

Resilient Repair Guide Source Report: Post-Earthquake Assessment of Reinforced Concrete Buildings

Prepared by

APPLIED TECHNOLOGY COUNCIL
201 Redwood Shores Parkway, Suite 240
Redwood City, California 94065
www.ATCouncil.org

Prepared for

FEDERAL EMERGENCY MANAGEMENT AGENCY
Michael Mahoney, Project Officer
William T. Holmes, Technical Monitor
Washington, D.C.

APPLIED TECHNOLOGY COUNCIL
Jon A. Heintz, Project Executive and Project Manager
Chiara McKenney, Assistant Project Manager

PROJECT TECHNICAL COMMITTEE

Ken Elwood (Project Tech. Director)
Nic Brooke*
Gregory G. Deierlein
Abbie Liel
Santiago Pujol Llano
James Malley
Jack P. Moehle
Bill Tremayne
John Wallace

PROJECT REVIEW PANEL

Santiago Pujol Llano
James Malley

WORKING GROUP

Saman Abdullah
Vishvendra (Jay) Bhanu
Ryo Kuwabara
Donovan Llanes
Kai Marder
Gonzalo Munoz
Polly Murray
Eyitayo Opabola
Matias Rojas Leon
Amir Safiey
Mehdi Sarrafzadeh
Prateek Shah
Tomomi Suzuki

*Support for participation provided by the Earthquake Commission (EQC) of New Zealand



FEMA



Notice

Any opinions, findings, conclusions, or recommendations expressed in this publication do not necessarily reflect the views of the Applied Technology Council (ATC), the Department of Homeland Security (DHS), or the Federal Emergency Management Agency (FEMA). Additionally, neither ATC, DHS, FEMA, nor any of their employees, makes any warranty, expressed or implied, nor assumes any legal liability or responsibility for the accuracy, completeness, or usefulness of any information, product, or process included in this publication. Users of information from this publication assume all liability arising from such use.

Cover photograph – N/A

Table of Contents

1. Introduction	1-1
1.1 ATC-145 Project Series.....	1-1
1.2 ATC-145 Documents	1-2
1.2.1 Source Report.....	1-2
1.2.2 Case Study Annex to Source Report	1-3
1.2.3 Repair Guidelines (Under Development).....	1-3
1.3 Report Organization and Content.....	1-3
2. Post-Earthquake Performance Objectives	2-1
2.1 Introduction	2-1
2.2 Background	2-2
2.3 ATC-145 Source Report Repair Assessment Process	2-2
3. Post-Earthquake Assessment Framework for Conforming Reinforced Concrete Moment Special Frames	3-1
3.1 Introduction	3-1
3.2 Inspection and Analysis Phase	3-4
3.2.1 Preliminary Inspection	3-6
3.2.2 Analyzing the Impact of the Damaging Earthquake ...	3-8
3.2.3 Determining Expected Damage Level from Initial Estimate of Deformation Demand.....	3-13
3.2.4 Detailed Inspection.....	3-15
3.2.5 Comparing Inspection Findings with Analysis Results	3-18
3.2.6 Final Estimate of Deformation Demands	3-19
3.3 Safety-assessment Phase	3-20
3.3.1 Reinforcement Fatigue Check	3-23
3.4 Serviceability-assessment Phase	3-28
3.4.1 Definition of Service Earthquake	3-30
3.4.2 Stiffness of Damage Components	3-31
3.4.3 Stiffness of Epoxy-repaired Components.....	3-32
3.4.4 Damping for Serviceability Analyses.....	3-33
3.4.5 Drift Limit for Nonstructural Components.....	3-33
3.5 Summary of Assessment Framework.....	3-34
4. Future Work	4-1
4.1 Expansion of Component Deformation Limits (Appendix H) to Other Reinforced Concrete Components and Other Materials.....	4-1
4.2 Refinement of Visual Damage Limits (Appendix I) and Expansion to Other Reinforced Concrete Components.....	4-1
4.3 Refinement of Inspection Procedures.....	4-2

4.4	Refinement of Damage Categorization Process (Using Component Damage Classes to Determine Building Damage Class)	4-3
4.5	Refinement and Expansion of Modelling and Acceptance Criteria	4-3
4.6	Development of Additional Case Studies	4-4
4.7	Development of Repair Technique Guidance	4-4
4.8	Development of an Improved Definition of Substantial Structural Damage	4-4
4.9	Development of Low Cycle Fatigue Assessment Procedure for Reinforced Concrete Walls	4-5
4.10	Advancement of Serviceability Check	4-5
4.11	Coordination with Functional Recovery and Reoccupancy Studies Outside of ATC-145	4-5
	References	5-1

Appendix A: Influence of Prior Loading on Deformation

	Capacity.....	A-1
A.1	Introduction and Objectives.....	A-1
A.2	Proposed Safe Deformation Limit, θ_{cap} , for Earthquake-Damaged Components	A-2
	A.2.1 Prior Research Investigating Significance of Deformation Cycles Below 0.02 Rad	A-3
A.3	Formation of a Database of Experimental Research on Ductile Components	A-11
	A.3.1 Database Overview	A-12
	A.3.2 Database Results Summary and Discussion	A-17
A.4	Another Look at the Rotational Capacity of ‘Conforming’ Columns.....	A-40
	A.4.1 What is a Conforming Column?	A-40
	A.4.2 What is the Rotational Capacity of a Conforming Column?.....	A-41
A.5	Conclusions and Recommendations	A-46

Appendix B: Influence of Prior Loading on System Response

B.1	Review of Analytical Studies of Duration and Aftershock response	B-2
	B.1.1 Aftershock Literature.....	B-3
	B.1.2 Ground Motion Duration Studies	B-3
B.2	Review of ‘Shake Table’ Test Data and Field Observations ...	B-7
	B.2.1 Laboratory Observations	B-7
	B.2.2 Field Observations	B-18
	B.2.3 Summary.....	B-29
	B.2.4 Description of Selected Tests	B-30
B.3	Effect of Loading History on Drift Demand.....	B-45
	B.3.1 Introduction	B-45
	B.3.2 Oscillator Properties	B-45
	B.3.3 Ground Motions.....	B-50
	B.3.4 Results	B-51
	B.3.6 Tables.....	B-53
	B.3.7 Figures	B-58

B.4	Summary of Torsion Studies	B-88
B.4.1	Introduction	B-88
B.4.2	Parametric Analysis for 2DOF Systems.....	B-88
B.4.3	Analysis Results	B-93
B.4.4	Summary and Conclusions.....	B-106
B.5	System Assessment to Determine Repair Triggers	B-108
B.5.1	Introduction	B-108
B.5.2	Methods.....	B-108
B.5.3	Single Degree of Freedom Study to Isolate Building Characteristics	B-113
B.5.4	RC Frame Buildings of Interest.....	B-117
B.5.5	Repair Trigger for RC Frames.....	B-120
Appendix C: Fatigue Capacity Models and Background.....		C-1
C.1	Overview	C-1
C.2	Fatigue Capacity Models for Reinforcing Bars.....	C-1
C.3	Definition of Acceptable Levels of Fatigue Damage	C-5
C.4	Assessment of Fatigue Degradation	C-6
C.4.1	Simplified Fatigue Life Assessment.....	C-7
C.4.2	Recommendations for Detailed Fatigue Damage Assessments	C-11
C.5	Parametric Analysis to Determine Thresholds Below Which Fatigue Damage is Not Consequential	C-11
C.6	Future Work: Incorporation of Reinforced Concrete Walls...	C-15
Appendix D: Stiffness of Damaged and Epoxy-repaired RC Components.....		D-1
D.1	Introduction	D-1
D.2	Stiffness of Damaged Beam-column Elements	D-1
D.3	Stiffness of Epoxy-repaired Frame Components	D-10
D.4	Cyclic Stiffness Degradation in Ductile Beam Elements.....	D-15
D.4.1	Methodology for Cyclic Stiffness Degradation Calculation	D-11
D.4.2	Component Stiffness Degradation.....	D-12
D.4.3	Marder et al. (2020).....	D-12
D.4.4	Sarrafzadeh (2021)	D-19
D.5	Discussion and Recommendations.....	D-23
D.5.1	Analysis of Moderately-damaged RC Ductile Frames	D-23
D.5.2	Analysis of Epoxy-repaired Ductile RC Frames Following Moderate Earthquake Damage.....	D-24
Appendix E-1: Repair Database: Reinforced Concrete Walls.....		E1-1
E1.1	Database Format and Specifications	E1-3
E1.2	Digitization of Published Hysteresis Plots	E1-5
E1.3	Summary of Database Findings.....	E1-6
E1.3.1	Summary of Performance Modification Factors for Wall Specimens.....	E1-11
E1.4	Future Work	E1-19
Appendix E-2: Repair Database: Ductile Reinforced Concrete Frames		E2-1
E2.1	Introduction and Objectives	E2-1
E2.2	Database of Component Repair Tests	E2-1

E2.2.1	Digitization of Published Hysteresis Plots.....	E2-7
E2.3	Database Summary for Columns	E2-7
E2.3.1	Overall Effectiveness of Column Repairs	E2-10
E2.3.2	Effectiveness of Column Repair Based on Specific Damage	E2-13
E2.4	Database Summary for Beams.....	E2-27
E2.4.1	Overall Effectiveness of Beam Repairs	E2-30
E2.4.2	Effectiveness of Beam Repair Based on Specific Damage	E2-31
E2.4.3	Stiffness Recovery and Shear Span to Depth Ratio	E2-34
E2.5	Database Summary for Joints	E2-34
E2.5.1	Overall Effectiveness of Joint Repairs.....	E2-37
E2.5.2	Effectiveness of Joint Repair Based on Specific Damage	E2-40
E2.5.3	Beam-Joint Stiffness Contributions	E2-46
E2.5.4	Repair of Joints with Inadequate Seismic Design (Type-2)	E2-47
E2.6	Implications for Reparability of Seismic Frames	E2-48
E2.6.1	Low to Moderately-damaged Ductile Frames	E2-48
E2.6.2	Heavily Damaged Ductile Frames.....	E2-54
E2.6.3	Frames with Non-conforming or Brittle Elements .	E2-56

Appendix F: Influence of Deformation Capacity on the Repair

	Assessment of RC Frame Buildings	F-1
F.1	Overview	F-1
F.2	Design of Frames with Different Deformation Capacities	F-1
F.3	Nonlinear Modeling of Studied Frames.....	F-6
F.4	Summary of Framework for System-Level Repair Assessment	F-8
F.5	Repair Assessment Results	F-9
F.5.1	System-level Drift Amplification Results	F-9
F.5.2	Comparison of System and Component Limits in Repair Guidelines	F-13
F.5.3	Implications for Substantial Structural Damage	F-18
F.6	Conclusions and Summary	F-20

Appendix G: Wall System Studies

G.1	Introduction.....	G-1
G.2	Description.....	G-1
G.3	Design of Archetype Buildings.....	G-7
G.4	OpenSEES Modeling.....	G-9
G.5	Verification of the Dynamic Response of the Model	G-13
G.6	Results of System Assessment.....	G-14
G.6.1	Results for 4-story Building Archetype	G-14
G.6.2	Results for 8-story Building Archetype	G-22
G.6.3	Results for 12-story Building Archetype	G-30
G.7	Analysis of the Damage-to-Undamaged Ratio Trends	G-38
G.8	Implications for Substantial Structural Damage	G-40
G.9	Conclusions	G-41

Appendix H: Component Deformation Limits for RC Components .. H-1

H.1	Overview	H-1
H.2	Impact of Loading History on Residual Capacity of RC Components.....	H-2
H.2.1	When does the number of cycles starts influencing the cyclic behavior (strength and deformation capacity) of RC components?	H-2
H.2.2	When does prior loading history start influencing residual capacity?	H-7
H.3	Proposed Methodology.....	H-18
H.3.1	Defining the Ultimate Component Deformation Limit	H-18
H.3.2	Inspection Trigger	H-20
H.3.3	Repair Trigger	H-22
H.3.4	Components Always Requiring Inspection	H-23
H.4	Non-Ductile Frame Elements	H-23
H.4.1	Description of Database	H-23
H.4.2	Failure mode Classification.....	H-25
H.4.3	Defining the Deformation at Initiation of LSL.....	H-26
H.4.4	Proposed Inspection Trigger	H-30
H.4.5	Repair Trigger	H-35
H.5	Conforming Flexure-Controlled Walls.....	H-36
H.5.1	Description of Database	H-36
H.5.2	Deformation at Initiation of LSL for Conforming Flexure-Controlled Walls.....	H-41
H.5.3	Inspection Trigger	H-45
H.5.4	Repair Trigger	H-48
H.6	Conclusions and Recommendations.....	H-49
H.6.1	Impact of Loading Protocol on Residual Capacity of Concrete Components	H-49
H.6.2	Triggers	H-50

Appendix I: Visual Damage Limits I-1

I.1	Introduction and Objectives	I-1
I.2	Description of Key Damage States.....	I-1
I.2.1	Non-ductile Frame Elements.....	I-1
I.2.2	Conforming Flexure-Controlled Walls	I-5
I.3	Datasets of Component with Damage Photos	I-9
I.3.1	Frame Elements.....	I-9
I.3.2	Conforming Flexure-Controlled Walls	I-9
I.4	Undamaged Components	I-12
I.5	Future Work	I-13
I.6	Conclusions	I-13

Appendix J: List of Resources J-1

Appendix K: Inspection Reference Material..... K-1

The Federal Emergency Management Agency (FEMA) has the goal of reducing the cost that disasters inflict on the United States. Repair of earthquake damage is critical to the recovery of a community after an earthquake disaster, and in turn, overall resilience. The primary goal of the ATC-145 project, *Guide for Repair of Earthquake Damaged Buildings to Achieve Future Resilience*, is to update and improve the existing guidance for post-earthquake inspection, evaluation, and repair procedures. This Source Report presents:

- an earthquake damage assessment methodology for code-conforming reinforced concrete special moment frames, which has served as the inspiration for a broadly applicable assessment framework under development at the time of this writing (referred to in this report as the *Repair Guidelines*), and
- summaries of studies conducted during the first three years of the project about earthquake-damaged reinforced concrete structures that informed the assessment framework presented in this Source Report and the framework presently under development as the *Repair Guidelines*.

1.1 ATC-145 Project Tasks

The first three years of the ATC-145 project explored the impact of loading and damage from a prior earthquake on drift demand and capacity in a future earthquake. A wide range of studies to inform new inspection, evaluation, and repair guidance for earthquake-damaged buildings were conducted. An assessment framework for code-conforming special reinforced concrete frames was developed and then tested with two case study buildings. This assessment framework is currently being broadened to include other types of reinforced concrete structures and is envisioned to incorporate other structural materials in the future.

Year-1 studies identified the key conclusion that prior earthquake loading resulting in deformation demands below a specific limit (i.e., approximately 2% story drift depending on component and design detailing) is unlikely to result in significantly larger drift demands in future earthquakes (as compared to the building in its original state), and unlikely to impact the drift

capacity of damaged components. The repair database (Appendix E) was also developed in Year 1.

Year-2 studies (summarized in Appendices A to D) further explored the key conclusion about story drift from Year 1 using new analytical studies and review of previously published test data. The Year-2 work culminated in the development of the assessment methodology presented in Chapters 2 and 3 of this Source Report, which applies only to code-conforming, reinforced concrete special moment frames.

Year-3 studies (summarized in Appendices F to I) focused on expanding the assessment methodology developed in Year 2 to a wider range of reinforced concrete systems. Applications of the assessment framework presented in this Source Report to two case study buildings (reports included as the *Annex* to this report) were completed. A close review of the FEMA 306 series, *Evaluation of Earthquake Damaged Concrete and Masonry Wall Buildings*, was conducted, and a first draft of the *Repair Guidelines* (not included in this Source Report) was developed.

1.2 ATC-145 Documents

Three interrelated documents were created in the first three years of the ATC-145 project. This *Source Report* summarizes the findings of all major studies to-date (as of September 2021) and presents an assessment framework for code-conforming reinforced concrete special moment frames. The *Case Study Annex* to the Source Report is a separate document that presents results for two case study buildings assessed using the framework presented in the Source Report. The Annex also includes recommendations for changes to the assessment framework that will be integrated into the Repair Guidelines. The *Repair Guidelines* report is a separate document, still under development at the time of this writing, that builds and expands on the assessment framework in this Source Report.

The Repair Guidelines will supersede the assessment framework described in this Source Report.

1.2.1 Source Report

This Source Report summarizes all of the major studies conducted in the first three years of the ATC-145 project. The purpose is to document progress to-date and note topics and issues that require further consideration or study.

The centerpiece of the Source Report is an inspection and evaluation methodology for determining what post-earthquake damage conditions require repair for the case of a code-conforming reinforced concrete special

moment frame building. This assessment framework serves as a major developmental milestone in the project, but it will be superseded by a more expansive framework under development as the Repair Guidelines, which will cover a range of systems and also include repair guidance.

Topics that require further study are presented as a complete list in Chapter 4, *Future Work*. These topics will be addressed during the development of the Repair Guidelines.

Appendices of the Source Report summarize findings that support the Source Report framework (Appendices A to E) and expansion of the methodology to structural systems not covered by the Source Report methodology, for use in development of the Repair Guidelines (Appendices F to I).

1.2.2 Case Study Annex to Source Report

The *Case Study Annex* summarizes two applications of the Source Report assessment methodology to actual code-conforming special reinforced concrete frame structures that were subjected to earthquake ground motions. The Annex report presents the results of these case studies and key recommendations for future improvements to the methodology.

1.2.3 Repair Guidelines (Under Development)

The Repair Guidelines, which are currently under development, build and expand on the assessment methodology presented in Chapters 2 and 3 of this Source Report. When completed, these Guidelines will present the final ATC-145 methodology for inspection and evaluation of earthquake-damaged buildings, structural system-specific triggers for repair, and up-to-date repair technique guidance. The Repair Guidelines will supersede content related to reinforced concrete walls in the FEMA 306 series, *Evaluation of Earthquake Damaged Concrete and Masonry Wall Buildings*.

Though development of the Repair Guidelines is presently focused on addressing the wide range of reinforced concrete systems, it is envisioned that the Repair Guidelines could also incorporate steel, masonry, and wood systems in the future.

1.3 Report Organization and Content

The body of this report outlines the damage-assessment framework for reinforced concrete special moment-resisting frames.

Chapter 2 provides the post-earthquake performance objectives that form the basis of the damage-assessment framework presented in Chapter 3.

Chapter 3 describes the assessment framework for determining when repair is necessary for an earthquake-damaged reinforced concrete special moment frame building.

Chapter 4 presents plans for future project work.

Appendices A to F summarizes the technical background that supports the methodology in the Source Report:

- Appendices A to D provide relevant background and the derivation of criteria for the inspection, analysis, and assessment procedures that comprise the assessment methodology in Chapter 3.
- Appendix E presents a database on existing research on the efficacy of repair of reinforced concrete components.

Appendices F through I explore the future expansion of the methodology across other reinforced concrete systems and development of the Repair Guidelines. These systems are not covered under the assessment framework in Chapter 3 of this Source Report.

- Appendix F presents the findings of studies on less ductile moment-resisting frame systems and implications for inclusion of the system in the Repair Guidelines.
- Appendix G presents the findings of studies on special shear wall systems and implications for inclusion of the system in the Repair Guidelines.
- Appendix H presents a methodology for developing inspection and repair triggers for a wide range of reinforced concrete systems, for adoption into the Repair Guidelines.
- Appendix I presents a methodology for developing visual damage limits, for adoption into the Repair Guidelines.

Appendices J and K are reference material.

- Appendix J provides a list of the documents referenced in the body of the Source Report.
- Appendix K provides reference material for the inspection phase of the assessment framework.

Chapter 2

Post-Earthquake Performance Objectives

2.1 Introduction

To determine whether a building needs to be repaired after an earthquake, an objective for its performance in a future earthquake must first be established. If the expected performance of an earthquake-damaged building does not meet this *post-earthquake performance objective*, repair is required, and the repair shall be designed such the repaired building meets the post-earthquake performance objective.

Generally, provisions for post-earthquake assessment, including the one presented in this Source Report, consider if a building is *complying* (or *compliant*). A complying building is one designed to the current code or a recent code that provides seismic resistance similar to the current code. In the assessment methodology presented in Chapter 3, the complying designation is based on the Benchmark Building table of ASCE/SEI 41-17, *Seismic Evaluation and Retrofit of Existing Buildings*. This table defines complying concrete moment-resisting frame buildings as ones designed and constructed in accordance with the 1994 Uniform Building Code or a more recent standard. Such buildings are expected to have similar strength, detailing, and deformation capacity to buildings designed to current code, allowing for the formation of a strong-column-weak-beam plastic (or ductile) collapse mechanism governed by flexural deformations. In this Source Report, the terms *complying*, *compliant*, and *conforming* are used interchangeably.

In the assessment methodology presented in Chapter 3 for code-conforming special reinforced concrete frames, the post-earthquake performance objective consists of two criteria: one for safety and one for serviceability. Not passing the safety criteria will trigger a *safety repair*, while not passing the serviceability criteria will trigger a *non-safety repair*. Epoxy injection is not considered a safety repair as it has limited impact on the performance of ductile components except in service-level earthquakes (see Appendix D).

Provisions for post-earthquake assessment typically include a requirement to seismically retrofit non-complying buildings if damaged beyond a certain

threshold, the *retrofit trigger*. As the assessment methodology presented in Chapter 3 addresses code-conforming buildings only, a retrofit trigger and retrofit performance objective are not presented.

2.2 Background

The model building code that provides post-earthquake repair and retrofit requirements in the United States is the International Existing Building Code (IEBC). The final assessment framework developed under ATC-145 will ultimately fit within the confines of the IEBC or recommend modifications to the IEBC requirements.

The overall repair assessment process presented for use in this Source Report is based on the one in the ATC-52-4, *Here Today -- Here Tomorrow: The Road to Earthquake Resilience in San Francisco – Post-Earthquake Repair and Retrofit Requirements*, a report developed under the San Francisco Community Action Plan for Seismic Safety (CAPSS) to provide a clear and consistent methodology for post-earthquake repair and retrofit requirements.

2.3 ATC-145 Source Report Repair Assessment Process

The overall assessment process presented in this Source Report is summarized as Figure 2-1. The first step in the process is to determine if the damage exceeds the repair trigger, which represents the level of damage beyond which the post-earthquake performance objective is no longer met. The studies described in the report appendices informed the definition of the repair triggers defined in this Source Report.

The post-earthquake performance objective consists of two criteria:

- *Safety criterion*: Assessed performance of building under design earthquake and maximum-considered earthquake ground motions remains essentially unchanged after the damaging earthquake, and
- *Serviceability criterion*: Drift demands for a “service earthquake” do not exceed the median drift capacity of drift-sensitive nonstructural components present in the building (e.g., partition walls, exterior cladding) after the damaging earthquake.

Though new buildings designed to the current building code only have one earthquake performance objective, two performance objectives are included in the repair assessment framework, because the potential for significantly reduced stiffness in a damaged or repaired building may lead to unacceptable performance (e.g., nonstructural damage) in future smaller, more frequent earthquakes. It is expected that many authorities having jurisdiction (AHJs)

will be resistant to adopting serviceability criteria. Note that the intensity or return period of the service earthquake considered may be selected by the AHJ; Section 3.4.1 provides some options to consider. To assist engineers doing a serviceability assessment, this report provides recommendations to estimate member stiffness for damaged and epoxy-repaired components (Sections 3.4.2 and 3.4.3).

Passing the safety criterion implies that if one assessed the building after being damaged in the initial earthquake, the damaged building would still satisfy the performance objective of the code (e.g., less than 10% probability of collapse in MCE_R). Such a building would not require a safety repair. For the purpose of this Source Report, a building is assumed to satisfy the safety criterion when the median drift demand, assessed at design-basis earthquake (DBE) and maximum considered earthquake (MCE) levels, remains “essentially unchanged” after the damaging earthquake compared to that of the pre-damaged building. Furthermore, to meet the safety criterion, it is important to ensure the deformation capacity of all structural components have not been compromised.

The assessing engineer does not rely on independent judgment to determine what constitutes “essentially unchanged”. Rather, the engineer refers to Section 3.3 for deformation limits, which are based on analytical studies summarized in Appendix B. These studies considered several methods of determining in what cases median drift demands increase in the damaged building relative to the pre-damaged building. The studies focused on understanding the relationship between the drift demand in the damaging earthquake and the amplification in displacements in a subsequent earthquake, evaluated at both DBE and MCE levels. To define repair triggers, the studies described in this report seek to identify the deformation demands which indicate a building no longer satisfies the safety criterion.

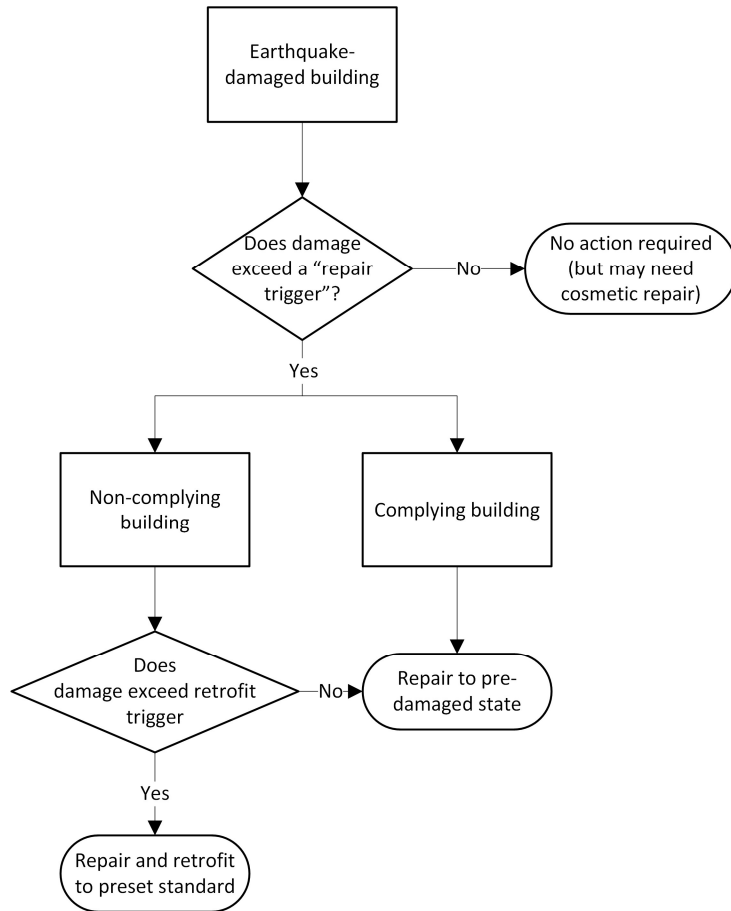


Figure 2-1 Flow chart of post-earthquake repair process.

Chapter 3

Post-Earthquake Assessment Framework for Conforming Reinforced Concrete Moment Special Frames

3.1 Introduction

The post-earthquake assessment framework presented in this chapter for reinforced concrete special moment-resisting frame buildings provides a systematic method for identifying the level of repair needed to meet the post-earthquake performance objectives defined in Chapter 2.

The level of repair is described using the following categories:

Category 0. No repair needed.

Category 1. Non-safety repairs: Repairs that are primarily intended to restore appearance, durability, and serviceability of a building. These include but are not limited to epoxy-injection, mortar patching, and replacement of cover concrete. Replacement of core concrete is considered beyond the scope of “non-safety repairs”.

Category 2. Safety repairs: Repairs that are primarily intended to restore safety of a building. These repairs may, or may not, involve replacement of reinforcement. The repair database (Appendix E) further categorizes these techniques based on whether the repair targets a similar capacity (strength and/or deformation) of the original component or a higher capacity. The latter is considered a repair *and* retrofit of the component.

While the assessment framework is intended to be applied to the entire structural system, it can also be used to identify repair categories for individual components with different levels of damage.

The assessment framework described below is not appropriate for a rapid post-earthquake assessment; rather, it is intended for a detailed assessment which is likely to take place in the weeks or months following an earthquake. The assessment may be commissioned voluntarily by the building owner or

triggered by a requirement of the Authority Having Jurisdiction (AHJ). It is beyond the scope of this report to recommend specific assessment triggers for the assessment procedure, but possible assessment triggers may include:

- Yellow or red tag from the rapid post-earthquake assessment, or
- Exceedance of specific ground motion intensity parameter used in design (e.g., comparison of $S_a(T1)$ from ShakeMap with $S_a(T1)$ for DBE), or
- Exceedance of a selected damage probability based on building fragility curves calculated according to HAZUS Earthquake Model Technical Manual (FEMA, 2020) (e.g., 15% chance of “slight” structural damage, or 5% chance of “moderate” structural damage using 0.3 second and 1.0 second spectral accelerations from ShakeMap).

As shown in Figure 3-1, the assessment framework involves three phases:

1. Inspection and Analysis Phase
2. Safety-assessment Phase
3. Serviceability-assessment Phase

The goal of the Inspection and Analysis Phase is to identify any *severe damage states* in the structure which clearly require safety repairs without further assessment and to estimate the peak drift demands from the damaging earthquake. Severe damage states in this context include crushing of core concrete or buckling of reinforcement, as described in Section 3.2.1.

The goal of the Safety-assessment Phase is to determine if the damage requires safety repairs to be able to satisfy the post-earthquake safety performance objective (Chapter 2). This is assessed based on comparisons of estimates of peak story drift demand and peak chord rotations with recommended repair triggers, and a simple fatigue-based assessment.

If the building and/or component satisfies the Safety-assessment Phase, a building owner may choose to also assess the expected performance of the building in a serviceability earthquake. Alternatively, an AHJ may require the Serviceability-assessment Phase to assess the risk of repeated damage to drift-sensitive nonstructural components in future small and moderate earthquakes. The Serviceability-assessment Phase uses estimates of stiffness of damaged and epoxy-repaired components to determine if epoxy repair and building stiffening is required to satisfy the post-earthquake serviceability performance objective (Chapter 2).

The following sections describe the three phases of assessment in detail.

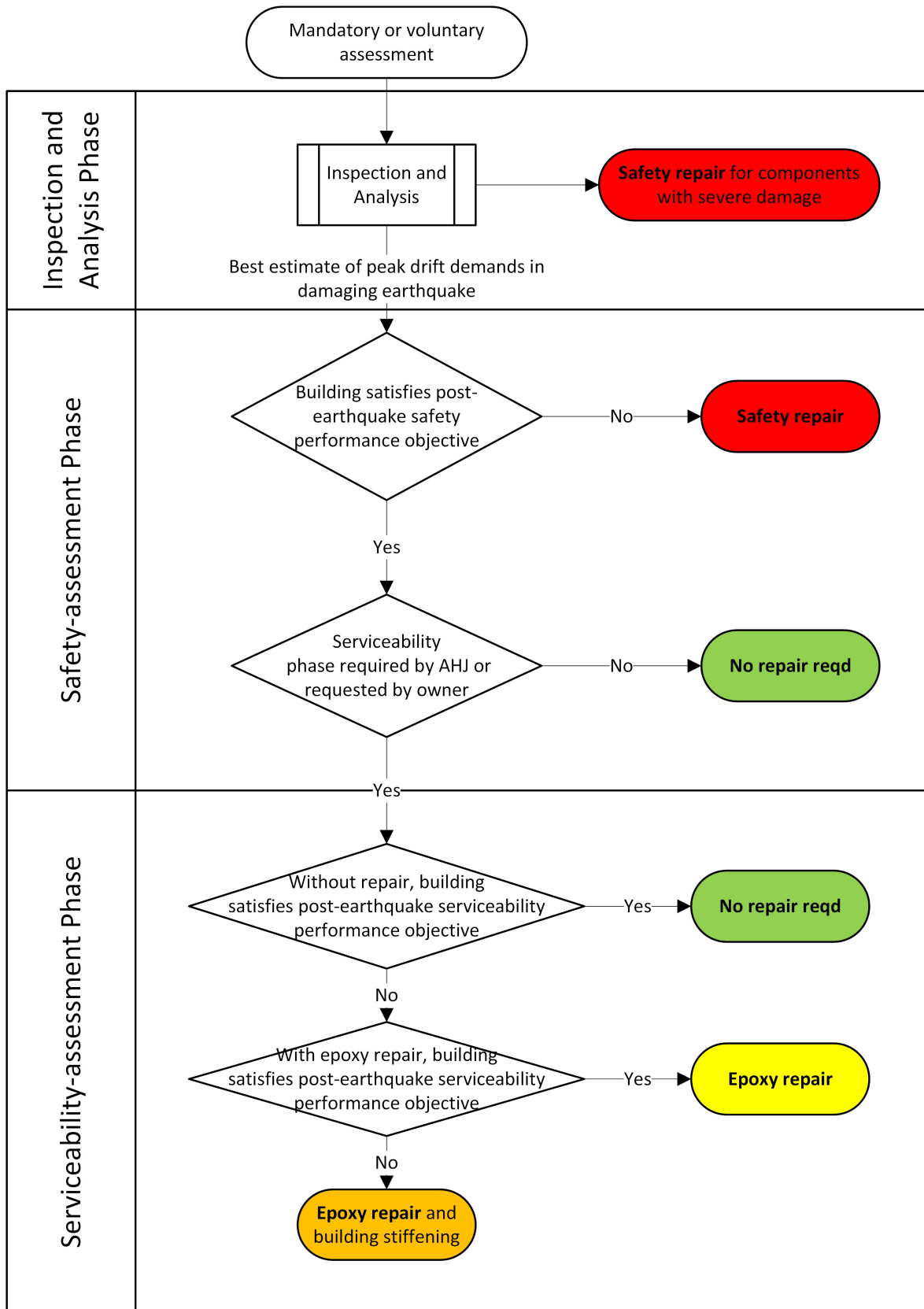


Figure 3-1 Assessment framework flowchart.

3.2 Inspection and Analysis Phase

The Inspection and Analysis Phase includes inspection and analysis of the damaged building with a goal of identifying any severe damage and estimating the peak drift demand experienced by the building in the earthquake. Figure 3-2 provides a flowchart for the steps of the Inspection and Analysis Phase. After a preliminary inspection to identify any severely damaged components and assess the general extent of damage in the building, the assessing engineer develops a numerical model of the building. The output of the model and relevant fragility curves are used to estimate the extent and distribution of damage in the building as analyzed by the model. The results of a detailed inspection of the building are used to validate the model, leading to potential modifications to the model or earthquake demand estimate to achieve a better match between predicted damage and observed damage. The final outcome is the best possible estimate of the peak deformation demands in the damaging earthquake.

Description of these steps and supporting background information is provided in the following sections.

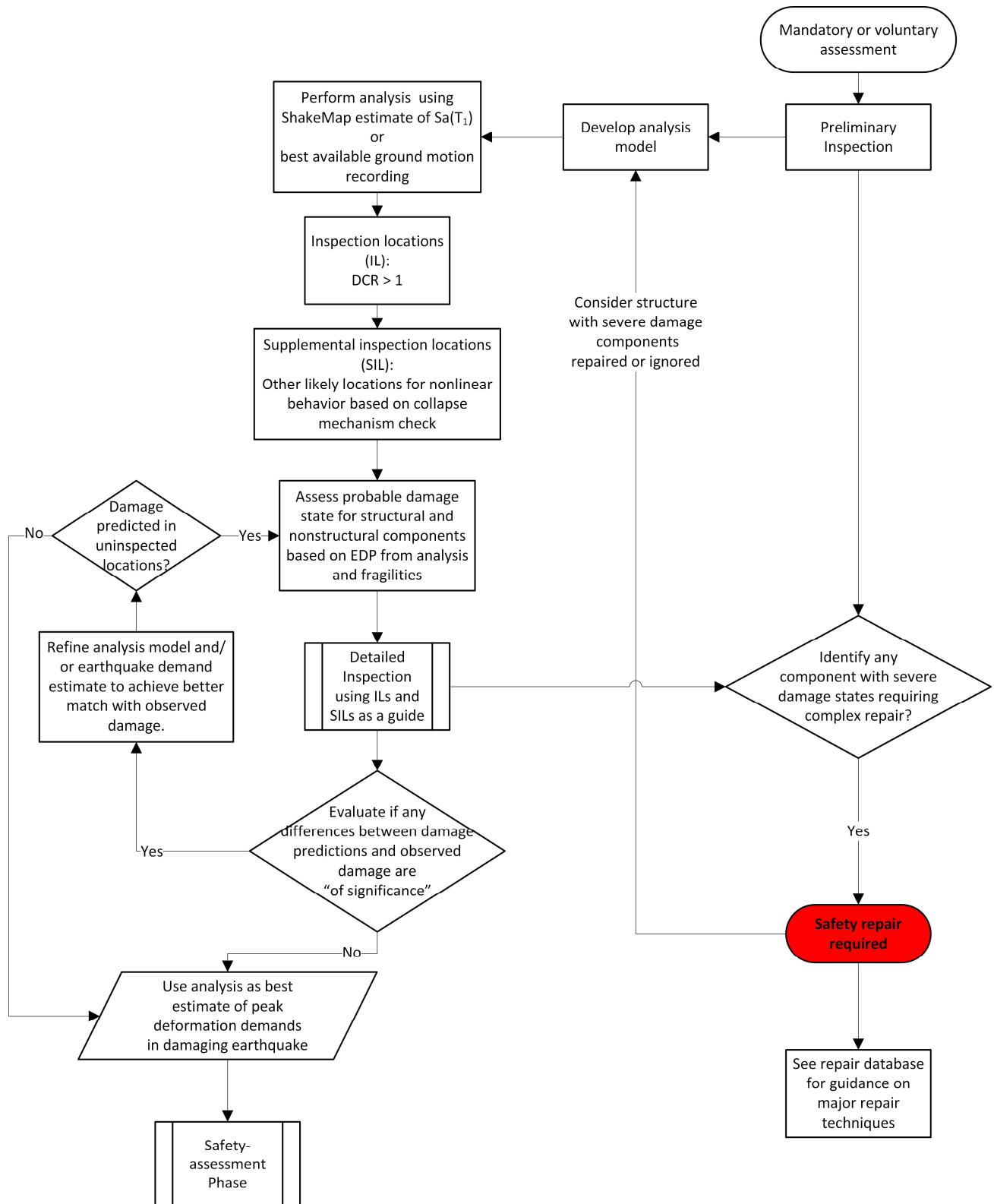


Figure 3-2 Inspection and Analysis Phase.

3.2.1 Preliminary Inspection

The first step, upon the triggering or commissioning of a post-earthquake damage assessment, is to perform a Preliminary Inspection of the building. This inspection is independent of any inspections required to identify potential life safety risks and placarding by the AHJ.

A site visit is made to the building and a visual inspection is performed to identify obvious indications of structural or nonstructural damage. Although quantification of nonstructural damage is not the primary objective of the ATC-145 inspection methodology, observation of such damage can serve as a proxy to infer peak drift demands from the earthquake. For example, relevant nonstructural damage includes: sliding/movement of joints, damage to gypsum-sheathed wall partitions, pounding (interaction) of secondary structural systems (e.g., stairs) with primary structural elements (e.g., walls or columns).

The ATC-38 *Post-earthquake Building Performance Assessment Form* (ATC, 2000) is recommended as a guide for the Preliminary Inspection process and to record observations. The ATC-38 methodology was developed following the 1994 Northridge earthquake to systematically collect and analyze data from buildings located in the vicinity of strong-motion recording instruments. The methodology was successfully updated and applied following the 2014 South Napa Earthquake, including collection of damage observations of buildings that were not located in close proximity to strong-motion recording instruments (FEMA, 2015b).

The ATC-38 forms were created to collect data including the structure size, age, location, structural framing system and other important structural characteristics, as well as information on nonstructural systems and performance, fatalities and injuries, estimated time to restore the facility to pre-earthquake usability, and placarding. Descriptions of observed structural irregularities, consistent with FEMA P-154, *Rapid Visual Screening of Buildings for Potential Seismic Hazards: A Handbook* (FEMA, 2015a), are also collected. Not all of this data is directly relevant to the needs of this inspection and damage assessment methodology (e.g., restoration time, placarding). A modified version of the ATC-38 form for use with this assessment framework is provided in Appendix K.

The Preliminary Inspection should include visual observation of both the building's interior and exterior. Selective removal of nonstructural finishes or coverings (e.g., ceiling tiles) may be required to assist with the identification of structural damage, if damage is suspected (e.g., the building appears out-

of-plumb, observation of nonstructural damage, evidence of spalled concrete, or prevalence of damage to similar buildings in the surrounding area).

Review of the existing structural drawings prior to performing the Preliminary Inspection is recommended. This will assist the assessing engineer with identification of potential structural irregularities and guide the inspection to prioritize observation of these elements/locations for evidence of damage (e.g., a soft or weak-story, plan irregularity). Additionally, the assessing engineer should verify, to the extent practicable with visual observation, that the as-built structure generally matches the existing drawings (e.g., typical column size and grid, beam size, floor system).

If the building is equipped with seismic instrumentation that is capable of reporting peak response incurred during the earthquake, the assessing engineer should review the data prior to performing the Preliminary Inspection. Locations of maximum component deformations or story-drift demand should be identified for visual inspection. If the instrumentation also reports accelerations at the base of building, the resulting response spectrum or ground motion may be used as a direct input to the analysis model (see Section 3.2.2). The model can then be calibrated with the recorded response over the building height.

The ATC-38 form requires the inspecting engineer to approximately estimate the degree of damage sustained to structural and nonstructural components. This is achieved through the assignment of ATC-13, *Earthquake Damage Evaluation Data for California*, Damage States (ATC, 1985) and estimated percentages of collapsed floor area and nonstructural damage (e.g., percentage of windows or cladding damaged).

Additionally, the ATC-38 form allows the identification of severe, non-ductile types, including (but not limited to):

- Concrete core crushing
- Shear failures
- Spalling with evidence of bar buckling and/or fracture
- Tearing or damage to floor diaphragms at points of high stress (e.g., re-entrant corners, perimeter column to slab connections), and
- Large residual story drifts or foundation settlement

Where these severe damage types are observed, safety repair and/or immediate temporary shoring may be required (without further assessment) as per Figure 3-1.

Additionally, the Preliminary Inspection should inform the development of the analysis model. As discussed in the following section, the analysis model is used to estimate component deformation demands and locations for Detailed Inspection. If significant or extensive evidence of degradation or yielding (e.g., beam hinging) are observed during the Preliminary Inspection, a linear analysis model may not be appropriate, and it may be advisable to proceed directly to a nonlinear analysis.

3.2.2 Analyzing the Impact of the Damaging Earthquake

The second step in the procedure is to use established analysis methods to obtain an estimate of the deformation demands incurred during the damaging earthquake. In buildings without evidence of severe/non-ductile damage, this step would encompass the entire building. In buildings where components are deemed potentially repairable despite some degree of severe/non-ductile damage or failure being observed during the preliminary inspection, this process may still be applicable to define the deformation demands on the remaining portions of the building not exhibiting such damage. For example, if a building exhibited severe diaphragm damage that is deemed repairable, this procedure could still be applicable to the lateral force resisting system. Alternatively, if the component experiencing severe damage is sufficiently damaged as to not to participate in the building response and can be ignored without loss of stability, the assessing engineer may decide to ignore the contribution of the failed component in the remainder of the assessment process (similar to that permitted in ASCE/SEI 41). In such situations, judgment must be used as to when the observed severe component damage prevents this procedure from being reasonable to apply.

3.2.2.1 Analysis Procedure

The analysis procedure should follow one of the methods described in ASCE/SEI 41, *Seismic Evaluation and Retrofit of Existing Buildings* (ASCE, 2017), namely linear static (LSP), linear dynamic (LDP), nonlinear static (NSP), or nonlinear dynamic (NDP).

It is recommended that a linear procedure generally be used as a starting point, with a modal analysis LDP being the preferred option. (For the rare cases that a ground motion recording is available at the building site, a response history LDP may be an appropriate alternative.) Only in cases of irregular buildings or those with considerable structural damage observed in the preliminary inspection are nonlinear procedures warranted for the initial analysis. The guidance given in ASCE/SEI 41-17 Section 7 on analysis procedure selection can be used to determine what constitutes an irregular building. Note that the current relevant sections of ASCE/SEI 41 may be

modified before the 2023 edition is released. The ATC-140 project, *Update of Seismic Evaluation and Retrofit of Existing Buildings Guidance*, may recommend updates to the guidance on analysis procedure selection.

Analysis requirements in ASCE/SEI 41 that may produce a conservative value of deformation or force demands should be treated with caution, as the goal of the analysis for this post-earthquake assessment procedure is to obtain a best estimate of the actual deformation demands incurred. For example, torsional amplification requirements in ASCE/SEI 41 will generally overstate the eccentricity of the center of mass relative to the center of lateral rigidity and thus artificially increase demands. Analysis in the ATC-134 project, *Performance-Based Seismic Engineering: Benchmarking of Existing Building Evaluation Methodologies*, indicates that ASCE/SEI 41 models are generally accurate in predicting the story with the most damage and that nonlinear models predict well drifts at critical locations (NIST, expected 2022).

3.2.2.2 Analysis Model

Development of the analysis model should generally be in accordance with the relevant sections of ASCE/SEI 41.

ASCE/SEI 41 modelling parameters are generally intended to provide median estimates of component behavior while acceptance criteria provide a conservative estimate of deformation capacity. Such conservatism embedded in the ASCE/SEI 41 acceptance criteria will not affect the procedure described herein, as the acceptance criteria are not utilized in this process. However, any conservatism embedded in the ASCE/SEI 41 modelling parameters may have an undue effect on the analysis results. If significant discrepancies between the inspection findings and the analysis results are observed, modifications to the model may be warranted. This is further discussed Section 3.2.5.1.

For symmetric or near-symmetric buildings, two-dimensional models of the lateral-force resisting systems in orthogonal directions may be sufficient. However, for linear analysis there may be little time savings or other practical benefits associated with using two-dimensional models. Three-dimensional models are therefore expected to be used in the majority of cases.

3.2.2.3 Representation of Seismic Demand

The representation of seismic demand used in the analysis is intended to simulate, as close as is practically possible, the actual ground shaking experienced by the building being evaluated. Estimating the site-specific

seismic demand due to a prior earthquake is a significantly different undertaking than estimating the site-specific seismic hazard for future earthquakes during the life of the building. There is, therefore, little guidance available for this purpose in existing standards addressing seismic design or assessment.

Unless a site-specific recording station is available, an estimate of site-specific ground shaking will include uncertainty due to attenuation and/or spatial interpolation and differences in ground conditions between building site and recording station sites.

In the absence of a site-specific recording station, there are two primary potential sources of information:

- The nearest ground motion recording station provided the site soil conditions are similar.
- Existing published estimates of shaking intensity that account for attenuation, spatial interpolation between recording stations, and variation in ground conditions. ShakeMap (USGS, 2021) is focused on here as the most comprehensive available resource.

ShakeMap already represents a good estimate of interpolated site-specific shaking (Worden et al, 2018). However, one preliminary observation made by the authors (Tremayne, 2020) showed that ShakeMap predicted a value of $S_a(0.3)$ at a grid encompassing two recording stations that was as much as 40% to 50% lower than the recorded values at the two stations. More comprehensive research into the prevalence of such inconsistencies is needed. ShakeMap also currently only provides $S_a(T)$ values at $T = 0.3s$, $1.0s$, and $3.0s$, thus requiring construction of an approximate response spectrum between those points. Procedures given in ASCE/SEI 7, *Minimum Design Loads and Associated Criteria for Buildings and Other Structures* (ASCE, 2016), are appropriate for construction of a design spectra based on this data, however the assumed shape of a design spectra may not be appropriate for representing the spectra a specific site in a specific earthquake. Conversations with ShakeMap developers, however, have confirmed that it would be straightforward to extract $S_a(T)$ values at user-defined periods, a useful functionality that would reduce this need for response spectrum interpolation.

Ground motion simulations, validated based on the available ground motion recordings, provide an option for estimating the ground motion at any site. For example, SeisFinder (Savarimuthu et al, 2017) is a web application to extract selected intensity measures from previously conducted ground motion

simulations of historical events. Ground motion simulation technology is rapidly evolving and may be in widespread use in the future, but currently such simulations are not generally available after every earthquake and extraction of waveforms/spectra for a user selected site may not be feasible. If using results from ground motion simulations, careful review of validation with available recordings is essential (Bradley et al, 2017).

Estimating demands incurred in a building as a result of a specific earthquake has additional uncertainty due to the potential for peaks and troughs in spectral acceleration within the period range of the building and the significant uncertainties associated with building period. This is most pronounced when using a response spectrum from a specific recording station. As ShakeMap (1) contains inherent smoothing due to its attenuation and spatial interpolation algorithms, and (2) currently requires interpolation between provided $Sa(T)$ values, the effects of peaks and troughs are less pronounced. This is illustrated in Figure 3-3.

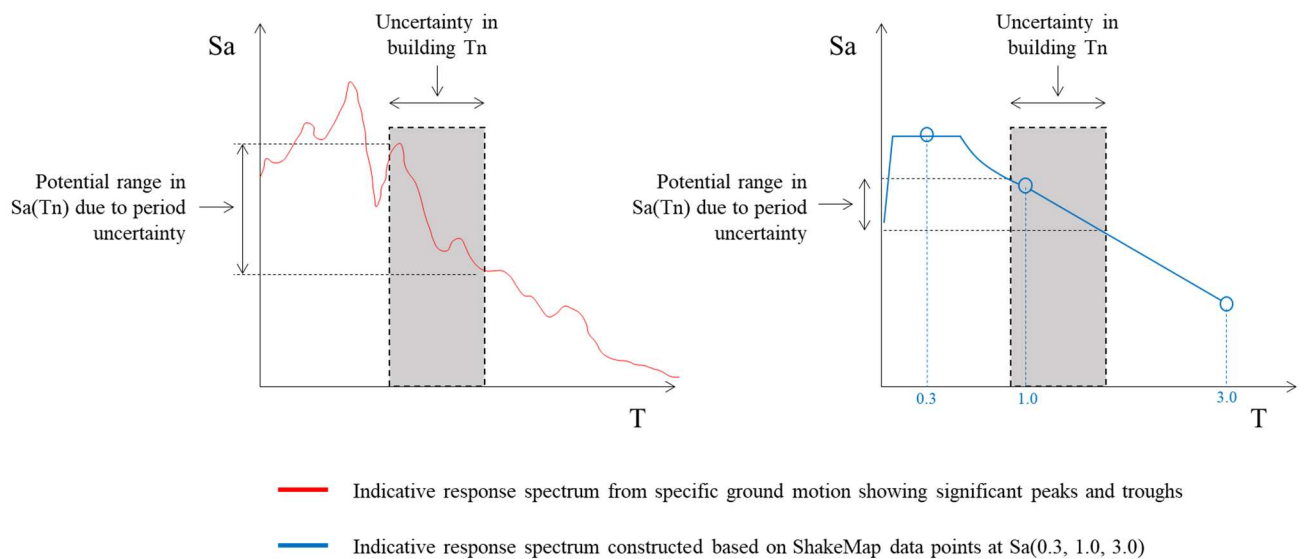


Figure 3-3 Estimating spectral demand on building from damaging earthquake.

Ultimately, clear guidance should be developed on when ShakeMap or the nearest recording station on a comparable site is the preferred tool. However, developing such guidance will require further consideration into the sources of error between the two metrics and the impact such errors have on seismic demands predicted for typical buildings. In the interim, the pros and cons of both options are discussed herein, but judgement should be left to the assessing engineer to select the preferred approach based on the specific building considered.

A simple preliminary procedure is to use the ShakeMap representation as the default value for the initial analysis, and only if significant discrepancies between inspection and analysis are obtained would nearby recording station spectra be analyzed in detail (see Section 3.2.5.1).

Another option would be to use non-ergodic (local) ground motion prediction equations to estimate spectral values from magnitude, distance, and site conditions. Such models can be used on their own, if there are no nearby recording stations, or the estimates from such models can be combined with data from recording stations to (a) help substantiate that the recorded motions are consistent with expectations, and (b) to help interpolate or extrapolate data from recording stations to other sites.

3.2.2.4 Initial Estimate of Deformation Demand

Upon completion of the analysis process, an estimate of peak deformation demands should be extracted from the results. Story drift is recommended as the deformation demand metric of choice because of its widespread use and familiarity in earthquake engineering. However, for ductile hinging elements the chord or plastic rotation is better correlated with the degree of structural damage observed.

3.2.2.5 Identification of Inspection Locations

An Inspection Location (IL) is defined as any structural component (e.g., beam, column, beam-column joint, slab) identified by the building analysis where the Demand Capacity Ratio (DCR) exceeds 1.0. The Demand Capacity Ratio shall be as defined by section 7.3.1.1 of ASCE/SEI 41-17. The building analysis shall identify Inspection Locations for use in the Detailed Inspection (Section 3.2.3).

3.2.2.6 Identification of Supplemental Inspection Locations

In addition to the Inspection Locations, Supplemental Inspection Locations (SIL) shall be identified. A SIL is defined as any structural component that is not already identified by the building analysis, but where nonlinear behavior is anticipated based on a frame-mechanism check (e.g., FEMA P-2018, *Seismic Evaluation of Older Concrete Buildings for Collapse Potential (FEMA, 2018b)*) or an observed structural configuration irregularity (e.g., based upon ATC-38 observations combined with review of structural drawings). The intent of identifying SILs is twofold:

- Avoid missing damage due to an underestimation of the ground motion shaking at the site, and

- Ensure the engineer has a good understanding of the likely progression of nonlinear behavior in the building prior to detailed inspection.

3.2.3 *Determining Expected Damage Level from Initial Estimate of Deformation Demand*

This step requires using the initial estimates of deformation demand from Section 3.2.2.4 to identify the expected component damage. Quantitative relationships between observable damage and deformation demand would be optimal tools for this purpose. Tools for developing quantitative estimates are discussed subsequently; however, the uncertainty involved in such an estimation means that even a notionally quantitative procedure would involve significant subjectivity. The experience and judgement of the assessing engineer is therefore perhaps the most important factor in developing such an estimate.

Perhaps the most comprehensive source of data that explicitly relates deformation demand to observable damage is the fragility curves developed as part of FEMA P-58, *Development of Next Generation Performance-Based Seismic Design Procedures for New and Existing Buildings* (FEMA, 2018a). These fragility curves cover many structural and nonstructural components found in typical buildings. Descriptions of damage states are provided, as are photographic examples in many cases. Using the estimate of deformation demand for the specific component being considered, it is straightforward to use the fragility functions to determine probabilities of being in various damage states (Figure 3-4).

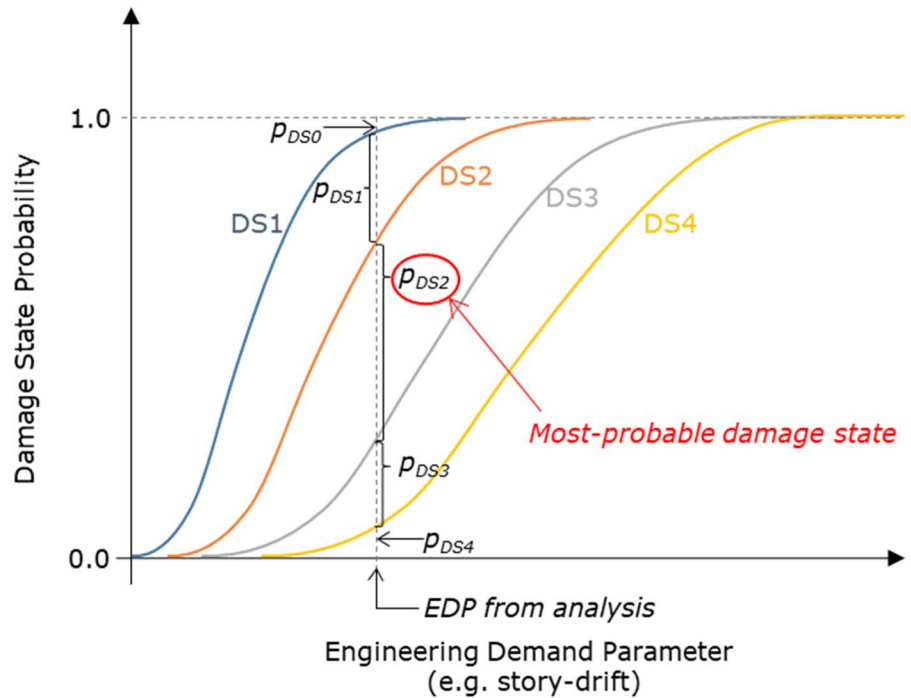


Figure 3-4 Use of fragility curves to identify probable damage state.

Use of fragility curves for nonstructural elements is of significant benefit for this process, as they can exhibit tighter ranges of drifts between visually distinct damage states. For example, the difference in damage observed in a ductile reinforced concrete plastic hinge subject to 1% or 2% drift may be limited, while such differences in drift would likely have a significant effect on partition walls.

It is noted that not all of the fragility curves contained within the FEMA P-58 database are relevant for this assessment framework (e.g., materials other than reinforced concrete). Some otherwise relevant fragility curves are also of limited practical use due to the high degree of dispersion in the data.

Other published relationships between deformation demand and observable damage exist, including FEMA 306, *Evaluation of Earthquake Damaged Concrete and Masonry Wall Buildings* (FEMA, 1998a), for walls and coupling beams and Bearman (2012) for columns. These are considered supplementary sources to FEMA P-58 and may enable slightly more refined estimates of expected damage to be identified (e.g., Bearman describes several more damage states for flexural reinforced concrete columns than the corresponding FEMA P-58 fragilities do).

All of the above-mentioned data sources, namely FEMA P-58, FEMA 306, and Bearman (2012), are largely based on experimental data from static cyclic loading tests. They also often rely on measured residual crack widths

as a metric for differentiating between damage states. Damage data from typical cyclic experiments are often only reported at cycle peaks or at “residual” states, where residual refers to the point of zero lateral force immediately following a cycle peak. In a building subject to a real earthquake, the observed damage will always correspond to the residual state of the building, but the residual deformation will not necessarily be representative of the peak deformation. Tests conducted by Marder et al. (2020) showed that crack widths are dependent on the level of axial load or axial restraint and the residual deformation, but not necessarily the peak deformation. Alternative metrics, such as the number cracks or distribution of cracking along a plastic hinge, may be better correlated with peak demands.

3.2.4 Detailed Inspection

The Detailed Inspection is informed by the results of the building analysis. Specifically, the Inspection Locations (IL) and Supplemental Inspection Locations (SIL), as identified by the analysis, are subjected to the following inspection steps:

- Visually inspect all IL and SIL starting with the story with the largest predicted drift demands. The surface of the structural component shall be exposed through the removal of nonstructural finishing to facilitate visual identification of surface damage, such as cracking, spalling and crushing. This may require the removal of nonstructural finishes, including ceilings, gypsum board enclosures and fireproofing. Chapter 3 of FEMA 306 provides guidance on applicable visual inspection techniques and recording of damage observations (FEMA, 1998a).
- Where any damage is observed to a component per Step 1, Intrusive Inspections shall be performed to inspect the concrete core and reinforcing bars. This is defined as an Intrusive Inspection Location (IIL.) Note that cover concrete should not be removed unless already spalled or loose; if the cover concrete is undamaged, the core and bars can be assumed to also be undamaged. The inspecting engineer shall document any instances of damage, including concrete core crushing or cracking, and buckled or fractured reinforcing bars. Chapter 3 of FEMA 306 provides guidance on applicable intrusive inspection techniques and recording of damage observations. At minimum, any removed spalled cover concrete shall be replaced with an equivalent material (e.g., repair mortar product of equivalent strength to base concrete).
- A sampling process, illustrated in in Figure 3-5, may be adopted to potentially reduce the number of Intrusive Inspections Locations (IILs).

The process shall start by requiring intrusive inspection of 100% of ILs and SILs identified as damaged, per step 2. If 5% of IL and SILs for one component type (e.g., beam, column, beam-column joint) are consecutively identified as undamaged, then the intrusive inspection frequency may be progressively reduced, if no damage continues to be found. If damage is identified, inspection shall revert to 100% of the damaged ILs and SILs. A minimum of 5% of the damaged ILs and SILs shall be intrusively inspected according to procedures in Step 2.

Material sampling and testing is not required as part of the Detailed Inspection but may be triggered by low-cycle fatigue evaluation (see Section 3.3.1).

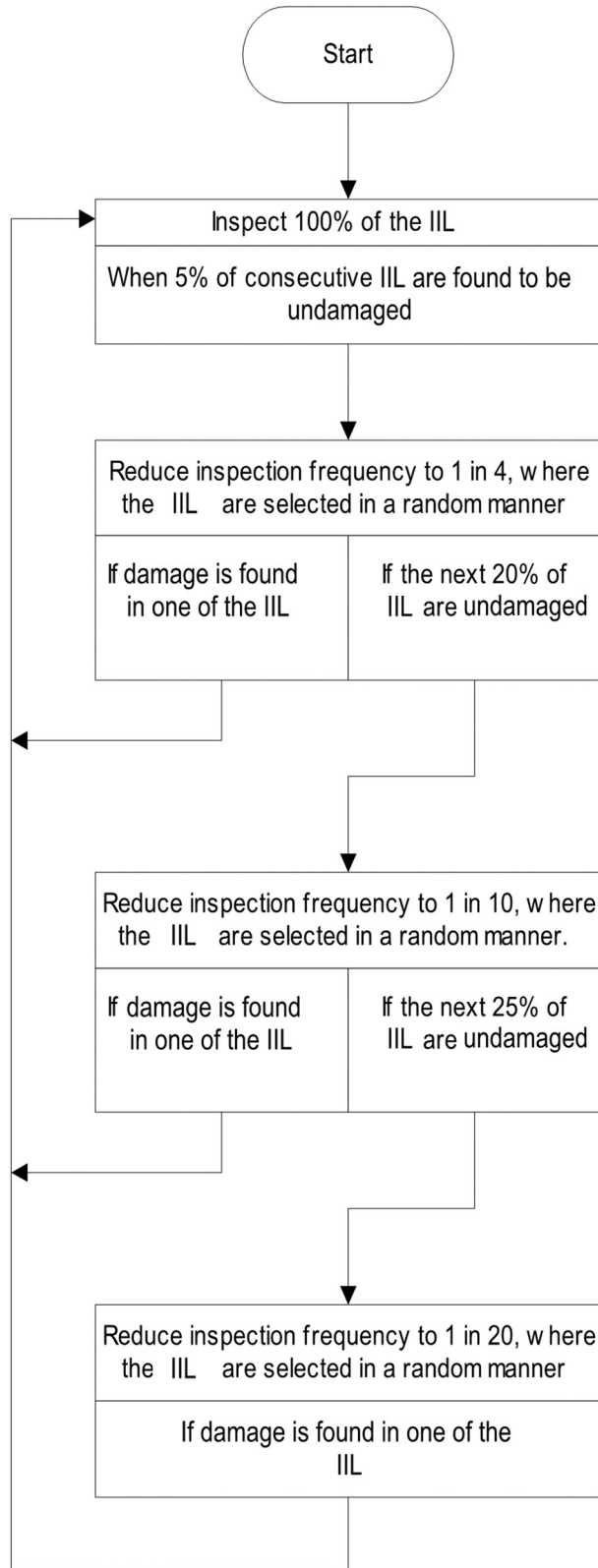


Figure 3-5 Intrusive Inspection Location (IIL) sampling process. (Adapted from AS/NZS 1554 – Structural Steel Welding Standard: Inspection Program for Welded Connections.)

3.2.5 Comparing Inspection Findings with Analysis Results

In this step, the expected damage based on the analysis estimate of deformation demand is compared against the actual damage observed during the detailed inspection. This is a critical step of validating the analysis, before proceeding further with its use in the assessment.

There are no prescriptive rules proposed as to what constitutes acceptable agreement. The engineer must exercise their judgment based on the particular situation. The following three possible scenarios are highlighted as warranting consideration:

1. The analysis results give deformation demands large enough to trigger the limiting criteria in the Safety-assessment Phase (i.e., greater than 2% drift), but the detailed inspection shows limited damage.
2. The analysis results give deformation demands small enough to not trigger any of the limiting criteria in the Safety-assessment Phase (i.e., less than 2% drift), but the detailed inspection shows considerable damage.
3. The distribution of damage observed in the detailed inspection does not align with the expected distribution based on the analysis.

If none of these three scenarios is observed, there is little rationale in attempting to refine the analysis as it would potentially have no effect on the overall outcome of the assessment procedure.

Of these three scenarios, the first is assumed to be the most likely to occur, due to the conservative nature of the seismic assessment provisions on which the analysis is based. At least one past study comparing analytical predictions with post-earthquake inspections showed that the analytical predictions tended to over-predict the observed damage (Bech et al, 2014). This study concluded that explicit inclusion of foundation flexibility and kinematic effects associated with soil-structure interaction (SSI) as permitted by ASCE/SEI 41, generally reduced the degree of over-prediction.

3.2.5.1 Analysis Refinement

The analysis refinement process is intended to reduce discrepancies between analysis results and inspection findings. However, it must be emphasized that the reduction of differences is not in itself the goal. The goal is to better represent the true seismic response of the building during the damaging earthquake, and thereby better understand the future seismic risk of the building. Any number of modifications to the analysis model or input demands could be made to reduce the discrepancies, but they should only be

considered if they are likely to influence the outcome of the overall assessment (i.e., the need to repair).

The logical areas for analysis refinement to investigate are dependent on the discrepancies observed.

If the distribution of damage observed does not align with the predicted locations from the analysis, nonlinear analysis may be an appropriate way of better understanding the post-yield response of the building. In particular, buildings observed to have exhibited localized damage (e.g., soft story mechanism) may be poorly predicted by linear analysis. Dominant collapse mechanism in a moment frame structure has been found to be ground motion dependent (Haselton et al, 2011) and such variation would not be captured by linear analyses.

If the deformation demands obtained from the analysis imply a higher level of damage not consistent with the damage observed in the inspection, conservatism in the modelling may be a contributing factor. The ongoing ATC-134 project, *Performance-Based Seismic Engineering: Benchmarking of Existing Building Evaluation Methodologies*, is expected to provide guidance on which modelling criteria in ASCE/SEI 41 may tend to yield conservative results (NIST, expected 2022). This may also be a situation in which the representation of seismic demand used for the analysis may be having an undue influence (e.g., if a peak in the response spectrum corresponds to the estimated natural period of the analysis model).

3.2.5.2 Re-Inspection

Re-inspection should typically not be required after comparison and/or analysis refinement. However, if the refined analysis indicates that damage is expected in locations not already covered by the initial inspection, an additional inspection covering these locations may be warranted.

3.2.6 Final Estimate of Deformation Demands

The Inspection and Analysis Phase, as described above, has provided an analysis consistent with the distribution of damage identified in the building. Thus, upon completion of the Inspection and Analysis Phase, the analysis can be considered to provide the best available estimates of the peak deformation demands during the damaging earthquake. The Safety-assessment Phase, described in the following section, will require the peak story drift, δ_{EQ} , from the aforementioned analysis. For assessment of component performance during the Safety-assessment Phase or estimate of reduced stiffness in the

Serviceability-assessment Phase, the peak chord rotations during the damaging earthquake, θ_{EQ} , will also be required.

3.3 Safety-assessment Phase

The goal of the Safety-assessment Phase is to determine if the prior earthquake demands on a building exceed a *repair trigger*, thus requiring safety repairs to satisfy the post-earthquake safety performance objective. Such repair may be triggered if an amplification in drift demands in a design-level earthquake ground motion is anticipated and the prior loading has resulted in a reduction of component deformation capacity. The assessment is done based on the peak story drift, δ_{EQ} , and peak chord rotations, θ_{EQ} , from the prior earthquake demands as estimated during the Inspection and Analysis Phase.

FEMA 307, *Evaluation of Earthquake Damaged Concrete and Masonry Wall Buildings – Technical Resources* (FEMA, 1998b), explored the amplification in drift demand resulting from prior earthquake damage using SDOF oscillators with a range of hysteretic models. For systems characterized by ductile flexural response having degrading stiffness, with and without pinching, and without negative post-yield stiffness, FEMA 307 concluded prior damage does not cause large increases in calculated median peak displacement demands. While the study did conclude prior damage can cause some increase in variability of calculated peak displacement, such variability due to uncertain ground motion and building modeling is inherent in earthquake engineering. For SDOF oscillators with negative post-yield stiffness, FEMA 307 concluded prior damage can lead to amplifications in peak displacement demands.

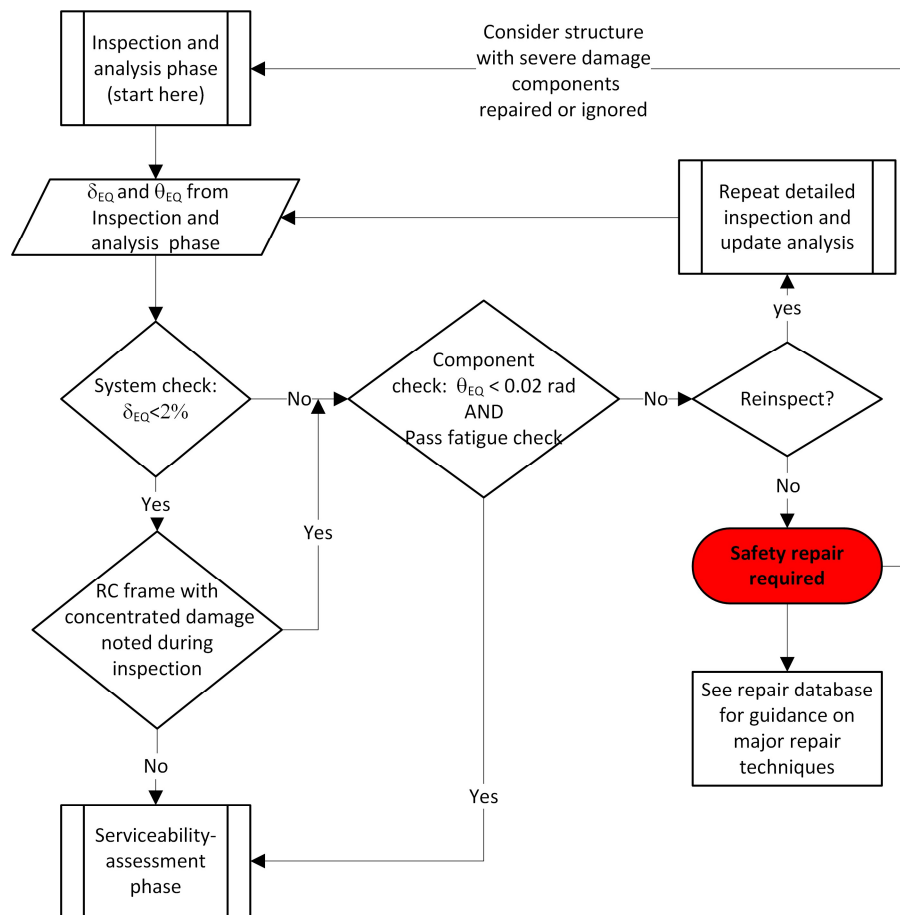


Figure 3-6 Safety-assessment phase. The 2% limit is likely system-dependent and will be updated in the *Repair Guidelines*.

Studies summarized in Appendices A, B, and C expand on the conclusions of FEMA 307 to identify prior demands which may impair the safety of the structure in future ground shaking. These studies include:

- System-level:
 - Collection of shake table test data for building structures subjected to sequences of ground motions to identify if amplifications in drift demand were observed (Appendix B).
 - SDOF and MDOF system analyses to determine when amplification in drift response in a repeated earthquake is anticipated (Appendix B).
- Component-level:
 - Assessment of reinforced concrete frame component tests with varying loading protocols to determine if prior loading will result in decrease in deformation capacity of the component (Appendix A).

- Assessment of conditions under which fatigue capacity of reinforcing bars may have been reduced such that fracture in subsequent earthquakes is anticipated (Appendix C).

Based on these studies, and as illustrated in Figure 3-6, two checks are considered in the Safety-assessment Phase: system-level check and component-level check.

System-level: Based on the studies summarized in Appendix B, the following criterion is adopted to identify if amplification in drift demand in a subsequent design-level ground motion is not anticipated:

$$\delta_{EQ} < 2\% \text{ story drift} \quad (3-1)$$

For most frame structures, this criterion alone should be sufficient to ensure the building satisfies the post-earthquake safety performance objective; however, for systems where large localized component deformation is anticipated, it is advisable to also complete the component-level check. In particular, if concentrated damage was noted during Detailed Inspection, a component-level check should be completed even if the above criterion is satisfied.

If the building does not pass the above system-level criterion, the component-level check should be evaluated.

Component-level. The component-level check assesses if the prior loading has resulted in a reduction of component deformation capacity, including the potential for bar fracture in a subsequent design-level earthquake. This check helps identify the specific components which require safety repair.

Two independent checks are required. First, based on studies summarized in Appendix A, if the following criterion is satisfied it is unlikely that the prior loading has detrimentally impacted the drift capacity of the component:

$$\theta_{EQ} < 0.02 \text{ rad} \quad (3-2)$$

The above criterion was developed considering a broad range of loading protocols but does not directly address fatigue of reinforcement. To ensure the reinforcement is unlikely to experience fracture in a subsequent design-level earthquake the fatigue check from Section 3.3.1 must also be satisfied.

If both component-level criteria are satisfied for all damaged components in the frame, then no repairs are required on the basis of the safety assessment, and the engineer can proceed to the Serviceability-assessment Phase (if required). For any components where the above criteria are not satisfied, safety repair will be required.

If the outcome of the assessment does not meet with the expectation of the engineer, the option is provided at this stage to reinspect and improve the estimate of deformation demands from the damaging earthquake.

3.3.1 Reinforcement Fatigue Check

While not commonly the case, low-cycle fatigue (LCF) of longitudinal reinforcement may limit the performance of a reinforced concrete element if other failure modes are suppressed by adequate detailing (Dutta and Mander 2001). Consequently, some consideration is required of the possibility that LCF has compromised reinforcement in an earthquake-damaged building.

The significance of LCF is greatly impacted by the occurrence of bar buckling. For this reason, consideration of reinforcement fatigue comprises two questions related to the condition of reinforcing steel in a structure:

1. Has bar buckling occurred?
2. Has the fatigue capacity of reinforcement been exceeded?

These questions are addressed sequentially below. The potential outcomes for the checks are summarized in Figure 3-7. In both cases, the questions should be addressed at a component level, i.e., with respect to specific locations within a structure. In particular, both buckling and fatigue of reinforcement are dependent on the magnitude of deformation (typically rotation) demands imposed on the plastic hinges in a structure. Investigations of these issues should therefore focus on regions of the structure where deformation demands are expected to be largest. This will generally mean the story (or stories) subjected to the largest drift demands based on the outcome of the Inspection and Analysis Phase (Section 3.2). The geometry of a structure (span lengths, etc.) may also lead to some parts being subject to larger deformations than others. As described in Section 3.2.4, Detailed Investigation of the condition of a building should begin by considering a sample of the critical regions. If neither buckling nor low cycle fatigue are identified in these critical regions then it may be assumed that the building is not affected by these issues. If buckling and/or low cycle fatigue are identified in the initially assessed regions, investigations should be undertaken of regions subjected to progressively smaller deformations as identified by the Detailed Inspection described in Section 3.2.4, proceeding until a level of deformation demand is identified that does not result in buckling or low cycle fatigue.

If the assessment process in Figure 3-7 leads to “safety repair required”, it is assumed this will typically involve replacement of impacted bars. Straightening in conjunction with heat treatment to relieve residual stresses

should be done with extreme caution. Although recommendations on repair techniques is beyond the scope of this report, the repair database (Appendix E) provides descriptions of tests of repaired components with bar replacement. It is noted that the performance of the repaired component is sensitive to the details of how the bars are replaced.

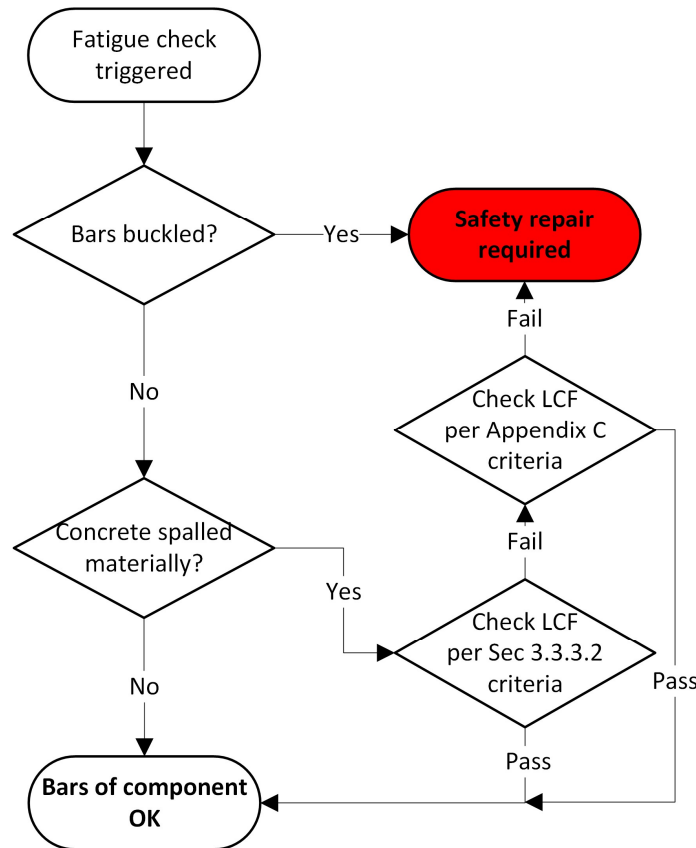


Figure 3-7 Fatigue and buckling assessment process.

3.3.3.1 Determination of Whether Bars Have Buckled

It is presumed that any material buckling of reinforcing bars would constitute damage requiring remediation of the buckled bar, and thus necessitating “safety repair”.

Reinforcing bars can be considered to be in one of three categories:

- Category 1. Bars with visible buckling and concrete spalling,
- Category 2. Bars in elements without cover spalling (i.e., unbuckled bars), and
- Category 3. Exposed bars without visible buckling (i.e., possibly buckled bars).

Bars with visible buckling. Bars should generally be considered to have buckled if there is visible separation between the full circumference of the bar and the surrounding concrete at any location, accompanied by visible bending of the bar.

Unbuckled bars. The occurrence of bar buckling involves lateral deformation of the bar. The occurrence of such deformation is inevitably associated with spalling of concrete in the vicinity of the buckle. Bars can therefore be considered to be unbuckled if the concrete surrounding the bar has not spalled to an extent that is consistent with the occurrence of buckling.

Assuming that the lateral displacement of a material buckle occurs over a length of at least a few bar diameters (e.g., Dhakal and Maekawa, 2002) it may conservatively be assumed that buckling has not occurred in a plastic hinge unless:

- Spalling to the depth of the longitudinal bar has occurred in the plastic hinge region, and
- The extent of spalling is sufficient such that at least 50% of the circumference of a bar is exposed over a continuous length of at least twice the bar diameter ($2d_b$).

For the purposes of considering the above criteria, spalling should be considered to include incipient spalling where cracking has created loose blocks of cover concrete that have not dislodged from the element.

Unbuckled bars may be assumed not to have sustained material fatigue damage.

Possibly buckled bars. Bars that do not meet the criteria in the preceding two sections may have buckled during earthquake shaking to an extent that causes fatigue damage, even if residual buckling may not be evident to the assessor.

In such situations (i.e., where sufficient spalling has occurred for buckling to be possible but where there is no visible evidence of buckling), the impact of LCF on the bar(s) should be considered as described in the next section. However, should LCF be determined not to have materially affected such bars, no remediation of the reinforcing bars is necessary.

3.3.3.2 Fatigue Demands on Reinforcing Bars

Based on analyses described in Appendix C, two performance measures are considered to represent reasonable alternatives for determining whether the

residual fatigue life of reinforcement in an earthquake-damaged structure is sufficient:

1. The fatigue life of the reinforcement not having been reduced by more than 10% by the imposed earthquake demands when measured as a Miner's sum (Miner, 1945), or
2. The residual fatigue life being sufficient to withstand the impacts of a future Maximum Considered Earthquake (MCE).

Fulfillment of either of these criteria is considered sufficient to demonstrate that the reinforcement has not been compromised by fatigue damage. It is not necessary for the reinforcing bar to fulfill both.

Appendix C describes a detailed procedure to assess if reinforcement satisfies either of the two criteria above. For reasonable deformation demands and typical number of cycles and plastic hinge lengths, it is unnecessary to follow the detailed procedure of Appendix C. If all of the following three conditions are met it may be deemed that the reinforcement meets Criterion 1 above and thus has not been compromised by fatigue damage.

- The maximum chord rotation is less than 0.02 rad,
- The significant duration (D_{5-95}) of the damaging earthquake was less than 45 sec¹, and
- The effective plastic hinge length (as defined in Equation 3-3) of an element is greater than 0.4 times the member depth.

It should be recognized that strain penetration to either side of the critical crack results in a practical lower bound on the effective plastic hinge length as discussed by Opabola et al. (2018). Accounting for this, the effective plastic hinge length may be calculated (NZSEE et al. 2018; Priestley et al. 2007) as

$$L_p = k_{lp}a + L_{sp} \geq 2L_{sp} \quad (3-3)$$

where:

$$k_{lp} = 0.2 \left(\frac{f_u}{f_y} - 1 \right) \leq 0.08 \quad (3-4)$$

a = shear span, i.e., the distance of the critical section from the point of contraflexure

¹ This limit (if considered necessary to better define this condition) is only a placeholder and requires further investigation.

L_{sp} = strain penetration length = $0.15f_y d_b$ where the units of f_y are ksi,
or $0.022f_y d_b$ if the units of f_y are MPa

f_y = probable yield strength of longitudinal reinforcement

d_b = diameter of longitudinal reinforcement

f_u = probable ultimate strength of the longitudinal reinforcement.

These considerations have been derived from analysis of cantilever elements (see Appendix C). This means that no account has been made for elastic deformations of other, non-yielding, elements of a frame, e.g., the columns or joints of a capacity designed ‘strong column-weak beam’ type frame. This is consistent with comparison to the maximum chord rotation of a frame element.

The findings above have been derived on the basis that the deflection of low aspect ratio (i.e., elements where the shear span to depth, a/d , is less than 4) is materially affected by the occurrence of bar slip, shear deformation and other phenomena not captured by conventional moment-curvature analysis. These effects have been accounted for following the recommendations of Opabola et al. (2020).²

If the reinforcement does not satisfy the preceding criteria (i.e., the fatigue capacity of a structural element may have been reduced by more than 10%), a more detailed consideration of the quantum of fatigue damage may be undertaken based on the methods summarized in Appendix C. Two methods to estimate the cyclic demands are described in Appendix C, namely:

- A simplified assessment approach based on the idealized displacement history described in FEMA 461, *Interim Testing Protocols for Determining the Seismic Performance Characteristics of Structural and Nonstructural Components* (FEMA, 2007), and
- More complex assessment requiring forensic response history analysis of the structure using the best available estimate of the ground motion that damaged the building.

The approach to low-cycle fatigue described here and in Appendix C is applicable to reinforcement that is not susceptible to strain aging, i.e., reinforcement includes trace amounts of Vanadium (Pussegoda, 1978; Restrepo-Posada, 1993). High strength reinforcing steel (Grade 60 and above) used in the United States is generally considered not to be susceptible to strain aging and can be assessed using the approach to low-cycle fatigue

² These recommendations have a significant impact on the calculated fatigue damage as outlined in Appendix C. See Appendix C for further discussion.

described in this document. Additional consideration, outside the scope of this report, would need to be given where structures contained longitudinal reinforcement produced from mild steel (Grade 40), high carbon steel without Vanadium, or high strength steel produced by cold working.

3.4 Serviceability-assessment Phase

After satisfying the Safety-assessment Phase, the building is deemed to meet the post-earthquake safety performance objective from Chapter 2. It is noted that the Safety-assessment Phase does not identify any need for Category 1 non-safety repairs (namely, epoxy injection). This is because epoxy injection has been found to have limited impact on the ultimate deformation capacity, and hence safety-related performance, of reinforced concrete components (see Appendix E). Epoxy injection can recover a portion of the original stiffness of the repaired component, but only for cycles at small deformations; for cycles above a chord rotation of approximately 0.01 rad, the stiffness of an epoxy-repaired component is similar to that of an unrepaired damaged component (see Appendix D). Hence, epoxy-injection repair is only considered useful for increasing stiffness and reducing drifts for service-level earthquakes.

Since serviceability is not considered in the design of new buildings in United States, the Serviceability-assessment Phase may be rarely required by an AHJ. In cases where the Serviceability Phase is not required, then a building not requiring safety repair from the Safety-assessment Phase may be left unrepaired from an earthquake safety perspective. Considerations, such as durability or aesthetics, may however still lead to an epoxy repair of damaged components regardless of the choice to consider the Serviceability-assessment Phase. This section provides a process for identifying if epoxy injection, or further intervention, would assist in meeting the serviceability post-earthquake performance objective from Chapter 2.

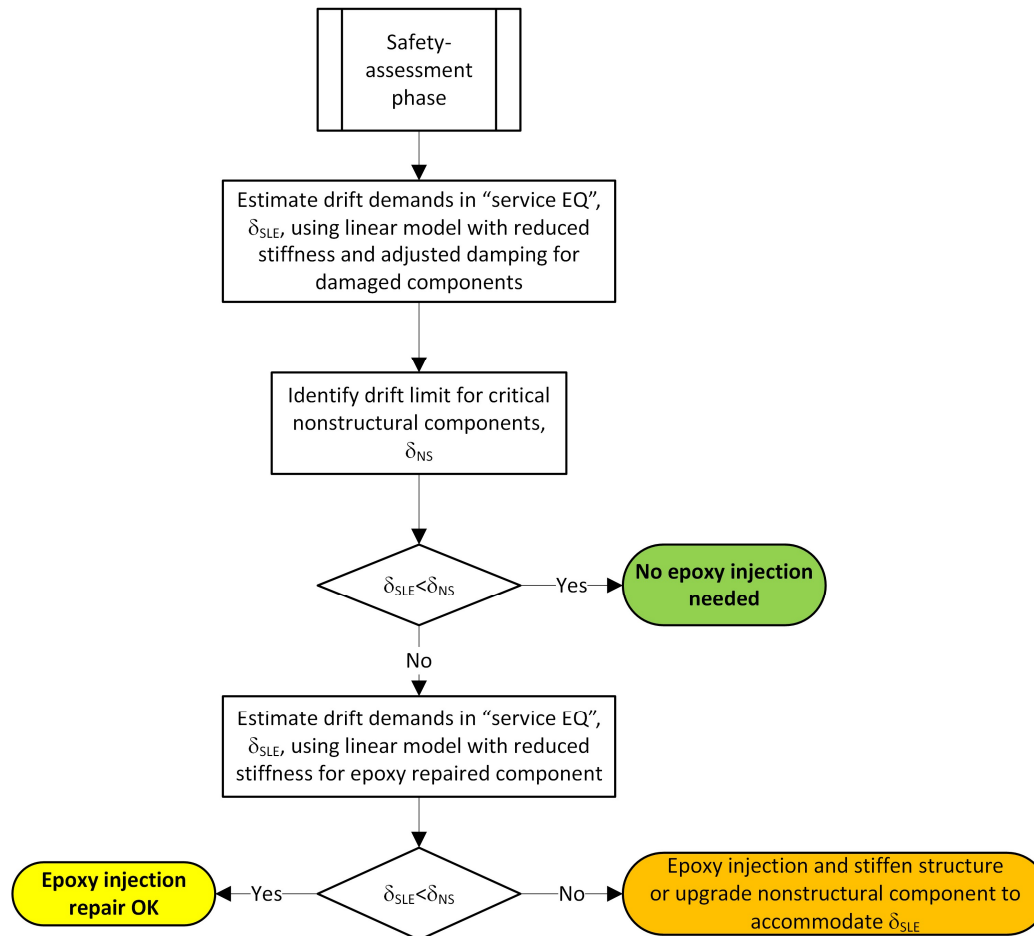


Figure 3-8 Serviceability-assessment phase.

Analyses summarized in Appendix B, considering a range of definitions for a service-level earthquake (SLE), have identified that a damaged building is expected to experience a larger drift in a service earthquake than an undamaged building in many cases. This amplification in displacement demand is not surprising given that the response of both the damaged and undamaged buildings due to a small service-level earthquake are expected to be essentially linear-elastic, but the damaged structure will be softer than the undamaged structure, albeit likely with more damping. However, such amplification of displacements is only a concern for a service earthquake if the amplification results in nonstructural damage in a service earthquake not experienced in the building prior to the damaging earthquake (i.e., for an undamaged building). Since the damaged building will be softer than the original building, it is expected that drift-sensitive nonstructural components, rather than acceleration-sensitive components, will be most impacted. It is, thus, recommended that the engineer compare drift demands from a linear analysis (using appropriately reduced stiffnesses and possibly increased damping) with

the drift capacity of the most critical drift sensitive component in the structure. This is anticipated to be either cladding or partition walls. The objective is to ensure that the structure stiffness has not reduced so much as to lead to repeated damage to such nonstructural components during every (frequent) service earthquake. It is noted that low-level earthquakes are more frequent during the months and years following a major earthquake until the aftershock rate decays to steady-state seismic activity, and repeated damage to recently repaired nonstructural components during aftershocks is not desirable.

Figure 3-8 provides a flowchart summarizing the key steps of the Serviceability-assessment Phase. As described above, the goal of this phase is to identify if the drift demands in a service-level earthquake, δ_{SLE} , are likely to exceed the drift capacity of critical drift-sensitive nonstructural components, δ_{NS} . The first step is to assess if the damaged building can satisfy $\delta_{SLE} < \delta_{NS}$ without any repair. If the damaged building does not meet this criterion, repair will be necessary. If drift demands using the stiffness of epoxy-repaired components is not sufficient to satisfy $\delta_{SLE} < \delta_{NS}$, either the building will need to be stiffened or the critical nonstructural components will need to be upgraded to be able to accommodate δ_{SLE} .

The following sections provide guidance on key inputs needed to follow the flowchart in Figure 3-8; namely, the definition of a service earthquake, stiffness of damaged and epoxy-repaired components, damping for serviceability analysis, and drift limits for critical nonstructural components.

3.4.1 Definition of Service Earthquake

The intensity or return period of the “service-level earthquake” considered in determining δ_{SLE} should be selected by the AHJ. Various standards and guidelines provide different recommendations for return periods for service-level earthquakes (see Table 3-1).

For the purpose of this assessment, the maximum intensity considered for a service-level earthquake need not exceed that which would likely cause cracking and yielding in a new building. Studies summarized in Appendix B.3 indicate that earthquakes over this intensity are unlikely to result in amplifications in drift demand for a damaged building relative to an undamaged building.

After a major earthquake, a damaged building is likely to be exposed to higher level of seismicity during the aftershock period (lasting months to years) and the time-dependent hazard during this period is not well represented by the steady-state hazard curve. In this environment, it may be prudent to select a higher ground shaking intensity than one would select for

otherwise use for design of a new building not in a period of heightened seismicity.

Table 3-1 Possible Definitions of a Service-level Earthquake

Reference	Return Period
NZS 1170.0:2002	25 years
TBI (2017)	43 years
Vision 2000	72 years

Note: See also discussion in Appendix B.5.4.3.

3.4.2 Stiffness of Damage Components

Reinforced concrete frame components will decay in stiffness with an increase in prior inelastic drift demand. Gulkan and Sozen (1974) suggested that the reduced stiffness of a component having experienced displacement ductility of μ could be estimated based on the origin-to-peak stiffness as shown in Figure 3-9.

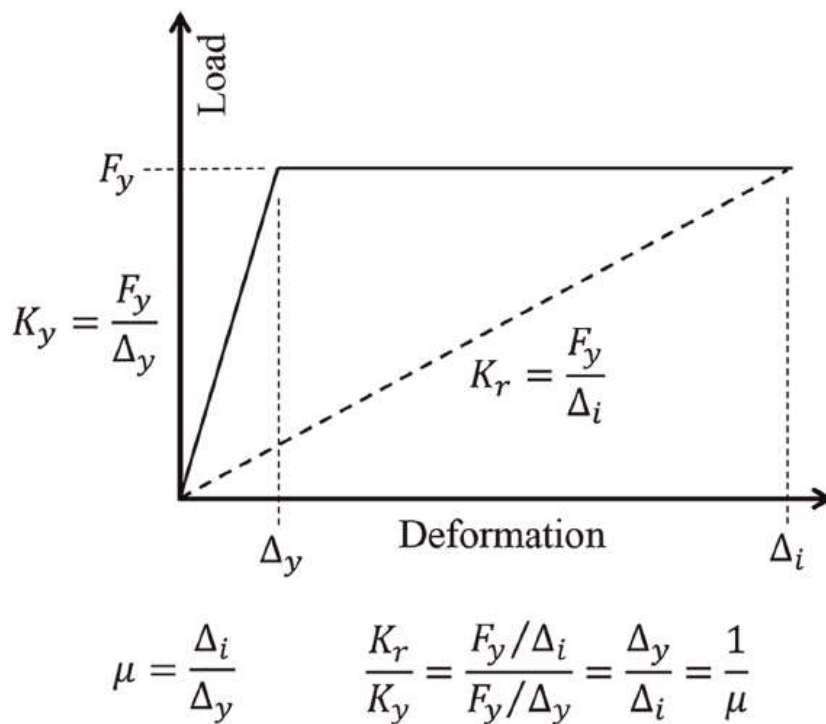


Figure 3-9 Origin-to-peak stiffness.

Data presented in Appendix D indicate that the Gulkan and Sozen model generally provides a reasonable lower bound to the measured stiffnesses of columns from repeated shake table tests, except for ductility demands less than two. Given uncertainties in estimating the prior ductility demand and

the overestimation of stiffness for ductility demands less than two, Marder et al (2020) recommended to determine the reduced stiffness as follows:

$$\frac{K_r}{K_y} = \begin{cases} 1.0, & \mu < 1.0 \\ 0.5, & 1.0 \leq \mu \leq 2.0 \\ 1/\mu, & \mu \geq 2.0 \end{cases} \quad (3-5)$$

The effective stiffness to yield, K_y , and the yield rotation of the component to determine the ductility can be estimated based on procedures in ASCE/SEI 41. The chord rotation demands should be based on the analysis from the Inspection and Analysis Phase.

As noted, the above model provides a lower bound on stiffness reduction based on limited data from shake table tests. A median model may be preferred to achieve a prediction of expected drift demands in the service earthquake, however, given the limited data used to develop the model the lower-bound is preferred approach at this time.

3.4.3 Stiffness of Epoxy-repaired Components

Epoxy-repair can help recover a portion of the stiffness loss due to prior earthquake demands. The extent of stiffness recovery depends on quality control and the ability to get epoxy into hairline cracks. Components with axial load (e.g., columns) typically have lower recovered stiffness because of challenges of achieving epoxy penetration in cracks closed by axial loads. Data discussed in Appendix D indicates that the stiffness recovery is not related to the prior inelastic drift demands, hence there is no need to relate the stiffness of a repaired component to the prior ductility demand as suggested above for damaged components.

Based on the data presented in Appendix D, the stiffness of epoxy-repaired beams can be estimated as:

$$K_{beam\ repair} = 0.8K_y \quad (3-6)$$

The effective stiffness to yield, K_y , can be estimated based on procedures in ASCE/SEI 41.

Few data exist for columns repaired by epoxy injection and, given the challenges of maintaining axial load in the laboratory during repair, it is unclear if all tests conducted repair under appropriate field conditions. Furthermore, Appendix D indicates wider variability in the recovery of stiffness with epoxy injection for columns. Given the above, it is recommended that in locations of epoxy repair for columns, the stiffness recovery be ignored and the stiffness of repaired columns be taken the same as that suggested in Equation 3-6 for damaged frame components.

3.4.4 Damping for Serviceability Analyses

It may be logical to conclude that the damping in a damaged structure would be higher than the damping in an undamaged structure. Gulkan and Sozen (1974) propose an increase in damping based on the ductility demand (Figure 3-10).

On the other hand, damping for serviceability-level analyses is typically assumed to be less than damping for a large earthquake demand causing nonlinear response. The Pacific Earthquake Engineering Research Center (PEER) Tall Building Initiative Guidelines (2017) recommends lower damping for SLE compared to MCE analyses for design of tall buildings. It is unclear if this reduction still applies for damaged buildings.

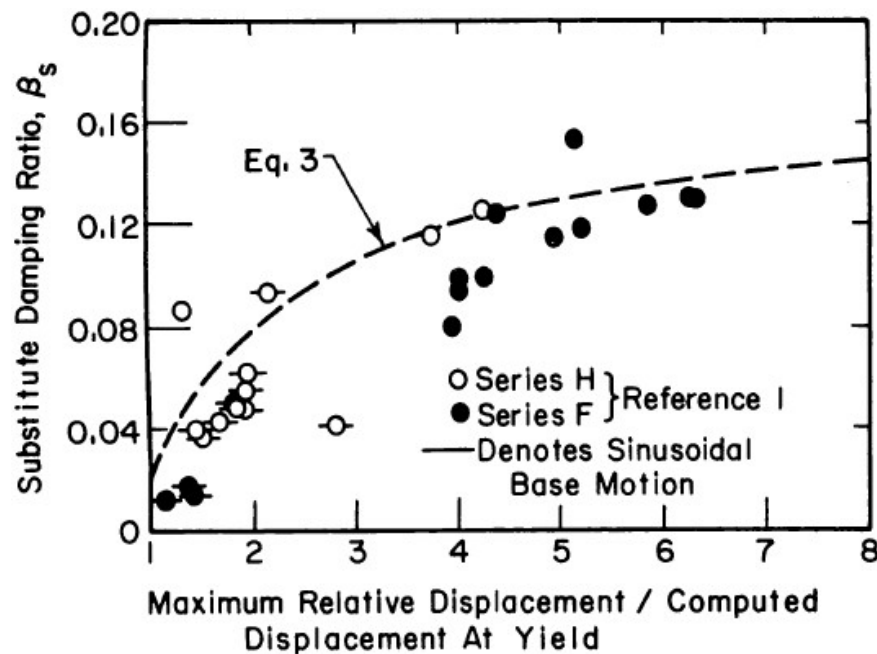


Figure 3-10 Damping versus ductility demand (Gulkan and Sozen, 1974).

The level of damping to be used in the linear analyses as part of the Serviceability-assessment Phase has not been systematically studied, but considering these two counteracting effects, it is provisionally recommended to use the same damping as typically done for linear analysis of undamaged buildings. (See recommendations of PEER Tall Building Initiative (2017)). It is recommended that this issue be studied further in the ATC-145 project.

3.4.5 Drift Limit for Nonstructural Components

A key parameter in the serviceability assessment is the limiting drift capacity of critical drift-sensitive nonstructural components, δ_{NS} . These are anticipated to be either cladding or partition walls. It is noted that the

sensitivity of partition walls to story drift is highly dependent on boundary conditions. Many partitions do not connect to the underside of the upper floor level, and thus may not be sensitive to story drift. These boundary conditions should be inspected before selecting δ_{NS} .

FEMA P-58 provides a wealth of fragility data which may be used to select an appropriate value of δ_{NS} (FEMA, 2018). Median values from appropriate fragility curves may be used. For partition walls, these fragility curves indicate median drifts for the first damage state of 0.5% to 1% drift.

In the absence of detailed investigations of the nonstructural components used in the building and review of appropriate P-58 fragilities, $\delta_{NS} = 0.5\%$ may be assumed based on the serviceability drift limit used in PEER Tall Building Initiative (2017). Uang and Bertero (1991)'s review of serviceability criteria also suggests 0.5% as an appropriate limit. This limit should be explored further in future development of ATC-145.

3.5 Summary of Assessment Framework

This chapter presented an assessment procedure to determine if repairs are required for code-conforming concrete moment frame buildings after an earthquake. For the purpose of this report, a code-conforming building is one which satisfies the Benchmark Building table of ASCE/SEI 41-17.

The assessment procedure includes three phases:

1. Inspection and Analysis Phase:

The goal of this phase is to estimate the peak drift demands that occurred during the damaging earthquake. This phase involves an iterative process by which the assessing engineer first does a preliminary inspection to identify severe damage, then builds a numerical analysis model of the building to predict the likely damage states in the building, and finally completes a detailed inspection of the building to see if the predicted damage states agree with the observed damage. If the predicted damage states do not agree with the observations in the building, refinement of the building model and/or the estimate of ground shaking at the site is required. Once satisfactory agreement is achieved, the analysis model is considered to provide the best estimate of the drift demands on the building during the damaging earthquake.

2. Safety-assessment Phase:

The goal of this phase is to determine if the building requires safety repairs (i.e., more than epoxy injection and mortar patching) or if the building

without repair is expected to perform satisfactorily from a life-safety perspective in a subsequent design-level earthquake. Two criteria are applied to assess if safety repairs are required: system-level and component-level criteria. Based on analytical studies summarized in Appendix B, the system-level criterion indicates that a building with story drift demands less than 2% is unlikely to require complex repairs. Based on further studies of frame components (Appendix A) and low-cycle fatigue of reinforcement (Appendix C), the component-level criteria indicate that if the chord rotation remained below 0.02 rad and bar buckling was not observed, the component would not require safety repairs. While this report does not provide specific guidance on designing safety repairs, the reader is directed to the repaired component database in Appendix E for examples of repair strategies tested in the laboratory.

3. Serviceability-assessment phase:

A building which passes the Safety-assessment phase may still be considerably softer after the damaging earthquake than it was before the earthquake. This may result in larger drifts in small frequent earthquakes than would be typically considered acceptable for a new concrete building . The serviceability-assessment phase addresses this concern by comparing the expected drift of the building in a serviceability earthquake with the drift capacity of nonstructural components. It is, however, noted that this phase may not be required by an AHJ since no serviceability check is included in the design of new buildings in the United States.

This Source Report documents the key studies conducted in the first three years of the ATC-145 project and a repair assessment framework for conforming special reinforced concrete moment frames. The purpose is to document progress on the project to-date and serve as a resource for future ATC-145 work. This chapter highlights areas that require further study (as of September 2021). These future tasks will be addressed in the development of the *Repair Guidelines*, which will present the final ATC-145 methodology for inspection and evaluation of earthquake-damaged buildings, structural system-specific triggers for repair, and up-to-date repair technique guidance.

4.1 Expansion of Component Deformation Limits (Appendix H) to Other Reinforced Concrete Components and Other Materials

Component Deformation Limits, which are used as inspection and repair triggers in the *Repair Guidelines*, will need to be expanded across other reinforced concrete components. Appendix H provides a methodology for assessing these limits and applies this methodology to non-ductile frame components and code-conforming flexure-controlled walls, but it is envisioned that this approach can be expanded across other components. The methodology is intended to be general enough such that it may be applied to materials other than reinforced concrete, but this will take careful consideration in the future.

4.2 Refinement of Visual Damage Limits (Appendix I) and Expansion to Other Reinforced Concrete Components

Visual Damage Limits, which are used to determine the damage classes of components in the *Repair Guidelines*, will need to be further refined through a trial application on a building with documented damage, then expanded across other reinforced concrete components. Furthermore, the process by which an engineer determines the Damage Class (Figure 4-1) using both the Visual Damage Limit and the Repair Trigger (median component deformation limit) needs to be explored. The scope of Appendix I is limited to non-ductile frame components and code-conforming flexure-controlled walls, but it is envisioned that this framework can be expanded across other

components and failure types. A tool will be developed to help the inspecting engineer query a database and find summaries of the most relevant tests for comparison with observed damage. Expanding the concept of Visual Damage Limits to materials other than reinforced concrete will be explored.

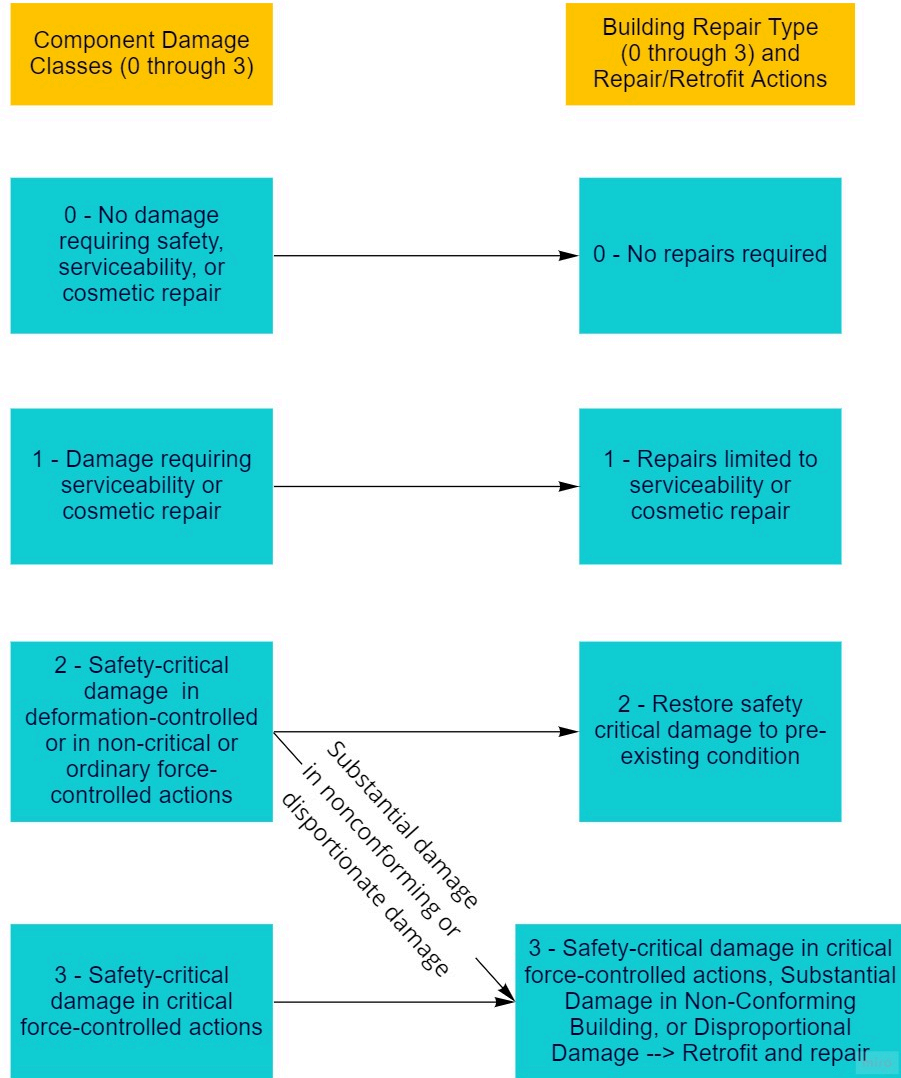


Figure 4-1 Summary of proposed relationship between Component Damage Classes and Building Repair Type from Chapter 4 of the first draft of the *Repair Guidelines*

4.3 Refinement of Inspection Procedures

Inspection procedures will need to be further refined. This includes the identification of possible damage locations, procedure of intrusive inspections, and use of Visual Damage Limits in damage categorization.

4.4 Refinement of Damage Categorization Process (Using Component Damage Classes to Determine Building Damage Class)

The *Repair Guidelines* methodology requires categorizing the Building Repair Types from the Component Damage Classes as illustrated in Figure 4-1. The proposed process is largely component-based (e.g., one component in Damage Class 2 would lead to classification in Building Repair Type 2); the limitations of this approach need to be explored. Furthermore, “critical force-controlled action”, which currently triggers repair and retrofit (Building Repair Type 3), need further definition.

4.5 Refinement and Expansion of Modelling and Acceptance Criteria

In the first draft of the *Repair Guidelines*, it is assumed that strength and deformation capacity modification factors are not required. This conclusion is based on component studies summarized in this Source Report (Appendices A and H) indicating that cycles with deformation demands below that of lateral strength loss that also do not cause significant low-cycle fatigue (Appendix C), do not impact the strength or deformation capacity of the component in future loading. Hence, there is no need to adjust strength or deformation capacity for modeling of a damaged structure where component deformation demands in the damaging earthquake were less than that at lateral strength loss. For components experiencing larger deformation demands, safety repair is required. Further guidance on modeling and acceptance criteria of these components with safety repairs is needed. It is currently assumed that the assessment of a building with safety repairs will be done according to ASCE/SEI 41, but this needs to be further validated.

In the first draft of the *Repair Guidelines*, it is also assumed that stiffness modification factors are not required for analyses of the damaged building subjected to design level (or higher) ground motions. This conclusion is based on system studies summarized in this Source Report (Appendices B, F, and G) which indicate that if the component deformation demands did not exceed lateral strength loss (i.e., the repair trigger) in the damaging earthquake, then amplification of drift demands in future design level earthquakes is not anticipated. Stiffness modification factors are provided, however, for analysis at serviceability levels. Guidance on serviceability-level assessment needs to be developed as indicated in 4.10.

4.6 Development of Additional Case Studies

Additional case studies are required to refine the *Repair Guidelines* methodology, especially the inspection process, reconciliation of inspection observations and analysis results, and use of Visual Damage Limits.

4.7 Development of Repair Technique Guidance

Updated comprehensive guidance for repair will need to be developed. The process will start with a thorough review of FEMA 308, *Repair of Earthquake Damaged Concrete and Masonry Wall Buildings*. Building on the Appendix E, an approach to determine when a repair technique is adequate to restore safety-related damage to pre-damage condition (i.e., $\lambda_D \geq 1$ and $\lambda_Q \geq 1$) will be developed.

4.8 Development of an Improved Definition of Substantial Structural Damage

The findings of system studies in Appendices B, F, and G indicate that drift amplification can occur before the 33% loss of lateral-load carrying story capacity that defines *Substantial Structural Damage* in the 2021 International Existing Building Code (IEBC). As summarized in Figure 4-2, Substantial Structural Damage presently serves as the repair and retrofit trigger for non-compliant buildings in the IEBC. As these findings indicate that buildings with damage less than Substantial Structural Damage can have amplified drift demands in a future earthquake, further investigation is required to develop an improved definition for Substantial Structural Damage that catches damaged buildings with significant performance degradation.

In the 2021 IEBC, if an earthquake-damaged building meets the definition of Substantial Structural Damage (SSD), the requirements are dependent on whether or not the pre-damaged building was complying, where compliance is defined in Section 304.3.2 as the ability to resist at least 75% of current IBC loads or ASCE/SEI 41 criteria for reduced seismic forces. Per Section 405.2.3, non-compliant buildings with SSD require repair and retrofit, but compliant buildings with SSD “shall be permitted to be restored to their predamage condition”.

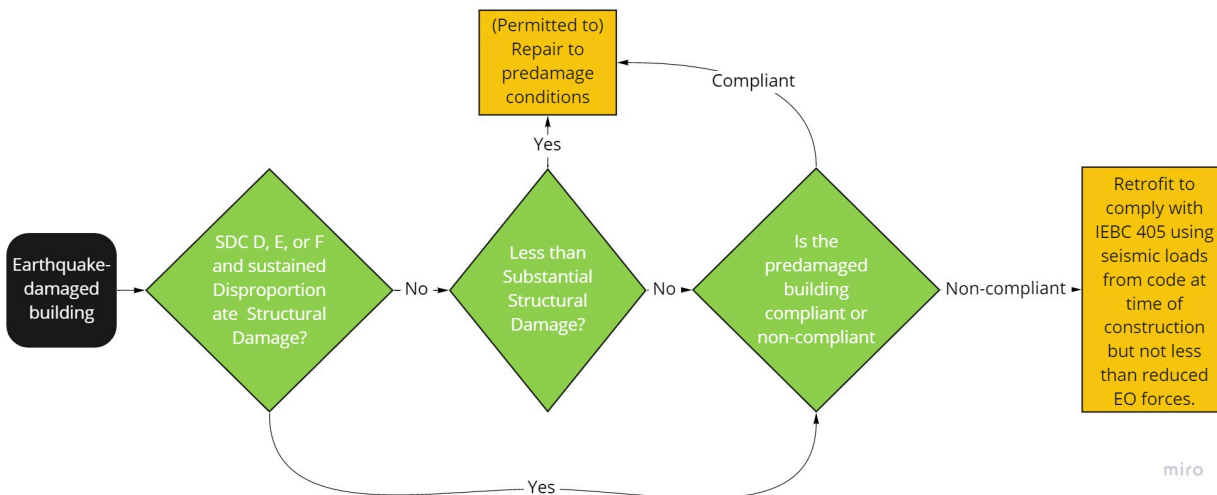


Figure 4-2 Summary of the post-earthquake assessment process in the 2021 IEBC.

4.9 Development of Low Cycle Fatigue Assessment Procedure for Reinforced Concrete Walls

The low cycle fatigue (LCF) assessment procedure in Source Report Chapter 3 and Appendix C was developed with a focus on conforming special reinforced concrete moment frames. This needs to be extended to other concrete components, in particular, lightly reinforced flexure-controlled walls. A significant portion of the material presented in Appendix C is generic and can be applied to RC walls, with little to no changes; however, strain concentrations which can happen in walls with light longitudinal reinforcement needs to be addressed.

The simplified assessment procedure of Source Report Chapter 3 (also incorporated in the first draft of the *Repair Guidelines*, Chapter 6) will also need to be reviewed in terms of applicability to walls. In particular, this simplified procedure relies on being able to say that if there is no significant spalling then there is no bar buckling and hence no LCF concerns. This may be valid for typical walls with sufficient longitudinal reinforcement to develop distributed cracking but may not work for walls with light longitudinal steel where high strains may be concentrated at limited number of cracks. An alternative simplified process will need to be developed for such walls noting that it is not practical to expect most components to be assessed using the details of Appendix C.

4.10 Advancement of Serviceability Check

System-level studies summarized in Appendix B indicate that an earthquake-damaged building will likely experience more drift in a service-level earthquake relative to that expected for an undamaged building. Chapter 3 of this Source Report proposes one possible approach to assessing the performance of an earthquake-damaged building in service-level earthquakes. Future studies should reassess if this proposed approach is fit for purpose. An alternative may be to consider a limit on changes in performance at a service-level due to earthquake damage.

4.11 Coordination with Functional Recovery and Reoccupancy Studies Outside of ATC-145

Assessment and repair of earthquake-damaged buildings is a critical step in the recovery of a community impacted by an earthquake. Efficient and effective means of assessing and making repair decisions on a building based on the *Repair Guidelines*, will enable faster return to function and hence contributes to Functional Recovery objectives. The *Repair Guidelines* will

need to be coordinated with work on other projects advancing Functional Recovery concepts.

References

References are provided here for Chapters 1 to 4 of the Source Report. Appendix references are listed within each Appendix.

- ATC, 1985, *Earthquake Damage Evaluation for California*, ATC-13, Applied Technology Council, Redwood City, California.
- ATC, 2000, *Database on Performance of Structures near Strong-motion recordings: 1994 Northridge California Earthquake*, ATC-38, Applied Technology Council, Redwood City, California.
- ASCE, 2016, *Minimum Design Loads and Associated Criteria for Buildings and Other Structures*, ASCE/SEI 7-16, American Society of Civil Engineers, Structural Engineering Institute, Reston, Virginia.
- ASCE, 2017, *Seismic Evaluation and Retrofit of Existing Buildings*, ASCE/SEI 41-17, American Society of Civil Engineers, Structural Engineering Institute, Reston, Virginia.
- Bearman, C., 2012, *Post-earthquake assessment of reinforced concrete frames (Master's thesis)*, University of Washington, Seattle, Washington.
- Bech, D., Cordova, P., Tremayne, B., Tam, K., Weaver, B., Wetzel, N., and Fisher, J., 2014, "Common Structural Deficiencies Identified in Canterbury Buildings and Observed versus Predicted Performance," *Earthquake Spectra*, Vol. 30, Issue 1, pp. 335–362.
- Bradley, B.A., Pettinga, J.D., Baker, J.W., and Fraser, J., 2017, "Guidance on the utilization of earthquake-induced ground motion simulations in engineering-practice," *Earthquake Spectra*, Vol 32, Issue 3, pp. 809-835.
- Dhakal, R. P., and Maekawa, K., 2002, "Modeling for Postyield Buckling of Reinforcement," *Journal of Structural Engineering*, Vol. 128, No. 9, pp.1139–1147.
- Dutta, A., and Mander, J. B., 2001, "Energy Based Methodology for Ductile Design of Concrete Columns," *ASCE Journal of Structural Engineering*, Vol. 127, No. 12, pp.1374–1381.
- FEMA, 1998a, *Evaluation of Earthquake Damaged Concrete and Masonry Wall Buildings*, FEMA 306, prepared by the Applied Technology

- Council for the Federal Emergency Management Agency,
Washington, D.C.
- FEMA, 1998b, *Repair of Earthquake Damaged Concrete and Masonry Wall Buildings*, FEMA 307, prepared by the Applied Technology Council for the Federal Emergency Management Agency, Washington D.C.
- FEMA, 1998c, *Evaluation of Earthquake Damaged Concrete and Masonry Wall Buildings*, FEMA 308, prepared by the Applied Technology Council for the Federal Emergency Management Agency, Washington, D.C.
- FEMA, 2007, *Interim Testing Protocols for Determining the Seismic Performance Characteristics of Structural and Non-Structural Components*, FEMA 461, prepared by the Applied Technology Council for the Federal Emergency Management Agency, Washington, D.C.
- FEMA, 2015a, *Rapid Visual Screening of Buildings for Potential Seismic Hazards: A Handbook*, FEMA P-154, prepared by the Applied Technology Council for the Federal Emergency Management Agency, Washington, D.C.
- FEMA, 2015b, *Performance of Buildings and Nonstructural Components in the 2014 South Napa Earthquake*, FEMA P-1024, prepared by the Applied Technology Council for the Federal Emergency Management Agency, Washington, D.C.
- FEMA, 2018a, *Development of Next Generation Performance-Based Seismic Design Procedures for New and Existing Buildings*, FEMA P-58, prepared by the Applied Technology Council for the Federal Emergency Management Agency, Washington D.C.
- FEMA, 2018b, *Seismic Evaluation of Older Concrete Buildings for Collapse Potential*, FEMA P-2018, prepared by the Applied Technology Council for the Federal Emergency Management Agency, Washington, D.C.
- FEMA, 2020, *Hazus Earthquake Model Technical Manual*, Federal Emergency Management Agency, Washington, D.C.
- Gulkan, P. and Sozen, M. A., 1974, "Inelastic responses of reinforced concrete structure to earthquake motions," *Journal proceedings*, Vol. 71, No. 12, pp. 604-610.
- Haselton, C., Liel, A., Deierlein, G., Dean, B., and Chou, J., 2011, "Seismic Collapse Safety of Reinforced Concrete Buildings. I: Assessment of

- Ductile Moment Frames”, *Journal of Structural Engineering*, Vol. 137, No. 4.
- ICC, 2021, *International Existing Building Code*, IEBC, International Code Council, Washington, D.C.
- Marder, K., 2018, *Post-Earthquake Residual Capacity of Reinforced Concrete Plastic Hinges (PhD Thesis)*, University of Auckland, Auckland, New Zealand.
- Marder, K., Elwood, K. J., Motter, C. J., and Clifton, G.C., 2020, “Post-earthquake assessment of moderately damaged reinforced concrete plastic hinges,” *Earthquake Spectra*, Vol. 36, Issue 1, pp. 299-321.
- Miner, M. A., 1945, “Cumulative Damage in Fatigue,” *Journal of Applied Mechanics*, Vol. 12, No. 3, pp. 159–164.
- NIST, expected 2022, *Benchmarking Evaluation Methodologies for Existing Reinforced Concrete Buildings*, ATC-134, prepared for the National Institute of Standards and Technology by the Applied Technology Council, Gaithersburg, Maryland.
- NZSEE, MBIE, EQC, NZGS, and SESOC, 2018, *Technical Proposal to Revise the Engineering Assessment Guidelines - Part C5 Concrete Buildings*, Ministry of Business, Innovation, and Employment, Wellington, New Zealand, pp. 252.
- Opabola, E., Best, T., Elwood, K. J., Hogan, L., and Synge, A. J., 2018, “Deformation Capacity of Reinforced Concrete Beams with a Single Crack,” *Proceedings of the NZSEE Conference*, New Zealand Society for Earthquake Engineering, Auckland, New Zealand, pp. 11.
- Opabola, E., and Elwood, K. J., 2020, “Simplified Approaches for Estimating Yield Rotation of Reinforced Concrete Beam-Column Components.” *ACI Structural Journal*, Vol. 117, No. 4, pp. 279–291.
- PEER, 2017, *Guidelines for Performance-Based Seismic Design of Tall Buildings*, Pacific Earthquake Engineering Research Center, Berkeley, CA.
- Priestley, M. J. N., Calvi, G. M., and Kowalsky, M. J., 2007, *Displacement-Based Seismic Design of Structures*, IUSS Press, Pavia, Italy, pp. 721.
- Pussegoda, L. N., 1978, *Strain Age Embrittlement in Reinforcing Steels (PhD Thesis)*, University of Canterbury, Christchurch, New Zealand, pp. 223.

- Restrepo-Posada, J. I., 1993, *Seismic Behaviour of Connections between Precast Concrete Elements*, Department of Civil Engineering, University of Canterbury, Christchurch, New Zealand, pp. 385.
- Savarimuthu, S., Lagrava, D., Bradley, B.A., Huang, J., Motha, J., Polak, V., Bae, S., 2017, "SeisFinder: A web application for extraction of data from computationally-intensive earthquake resilience calculations," *QuakeCoRE Annual Meeting 3-6 September 2017*, Taupo, New Zealand.
- Tremayne, W., 2020, Personal Communication, August 6, 2020.
- Worden, C.B., Thompson, E.M., Baker, J.W., Bradley, B.A., Luco, N., and Wald, D.J., 2018, "Spatial and spectral interpolation of ground motion intensity measure observations," *Bulletin of the Seismological Society of America*, Vol. 108, No 2, pp. 866-875.
- Uang, C. and Bertero, V, 1991. "UBC seismic serviceability regulations: Critical review," *Journal of Structural Engineering*, Vol. 117, No. 7, pp. 2055-2068.
- USGS, 2021, *ShakeMap*, U.S. Geological Survey Earthquake Hazards Program, <https://earthquake.usgs.gov/data/shakemap/>.

Appendix A

Influence of Prior Loading on Deformation Capacity of Reinforced Concrete Beams and Columns

A.1 Introduction and Objectives

As described in Chapter 3 of this report, the framework is divided into three phases: inspection, safety assessment and serviceability assessment. As part of the safety-assessment phase, the post-earthquake capacity of RC components is required to be checked to ensure that the capacity of components, which are expected to undergo inelastic deformations in future damaging earthquakes, has not been significantly impacted. As indicated in Section 3.3 and flowchart in Figure 3-6, the component-capacity assessment includes two checks:

1. ensure that the estimated earthquake deformation demands, θ_{EQ} , have not exceeded a safe deformation capacity limit, θ_{cap} , and
2. ensure that the component reinforcement has sufficient reserve fatigue capacity for a repeated design-level earthquake.

A simplified summary of check #1 of the component-level safety assessment is shown in Figure A-1.

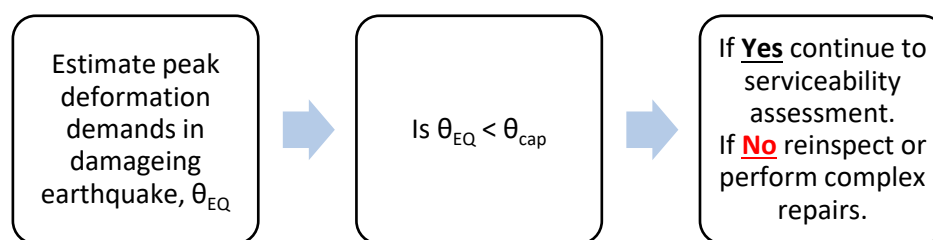


Figure A-1 Summary of component-level safety check #1 in assessment framework.

This appendix describes the studies undertaken to identify the safe deformation capacity limit, θ_{cap} , defined here as the deformation below which prior cycles do not influence the ultimate drift capacity of the component. In order to determine θ_{cap} , a thorough investigation of available experimental data on the impact of various loading protocols on the deformation capacity of damaged RC components was undertaken.

The focus of this investigation is on the performance of ductile RC frame components including columns, joints, and beams.

It should be noted, as this is a component-level assessment, the deformations applied in the experiments assessed in this study represent chord rotations of components in an actual frame structure. For regular moment-frame structures, story drift ratios (as used in the system-level assessment in Chapter 3 and Appendix B) will typically be larger than the corresponding component-level chord rotations referred to in this appendix; however, for some frames with short beam spans or irregularities the chord rotations can be larger than the story drift ratio.

A.2 Proposed Safe Deformation Limit, θ_{cap} , for Earthquake-Damaged Components

Typical experimental investigations of RC components for seismic performance involve the application of reversed-cyclic demands of increasing magnitude. Such a loading protocol allows for the assessment of energy-dissipation capacity, strength, stiffness, and deformation capacity, all of which allow inferences to be made about the performance of such components under real seismic action.

In a post-earthquake safety assessment, an engineer needs to determine if the prior loading from the damaging earthquake has reduced the deformation capacity of any components in the structure. For this purpose, it is desirable to identify a safe deformation limit below which it can be reliably assumed that the prior earthquake loading has not impacted the component-deformation capacity. To propose such a safety limit, θ_{cap} , loading cycles at or below any proposed limit must be investigated to assess if such cycles will impact the component performance in future earthquakes. In particular, this investigation is focused on assessing any significant impacts on deformation capacity of frame components.

Key components of performance that are investigated in this appendix include the following, which are further defined in Section A.3.1.3.4:

- Impact of cyclic loading on onset of strength degradation
- Impact of cyclic loading on deformation capacity (defined as the displacement at which a 20% reduction in lateral load carrying capacity is recorded).
- Role of detailing or other specimen characteristics on the impact of cyclic loading

Four experimental studies by El-Bahy et al. (1999), Pujol et al. (2006), Marder (2018) and Opabola et al. (2019) were identified as providing key evidence on the limited impact of prior deformation cycles below

approximately 0.02 rad. An overview of these studies is outlined below, followed by a recommendation for θ_{cap} .

A.2.1 Prior Research Investigating Significance of Deformation Cycles Below 0.02 rad

A.2.1.1 El-Bahy et al. (1999)

This study included an experimental program on 12 nominally identical reinforced concrete column specimens, tested in single curvature. These specimens were scaled versions of a prototype column, designed in accordance with the AASHTO guidelines (1989). The objective of the study was assessing the low-cycle fatigue performance of the columns in the absence of buckling in the reinforcement. The columns were all of circular cross section with shear span to depth ratios of 4.5, reinforcement ratios of 2.08%, and a transverse spiral reinforcement with center-center spacing (s) equal to two times the longitudinal bar diameter, d_b . This is a significantly lower s/d_b ratio than would be used in most ductile columns (typically $s/d_b \geq 4$), but enabled investigation of the impact of low-cycle fatigue in the absence of bar buckling. All specimens were tested under a constant axial load ratio of 10% ($P/A_g f'_c$).

A variety of loading histories were applied to the columns to investigate the impact of low-cycle fatigue and damage accumulation on their response to repeated inelastic loading cycles. A reference specimen (A1), subjected to monotonic loading, achieved a lateral displacement of 11% chord rotation, prior to failure (defined as a 20% reduction in lateral resistance). Five other protocols were used in the study, including a standard cyclic loading protocol, as well as multiple constant amplitude loading histories with cycles to failure at 2%, 4%, 5.5% and 7% chord rotation (Figure A-2). The results for these specimens are summarized in Figure A-3. Of specific interest, is the result for specimen A3 with 150 constant amplitude cycles of 2% chord rotation without experiencing failure or significant reduction in resistance ($< 5\%$). Following these cycles, the specimen was subjected to a monotonic push to $\sim 10\%$ prior to the test being stopped without a 20% or greater drop in strength. In contrast, specimens subjected to larger constant amplitude cycles, failed at a significantly lower number of cycles, ranging between 3 (for 7% chord rotation) and 26 (for 4% chord rotation). The results outlined above support the conclusion that, as long as bar buckling is restrained, cycles at or below 2% do not impact the deformation capacity of an RC column.

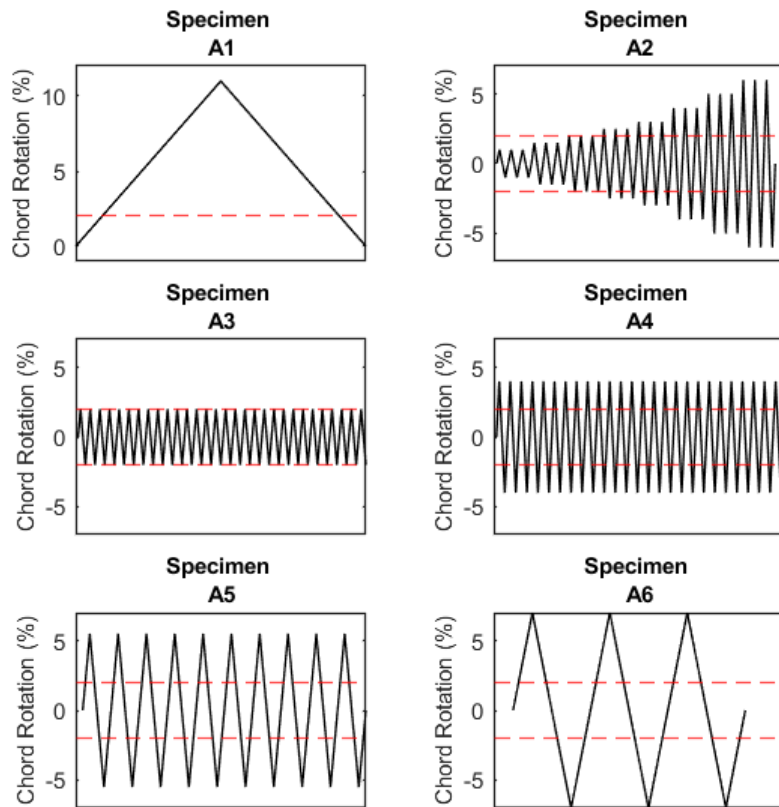


Figure A-2 Variation in loading protocol applied to column specimens A2, A4, A5 and A6 by El-Bahy et al. (1999). Dashed red lines represent +/- 2% chord rotation.

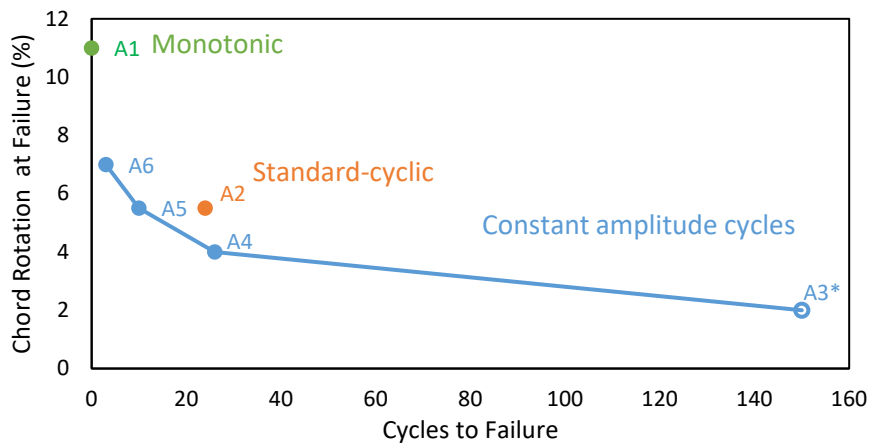


Figure A-3 Variation in cycles to failure for column specimens tested by El-Bahy et al. (1999).
 * Specimen A3, shown as a hollow datapoint, did not fail and cyclic loading was stopped following the application of 150 cycles at 2%.

A.2.1.2 Pujol et al. (2006)

This study conducted an experimental investigation on the seismic performance of 8 column assemblies. The specimens consisted of two cantilever column specimens connected to a central stub and tested under a constant axial load ratio ($P/A_g f'_c$) of 10% or 20%. Lateral loading was

applied to both specimens simultaneously through displacements induced via the central stub. In addition, specimens were constructed with 3 different transverse reinforcement spacings corresponding to s/d_b ratios of 2, 3 and 4. Varying displacement histories were applied to the columns consisting of initial cycles at chord rotations of 1%, 2% or 3% , followed by cycles to failure at either 3% or 4%.

The applied cycles for each specimen are presented in Table A-1 along with the summary of specimen parameters and experimental results. Each specimen eventually failed at the drift ratio corresponding to the last set of cycles listed in the table.

Table A-1 Pujol et al. (2006) Experimental Results Summary

Specimen ID	s/d_b	Axial Load Ratio (%)	No of Cycles at Chord Rotation				No. of cycles to failure at largest chord rotation
			1%	2%	3%	4%	
10 – 3 - 1.5	2	10	-	-	7	11	10
20 – 3 - 1.5	2	20	-	-	7	10	9
10 – 3 - 2.25	3	10	-	-	19	-	15
10 – 1 - 2.25	3	10	7	-	20	-	15
10 – 2 - 2.25	3	10	-	7	16	-	12
10 – 3 - 3	4	10	-	-	9	-	7
10 – 2 - 3	4	10	-	7	7	-	5
20 – 3 - 3	4	20	-	-	9	-	8

Two specimens were tested with an s/d_b ratio of 2. Both specimens were subjected to seven full cycles at a chord rotation of 3%, followed by cycles at 4%. These specimens were able to withstand 9-10 cycles at 4% prior to observation of a 20% drop in lateral resistance. An increase in axial load ratio from 10% to 20% in these specimens only resulted in a reduction of a single 4% cycle prior to failure. These specimens indicate that for tight transverse reinforcement spacing, likely precluding bar buckling, increases to axial load ratios up to 20% do not cause any significant reductions in cyclic capacity to failure. As identical loading was applied to both specimens, no specific inferences with respect to the impact of lower level cyclic loading can be made from these results.

Three specimens were tested with an s/d_b ratio of 3, all tested at 10% axial load ratio. The focus with these specimens was the impact of variation in applied cyclic content. A benchmark specimen was tested to failure at constant amplitude loading at 3% chord rotation and was able to withstand 15 cycles prior to failure. Two other specimens were subjected to seven initial cycles at 1% or 2% chord rotation respectively, prior to cycling to failure at 3% chord rotation. The cycles at 1% did not show any impact on the number of cycles to failure, while the cycles at 2% saw

a slight reduction, with the number of cycles to failure at 3% chord rotation reducing from 15 to 12.

This result indicates clearly that the prior cycles at 1% chord rotation had no impact on the cyclic capacity to failure, while limited impact was noted from prior cycles at 2% chord rotation. While this reduction should be noted, a total of 19 full cycles at 2 and 3% were still withstood prior to a 20% drop in strength in the latter specimen, considerably larger cyclic content than expected in design-level and even MCE ground motions.

Three other specimens were tested with an s/d_b ratio of 4. Two specimens were not subjected to any initial cycles and were instead cycled at 3% chord rotation to failure, at a constant axial load ratio of 10% or 20%, respectively. A third specimen was subjected to seven cycles at a chord rotation of 2% prior to being cycled at 3% to failure with an axial load ratio of 10%. The results showed that the cycles at 2% caused a reduction of two cycles at 3% prior to failure. The increase in axial load did not show any evidence of impacting the number of cycles to failure at 3%.

These results indicate that the initial cycles at a chord rotation of 2% did have some impact on the number of cycles to failure (reducing from 9 to 7 cycles at 3%), however similar to the previous set of columns and considering an estimated yield drift of 0.84% drift, the specimen was subjected to a significant number of inelastic cycles (12 in total) prior to a degradation in stiffness resulting in a 20% reduction in resistance.

It should be noted that as the specimens in this study do not apply conventional cyclic loading protocols, it is not possible to assess direct changes in deformation capacity. Rather, the results assess the number of cycles which cause a large enough degradation in stiffness resulting in a 20% reduction in resistance which sheds light on changes in deformation capacity while not providing a direct quantitative change.

Overall, the study shows that variations in axial load up to 20% did not have any impact on specimen performance while variations in s/d_b ratio caused a reduction in the number of cycles to failure. At s/d_b ratios of 3 and 4, initial cycles at 2% chord rotation resulted in ~20-30% reduction in the number of cycles to failure, in comparison to benchmark specimens. It is noted, however, that in both cases where this was recorded, the specimens were subjected to a larger number of inelastic cycles prior to a 20% reduction in resistance than their benchmark counterparts, and thus it can reasonably be assessed that the impact of cycles even up to 2% drift had a limited impact on the performance of the specimens. A more detailed analysis of the number of inelastic cycles applied is provided in section A3.2.2.1 of this appendix where the concept of an equivalent number of cycles is introduced.

A.2.1.3 Marder (2018)

As part of a study on the residual capacity and repair of reinforced concrete beams, Marder investigated 17 different combinations of loading histories, axial restraint and loading rate on the behavior of ductile, flexure-controlled beam elements. The specimens were constructed as 80% scale replicas of beams from a typical ductile RC frame structure in New Zealand, with $s/d_b = 6$ and shear-span to depth ratio of 3.58. Variations of passive axial restraint systems were applied to the specimens with unstressed post-tensioning rods which applied restraint to the beams with increasing beam elongation. A maximum axial load of $0.05A_g f'_c$ resulted from the restraint systems.

The prototype building used for the design of the specimens, was a perimeter moment-frame structure in Christchurch, New Zealand designed in accordance with NZS 3101:2006 and NZS 1170.5:2004 (Bull, 2008), using a design ductility (similar to R-factor) of 4, resulting in a base shear coefficient of 3.2% of building weight.

A variety of loading protocols were developed in this study, ranging from standard cyclic loading, to the application of earthquake displacement histories which were derived from response-history analysis of the prototype building. Beam-end rotations extracted from the analysis of the model were applied to the specimens. A full summary of the specimen loading protocols, and deformation capacities is provided in Table A-2. Two acceleration records, one for a long duration (LD) and another for a pulse-type (P) earthquake were selected for the building analysis. These records were then scaled to produce peak beam chord rotation from the response history analysis of 1.4% (P-1, LD-1) and 2.2% (P-2, LD-2). In specimens where these displacement histories were applied, a cyclic protocol, omitting all cycles at or below the peak displacement of the earthquake history were also applied.

In addition, a cyclic loading protocol was applied to an undamaged specimen, omitting all cycles at or below 2.2% chord rotation (specimen CYC-NOEQ). Figure A-4 presents a comparison of the hysteretic behaviour of the monotonic (Mono), standard cyclic (CYC) and cyclic omitting cycles below 2.2% (CYC-NOEQ) specimens. A clear difference is seen between the cyclic and monotonic specimens; however, the figure clearly demonstrates there was no difference in the performance of the cyclic specimens, regardless of the omission of cycles at or below 2.2% chord rotation, highlighting the limited impact of these lower-deformation cycles.

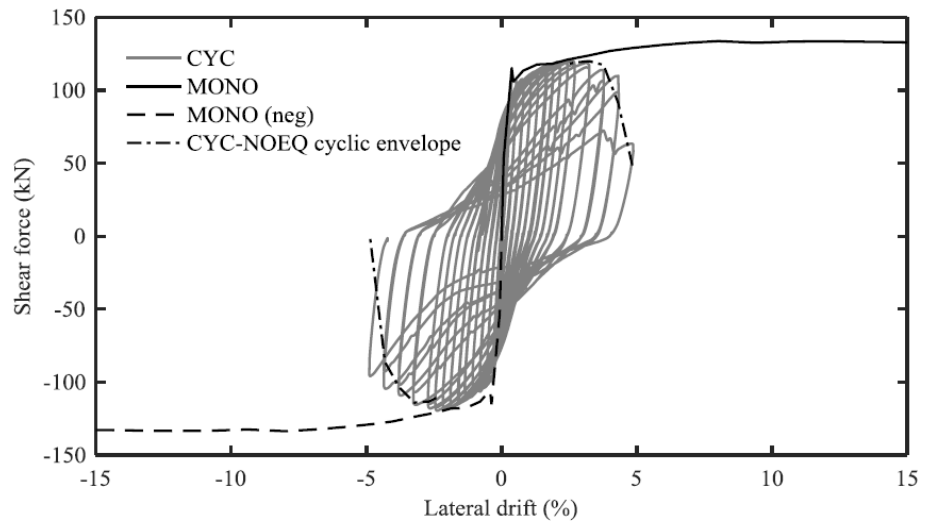


Figure A-4 Comparison of specimen hysteresis from beams tested by Marder (2018). Figure adapted from Marder (2018).

Marder concluded that cycles up to 2.2% chord rotation did not have a significant impact on the deformation capacity of the specimens and noted that in no cases was the slope of the load-deformation envelope for any specimen negative during cycles at or below 2.2%. There was a reduction in the displacement capacity in 4 of the 17 specimens following earthquake-type loadings (both P and LD ground motions), however this was attributed to localized concentration of damage with excessive shear sliding, rather than failure due to the applied number of cycles. It should be noted, however, that in cases where a reduction in deformation capacity was observed, similar specimens with a higher number of loading cycles saw larger deformation capacities, where localized damage concentration was not observed. Marder concluded that these variables can be regarded as independent of each other.

Table A-2 Marder (2018) Experimental Results Summary

Specimen ID	Peak Drift of Earthquake Displacement History (%)	No. Effective Cycles up to 2% Chord Rotation*	Drift at 20% Drop in Resistance (%)	Cause of Loss in Resistance
CYC	N/A	5.6	4.34	Cyclic Degradation
CYC-DYN	N/A	5.6	3.26	Cyclic Degradation
CYC-NOEQ	N/A	0	4.34	Cyclic Degradation
CYC-ER	N/A	5.6	4.34	Bar Rupture
CYC-LER	N/A	5.6	4.34	Cyclic Degradation
P-1	1.4%	4.1	4.88	Bar Rupture
P-2	2.2%	0.5	3.26	Cyclic Degradation
P-2-S	2.2%	0.5	3.8	Bar Rupture
LD-1	1.4%	7	4.34	Cyclic Degradation
LD-1-R	1.4%	7	4.34	Cyclic Degradation
LD-2	2.2%	5.4	3.26	Cyclic Degradation
LD-2-S	2.2%	5.4	3.8	Cyclic Degradation
LD-2-R	2.2%	5.4	4.34	Cyclic Degradation
LD-2-ER	2.2%	5.4	4.34	Bar Rupture
LD-2-LER	2.2%	5.4	4.34	Bar Rupture
LD-2-LER-R	2.2%	5.4	4.34	Bar Rupture

* Notes: The number of effective cycles at 2% chord rotation were calculated by Marder using a range counting methodology introduced in Section A3.1.1.

The notation ‘S’ indicates displacement histories which were applied statically. ‘DYN’ indicated a dynamic loading rate for specimens with cyclic loading histories. ‘NOEQ’ indicates the omission of cycles below the peak drift of the earthquake displacement history. ‘R’ indicates specimens which were repaired using epoxy injection and mortar patching following application of earthquake displacement history. ‘ER’ represents specimens with application of axial elongation restraint. ‘LER’ indicates those specimens which has ‘Limited Elongation Restraint’, representing a lower level of axial restraint to ‘ER’ specimens.

A.2.1.4 Opabola et al. (2019)

This study focused on the performance of RC beam elements which formed single-crack mechanisms at the beam-joint interface region. The study investigated the low-cycle fatigue behavior of the beams as well as the impact of epoxy injection on their post-earthquake performance. The beams were all constructed to form a single interface crack with intermediate reinforcement terminating at the beam-joint interface, and a cold-joint representing the connection between cast-in place columns and pre-cast beams. The specimens were damaged under simulated

earthquake loading and were designed with an s/d_b ratio of 4.8 and tested at a shear-span to depth ratio of 2.8.

As part of the applied loading protocols, an earthquake-type beam displacement history was derived from time-history analysis of a building model. This was similar to the methodology utilized by Marder (2018) in the previous study but using a ground motion from the 2016 Kaikoura earthquake and a model for a RC frame building located in Wellington, New Zealand. The derived displacement history was subsequently scaled to represent two earthquake intensities having peak chord rotation of 1% and 3%. One of the beam specimens was subjected to both records to simulate earthquake damage. Following the application of these displacement records, the critical crack at beam-joint interface was injected with epoxy resin.

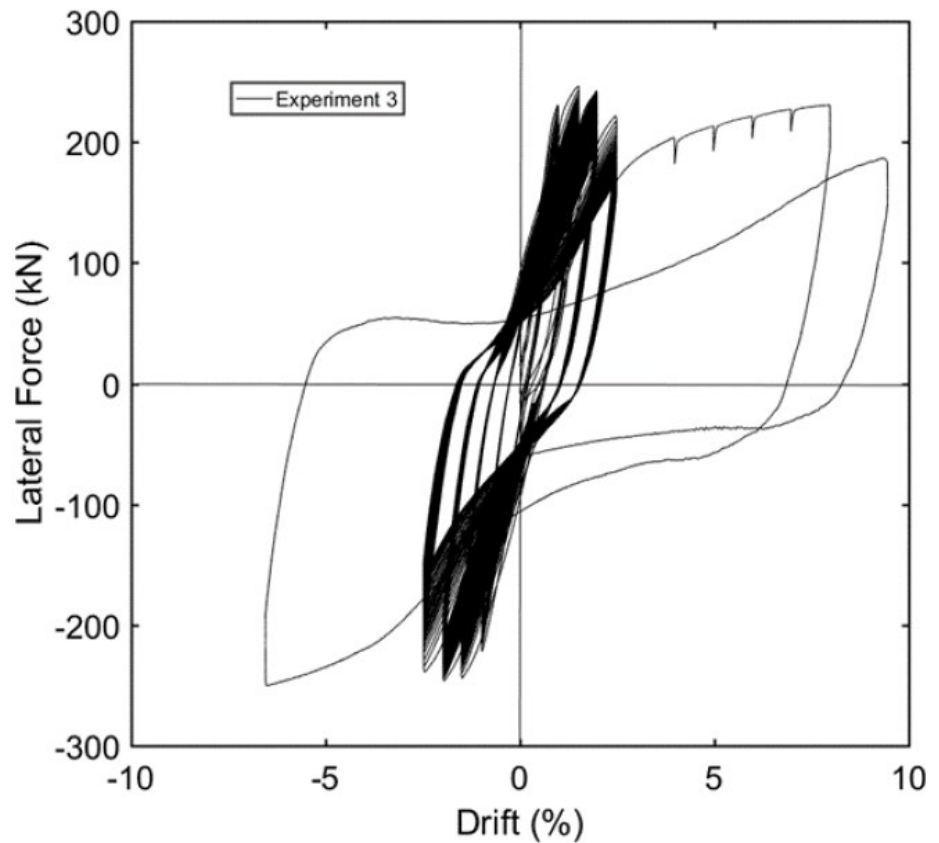


Figure A-5 Hysteretic behavior of beam specimen tested by Opabola et al. (2019). Figure adapted from Opabola et al. (2019). Note drift in this figure is in reference to a component drift.

A passive axial restraint system, similar to that used by Marder (2018), was applied to the specimen to avoid a sliding shear failure and the repaired specimen was then subjected to displacement cycles ranging from a chord rotation of 1 to 2.5%. In total, the repaired specimen was subjected to 15 cycles at 1%, 25 cycles at 1.5%, 40 cycles at 2% and 30 cycles at 2.5%. The specimen was then pushed to a chord rotation of 9.5% prior to seeing a 20% reduction in resistance (Figure A-5). No

buckling of the reinforcement was observed until a chord rotation of 4%. It should be noted that the specimen did see a reduction in resistance during the cycles at 2.5%, however the application of a large monotonic push resulted in the specimen regaining its resistance prior to failure. The results of the test described above shows that the beam was able to withstand 80 full cycles at or below 2% chord rotation without any notable reductions in strength. The results are in line with those observed in the previously outlined studies, where a limited impact is observed on the performance of the beam from cycles at or below a chord rotation of 2%.

A.2.1.5 Implications of Prior Experimental Studies on a Proposed θ_{cap}

The studies outlined above all provide evidence that displacement cycles at or below a chord rotation of 0.02 rad have limited impact on the deformation capacity of the frame elements. This was observed under a variety of configurations with s/d_b ratios ranging from 2 to 6, shear span to depth ratios ranging from 2.8 to 4.5, axial load ratios of 0 to 20% and shear stress/ $\sqrt{f'_c}$ ratio of 0.08 to 0.48 (in MPa).

Based on this initial investigation of prior experimental research, a hypothesized chord rotation limit of $\theta_{cap} = 0.02$ rad was proposed. This limit represents the component deformation demand for ductile RC frame components below which cyclic loading is not expected to have an impact on the deformation capacity.

As described in the next section, a larger database of tests was compiled with a variety of specimen and loading characteristics to more thoroughly assess the validity of the proposed limit of $\theta_{cap} = 0.02$ rad.

A.3 Formation of a Database of Experimental Research on Ductile Components

A database of existing experimental work was formed, focusing on studies on ductile frame elements with variations in loading protocols. A secondary focus was placed on obtaining specimens of various design characteristics such as detailing and applied axial load levels. In total, the selected database includes 24 beam specimens, 29 joint specimens, and 52 column specimens. The details for each specimen in addition to all data discussed in this appendix can be found tabulated in Section A.6.

The following requirements based on the provisions of the New Zealand Concrete Design Standards (NZS 3101:2006) ACI-318-19 Design Guidelines were placed on the characteristics of the selected specimens. The restrictions were placed to ensure that the database is representative of frames with ductile flexural response in beam and column elements, avoiding brittle failure mechanisms.

- $s/d_b \leq 6$ in potential plastic hinge regions of beams and columns
- axial load ratio, $(P/A_g f_c) \leq 40\%$ for columns
- No splicing of reinforcement in potential plastic hinge regions
- Joint or beam-column subassembly tests should form ductile flexural yielding mechanism in their beams and satisfy minimum joint transverse reinforcement requirements of the latest codes which the specimens are designed to, in addition to a minimum meeting the joint reinforcement recommendations of the Joint ACI-ASCE Committee 352 - 1976.

The database can be found in M. Sarrafzadeh’s PhD Thesis (under review) entitled “Residual Capacity and Reparability of Moderately-Damaged Reinforced Concrete Ductile Frame Structures” (Sarrafzadeh, 2021).

A.3.1 Database Overview

The database of ductile RC frame component tests was compiled to assess the impact of cyclic loading at or below the proposed θ_{cap} of 2% chord rotation. In order to evaluate a range of experimental procedures with multiple variations across specimen and loading characteristics, a consistent assessment approach was selected to allow a fair comparison of the available data. For each study identified as meeting the initial criteria, all study metadata and loading characteristics were collected and used in the analysis as outlined below.

A.3.1.1 Assessment of Applied Loading Protocol

In order to assess the impact of different loading histories in a consistent manner, a range counting methodology was used to provide a normalized value of the number of cycles applied to each specimen.

To achieve this, the concept of an effective number of cycles at a benchmark chord rotation was used. Malhotra et al. (2002) proposed a range counting equation where each displacement range in a loading protocol could be presented as a proportion of a chosen benchmark displacement (e.g., equivalent number of cycles at 2% chord rotation). The equation proposed by Malhotra et al. is presented below in equation A-1.

$$N_{eff} = \frac{1}{2} \sum_{i=1}^{2n} \left| \frac{u_{r,i}}{u_{r,max}} \right|^C \quad (A-1)$$

where:

n = represents the number of half cycles experienced by the element.

- $u_{r,i}$ = peak displacement for each half cycle, i ,
- $u_{r,max}$ = $2 \times$ the peak drift experience by the element and
- C = constant used to give higher weighting to larger displacement cycles. The study by Malhotra et al. proposed $C = 2$.

As outlined in Malhotra et al. (2002) the equation was derived using the damage accumulation model proposed by Miner (1945) and low-cycle fatigue relationships for steel proposed by Coffin (1954) and Manson (1954).

As such, the determination of an effective number of cycles is primarily based on the consumption of reinforcement fatigue life by each half cycle of displacement. As stated above, the use of effective number of cycles in this appendix is intended as a tool for the comparison of various dissimilar loading protocols. While effective number of cycles values will be presented throughout this appendix, the values are relied on in a relativistic manner and are used to capture variations in cyclic loading applied to specimens.

For the purposes of this study, a benchmark chord rotation of 2% was selected, to allow the representation of each loading protocol as an effective number of cycles at 2%. Unless specified otherwise, where an effective number of cycles (N_{eff}) is referred to in this appendix, the effective number of cycles at a chord rotation of 2% is being referenced.

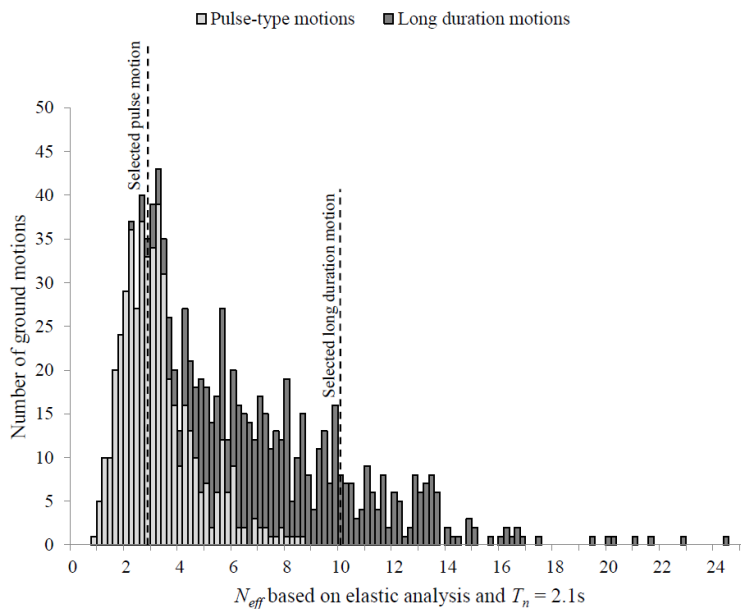


Figure A-6 Distribution of N_{eff} at peak displacement for a range of ground motion records as analyzed by Marder (2018).

Based on the methodology proposed by Malhotra et al. (2002), Marder (2018) conducted analysis of 972 ground motions to provide insight on

the typical number of cycles that are expected from a wide range of earthquake records.

Marder extracted displacement histories for each ground motion for an elastic single degree of freedom with $T=2.1$ sec (corresponding to the period of the prototype building described previously), with a C constant of 2 used in equation A-1. Calculating the effective number of cycles at peak displacement for each ground motion, a distribution of the number of cycles expected in a variety of different ground motion types was obtained as shown in Figure A-6. The analysis found that 87% of the considered ground motions had an effective number of cycles at peak drift below 10.

A.3.1.2 Extraction of Backbone Data

In order to use the published materials to assess all specimens in a consistent manner, the backbone curves for each specimen in the database were extracted using a manual digitization tool. The plots of specimen force-displacement response were used to trace the overall backbone curves for each specimen in both the positive and negative loading directions. An example of the digitized backbone curves is shown in Figure A-7. The backbones presented in this figure have been normalized based on the peak strength of each individual specimens, in order to present a clear comparison of the deformation capacity of each specimen. In addition, each backbone is color coded based on the N_{eff} value calculated based on the specific loading protocol applied to the specimen, as outlined in the previous section. Colors ranged from green to red representing an increase in N_{eff} . This is further detailed in the discussion of the results below.

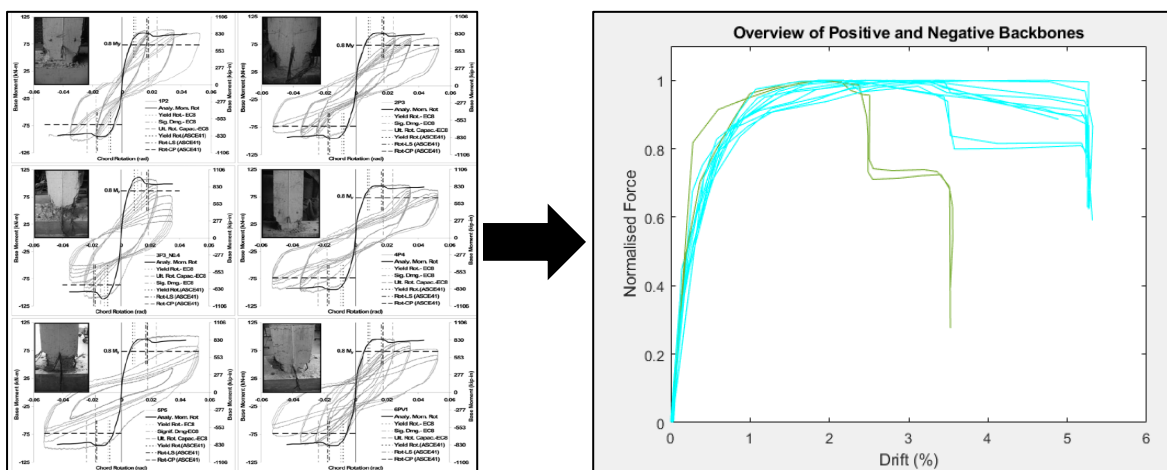


Figure A-7 Example of digitization of backbone data from hysteresis plots. Hysteresis plots were obtained from Acun and Sucuoglu (2010).

A.3.1.3 Determination of Component Performance Characteristics

To assess the performance of specimens and any potential impacts of the various loading protocols, the following performance characteristics were extracted from the digitized backbone data:

- Deformation Capacity
- Chord Rotation at Observation of Bar Buckling
- Maximum Chord Rotation Prior to Lateral Resistance Degradation
- Estimated Yield Rotation
- Maximum Plastic Rotation Prior to Strength Degradation

A.3.1.3.1 Deformation Capacity

The deformation capacity for each component was determined based on the backbone data. The conventional approach to assessing failure as a 20% drop in resistance for each specimen was adopted (see Figure A-8). This was determined in both the positive and negative direction of loading for each specimen and the minimum chord rotation was adopted as the deformation capacity for each specimen. In a minority of cases where specimens did not fail in either loading direction, the higher of the maximum displacement values in the two directions was adopted to represent a lower bound on the deformation capacity of the specimen.

A.3.1.3.2 Chord Rotation at Observation of Bar Buckling

Where data was provided by the original reference, the point in the loading of each specimen at which buckling was observed in the longitudinal reinforcement was recorded. No buckling was reported in the beams of any of the joint subassemblies documented in the database and was only reported or observed in approximately 50% of the beam and column specimens in the database.

A.3.1.3.3 Maximum Chord Rotation Prior to Lateral Resistance Degradation

An important characteristic in ductile elements is the ability to maintain lateral resistance during repeated inelastic deformations. As such, a key performance indicator is the level of deformation that a specimen can sustain without experiencing any degradation in resistance. This was simply determined as the maximum chord rotation prior to a reduction in resistance from the digitized backbones (see Figure A-8). This point did not always imply a negative slope in the backbone curve of the specimen as the digitized backbone does not distinguish in-cycle and between-cycle degradation in resistance.

A.3.1.3.4 Estimated Yield Rotation

The ACI 369 rectangular column database (Ghannoum et al., 2010) estimates the yield rotation of a RC component based on a secant line to 70% of peak strength. Because of its simplicity, this methodology was adopted in this study as illustrated in Figure A-8.

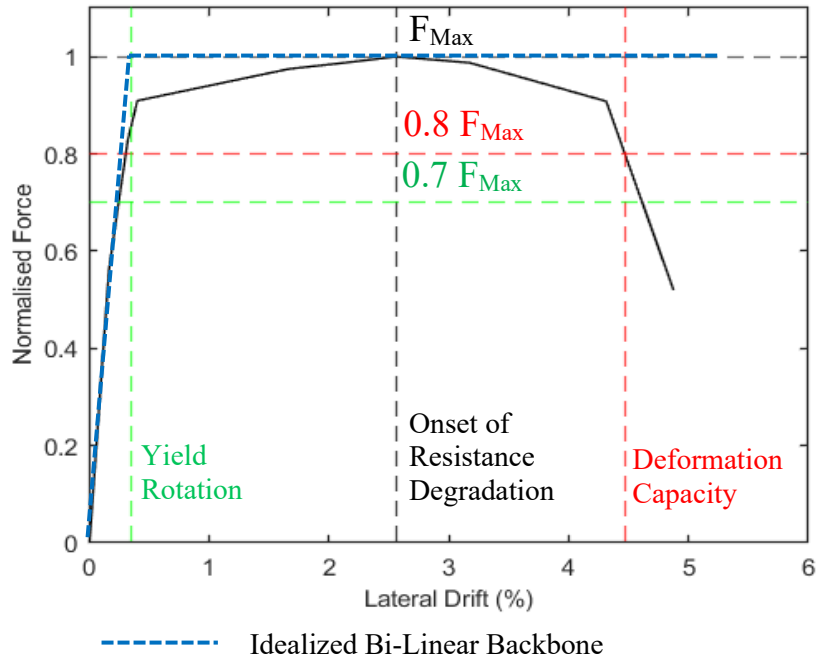


Figure A-8 Methodology used to estimate yield rotation, onset of strength degradation and deformation capacity from backbone data.

A.3.1.3.5 Maximum Plastic Rotation Prior to Strength Degradation

In order to assess the plastic rotation experienced by each specimen, the backbone data was converted to shear force vs. plastic chord rotation. The methodology used to convert the backbones is outlined below and shown in Figure A-9. The plastic rotation for deformations greater than the estimated yield rotation were calculated in accordance with equations A-2 to A-4. Note, all equations are based on units of mm, rad and MPa.

$$Inelastic\ Rotation = \left(\frac{\Delta_{Tot}}{L} - \theta_y \right) \cdot \frac{L}{L_{Plas}} \quad (A-2)$$

$$L_{Plas} = L - \left(\frac{l_p}{2} - 0.022 \cdot f_y \cdot d_b \right) \quad (A-3)$$

$$l_p = k_{lp} L_c + L_{sp} \geq 2L_{sp} \quad (A-4)$$

where:

Δ_{Tot} = total end deformation of the specimen in mm

L = total shear span of the specimens in mm

θ_y = yield rotation in rad

f_y = longitudinal steel yield strength

d_b = longitudinal bar diameter

$k_{lp} = 0.2(f_u/f_y - 1) \leq 0.08$

L_c = distance of the critical section from the point of contraflexure

$L_{sp} = 0.022 \cdot f_y \cdot d_b$, represents the depth of strain penetration included in the plastic hinge length (Priestley et al. 2007), with f_y being the probable yield strength of longitudinal reinforcement and d_b being the average longitudinal bar diameter.

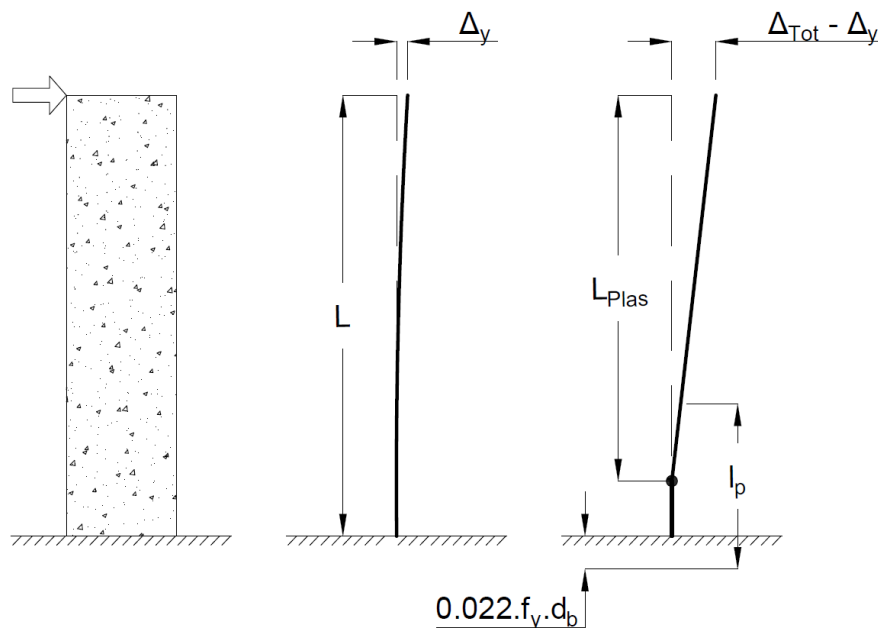


Figure A-9 Deformation model used to estimate plastic rotation concentrated at center of rotation.

A.3.2 Database Results Summary and Discussion

A.3.2.1 Column Specimens

In total, 52 column specimens which met the modern ductile detailing requirements outlined in Section A.3 were processed from 10 separate experimental investigations. Studies by El-Bahy et al. (1999), Lehman et al. (2001), Esmacily et al. (2004), Hindi et al. (2006), Pujol et al. (2006), Acun & Sucuoglu (2010), Goodnight et al. (2013), Ou et al. (2014), Nojavan et al. (2015) and Xing et al. (2017) were analyzed. Of the 52 specimens, 52% of the specimens had a s/d_b ratio of 4 or less. The shear span to depth ratio that the specimens were tested at ranged between 2.25 to 5.71 and the applied axial load ratio during testing ranged between 2 to 28.5%. A general summary of specimen properties is presented in Figure A-10 with full details provided in Section A.6 Table A-4 to A-6.

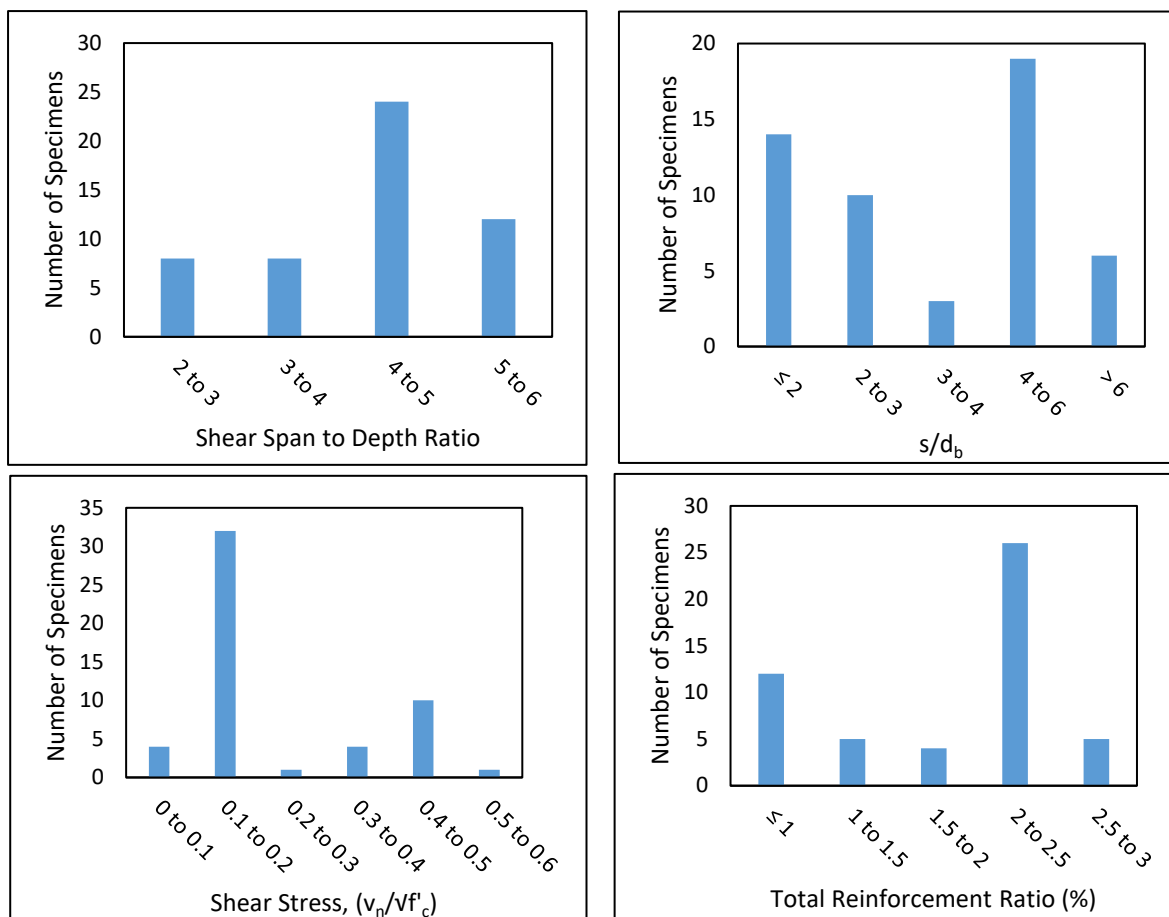


Figure A-10 General overview of specifications for column specimens included in database.

A.3.2.2 Studies with Constant Amplitude Loading Cycles

The studies by El-Bahy et al. (1999), Pujol et al. (2006) and Xing et al. (2017) all used loading protocols with the application of constant amplitude cycles, typically used to assess the low cycle fatigue performance of specimens. The nature of such loading protocols dictates that the specimens will fail at the deformation level they are being cycled at. Such results do not present a direct deformation capacity, like that obtained through loading protocols with gradually increasing displacement amplitudes, and as such these tests are analyzed in this section separately.

El-Bahy et al. (1999)

The details of this study were outlined previously in Section A.2.1.1 where it was shown that a significant reduction in the number of cycles to failure were observed when the amplitude of the applied loading cycles was increased from 2 to 4% chord rotation and beyond. Figure A-11 presents the effective number of cycles at 2% chord rotation prior to failure (N_{eff}) at the various constant amplitude magnitudes. A clear trend is seen in the reduction of N_{eff} to failure as the magnitude of the constant amplitude cycles is increased. This provides good evidence to show that

large amplitude cycles do result in detrimental impact on the deformation capacity of the columns. It should be noted that no column was tested at 3% chord rotation and Specimen A3 which was cycled at 2% drift, did not fail after being subjected to 150 cycles as indicated in Figure A-11.

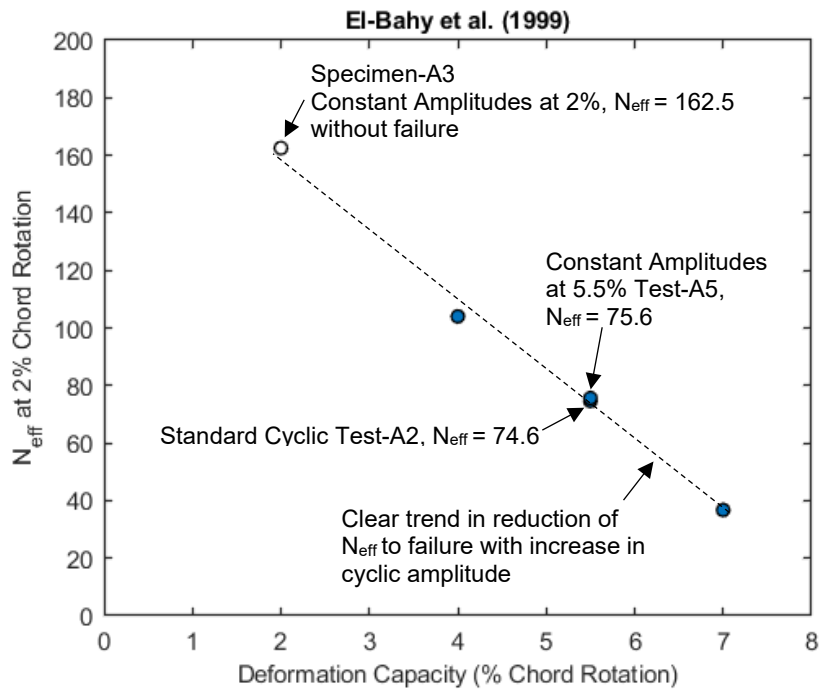


Figure A-11 Comparison of the total Number of effective cycles prior to failure at various constant amplitude displacements for columns tested by El-Bahy et al. (1999) [REF]. Specimen A3 is represented by a white data point to indicate it did not experience failure at the plotted N_{eff} .

In addition to the constant amplitude tests, the standard cyclic specimen, A2 is also plotted on Figure A-11. This specimen achieved a deformation capacity of 5.5%, the same as the magnitude of constant amplitudes applied to specimen A5. Interestingly, the standard cyclic specimen A2 also displayed nearly the same N_{eff} as the constant amplitude specimen A5.

Overall, the results outlined here show a clear trend in a reduction of N_{eff} to failure as the magnitude of the constant amplitude cycles above 2% chord rotation is increased.

Pujol et al. (2006)

As outlined in Section A.2.1.2 for the specimens in this study, the application of initial cycles at 2% chord rotation appeared to result in a reduction in the number of cycles at 3% chord rotation. It was observed that a virgin specimen with an s/db ratio of 3 was able to resist 15 cycles at 3% prior to failure.

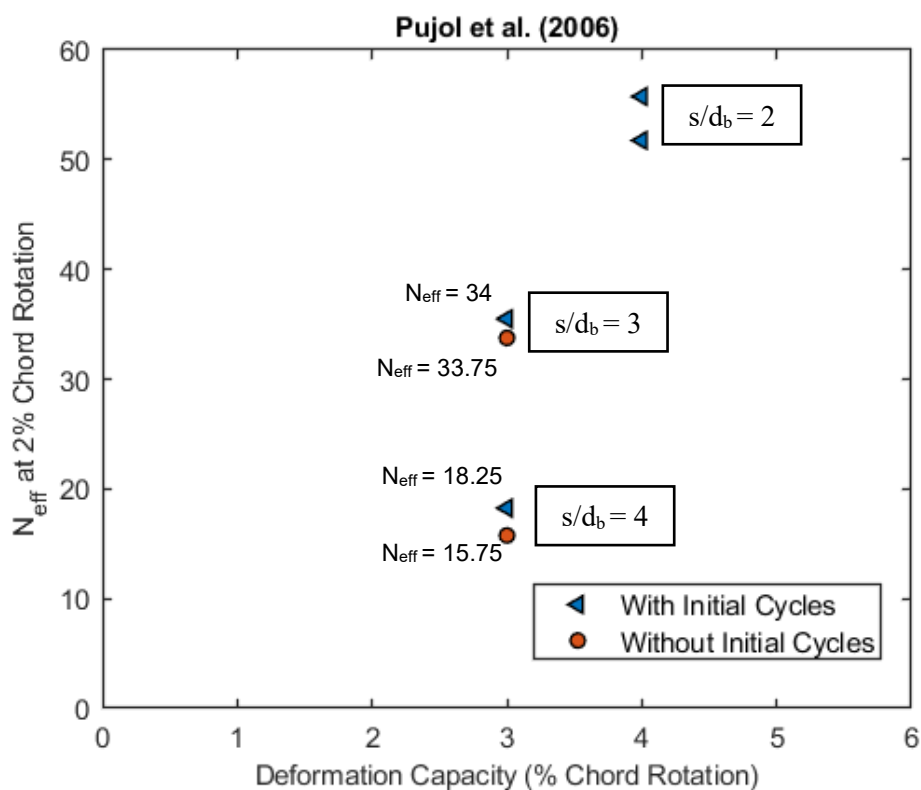


Figure A-12 Comparison of the total Number of effective cycles prior to failure at various constant amplitude displacements for columns tested by Pujol et al. (2006).

As outlined in Table A-1, a similar specimen subjected to 7 initial cycles at 1% chord rotation also resisted 15 cycles at 3% prior to failure, while a specimen with 7 initial cycles at 2% chord rotation, failed following 12 cycles at 3%. A similar trend was observed in specimens with an s/d_b of 4 where the number of cycles to failure at 3% chord rotation reduced from 7 to 5 with initial cycles applied at 2%. These numbers seem to suggest a detrimental impact due to the initial cycles at 2% chord rotation, however, the N_{eff} prior to failure for each specimen, refutes this observation, as shown in Figure A-12. Using N_{eff} values for the various loading protocols in this study suggests that the specimen with initial cycles at 2% chord rotation, resisted the same or a higher number of effective cycles prior to failure in comparison to the specimens without the initial cycles. Hence, while the number of cycles at 3% chord rotation to failure reduced between the pairs of specimens outlined above, the N_{eff} values prior to failure are essentially unchanged regardless of the presence of cycles at 1 or 2% chord rotation.

In addition to the observation with regards to initial cycles, it can also be seen in Figure A-12 that the reduction s/d_b resulted in a clear increase in the number of effective cycles to failure. Further analysis of the impact of transverse reinforcement spacing on the deformation capacity of column specimens is outlined later in this section of the appendix.

Xing et al. (2017)

This study focused on the application of low cycle fatigue type loading histories on columns specimens. As part of a larger subset of studies, the results for 5 of the columns are presented in this chapter. All columns were tested under identical conditions with axial load ratios of 20%, $s/d_b = 4.55$ and a shear span to depth ratio of 4.38. The specimens discussed here were subjected to constant amplitude cycles at 5.1%, 4.1%, 3.1%, 2.4% chord rotation, as well as one specimen subjected to a combination of cycles at 1.4% and 2.5% chord rotation. The results for these columns are shown below in Figure A-13 in the form of N_{eff} vs. deformation capacity. Similar to the tests by El-Bahy et al. (1999), a progressive reduction in the number of cycles to failure is observed as the magnitude of the constant amplitude cycles is increased.

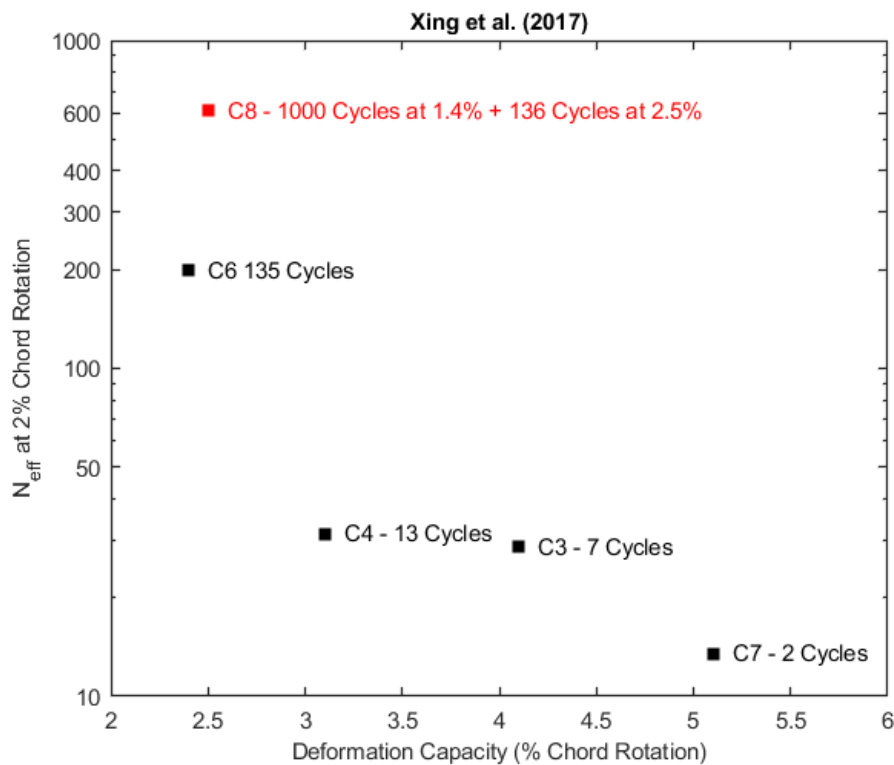


Figure A-13 Variation in cycles to failure for column specimens tested by Xing et al. (2017).

The results show that there is a marked reduction in N_{eff} when the deformation level is increased from 2.5% drift to 3% drift going from $N_{eff} = 200+$ in specimens C6 and C8 to $N_{eff} = 31.4$ in specimen C4. The number of effective cycles for specimens C6 and C8 are also significantly beyond what would reasonable be expected in even a long duration earthquake. In addition, the 1000 additional cycles at 1.4% chord rotation in specimen C8, had no impact on the number of cycles to failure at 2.5% chord rotation (135 and 136 for specimens C6 and C8, respectively). The results outlined here provide strong evidence that

cycles up to 1.4% chord rotation had no impact on the cyclic capacity of the tested columns, while the columns were also able to withstand a significant number of cycles at up to 2.5% chord rotation prior to failure.

A.3.2.2.3 Overall Column Database Results

This section outlines overall trends in the data collected from column specimens. The scatter plots in this section have omitted six specimens from a study by Hindi et al. (2010) and two specimens from Nojavan (2015), which had deformation capacities far exceeding the remaining specimens in the database. In addition, all specimens which were subjected to constant amplitude cycles in studies by El-Bahy et al. (1999), Pujol et al. (2006) and Xing et al. (2017) were also omitted as the deformation capacity for such cases is predetermined by the selected amplitude of the constant cycles.

A.3.2.2.4 Onset of Strength Degradation

Figure A-14 shows the distribution of chord rotation at the onset of decay in strength vs. the number of effective cycles at or below a chord rotation of 2%. On average, the specimens did not begin to decay in strength prior to a chord rotation of 3.25% +/- 1.3% (1 standard deviation) as illustrated in Figure A-14. Among individual studies, no trend was observed between the number of effective cycles applied, and a reduction in chord rotation at the onset of strength degradation. Only the study by Ou et al. (2014) suggests the possibility of earlier onset of degradation with an increase in the number of effective cycles applied, but this trend is not supported by the other studies. Closer examination of the Ou et al. (2014) study show that the specimen with a lower chord rotation prior to strength degradation was subjected to 10 cycles at 3% chord rotation, in comparison to the better performing specimen which was subjected to only one cycle at each displacement amplitude. The reduction observed in this study is thus likely due to loading above 2% chord rotation.

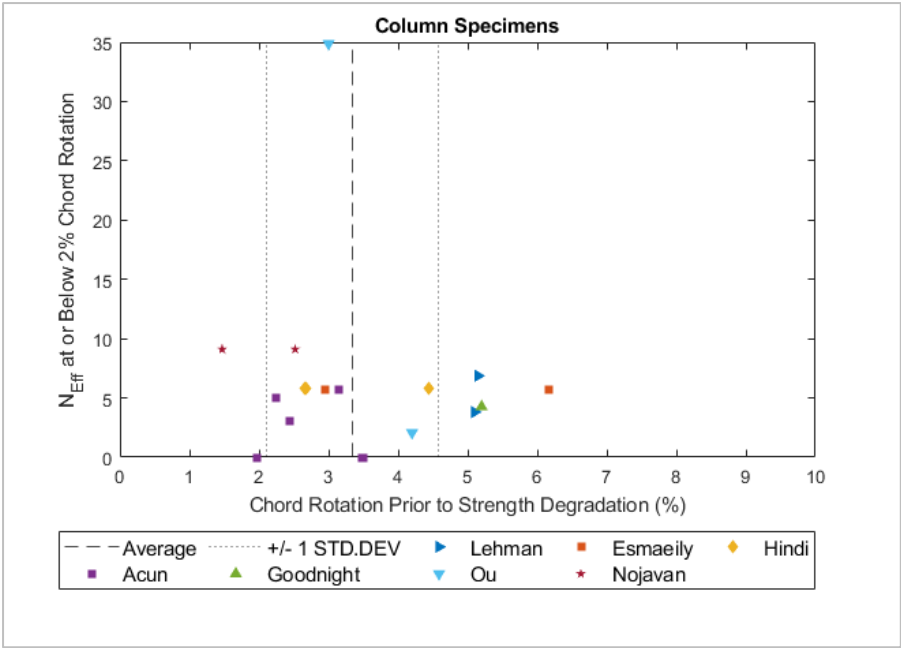


Figure A-14 Chord Rotation Prior to Strength Degradation vs. Number of effective cycles at 2% chord rotation for column specimens.

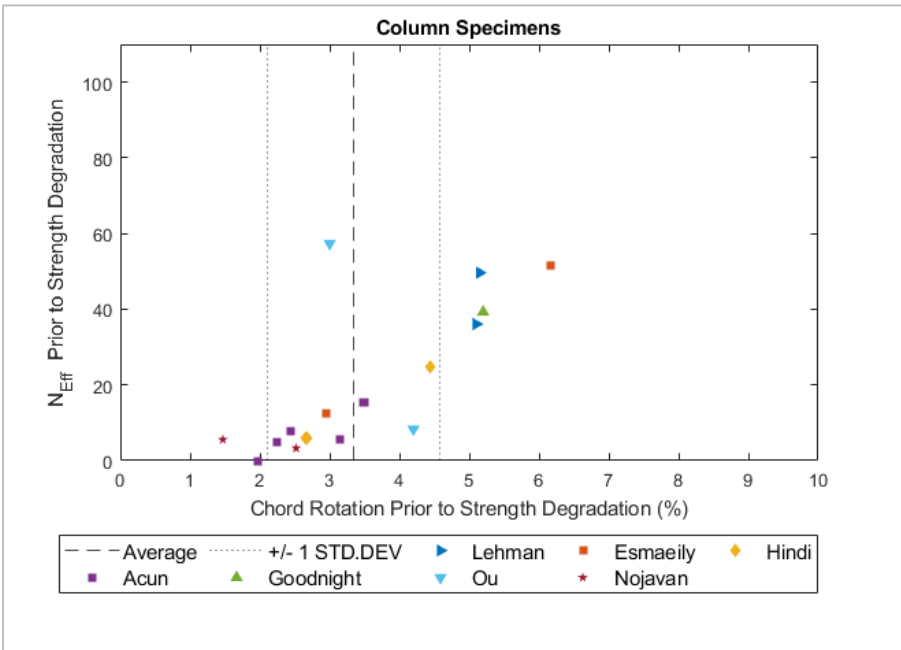


Figure A-15 Chord Rotation Prior to Strength Degradation vs. Number of effective cycles prior to strength degradation.

Figure A-15 presented N_{Eff} values due to all cycles prior to the onset of strength degradation. A positive trend is observed in this figure. Unless caused by an increase in bond slip due to lower amplitude cycles, this result appears to be a fallacy due to variation on other variables. In any case, the results support the conclusion that the cycles prior to onset of degradation do not detrimentally impact the deformation demand at onset of degradation.

A.3.2.2.5 Deformation Capacity

Alternative Methodology for Assessment of Deformation Capacity

A challenge in assessing changes in deformation capacity with standard cyclic loading protocols, is the inconsistency in the number and amplitude of cycles between different tests. When assessing the impact of smaller amplitude cycles on overall deformation capacity of components, differences in loading at larger amplitude cycles makes comparison of deformation capacities challenging. This was outlined previously in discussion of the prior literature, where clear evidence was presented on the detrimental impact of cycles greater than 2% chord rotation on deformation capacity. Figure A-16 uses the loading protocols applied to two specimens CLC (Loading Protocol 1) and COC (Loading Protocol 2) by Ou et al. (2017) to illustrate the challenges of comparing dissimilar loading protocols.

The loading histories shown in Figure A-16 consist of drastically different number of cycles. When calculating N_{eff} using only cycles at or **below** 2% chord rotation, it would appear that when N_{eff} increased from 2 to 35, a reduction in deformation capacity from 6.4% to 4.8% was observed. On closer observation, we can see that Loading Protocol 1 was subjected to a N_{eff} of 50 due to cycles **above** 2% chord rotation prior to failure, in comparison to 34 in Loading Protocol 2. This result suggests that the reduction in the absolute chord rotation at failure in Loading Protocol 1 is more likely a consequence of the higher number of cycles **above** 2% drift.

To isolate the influence of cycles below 2% chord rotation, on the cyclic capacity of the specimens between 2% and the deformation capacity, the results of the database will be presented as N_{eff} due to cycles **below** 2% vs. N_{eff} due to cycles **above** 2% prior to failure. If an increase in cyclic content below 2% chord rotation results in a decrease in cyclic content above 2% chord rotation to failure, this would suggest that lower level cycles had a detrimental impact on cyclic capacity to failure.

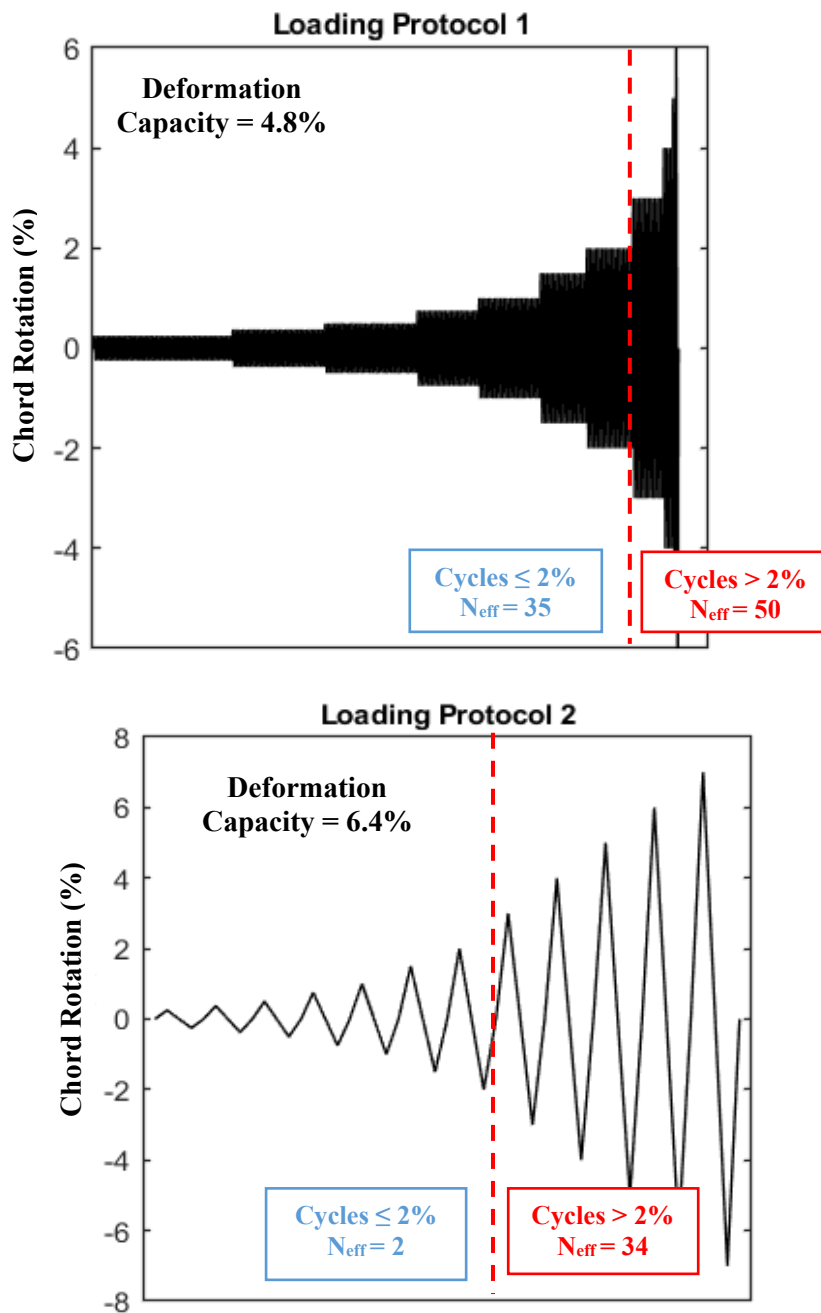


Figure A-16 Comparison of loading protocols used by Ou et al. (2014) used to illustrate proposed methodology for comparison of dissimilar loading histories. Loading Protocol 1 represents the history applied to specimen CLC and Loading Protocol 2 represents the history applied to specimen COC.

Deformation Capacity of Column Specimens

In line with the methodology outlined above, the results for the columns subjected to variable amplitude loading in the database are shown below in Figure A-17.

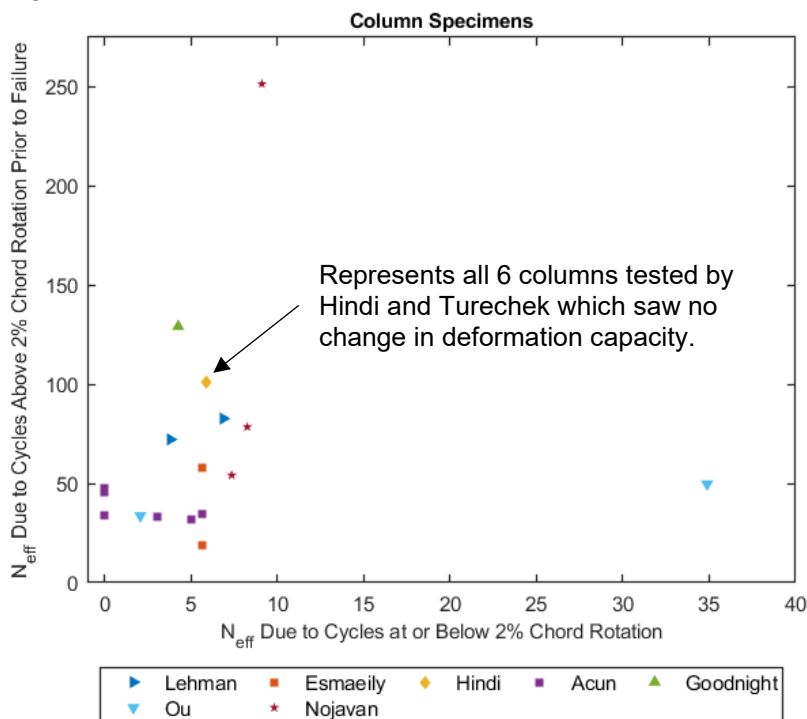


Figure A-17 Impact of variations in loading on deformation capacity of columns subjected to variable amplitude loading.

Observing the overall dataset, a weak trend may be observed where increases in N_{eff} below 2% chord rotation is resulting in an increase in N_{eff} above 2% prior to failure. This is obviously counterintuitive and as such suggests a lack of influence of the cycles below 2% on the cyclic capacity of the specimens. Taking a closer look at individual studies, a similar conclusion is drawn. Among the seven studies shown in Figure A-17, no trend of a detrimental impact due to varying N_{eff} below 2% chord rotation on cyclic capacity is observed. Similar to the results shown for onset of degradation in resistance, the data for cyclic capacity also supports the proposed safe deformation limit, θ_{Lim} of 2% chord rotation.

A.3.2.2.6 Buckling of Longitudinal Reinforcement

The presence of damage or significant inelastic deformation in steel reinforcement is a key issue during post-earthquake assessment of RC structures. Buckling of reinforcement indicates a high likelihood of bar fracture in subsequent earthquakes due to high localized strains, as indicated in Chapter 3. As such, it is of value to assess typical chord rotations at the onset of bar buckling, in relation to the proposed safe deformation limit of 2% .

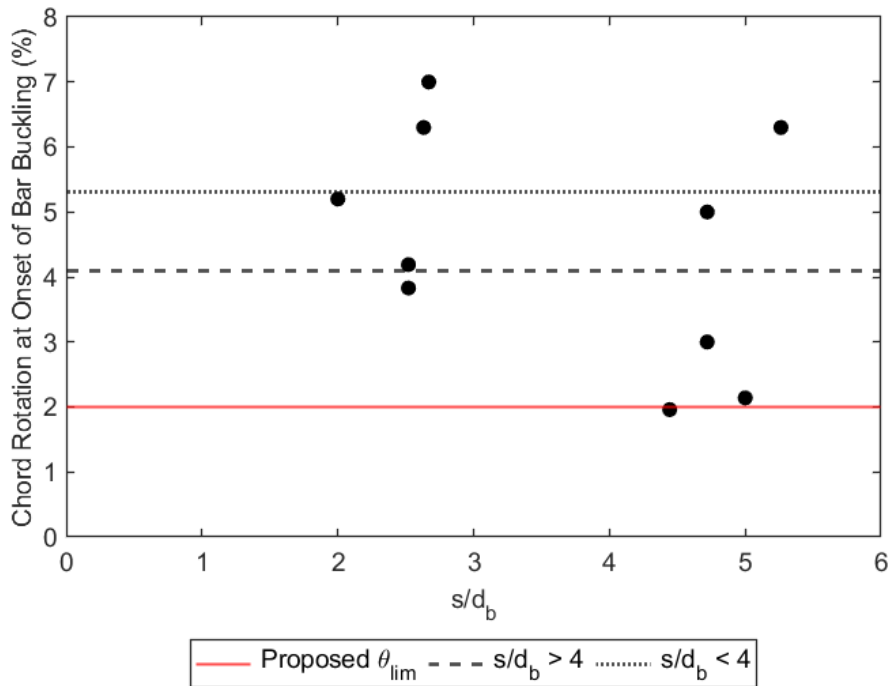


Figure A-18 Chord rotation at onset of bar buckling vs. s/d_b .

The chord rotation at the onset of bar buckling was only reported for 12 of the column specimens in the database. Figure A-18 presents the data for these specimens in relation to s/d_b ratio. The presented data is for specimens ranging in axial load ratio between 2 to 30% and s/d_b ranging from 2 to 5.3.

On average, the peak chord rotation at the onset longitudinal bar buckling in specimens with s/d_b below 4 was 5.3%, while for specimens with s/d_b greater than 4 this was lower at 4.1%. Two of the specimens suffered bar buckling at a chord rotation close to 2%, both from the study by Nojavan (2015), however, neither saw a 20% or greater reduction in strength until at least a chord rotation of 5.5%. The remainder of the specimens achieved a chord rotation of at least 3% prior to any observation of longitudinal bar buckling. Based on the limited data available here, it can be assumed that it is unlikely buckling of longitudinal reinforcement will be observed at or below the proposed safety limit of 2% chord rotation for ductile RC columns with $s/d_b \leq 6$.

A.3.2.2.7 Impact of Transverse Reinforcement Spacing and Axial Load

As previously outlined, a limit was placed on the specimens in the database to not exceed an s/d_b of 6, in line with the requirements of modern seismic detailing of current US and New Zealand design codes.

Figure A-19 presents the range of s/d_b ratios included in the database with the chord rotation prior to strength degradation. A clear trend is observed linking a decrease in chord rotation at onset of strength

degradation to an increase in s/d_b . The trend is shown in the figure with a blue trendline and coincides with the $2\% \theta_{cap}$ limits at an s/d_b of 6. This is of significance, as it was previously highlighted in Figure A-15 that prior to the onset of strength degradation there is a clear indifference to number of loading cycles, thereby validating again the proposed safety limit for specimens with s/d_b of 6 or lower. A subset of specimens with s/d_b marginally above 6 was included here, as considering construction tolerances these can be considered to be in line with modern seismic detailing requirements. The data shows that the chord rotation at the onset of strength degradation for these specimens is comparable to specimens with s/d_b of 5.

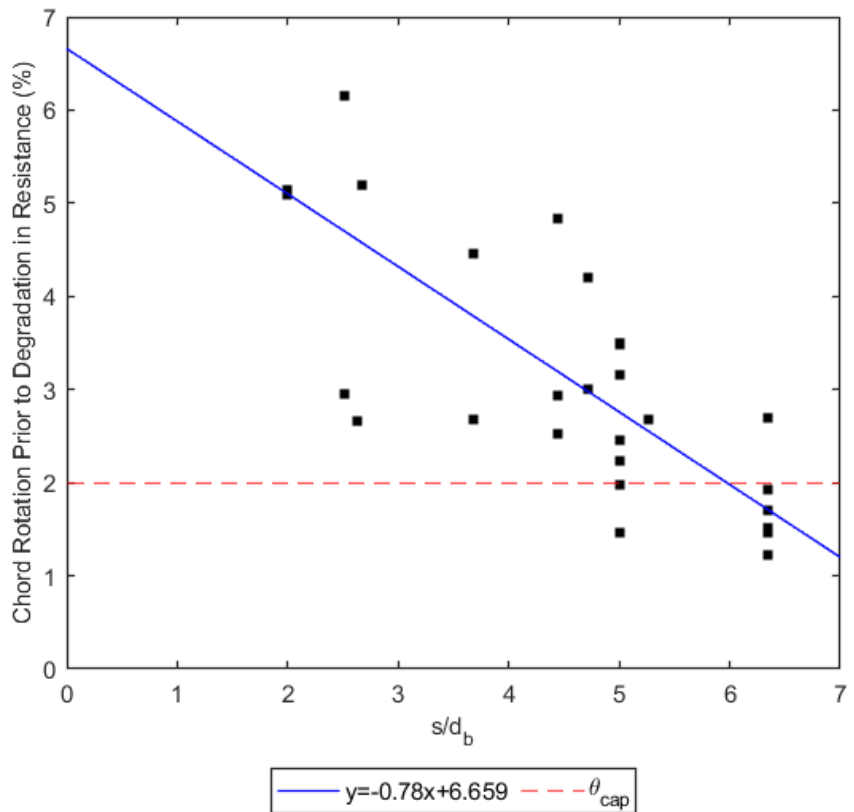


Figure A-19 Chord rotation at onset of strength degradation vs. s/d_b .

Like the plots for s/d_b , variation of chord rotation at onset of strength degradation vs. axial load ratio are presented below in Figure A-20. A relationship was developed by fitting a quadratic curve to the presented data as shown in Figure A-20. Based on the fitted quadratic relationship, the chord rotation at onset of degradation is below the θ_{cap} safety limit once an axial load of 33% is exceeded. It should be noted that considering both loading and strength reduction factors, the effective axial load limit on columns designed in according to ACI-318 is 37%.

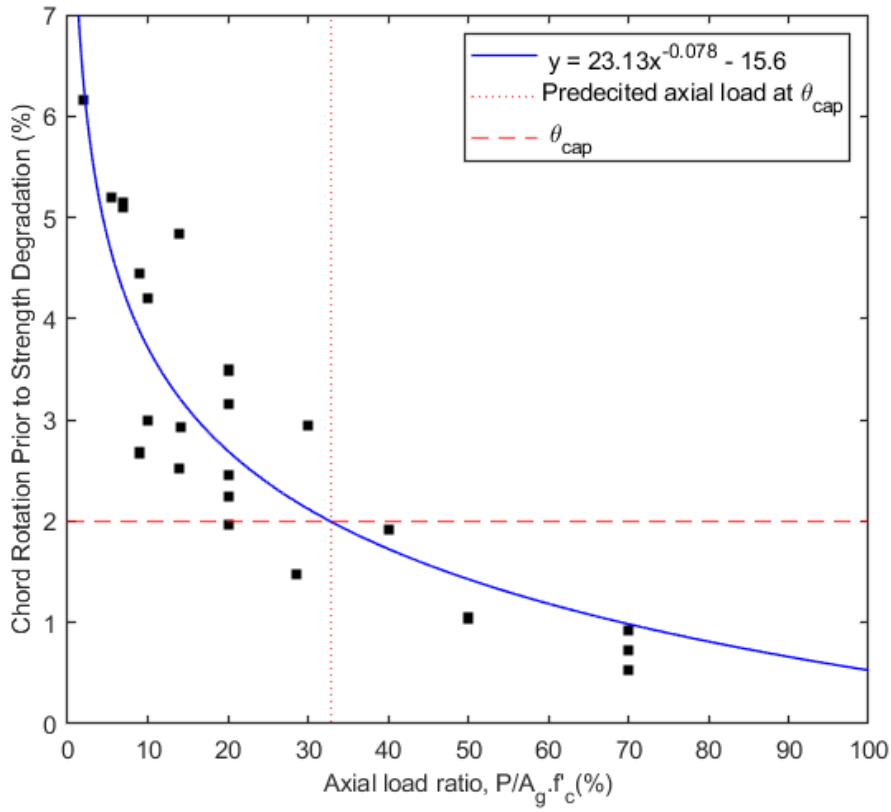


Figure A-20 Chord rotation at onset of strength degradation vs. Axial load ratio.

A.3.2.2.8 Overall Beam Database Results

In total, 24 beam specimens, which all met the requirements for ductile elements outlined in Section A.3, from studies by Ma et al. (1976), Ingham et al. (2001) and Marder (2018) are discussed in this section. As previously mentioned, then details of all specimens can be found in Section A.6 Table A-7 to A-9.

All beam specimens were tested under single curvature, with various restraint methods. The beams in the studies by Ingham et al. and Marder were all based on a prototype typical ductile moment frame structure in New Zealand and were tested at a shear span to depth ratio of 3.58. Ma et al. (1976) tested beams at a shear span to depth ratio of 3.9. The s/d_b ratio of the tested beams ranged from 3.1 to 6. All 24 beams were constructed with a total reinforcement ratio, A_s/bd , of ~1%. A general summary of specimen properties is presented in Figure A-21.

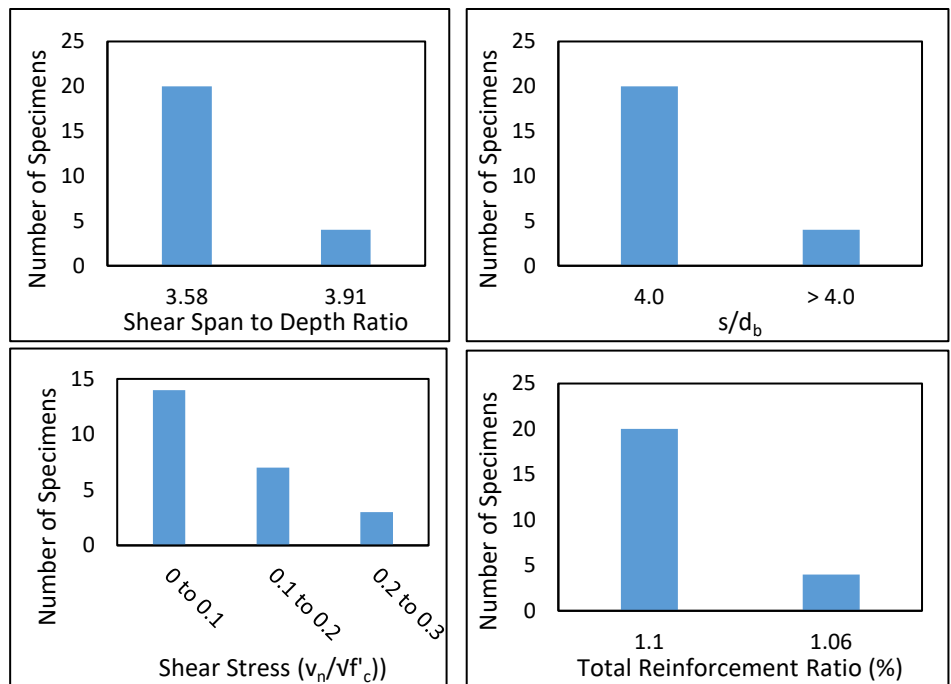


Figure A-21 General overview of specifications for beam specimens included in database.

A.3.2.2.9 Onset of Strength Degradation

Figure A-22 plots the chord rotation at onset of strength degradation in relation to the number of effective cycles at or below 2% chord rotation applied to each specimen. On average, the beams were able to achieve a chord rotation of 2.9% prior to onset of strength degradation.

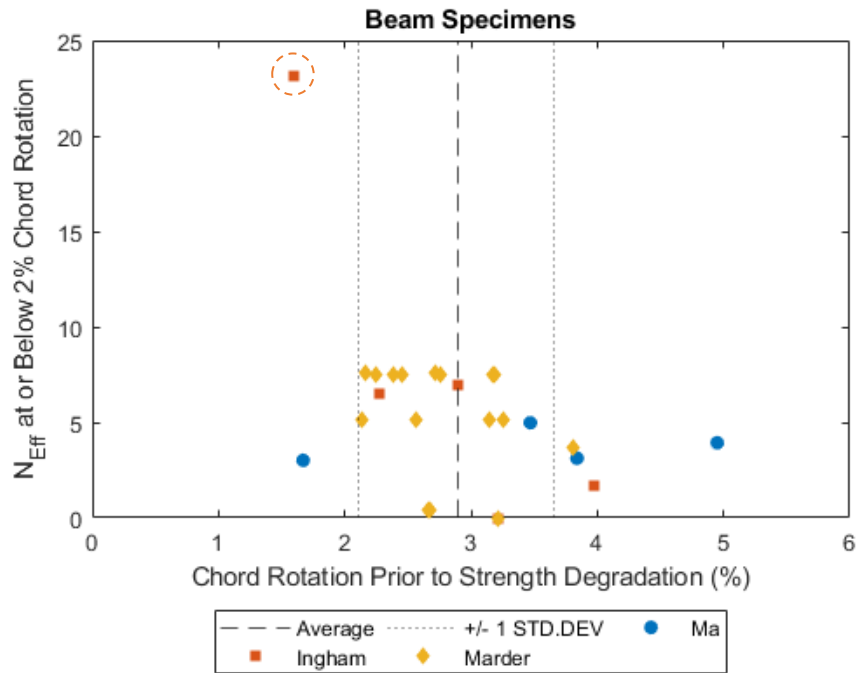


Figure A-22 Chord rotation prior to strength degradation vs. number of effective cycles at or below 2% chord rotation for tested beam specimens.

From the data presented in Figure A-22, an overall trend is not observed, however a trend is observed in the study by Ingham et al. (2001). No variation in axial load, transverse reinforcement spacing, or reinforcement ratio existed between the specimens in the Ingham et al. (2001) study. The data shows that the specimen highlighted with a dashed circle in Figure A-22 seems to indicate that a reduction in deformation capacity has occurred as a result of a N_{eff} of ~24. The remainder of the specimens do not show such a trend and this is also not observed in column specimens discussed in the previous section and as such this specimen is considered an outlier.

A.3.2.2.10 Deformation Capacity

Figure A-23 plots the deformation capacity of the beam specimens with respect to the cyclic loading applied. On average, the beams were able to sustain a chord rotation of 4% prior to failure (+/- 1 standard deviation of 0.64%). No trend in a decrease in deformation capacity with an increase in the total number of effective cycles was observed for the dataset as a whole. Once again, the specimen with a high N_{eff} in the study by Ingham et al., highlighted in Figure A-23 with a dashed circle, indicated a reduced deformation capacity.

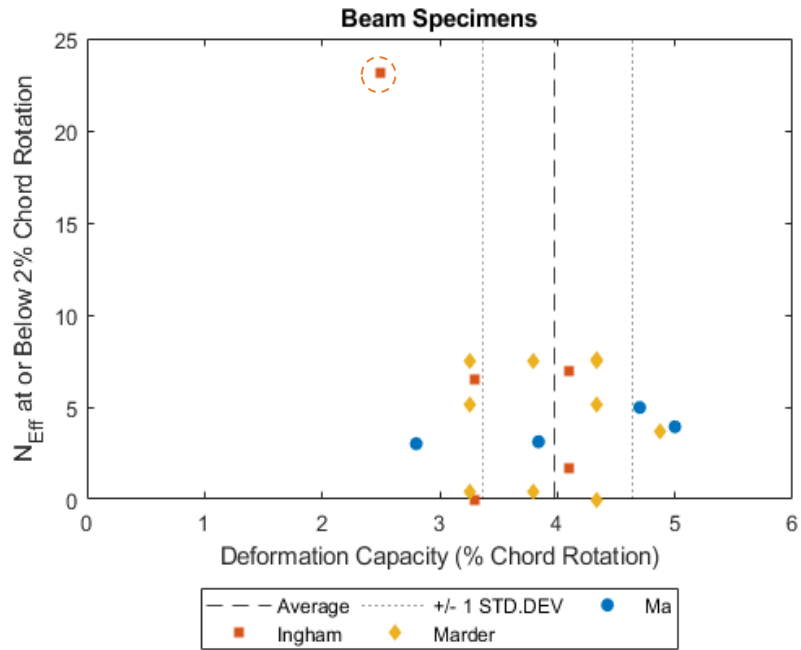


Figure A-23 Drift prior to strength degradation vs. number of effective cycles at or below 2% drift for tested joint specimens.

In line with the methodology outlined in the results section for column specimens, the deformation capacity for beam specimens is presented below in the form of N_{eff} due to cycles above 2% chord rotation prior to failure in Figure A-24.

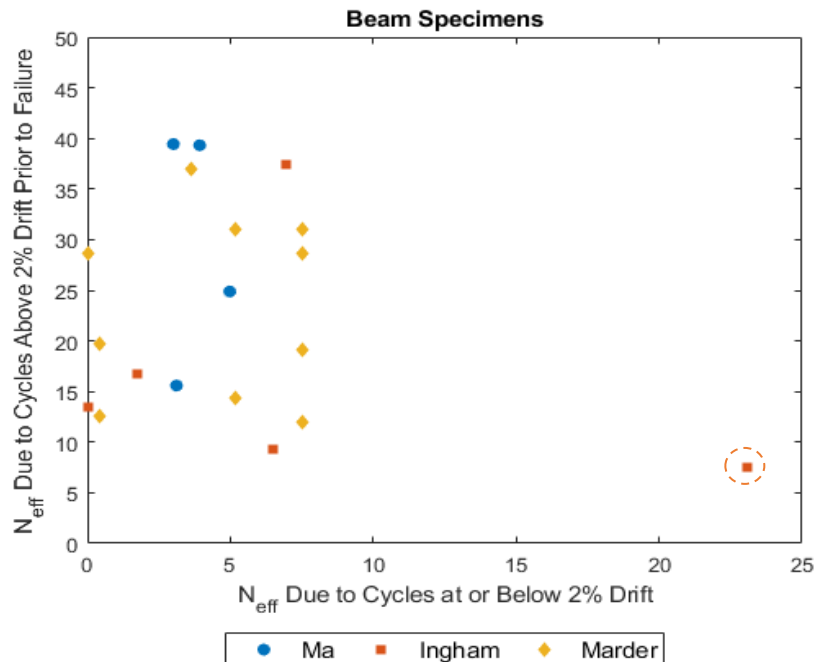


Figure A-24 Impact of variations in loading on the deformation capacity of ductile beam specimens.

This was done to ensure that variations in cyclic loading above 2% chord rotation were not impacting the results presented in Figure A-23, particularly with respect to specimens from Ingham et al. (2001). Once

again, no trend is observed showing a detrimental impact of loading cycles at or below 2% drift on the deformation capacity for the dataset. The beam specimen with a high N_{eff} due to cycles below 2% chord rotation from the study by Ingham et al. (2001) still seems to indicate a slight reduction in deformation capacity, however the reduction is less pronounced when presenting the data based on N_{eff} . The remaining specimens from the study achieved an N_{eff} due to cycles above 2% chord rotation between 9.4-37.4 while the outlier specimen achieved a value of 7.6. Based on evidence presented for column specimens, in addition to the beams tested by Opabola et al. (2019), where a significant number of cycles were applied without such reductions being observed, this specimen is deemed to be an outlier here and not of concern to the overall study outcomes. In addition, the beams in the Ingham et al. (2001) study made use of welded studs in their instrumentation, which were reported to cause premature failure and bar rupture in identical specimens not discussed in this study. It is likely that the reinforcement performance was compromised due to the welded studs in the outlier beam discussed above as well.

Story Drift vs. Chord Rotation

Typically, the chord rotation at the component level is smaller than the overall inter-story drift ratio in a regular frame structure.

The study by Shin and LaFave (2004) presented the results of their testing in both inter-story drift ratio and beam rotation. While the relationship between the two is not linear, the results from this study provide some evidence of the difference in magnitude between the two metrics.

In this study a beam chord rotation of 0.02, in line with the proposed θ_{cap} safety limit, corresponded to ~ 3.5-4% inter-story drift ratio in the tested joints.

On average, the column/beam moment capacity ratio for the specimens in this study was 1.35.

A.3.2.3 Overall Joint Database Results

In total, 29 joint specimens which met the requirements for ductile detailing outlined in Section A.3 of this appendix were processed from 6 individual investigations. Studies by Meinheit (1977), Beckingsale (1980), Park & Milburn (1983), Oka & Shiohara (1992), Noguchi & Kashiwazaki (1992) and Shin & LaFave (2004). All joints in the database were designed to form plastic hinges in the beam regions in line with modern design practices with a weak-beam strong column approach.

Some of the basic joint specimen characteristics are summarized in Figure A-25 with full details provided in Section A.6 Table A-10 to A-12. Specimens included beam shear span to depth ratios ranging from 3.6 to 5.8, beam total reinforcement ratios from 0.5 to 3.2% (A_s/bd) and joint transverse reinforcement ratios ranging between 0.78 – 2.38%. s/d_b ratios in beam potential plastic hinge regions ranged between 2.7 to 5.6.

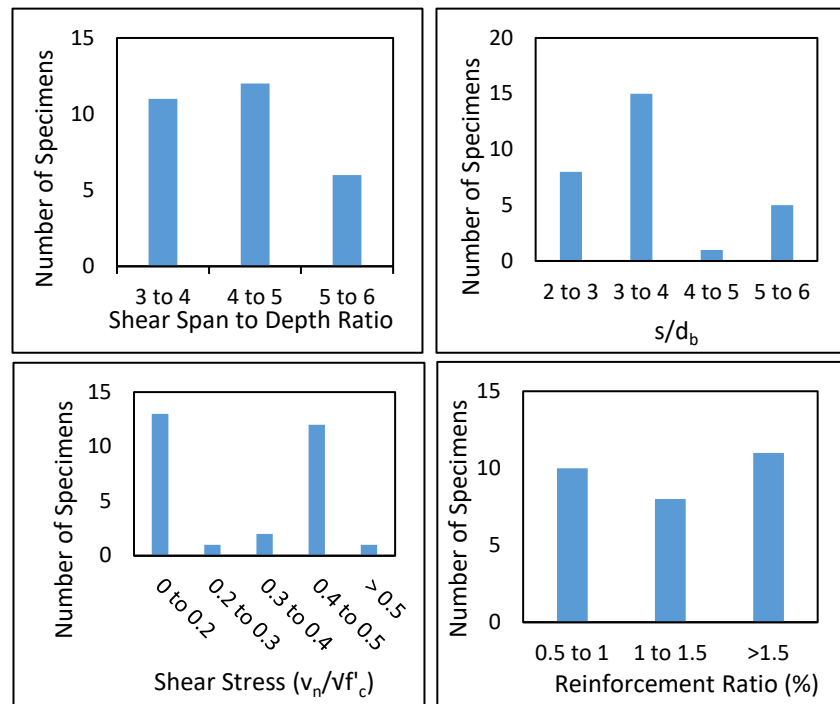


Figure A-25 General overview of specifications for joint specimens included in database.

All specimens included in this category were cruciform specimens or T-shaped specimens representing interior and exterior beam-column joints, respectively. While often joint tests will report the deformation applied to the column stub as a percentage of full specimen height, representing an effective story drift, two of the studies by Meinheit (1977) and Beckingsale (1980) reported the individual beam rotations, representing chord rotations in a frame as illustrated in Figure A-26. The results for these specimens are presented separate to the remainder of the joints in the proceeding sections.

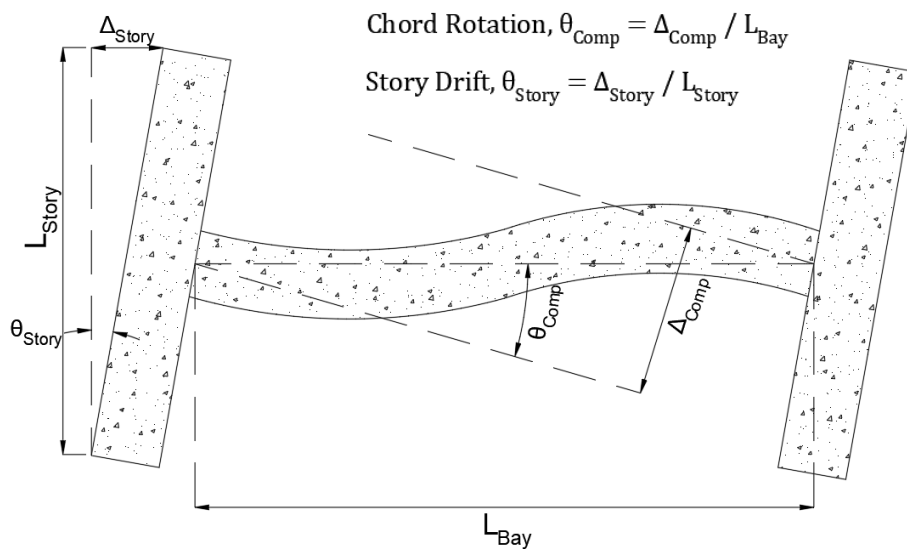


Figure A-26 Distinction between story drift ratio and chord rotation in frames.

Context with regards to the differences in magnitude between component chord rotation and inter-story drift ratios is presented in the callout box.

A.3.2.3.1 Onset of Degradation – Isolated Beam Rotation Specimens

Figure A-27 shows the beam chord rotation prior to strength degradation vs the number of effective cycles applied to the specimens for the beam rotations reported by Meinheit and Beckingsale. On average, a chord rotation of 4.4% was achieved prior to any degradation in resistance, with only one specimen seeing any degradation below 3% chord rotation. An earlier onset of strength degradation was not observed even in specimens with an effective number of cycles at 2% chord rotation as high as ~21.

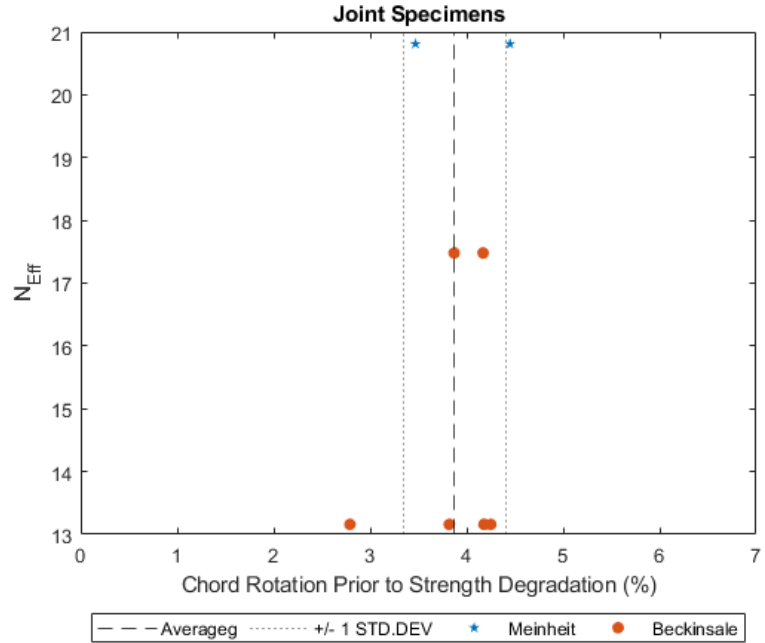


Figure A-27 Chord rotation at onset of strength degradation vs. effective number of cycles at 2% chord rotation for specimens tested by Meinheit (1977) and Beckingsale (1980).

A.3.2.3.2 Deformation Capacity - Isolated Beam Rotation Specimens

Similar to the results based on the chord rotation at onset of degradation, comparisons between the deformation capacity and number of effective cycles applied to each specimens show no observable detrimental impact whether assessing the total number of cycles applied or the number of effective cycles due to loading at or below a chord rotation of 2%. On average a chord rotation of 4.6% was achieved prior to failure, as shown in Figure A-28. Once again this is significantly higher than the proposed safety limit of 2%.

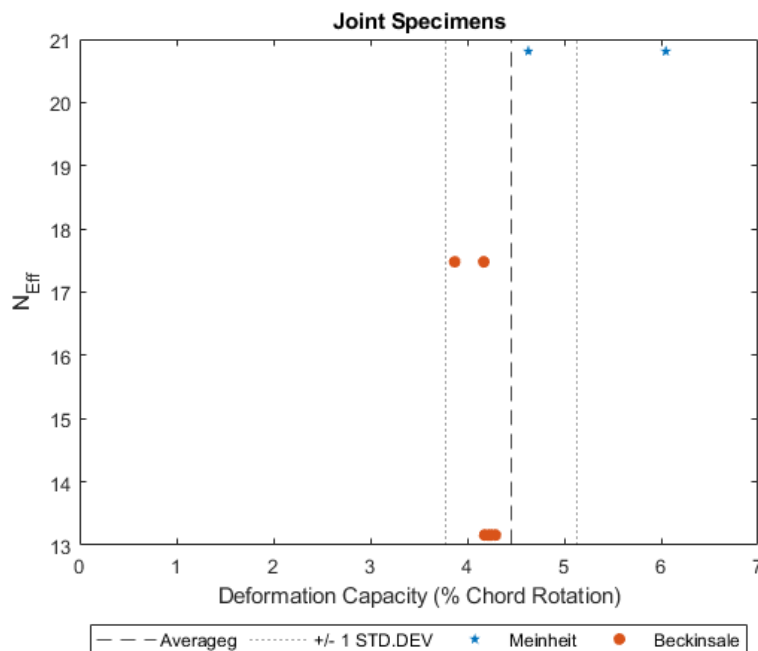


Figure A-28 Deformation capacity vs. effective number of cycles at 2% chord rotation for specimens tested by Meinheit (1977) and Beckingsale (1980).

A.3.2.3.3 Strength Degradation –Story Drift Specimens

As outlined previously, the results in this section represent distributions in story-drift ratio rather than the chord rotations that have been reported to this stage. The results come from 21 joint elements from the studies by Park & Milburn (1983), Oka & Shiohara (1992), Noguchi & Kashiwazaki (1992) and Shin & LaFave (2004). Figure A-29 presents the distribution of story-drift ratio at onset of degradation versus the effective number of cycles applied to each specimen. The data shows that with respect to the number of effective cycles at a story drift of 2%, no observable trend is present among individual studies, with an average drift at the onset of degradation in resistance of 3.2% (+/- 1 standard deviation of 0.74%).

A.3.2.3.4 Deformation Capacity – Story Drift Specimens

The observations discussed with respect to drift at onset of degradation once again hold here when considering changes in deformation capacity. No clear trends are seen within individual studies. On average specimens reached a story drift of 4.9% prior to failure (+/- 1 standard deviation of 0.93%). These results are presented in Figure A-30 and Figure A-31.

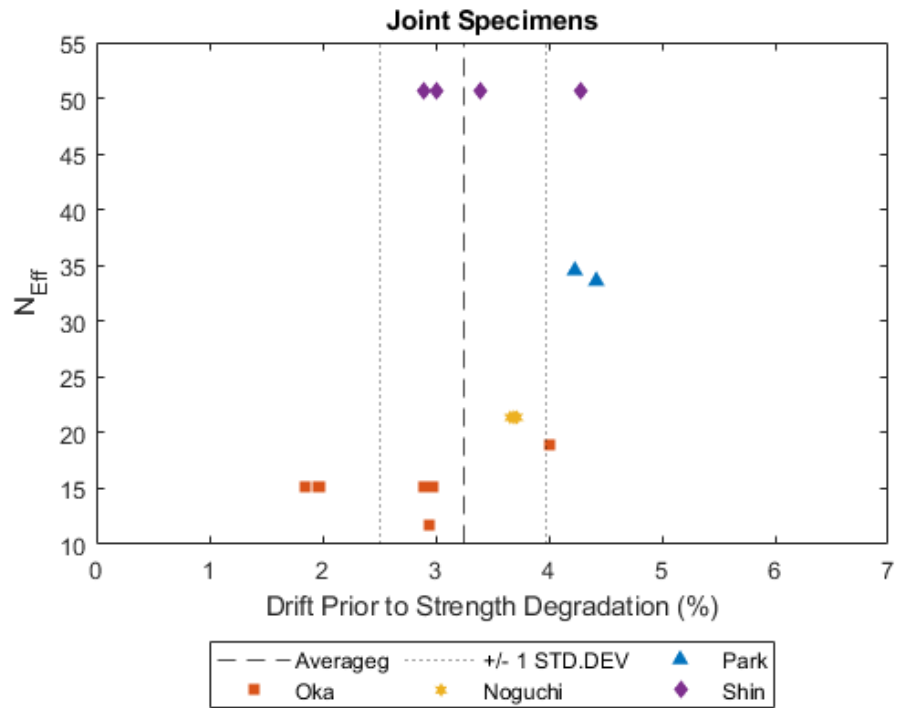


Figure A-29 Drift prior to degradation in resistance vs. number of effective cycles at 2% drift for tested joint specimens.

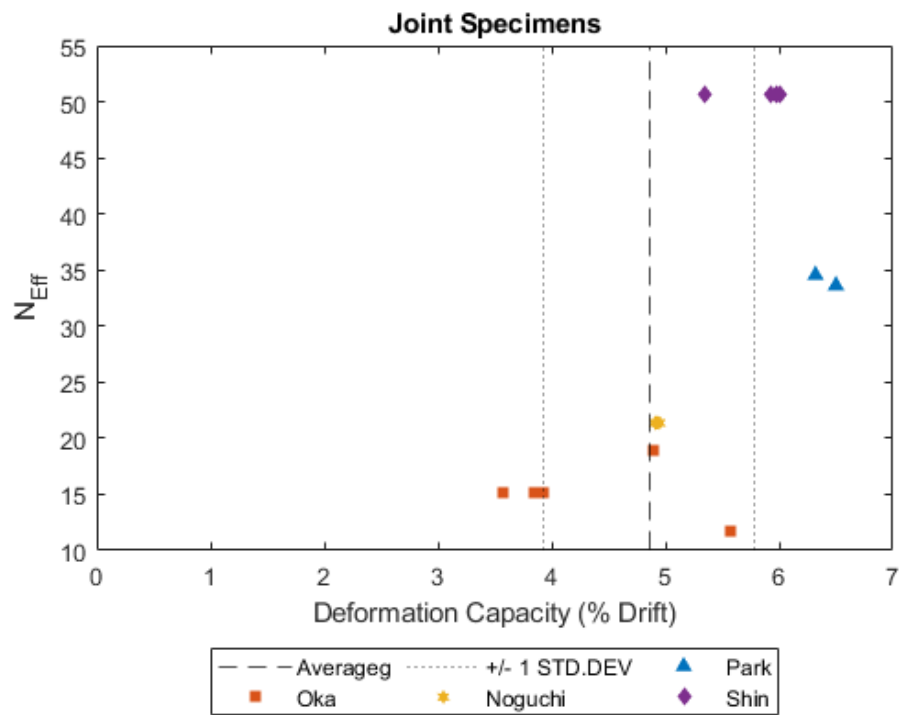


Figure A-30 Deformation Capacity vs. number of effective cycles at 2% drift for tested joint specimens.

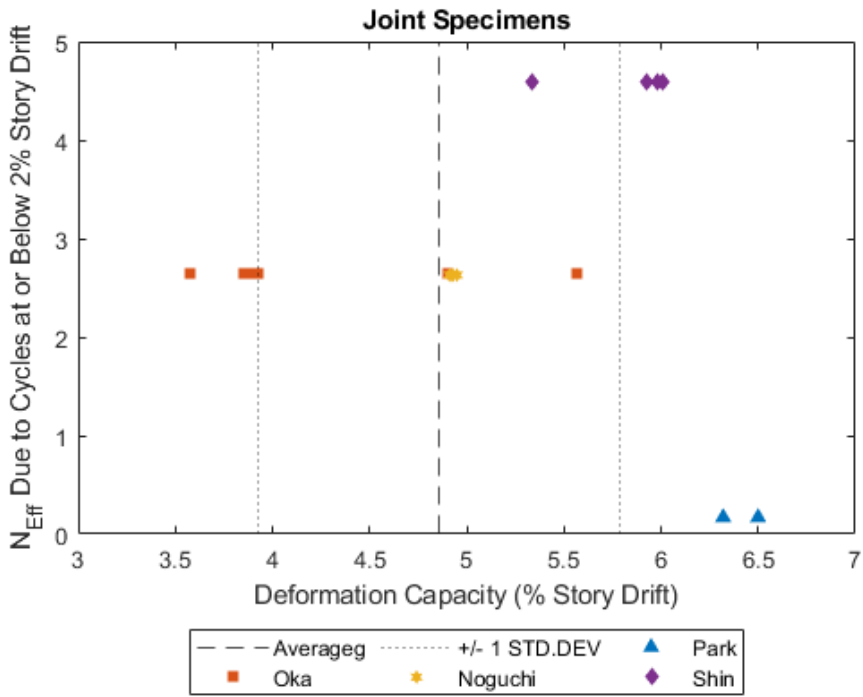


Figure A-31 Deformation Capacity vs. number of effective cycles at or below 2% drift for tested joint specimens.

A.4 Another Look at the Rotational Capacity of ‘Conforming’ Columns

A.4.1 What is a Conforming Column?

The previous section suggests that the rotational capacity of RC ‘conforming’ elements (with reinforcement details to avoid shear and bond failures) has been observed to exceed 2% in cyclic tests. But rotational capacity can vary with variations in detailing and axial load and, as result, the suggested threshold (2%) may vary depending on what is deemed to be ‘conforming,’ which in turn varies with time and location as local traditions vary. To address that issue, this section takes a different look at the question of *what is the minimum rotational capacity that can be expected from columns comparable to those classified as conforming now?* For this purpose, six hypothetical conforming columns are considered. The mentioned columns were defined by Moehle (2014) as illustrated in Figure A-32 and span a wide range of possibilities. The figure illustrates calculated relationships between moment and rotation (obtained as the product of curvature and half the cross-sectional depth). In all cases, a sharp decrease in capacity was not calculated to occur at rotations smaller than 0.03. The calculation results are based on the idea that column response is controlled by flexure. Other mechanisms of failure are plausible. Formulations calibrated to capture other modes of failure are examined next.

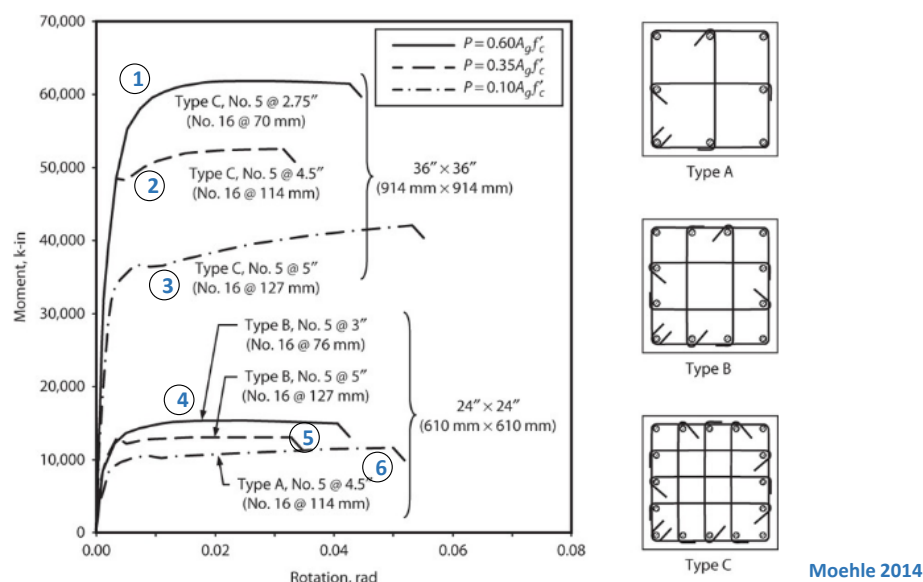


Figure A-32 Estimated moment-rotation relationships calculated for considered hypothetical ‘conforming’ columns. Yield stress = 70 ksi (long. bars) and 60 ksi (trans. bars), concrete cylinder compressive strength = 6 ksi.

A.4.2 What is the Rotational Capacity of a Conforming Column?

Rotational capacity (or drift capacity in the case of a column framing into stiff beams) is defined here as the rotation (or drift ratio - DR_{max}) corresponding to a reduction in lateral resistance of 20% as inferred from the envelope of load-deflection hysteresis loops.

Four formulations are used to estimate the drift capacity of the considered conforming columns defined in Figure A-32:

- Method 1 – Pujol et al. 1999 (Pujol, Ramfrez, & Mete A, 1999)

$$DR_{max} (\%) = \frac{r * f_y}{v_{max}} * \frac{a}{d} \leq \left\{ \frac{a}{d} \right. \quad (A-5)$$

- Method 2 – Elwood and Moehle 2005 (Elwood & Moehle, 2005)

$$DR_{max} = 3\% + 4r - 0.2\% \frac{v_{max}}{\sqrt{f'_c}} - 2.5\% \left(\frac{P}{A_g f'_c} \right) \geq 1\% \quad (A-6)$$

- Method 3 – Ghannoum and Matamoros 2014 (Ghannoum & Matamoros, Nonlinear modeling parameters and acceptance criteria for concrete columns, 2014)

$$DR_{max} = \theta_y + 0.042 - 0.043 \left(\frac{P}{A_g f'_c} \right) + 0.63r - 0.023 * \frac{V_{max}}{V_0} \quad (A-7)$$

- Method 4 – Haselton et al. 2016 (Haselton, Curt B. et al., 2016)

$$DR_{max} = \theta_y + 0.1(0.16)^{\frac{P}{A_g f'_c}} (0.02 + 40r)^{0.43} (0.54)^{0.069 f'_c} \quad (A-8)$$

where P is the Axial Load, A_g is the gross cross-sectional area of the column, f'_c is the concrete compressive strength, r is the transverse reinforcement ratio, f_y is the transverse reinforcement yield stress, v_{max} is the maximum nominal shear stress, V_{max} is the maximum lateral load, a is the shear span, and d is the depth to the centreline of the outermost tension reinforcement. θ_y is the yield drift, computed as $0.5\epsilon_y a \div d$ from Sullivan 2019 (Sullivan, 2019). V_0 is evaluated using the shear-strength equation of ASCE 41-06 (ASCE, 2007) for reinforced concrete columns. Note that Method 4 was calibrated to produce rotation at peak lateral force instead of rotation at a decay in lateral resistance of 20%. In general, these methods were not developed for exclusive application to columns that classified (today) as ‘conforming’.

The listed methods were conceived a) for different purposes (with some meant to be more conservative), b) for domains that may not include all the cases in Figure A-32, and c) using data samples with wide dispersion in test results. For these reasons, the results produced by Equations A-5 to A-8 for the cases in Figure A-32 were not taken at face value. Instead, they were used to organize experimental data through this question:

If the estimate of drift capacity produced by a given formulation for a column classified as ‘conforming’ is X, how often do test columns expected to be as good or better –according to the same formulation– reach rotational capacities exceeding the proposed threshold of 2%?

For that purpose, the following steps were followed for each formulation (1 through 4):

- a) identify the minimum drift-capacity estimate DR_{max} produced by the formulation for the cases in Figure A-32
- b) identify columns tested in the laboratory for which the formulation produces the same or larger estimates of drift capacity DR_{max} (relative to a.)
- c) count how many of the columns identified in b) reached measured drift capacities exceeding 2%.

The columns identified in b) could be said to be as good as ‘conforming columns’ (as defined today) from the perspectives of each of the formulations represented by Eq. A-5 to A-8. In that sense, the criterion stated in b) can be thought of as an alternative way to define ‘conforming’ different from checking every requirement in the current standard.

A total of 177 test columns (ACI Columns) were considered from the ACI 369 Rectangular Column Database (Ghannoum, et al., 2015) that satisfy the following conditions:

- Axial Load Ratio (ALR): $P/A_g f'_c \leq 0.5$
- Aspect Ratio (AR): $a/d < 4$
- No lap slices

Figure A-33 through Figure A-36 contain plots of measured drift or rotational capacity (as defined) v. drift capacity estimated using each of the listed expressions (A-5 to A-8). The figures also contain symbols representing the hypothetical conforming columns from Figure A-32. The x coordinate of each of these symbols (for hypothetical columns) is the value for DR_{max} obtained from one of the available expressions (A-5 through A-8). The y coordinate (that is less relevant) is the limiting rotation from Figure A-32 obtained as limiting curvature times half the column cross-sectional depth. Expressions A-5 to A-8 produce estimates of drift capacity as low as 1.3% and as high as 5.5% for the cases in Figure A-32. Even if attention is given exclusively to the most critical cases, values range widely: from 1.3% to ~4%. This variation is related to the mentioned differences among formulations and is not as

informative as measurements of drift capacity obtained from columns deemed comparable according to bullet b).

For each of the methods for estimation of drift or rotational capacity considered, Table A-3 lists the percentage of test columns (1) deemed comparable to the hypothetical columns (i.e., with estimated drift capacities equal to or larger than the smallest result obtained for cases in Figure A-32); and (2) with observed drift capacity larger than 2%.

In all the cases considered, more than ~80% of test columns deemed comparable to the hypothetical columns considered reached drift capacities exceeding 2% in laboratory tests supporting, in general, the conclusion from the previous section. The consistency in Table A-3 is remarkable because the considered formulations differ much in origin and intent, and because the laboratory data considered here includes columns with a wide range of properties.

Table A-3 Minimum Drift Capacity Computed for a hypothetical Code-Compliant RC Column (DC_{minCC}) and the Corresponding Percentage of Comparable Test Columns with Measured Drift Capacities Exceeding Than 2%.

Method	DC_{minCC} (%) (1)	No. of comparable test columns (2)	% of (2) with observed drift capacity > 2% (3)
	1.40	121	91%
	4.10	58	93%
	1.57	138	82%
	2.36	138	79%

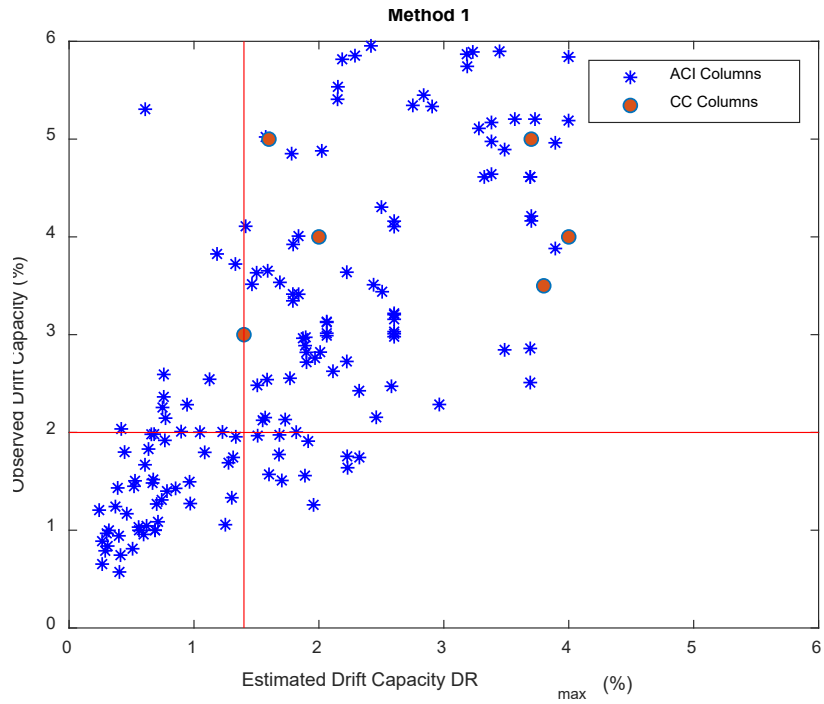


Figure A-33 Plots of observed drift capacity from experimental results against estimated drift capacity (DRmax) computed using Method 1 – Pujol et al. 1999 [2]. Vertical line indicates smallest drift capacity estimated for cases in Figure A-32. Horizontal line indicates proposed threshold of 2%.

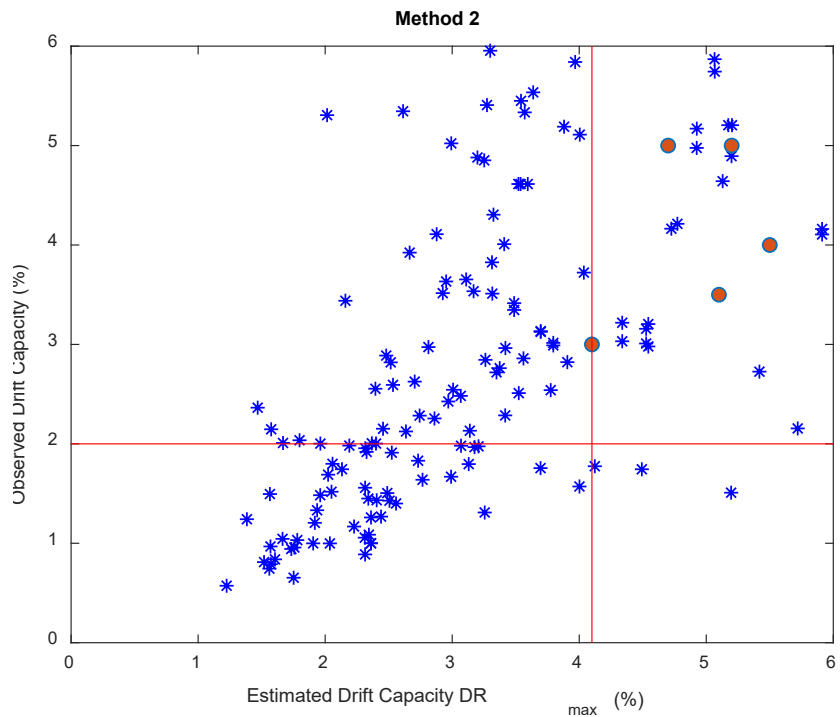


Figure A-34 Plots of observed drift capacity from experimental results against estimated drift capacity (DR max) computed using Method 2 – Elwood and Moehle 2005 [3]. Vertical line indicates smallest drift capacity estimated for cases in Figure A-32. Horizontal line indicates proposed threshold of 2%.

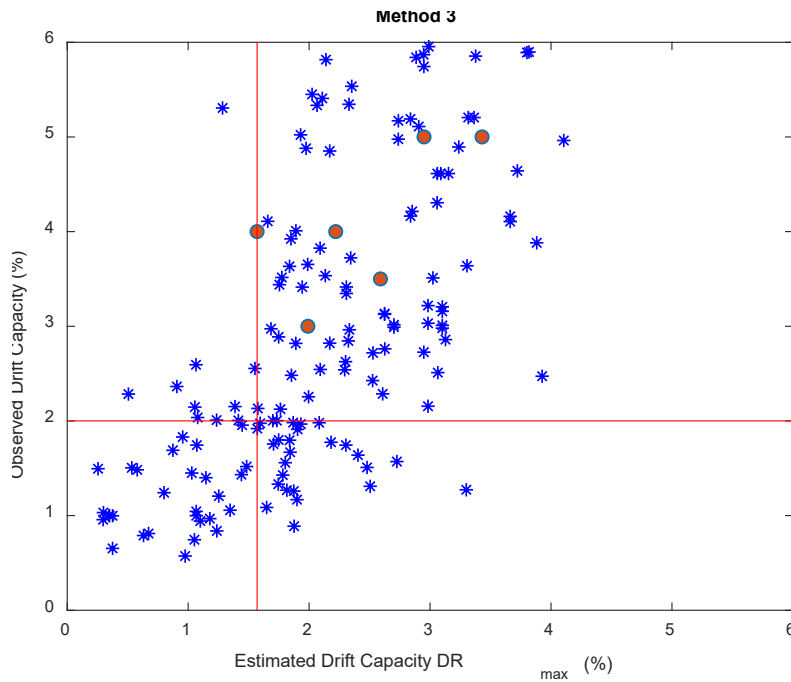


Figure A-35 Plots of observed drift capacity from experimental results against estimated drift capacity (DR_{max}) computed using Method 3 – Ghannoum and Matamoros 2014 [4]. Vertical line indicates smallest drift capacity estimated for cases in Figure A-32. Horizontal line indicates proposed threshold of 2%.

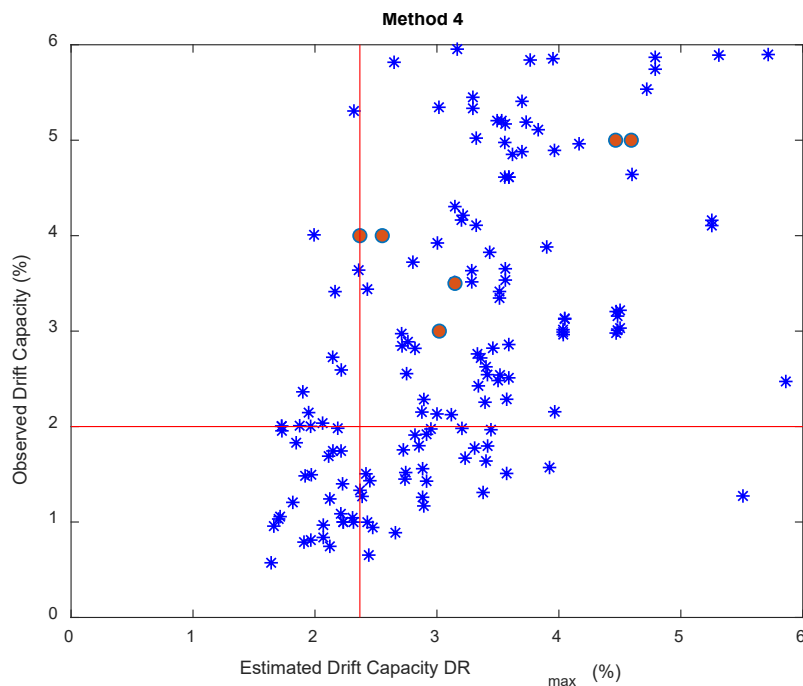


Figure A-36 Plots of observed drift capacity from experimental results against estimated drift capacity (DR_{max}) computed using Method 4 – Haselton et al. 2016 [5]. Vertical line indicates smallest drift capacity estimated for cases in Figure A-32. Horizontal line indicates proposed threshold of 2%.

A.5 Conclusions and Recommendations

Based on experimental observations of variations in cyclic loading on beam and column specimens, a safe deformation limit, θ_{cap} of 0.02 chord rotation was proposed. This was based on data pointing to an insignificant impact of cycles at or below this chord rotation on the deformation capacity of ductile RC components.

Observations of test data from a database of column, beam and joint tests collected for this study, largely supported this proposed safety limit.

- Column specimens with a range of axial loads up to 30% and transverse reinforcement spacing with s/d_b between 2 and 5.3 did not show trends in reduction of deformation capacity or chord rotation at onset of degradation.
- Based on relationships developed with respect to axial load ratios, a proposed limit of 30% $A_g F_c$ should also be considered in conjunction with the θ_{cap} of 0.02 chord rotation.
- The test data collected for beam and joint specimens also confirmed the proposed safety limit with the joint specimens highlighting that the limit maintained even when considering story drift ratios, noting that story drift ratios are typically greater in magnitude than component chord rotations for regular moment-frame structures without irregularities or particularly short beam spans.

References

- Acun, B. and Sucuoglu, H., 2010, "Performance of reinforced concrete columns designed for flexure under severe displacement cycles," *ACI Structural Journal*, Vol. 107, No. 3, pp. 364-371.
- ACI, 2019, *Building code requirements for structural concrete*, ACI 318-19, American Concrete Institute, Committee 318, Farmington Hills, USA.
- ASCE, 2006, *Seismic Rehabilitation of Existing Structures*, ASCE/SEI 41-06, American Society of Civil Engineers, Structural Engineering Institute, Reston, Virginia.
- Beckingsale, C.W., 1980, *Post elastic behaviour of reinforced concrete beam-column joints*, University of Canterbury, Christchurch, New Zealand.
- Coffin L.F., Jr., 1954, "A study of the effect of cyclic thermal stresses in ductile metals," *Transactions of ASME*, Vol. 76, pp. 931– 950.
- El-Bahy, A., Kunnath, S. K., Stone, W. C., and Taylor, A. W., 1999, "Cumulative seismic damage of circular bridge columns:

- Benchmark and low-cycle fatigue tests,” *ACI Structural Journal*, Vol. 96, pp. 633-641.
- Elwood, K. J., and Moehle, J.P., 2005, "Drift capacity of reinforced concrete columns with light transverse reinforcement," *Earthquake Spectra*, Vol. 21, No. 1, pp. 71-89.
- Esmaeily, A. and Xiao, Y., 2005, “Behavior of reinforced concrete columns under variable axial loads: analysis,” *ACI Structural Journal*, Vol. 102, No. 5, pp. 736.
- Ghannoum, W., Sivaramakrishnan, B., Pujol, S., Catlin, A. C., Fernando, S., Yoosuf, N., and Wang, Y, 2012, “ACI 369 rectangular column database,” *Network for Earthquake Engineering Simulation (database), Dataset, DOI, 10, D36688J50*.
- Ghannoum, W., Sivaramakrishnan, B., Pujol, S., Catlin, A.C., Fernando, S., Yoosuf, N., and Wang, Y., 2015, "NEES: ACI 369 Rectangular Column Database," <https://datacenterhub.org/resources/255>
- Ghannoum, W. and Matamoros, A.B., 2014, “Nonlinear modeling parameters and acceptance criteria for concrete columns," *ACI Special Publication*, Vol. 291, No. 1, pp. 1-24.
- Goodnight, J.C., 2015, *The effects of load history and design variables on performance limit states of circular bridge columns*, North Carolina State University, Raleigh, North Carolina.
- Haselton, Curt B. et al., 2016, "Calibration of model to simulate response of reinforced concrete beam-columns to collapse," *ACI Structural Journal*, Vol. 113, No. 6.
- Hindi, R. and Turechek, W., 2008, “Experimental behavior of circular concrete columns under reversed cyclic loading,” *Construction and Building Materials*, Vol. 22, No. 4, pp. 684-693.
- Ingham, J. M., Liddell, D., and Davidson, B. J., 2001, “Influence of loading history on the response of a reinforced concrete beam,” *Bulletin of the New Zealand Society for Earthquake Engineering*, Vol. 34, No. 3, pp. 107-124.
- Lehman, D. E., Gookin, S. E., Nacamuli, A. M., and Moehle, J.P., 2001, “Repair of earthquake-damaged bridge columns,” *Structural Journal*, Vol. 98, No. 2, pp. 233-242.
- Ma, S.Y.M., Bertero, V.V., and Popov, E.P., 1976, “*Experimental and analytical studies on the hysteretic behavior of reinforced concrete rectangular and T-beams*,” Earthquake Engineering Research Center, College of Engineering, University of California, Berkeley, California.

- Marder, K., 2018, *Post-earthquake residual capacity of reinforced concrete plastic hinges (Doctoral dissertation)*, University of Auckland, Auckland, New Zealand.
- Malhotra, P.K., 2002, "Cyclic-demand spectrum," *Earthquake Engineering and Structural Dynamics*, Vol. 31, No. 7, pp. 1441-1458.
- Manson, S.S., 1954, "Behavior of materials under conditions of thermal stress," *NACA Technical Notes*, No. 2933.
- Marquis, F., Kim, J. J., Elwood, K.J., & Chang, S.E., 2017, "Understanding post-earthquake decisions on multi-storey concrete buildings in Christchurch, New Zealand," *Bulletin of Earthquake Engineering*, Vol. 15, No. 2, pp. 731-758.
- Meinheit, D.F., 1978, *The Shear Strength of Reinforced Concrete Beam-Column Joints*, University of Texas, Austin.
- Miner, M. A., 1945, "Cumulative Damage in Fatigue," *Journal of Applied Mechanics*, Vol. 12, No. 3, pp. 159–164.
- Noguchi, H., and Kashiwazaki, T., 1992, "Experimental studies on shear performances of RC interior column-beam joints with high-strength materials," *10th World Conference on Earthquake Engineering Proceedings*, pp. 3163-3168.
- Nojavan, A., 2015, *Performance of full-scale reinforced concrete columns subjected to extreme earthquake loading*, University of Minnesota, Minneapolis, Minnesota.
- Oka, K., and Shiohara, H., 1992, "Tests of high-strength concrete interior beam-column joint subassemblages," *10th World Conference on Earthquake Engineering Proceedings*, pp. 3211-3217.
- Opabola, E. A., Best, T., Elwood, K. J., Hogan, L., and Synge, A. J., 2018, "Deformation capacity of reinforced concrete beams with single crack," *New Zealand Society for Earthquake Engineering Conference*, Auckland, New Zealand.
- Ou, Y.C., Song, J., Wang, P.H., Adidharma, L., Chang, K.C., and Lee, G.C., 2014, "Ground motion duration effects on hysteretic behavior of reinforced concrete bridge columns," *Journal of Structural Engineering*, Vol. 140, No. 3.
- Park, R., and Milburn, J. R., 1983, "Comparison of recent New Zealand and United States seismic design provisions for reinforced concrete beam-column joints and test results from four units designed according to the New Zealand code," *Bulletin of the New Zealand National Society for Earthquake Engineering*, Vol. 16, No. 1, pp. 3-24.

- Priestley, M. J. N., Calvi, G. M., and Kowalsky, M. J., 2007, Displacement-Based Seismic Design of Structures, IUSS Press, Pavia, Italy, pp. 721.
- Pujol, S., Ramfrez, J. A., and Mete A.S., 1999, "Drift capacity of reinforced concrete columns subjected to cyclic shear reversals," *ACI Special Publication*, Vol. 187, pp. 255-274.
- Pujol, S., Sozen, M.A., & Ramirez, J.A., 2006, "Displacement history effects on drift capacity of reinforced concrete columns," *ACI Materials Journal*, Vol. 103, No. 2, pp. 253.
- Sarrafzadeh, M.M., 2021, *Residual Capacity and Reparability of Moderately-Damaged Reinforced Concrete Ductile Frame Structures*, PhD Thesis (under review), University of Auckland, Auckland, New Zealand.
- Shin, M., and LaFave, J. M., 2004, "Testing and modeling for cyclic joint shear deformations in RC beam-column connections," *13th World Conference on Earthquake Engineering Proceedings*.
- Standards New Zealand, 2006, *Concrete Structures Standard, NZS 3101:2006, Incorporating amendment No. 1, 2, and 3*, Wellington, New Zealand.
- T. Sullivan, 2019, "Rapid Assessment of Peak Storey Drift Demands on Reinforced Concrete Frame Buildings," *Bulletin of the New Zealand Society for Earthquake Engineering*, Vol. 52, No. 3, pp. 109-118.
- Xing, G., Ozbulut, O. E., Lei, T., and Liu, B., 2017, "Cumulative seismic damage assessment of reinforced concrete columns through cyclic and pseudo-dynamic tests," *The Structural Design of Tall and Special Buildings*, Vol. 26, No. 2.

Appendix B

Influence of Prior Loading on System Response

This Appendix describes investigations conducted to quantify the drift threshold beyond which life safety performance in a future earthquake is impaired for RC frames systems. This drift threshold constitutes a system level “repair trigger”, indicating structural repairs beyond epoxy injection and mortar patching are needed, which will be related to component and other threshold limits in future guideline development.

For code-conforming reinforced concrete (RC) frame building structures, a repair trigger is defined as 2% story drift, indicating that drifts demands beyond that level are associated with impaired performance. The project team also hypothesized that certain structural characteristics would influence the repair trigger. Structural characteristics investigated were: building fundamental period, structures with torsional and elevation irregularities, and structures sensitive to P-Delta effects.

Several studies were conducted to support this repair trigger and explore the effects of these building characteristics. These were:

- Review of previous literature on influence of ground motion duration and aftershocks on drift demands and collapse capacity (Section B.1). This review suggests that modern ductile buildings can withstand drifts on the order of 2% without a reduction in collapse capacity or an increase in drift demands in future events. Building deformation capacity is identified as a key building characteristic influence aftershock and duration response.
- Review of shake table experimental studies and field observations that involved repeated ground shaking (Section B.2). This review shows that, for structures in which drift demand does not exceed drift capacity, there is not a significant increase in drift demands in a subsequent motion.
- Single degree-of-freedom analyses with varying ground motion and hysteresis characteristics subjected to repeated ground shaking (Section B.3). These analyses showed that, for sequences of intense motions and for stable oscillators, the relative increase in drift

(occurring in the second motion) was, on average, no more than 20%. Larger increases in drift occurred primarily in oscillators with effective periods below 1 second.

- Simple torsional models subjected to repeated ground shaking (Section B.4) These models find that torsional response did not significantly affect the amplification of displacement demand for the irregular systems considered in this study.
- System analyses of archetype code-conforming RC frame structures (Section B.5). These analyses show that deformation capacity of the structure is a key factor influencing the drift demands at which future performance is impaired, and that 2% drift is a conservative limit as repair trigger (bounding cases when performance is significantly impaired).

While building characteristics influence drift demand and damage propagation, none of the code-conforming RC frame structures assessed or reviewed in the various studies, regardless of the above characteristics, indicated the need for a repair trigger below 2% drift. Rather, the studies conducted here indicate that the key characteristic of the structure influencing the 2% drift value is the building's deformation capacity. When the guidelines are extended to other systems, it may be appropriate to provide a normalized repair trigger that considers the drift as a function of the onset of global softening in the structure or relates these limits to component(s)' deformation capacities.

There is some conservatism in the 2% drift threshold, as described in the subsequent sections. While excessive conservatism is to be avoided, it is preferable that structures evaluated by these guidelines be falsely identified as candidates for repair than that these structures be classified as safe when in fact future investigations are needed.

Several of the studies also examined how damage in an earthquake may impair performance in serviceability-level earthquakes. These studies did not influence the selected repair trigger, but are described here to inform the development of serviceability-assessment procedures.

B.1 Review of Analytical Studies of Duration and Aftershock response

The team conducted a review of literature on aftershocks and ground-motion duration and their influence on structural response to summarize what is known about how damaged buildings respond to future earthquake events. Of

particular interest was the identification of thresholds in that literature beyond which damage is severe enough that repair may be important.

B.1.1 Aftershock Literature

We reviewed 22 papers that examine aftershock performance of damaged buildings. These papers considered concrete moment frames (including those with and without infill), steel moment frames, and wood frame construction; there have also been a number of studies with single-degree-of freedom models of generic buildings. Most of the building models were in 2D or “pancake” 3D models involving a degenerated planar analysis with two horizontal degrees of freedom, and most use concentrated plasticity. A variety of hysteresis models are used in these studies. Damage in the first (mainshock) event was primarily quantified using peak or residual drifts or ASCE/SEI 41 limit states.

An example of results, from Raghunandan et al. (2015), is provided in Figure B-1. These results show about a 10% change in collapse capacity when drifts experienced by the building (before collapse capacity is assessed) are less than about 1.5%. At 4% drift in the mainshock, there is as much as 30% difference in collapse capacity. That study also showed that drift demands in aftershock ground motions did not increase until the mainshock damage exceeded peak story drifts of about 2%.

Some of the most relevant studies are summarized in Table B-1. These studies show that several building properties affect aftershock response: P-delta (i.e., more damage can be expected in aftershocks buildings with higher axial load or that are more flexible due to P-delta effects), strength (weaker buildings are more susceptible to damage), and deformation capacity (for less ductile buildings, effect of damage begins earlier). They also show that it is important to account in models for mechanism of deterioration of strength and stiffness, including P-delta effects, (in-cycle) negative stiffness, and cyclic deterioration to capture mainshock-aftershock trends.

B.1.2 Ground Motion Duration Studies

There are an increasing number of studies that show that duration of ground shaking can increase vulnerability of buildings (e.g., Raghunandan et al., 2013; Chandramohan et al., 2013; Chandramohan et al., 2016). In particular, duration seems to matter for damage measures assessing cumulative energy or collapse. However, studies focusing on peak response do not find trends with duration, unless drift demands are associated with response in the highly nonlinear range of structural response (see e.g., Chandramohan et al., 2016). These observations suggest that structural deformation capacity – and

demands exceeding this capacity – is the key characteristics that influences the relationship between duration and structural response. However, these studies do not suggest a particular value of repair trigger or drift demand at which future performance is impaired.

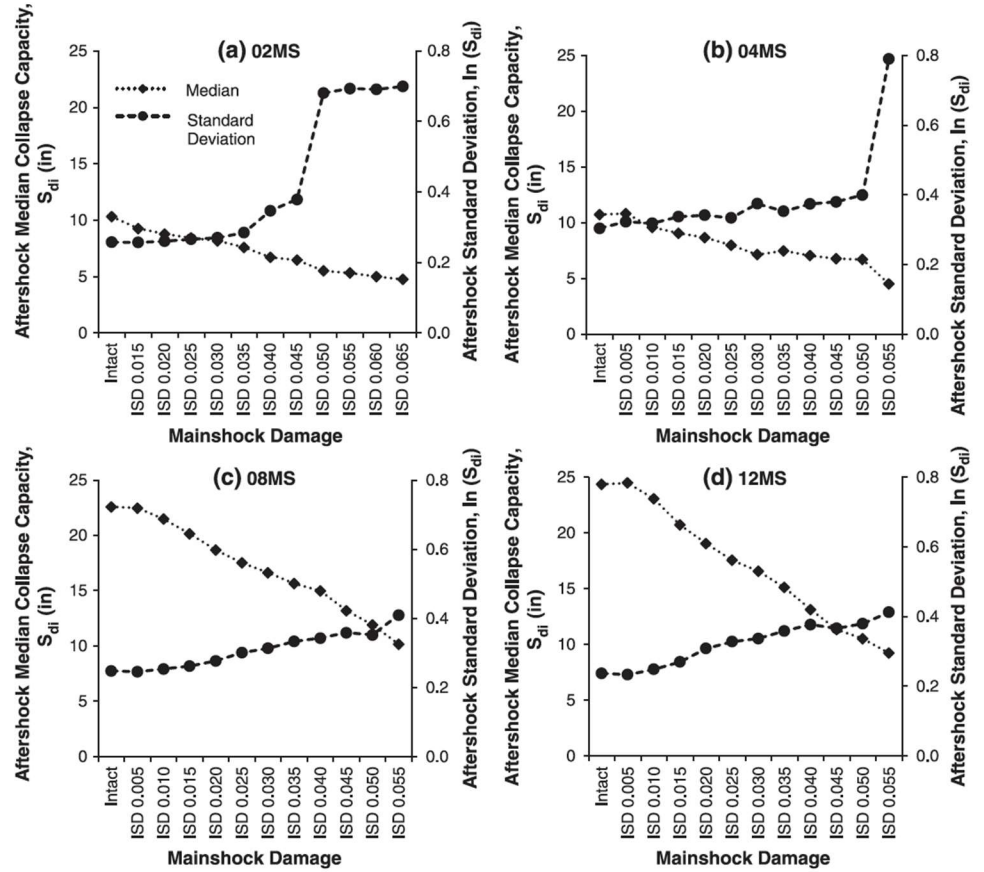


Figure B-1 Change in median collapse capacity as a function of drifts (“ISD”) experienced in the mainshock. These results are for four different buildings with heights of 2, 4, 8 and 12 stories. (From Raghunandan et al. 2015).

Table B-1 Summary of Selected Relevant Aftershock Studies

Bldg. type	Authors	At what level of damage does response change?
RC (Modern) Frames	Raghubandan et al.	Response (in terms of drifts in second event and residual capacity) starts to change after 2% Story Drift or 1% Residual Roof Drift
	Hosseinpour and Abdelnaby	"Life safety" response causes changes of about 20% in collapse capacity in second event
	Zhang et al.	1% drift has about a 7% change in the collapse capacity; 3% drift has a 40% change
RC (Older) Frames	Jeon et al.	Fragilities start to shift when drift is 1.2% in first earthquake
RC Frames with Infill	Tesfamariam et al.	Presence of infill affects how aftershock impacts response
	Burton et al.	Mainshock with intensity of 0.5*collapse capacity causes reduction of about 20% in capacity
Steel (Modern) Frames	Ruiz-Garcia and Aguilar	1.4% Residual Drift leads to a 10% reduction in median Sa at which Demolition Threshold is reached
	Li and Song	Peak Story Drift of 2-2.5% or "Moderate Damage" (Life Safety) leads to about 20% reduction in collapse capacity
Wood	Nazari et al.	Earthquakes smaller than Design Earthquake don't affect subsequent response; mainshock damage exceeding 2% drift may alter fragility in subsequent events
	Goda and Salami	2% or 3% drift needed before drifts increase in aftershock

References

- ASCE, 2016, Minimum Design Loads and Associated Criteria for Buildings and Other Structures, ASCE/SEI 7-16, American Society of Civil Engineers, Structural Engineering Institute, Reston, Virginia.
- Baker, J. W., 2011, "Conditional mean spectrum: Tool for ground-motion selection," *Journal of Structural Engineering*, Vol. 137, No. 3, pp. 322-331.
- Chandramohan, R., Baker, J.W., and Deierlein, G.G., 2016, "Impact of hazard-consistent ground motion duration in structural collapse risk assessment," *Earthquake Engineering & Structural Dynamics*, Vol. 45, No. 8, pp. 1357-1379.
- Chandramohan, R., Baker, J.W., and Deierlein, G.G., 2016, "Quantifying the influence of ground motion duration on structural collapse capacity using spectrally equivalent records," *Earthquake Spectra*, Vol. 32, No. 2, pp. 927-950.
- Eads, L., Eduardo M., and Lignos, D., 2016, "Spectral shape metrics and structural collapse potential," *Earthquake Engineering & Structural Dynamics*, Vol. 45, No. 10, pp. 1643-1659.
- FEMA, 2009, *Quantification of Building Seismic Performance Factors*, , FEMA P-695, prepared by the Applied Technology Council for the Federal Emergency Management Agency, Washington, D.C.

- FEMA, 2018a, *Assessing Seismic Performance of Buildings with Configuration Irregularities*, FEMA P-2012, prepared by the Applied Technology Council for the Federal Emergency Management Agency, Washington, D.C.
- FEMA, 2018b, *Seismic Performance Assessment of Buildings*, FEMA P-58, prepared by the Applied Technology Council for the Federal Emergency Management Agency, Washington, D.C.
- Haselton, C.B, Liel, A.B., Taylor-Lange, S.C., and Deierlein, G.G., 2016, "Calibration of Model to Simulate Response of Reinforced Concrete Beam-Columns to Collapse," *ACI Structural Journal*, Vol. 113, No. 6.
- Ibarra, L.F., Ricardo, A. M., and Krawinkler, H., 2005, "Hysteretic models that incorporate strength and stiffness deterioration," *Earthquake Engineering & Structural Dynamics*, Vol. 34, No. 12, pp. 1489-1511.
- Malhotra, P.K., 2002, "Cyclic-demand spectrum." *Earthquake Engineering & Structural Dynamics*, Vol. 31, No. 7, pp. 1441-1457.
- Parsons, V.L., 2014, "Stratified sampling." *Wiley StatsRef: Statistics Reference Online*.
- Raghunandan, M., and Liel, A.B., 2013, "Effect of ground motion duration on earthquake-induced structural collapse," *Structural Safety*, Vol 41, pp. 119-133.
- Raghunandan, M., Liel, A.B., and Luco, N., 2015, "Aftershock collapse vulnerability assessment of reinforced concrete frame structures," *Earthquake Engineering & Structural Dynamics*, Vol. 44, No. 3, pp. 419-439.
- Uang, C.M., and Bertero, V.V., 1991. "UBC seismic serviceability regulations: Critical review," *Journal of Structural Engineering*, Vol. 117, No. 7, pp. 2055-2068.
- Vamvatsikos, D., and Cornell, A.C., 2002, "Incremental dynamic analysis," *Earthquake Engineering & Structural Dynamic*, Vol. 31, No. 3, pp. 491-514.

B.2 Review of 'Shake-Table' Test Data and Field Observations

This appendix presents experimental evidence to address whether drift demand, for a given ground motion, is larger in structures that have experienced previous earthquake motions compared with structures that have not. The stated question is examined almost exclusively using observations:

1. from dynamic experiments in the laboratory (i.e. physical simulations also known as 'shake-table' tests),
2. from field surveys, and
3. from engineers with experience dealing with buildings affected by more than one earthquake.

The examined laboratory data come predominantly from dynamic tests on RC specimens detailed to avoid decay in resistance caused by large drift demand.

B.2.1 Laboratory Observations

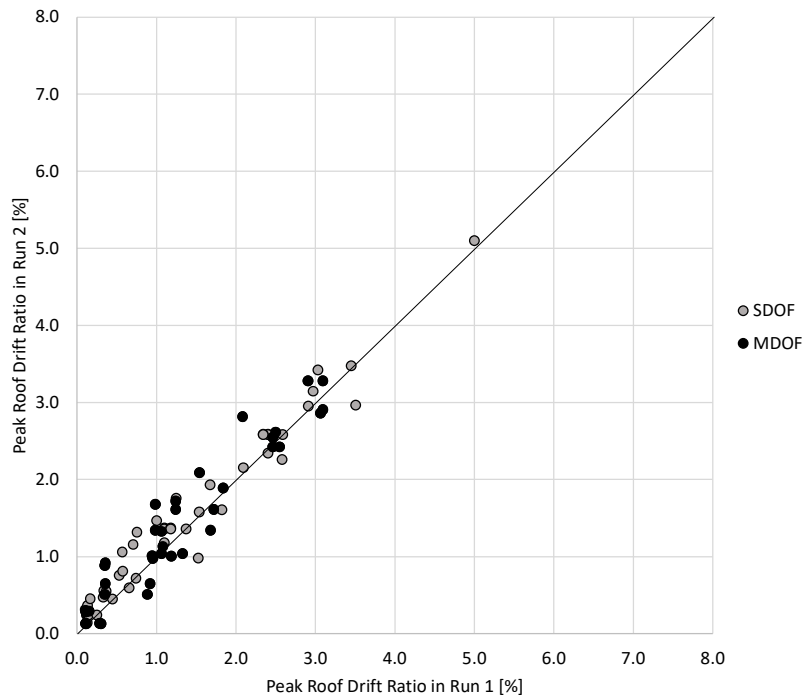


Figure B-2a Measured Roof Drift Ratios. The solid line represents a 1-1 relationship.

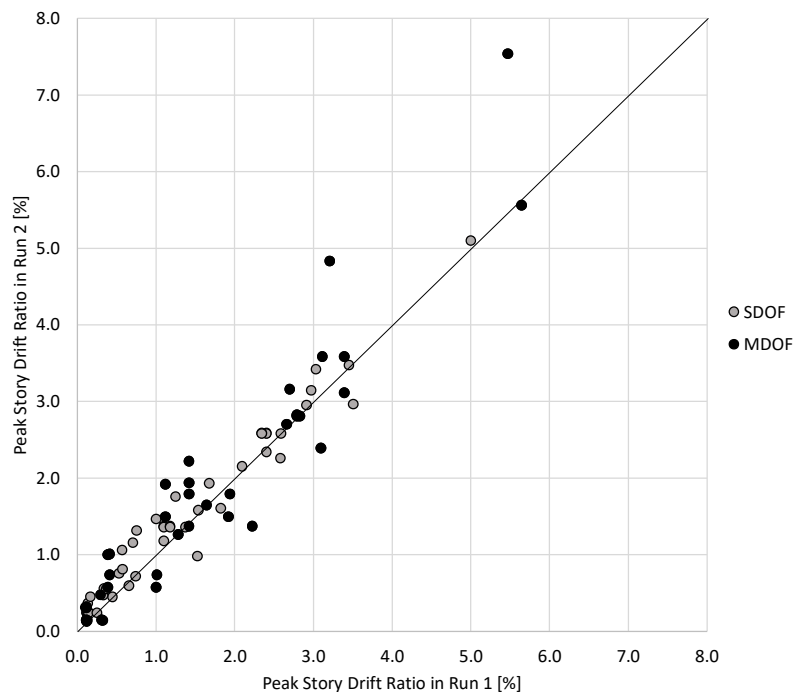


Figure B-2b Measured Story Drift Ratios. The solid line represents a 1-1 relationship.

As described in the next paragraphs, a database with results from dynamic earthquake simulations (or “shake-table” tests) on RC test structures has been compiled (Table B-2). Figures B-2 and B-3 illustrate the main test results. Details of selected tests are provided in B.2.4. The simulations have been organized in 88 pairs (Table B-2). Each pair includes two simulations (dynamic tests) done with the same base motion. For 53 of the pairs, the second simulation was done after the first with at least enough time in between for the test specimen to return to rest. In the remaining 35 pairs, one or more additional simulation(s) of higher intensity was (were) done in between the two motions in the pair (Figure B-3a).

Of the 88 pairs of simulations mentioned, 37 come from tests of MDOF systems (physical models of building structures with 2 to 10 stories). The rest come from SDOF systems with a concentrated mass supported by one or two RC columns. Thirty (30) pairs come from five large-scale structures. The rest come from tests reduced-scale structural models.

The results presented here refer to drifts measured relative to the shape of the structure at the beginning of the motion in consideration. That is: they exclude permanent drifts from previous simulations. This choice is rather arbitrary, but it can be argued that repairs done after strong ground motion are sensitive to increases in drift relative to the shape of the structure at the time of repair and not to ‘cumulative’ drift.

In all cases, the test structures had sufficient reinforcement detailing to survive the applied motions without brittle failures. They were structures dominated mostly by flexure producing cracking and yielding of longitudinal reinforcement and presumably stable hysteresis force-displacement loops as intensity increased (except –likely– for drift ratios exceeding 4%). More details about the test structures can be found in the sources listed in Table B-2. Section B.2.4 describes some of the mentioned tests in more detail. The MDOFs included structural models of structures with soft stories (Schultz, Suzuki – Figure B-3b), regular and irregular frames (Cecen, Wood, Yang - Figure B-3b), dual wall-frame systems (Abrams, Kajiwara), and a structure in which masonry infill walls induced severe torsional response (Suzuki - Figure B-3b). The specimens tested by Laughery and Monical were single-bay frames. The specimen tested by Schoettler was a single column supporting a large mass atop. The specimens tested by Yang were single-bay, two-story frames.

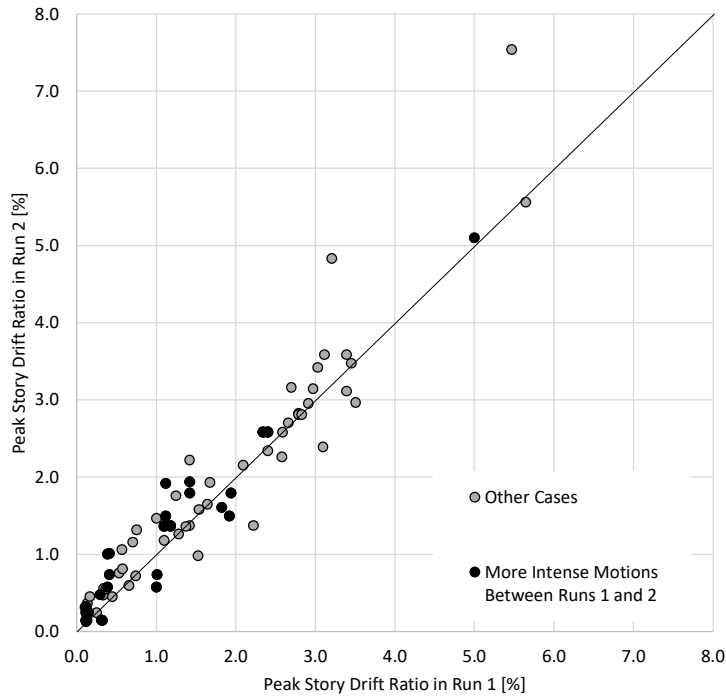


Figure B-3a Measured Drift Ratios. Black circles represent story drift ratios measured in runs straddling one or more runs of higher intensity (See Table B-2).

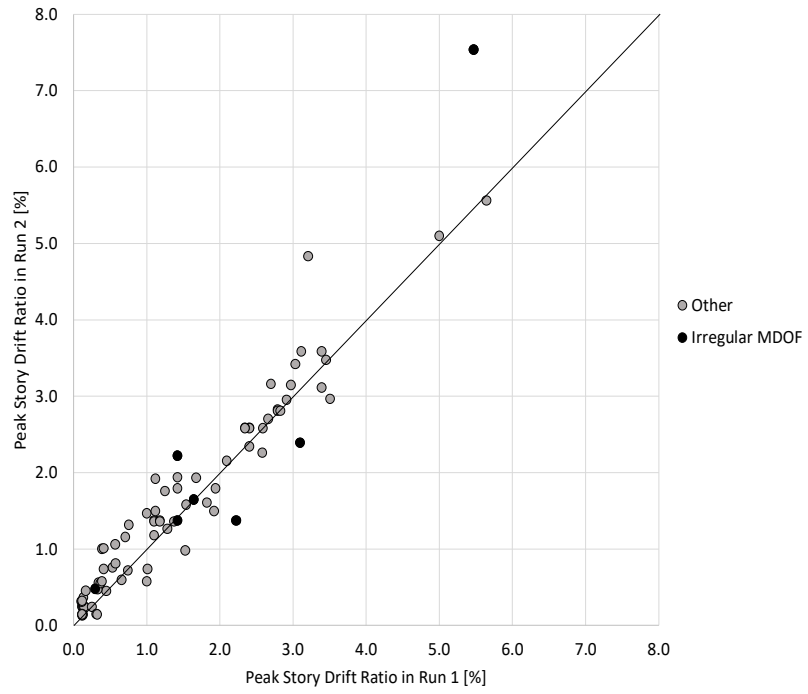


Figure B-3b Measured Drift Ratios. Black circles represent story drift ratios measured in irregular MDOFS (See Table B-2).

Table B-2 Properties of Test Specimens and Ground Motions Considered (after Shah, 2021)

Experiment	Direction / Specimen	DOF	Mea. Period, sec.	Time Scale Factor	Base Shear Coeff.	Ground Motion	Scaled Tg, sec.	Type of Specimen	Irregularities? 1=Y	Intensity Motion in		Run 1 ID	Run 2 ID	Run 1 mea. PGA g	Run 1 mea. PGV cm/s	Run 2 mea. PGA g	Run 2 mea. PGV cm/s	Run 1 Roof DR, %	Run 2 Roof DR, %	Run 1 Max. Story DR, %	Run 2 Max. Story DR, %	Run2/Run1 Roof DR, %	Run2 - Run1 Roof DR, %	Run2/Run1 Story DR, %	Run2 - Run1 Story DR, %
										1=Y	1=Y														
Abrams, 1979	FW1	10	0.31	2.5	0.42	1940 El Centro NS	0.22	Frames	0	0	3	4	2.2	29	2.0	33	3.07	2.86	8.51	6.94	0.93	-0.20	0.82	-1.57	
Abrams, 1979	FW2	10	0.30	2.5	0.29	1940 El Centro NS	0.22	Frames	0	0	2	3	0.9	25	1.1	23	2.50	2.61	5.64	5.56	1.05	0.12	0.99	-0.08	
Abrams, 1979	FW4	10	0.29	2.5	0.42	1952 Taft N21E	0.29	Frames	0	0	2	3	0.9	32	1.3	31	2.08	2.82	3.21	4.83	1.35	0.73	1.51	1.63	
Cecen, 1979	H2	10	0.23	2.5	0.26	1940 El Centro NS	0.22	Frames	0	0	3	4	0.5	16	0.4	16	1.08	1.13	2.70	3.16	1.05	0.05	1.17	0.46	
Wood, 1983	STP	9	0.17	2.5	0.58	1940 El Centro NS	0.22	Frames w. Setbacks	1	1	1	3	0.3	6	0.1	3	0.15	0.29	0.29	0.48	1.91	0.14	1.62	0.18	
Wood, 1983	STP	9	0.17	2.5	0.58	1940 El Centro NS	0.22	Frames w. Setbacks	1	0	2	4	1.5	21	0.4	16	0.95	1.01	1.64	1.65	1.07	0.07	1.00	0.01	
Schultz, 1985	SS1	9	0.26	2.5	0.3	1940 El Centro NS	0.22	Frames w. Soft Story	1	0	1	2	0.3	16	0.3	15	1.19	1.01	3.10	2.39	0.85	-0.18	0.77	-0.70	
Schultz, 1985	SS2	9	0.22	2.5	0.43	1940 El Centro NS	0.22	Frames w. Soft Story	1	0	1	2	0.3	13	0.4	13	1.06	1.33	1.42	2.22	1.25	0.26	1.57	0.80	
Schultz, 1985	SS2	9	0.22	2.5	0.43	1940 El Centro NS	0.22	Frames w. Soft Story	1	0	1	3	0.3	13	0.3	12	1.06	1.04	1.42	1.37	0.98	-0.02	0.97	-0.04	
Schultz, 1985	SS2	9	0.22	2.5	0.43	1940 El Centro NS	0.22	Frames w. Soft Story	1	0	2	3	0.4	13	0.3	12	1.33	1.04	2.22	1.37	0.78	-0.29	0.62	-0.85	
Schoettler, 2012	Col. 1	1	0.79	1	0.26	1989 Loma Prieta EW	0.58	Single Column	0	1	2	4	0.4	36	0.4	38	1.82	1.61	1.82	1.61	0.88	-0.21	0.88	-0.21	
Schoettler, 2012	Col. 1	1	0.79	1	0.26	1989 Loma Prieta NS	0.68	Single Column	0	1	3	6	0.5	80	0.5	78	5.00	5.10	5.00	5.10	1.02	0.10	1.02	0.10	
Schoettler, 2012	Col. 1	1	0.79	1	0.26	1995 Kobe NS	1.23	Single Column	0	0	8	9	0.8	128	0.8	129	9.94	7.04	9.94	7.04	0.71	-2.90	0.71	-2.90	
Laughery, 2016	C1	1	0.16	3	0.92	1994 Northridge EW	0.35	One-Bay Frame	0	0	4	5	1.8	28	1.5	30	3.51	2.97	3.51	2.97	0.85	-0.54	0.85	-0.54	
Laughery, 2016	C2	1	0.16	3	0.92	1994 Northridge EW	0.35	One-Bay Frame	0	0	1	5	1.9	30	1.7	29	3.45	3.48	3.45	3.48	1.01	0.03	1.01	0.03	
Laughery, 2016	H1	1	0.13	3	1.02	1994 Northridge EW	0.35	One-Bay Frame	0	0	4	5	1.4	31	1.4	31	3.03	3.42	3.03	3.42	1.13	0.39	1.13	0.39	
Laughery, 2016	H2	1	0.13	3	1.02	1994 Northridge EW	0.35	One-Bay Frame	0	0	1	5	1.6	30	1.6	29	2.97	3.15	2.97	3.15	1.06	0.17	1.06	0.17	
Kajiwara, 2017	2018-Short	10	0.42	1	0.4	1995 Kobe EW	0.74	10-Story Building	0	0	4	5	0.6	73	0.9	78	0.95	0.98	1.28	1.27	1.02	0.02	0.99	-0.02	
Kajiwara, 2017	2018-Long	10	0.53	1	0.39	1995 Kobe NS	0.82	10-Story Building	0	0	4	5	0.8	93	1.2	96	1.84	1.89	2.66	2.70	1.03	0.05	1.02	0.05	
Suzuki, 2021	Spec. 1, E. Corner	7	--	1.41	--	1999 Chichi, CHY101EW	---	Frame with Infill	1	0	3	4	0.5	73	0.5	73	1.54	2.09	5.47	7.54	1.36	0.55	1.38	2.07	

Table B-2 Properties of Test Specimens and Ground Motions Considered (continued)

Experiment	Direction / Specimen	DOF	Mea. Period, sec.	Time Scale Factor	Base Shear Coeff.	Ground Motion	Scaled Tg, sec.	Type of Specimen	Irregularities? 1=Y	Intensity Motion in 1=Y	Run 1 ID	Run 2 ID	Run 1	Run 1	Run 2	Run 2	Run 1	Run 2	Run 1	Run 2	Run 2/Run 1	Run 2/Run 1	Run 2/Run 1	Run 2/Run 1
													mea. PGA g	mea. PGV cm/s	mea. PGA g	mea. PGV cm/s	Roof DR, %	Roof DR, %	Max. Story DR, %	Max. Story DR, %	Roof DR	Roof DR, %	Story DR	Story DR, %
Monical, 2021	F1-B	1	0.17	2	0.47	1940 El Centro NS	0.24	One-Bay Frame	0	0	1	2	0.1	3	0.1	3	0.12	0.13	0.12	0.13	1.11	0.01	1.11	0.01
Monical, 2021	F1-B	1	0.17	2	0.47	1940 El Centro NS	0.24	One-Bay Frame	0	0	1	3	0.1	3	0.1	3	0.12	0.14	0.12	0.14	1.24	0.03	1.24	0.03
Monical, 2021	F1-B	1	0.17	2	0.47	1940 El Centro NS	0.24	One-Bay Frame	0	1	1	5	0.1	3	0.1	3	0.12	0.25	0.12	0.25	2.14	0.13	2.14	0.13
Monical, 2021	F1-B	1	0.17	2	0.47	1940 El Centro NS	0.24	One-Bay Frame	0	1	1	6	0.1	3	0.1	4	0.12	0.24	0.12	0.24	2.08	0.13	2.08	0.13
Monical, 2021	F1-B	1	0.17	2	0.47	1940 El Centro NS	0.24	One-Bay Frame	0	0	2	3	0.1	3	0.1	3	0.13	0.14	0.13	0.14	1.12	0.02	1.12	0.02
Monical, 2021	F1-B	1	0.17	2	0.47	1940 El Centro NS	0.24	One-Bay Frame	0	1	2	5	0.1	3	0.1	3	0.13	0.25	0.13	0.25	1.93	0.12	1.93	0.12
Monical, 2021	F1-B	1	0.17	2	0.47	1940 El Centro NS	0.24	One-Bay Frame	0	1	2	6	0.1	3	0.1	4	0.13	0.24	0.13	0.24	1.88	0.11	1.88	0.11
Monical, 2021	F1-B	1	0.17	2	0.47	1940 El Centro NS	0.24	One-Bay Frame	0	1	3	5	0.1	3	0.1	3	0.14	0.25	0.14	0.25	1.73	0.11	1.73	0.11
Monical, 2021	F1-B	1	0.17	2	0.47	1940 El Centro NS	0.24	One-Bay Frame	0	1	3	6	0.1	3	0.1	4	0.14	0.24	0.14	0.24	1.68	0.10	1.68	0.10
Monical, 2021	F1-B	1	0.17	2	0.47	1940 El Centro NS	0.24	One-Bay Frame	0	0	5	6	0.1	3	0.1	4	0.25	0.24	0.25	0.24	0.97	-0.01	0.97	-0.01
Monical, 2021	F1-B	1	0.17	2	0.47	1940 El Centro NS	0.24	One-Bay Frame	0	0	4	7	0.2	8	0.2	6	0.34	0.56	0.34	0.56	1.65	0.22	1.65	0.22
Monical, 2021	F1-B	1	0.17	2	0.47	1940 El Centro NS	0.24	One-Bay Frame	0	0	8	9	0.3	11	0.2	12	1.10	1.18	1.10	1.18	1.07	0.08	1.07	0.08
Monical, 2021	F1-B	1	0.17	2	0.47	1940 El Centro NS	0.24	One-Bay Frame	0	1	8	14	0.3	11	0.2	12	1.10	1.37	1.10	1.37	1.25	0.27	1.25	0.27
Monical, 2021	F1-B	1	0.17	2	0.47	1940 El Centro NS	0.24	One-Bay Frame	0	1	8	15	0.3	11	0.3	13	1.10	1.36	1.10	1.36	1.24	0.26	1.24	0.26
Monical, 2021	F1-B	1	0.17	2	0.47	1940 El Centro NS	0.24	One-Bay Frame	0	1	9	14	0.2	12	0.2	12	1.18	1.37	1.18	1.37	1.16	0.19	1.16	0.19
Monical, 2021	F1-B	1	0.17	2	0.47	1940 El Centro NS	0.24	One-Bay Frame	0	1	9	15	0.2	12	0.3	13	1.18	1.36	1.18	1.36	1.15	0.18	1.15	0.18
Monical, 2021	F1-B	1	0.17	2	0.47	1940 El Centro NS	0.24	One-Bay Frame	0	0	14	15	0.2	12	0.3	13	1.37	1.36	1.37	1.36	0.99	-0.01	0.99	-0.01
Monical, 2021	F1-B	1	0.17	2	0.47	1940 El Centro NS	0.24	One-Bay Frame	0	0	10	11	0.3	18	0.4	17	1.68	1.93	1.68	1.93	1.15	0.25	1.15	0.25
Monical, 2021	F1-B	1	0.17	2	0.47	1940 El Centro NS	0.24	One-Bay Frame	0	0	12	13	0.4	21	0.4	21	2.58	2.26	2.58	2.26	0.88	-0.32	0.88	-0.32
Monical, 2021	F1-C	1	0.17	2	0.47	1940 El Centro NS	0.24	One-Bay Frame	0	0	16	17	0.1	3	0.1	3	0.45	0.45	0.45	0.45	1.00	0.00	1.00	0.00
Monical, 2021	F1-C	1	0.17	2	0.47	1940 El Centro NS	0.24	One-Bay Frame	0	0	18	19	0.2	5	0.2	6	0.74	0.72	0.74	0.72	0.97	-0.02	0.97	-0.02
Monical, 2021	F1-C	1	0.17	2	0.47	1940 El Centro NS	0.24	One-Bay Frame	0	0	20	21	0.3	10	0.3	11	1.54	1.58	1.54	1.58	1.03	0.04	1.03	0.04
Monical, 2021	F1-C	1	0.17	2	0.47	1940 El Centro NS	0.24	One-Bay Frame	0	0	22	23	0.3	17	0.3	15	2.09	2.15	2.09	2.15	1.03	0.06	1.03	0.06
Monical, 2021	F1-C	1	0.17	2	0.47	1940 El Centro NS	0.24	One-Bay Frame	0	0	24	25	0.4	20	0.4	20	2.40	2.34	2.40	2.34	0.97	-0.06	0.97	-0.06
Monical, 2021	F1-C	1	0.17	2	0.47	1940 El Centro NS	0.24	One-Bay Frame	0	1	24	28	0.4	20	0.4	21	2.40	2.59	2.40	2.59	1.08	0.18	1.08	0.18
Monical, 2021	F1-C	1	0.17	2	0.47	1940 El Centro NS	0.24	One-Bay Frame	0	1	24	29	0.4	20	0.4	21	2.40	2.58	2.40	2.58	1.07	0.18	1.07	0.18
Monical, 2021	F1-C	1	0.17	2	0.47	1940 El Centro NS	0.24	One-Bay Frame	0	1	25	28	0.4	20	0.4	21	2.34	2.59	2.34	2.59	1.10	0.25	1.10	0.25
Monical, 2021	F1-C	1	0.17	2	0.47	1940 El Centro NS	0.24	One-Bay Frame	0	1	25	29	0.4	20	0.4	21	2.34	2.58	2.34	2.58	1.10	0.24	1.10	0.24
Monical, 2021	F1-C	1	0.17	2	0.47	1940 El Centro NS	0.24	One-Bay Frame	0	0	28	29	0.4	21	0.4	21	2.59	2.58	2.59	2.58	1.00	0.00	1.00	0.00
Monical, 2021	F1-C	1	0.17	2	0.47	1940 El Centro NS	0.24	One-Bay Frame	0	0	26	27	0.5	24	0.5	25	2.91	2.95	2.91	2.95	1.02	0.04	1.02	0.04

Table B-2 Properties of Test Specimens and Ground Motions Considered (continued)

Experiment	Direction / Specimen	DOF	Mea. Period, sec.	Time Scale Factor	Base Shear Coeff.	Ground Motion	Scaled Tg, sec.	Type of Specimen	Irregularities? 1=Y	Intensity Motion in		Run 1 ID	Run 2 ID	Run 1 mea. PGA g	Run 1 mea. PGV cm/s	Run 2 mea. PGA g	Run 2 mea. PGV cm/s	Run 1 Roof DR, %	Run 2 Roof DR, %	Run 1 Max. Story DR, %	Run 2 Max. Story DR, %	Run2/Run1 Roof DR	Run2 - Run1 Roof DR, %	Run2/Run1 Story DR	Run2 - Run1 Story DR, %
										1=Y	1=Y														
Monical, 2021	F2-C	1	0.17	5	0.47	2010 Darfield NS	0.05	One-Bay Frame	0	0	1	8	0.1	5	0.1	6	0.10	0.31	0.10	0.31	3.03	0.21	3.03	0.21	
Monical, 2021	F2-C	1	0.17	2	0.47	1971 San Fernando NS	0.19	One-Bay Frame	0	0	2	9	0.1	6	0.1	5	0.13	0.37	0.13	0.37	2.77	0.23	2.77	0.23	
Monical, 2021	F2-C	1	0.17	2.5	0.47	2002 Denail NW	0.44	One-Bay Frame	0	0	3	10	0.1	5	0.1	5	0.17	0.45	0.17	0.45	2.74	0.29	2.74	0.29	
Monical, 2021	F2-C	1	0.17	4	0.47	1940 El Centro NS	0.12	One-Bay Frame	0	0	4	11	0.2	4	0.2	5	0.33	0.47	0.33	0.47	1.44	0.15	1.44	0.15	
Monical, 2021	F2-C	1	0.17	2	0.47	1940 El Centro NS	0.24	One-Bay Frame	0	0	5	12	0.1	5	0.1	5	0.37	0.55	0.37	0.55	1.50	0.18	1.50	0.18	
Monical, 2021	F2-C	1	0.17	1	0.47	1994 Northridge EW	0.30	One-Bay Frame	0	0	6	13	0.1	5	0.1	5	0.53	0.76	0.53	0.76	1.42	0.23	1.42	0.23	
Monical, 2021	F2-C	1	0.17	1.25	0.47	1972 Managua NS	0.30	One-Bay Frame	0	0	7	14	0.1	4	0.1	5	0.66	0.60	0.66	0.60	0.91	-0.06	0.91	-0.06	
Monical, 2021	F2-C	1	0.17	5	0.47	2010 Darfield NS	0.05	One-Bay Frame	0	0	15	22	0.2	10	0.2	9	0.57	0.81	0.57	0.81	1.41	0.24	1.41	0.24	
Monical, 2021	F2-C	1	0.17	2	0.47	1971 San Fernando NS	0.19	One-Bay Frame	0	0	16	23	0.2	9	0.2	9	0.57	1.06	0.57	1.06	1.86	0.49	1.86	0.49	
Monical, 2021	F2-C	1	0.17	2.5	0.47	2002 Denail NW	0.44	One-Bay Frame	0	0	17	24	0.1	10	0.1	10	0.71	1.16	0.71	1.16	1.64	0.45	1.64	0.45	
Monical, 2021	F2-C	1	0.17	4	0.47	1940 El Centro NS	0.12	One-Bay Frame	0	0	18	25	0.4	10	0.3	10	0.75	1.32	0.75	1.32	1.75	0.56	1.75	0.56	
Monical, 2021	F2-C	1	0.17	2	0.47	1940 El Centro NS	0.24	One-Bay Frame	0	0	19	26	0.2	10	0.3	11	1.00	1.47	1.00	1.47	1.47	0.47	1.47	0.47	
Monical, 2021	F2-C	1	0.17	1	0.47	1994 Northridge EW	0.30	One-Bay Frame	0	0	20	27	0.2	9	0.2	11	1.25	1.76	1.25	1.76	1.41	0.51	1.41	0.51	
Monical, 2021	F2-C	1	0.17	1.25	0.47	1972 Managua NS	0.30	One-Bay Frame	0	0	21	28	0.2	9	0.2	9	1.53	0.98	1.53	0.98	0.64	-0.54	0.64	-0.54	

Table B-2 Properties of Test Specimens and Ground Motions Considered (continued)

Experiment	Direction / Specimen	DOF	Mea. Period, sec.	Time Scale Factor	Base Shear Coeff.	Ground Motion	Scaled Tg, sec.	Type of Specimen	Irregularities? 1=Y	Intensity Motion in 1=Y	Run 1 ID	Run 2 ID	Run 1	Run 1	Run 2	Run 2	Run 1	Run 2	Run 1	Run 2	Run 2/	Run 2 -	Run 2/	Run 2 -
													PGA g	PGV cm/s	PGA g	PGV cm/s	Roof DR, %	Roof DR, %	Max. Story DR, %	Max. Story DR, %	Roof DR	Roof DR, %	Story DR	Story DR, %
Yang, 2021	C1	2	0.30	1.5	0.87	1940 El Centro NS	0.37	Two-Story Frame	0	1	1	7	0.1	7	0.1	7	0.11	0.28	0.12	0.31	2.56	0.17	2.68	0.19
Yang, 2021	C1	2	0.30	1.5	0.87	1940 El Centro NS	0.37	Two-Story Frame	0	1	2	8	0.3	18	0.3	18	0.35	0.89	0.39	1.00	2.53	0.54	2.59	0.61
Yang, 2021	C1	2	0.30	1.5	0.87	1940 El Centro NS	0.37	Two-Story Frame	0	1	3	9	0.5	37	0.5	37	0.98	1.68	1.12	1.92	1.71	0.69	1.71	0.80
Yang, 2021	C1	2	0.30	1.5	0.87	1940 El Centro NS	0.37	Two-Story Frame	0	0	5	6	1.0	74	1.0	74	2.46	2.55	2.79	2.83	1.03	0.09	1.01	0.04
Yang, 2021	C1-R	2	0.30	1.5	0.87	1940 El Centro NS	0.37	Two-Story Frame	0	1	1	10	0.1	7	0.1	7	0.11	0.13	0.12	0.15	1.22	0.02	1.29	0.03
Yang, 2021	C1-R	2	0.30	1.5	0.87	1940 El Centro NS	0.37	Two-Story Frame	0	1	2	11	0.3	18	0.3	18	0.35	0.51	0.39	0.58	1.46	0.16	1.49	0.19
Yang, 2021	C1-R	2	0.30	1.5	0.87	1940 El Centro NS	0.37	Two-Story Frame	0	1	3	12	0.5	37	0.5	36	0.98	1.34	1.12	1.50	1.36	0.36	1.34	0.38
Yang, 2021	C1-R	2	0.30	1.5	0.87	1940 El Centro NS	0.37	Two-Story Frame	0	0	5	13	1.0	74	1.0	74	2.46	2.42	2.79	2.81	0.98	-0.04	1.01	0.02
Yang, 2021	C1-R	2	0.30	1.5	0.87	1940 El Centro NS	0.37	Two-Story Frame	0	1	7	10	0.1	7	0.1	7	0.28	0.13	0.31	0.15	0.48	-0.15	0.48	-0.16
Yang, 2021	C1-R	2	0.30	1.5	0.87	1940 El Centro NS	0.37	Two-Story Frame	0	1	8	11	0.3	18	0.3	18	0.89	0.51	1.00	0.58	0.57	-0.38	0.57	-0.43
Yang, 2021	C1-R	2	0.30	1.5	0.87	1940 El Centro NS	0.37	Two-Story Frame	0	1	9	12	0.5	37	0.5	36	1.68	1.34	1.92	1.50	0.80	-0.34	0.78	-0.42
Yang, 2021	C1-R	2	0.30	1.5	0.87	1940 El Centro NS	0.37	Two-Story Frame	0	0	6	13	1.0	74	1.0	74	2.55	2.42	2.83	2.81	0.95	-0.12	0.99	-0.02
Yang, 2021	H1	2	0.30	1.5	0.95	1940 El Centro NS	0.37	Two-Story Frame	0	1	1	7	0.1	7	0.1	7	0.11	0.30	0.11	0.32	2.79	0.19	2.81	0.21
Yang, 2021	H1	2	0.30	1.5	0.95	1940 El Centro NS	0.37	Two-Story Frame	0	1	2	8	0.3	18	0.3	18	0.36	0.92	0.41	1.01	2.58	0.56	2.47	0.60
Yang, 2021	H1	2	0.30	1.5	0.95	1940 El Centro NS	0.37	Two-Story Frame	0	1	3	9	0.5	37	0.5	37	1.24	1.72	1.42	1.94	1.39	0.48	1.36	0.52
Yang, 2021	H1	2	0.30	1.5	0.95	1940 El Centro NS	0.37	Two-Story Frame	0	0	5	6	1.0	74	1.0	74	3.09	2.91	3.39	3.11	0.94	-0.19	0.92	-0.28
Yang, 2021	H1-R	2	0.30	1.5	0.95	1940 El Centro NS	0.37	Two-Story Frame	0	1	1	10	0.1	7	0.1	7	0.11	0.13	0.11	0.14	1.21	0.02	1.26	0.03
Yang, 2021	H1-R	2	0.30	1.5	0.95	1940 El Centro NS	0.37	Two-Story Frame	0	1	2	11	0.3	18	0.3	18	0.36	0.65	0.41	0.74	1.83	0.30	1.80	0.33
Yang, 2021	H1-R	2	0.30	1.5	0.95	1940 El Centro NS	0.37	Two-Story Frame	0	1	3	12	0.5	37	0.5	36	1.24	1.61	1.42	1.79	1.30	0.37	1.26	0.37
Yang, 2021	H1-R	2	0.30	1.5	0.95	1940 El Centro NS	0.37	Two-Story Frame	0	0	5	13	1.0	74	1.0	74	3.09	3.28	3.39	3.59	1.06	0.19	1.06	0.20
Yang, 2021	H1-R	2	0.30	1.5	0.95	1940 El Centro NS	0.37	Two-Story Frame	0	1	7	10	0.1	7	0.1	7	0.30	0.13	0.32	0.14	0.43	-0.17	0.45	-0.18
Yang, 2021	H1-R	2	0.30	1.5	0.95	1940 El Centro NS	0.37	Two-Story Frame	0	1	8	11	0.3	18	0.3	18	0.92	0.65	1.01	0.74	0.71	-0.27	0.73	-0.27
Yang, 2021	H1-R	2	0.30	1.5	0.95	1940 El Centro NS	0.37	Two-Story Frame	0	1	9	12	0.5	37	0.5	36	1.72	1.61	1.94	1.79	0.94	-0.11	0.92	-0.15
Yang, 2021	H1-R	2	0.30	1.5	0.95	1940 El Centro NS	0.37	Two-Story Frame	0	0	6	13	1.0	74	1.0	74	2.91	3.28	3.11	3.59	1.13	0.37	1.15	0.47

Notes:

For Monical 2021, runs after the first 30 runs (for a single specimen) are not included.

For Yang 2021: R denotes repair of cracks with epoxy, listed PGV and PGA values are 'target' instead of 'measured' values. R denotes repair of cracks with epoxy.

For Suzuki, 2021: listed PGV and PGA values are 'target' instead of 'measured' values.

Duration of records and time increments were divided by the Time Scale Factor.

Tg = characteristic period of ground (near intersection between regions of nearly constant spectral acceleration and velocity).

Figures B-4 and 5 illustrate increases in drift ratio. Figure B-4 refers to differences between drift ratios measured in the repetition of a motion (Run 2) and drift measured in the first instance of the same motion (Run 1). Figure B-5 refers to ratios of the former to the latter.

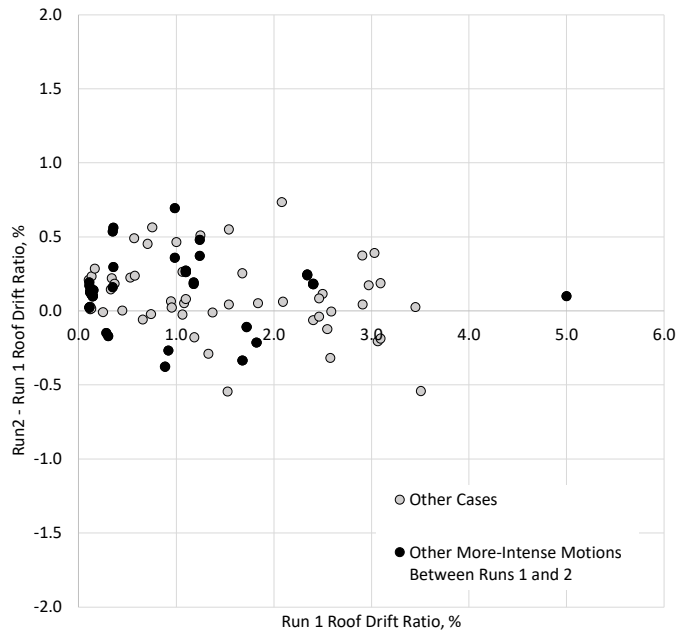


Figure B-4a Differences in Measured Roof Drift Ratios. Black circles represent roof drift ratios measured in motions straddling other more intense motions..

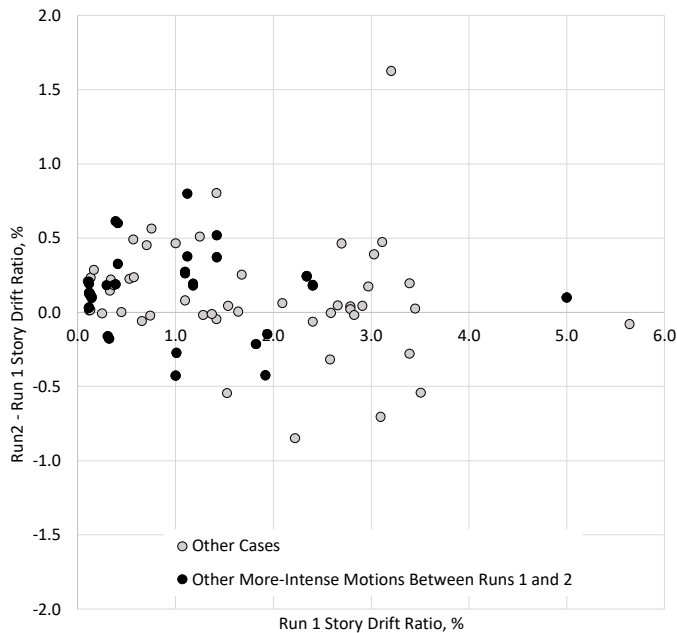


Figure B-4b Differences in Measured Story Drift Ratios. Black circles represent roof drift ratios measured in motions straddling other more intense motions..

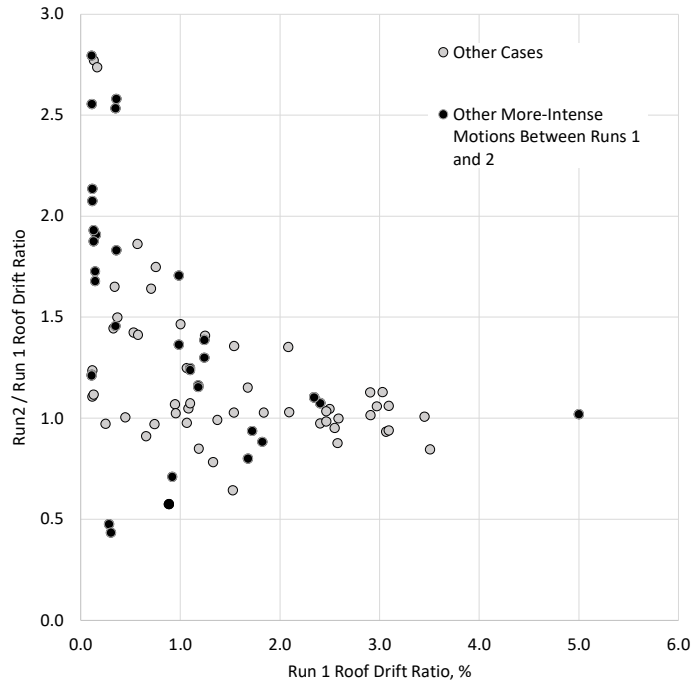


Figure B-5a Ratio of Final to Initial Roof Drift. The black circles represent repeated runs straddling one or several more intense run(s).

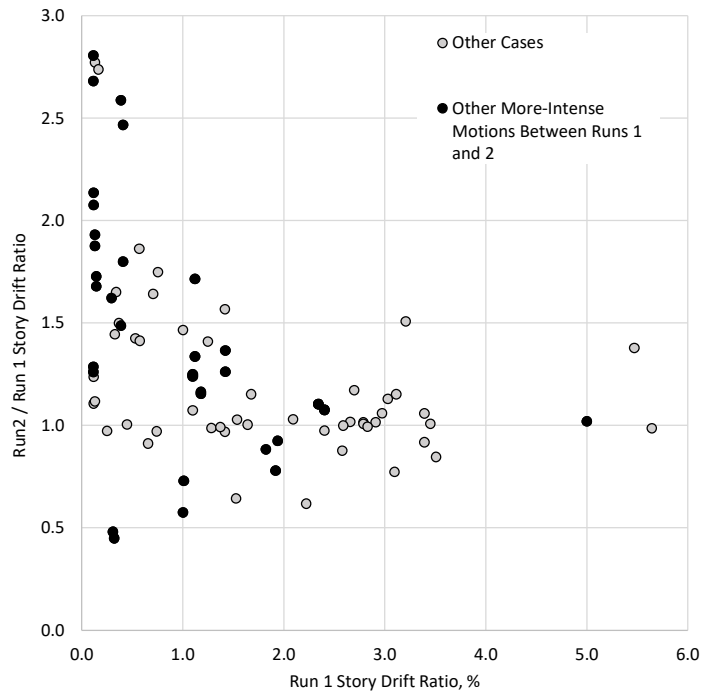


Figure B-5b Ratio of Final to Initial Story Drift. The black circles represent repeated runs straddling one or several more intense run(s).

There are a few apparent trends in the experimental data:

For comparison pairs in which the first simulation produced a drift ratio exceeding approximately 1%, there was no consistent increase in drift in the second run even if that run occurred after a larger intensity intermediate run(s).

There is scatter in the test data, especially for story drift ratios, and it may be attributable in part to at least two issues: 1) the variability in the demand for structures with different or varying periods produced by each of the chosen records, and 2) the ability of earthquake simulators (or ‘shake tables’) to reproduce a given base motion.

For pairs in which the first simulation produced a drift ratio **not** exceeding 1%, there was an increase in drift ratio (of 60% to 70% on average and as high as 300%). The relative increase in drift was larger if the initial run occurred in a pristine specimen, especially if stronger in-between simulation(s) preceded the second simulation in the pair.

In 80% of cases, the increase in drift ratio (for roof and story drift) was smaller than 0.3% (in absolute terms). In a number of cases the repeat caused less drift even in runs occurring after a higher-intensity intermediate simulation. Results were not worse in irregular structures.

In a nutshell: the apparent relative increases in drift occurred when the denominator in the ratio of drift in second run to drift in first run approached zero. The worst cases occurred when 1) the second run followed intermediate run(s) that caused cracking and yielding, while 2) the first run was mild enough to not cause either. This observation seems to be in agreement with tests indicating that in nonlinear structures drift increases faster with increases in initial period than it does in linear structures (Bonacci, 1989).

Note:

In the subject tests, the relative increase in drift did not increase with increments in initial drift as suggested from numerical analyses described in Section B.5. One could expect that as the drift reached in the first run increases, its consequences may handicap the structure causing more drift in the repeat or second run in the comparison pair. The laboratory observations available do not support that idea. The SDOF analyses described in B.3 do not support it either. The results from detailed numerical dynamic analyses described in B.5 differ from the evidence presented in this Appendix B.2. The cause is likely that the algorithms used in B.5 reduce lateral resistance with extent and number of cycles while the test structures and the SDOF did not experience such ‘decay.’ Decay in lateral resistance can affect drift demand as illustrated by Pujol and Sozen (2006).

B.2.2 Field Observations

In Chile, scores of buildings have subjected to strong ground motion at least twice: once in 1985, and once in 2010. In Viña del Mar and Valparaiso, the intensities of these two ground motions were similar from a number of points of view. The mean PGV in the region was 21 cm/s in 1985 and 20 cm/s in 2010 (Table B-3). The mean PGA was 0.24 g in 1985 and 0.22 g in 2010 (Table B-3). The reported Modified Mercalli Intensity was VII-VIII in 1985 (Wood et al. 1987) and VI-VII in 2010 (USGS 2020). And linear displacement spectra for the records obtained in downtown Viña del Mar were also similar (Figure B-6).

Table B-3 Values of PGV and PGA measured in Viña del Mar and Valparaiso

EQ	YR	STA	DIR	AZI	PGV (CM/S)	PGA (G)
Valparaiso	1985	Viña Centro	N70W	290	26	0.24
Valparaiso	1985	Viña Centro	S20W	200	31	0.36
Valparaiso	1985	Valparaiso	S20E	160	9	0.17
Valparaiso	1985	Valparaiso	N70E	70	15	0.18
Valparaiso	1985	El Almendral	N50E	50	29	0.30
Valparaiso	1985	El Almendral	S40E	140	17	0.17
					21	0.24
Maule	2010	Viña Centro	EW	90	33	0.33
Maule	2010	Viña Centro	NS	0	21	0.22
Maule	2010	Valparaiso	L	--	7	0.13
Maule	2010	Valparaiso	T	--	16	0.30
Maule	2010	El Almendral	L	--	29	0.22
Maule	2010	El Almendral	T	--	11	0.14
					20	0.22

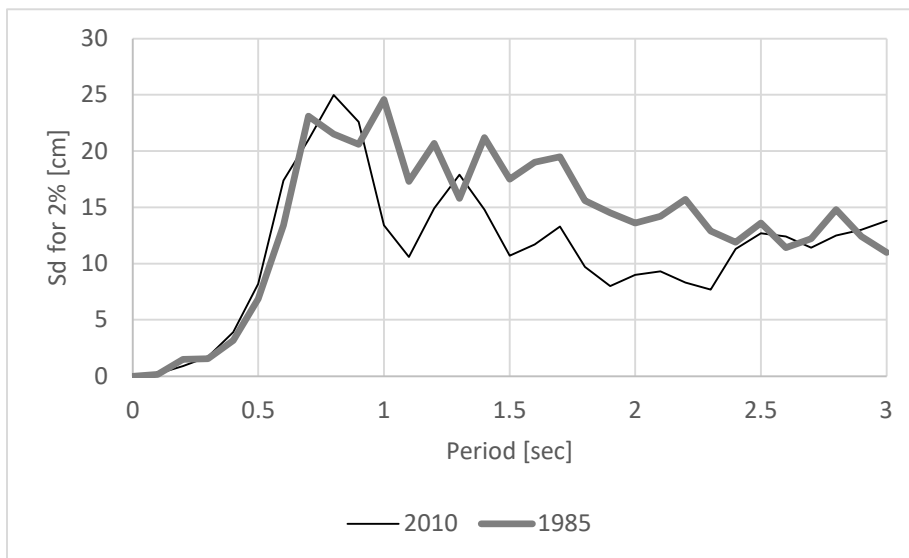


Figure B-6 Spectra for Records from Downtown Viña del Mar.

Given the similarities between the motions that occurred in 1985 and 2010, it may be useful to compare observations on the performance of buildings in the two earthquakes to address the question of how the response to the first motion may have affected the response to the second motion.

Ridell, Wood, and De La Llera (1987) summarized information from 178 buildings from Viña del Mar after the 1985 earthquake. The information was obtained from inspections completed by the Municipality. They wrote:

In most cases the damage reports are not as complete as desired. The Municipality inspection was carried out with the main purpose of determining the most critical situations that required prompt action after the earthquake. Therefore, no attempt was made to document damage in detail. On the basis of the available information, the level of damage in each building was classified in four categories: None, Light, Moderate, Severe. Buildings classified in the “None” category correspond to buildings for which there was no available information. It does not necessarily mean that there was positive evidence that these buildings were undamaged. It is unlikely, however, that any of these buildings could have suffered moderate or severe damage and remained unnoticed.

The subject buildings are described by Ridell et al. (1987). More detail is given for 12 of these buildings by Wood et al. (1987).

Five Chilean engineers were asked the question: “In your experience in the Maule Earthquake of 2010, did RC buildings that survived the 1985 (or previous) earthquake(s) without structural failures perform worse than buildings built after 1985?” All five replied “no.”

After the earthquake in 2010, Lepage and Pujol (2010) surveyed and classified the damage for 31 of the buildings surveyed earlier as reported by Ridell and Wood (Table B-4). A database with photographs from 2010 and more information about buildings in Chile is described in ATC 93 and is available here: <https://disasterhub.nist.gov/resources/5/>

The 31 buildings surveyed twice (in 1985 and 2010) varied in height from 8 to 23 stories. As most buildings in Chile, they were RC buildings with abundant structural walls. Wood et al. (1987) reported for these buildings ratios of wall cross-sectional area to floor area averaging 3% in each direction, and fundamental periods of vibration approaching 1/20 times the number of stories.

Table B-4 lists the damage ratings assigned to the 31 buildings surveyed in 1985 and 2010. A number of issues need consideration to interpret the ratings:

1. They were assigned by different engineers, with different perspectives and objectives.

2. The ratings from 1985 corresponding to ‘none’ and ‘light’ damage were grouped in a single category corresponding to a score of 1. ‘None’ and ‘light’ were treated as equivalent because ‘none’ did not imply absence of damage, as noted above. For instance, for Torres del Pacifico, the 1985 report classified the damage as 'none,' yet the available narrative speaks of cracks in beams and slabs. The rating ‘moderate’ was given a score of 2, and ‘Severe’ was given a score of 3.
3. The ratings are subjective and consider not only the severity of damage but the spread and potential consequences of the damage. The subjectivity is clear in the case of Marina Real: the original description of damage in 1985 seems to capture well what was photographed in 2010, yet the ratings assigned in 1985 (1) and 2010 (2) were different.
4. Once a building has been damaged, if said damage has been simply patched up with mortar (as was apparent in a number of cases in Viña del Mar), it seems quite unlikely that additional ground motion would lead to less observable damage even if the additional motion causes less drift than the initial motion. Said in a different way, even for an ideal objective surveyor, the mentioned damage ratings were likely to not change or change in a single ‘direction:’ up.
5. The buildings constructed in Chile before modifications made to the local design code after 2010 were not always well detailed and were prone to brittle response. By definition, in a brittle structure, a small increase in drift can cause a large increase in apparent damage. That damage can in turn cause reduction in resistance leading to more drift in a feedback loop that can result in disproportionate consequences. In a ductile structure, on the other hand, lateral resistance is sustained through displacement reversals, making the mentioned feedback loop and disproportionate damage less likely.




With these issues in mind, the most salient features of the observations made through comparison of the 1985 and 2010 post-earthquake surveys include:

1. Of the 31 buildings surveyed twice, three had a radical increase in the assigned score: Galleria Libertad Centro (1.5 to 3), Maya (1 to 3), Villa Real (1 to 2.5). The latter two had clear signs of previous repairs in elements with damage visible in 2010. For Villa Real Building, the description of the damage in 1985 (“inclined cracks in walls in lower 3 stories and spalling of cover from lintel beams”) can be interpreted to match what the photos taken in 2010 show. The same photos reveal mortar patching suggesting the damage in 2010 occurred at locations damaged before. Maya building had a single localized instance of



crushing and bar buckling with signs of severe corrosion and old concrete patching suggesting the problem may have started before 2010. That leaves one building of 31 in which there may have been a clear increase in damage. The damage occurred in short wall piers susceptible to brittle shear failure that, as explained above, results in dramatic damage that may not unequivocally indicate large increases in drift demand.



2. Of the 31 buildings surveyed twice, one had to be demolished: Festival building. Festival was classified as having severe damage both in 1985 and 2010. But the building seemed to have had much more widespread damage in 2010 than in 1985 despite having increases in thickness in a number of walls that were intervened after 1985. If one assumes these repairs/interventions to have been effective, then one may conclude that the apparently large increase in damage suggests also large increases in drift demand. On the other hand, the additional damage may be interpreted as the result of the snowballing process mentioned above in which previous damage causes additional drift that in turn causes more damage. Festival had a number of lap splices that failed at wall bases in 2010. In a wall with poorly confined lap splices in its longitudinal reinforcement, which are known to lead to brittle response, an infinitesimal increase in demand can result in dramatic changes in response and damage (Pankow 2020).
3. The mean damage rating (as defined) increased by approximately 30%. Given the discussed limitations of the data, this increase cannot be interpreted to be irrefutable evidence of critical consequences from the earthquake of 1985. Instead, the surveys discussed, in general, support the views of the interviewed engineers who stated that buildings that survived the earthquake of 1985 without structural failures performed as well as buildings built after 1985.



Table B-4


BUILDING	DAMAGE LEVEL		Number of Stories	NOTES	Photos from 2010	
	1985	2010				
PLAZA DEL MAR	1	1	23			
TORRES DEL SOL	1	1	22			
TORRES DE MIRAMAR	1	1	21			
MARINA REAL	1	2	20	Damage was described in 1985 as: 'the only major damage occurred in the curved portion of the perimeter walls...this damage was initiated by straightening under tension of the wall boundary reinforcement that had been placed to follow the curve of the wall. In addition minor damage was observed in some of the lintels.' These descriptions match what was photographed in 2010.		
TORRES DEL PACIFICO	1	1	17	The original report classified the damage as 'none' yet the narrative spoke of cracks in beams and slabs.		
ACAPULCO	3	3	15			
FESTIVAL	2	3	14	In 1985 the reports available speak of cracking in lintels, diagonal cracks in shear walls, and crushing of a wall boundary. In 2010 the damage was severe and widespread.		
PUESTA DE SOL	1	1	14			
O'HIGGINS	1	1	14			

BUILDING	DAMAGE LEVEL		Number of Stories	NOTES	Photos from 2010
	1985	2010			
GALERIA LIBERTAD CENTRO	1.5	3	13		
ATALAYA	1	1	12	Photographic record from 2010 does not reveal structural damage	
MEDITERRANEO	1	2	12		
PONTECASINO	1	1	11		
SOLIMAR	1	1	11		

BUILDING	DAMAGE LEVEL		Number of Stories	NOTES	Photos from 2010
	1985	2010			
MAYA	1	3	11	Damage in 2010 concentrated on one exterior column (showing crushing and buckling of bars) with clear signs of severe corrosion and existing patching suggesting the problem existed before	
TOSSA DEL MAR	1	1	11		
CENTROMAR	1	2	11		
MIRADOR	1	1	11		
ISAMAR	1	1	10		
ANTUMALAL	1	1	10		

BUILDING	DAMAGE LEVEL		Number of Stories	NOTES	Photos from 2010
	1985	2010			
VILLAREAL	1	2.5	10	Damage report from 1985 speaks of inclined cracks in walls in lower 3 stories and spalling of cover from lintel beams. The most noticeable damage in 2010 occurred in lintel beams. The photos taken in 2010 revealed previous repairs in affected areas suggesting similar damage.	
LAS PALMAS	1	1	10		
COPACABANA	1	1	10		
ALTAMAR	1	1	9		
ANCONA	1	1	9		
FONTANA	1	1	9		
LAS ACHIRAS	1	2	9		
RIVIERA	1	1	9		

BUILDING	DAMAGE LEVEL		Number of Stories	NOTES	Photos from 2010
	1985	2010			
MONTECARLO	2	2	8		
ROTONDA	1	1.5	8		

BUILDING	DAMAGE LEVEL		Number of Stories	NOTES	Photos from 2010
	1985	2010			
CAPRI	1	2	8		
Average	1.1	1.5			

B.2.3 Summary

The views expressed in this appendix are based on the idea that seismic drift demand and seismic drift capacity (or drift affecting lateral resistance) can be treated separately if they do not intersect. The question being addressed is whether drift demand, for a given ground motion, is larger in structures that have experienced previous motions compared with structures that have not.

The test data presented suggest that a structure that has experienced strong ground shaking is unlikely to perform consistently worse than a pristine structure in a future motion if:

- The drift capacity of the structure (or drift affecting lateral resistance) is not exceeded during the strong ground shaking.
- The intensity of the future motion in question is sufficient to cause cracking and/or drift exceeding 1% in the pristine structure.

When increases in drift demand were observed after repeated ground motion, they were smaller than 0.3% in 80% of the reported cases (for both roof and story drift ratio). Realize that our methods to estimate future ground motion and/or drift (given a ground motion) may not have the accuracy to produce estimates of drift within 0.3% with reliability. All the mentioned figures refer to drift measured relative to the shape of the structure at the beginning of each ground motion. It is assumed that repairs occurring after an earthquake are more sensitive to changes in drift than to absolute (cumulative) drift, and the trends described do not change radically for absolute (cumulative) drift.

The field evidence obtained and opinions of engineers who have dealt with structures affected by at least two strong earthquakes also supported the idea that a ductile, well-detailed structure, in general, does not lose its ability to resist future motions of moderate and large intensity once they go through an initial strong earthquake (without failure).

The evidence presented suggests that, unless the engineer requires the building to remain uncracked during earthquake motion, they need not assume that the building (especially if ductile) loses its ability to resist future ground motions after an initial earthquake occurs. It is implied that the mentioned motions are not expected to cause drift demands exceeding the drift capacity of the structure. If deemed prudent, it appears sufficient to assume that the future motion may cause an increase of approximately 0.3% in the drift that would be expected in a pristine (uncracked) structure.

B.2.4 Description of Selected Tests

This section describes in more detail tests mentioned in the previous sections B.2.1-3 (by Cecen 1979, Laughery 2016, Kajiwara 2017, Schultz 1986), and additional tests by Suita (2015) and Bonacci (1989).

B.2.4.1 Cecen, 1979

Haluk Cecen working with Mete Sozen tested two RC models with base-shear coefficients approaching 0.4. Their work was perhaps the first to address this question:

If a building is subjected to strong ground motion, does it lose its ability to survive future ground motion?

Cecen and Sozen did not have buildings near failure in mind. Those have been observed to be sensitive to repetition. They had in mind instead buildings that may crack and yield without experiencing damage compromising their capacity to resist lateral forces. The question they addressed was whether the softening caused by cracking and yielding (or ‘stiffness decay’ as it is called sometimes) comes with additional seismic displacement demands.

The specimens tested by Cecen were designed so that ‘*shear and bond failures could be avoided* and the structural response could be ‘confined’ primarily to axial and bending effects.’

Each specimen had two small-scale¹ ten-story moment frames flanking ten 1000-lb steel masses supported by pins going through the beam-column joints of the frames. The specimens were tested with uniaxial base motion. Out-of-plane motions were restricted by ‘bellows’ attached by hinges to the steel masses (Figure B-7). The test models (Figure B-7) were said to be ‘physical models of idealized structural concepts’ instead of ‘direct models of existing structures.’

Initial periods measured in the test structures ranged from approximately 1/3 to 1/4 sec. The record used to shake the test structures was the NS component of the acceleration record obtained in 1940 in El Centro, California. The time step of the record was reduced by dividing it by 2.5 ‘to excite the test models in a manner comparable to the excitation of actual structures by real earthquakes.’ Spectra for scaled records are shown in Figure B-8.

¹ Story height = 9 in. = 229 mm.

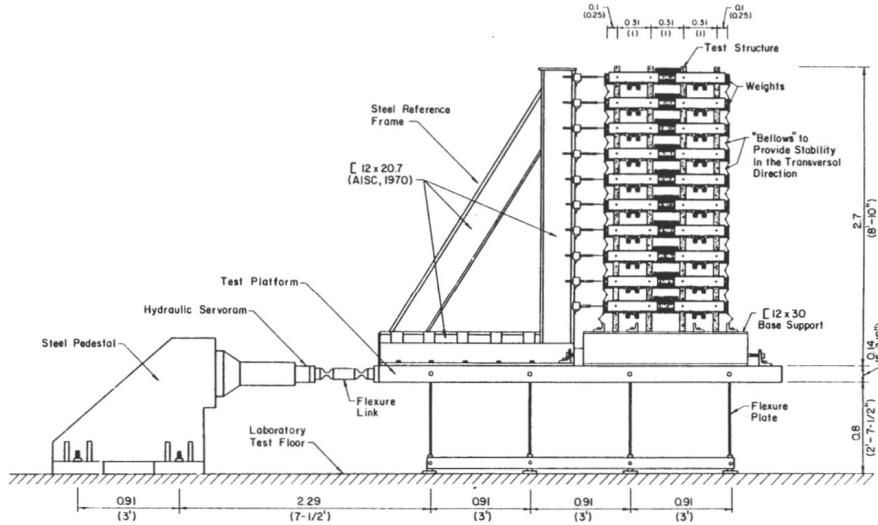


Fig. 3.1 General View of the Test Setup

Figure B-7 Specimen Tested by Cecen.

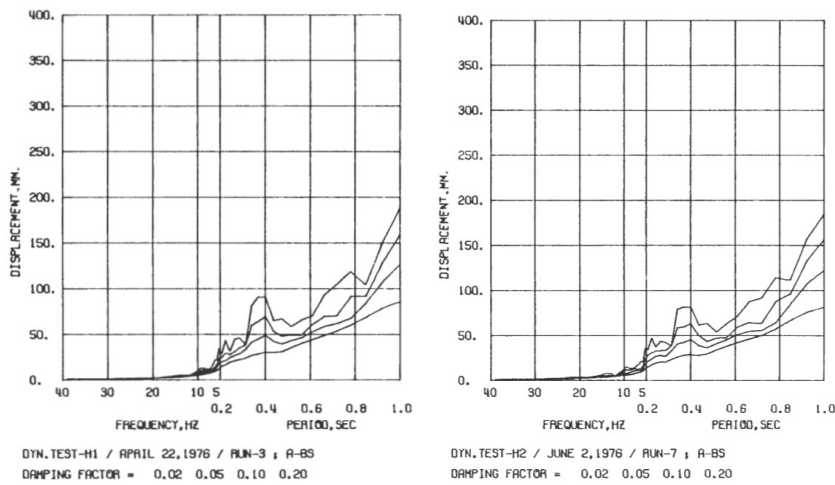


Figure B-8 Spectra of Run 3, Specimen H1, and Run 7, Specimen H2. (After Cecen).

The test specimens were labeled H1 and H2. Specimen H1 was subjected to 3 base motions or ‘runs’ while H2 was subjected to 7 motions. The last runs in both specimens were meant to have the same shaking intensity (Figure B-8). Runs 3 and 4 for H2 were also meant to have the same intensity as one another. In both cases, displacements and accelerations measured on the structure were remarkably similar (Figures B-9 to B-11). Notice the structures reached large drift ratios well into their ranges of nonlinear response.

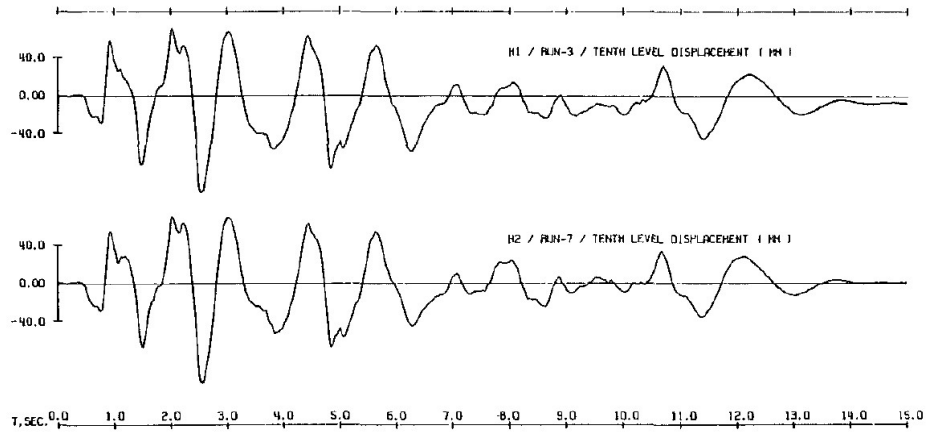


Figure B-9 Recorded top displacements (After Cecen).

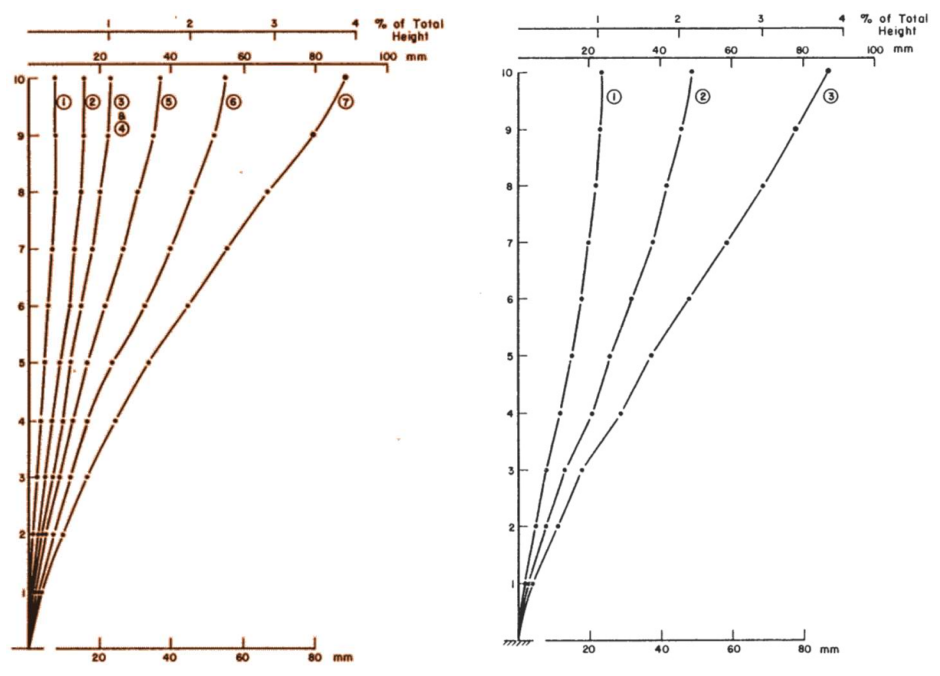


Figure B-10 Measured Drift Profiles (H2 left, H1 right) (After Cecen).

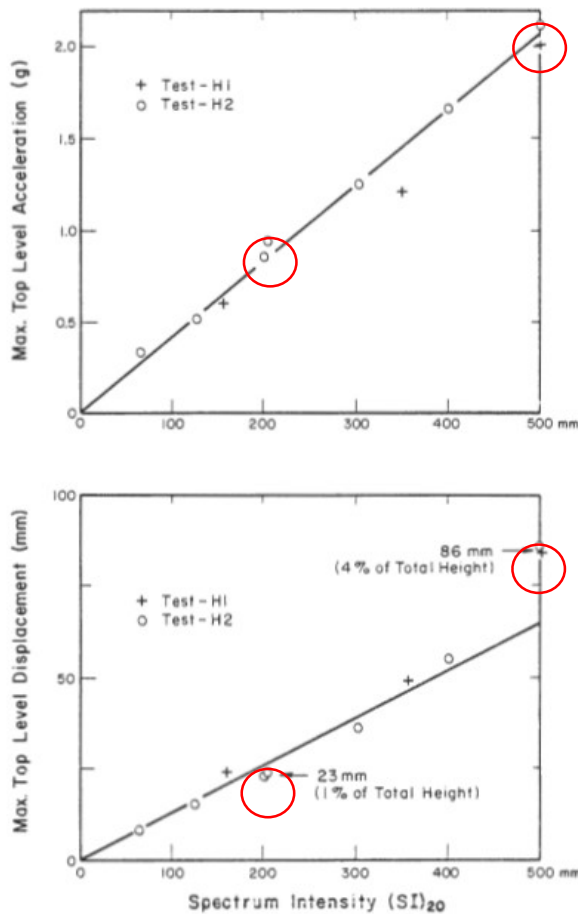


Figure B-11 Comparisons of Responses of Specimens H1 and H2. (After Cecen)

The similarities between the responses of specimens H1 and H2 are remarkable. It was concluded that the same base motion produces ‘basically’ the same response regardless of differences in previous loading histories. This observation was qualified with this statement: ‘provided that all of the previous loadings had intensities less than or equal to that of the loading under consideration.’ Nearly 40 years later Laughery (2016) reexamined this question as discussed in the following section.

Notice that both records in Figure B-9 start from zero indicating measurements were relative to displacements present at the start of the simulations shown. These initial displacements caused by previous motions were nearly an order of magnitude smaller than the displacements in Figure B-11. Yet they were not equal in Models H1 and H2. It is conceivable that differences in permanent drift may lead to differences in total accumulated drift larger than what is implied by Figure B-11. Nevertheless, if building contents are repaired without ‘re-plumbing’ the building (a difficult feat),

increase in drift may be a better indicator of potential for additional nonstructural damage than total (accumulated) drift.

B.2.4.2 Laughery, 2016

Laughery tested four one-story, one-bay reinforced concrete frames using the same earthquake simulator that Cecen used. Figure B-12 shows the specimen geometry and the test setup. The frames were identical except for column longitudinal reinforcement, of which there were two types: high-strength or conventional. Both frame types were designed to have similar nominal lateral strength (with a base shear coefficient close to 1). All base motions used in tests were adapted from the east-west component of the ground motion recorded at Sun Valley – Roscoe Boulevard during the 1994 Northridge earthquake. The original acceleration record was compressed by reducing its time step (by a factor of 1/3), and then scaled in amplitude (by a factor of 3).

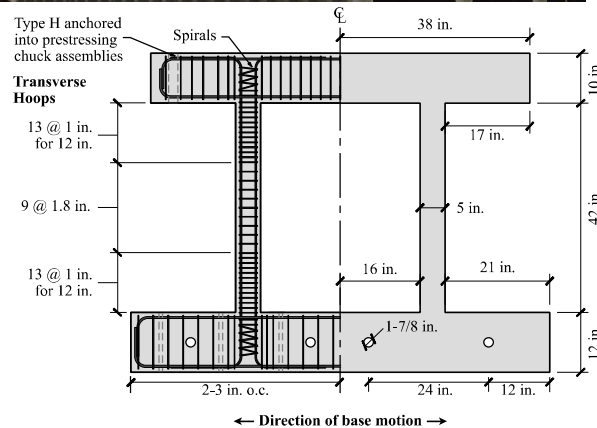


Figure B-12 Specimens Tested by Laughery (2016).

The frames were tested in two series, the difference between series being the order of intensity of ground motions. In test Series 1, frames were shaken with motions of increasing demand: 25%, 50%, 75%, 100%, and 100% again. In test Series 2, frames were shaken with four motions of decreasing demand (100%, 75%, 50%, 25%), followed by a fifth motion at 100%. The

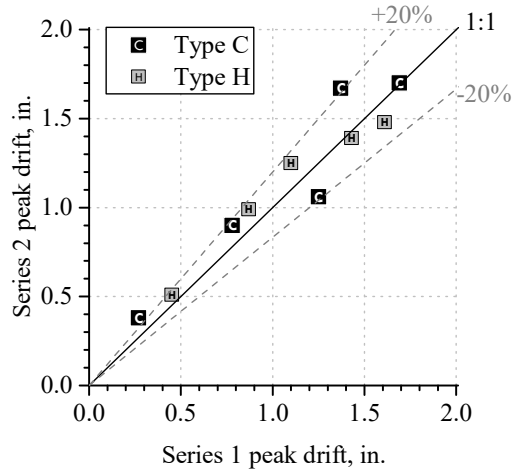
purpose of varying motion order was to create points of comparison between frames of the same type but with different levels of initial ‘damage.’ For example, before the test at 25%, Series 1 frames had not experienced any motions and were undamaged. In contrast, Series 2 frames were damaged, having experienced three motions of larger intensity before this test.

In Figure B-13a, the peak drifts² of Series 2 frames are plotted against the peak drifts of corresponding Series 1. This figure shows that peak relative drifts were comparable between the two series (typically within 20%), suggesting that softening caused by damage from previous ground motions did not lead to consistent increases in drift. That is, apart from permanent drift from previous strong motion, drift demand was not strongly dependent on loading history, with test frames reaching similar relative drifts despite some having been pushed farther into their inelastic range of response beforehand.

The drifts in Figure B-13a were measured relative to positions at the start of each test. They do not include permanent drifts from previous simulations. Figure B-13b shows total drift accumulated from simulation to simulation relative to the pristine condition preceding all simulations. In this case an increase in drift demand is apparent. The increase is attributable –for the most part- to the permanent offset reached in the first (the strongest) simulation in Series 2. Nevertheless, in nine out of ten cases (excluding the least demanding motion that caused only limited cracking and no yielding in the very first simulation of Series 1), the mean increase in drift was 12%. Although this increase appears modest given the uncertainty in matters related to earthquake drift, it prompts the following question:

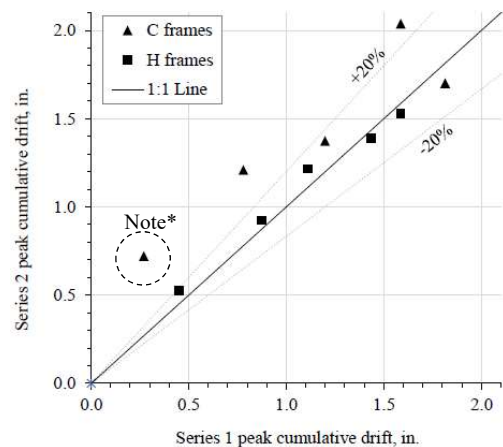
If the initial motion does not cause failure and it triggers no more than ‘cosmetic repairs’ (crack patching and painting), what matters most when it comes to reuse of the structure after future earthquakes: the increase in drift or the total drift? The increase in drift may be more critical for the mentioned cosmetic repairs. In contrast, total drift, that is sensitive to previous permanent drift, is more likely to be a better indicator of potential for failure.

² measured relative to positions at the start of each test



Note: Type C indicates Grade 60 reinforcement, and type H indicates Grade 120 reinforcement.

Figure B-13a Results by Laughery (2016) – **In-run** drift. (1 in. represents a drift ratio of 2.4%)



*This point represents the first simulation in Series 1 and the second in Series 2. In Series 1, caused limited cracking, and no yielding.

Figure B-13b Results by Laughery (2016) – **Cumulative** drift. (1 in. represents a drift ratio of 2.4%)

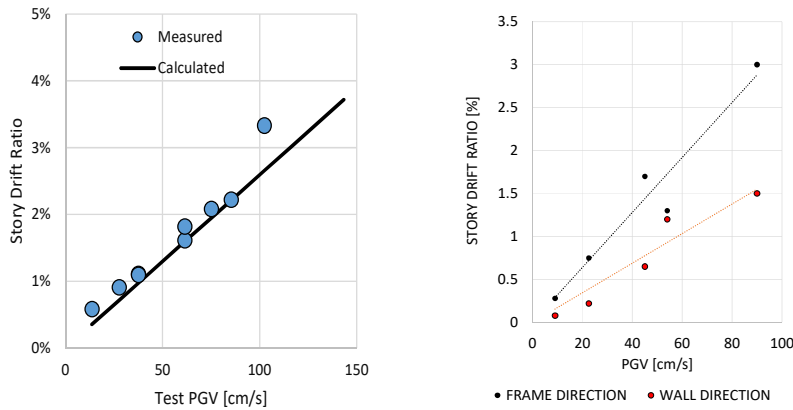
B.2.4.3 Suita et al., Kajiwara et al.

The tests by Cecen and Laughery described above were tests of RC SDOFs and small-scale MDOFs. Suita et al. (2015), as well as Kajiwara et al. (2017) tested large-scale multi-story building models.

Suita et al. tested an 18-story steel-frame model with ‘pre-Northridge’ connections. The uni-axial base motion used was ‘synthetic,’ with a nearly bilinear response velocity spectrum with a transition period T_g (between ranges for nearly constant response acceleration and velocity) of approximately 2/3 s.

Kajiwara et al. tested a ‘modern’ 10-story RC structure using the records obtained at the JMA station during the Kobe 1995 Earthquake. Base motion was applied along three axes.

The large-scale specimens tested by Suita and Kajiwara had base-shear coefficients exceeding 0.4. Figures B-14a and b show how drift varied with intensity (quantified in terms of peak ground velocity PGV) in their tests.



(a) Measurements Reported by Suita et al. (b) Measurements Reported by Kajiwara et al.

Figure B-14 Measurements from Large-Scale Building Models.

The data plotted come from consecutive runs applied to a given specimen. The linearity observed between drift and intensity suggests that drift is not sensitive to history (from previous motions of smaller intensity). The linearity is remarkable in the tests by Suita up to a drift ratio of approximately 2%. After that drift, fractures occurred in welds. This observation indicates that lateral-resistance decay causes increases in drift demand. That is: if the system reaches its drift capacity, damage accumulates from there on and drift demand increases as a result. The consequences are likely to lead (eventually) to instability.

B.2.4.4 Bonacci, 1989

Most tests on the effects of loading history on drift demand have dealt with structures with moderate periods (exceeding the period T_g at the transition between the ranges of ‘nearly constant response acceleration’ and ‘nearly constant response velocity’). Bonacci tested SDOF structural assemblies with relatively short periods and base shear coefficients of 1/3 or larger. Each oscillator was subjected to at least two consecutive base motions (runs) with different intensities. Figure B-15 shows a summary of results for specimens that 1) were weaker, and 2) had shorter initial periods than the rest.

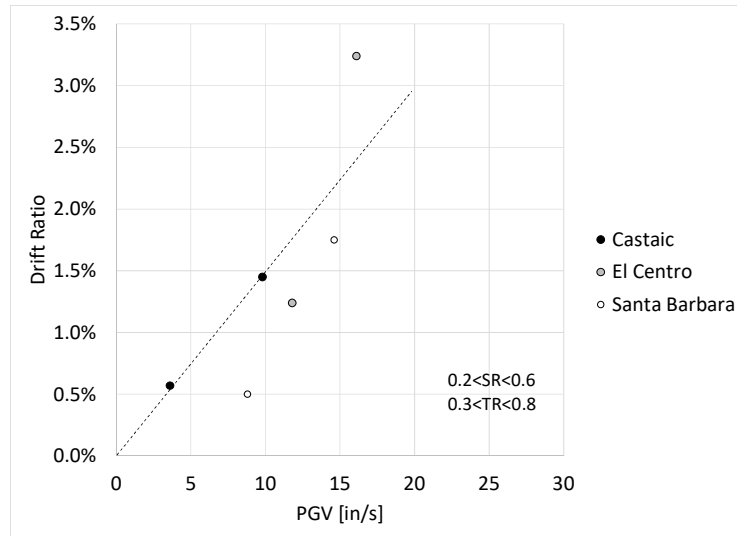


Figure B-15 Note: SR is ratio of base shear strength to demand for a linear oscillator, and TR is ratio of initial period to T_g .

The general trend observed indicated a mostly linear variation between drift and peak ground velocity PGV even in the scatter introduced by the use of different ground motions. The sensitivity of the results to the properties of the ground motion requires additional study. Nevertheless, the apparent general trend, albeit weak, suggests again that drift tends to be linearly proportional to intensity measured in terms of PGV for short-period oscillators. Given that test specimens were tested in sequences of increasing intensity, this observation, as discussed above, is an indication that –within a wide domain of structures with sufficient ‘toughness’– drift is not always critically sensitive to ‘history.’

B.2.4.5 Schultz, 1982 - The Plausible Accumulation of Deformation in Structures with Discontinuities in Stiffness and Strength

It seems plausible that structures with discontinuities may be more prone to accumulation of damage and deformation. Especial attention is given to the matter in this subsection in reference to tests by A. Schultz (1982). Schultz tested two small-scale nine-story three-span frame structures (called SS1 and SS2) subjected to simulated earthquake motions. Each specimen had two parallel frames and stiff 1100-lb masses at each story and between the mentioned frames (Figure B-16). The masses did not restrict rotations of beam-column joints where pins connected masses and frames. Shaking occurred along a single axis parallel to the frames.

In the test frames, columns were weaker than beams by design. Beams were 50% deeper than columns while cross-sectional thickness was equal. Column axial force caused by gravity was smaller than one tenth of the product of

concrete compressive strength and gross cross-sectional area ($f'_c A_g \div 10$). The first story was taller than other stories, and cross-sectional dimensions and materials were nominally equal in both test structures. The reinforcement ratio in first-story columns in Specimen SS2 (4.7%) was 60% larger than the reinforcement ratio in first-story columns in Specimen SS1 (2.9%).

Transverse reinforcement was provided by continuous rectangular spirals. The amount of transverse reinforcement was enough to produce an expected resistance to shear of four times the expected shear demands assuming no contribution from the concrete to resistance. Beam column joints were confined by helical spirals.

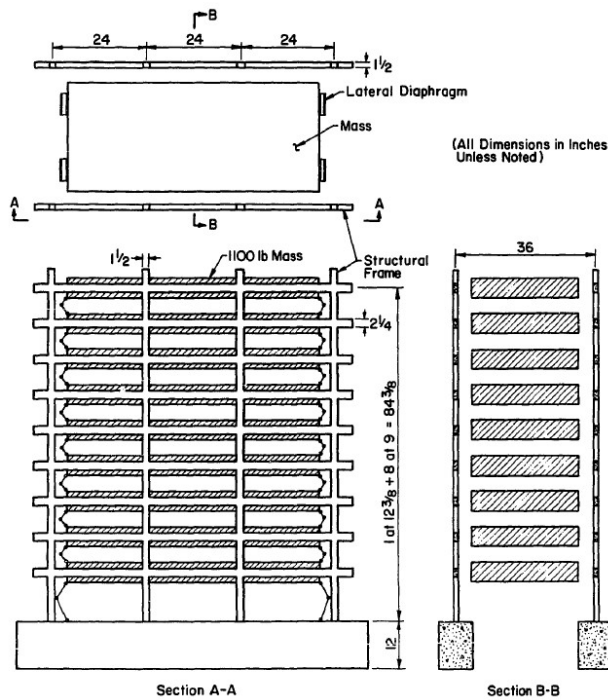


Figure B-16 Test structure (After Schultz).

The test structures were subjected to scaled versions of the N-S Component of recording obtained in El Centro, California, in the 1940 Imperial Valley. The time step was compressed by a factor of 1/2.5. The peak acceleration in the initial motion (Run 1) that was labelled 'design' motion was adjusted to $PGA = 0.35g$. The intensity of following motions was adjusted as follows relative to the intensity of the initial (design) motion:

Specimen	Run 1	Run2	Run3	Run 4	Run 5	Run 6
SS1:	1x	1x	1.5x	4x	N/A	N/A
SS2:	1x	1x	1x	2x	3x	4x

Story drift ratios reached nearly 3% in Run 1. Permanent deformations were observed at the end of simulations, but the measuring system was re-zeroed at the beginning of each simulation.

The response of Specimen SS1 to the first two (design) motions is summarized in Figure B-17.

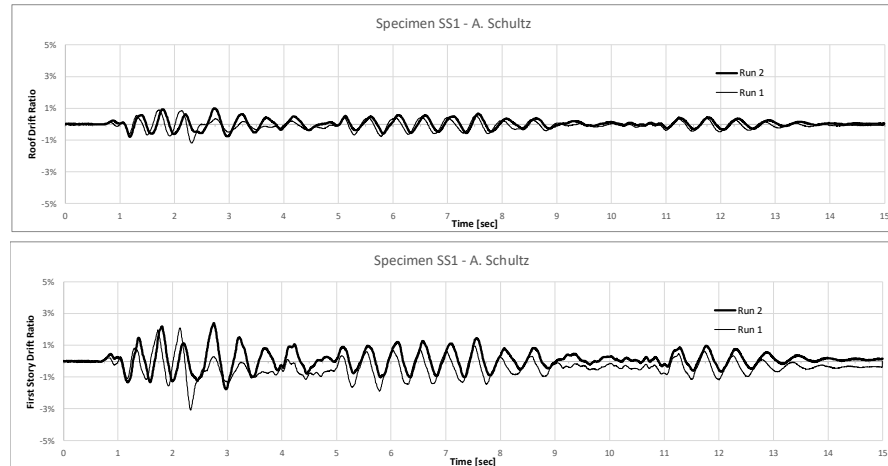


Figure B-17 Drift in Repeated Motions in Specimen SS1.

The similarities between the motions recorded for Specimen SS1 in its two initial runs are remarkable. Interestingly, “in-run” roof drift ratio was larger in the first simulation (1.2%) than in the second (1.0%) and the same was observed for first-story drift ratio (3.1% v. 2.4%). The repetition of motion did not lead to either increases in overall deformation or deformation in the first (soft) story, nor increases in damage that was limited to cracking.

In the third simulation, Specimen SS1 reached roof and first-story drift ratios of 1.5% and 4.3%, respectively. Specimen SS1 collapsed during Run 4 through a first-story failure mechanism.

Peak roof drift ratios reached in the initial (design) simulations for Specimen SS2 were 1.1, 1.3 and 1.0% (Figure B-18). Peak story drift ratios were 1.4, 2.2 and 1.4 % in that order. Again, it is hard to argue that the observations indicate repeated motions created additional deformation. Observed damage did not increase either.

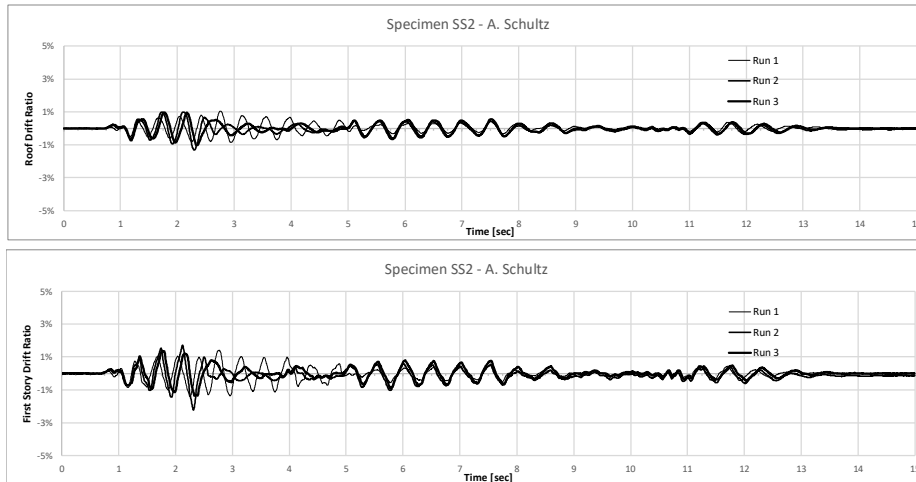


Figure B-18 Drift in Repeated Motions in Specimen SS2.

In runs 4 to 6 peak roof drift ratio was 1.8, 2.4 and 4% but the last number is of limited relevance (if any) because instruments went off scale. With the same caveat, peak first-story drift ratio was 2.9, 2.5 and 4.6% but larger drift ratios were observed in upper stories.

To study how deformation accumulated in specific stories the ratio of two drift ratios was plotted for each simulation discussed:

- Maximum story drift ratio
- Maximum (or peak) roof drift ratio

The ratio of these two ratios is called quotient to simplify the language. This quotient is an indicator for how much concentration of deformation there is. For a regular frame it is often close to 1.5. A numerical linear idealization of test structures SS1 and SS2 yields a calculated ratio ranging from 1.8 to 2.5 depending on what is assumed about the stiffness of the beam-column joints.

In the initial (design) simulations (Runs 1 and 2) of Specimen SS1 the described quotient was 2.4 and 2.3 in that order. For SS2, the quotient was 1.3, 1.6 and 1.3 in that order. The variation in quotients does not suggest accumulation of deformation in a single story with repeated ground motion. In all the described cases the quotient was calculated for the maximum story drift ratio occurring at the time peak roof drift was reached. That time did not always coincide with the time at which peak story drift ratio was reached. The quotient changes to 2.6 and 2.4 for SS1 and 1.3, 1.7 and 1.4 for SS2 if peak story drift ratio is used instead of maximum drift ratio at time of peak roof drift. The conclusion is the same: there was no discernible accumulation of deformation with repeated motions.

How the described quotient changes from test to test can help understand how the distribution of deformation changed in runs with more intense base motion than the initial (design) motions. Figure B-19 shows the ratio of the described quotient (of drift ratios) for simulation i to the quotient for the first simulation. The reported ratios correspond to the time at peak roof drift. For Simulation 4 in SS1 that led to collapse, the quotient plotted corresponds to the initial cycles of response only.

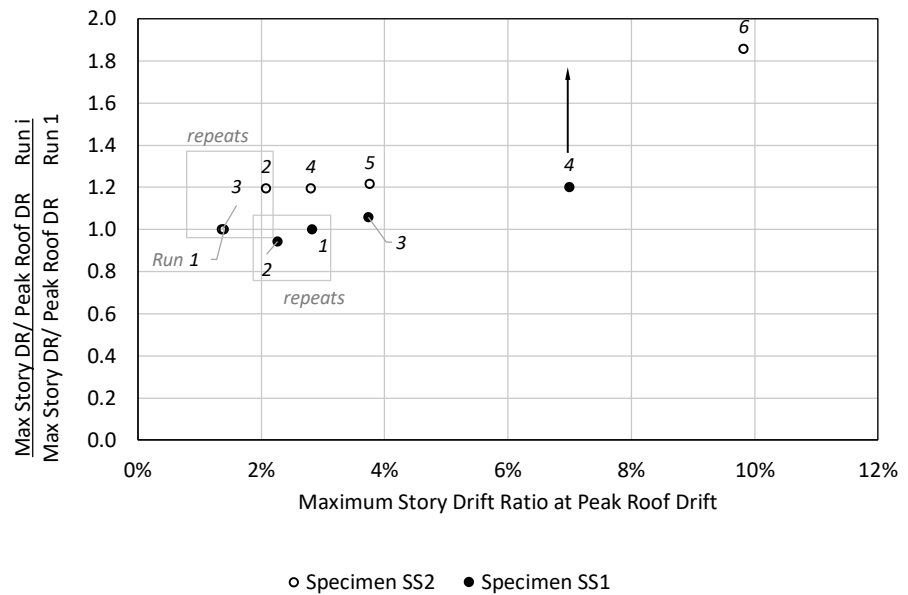


Figure B-19 Accumulation of Deformation. Markers indicate run number. Run 4 in SS1 led to collapse: reported ratio refers to measurements made in initial response cycles.

The most salient feature of Figure B-19 is that additional concentration of drift beyond the scatter in the data in initial runs occurred only after a story drift ratio of 4% was exceeded. Concrete spalling is reported to have started in Runs 3 –SS1– and Run 5 –SS2– that caused drift ratios close to 4%. Spalling increased in Run 4 –SS1– and Run 6 –SS2–. Quotients calculated for peak story and peak roof drift ratios (that occur at different times) increase the dispersion in the data but does not change this conclusion.

References

Abrams D.P., and Sozen M.A., 1979, “Experimental Study of Frame-Wall Interaction in Reinforced Concrete Structures Subjected to Strong Earthquake Motions,” *Civil Engineering Studies, Structural Research Series*, No. 460, University of Illinois at Urbana-Champaign, Urbana-Champaign, Illinois.

- Bonacci, J. F., 1989, *Experiments to Study Seismic Drift of Reinforced Concrete Structures (PhD Dissertation)*, University of Illinois at Urbana-Champaign, Urbana-Champaign, Illinois.
- Cecen, H., 1979, *Response of Ten Story, Reinforced Concrete Model Frames to Simulated Earthquakes (PhD Dissertation)*, University of Illinois at Urbana-Champaign, Urbana-Champaign, Illinois.
- Gulkan, P., and Sozen, M.A., 1971, “Response and Energy-Dissipation of Reinforced Concrete Frames Subjected to Strong Base Motions”, *Civil Engineering Studies, Structural Research Series No. 377*, University of Illinois at Urbana-Champaign, Urbana-Champaign, Illinois.
- Kajiwara, K., Tosauchi, Y., Sato, E., Fukuyama, K., Inoue, T., Shiohara, H., Kabeyasawa, T., Nagae, T., Fukuyama, H., Kabeyasawa, T., and Mukai, T., 2017, “2015 Three-dimensional Shaking Table Test of a 10-story Reinforced Concrete Building on the E-Defense, Part 1: Overview and Specimen Design of the Base Slip and Base Fixed Tests,” *16th World Conference on Earthquake Engineering*.
- Laughery, L.A., 2016, *Response of High-Strength Steel Reinforced Concrete Structures to Simulated Earthquakes (PhD Dissertation)*, Purdue University, West Lafayette, Indiana.
- Lepage, A., and Pujol S, 2010, *Reconnaissance of the Maule, Chile, Earthquake of 2010*. Personal Communications.
- Monical, J., 2021, *An Experimental Study of The Response of Reinforced Concrete Frames and Frames Containing Masonry Infill Walls to Simulated Earthquakes (PhD Dissertation)*, Purdue University. West Lafayette, Indiana.
- Otani, S., and Sozen, M.A., 1972, “Behavior of Multistory Reinforced Concrete Frames during Earthquakes,” *Civil Engineering Studies, Structural Research Series, No. 392*, University of Illinois at Urbana-Champaign, Urbana-Champaign, Illinois.
- Pujol, S., and Sozen, M.A., 2006, “Effect of Load Reversals on Dynamic Demand and Resistance of Reinforced Concrete Elements,” *ACI Special Publication, No. 236*.
- Riddell, R., Wood, S.L., and de la Llera, J. C., 1987, “The 1985 Chile Earthquake: Structural Characteristics and Damage Statistics for the Building Inventory in Viña del Mar”, *Civil Engineering Studies, Structural Research Series, No. 534*. University of Illinois at Urbana-Champaign, Urbana-Champaign, Illinois.

- Schoettler, M. J., Restrepo, J. I., Guerrini, G., Duck, D. E., and Carrea, F., 2012, *A Full-Scale, Single-Column Bridge Bent Tested by Shake-Table Excitation*, Center for Civil Engineering Earthquake Research, Department of Civil Engineering, University of Nevada. Reno, Nevada.
- Schultz, A.E., 1986, *An Experimental and Analytical Study of the Earthquake Response of R/C Frames with Yielding Columns (PhD Dissertation)*. University of Illinois at Urbana-Champaign, Urbana-Champaign, Illinois.
- Shah, P., 2021, *Seismic Drift Demands (PhD Dissertation)*, Purdue University, West Lafayette, Indiana.
- Suita, K., Suzuki, Y., and Takahashi, M., 2015, “Collapse Behavior of an 18-Story Steel Moment Frame During a Shaking Table Test,” *International Journal of High-Rise Buildings*, Vol. 4, No. 3.
- Suzuki, T., Puranam, A.Y., Elwood, K.J., Lee, H.J., Hsiao, F.P., Hwang, S.J., 2021, “Shake-Table Tests of Seven-story Reinforced Concrete Structures with Torsional Irregularities: Test program and datasets,” *Earthquake Spectra*.
- Wood, S. L., 1985, *Experiments to Study the Earthquake Response of Reinforced Concrete Frames with Setbacks (PhD Dissertation)*, University of Illinois at Urbana-Champaign, Urbana-Champaign, Illinois.
- Wood, S.L., Wight, J. K., and Moehle, J. P., 1987, “The Chilean Earthquake: Observations on Earthquake-Resistant Construction in Vina del Mar”, *Civil Engineering Studies, Structural Research Series*, No. 532. University of Illinois at Urbana-Champaign, Urbana-Champaign, Illinois.
- Yang, Y.H., Puranam, A.Y., Pujol, S., 2021, “Seismic Drift Demands in Concrete Structures Reinforced With High-Strength Steel,” *16th World Conference on Earthquake Engineering*.

B.3 Effect of Loading History on Drift Demand

B.3.1 Introduction

FEMA 307 (FEMA, 1999) addressed whether seismic drift demand is larger in structures that have experienced previous earthquakes, compared with structures that have not. That study focused on comparing initial response to high intensity shaking and subsequent response to shaking of similar intensity. This section describes an additional study considering 1) an expanded set of ground motion records, 2) variation in the intensities of the initial and subsequent motions, and 3) different methods to define base-shear strength and hysteretic behavior. For these purposes and following the format of FEMA 307, idealized SDOF oscillators were studied through numerical dynamic simulations for:

1. Four sets of 30 ground motions, with each set representing one of two different soil classes in one of two different seismic environments (Seattle and Berkeley),
2. Oscillator periods ranging from 0.1 seconds to 3 seconds,
3. Oscillator strengths defined using three methods,
4. Oscillators with three types of hysteretic behavior, and
5. Oscillators subjected to ground motions with different intensities.

B.3.2 Oscillator Properties

An SDOF oscillator can be defined using five different properties: 1) the period of vibration of the oscillator, 2) the strength of the oscillator, 3) the shape of its primary (or backbone) force-displacement curve, 4) the loading, unloading and reloading rules (or hysteretic rules) that the force-displacement response of the oscillator follows, and 5) damping. This section describes the properties of the oscillators considered.

B.3.2.1 Period

SDOF oscillators with effective periods of vibration ranging from 0.1 seconds to 3 seconds (in increments of 0.1 seconds) were considered. Effective periods instead of initial periods were used to facilitate direct comparison between uncracked and cracked oscillators. Effective periods of vibration were defined as the periods corresponding to the stiffness defined as the slope of the secant to the load-deflection curve drawn from zero force and displacement to force and displacement at yield as expressed below.

$$T_{eff} = 2\pi \sqrt{\frac{m}{F_y/\delta_y}}$$

Where,

T_{eff} = Effective period of SDOF oscillator,

m = Mass of SDOF oscillator,

F_y = Yield force of SDOF oscillator, and

δ_y = Yield displacement of SDOF oscillator.

B.3.2.2 Strength

SDOF strength was defined using three different procedures:

1. reducing the idealized linear spectral response (containing ranges of constant response acceleration, velocity and displacement) by a reduction factor R as it is common in design codes,
2. iterating to reach a given ductility demand (or ratio of maximum response displacement to yield displacement) for each considered record, and
3. reducing the linear spectral response by a reduction (or R) factor using as reference the spectra produced for each of the records considered (instead of their idealized ‘average’ used in 1).

The ratio of the defined strength to weight, or base-shear coefficient C_y , was used to define the yield force and displacement of each oscillator as follows:

$$F_y = C_y \left(\frac{T_{eff}}{2\pi} \right)^2 \times k_{SDOF} \times g$$

$$\delta_y = \frac{F_y}{k_{SDOF}}$$

Where T_{eff} , F_y , δ_y , are defined above, and

C_y = Base-shear coefficient,

k_{SDOF} = Stiffness of the SDOF oscillator set to a constant value of $4\pi^2$, and

g = Acceleration of gravity.

B.3.2.2.1 Code-Like R Factor Method

In this method, the base-shear coefficient for each oscillator was obtained using the procedure outlined in ASCE 7-16 (American Society of Civil Engineers, 2017). Three R factors of 2, 4 and 8 were used to obtain oscillators with different levels of strength. An example of the base shear coefficient versus period relationship obtained using this method is shown in Figure B-20.

This method of defining strength is based on an idealized ‘smooth’ design spectrum that does not have the radical variations in spectral shapes common in spectra produced from measured ground motion. As a consequence, oscillators with the same nominal strength can have considerably different displacement ductility when subjected to different ground motions. The smooth spectrum used was defined as explained in the subsection ‘Ground Motions.’

B.3.2.2.2 Constant Ductility Method

In this method, base-shear strength is defined such that the oscillator reaches a target displacement ductility (ratio of maximum displacement to yield displacement) for a given ground motion and a given set of hysteretic ‘rules.’ As a result, and after iteration, a different base-shear coefficient is obtained for each combination of ground motion and assumed hysteresis. To reduce the required computational effort, this definition of strength was used with only one set of hysteretic rules (TAKC described later in this section). The mentioned iteration was accomplished through these steps:

1. For a given period, run nonlinear dynamic analysis for SDOF oscillators with base shear coefficients ranging from 0.001 to 2,
2. Calculate displacement ductility values for each oscillator in 1),
3. Produce a plot of displacement ductility versus base shear coefficient. From the plot, interpolate the base shear coefficient value for given values of displacement ductility. In cases where multiple base shear coefficients are obtained for a given displacement ductility, use the smallest coefficient.
4. Repeat steps 1) through 3) for all periods under consideration.

An example of the base shear coefficient versus period relationship obtained using this method is shown in Figure B-21. Strengths were defined for values of displacement ductility of 2, 4 and 8.

The described procedure can produce large variations in base shear coefficient for oscillators with the same target ductility. It is more difficult to implement, and it requires more computational effort.

B.3.2.2.3 Constant R Factor Method

In this procedure, base shear coefficient for a given period and ground motion is obtained by dividing the maximum absolute acceleration (expressed in units of g) for linear response by a factor R (equal to 2, 4, or 8) as shown below.

$$C_y = \frac{\ddot{x}_{max}^{linear}}{R \times g}$$

Where C_y and g are defined above, and

\ddot{x}_{max}^{linear} = Maximum absolute acceleration for linear response of SDOF oscillator, and

R = Reduction factor

This procedure also produced a different base-shear coefficient for each combination of period and ground motion considered. An example of the relationship between base shear coefficient and period obtained using this method is shown in Figure B-22.

This method of defining strength was chosen because it accounts for variations in spectral shape and it does not require iteration.

B.3.2.3 Hysteretic Model

Three different sets of ‘rules’ to idealize the relationship between load and deflection were used to study the effect of cracking and ‘pinching’ on drift demands of SDOF oscillators subjected to multiple ground motions. Because the focus of the investigation was on drift demand for ductile systems, the rules chosen did not include any decay in lateral resistance. The studies described in FEMA 307 indicated clear increases in displacement response for systems with decaying resistance subjected to multiple motions. For the systems considered here, the envelope of the hysteresis loops matched the curve expected for monotonic loading. To facilitate comparison with results from FEMA 307, oscillators in this study were defined to be similar to those used in FEMA 307. The three hysteretic models used in this investigation were:

1. **Uncracked Takeda Model (TAKU):** This hysteretic model was used to represent structures that are uncracked before being subjected to ground motions. In this hysteretic model, the primary force-displacement curve was symmetric about its origin and contained three break points to represent cracking, yielding and a limit termed ‘ultimate’ although it did not represent a point of failure. Force at cracking was defined to be equal to half that at yield and displacement at cracking was defined assuming that the stiffness before cracking was twice the effective stiffness (measured from zero force and displacement to force and displacement at yield). The post-yield stiffness was set at five percent of the effective stiffness. At displacements exceeding the ‘ultimate’ limit, the force in the oscillator was held equal to the force at the limit. The loading, unloading and load reversals were governed by the hysteretic rules proposed by

Takeda (Takeda, Sozen, & Nielsen, 1971) which incorporate softening or stiffness decay. A plot of force versus displacement for this hysteretic model is shown in Figure B-23.

2. Cracked Takeda Model (TAKC): This hysteretic model was used to represent structures that are cracked before being subjected to a given ground motion. In this hysteretic model, the primary force-displacement curve was symmetric about its origin and contained two break points to represent yielding and ‘ultimate’ similar to 1). A post-yield stiffness equal to five percent of the effective stiffness was used again. At displacements beyond ultimate, the force in the oscillator was held equal to the force at ultimate. The loading, unloading and load reversals were governed by the hysteretic rules by Takeda. A plot of force versus displacement for this hysteretic model is shown in Figure B-23.
3. Uncracked Takeda Model with Pinching (TAKP): This hysteretic model was used to represent structures that are uncracked before being subjected to ground motions and are susceptible to the narrowing of the hysteresis loops called ‘pinching.’ Again, the primary force displacement curve was symmetric about its origin and contained three break points to represent cracking, yielding and ‘ultimate’ similar to 1). To facilitate comparisons between oscillators with and without pinching, the envelope of the force-displacement loops was defined to be the same as that in 2). The displacement triggering ‘pinching’ was set to approximately 30% of the current maximum displacement in each direction and the associated force was set to approximately 10% of the maximum force reached up to that instant in each direction. Once more, the loading, unloading and load reversals were governed by the rules by Takeda. A plot of force versus displacement for this hysteretic model is shown in Figure B-23.

All SDOF analyses were conducted using OpenSees, an open source finite element software for simulation of response of structures subjected to ground motions (McKenna, Fenves, & Scott, 2000). In OpenSees, the described hysteresis idealizations were implemented using OpenSees’ Hysteretic Material model because it can be configured to follow hysteretic rules similar to those defined by Takeda as shown in Figure B-24 (Takeda, Sozen, & Nielsen, 1971). The Hysteretic Material parameters used to define the oscillators in this investigation are listed in Table B-5.

B.3.2.4 Damping

Damping of SDOF models was defined using only the stiffness-proportional part of Rayleigh Damping because 1) SDOF models have a single period making it difficult to define both mass and stiffness proportional damping, 2)

mass proportional damping can overdamp the response of nonlinear systems as they yield, and 3) stiffness proportional damping produces a lower-bound estimate of damping for nonlinear systems (Chopra, 2017). A damping coefficient equal to 2% of critical was assumed and the stiffness used to calculate damping was updated at each time interval. The coefficient used for the stiffness-proportional part of Rayleigh Damping was held constant throughout the analysis and was calculated using the expression shown below.

$$a_1 = \frac{2\xi}{\omega}$$

where

a_1 = Coefficient for stiffness proportional part of Rayleigh damping for SDOF oscillators,

ω = Initial natural frequency of SDOF oscillator, and

ξ = Viscous damping ratio.

B.3.3 Ground Motions

One of the primary goals of the investigation was to study the effect of changes in drift demand of SDOF oscillators subjected to multiple ground motions with a wide range of spectral shapes and properties. To do so, 120 ground motions, organized in four sets of 30, were selected for two different site types representing areas with high and moderate seismicity, and two different soil classifications representing stiff and soft soils. This section describes the procedure used to select ground motions for the SDOF analyses and the sequences of ground motions used in them.

B.3.3.1 Ground Motion Selection

Test sites in Berkeley, CA and Seattle, WA were chosen to represent regions with high and moderate seismicity, respectively. For each site type, records were selected to represent plausible motions in stiff soils (soil class B) and soft soils (soil class D). A set of 30 ground-motion records were selected for each of the four combinations of site type and soil class.

To begin the selection of ground motions, an idealized ‘smooth’ spectrum corresponding to the Maximum Considered Earthquake (MCE) was first defined following the guidelines in ASCE 7-16 for each combination of site type and soil classification (American Society of Civil Engineers, 2017). This smooth spectrum was used as a ‘target’ for selection of records. Information about the locations and parameters used to define the target spectrum is listed in Table B-6. For each of the four target spectra, a set of 30 ground-motion records were selected from the PEER NGA West (Ancheta,

et al., 2013) to minimize the deviations between their spectra and the target in the entire range of periods considered (Baker & Lee, 2017). Only ground-motion records from events with moment magnitudes larger than six were considered. Records were amplified by scaling them with multipliers not exceeding five. Comparisons of target spectrum and linear spectra computed for the records selected for each site type and soil class are shown in Figure B-25 through Figure B-28. Properties of the selected ground motions are listed in Table B-7 through Table B-10.

B.3.3.2 Sequence of Ground Motions

To study the plausible effects of loading history on drift demand, each SDOF was subjected to two sequences of ground motions at 24 ground motion intensity levels ‘X’, ranging from 5% of MCE to 120% of MCE in increments of 5%. The first ‘sequence’ (Sequence A) was comprised of a single ground motion of intensity level ‘X’. The second sequence (Sequence B) was comprised of two ground motions: the first at an intensity of 100% of the prescribed MCE motion and the second corresponding to the intensity level ‘X’. Enough time (approximately 100 seconds) was provided between the motions in Sequence B to allow for the oscillator to come to rest.

B.3.4 Results

For SDOF oscillators subjected to multiple ground motions, displacements can be defined as either in-run displacements or cumulative displacements. In-run displacements are defined as displacements occurring during a given ground motion with respect to the position of the oscillator before the beginning of the ground motion. This definition of an oscillator’s displacement does not include permanent (residual) displacements that the oscillator might have experienced during previous motions. Cumulative displacements, in contrast, are displacements an oscillator undergoes during a ground motion with respect to the initial position of the oscillator before it was subjected to any ground motion. Cumulative displacements include permanent displacements caused by previous ground motions.

The observations below refer to in-run displacements exclusively. To compare in-run displacements obtained for SDOFs with different periods, they were expressed as ‘drift ratios’ using the expression shown below.

$$Drift = \frac{\delta_{SDOF}}{N \cdot H} * \Gamma$$

where,

Drift = Drift ratio of SDOF oscillator,

δ_{SDOF} = Displacement of SDOF oscillator,

N = Number of stories,

H = Story height, and

Γ = Fundamental mode participation factor (set equal to 1.25)

The following assumptions were made to arrive at this definition of drift:

1. Displacements estimated for an idealized SDOF, δ_{SDOF} , can serve as a measure of displacements occurring in building frames with the same initial period as the SDOF,
2. Roof displacement is equal to $\Gamma \times \delta_{SDOF}$
3. The number of stories N of the mentioned frames can be approximated as 10 times the initial period in seconds,
4. Total building height is N times story height $H = 10$ feet,
5. Roof drift ratio is roof displacement estimated as $\Gamma \times \delta_{SDOF}$ divided by the product $N \times H$.

To compare drift demands at an intensity level 'X', the projected peak 'drift ratio' in the first ground motion in Sequence A was compared with the projected peak 'drift ratio' calculated for the second ground motion in Sequence B. Comparisons between the two drifts were made in terms of 1) the ratio of drift from Sequence B to drift from Sequence A, and 2) the difference between the drift in Sequence B and Sequence A. Figure B-29 through Figure B-52 show the mean ratio of drifts and mean difference in drifts for different intensity levels, periods and hysteresis models for all combinations of site types, soil classifications, and strength definitions. Based on these figures, the following observations were made:

1. For sequences of intense motions and for stable oscillators (without pinching), the relative increase in drift (occurring in the second motion) was, on average, no more than 20%, in agreement with the findings of FEMA 307.
2. For the entire range of intensities considered, and for oscillators with effective periods longer than approximately 1 second, the average increase in drift demand was smaller than 50%.
3. Larger increases in drift (exceeding 100%) occurred primarily in oscillators with effective periods between approximately 0.1 seconds and 1 second. Low-strength oscillators with pinching were calculated to be the most susceptible to large increases in drift demands. Otherwise, the absolute increase in drift demand was, on average, less than 0.5% (in terms of drift ratio).

4. The largest relative increases in drift were calculated to occur for low-intensity motions a) occurring after intense motions, and b) for cases in which the low-intensity motion did not induce displacements exceeding the thresholds associated with cracking and yielding in the pristine oscillator (Sequence A). That is: once cracked, a structure is likely to drift more than a similar but uncracked and pristine structure as long as the motion causing drift is mild enough not to cause cracking and yielding in the latter.
5. General trends of changes in drift were similar for the different methods of defining strength and different site and soil types considered.

B.3.5 Tables

Table B-5 Hysteretic Material parameters Used to Define SDOF Oscillators in this Investigation

Parameters	Model		
	TAKU	TAKC	TAKP
PinchX	1	1	0.72
PinchY	1	1	0.1
Damage1	0	0	0
Damage2	0	0	0
Beta	0.4	0.4	0.4

Table B-6 Parameters Used to Define Target Spectrum According to ASCE 7-16. Two Site Types Were Used to Define Target Spectrum for Regions with High (Berkeley) and Moderate (Seattle) Seismicity. For Each of These Site Types, Two Soil Classifications (Site Class B and D) Were Used

Parameter	Berkeley, CA		Seattle, WA	
	Site Class B	Site Class D	Site Class B	Site Class D
S_s	2.257	2.257	1.396	1.396
S_t	0.871	0.871	0.487	0.487
F_a	0.9	0.9	0.9	0.9
F_v	0.8	0.8	0.8	0.8
T_0	0.07	0.07	0.06	0.06
T_s	0.34	0.51	0.31	0.47
T_L	8	8	6	6

Table B-7 Key Parameters for Ground Motions Used for Seattle Site B

EQ	RSN	Scale	PGA, g	PGV, in/sec	PGD, in	Arias Int. m/s	Hous-ner Int., in	D5-75, sec	D5-95, sec
1	3750	1.7	0.44	20.1	11.2	2.0	63.0	5.7	12.0
2	762	4.0	0.42	15.2	8.6	4.1	54.6	7.2	16.8
3	5829	0.9	0.36	18.6	17.9	3.2	51.7	15.5	25.7
4	1549	0.7	0.70	17.3	16.8	4.5	57.3	14.5	27.3
5	1521	1.2	0.42	16.5	8.8	4.3	61.4	19.3	24.1
6	8062	3.3	0.61	22.4	6.3	3.5	58.9	3.5	12.6
7	761	3.0	0.42	17.0	13.6	2.9	53.8	7.2	17.9
8	68	2.7	0.53	18.0	13.7	3.4	57.7	5.0	13.4
9	8133	4.5	0.47	16.4	6.8	3.2	59.7	4.8	10.6
10	2619	4.1	0.86	17.4	11.5	1.8	52.8	5.3	6.6
11	3852	4.1	0.45	15.7	9.9	2.8	53.8	5.7	16.4
12	5990	1.8	0.46	15.3	11.0	5.2	48.2	15.3	31.0
13	725	1.5	0.43	17.1	6.7	3.9	66.6	11.2	13.6
14	4016	4.6	0.54	15.4	6.6	2.7	55.9	5.0	11.0
15	5259	3.3	0.36	11.2	6.2	3.9	61.9	12.9	70.0
16	172	4.5	0.61	19.4	12.6	4.5	59.1	7.0	19.5
17	3752	4.8	0.42	17.4	9.5	6.4	62.5	18.3	27.3
18	5773	2.9	0.63	16.5	7.9	6.7	49.2	7.9	16.7
19	174	1.3	0.49	22.8	10.9	2.8	54.5	4.6	7.9
20	6961	2.8	0.54	19.7	12.9	4.0	57.7	13.2	20.3
21	93	4.1	0.44	17.0	10.4	2.9	48.7	7.2	21.5
22	162	2.1	0.43	15.4	13.1	3.3	54.6	7.1	14.8
23	4881	2.5	0.41	12.9	7.8	4.0	64.1	10.0	19.6
24	5678	2.2	0.57	16.4	9.9	3.5	62.2	3.8	9.0
25	762	3.3	0.42	18.3	12.2	3.0	60.6	8.5	18.2
26	5969	2.0	0.38	19.8	15.2	4.8	61.1	21.5	38.3
27	183	0.9	0.55	19.3	14.8	1.3	65.1	3.0	6.8
28	1521	1.6	0.37	20.9	16.3	4.0	59.8	21.8	24.9
29	1301	4.9	0.53	19.7	23.0	4.5	48.2	9.5	16.2
30	180	0.9	0.48	17.3	17.3	1.4	59.7	3.6	8.3

Table B-8 Key Parameters for Ground Motions Used for Seattle Site D

EQ	RSN	Scale	PGA, g	PGV, in/sec	PGD, in	Arias Int. m/s	Hous-ner Int., in	D5-75, sec	D5-95, sec
1	183	1.3	0.79	27.9	21.4	2.8	94.1	3.0	6.8
2	5969	2.7	0.52	26.7	20.5	8.7	82.5	21.5	38.3
3	161	2.5	0.55	40.3	16.0	2.8	94.6	3.0	14.4
4	6948	4.7	0.69	21.2	22.2	9.0	86.9	17.7	23.0
5	180	1.2	0.63	23.1	23.1	2.4	79.6	3.6	8.3
6	6961	3.7	0.71	26.0	17.0	6.9	76.3	13.2	20.3
7	2714	4.0	0.45	25.3	16.0	3.6	79.6	4.4	11.7
8	762	4.4	0.56	24.4	16.2	5.3	80.7	8.5	18.2
9	1762	2.7	0.40	21.0	16.4	5.0	83.0	11.0	24.1
10	8119	1.0	0.67	38.0	15.9	2.3	103.7	2.2	3.1
11	728	2.4	0.41	22.2	14.1	4.8	76.6	11.9	23.5
12	5827	1.1	0.59	26.6	15.0	7.4	94.4	19.8	32.7
13	169	2.0	0.47	20.7	11.6	9.6	86.0	24.4	51.4
14	1521	2.2	0.50	28.7	22.4	7.5	82.2	21.8	24.9
15	1521	1.7	0.60	23.4	12.5	8.7	87.0	19.3	24.1
16	176	4.1	0.48	26.0	17.6	4.6	86.4	8.1	21.4
17	15	3.5	0.63	25.7	12.9	7.3	90.5	10.2	28.8
18	5284	3.9	0.72	34.6	9.2	4.2	94.5	12.1	37.8
19	5259	4.4	0.48	14.9	8.3	6.9	82.5	12.9	70.0
20	5829	1.3	0.52	26.8	25.8	6.7	74.7	15.5	25.7
21	725	2.0	0.57	22.8	8.9	7.0	88.8	11.2	13.6
22	4866	2.0	0.65	27.6	13.0	6.8	98.2	7.2	13.6
23	761	4.6	0.88	23.1	10.9	6.6	88.5	7.2	17.2
24	4203	3.6	0.47	17.0	9.3	5.9	87.3	16.1	67.3
25	4881	3.3	0.53	17.0	10.3	6.9	84.6	10.0	19.6
26	4872	3.7	0.54	33.8	10.5	4.3	97.7	8.0	22.7
27	187	4.1	0.84	28.6	19.7	3.8	75.6	6.0	16.9
28	3750	2.3	0.60	27.2	15.2	3.7	85.3	5.7	12.0
29	178	1.7	0.45	32.1	13.9	3.3	98.5	4.3	11.9
30	169	1.6	0.56	20.8	12.7	8.4	97.9	22.5	50.5

Table B-9 Key Parameters for Ground Motions Used for Berkeley Site B

EQ	RSN	Scale	PGA, g	PGV, in/sec	PGD, in	Arias Int. m/s	Hous-ner Int., in	D5-75, sec	D5-95, sec
1	5829	1.7	0.67	35.1	33.8	11.5	97.7	15.5	25.7
2	180	1.6	0.85	30.8	30.8	4.3	106.1	3.6	8.3
3	162	3.8	0.77	27.9	23.8	10.9	98.8	7.1	14.8
4	3750	3.1	0.81	36.7	20.5	6.8	114.9	5.7	12.0
5	5969	3.7	0.71	36.6	28.0	16.4	113.1	21.5	38.3
6	1521	2.9	0.67	37.8	29.5	13.0	108.3	21.8	24.9
7	1549	1.2	1.21	29.7	28.8	13.3	98.3	14.5	27.3
8	1521	2.2	0.78	30.3	16.2	14.5	112.6	19.3	24.1
9	183	1.7	1.04	36.5	27.9	4.7	123.0	3.0	6.8
10	5678	3.9	1.01	29.1	17.6	11.0	110.3	3.8	9.0
11	15	4.6	0.83	33.7	16.9	12.7	118.9	10.2	28.8
12	4881	4.4	0.71	22.7	13.7	12.3	112.8	10.0	19.6
13	725	2.7	0.77	30.8	12.1	12.8	119.9	11.2	13.6
14	5990	3.3	0.84	28.0	20.2	17.5	88.4	15.3	31.0
15	174	2.2	0.83	38.6	18.5	7.9	92.2	4.6	7.9
16	1762	3.6	0.54	28.0	21.8	8.8	110.6	11.0	24.1
17	161	3.3	0.72	53.2	21.1	4.9	124.8	3.0	14.4
18	728	3.3	0.57	30.5	19.4	9.0	105.4	11.9	23.5
19	68	4.9	0.96	32.7	24.8	11.1	104.7	5.0	13.4
20	5969	2.8	0.77	21.5	22.9	14.5	90.4	15.0	31.2
21	4866	2.6	0.84	35.9	16.9	11.5	127.7	7.2	13.6
22	1549	2.0	1.25	41.7	23.3	22.2	100.4	19.0	30.8
23	169	2.1	0.73	27.3	16.7	14.4	128.5	22.5	50.5
24	1787	3.2	0.85	32.8	24.9	8.5	128.8	6.4	11.7
25	68	3.3	0.74	28.2	20.7	7.4	102.9	5.2	13.2
26	178	2.3	0.62	43.4	18.8	6.1	133.3	4.3	11.9
27	4860	3.3	0.86	24.1	20.1	11.8	127.1	10.9	23.2
28	5827	1.9	0.78	32.6	15.5	17.4	125.0	22.8	34.5
29	5827	1.5	0.81	36.3	20.4	13.7	128.7	19.8	32.7
30	143	0.9	0.77	35.0	13.3	9.6	116.1	8.3	16.5

Table B-10 Key Parameters for Ground Motions Used for Berkeley Site D

EQ	RSN	Scale	PGA, g	PGV, in/sec	PGD, in	Arias Int. m/s	Hous-ner Int., in	D5-75, sec	D5-95, sec
1	5969	4.8	0.92	47.4	36.4	27.6	146.7	21.5	38.3
2	180	2.0	1.06	38.5	38.5	6.8	132.6	3.6	8.3
3	183	2.2	1.34	47.2	36.2	7.9	159.2	3.0	6.8
4	1762	4.7	0.70	36.5	28.5	15.1	144.5	11.0	24.1
5	5827	2.0	1.08	48.4	27.2	24.4	171.6	19.8	32.7
6	721	2.8	1.00	53.0	21.2	8.7	152.9	7.0	28.0
7	728	4.3	0.74	39.8	25.3	15.3	137.3	11.9	23.5
8	5836	3.3	0.96	35.5	23.3	20.0	127.6	11.2	24.7
9	161	4.4	0.97	70.9	28.1	8.7	166.4	3.0	14.4
10	8119	1.7	1.14	64.7	27.0	6.7	176.2	2.2	3.1
11	5832	3.3	0.68	45.4	25.5	23.3	164.9	27.1	44.1
12	8134	4.9	0.69	46.2	31.5	10.1	161.2	7.0	12.6
13	5829	2.2	0.87	45.4	43.7	19.3	126.4	15.5	25.7
14	4847	2.8	0.85	54.0	27.7	10.3	179.6	7.3	20.3
15	169	2.7	0.94	35.1	21.4	23.9	165.2	22.5	50.5
16	1521	2.9	1.02	39.9	21.3	25.3	148.4	19.3	24.1
17	6	4.1	0.86	50.5	39.0	19.6	185.0	17.7	24.1
18	1521	3.9	0.89	50.9	39.6	23.5	145.6	21.8	24.9
19	1511	2.6	0.90	53.0	34.0	23.8	130.3	17.5	29.5
20	169	3.4	0.80	35.2	19.7	27.6	146.3	24.4	51.4
21	900	4.2	0.64	48.1	38.3	11.9	150.8	10.9	18.9
22	1511	2.4	1.03	56.4	40.9	21.0	176.6	16.5	28.1
23	8134	4.6	0.85	64.4	21.9	8.8	169.4	4.4	14.5
24	5991	2.6	0.95	46.7	24.0	20.4	139.8	13.1	24.2
25	8161	2.3	0.76	65.7	49.5	14.7	153.8	14.1	33.0
26	1489	3.1	0.86	65.3	90.6	12.9	132.9	17.7	21.6
27	178	3.0	0.80	56.6	24.5	10.4	173.9	4.3	11.9
28	6953	4.2	0.83	48.6	33.2	18.2	150.5	11.2	22.0
29	802	2.9	0.95	52.5	38.0	9.2	127.2	4.1	8.2
30	1787	4.2	1.11	43.0	32.7	14.6	169.0	6.4	11.7

B.3.6 Figures

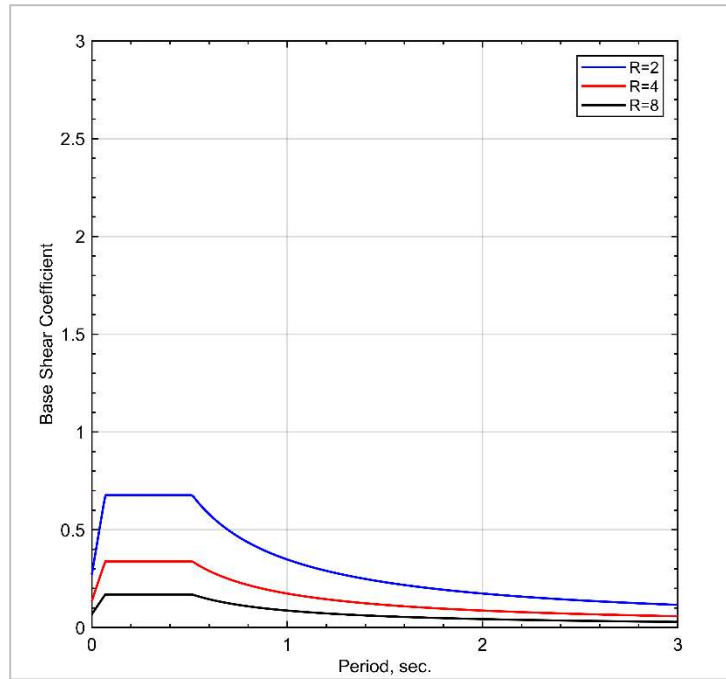


Figure B-20 Plot of base shear coefficient versus period for the ASCE R factor method. Base shear coefficients for R factors of 2, 4 and 8 are shown.

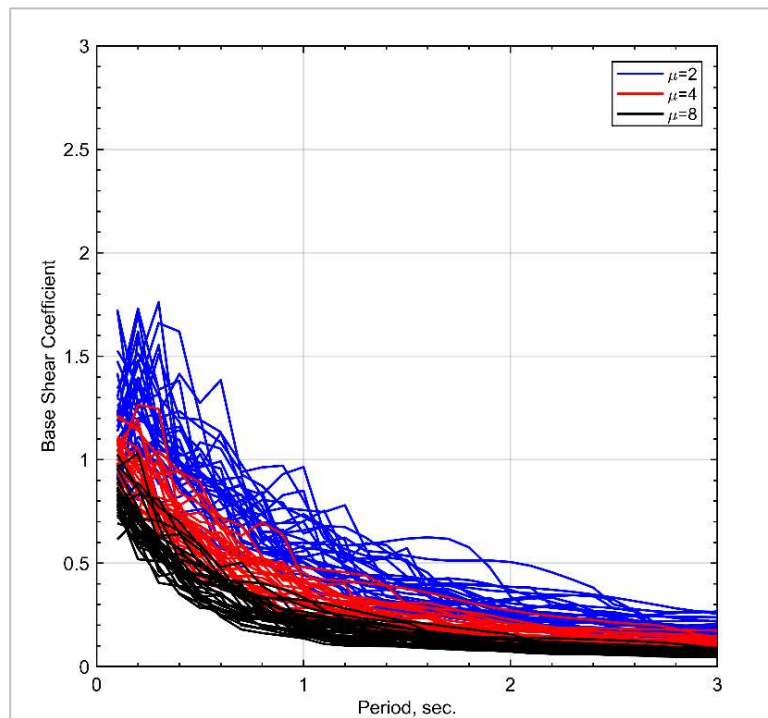


Figure B-21 Plot of base shear coefficient versus period for the constant ductility method. Base shear coefficients for ductility values of 2, 4 and 8 are shown.

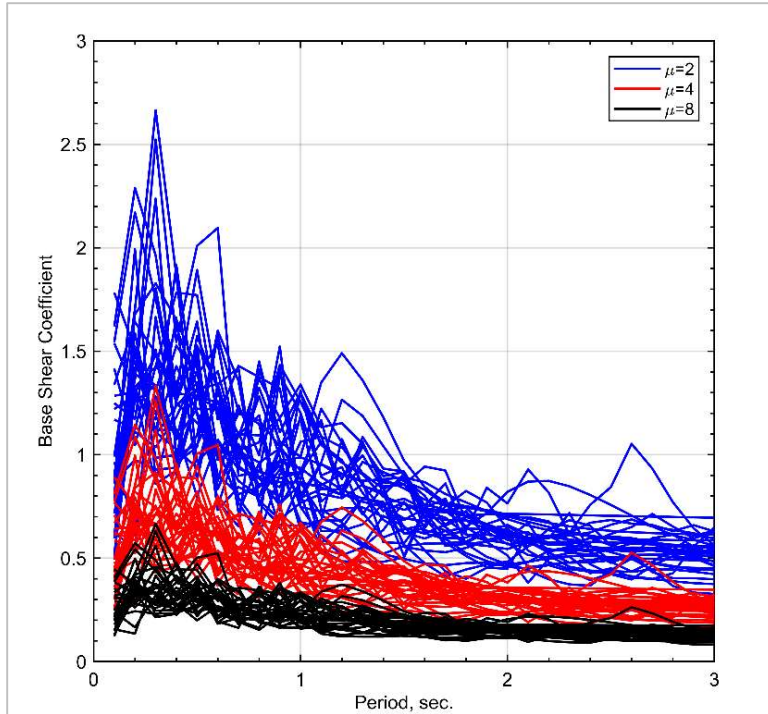


Figure B-22 Plot of base shear coefficient versus period for the constant R factor method. Base shear coefficients for R factors of 2, 4 and 8 are shown.

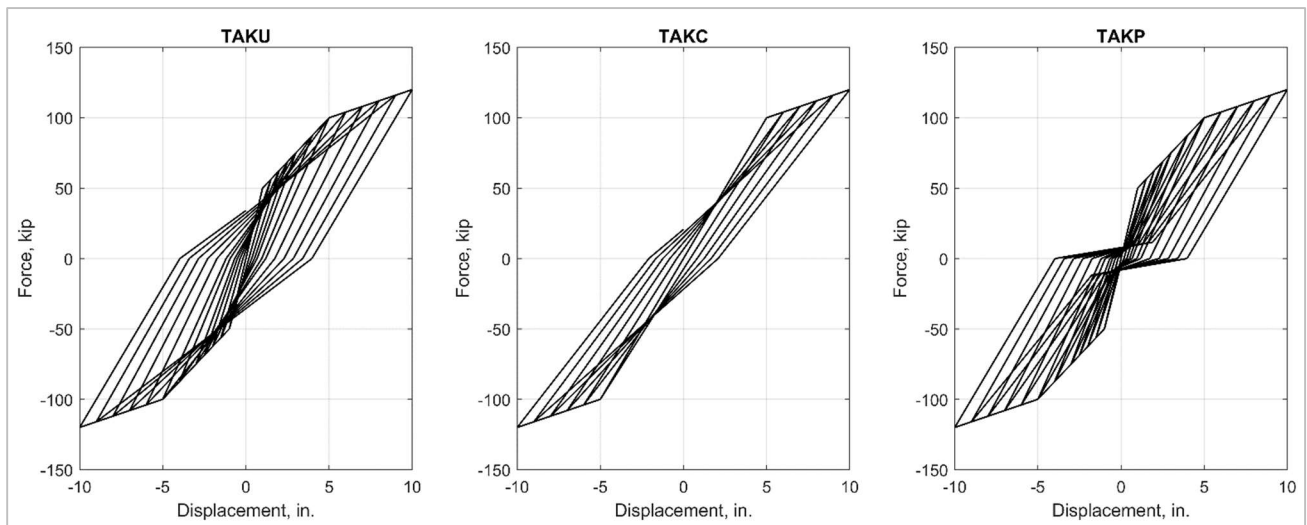


Figure B-23 Hysteresis models used in SDOF analyses.

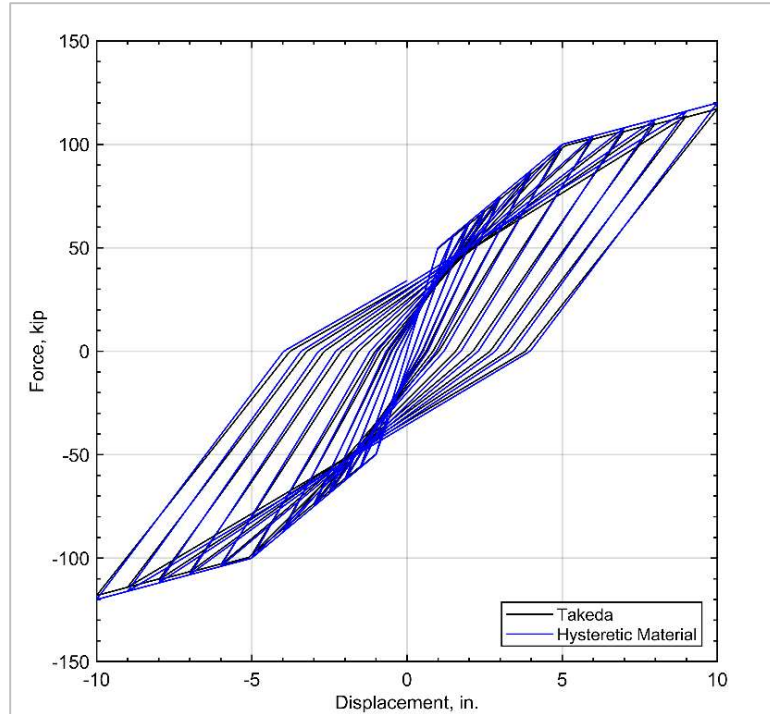


Figure B-24 Comparison of hysteresis produced using Takeda hysteretic rules and Hysteretic Material model in OpenSees.

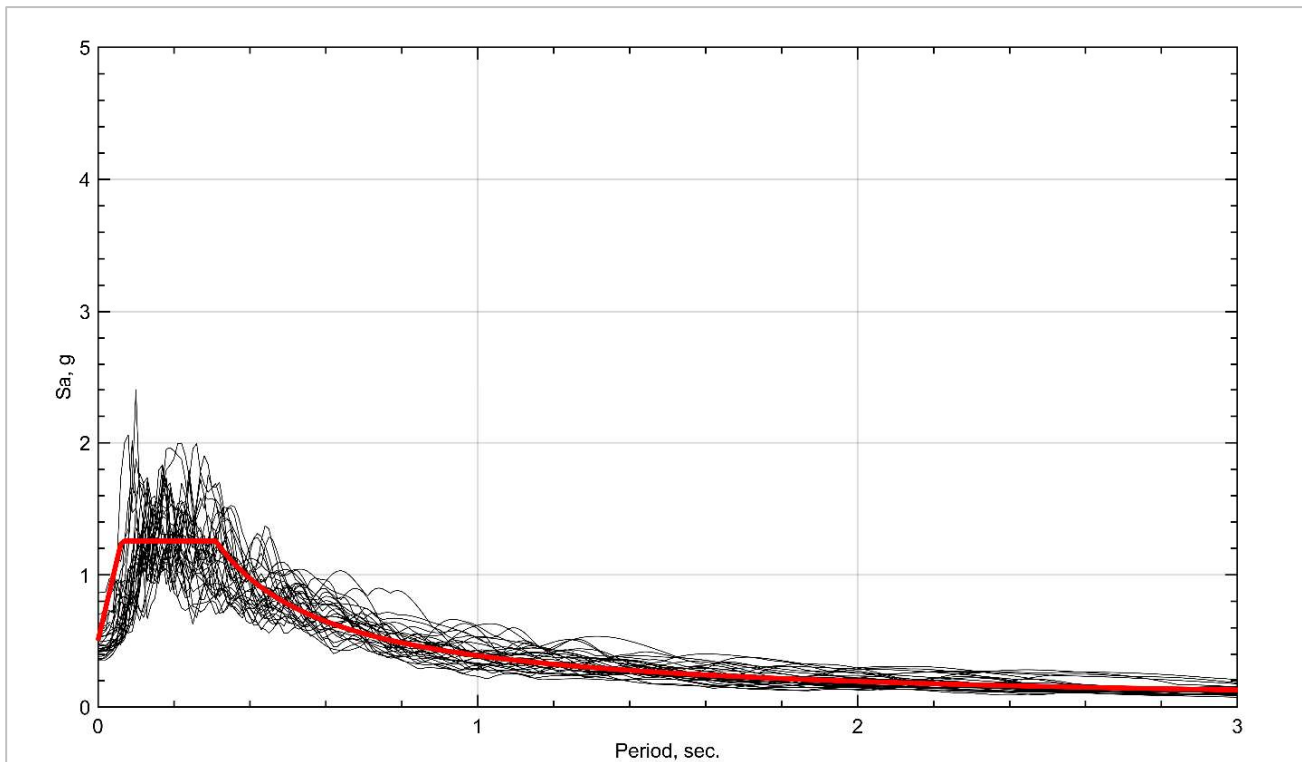


Figure B-25 Plot of spectral acceleration versus period for ground motions used for Seattle Site B. Target spectrum is shown in red whereas spectra from selected ground motions is shown in black.

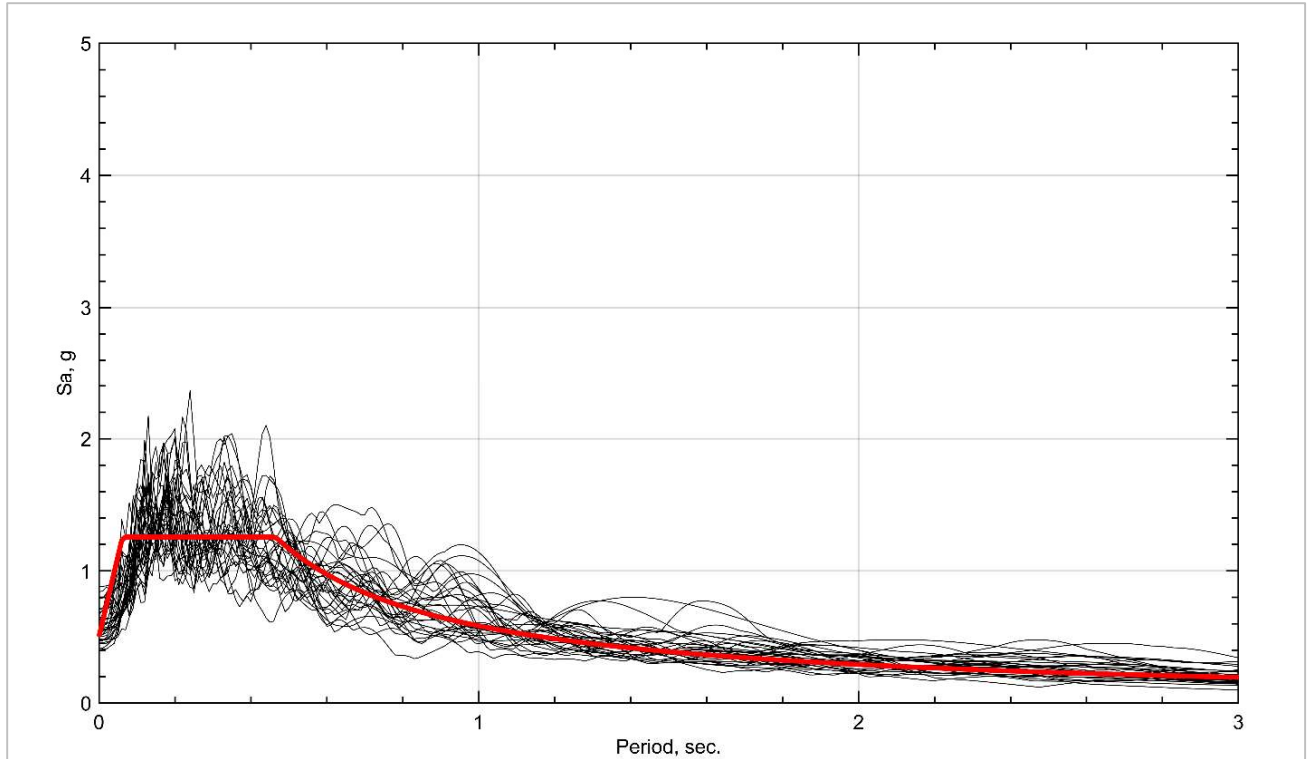


Figure B-26 Plot of spectral acceleration versus period for ground motions used for Seattle Site D. Target spectrum is shown in red whereas spectra from selected ground motions is shown in black.

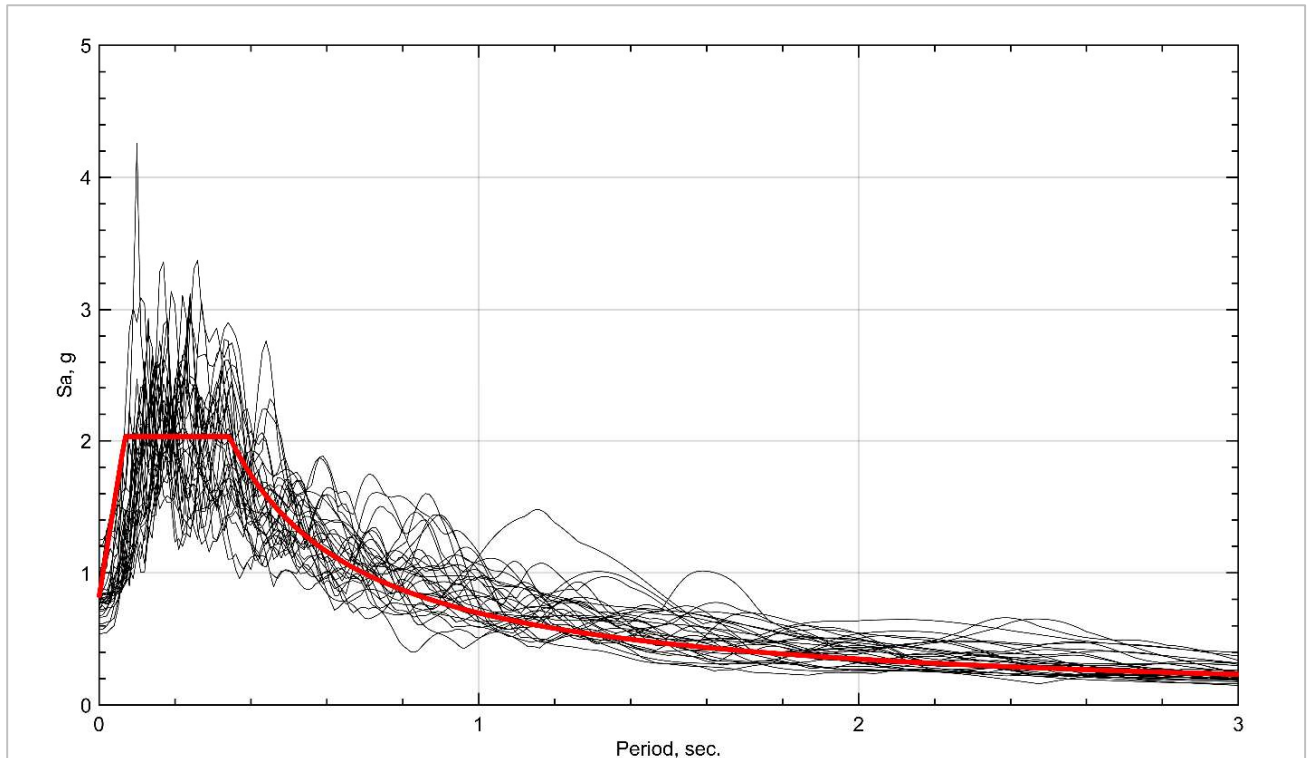


Figure B-27 Plot of spectral acceleration versus period for ground motions used for Berkeley Site B. Target spectrum is shown in red whereas spectra from selected ground motions is shown in black.

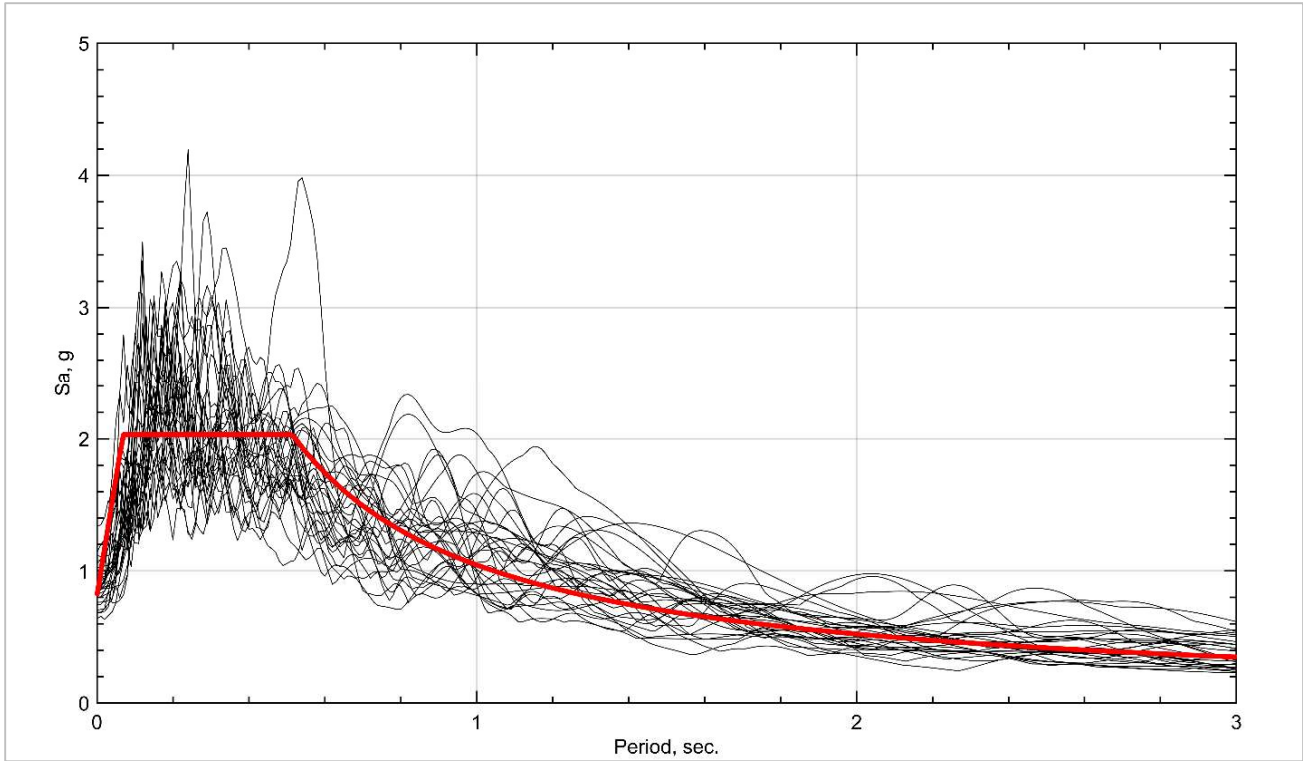


Figure B-28 Plot of spectral acceleration versus period for ground motions used for Berkeley Site D. Target spectrum is shown in red whereas spectra from selected ground motions is shown in black.

ASCE Method (Berkeley Site B)

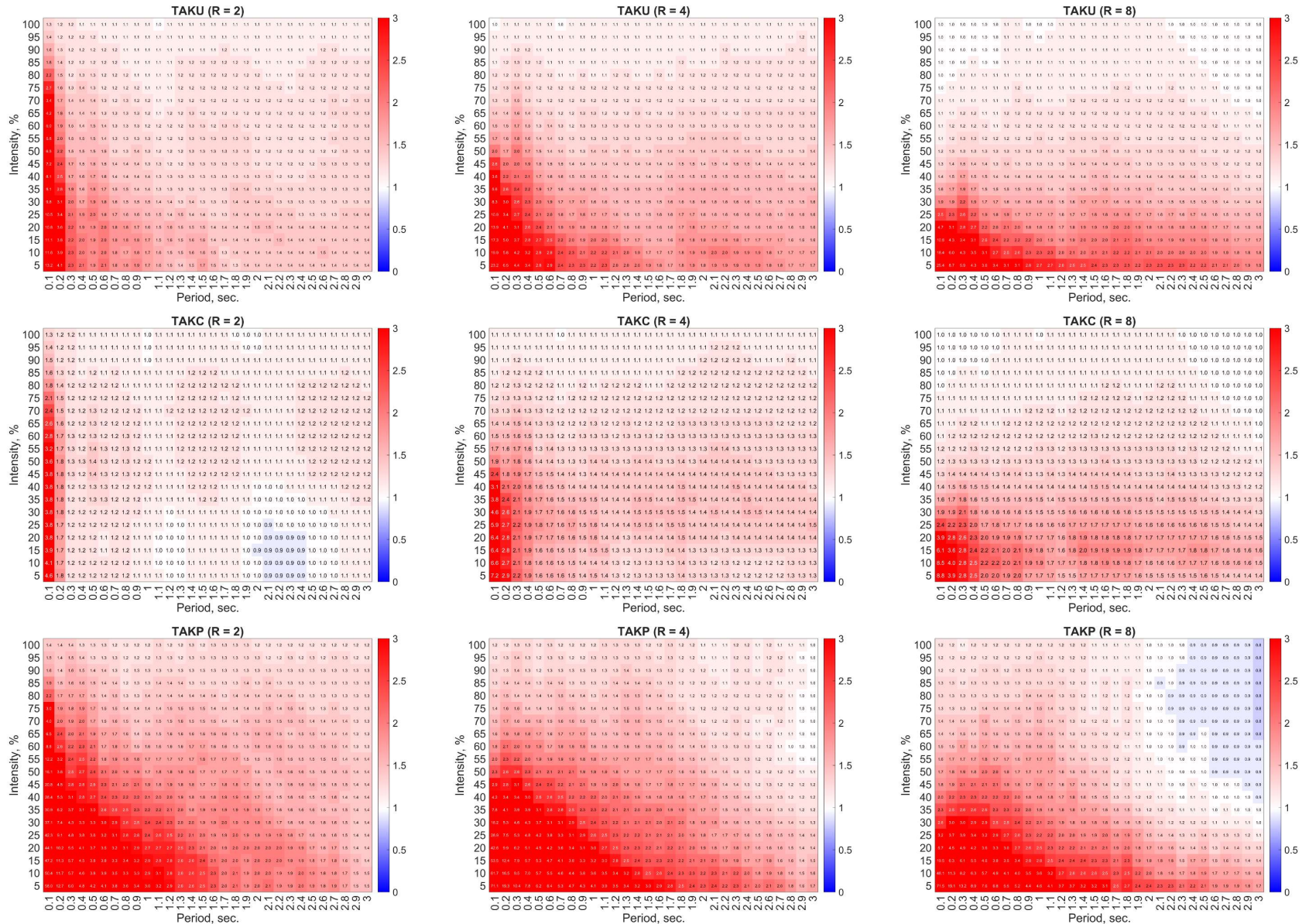


Figure B-29 Mean of ratio of drift from sequence B to drift from sequence A for different intensity levels, periods and hysteresis models for oscillators whose strengths were defined using the ASCE method and were subjected to ground motions from Berkeley Site B. Colors and numbers in each cell correspond to the value of the mean ratio of drifts.

ASCE Method (Berkeley Site B)

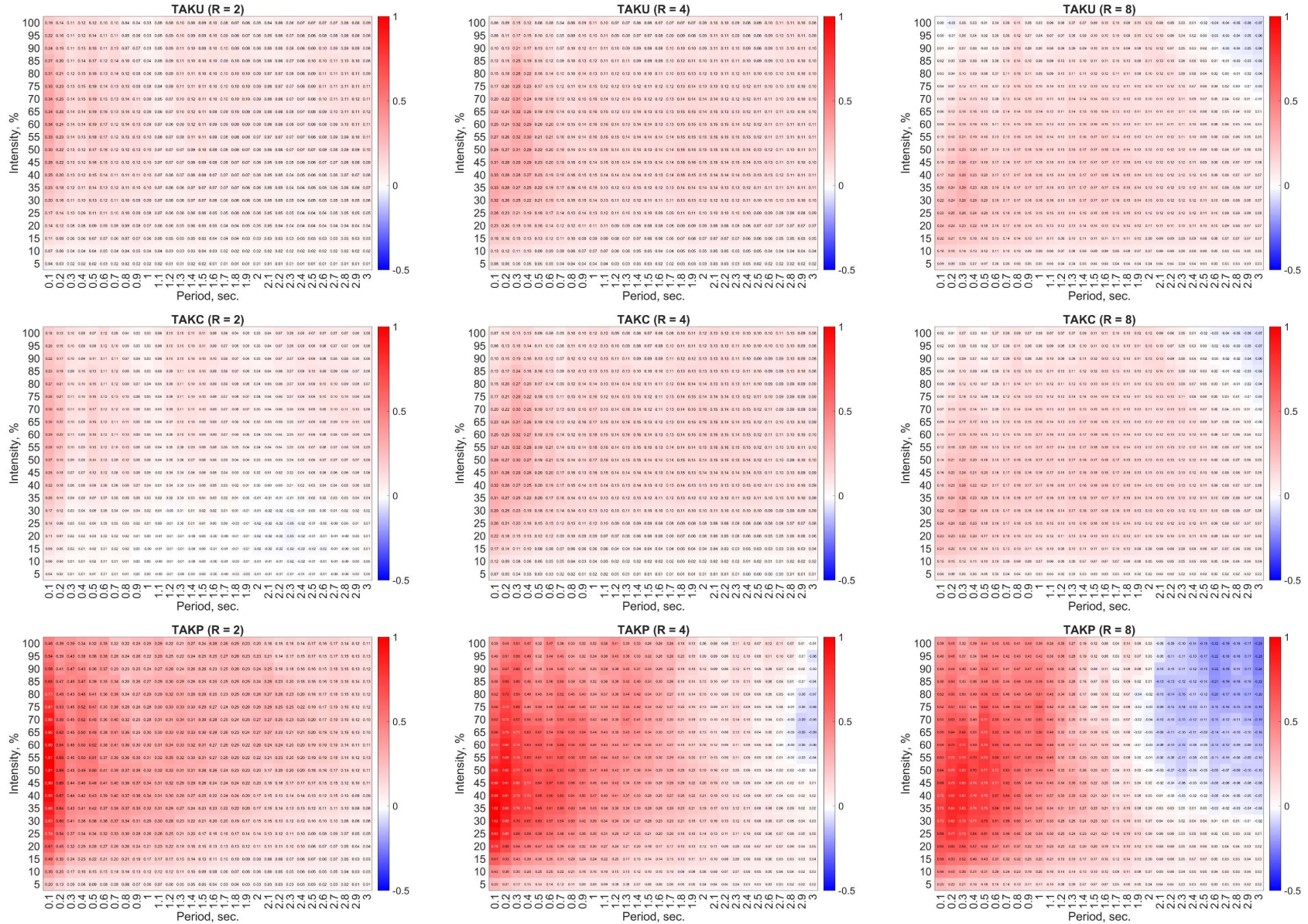


Figure B-30 Mean of difference in drifts between sequence B and sequence A for different intensity levels, periods and hysteresis models for oscillators whose strengths were defined using the ASCE method and were subjected to ground motions from Berkeley Site B. Colors and numbers in each cell correspond to the value of the mean difference of drifts.

ASCE Method (Berkeley Site D)

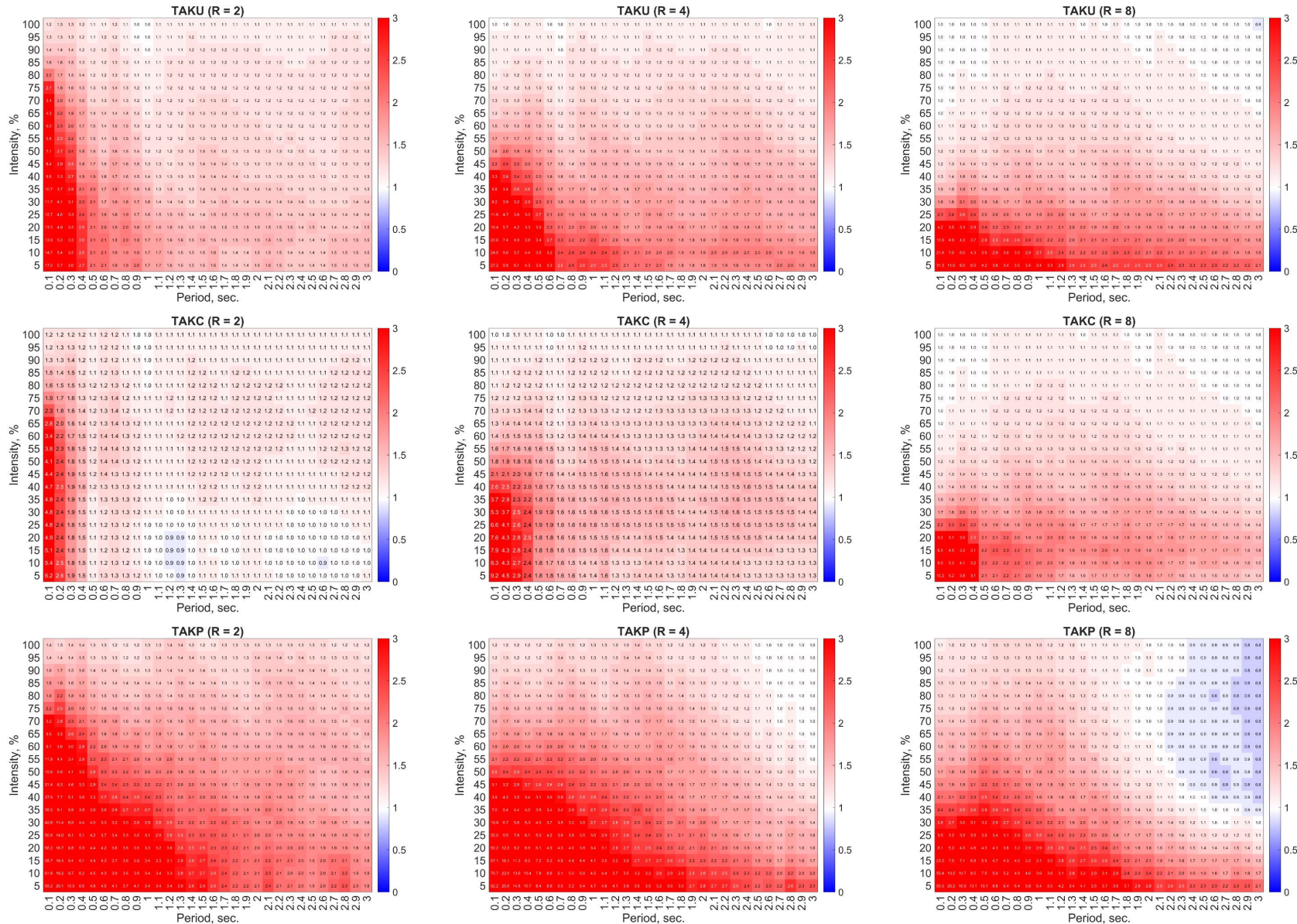


Figure B-31 Mean of ratio of drift from sequence B to drift from sequence A for different intensity levels, periods and hysteresis models for oscillators whose strengths were defined using the ASCE method and were subjected to ground motions from Berkeley Site D. Colors and numbers in each cell correspond to the value of the mean ratio of drifts.

ASCE Method (Berkeley Site D)

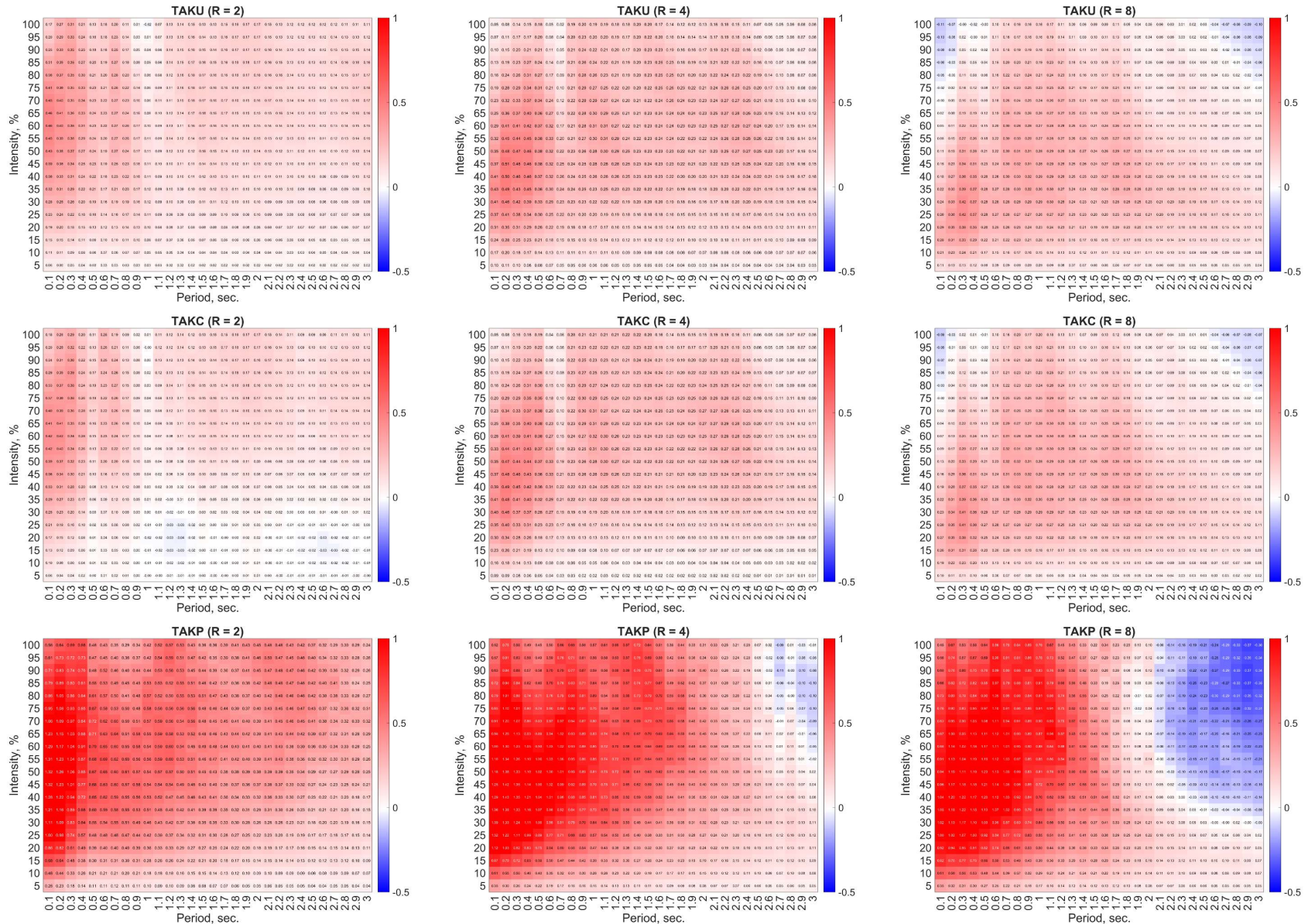


Figure B-32 Mean of difference in drifts between sequence B and sequence A for different intensity levels, periods and hysteresis models for oscillators whose strengths were defined using the ASCE method and were subjected to ground motions from Berkeley Site D. Colors and numbers in each cell correspond to the value of the mean difference of drifts.

ASCE Method (Seattle Site B)

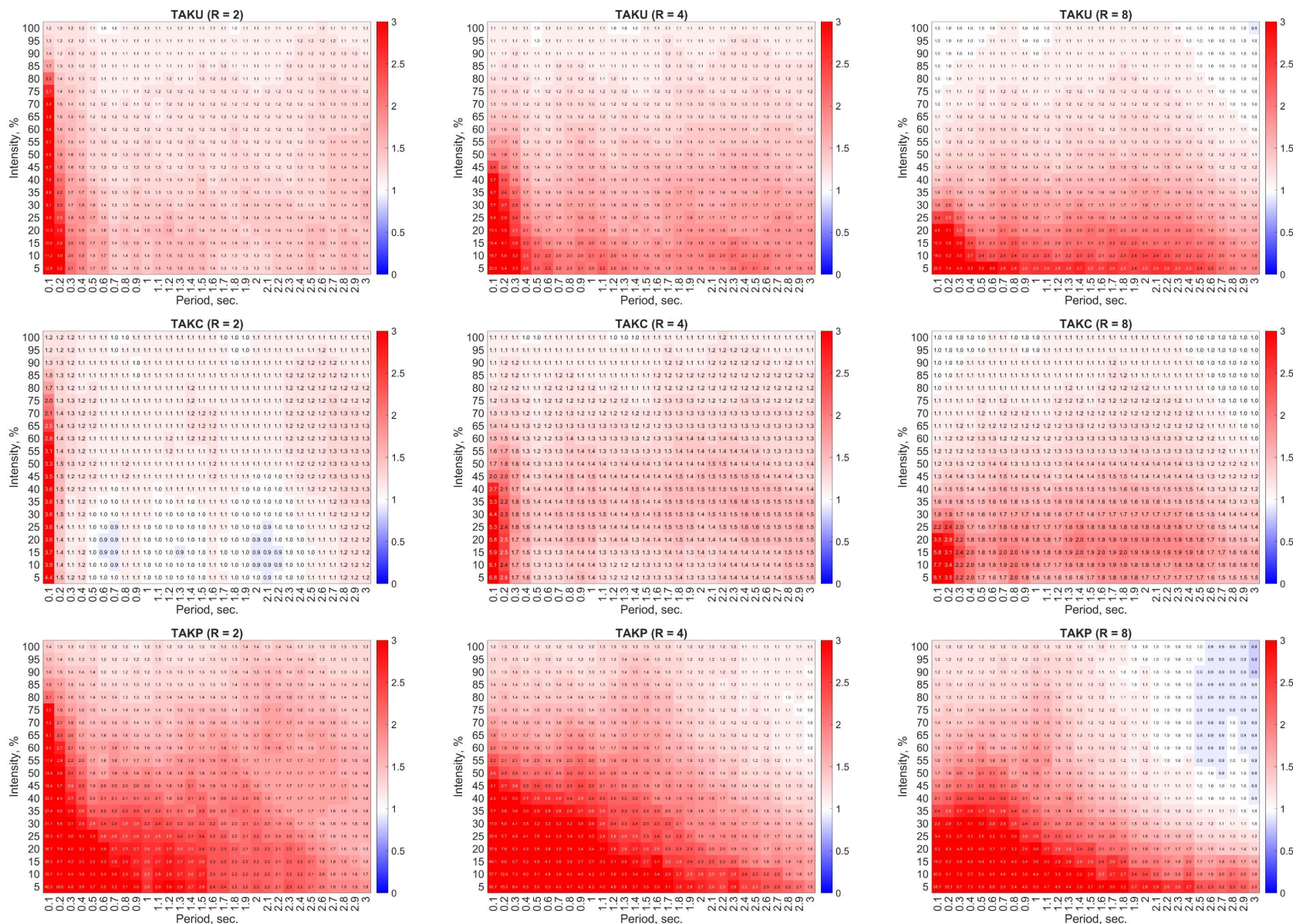


Figure B-33 Mean of ratio of drift from sequence B to drift from sequence A for different intensity levels, periods and hysteresis models for oscillators whose strengths were defined using the ASCE method and were subjected to ground motions from Seattle Site B. Colors and numbers in each cell correspond to the value of the mean ratio of drifts.

ASCE Method (Seattle Site B)

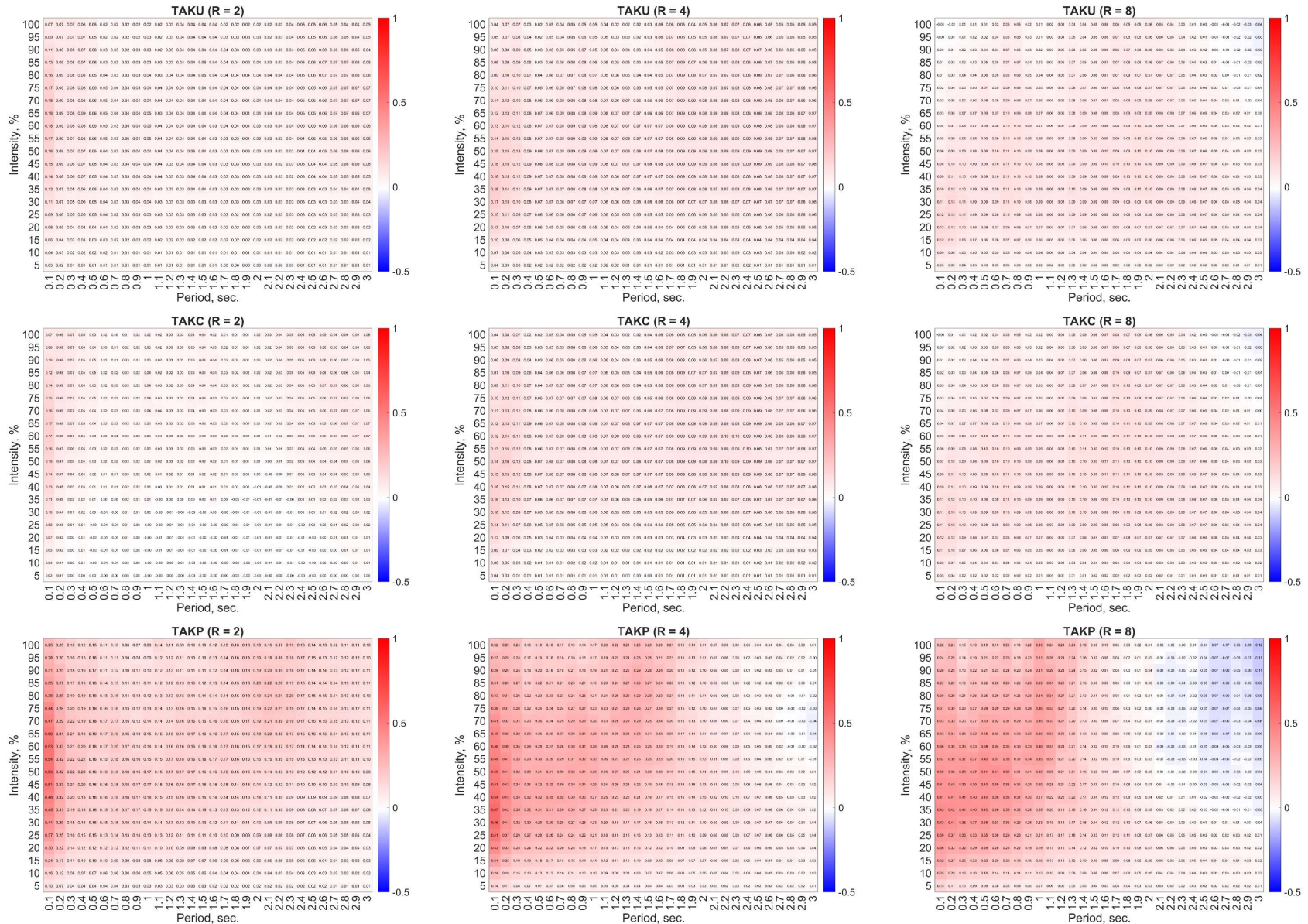


Figure B-34 Mean of difference in drifts between sequence B and sequence A for different intensity levels, periods and hysteresis models for oscillators whose strengths were defined using the ASCE method and were subjected to ground motions from Seattle Site B. Colors and numbers in each cell correspond to the value of the mean difference of drifts.

ASCE Method (Seattle Site D)

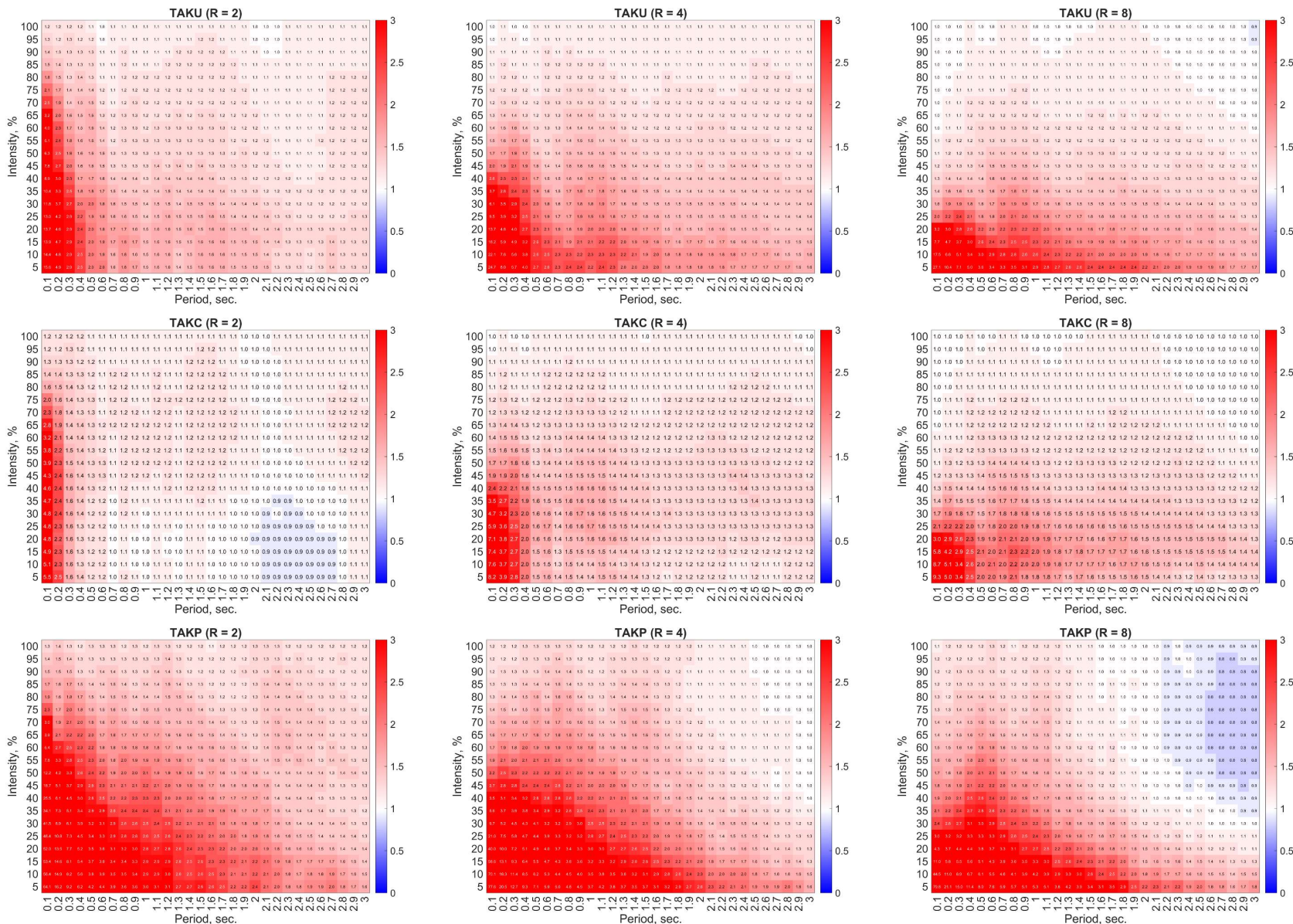


Figure B-35 Mean of ratio of drift from sequence B to drift from sequence A for different intensity levels, periods and hysteresis models for oscillators whose strengths were defined using the ASCE method and were subjected to ground motions from Seattle Site D. Colors and numbers in each cell correspond to the value of the mean ratio of drifts.

ASCE Method (Seattle Site D)

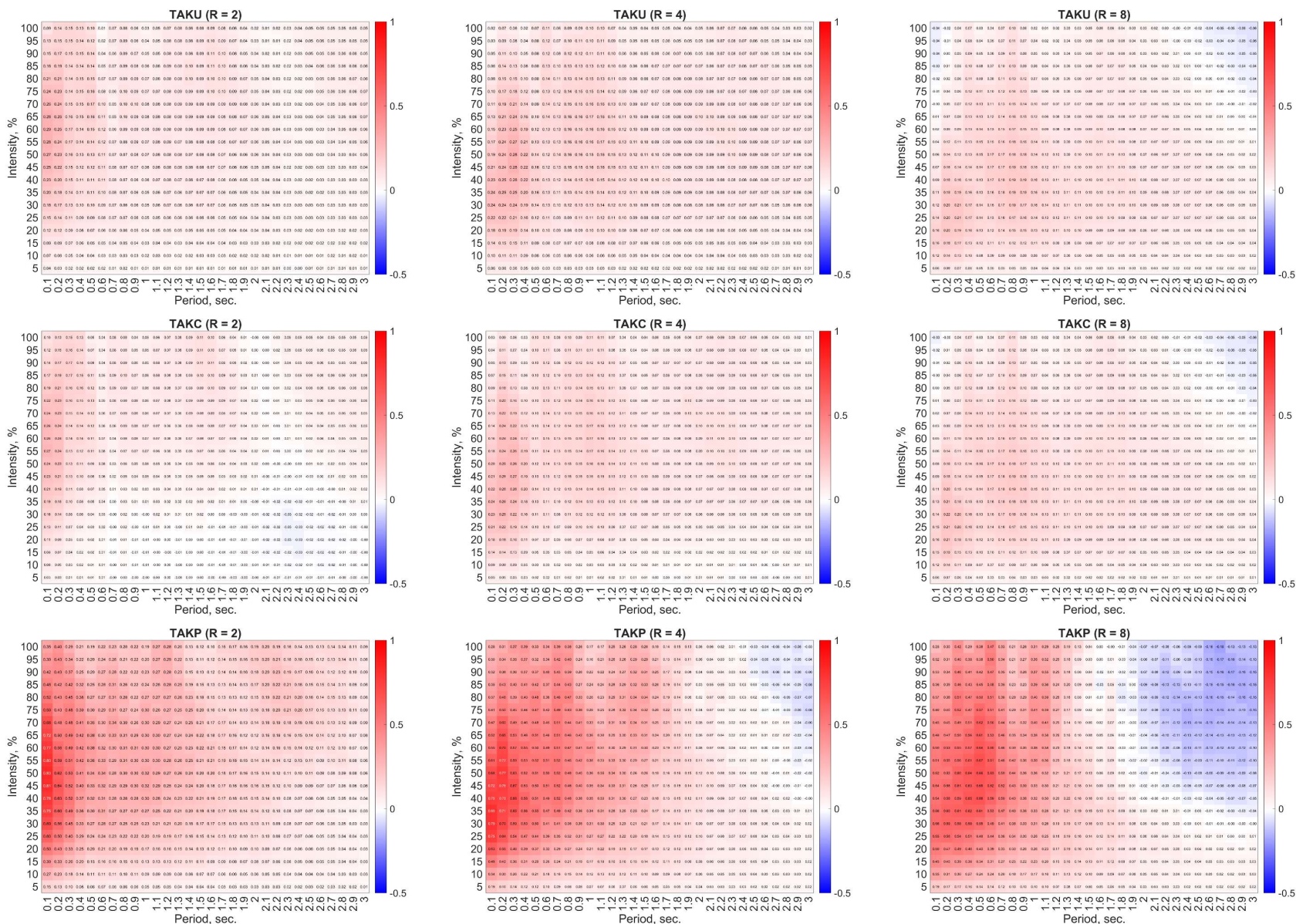


Figure B-36 Mean of difference in drifts between sequence B and sequence A for different intensity levels, periods and hysteresis models for oscillators whose strengths were defined using the ASCE method and were subjected to ground motions from Seattle Site D. Colors and numbers in each cell correspond to the value of the mean difference of drifts.

Constant Ductility Method (Berkeley Site B)

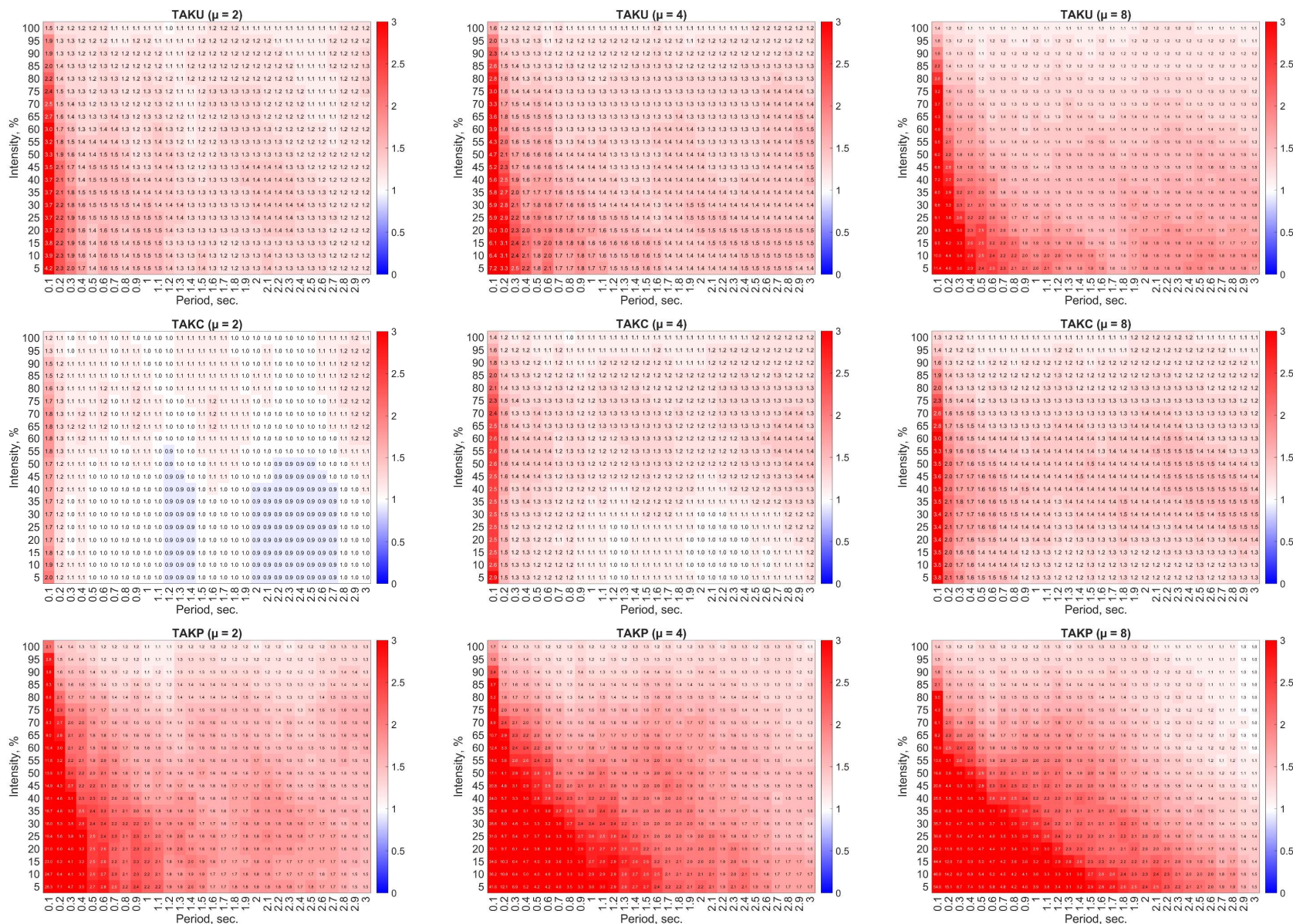


Figure B-37 Mean of ratio of drift from sequence B to drift from sequence A for different intensity levels, periods and hysteresis models for oscillators whose strengths were defined using the constant ductility method and were subjected to ground motions from Berkeley Site B. Colors and numbers in each cell correspond to the value of the mean ratio of drifts.

Constant Ductility Method (Berkeley Site B)

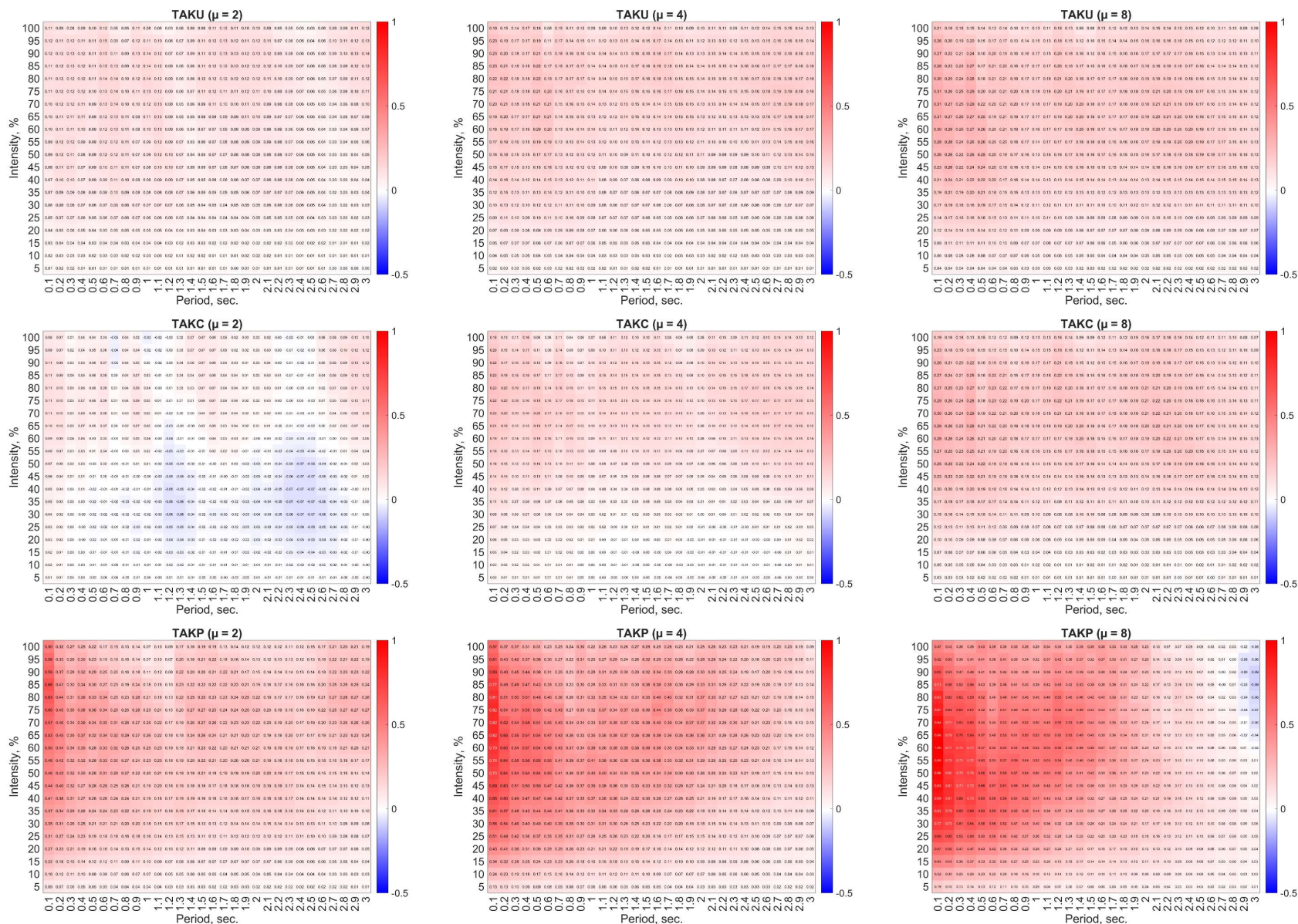


Figure B-38 Mean of difference in drifts between sequence B and sequence A for different intensity levels, periods and hysteresis models for oscillators whose strengths were defined using the constant ductility method and were subjected to ground motions from Berkeley Site B. Colors and numbers in each cell correspond to the value of the mean difference of drifts.

Constant Ductility Method (Berkeley Site D)

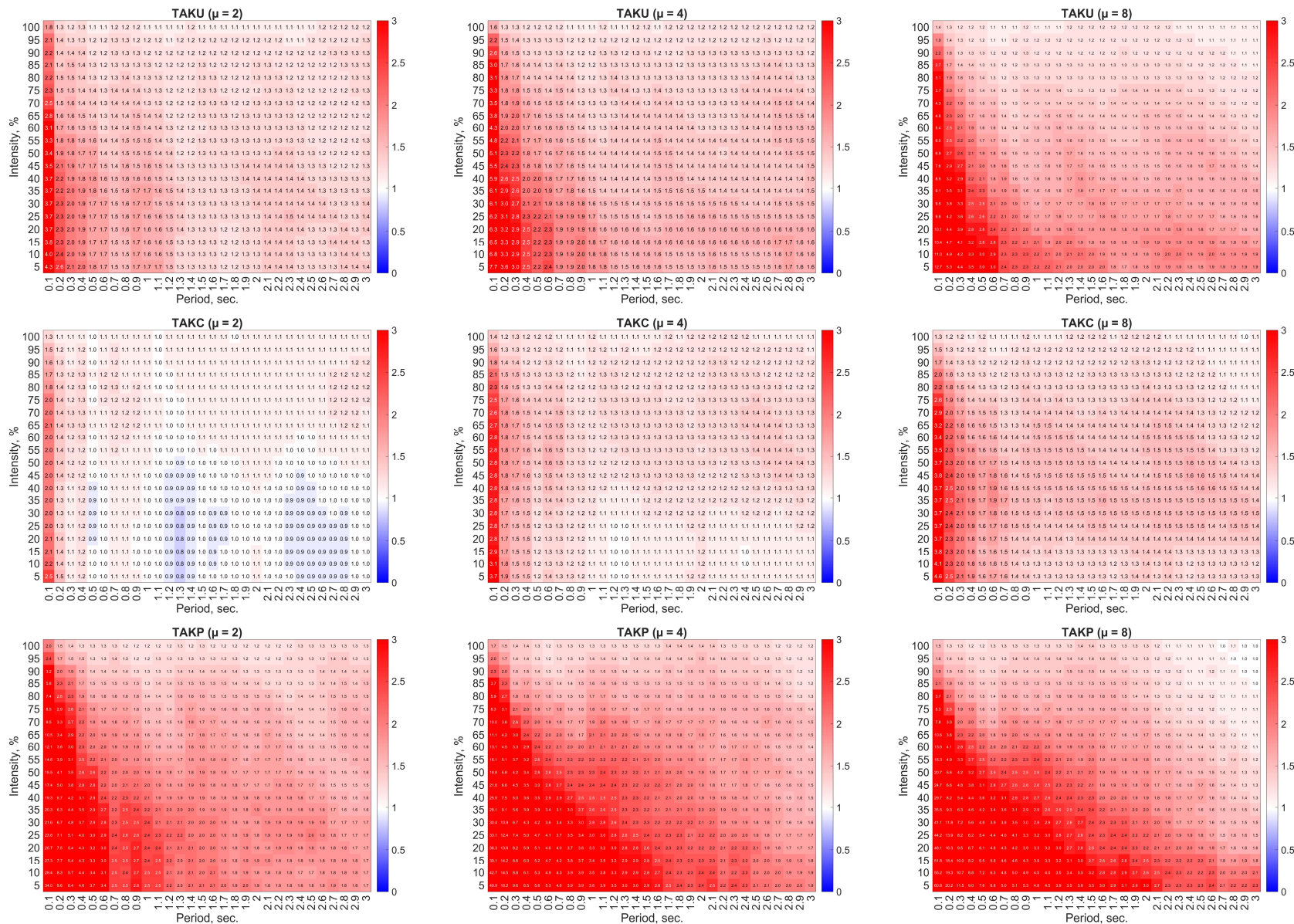


Figure B-39 Mean of ratio of drift from sequence B to drift from sequence A for different intensity levels, periods and hysteretic models for oscillators whose strengths were defined using the constant ductility method and were subjected to ground motions from Berkeley Site D. Colors and numbers in each cell correspond to the value of the mean ratio of drifts.

Constant Ductility Method (Berkeley Site D)

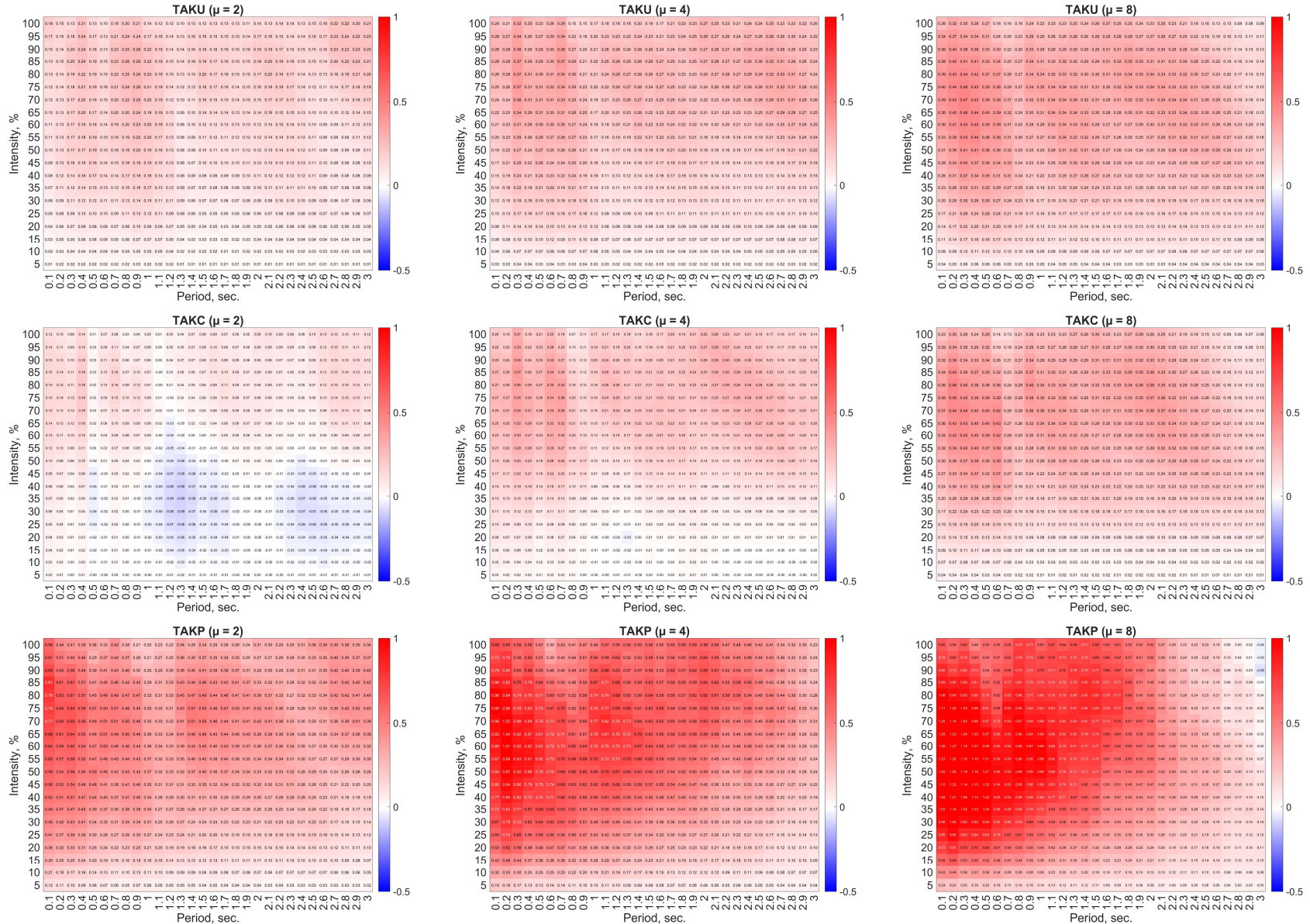


Figure B-40 Mean of difference in drifts between sequence B and sequence A for different intensity levels, periods and hysteresis models for oscillators whose strengths were defined using the constant ductility method and were subjected to ground motions from Berkeley Site D. Colors and numbers in each cell correspond to the value of the mean difference of drifts.

Constant Ductility Method (Seattle Site B)

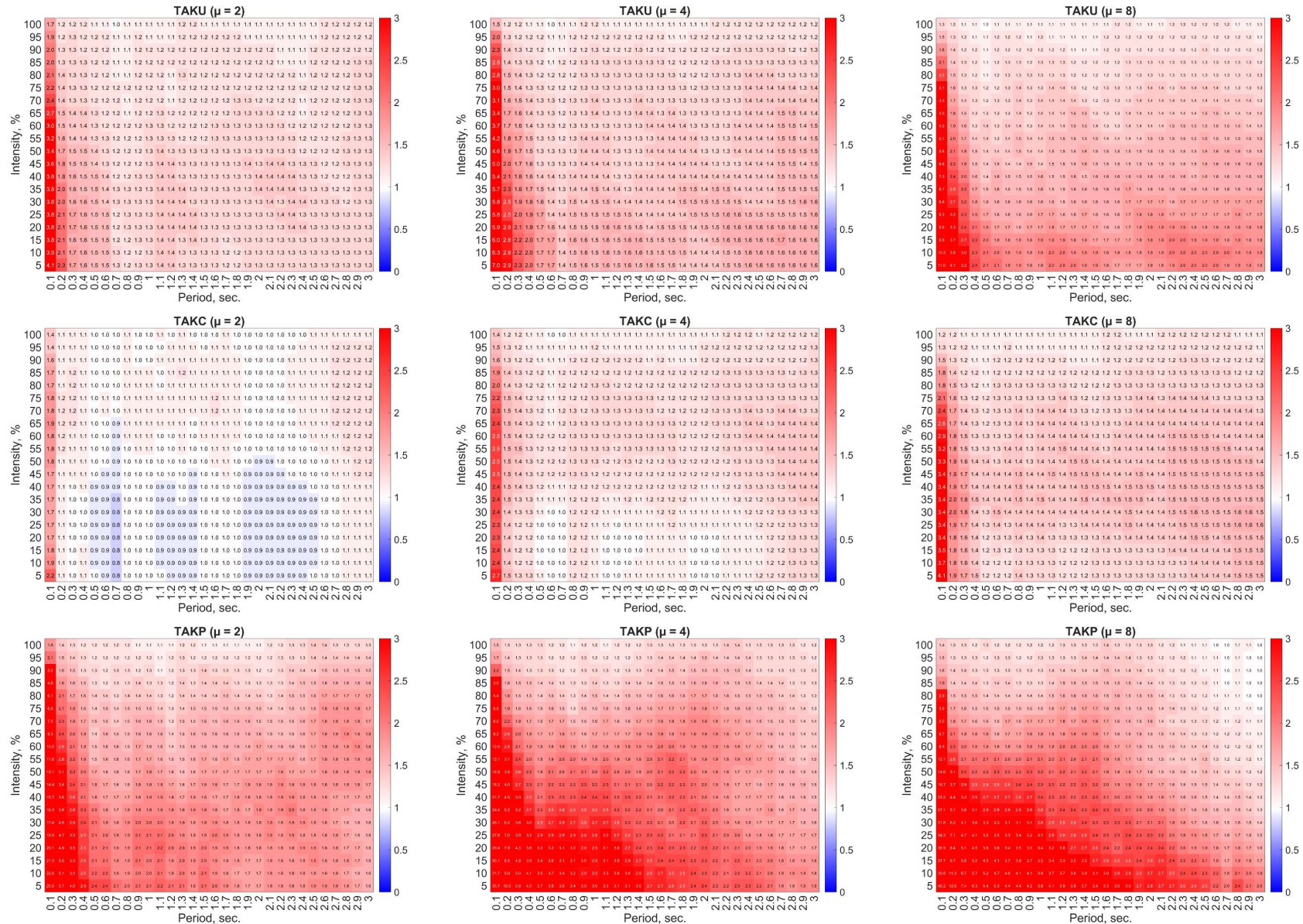


Figure B-41 Mean of ratio of drift from sequence B to drift from sequence A for different intensity levels, periods and hysteresis models for oscillators whose strengths were defined using the constant ductility method and were subjected to ground motions from Seattle Site B. Colors and numbers in each cell correspond to the value of the mean ratio of drifts.

Constant Ductility Method (Seattle Site B)

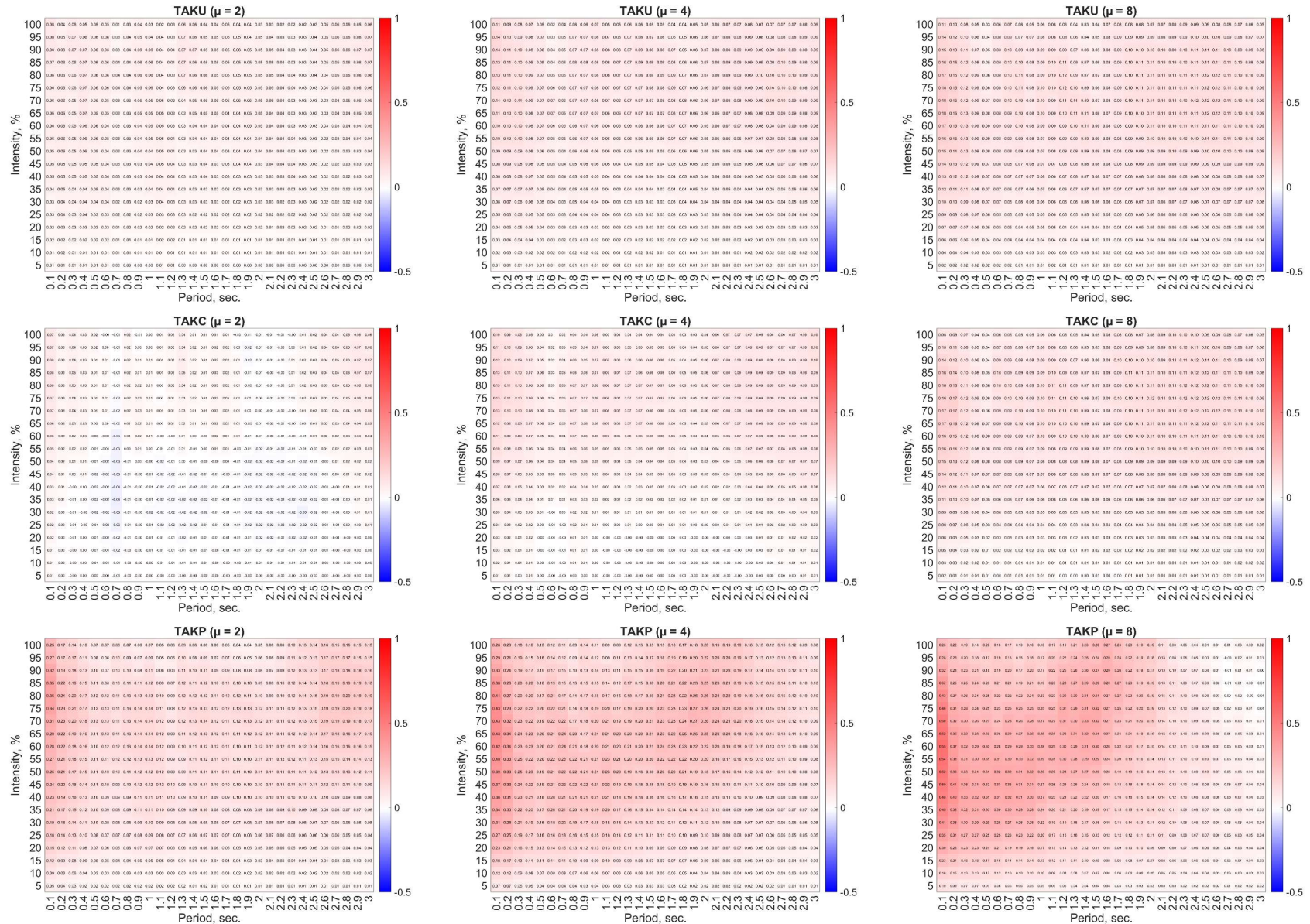


Figure B-42 Mean of difference in drifts between sequence B and sequence A for different intensity levels, periods and hysteresis models for oscillators whose strengths were defined using the constant ductility method and were subjected to ground motions from Seattle Site B. Colors and numbers in each cell correspond to the value of the mean difference of drifts.

Constant Ductility Method (Seattle Site D)

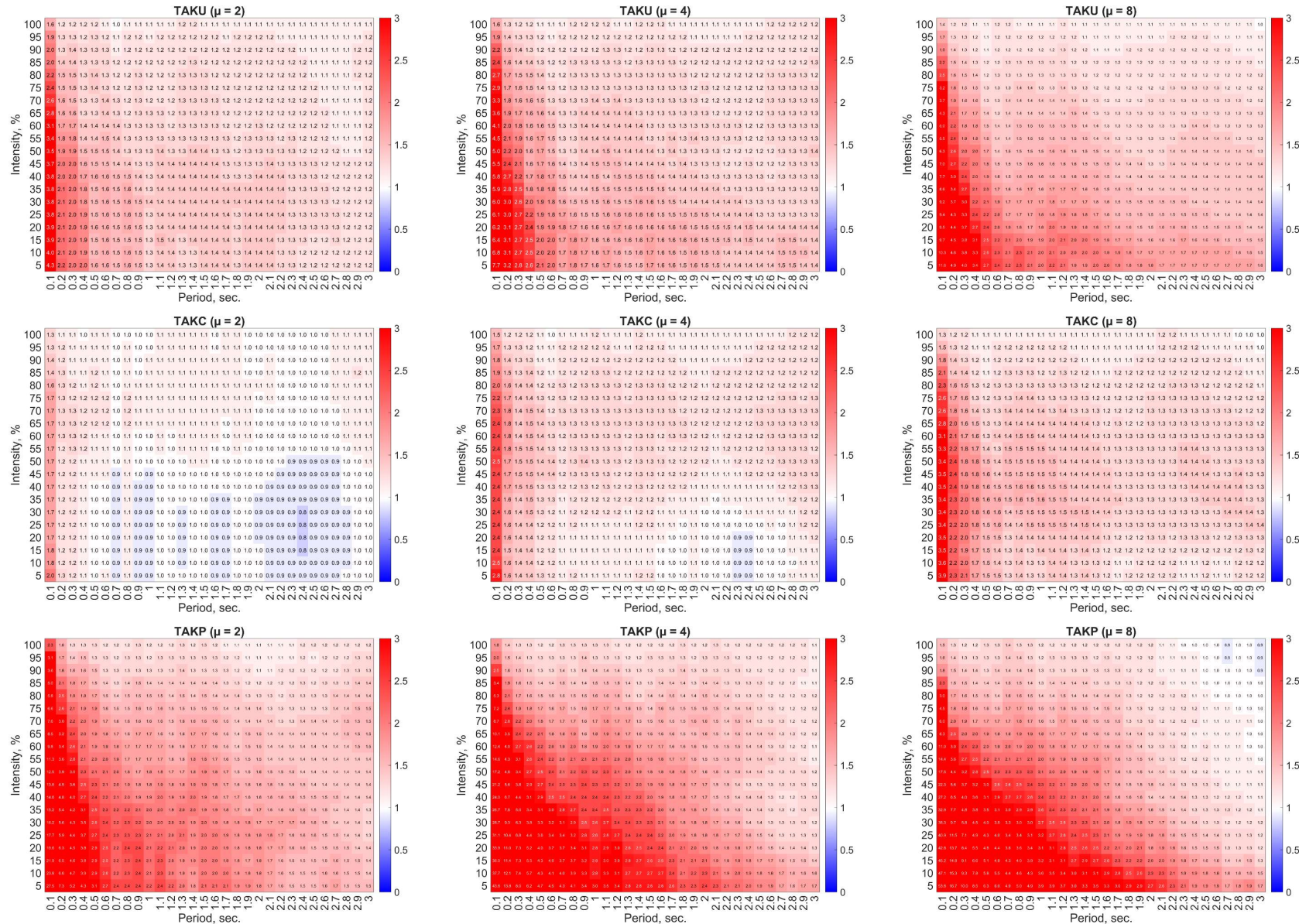


Figure B-43 Mean of ratio of drift from sequence B to drift from sequence A for different intensity levels, periods and hysteresis models for oscillators whose strengths were defined using the constant ductility method and were subjected to ground motions from Seattle Site D. Colors and numbers in each cell correspond to the value of the mean ratio of drifts.

Constant Ductility Method (Seattle Site D)

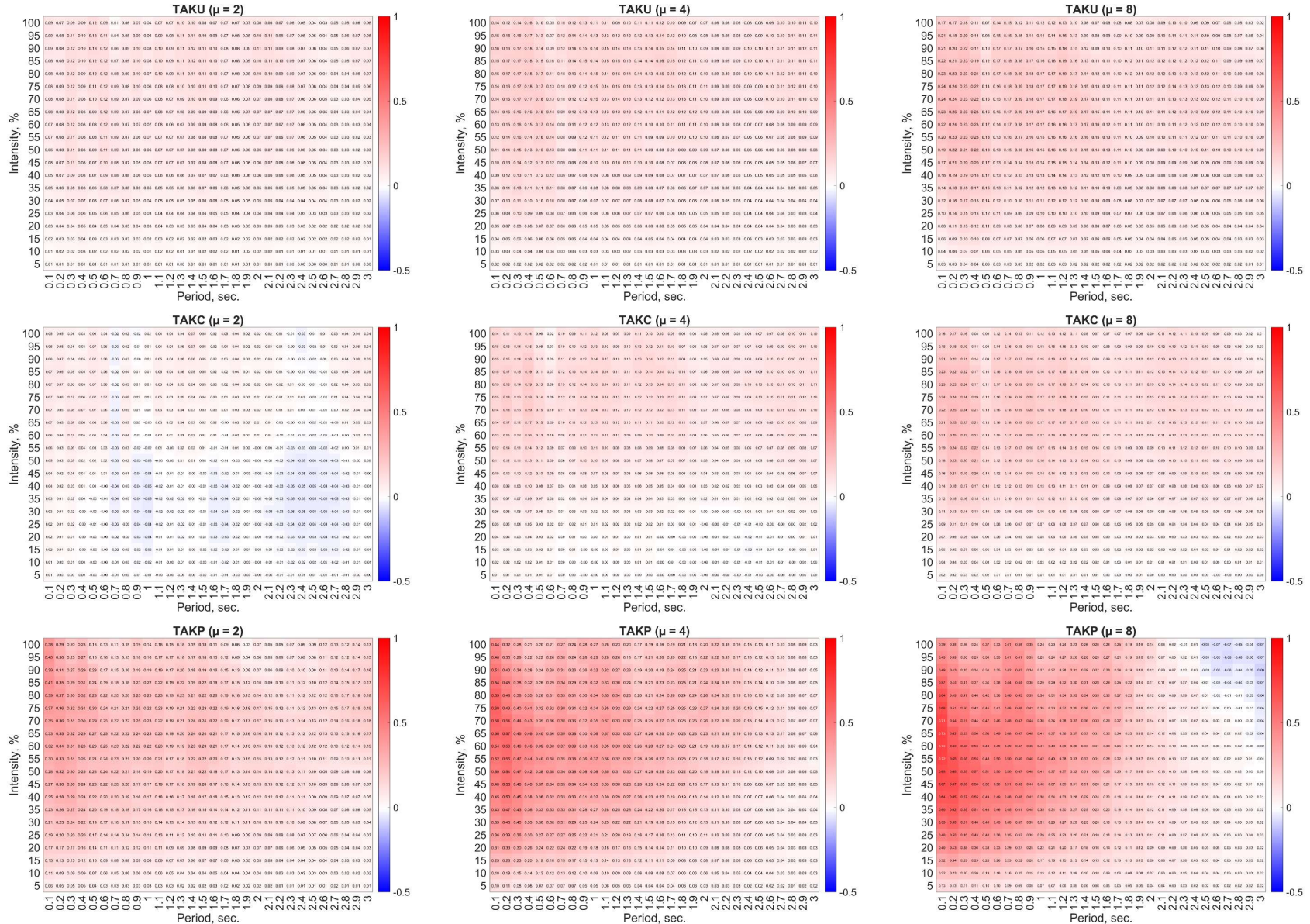


Figure B-44 Mean of difference in drifts between sequence B and sequence A for different intensity levels, periods and hysteresis models for oscillators whose strengths were defined using the constant ductility method and were subjected to ground motions from Seattle Site D. Colors and numbers in each cell correspond to the value of the mean difference of drifts.

Constant R Factor Method (Berkeley Site B)

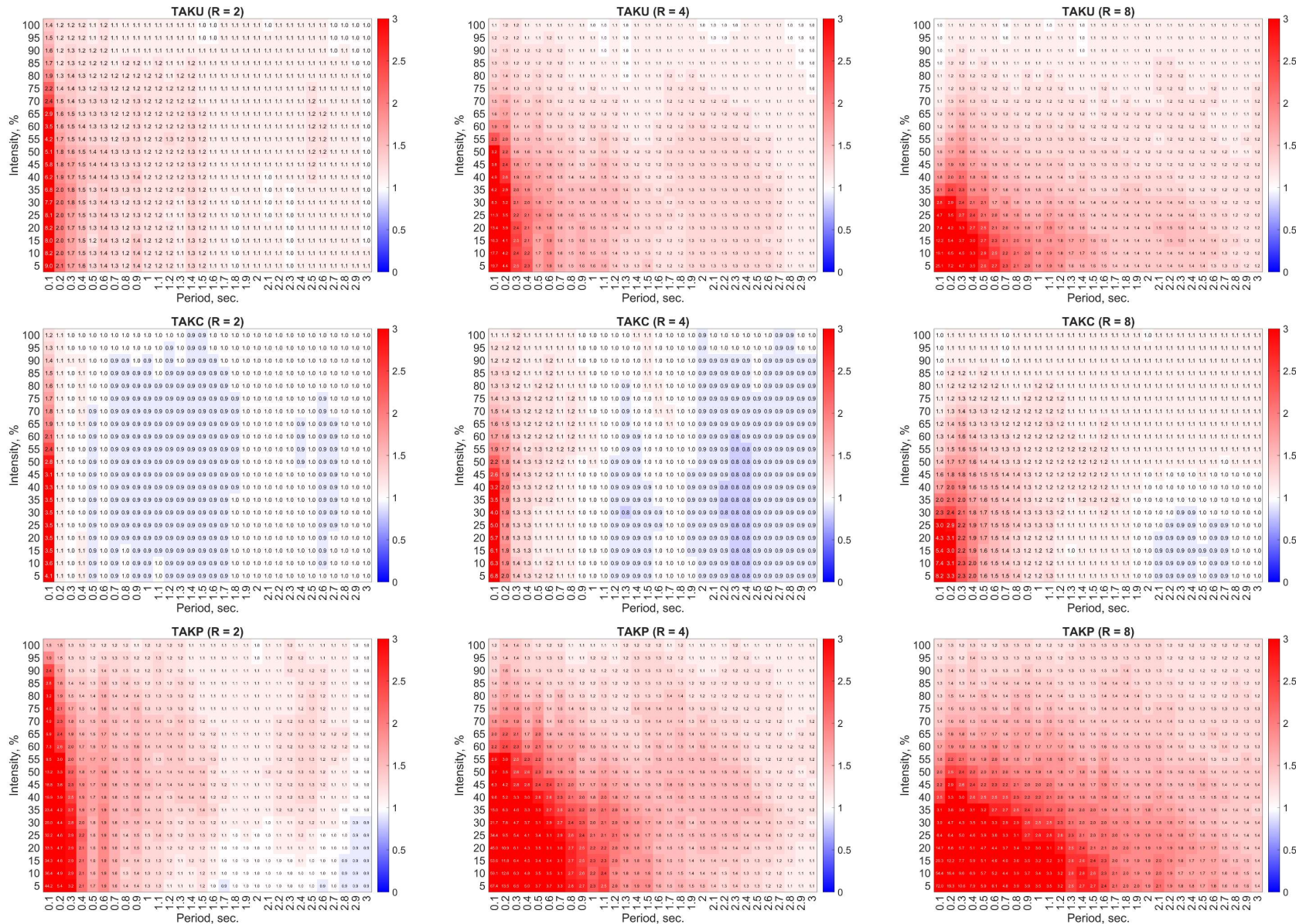


Figure B-45 Mean of ratio of drift from sequence B to drift from sequence A for different intensity levels, periods and hysteresis models for oscillators whose strengths were defined using the constant R factor method and were subjected to ground motions from Berkeley Site B. Colors and numbers in each cell correspond to the value of the mean ratio of drifts.

Constant R Factor Method (Berkeley Site B)

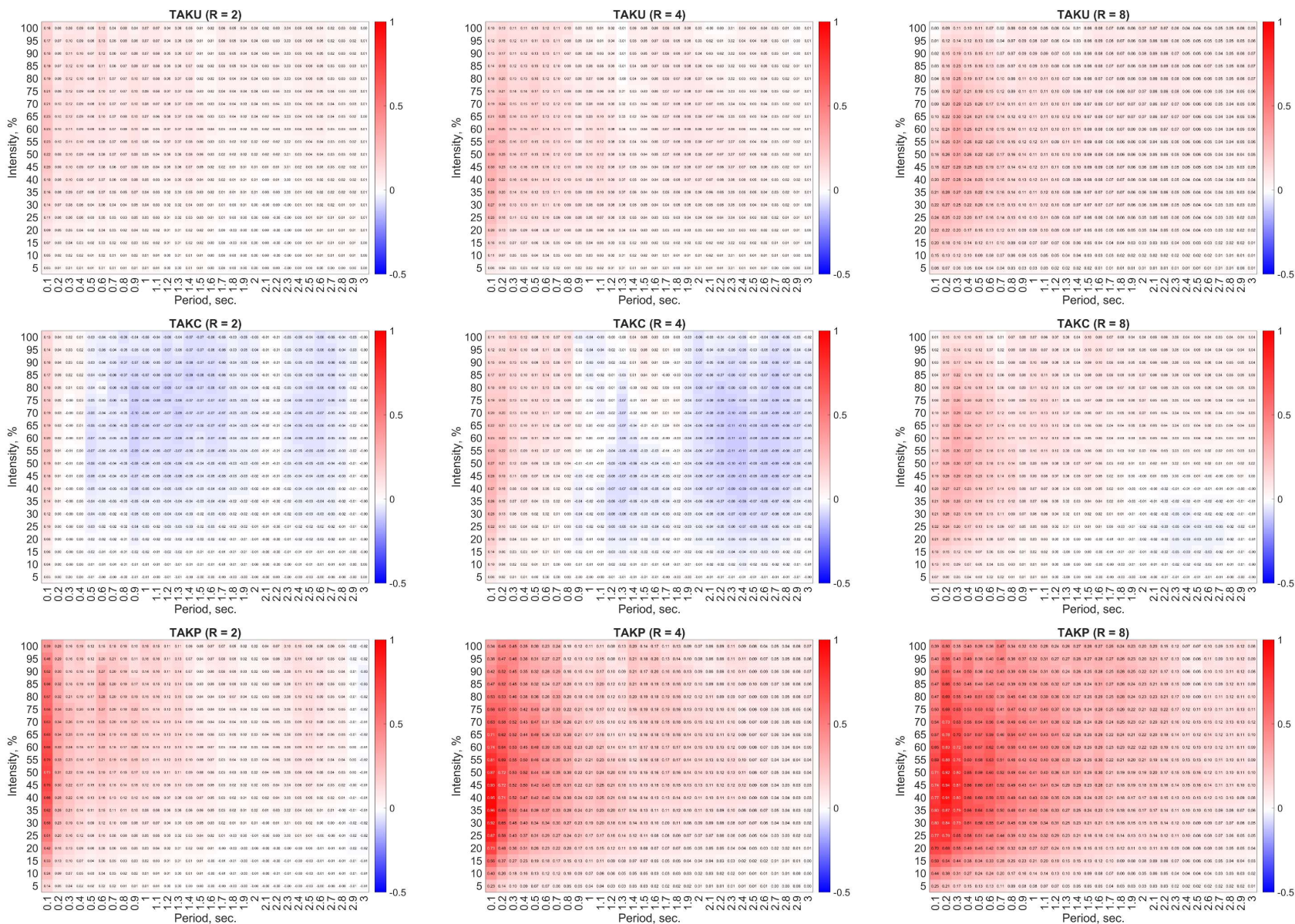


Figure B-46 Mean of difference in drifts between sequence B and sequence A for different intensity levels, periods and hysteresis models for oscillators whose strengths were defined using the constant R factor method and were subjected to ground motions from Berkeley Site B. Colors and numbers in each cell correspond to the value of the mean difference of drifts.

Constant R Factor Method (Berkeley Site D)

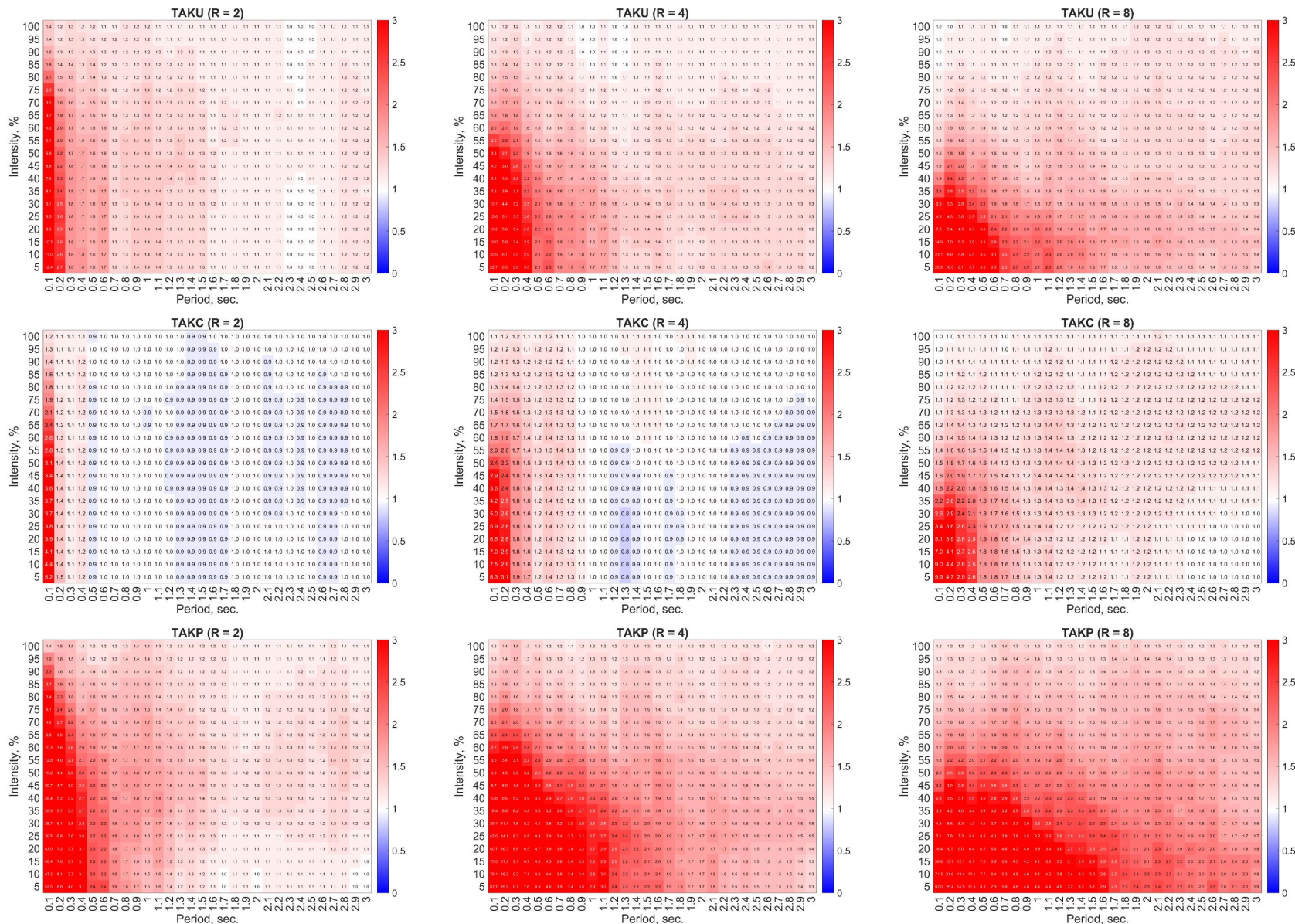


Figure B-47 Mean of ratio of drift from sequence B to drift from sequence A for different intensity levels, periods and hysteresis models for oscillators whose strengths were defined using the constant R factor method and were subjected to ground motions from Berkeley Site D. Colors and numbers in each cell correspond to the value of the mean ratio of drifts.

Constant R Factor Method (Berkeley Site D)

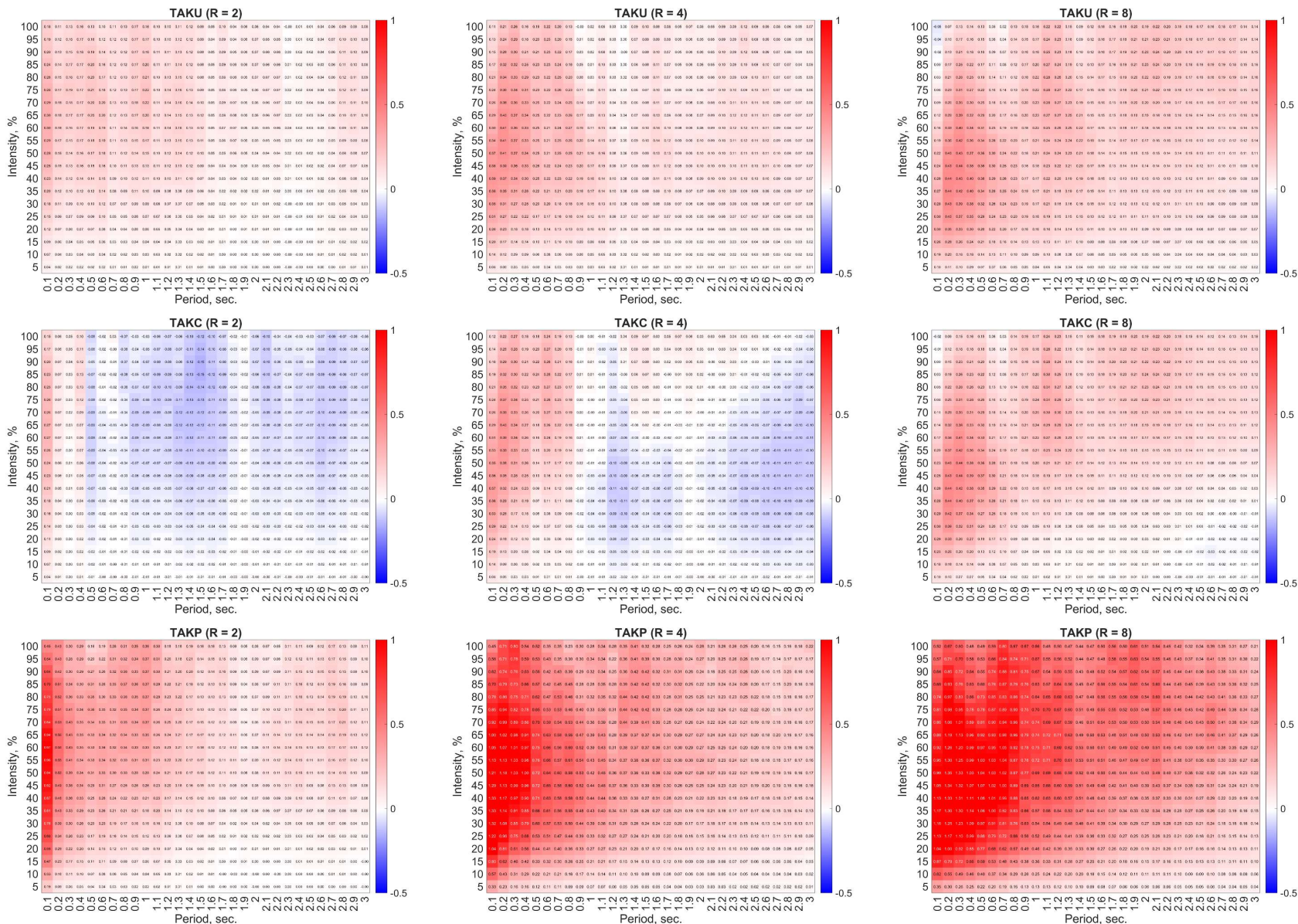


Figure B-48 Mean of drifts between sequence B and sequence A for different intensity levels, periods and hysteresis models for oscillators whose strengths were defined using the constant R factor method and were subjected to ground motions from Berkeley Site D. Colors and numbers in each cell correspond to the value of the mean difference of drifts.

Constant R Factor Method (Seattle Site B)

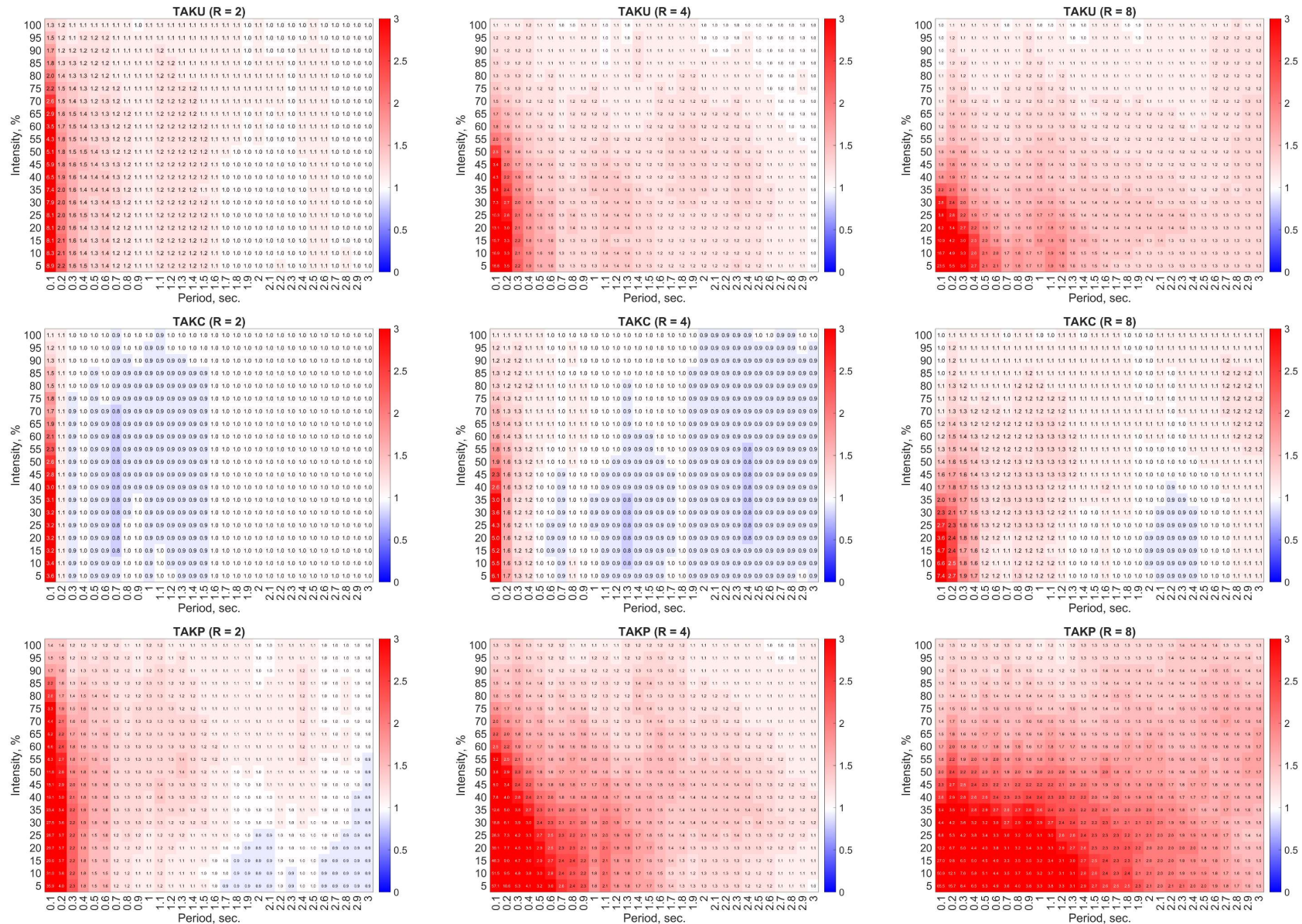


Figure B-49 Mean of ratio of drift from sequence B to drift from sequence A for different intensity levels, periods and hysteresis models for oscillators whose strengths were defined using the constant R factor method and were subjected to ground motions from Seattle Site B. Colors and numbers in each cell correspond to the value of the mean ratio of drifts.

Constant R Factor Method (Seattle Site B)

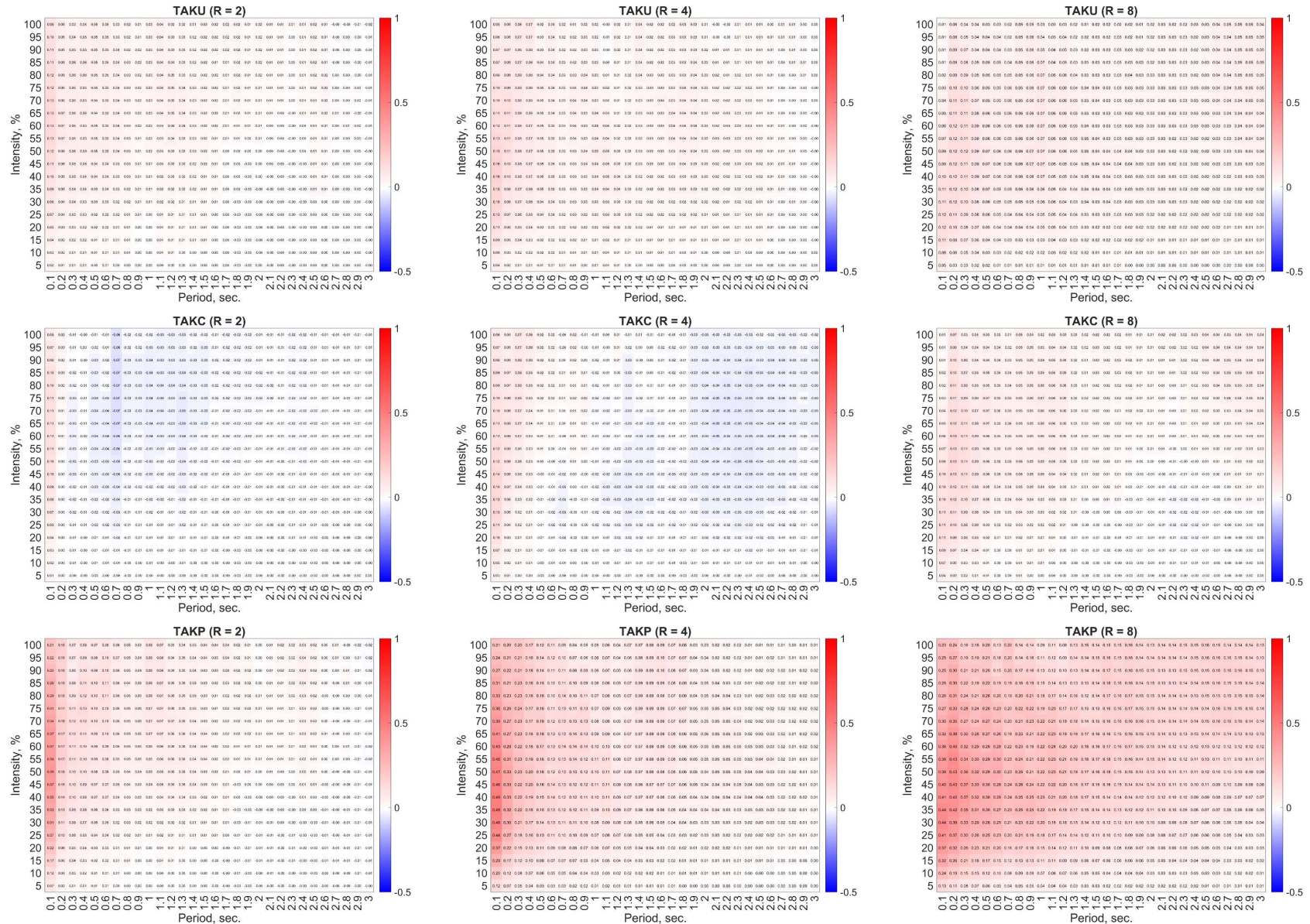


Figure B-50 Mean of difference in drifts between sequence B and sequence A for different intensity levels, periods and hysteresis models for oscillators whose strengths were defined using the constant R factor method and were subjected to ground motions from Seattle Site B. Colors and numbers in each cell correspond to the value of the mean difference of drifts.

Constant R Factor Method (Seattle Site D)

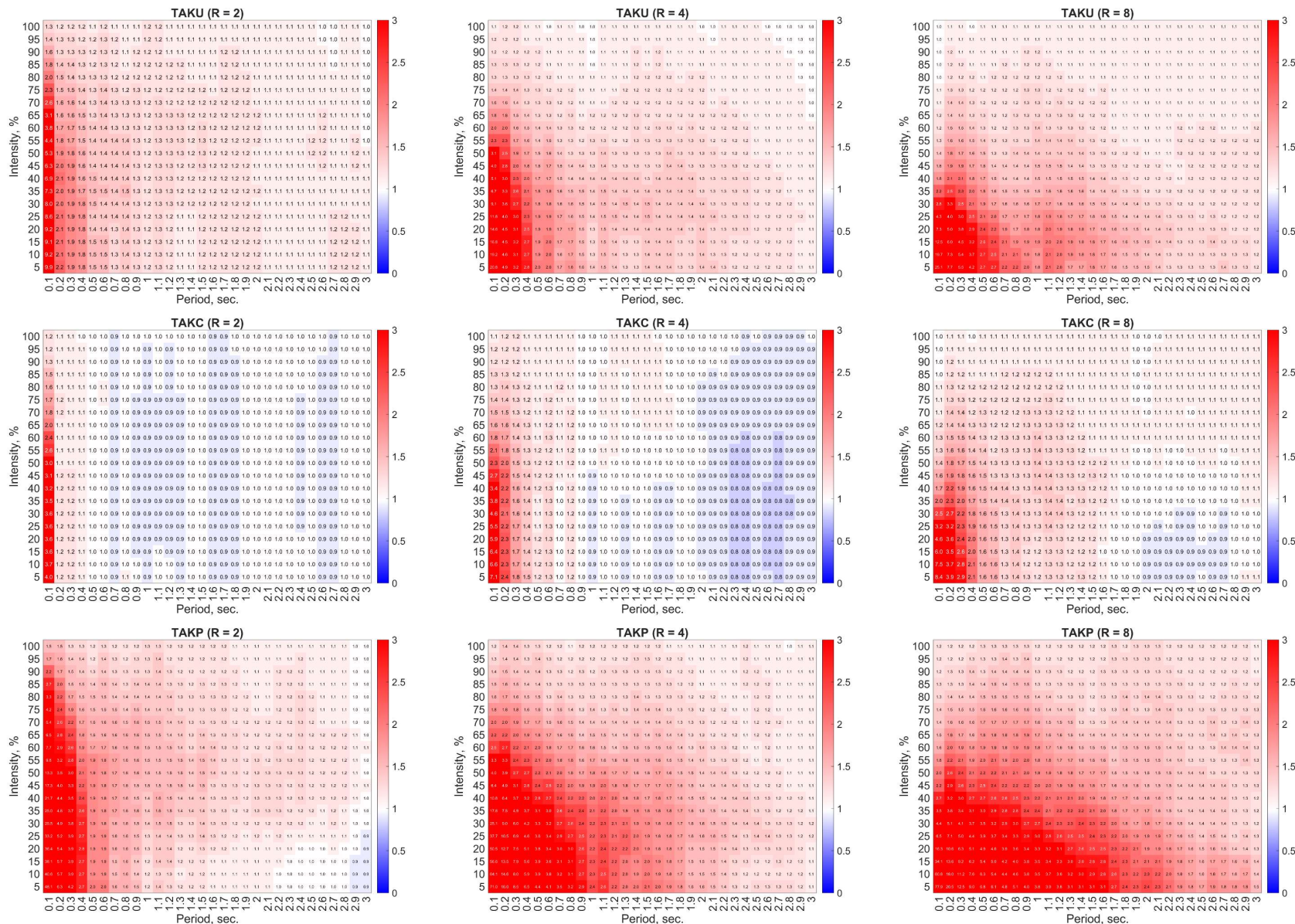


Figure B-51 Mean of ratio of drift from sequence B to drift from sequence A for different intensity levels, periods and hysteresis models for oscillators whose strengths were defined using the constant R factor method and were subjected to ground motions from Seattle Site D. Colors and numbers in each cell correspond to the value of the mean ratio of drifts.

Constant R Factor Method (Seattle Site D)

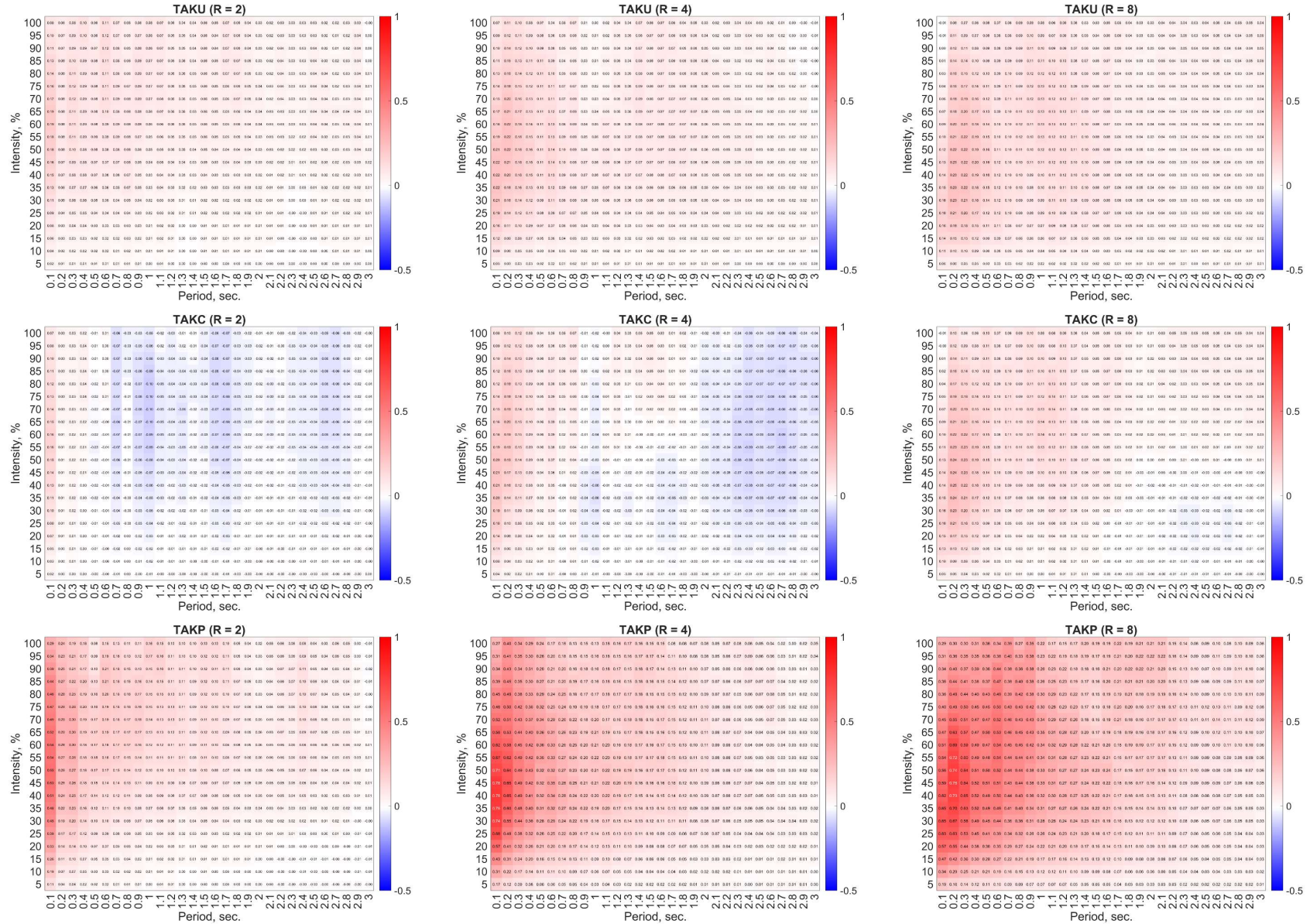


Figure B-52 Mean of difference in drifts between sequence B and sequence A for different intensity levels, periods and hysteresis models for oscillators whose strengths were defined using the constant R factor method and were subjected to ground motions from Seattle Site D. Colors and numbers in each cell correspond to the value of the mean difference of drifts.

References

- Ancheta, T.D., Darragh, R.B., Stewart, J.P., Seyhan, E., Silva, W.J., Chiou, B.S., and Boore, D.M., 2013, *PEER NGA-West2 Database*, Pacific Earthquake Engineering Research Center, Berkeley, California.
- ASCE, 2016, Minimum Design Loads and Associated Criteria for Buildings and Other Structures, ASCE/SEI 7-16, American Society of Civil Engineers, Structural Engineering Institute, Reston, Virginia.
- Baker, J.W., and Lee, C., 2017, “An Improved Algorithm for Selecting Ground Motions to Match a Conditional Spectrum,” *Journal of Earthquake Engineering*.
- Chopra, A. K., 2017, *Dynamic of Structures: Theory and Applications to Earthquake Engineering*, Pearson, New York, New York.
- FEMA, 1999, Repair of Earthquake Damaged Concrete and Masonry Wall Buildings, FEMA 307, prepared by the Applied Technology Council for the Federal Emergency Management Agency, Washington D.C.
- McKenna, F., Fenves, G., and Scott, M., 2000, *Open System for Earthquake Engineering Simulation*, Pacific Earthquake Engineering Research Center, Berkeley, California.
- Takeda, T., Sozen, M.A., and Nielsen, N.N., 1971, *Reinforced Concrete Response to Simulated Earthquakes*, OHBAYASHI-GUMI, Tokyo, Japan.

B.4 Summary of Torsion Studies

B.4.1 Introduction

The SDOF studies (Appendix B.3) concluded that systems damaged by MCE/DBE level earthquakes will not result in significant increase in drift demand during subsequent MCE/DBE level input; however, amplification can occur for subsequent smaller inputs. SDOF oscillators cannot represent the localization of deformation demands that can occur in some multi-story buildings, including those with torsional irregularities. Furthermore, building structures can also experience accidental eccentricities resulting from variations in strength and stiffness or because of multi-directional earthquake input (De la Llera and Chopra, 1995). Some post-earthquake investigations have also suggested that damage during significant earthquakes may have resulted from torsional response in a building with nearly symmetric plan (Kam et al, 2011). Regardless of the irregularities or eccentricities building structures may have, the buildings are more susceptible to localized damage when experiencing torsional response. Hence, it may be possible that localized damage during prior earthquake events due to torsional response may affect the response of the building in future earthquake events.

Consequently, the studies described in this appendix investigate the effects of torsional irregularities on amplification in drift demand in subsequent earthquake events due to damage during prior earthquake events. Numerical analyses were conducted for simple two degree-of-freedom (2DOF) oscillators with variations in stiffness and strength irregularities, for a range of different earthquake sequences.

B.4.2 Parametric Analysis for 2DOF Systems

B.4.2.1 Target Spectrum

Figure B-53 shows target spectra for Berkeley Site Class D and design base shear coefficient for $R = 2$. The target spectra for MCE and DE criteria corresponds to those used in SDOF study described in B.3.

The use of R-factor method to define base shear coefficient is preferred for its simplicity compared to constant ductility method (used in SDOF study) as the SDOF study revealed that the two methods did not result in different conclusions regarding drift amplification. A higher R-factor was also used (i.e., $R=6$) in this study, which showed generally same results in terms of displacement demand amplification. Hence this section presents only the results for $R = 2$. Target period range selected for these studies is from 0.1 to 3.0 sec., and 2DOF oscillators were created for nine target periods (i.e., 0.1,

0.3, 0.5, 0.8, 1.0, 1.5, 2.0, 2.5 and 3.0 sec.), as indicated by dash lines in Figure B-53.

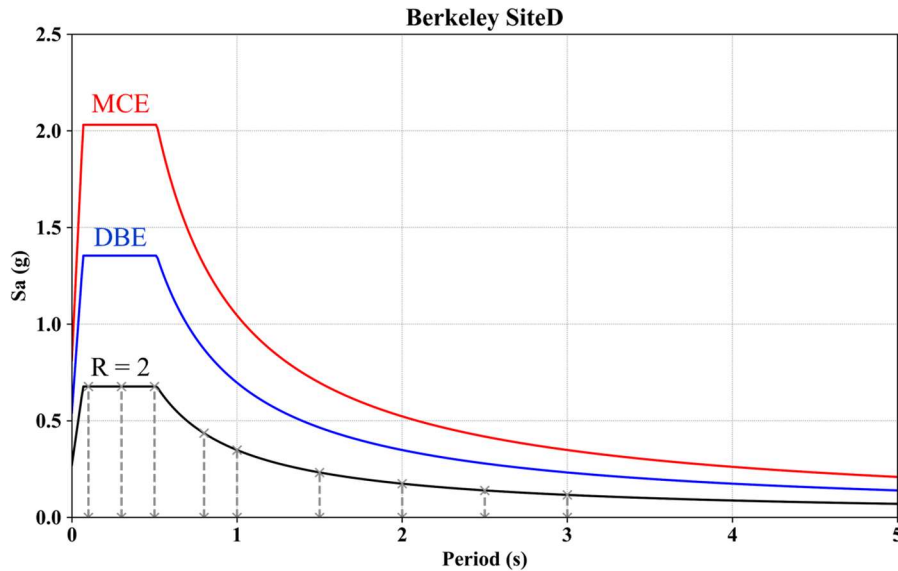


Figure B-53 Target spectra for Berkeley Site D (red and blue lines) and base shear coefficient for 2DOF oscillators (black line) based on R-factor method

B.4.2.2 Analysis Model and Irregular Systems

B.4.2.2.1 Modelling of 2DOF Oscillators

Figure B-54 illustrates 2DOF oscillator created using OpenSeesPy (Zhu et al., 2018). The system comprises two zero-length elements: Element-1 and Element-2 representing a more critical side (i.e., soft or weak side) and a non-critical side, respectively. One node of each element was fixed, while the other node was connected to a rigid beam. Top nodes were restrained such that only movement in in Y-direction was permitted.

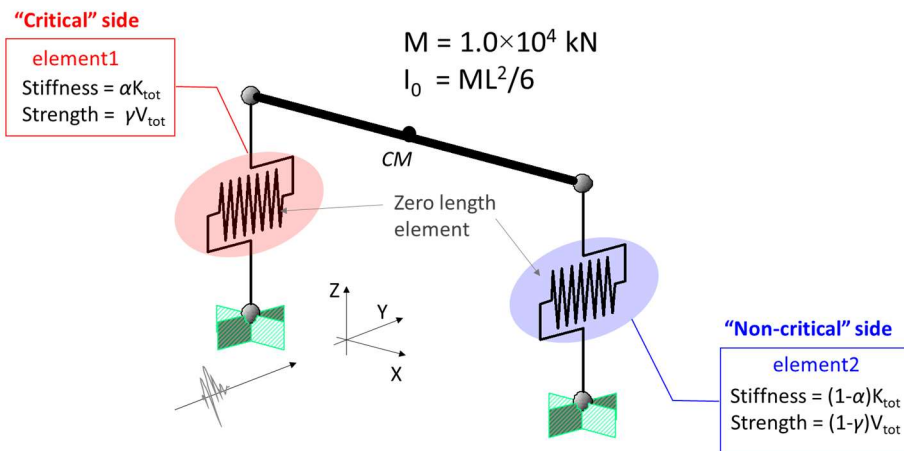


Figure B-54 Illustration of a 2DOF Oscillator.

The strength of the system, V_{tot} , was based on the base shear coefficient for each target period, T_{target} (Figure B-53) and assigned seismic mass ($=1.0 \times 10^4$ kN for this study). The system translation stiffness, K_{tot} , was computed based on each target period, i.e., K_{tot} should satisfy $T_{target} = 2\pi(M/K_{tot})^{0.5}$ and corresponds to the translational stiffness of a symmetric system. The mass moment of inertia, I_0 , of the system was defined assuming uniform mass distribution over a 10 meter by 10 meter square diaphragm, resulting in $I_0 = 1.7 \times 10^5$ kN.m².

Takeda model with post yield stiffness with 5% of the initial stiffness (i.e., TAK05 in FEMA 307) was used as the hysteresis model of the zero-length elements (Figure B-55). The unloading stiffness coefficient, $\beta = 0.4$ was used for this study based on Takeda et al. (1970) while FEMA 307 (ATC, 1998) shows $\beta = 0.5$. The analysis results presented in this section used the bilinear backbones for the hysteresis model.

To create irregularities in the 2DOF system, initial stiffness of Element-1 was controlled by coefficient α ($K_1 = \alpha K_{tot}$ for $0 < \alpha \leq 0.5$), while stiffness for Element-2 is $K_2 = (1 - \alpha)K_{tot}$. In addition, the strengths of the zero-length elements were controlled by a factor γ ($0 < \gamma \leq 0.5$) relative to the system strength capacity V_{tot} . Namely, the strength capacities of Element-1 and -2 were γV_{tot} and $(1 - \gamma)V_{tot}$, respectively.

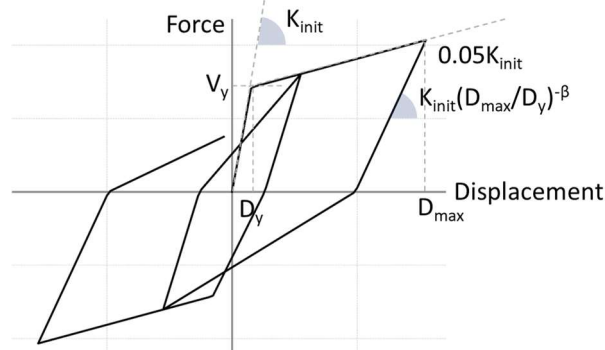


Figure B-55 Hysteresis model with a bilinear backbone (TAK05 in FEMA 307, with coefficient of unloading stiffness, β , = 0.4 based on Takeda et al., 1970)

B.4.2.2.2 Irregular Systems

Stiffness and strength irregularities are considered in this study using $\alpha = 0.5$ or 0.45 and $\gamma = 0.5$ or 0.4 to define the element stiffness and yield strength, respectively. All irregular systems considered are listed in Table B-11: Stiff I-E and Stiff I-I or Strength I-I05 and Strength I-I10 for initial stiffness or strength irregularities, respectively, and Stiff & Strength as a combined

stiffness and strength irregularity. Figure B-56 schematically illustrates the backbone of each element for the 2DOF system.

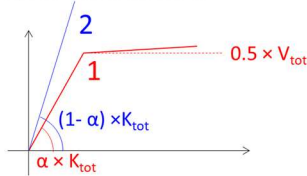
Table B-11 Irregular Systems

Type of Irregularity	Irregular Systems	α	γ	Element-1 (Critical)	Element-2 (non-critical)
Initial Stiffness Irregularity	Stiff I-E	0.5 0.45	0.5	Inelastic ($\eta = 0.05$)	Elastic
	Stiff I-I	0.45	0.5	Inelastic ($\eta = 0.05$)	Inelastic ($\eta = 0.05$)
Strength Irregularity	Strength I-I05	0.5	0.4	Inelastic ($\eta = 0.05$)	Inelastic ($\eta = 0.05$)
	Strength I-I10	0.5	0.5 0.4	Inelastic ($\eta = 0.05$)	Inelastic ($\eta = 0.1$)
Combined Stiffness and Strength Irregularity	Stiff & Strength	0.45	0.4	Inelastic ($\eta = 0.05$)	Inelastic ($\eta = 0.05$)

Note: η = hardening ratio for inelastic element

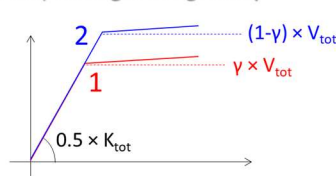
Stiffness irregularity

I-E) Elastic & Inelastic

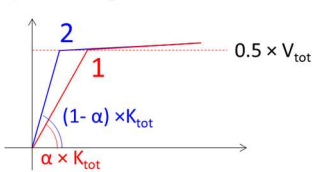


Strength irregularity

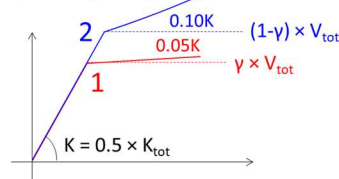
I-I05) Strength irregularity



I-I) Both edge inelastic



I-I10) Strength + post yield stiffness



Combined Stiffness & Strength irregularity

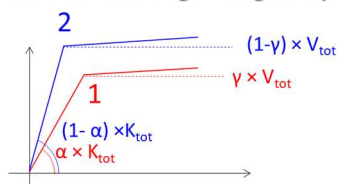


Figure B-56 Illustration of Irregular Systems. K_{tot} is the stiffness in translation of the 2DOF system based on each target period; V_{tot} is the strength capacity of the 2DOF system based on a base shear coefficient for each target period.

Stiff I-E. This system consists of an inelastic element (i.e., Element-1) and an elastic element (i.e., Element-2). Element-1 has an initial stiffness of αK_{tot} and yield strength of $0.5V_{tot}$. In contrast, Element-2 has an initial stiffness of $(1-\alpha)K_{tot}$ with no yielding modeled. Since Element-2 is elastic, this system will have larger base shear coefficient than designed.

Stiff I-I. This system consists of two inelastic elements at both edges with a variation of initial stiffness defined by the coefficient α . Element-1 and Element-2 have initial stiffness of αK_{tot} and $(1-\alpha)K_{tot}$, respectively, and each element has a yield strength of $0.5V_{tot}$. The system is symmetric when $\alpha = 0.5$ and referred to as the “symmetric case” in the analysis results presented in the subsequent sections.

Strength I-I05. This system consists of two inelastic elements at both edges with a variation of strength capacities defined by the coefficient γ . Element-1 and Element-2 have yield strengths of γV_{tot} and $(1-\gamma)V_{tot}$, respectively, and each element has stiffness of $0.5K_{tot}$. The system is symmetric when $\gamma = 0.5$.

Strength I-I10. This system is an extension of Strength I-I05. While Strength I-I05 has no stiffness irregularity in nonlinear range once both elements yield, Strength I-I10 introduces variation in the post-yield stiffness, in addition to different yield strengths for the two elements. Element-1 has post yield stiffness of $0.05 K_{init}$ which corresponds to that in other irregular systems. The post-yield stiffness of Element-2 is $0.10 K_{init}$.

Stiff & Strength. This system is a combination of Stiff I-I and Strength I-I05. Namely, Element-1 in this system has an initial stiffness of αK_{tot} and strength capacity of γV_{tot} , while Element-2 has an initial stiffness of $(1-\alpha)K_{tot}$ and yield strength of $(1-\gamma)V_{tot}$.

B.4.2.3 Input Earthquakes

Thirty earthquake records scaled to fit the MCE target spectrum for Berkeley Site D were used in this study. The ground motions and response spectra are available in Table 5 and Figure B-61 of Appendix B.3. Although the results in this study focused on the median demand obtained from different earthquake inputs, the ranges in the ground motion characteristics may be of interest in future studies considering ground motion characteristics which may drive larger amplification in response in damaged structures.

Input Sequences. The 2DOF oscillators were subjected to a single input motion or a sequence of two inputs. For sequences, the same ground motion was used for both inputs, only the intensity of the motion was modified. Table B-12 shows the definition of each input motion sequence with the

intensities relative to the MCE spectrum. Each sequence ID stands for the intensity of the first input (e.g., MCE or DBE) and a subsequent input (i.e., 10 through 100%); for example, MCE67 is a sequence with 100% input followed by 67% input. DBE stands for design-basis earthquake which is two third of the MCE level (i.e., 67%). Ind50 is an individual earthquake input with 50% of MCE intensity.

Table B-12 Earthquake input sequence

Name*	Input 1	Input 2
<i>MCE100</i>	100%	100%
<i>MCE67</i>	100%	67%
<i>MCE50</i>	100%	50%
<i>MCE40</i>	100%	40%
<i>MCE30</i>	100%	30%
<i>MCE20</i>	100%	20%
<i>MCE10</i>	100%	10%
<i>DBE67</i>	67%	67%
<i>Ind50</i>	50%	N/A
<i>Ind40</i>	40%	N/A
<i>Ind30</i>	30%	N/A
<i>Ind20</i>	20%	N/A
<i>Ind10</i>	10%	N/A

*Note: 100% relative to MCE. DBE is design level earthquake which is 2/3 of MCE. Ind stands for individual earthquake input for undamaged oscillators. Gray shaded cases for DBE were not discussed in this report.

The input sequences were selected to obtain displacement-demand amplification for repeated earthquake inputs, consistent with the post-earthquake performance objectives defined in Chapter 2. There is no consensus on the definition of intensity level for a “Serviceability Earthquake”, and therefore this study considered a range of intensities from 10% to 50% to investigate the effect of prior earthquake events on serviceability performance.

B.4.3 Analysis Results

B.4.3.1 Introduction

This subsection presents the results obtained from numerical analyses for 2DOF oscillators.

First, response of symmetric systems ($\alpha = 0.5$, $\gamma = 0.5$) is discussed to confirm the validity of the 2DOF oscillator relative to the SDOF oscillators

discussed in the previous section. The results include ductility/displacement demand, amplification for MCE100, as well as the amplification for smaller subsequent events.

Second, response of the five irregular systems from Table B-11 shall be presented for the same parameters considered for the symmetric systems.

Finally, the amplifications in displacement demand are compared between the symmetric and irregular systems to identify the effect of torsional response on the amplification in displacement demand.

B.4.3.2 Response of Symmetric Systems

Ductility Demand from Single Earthquake Inputs. Figure B-57 presents ductility demands (= peak displacement demand/ yield displacement) during the first MCE input (i.e., 100%). In a period-range of 0.5 to 3.0 sec., ductility demand under the thirty-earthquake input ranged from 2 to 8, with a median consistently around 4. Although short period range (i.e., $T_{target} < 0.5$) shows median ductility demand higher than longer period range, this is a well-known phenomenon related to normalizing by small yield displacements.

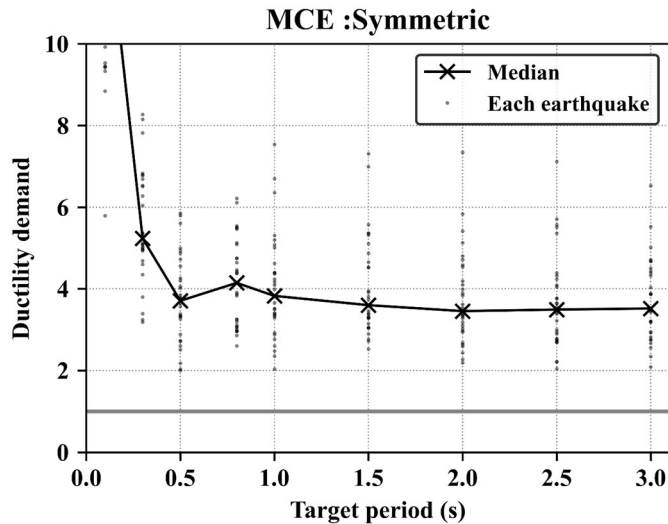


Figure B-57 Ductility demand in individual MCE input VS Target period for symmetric systems.

Displacement Demand Amplification. Figure B-58 compares ductility demands in individual 100% input with those in subsequent 100% input. In MCE100, the ductility demands were larger than 2. Figure B-59 shows the same plots for MCE30 representing the cases with big earthquake event followed by smaller earthquake event. The 30% individual runs resulted in median ductility demand of 1 while subsequent 30% input to MCE event showed the median ductility demand larger than 1.0.

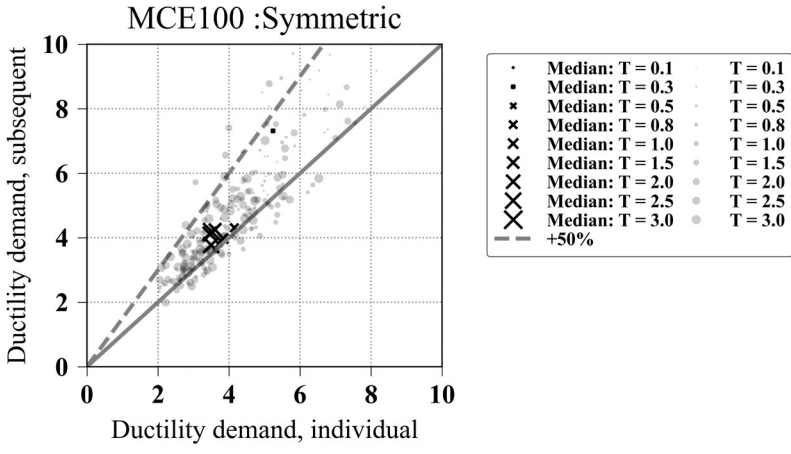


Figure B-58 Peak ductility from individual earthquake input VS Peak ductility demand from subsequent input for MCE100.

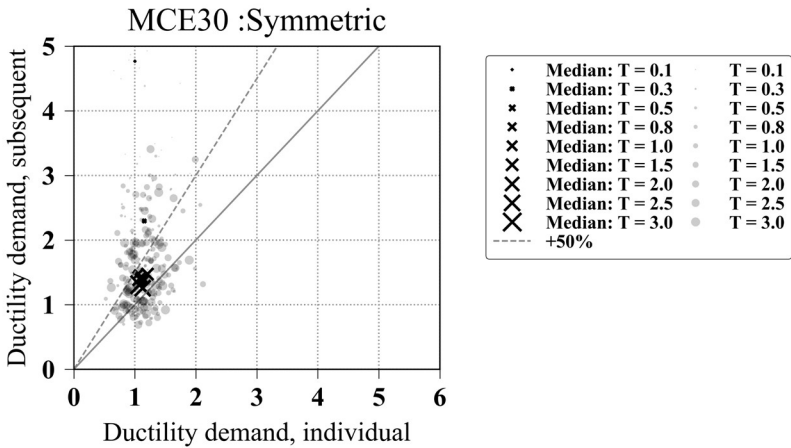


Figure B-59 Peak ductility from individual earthquake input VS Peak ductility demand from subsequent input for MCE30.

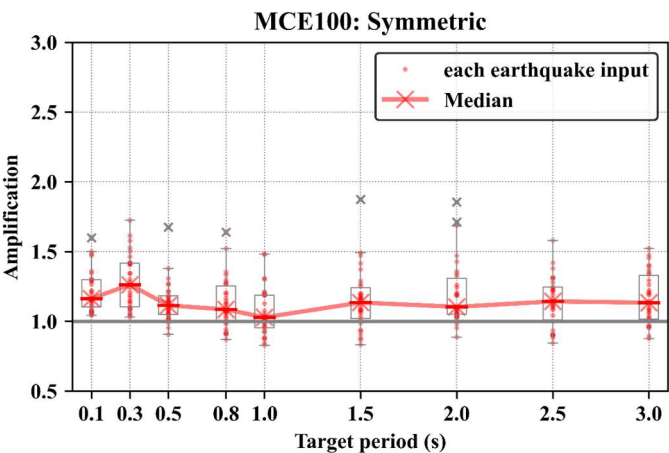


Figure B-60 Amplification VS Target period for symmetric systems, MCE100. The box-and-whisker plots with 25th-75th percentile. x shows outliers.

The ratio of the values in Y-axis to those in X-axis in Figure B-58 provide the amplification in displacement demand due to prior earthquake events for the case MCE100, which is shown in Figure B-60. In this figure, 30 red dots for each target period represent the amplification in each earthquake input, and the red line shows median amplification of the 30 cases. MCE100 did not result in significant amplification in displacement demand: the median amplifications for each target period were between 1.0 and 1.25, while the 25th to 75th-percentile edges of the box plots remains within 0.9 to 1.4. It is noted that amplifications for outlier ground motions can be as high as 1.9, but this range of variability is anticipated in earthquake engineering.

The median amplification was extracted for other sequence cases with initial MCE input. Figure B-61 presents the median amplification of symmetric systems for MCE100, MCE67 and MCE30. Displacement demands were amplified in the subsequent motion over the individual motion for small subsequent earthquake events, particularly in the short target period range (i.e., < 0.5 sec.).

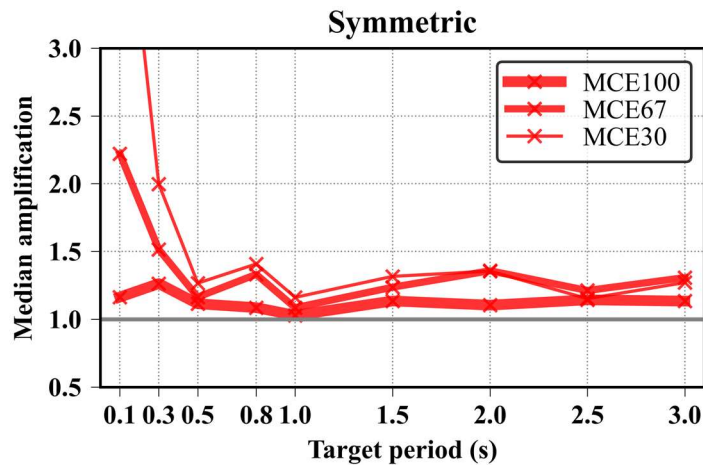


Figure B-61 Median amplification VS Target period for symmetric systems, MCE30, MCE67 and MCE100.

Figure B-62 shows the median amplification versus median ductility demand in individual run for the 2DOF system with the target period ≥ 0.5 seconds to look at the effect of ductility demand in individual run. Some data points with the ductility demand in individual input is less than 1 showed large amplification (>1.5), while that ranged from 1.0 to 1.5 when ductility demand in individual run was larger than 1.0.

These results for symmetric systems are consistent with the overall outcomes from constant ductility method applied for the SDOF studies (see Section B.3 of Appendix B) and the result from FEMA 307 studies. These results shall be

used in Section B.4.3.3 as a reference when assessing the performance of irregular systems in sequential ground motions relative to symmetric systems.

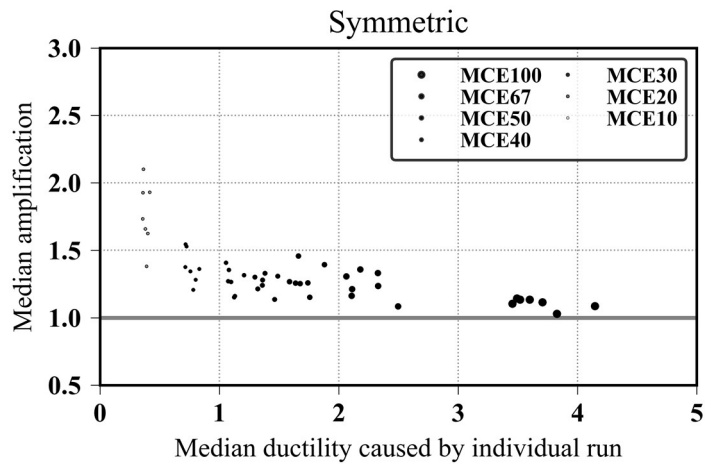


Figure B-62 Median amplification VS Median ductility caused by Individual Run. Excluding the data points for T = 0.1 s and 0.3 s.

B.4.3.2 Response of Irregular Systems

This section covers the analysis results for irregular systems listed in Table B-11. The results include the ductility demand due to individual and subsequent inputs, and amplification in displacement demand due to a prior MCE input. The plots presented in this section can be compared with those for the symmetric system discussed in B.4.3.1.

Ductility Demand under MCE input. Figure B-63 shows the ductility demand during the first MCE input from all the irregular systems. Red and blue lines/dots in Figure B-63 represent the ductility demand in the critical and non-critical elements, respectively. The black lines and dots are ductility demand at center of mass (CM) where the yield displacement was defined as a yield point of a bilinear backbone of the system performance ($= V_{tot}/K_{tot}$). Further, Stiff I-E does not have yield displacement for a non-critical element and at CM since the non-critical element is elastic, the same yield displacements as Stiff I-I were used to normalize the ductility demand.

According to the figure, all the irregular systems were subjected to median ductility demand of approximately 3 to 4 at CM in a period range of 0.5 to 3.0 seconds. High ductility demands are noted for target periods from 0.1 or 0.3 seconds which was also seen in the symmetric system. In addition, critical side overall presented higher ductility demand in irregular systems, because of torsional responses.

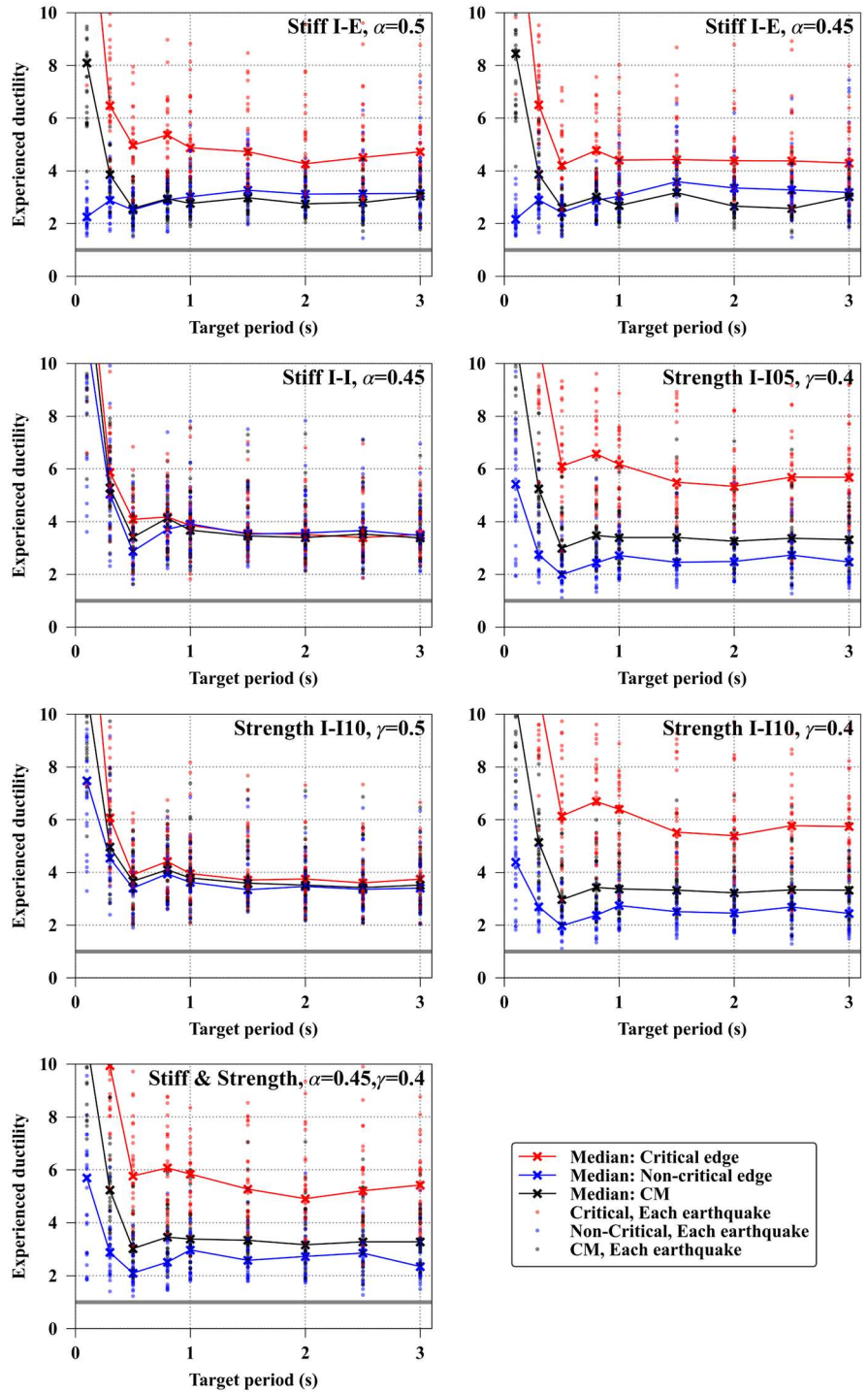


Figure B-63 Ductility demand under MCE inputs VS Target period for irregular systems

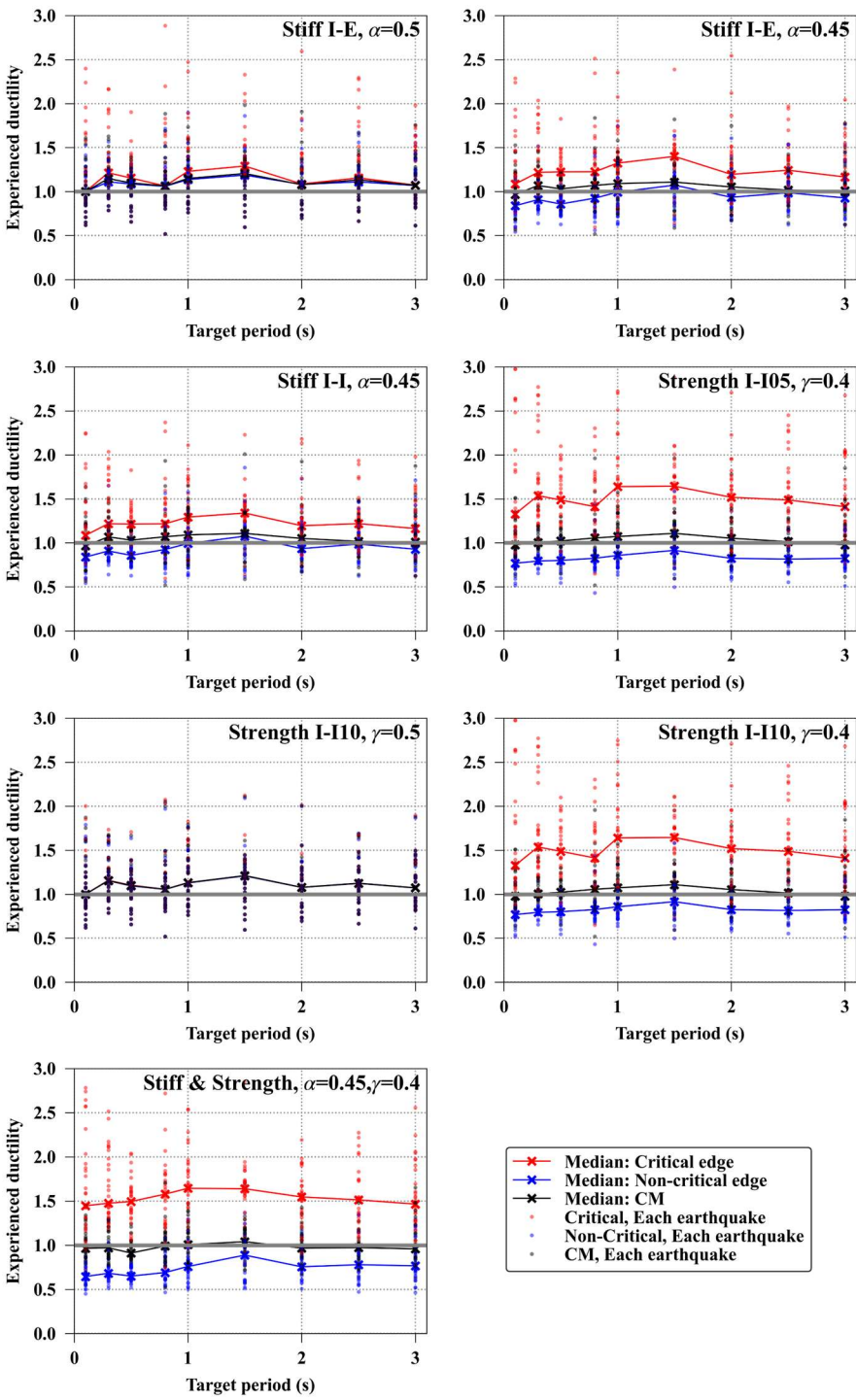


Figure B-64 Ductility demand under Ind30 VS Target period for irregular systems (scale of Y axis is different from Figure B-63)

Ductility Demand in Individual Small Input: Similar to Figure B-63, Figure B-64 shows the ductility demand in individual 30% input for each target period to represent the ductility demand on undamaged oscillator

during small earthquake input. The 30% inputs resulted in median ductility demand of around 1 at CM with higher demand in the critical side. The ductility demand on the non-critical side was slightly less than 1.

Amplification in Subsequent Inputs (MCE100). Figure B-65 shows the amplification in displacement demand in MCE100 for all the irregular systems. Red and blue lines/dots represent the amplification in the critical and non-critical elements, respectively, while the black lines, dots and box-and-whisker plots are the amplification at CM. MCE100 overall resulted in small amplification; the median amplification for each target period stays between 0.9 and 1.4, and each earthquake input resulted in amplification of between 0.75 and 2.0.

Amplification in Smaller Subsequent Inputs. Median amplification in MCE30 is shown in Figure B-66, representing trend in amplification in the cases with big earthquake input followed by small subsequent input. In MCE30, median amplification at CM for the oscillators with yielding elements and $T_{\text{target}} > 0.3$ was between 1.0 to 1.5, while the oscillators with elastic element in one side showed around 1.0 amplification at CM. The critical side was generally subjected to higher amplification than CM, while Stiff I-I showed larger amplification in the non-critical side. As seen in the symmetric system, large amplification in the system with shorter target period ($T_{\text{target}} < 0.5$) was observed.

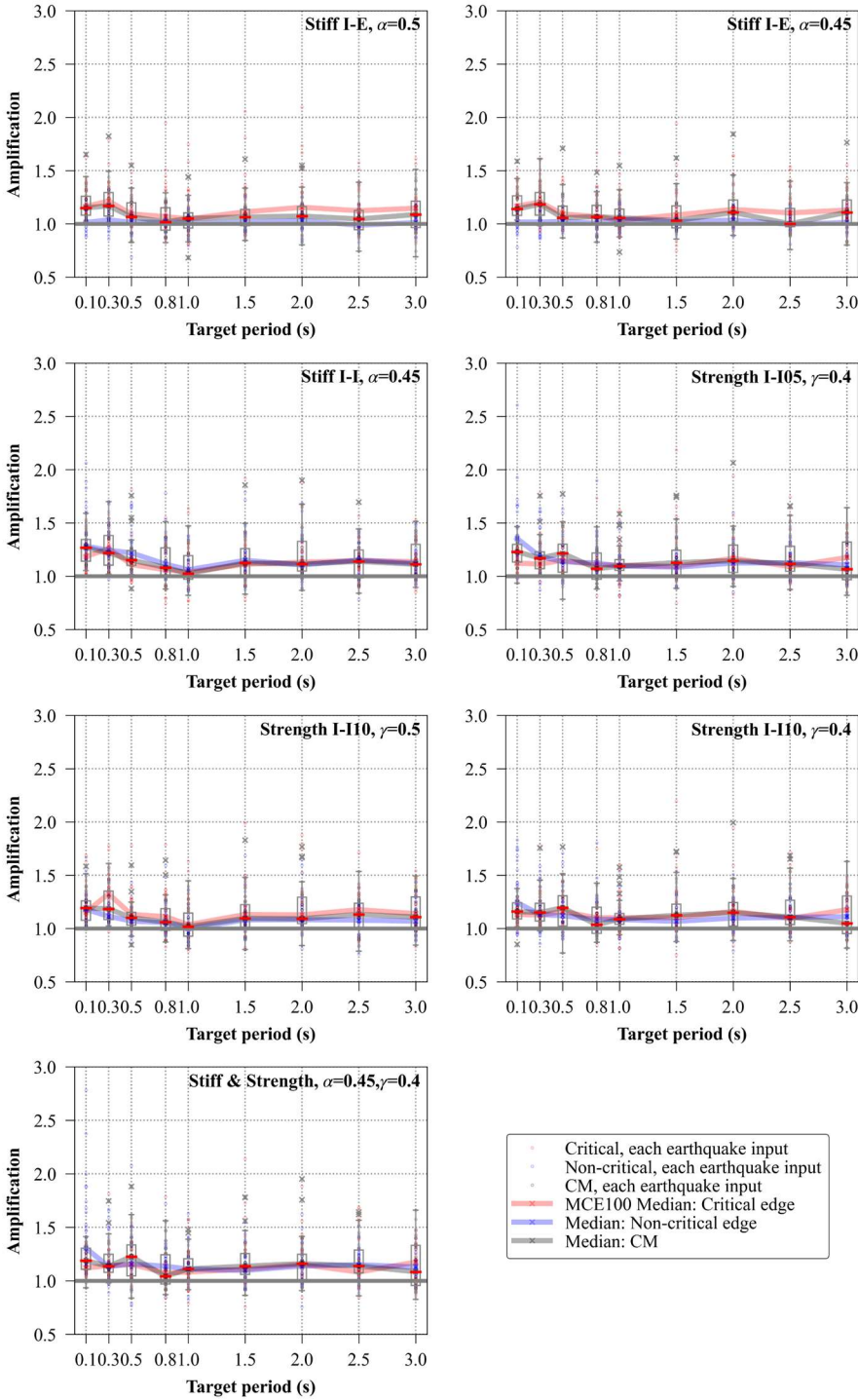


Figure B-65 Amplification in MCE100 for the irregular systems. Box-and-whisker plots (25th-75th percentiles) are for CM.

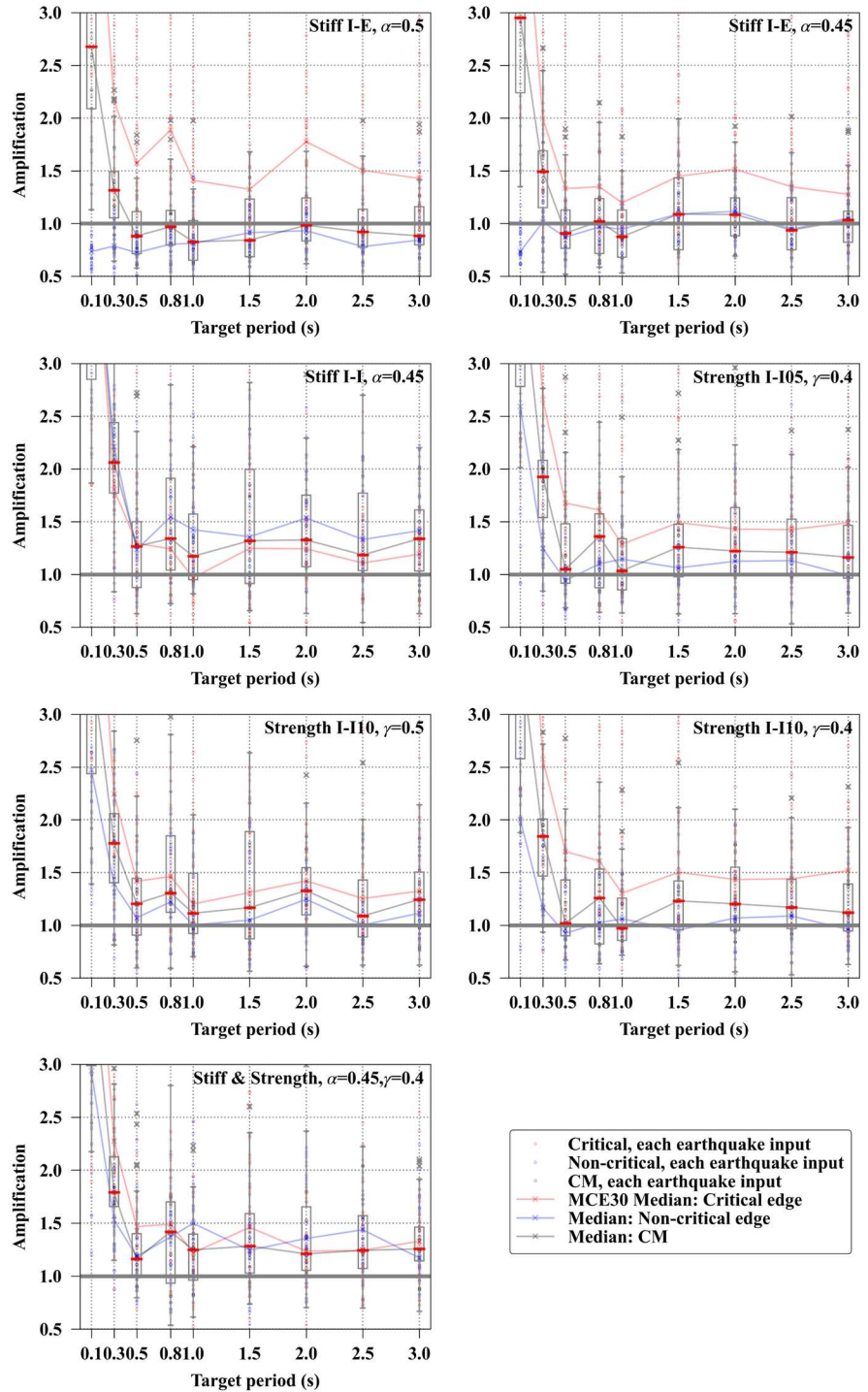


Figure B-66 Amplification in MCE30 for the irregular systems. Box-and-whisker plots (25th-75th percentiles) are for CM.

B.4.3.3 Displacement Demand Amplification in Symmetric and Irregular Systems

This section compares the amplification in displacement demand between symmetric and irregular systems. Figure B-67 plots the amplification in irregular systems versus the amplification in the corresponding symmetric system, from MCE100. Red, blue and black markers represent the amplification for critical side, non-critical side or at CM.

The data points for the amplifications in symmetric and irregular systems distribute approximately along the line corresponding to equal amplification in symmetric and irregular systems for MCE100. Non-critical side of Stiff I-E showed the data points lining up around 1.0 amplification regardless of amplification in symmetric systems. Not many outliers exist from each earthquake case: most of the points for the amplification in the critical side stay within $\pm 20\%$ of the amplification in the symmetric systems.

To demonstrate the case of a big earthquake input followed by a smaller earthquake input, Figure B-68 shows the same data as Figure B-67 but for MCE30. As already discussed in B4.3.1 and B4.3.2, more amplification was observed compared to MCE100, however, the amplification in irregular systems was overall within $\pm 20\%$ of the median amplifications in symmetric systems.

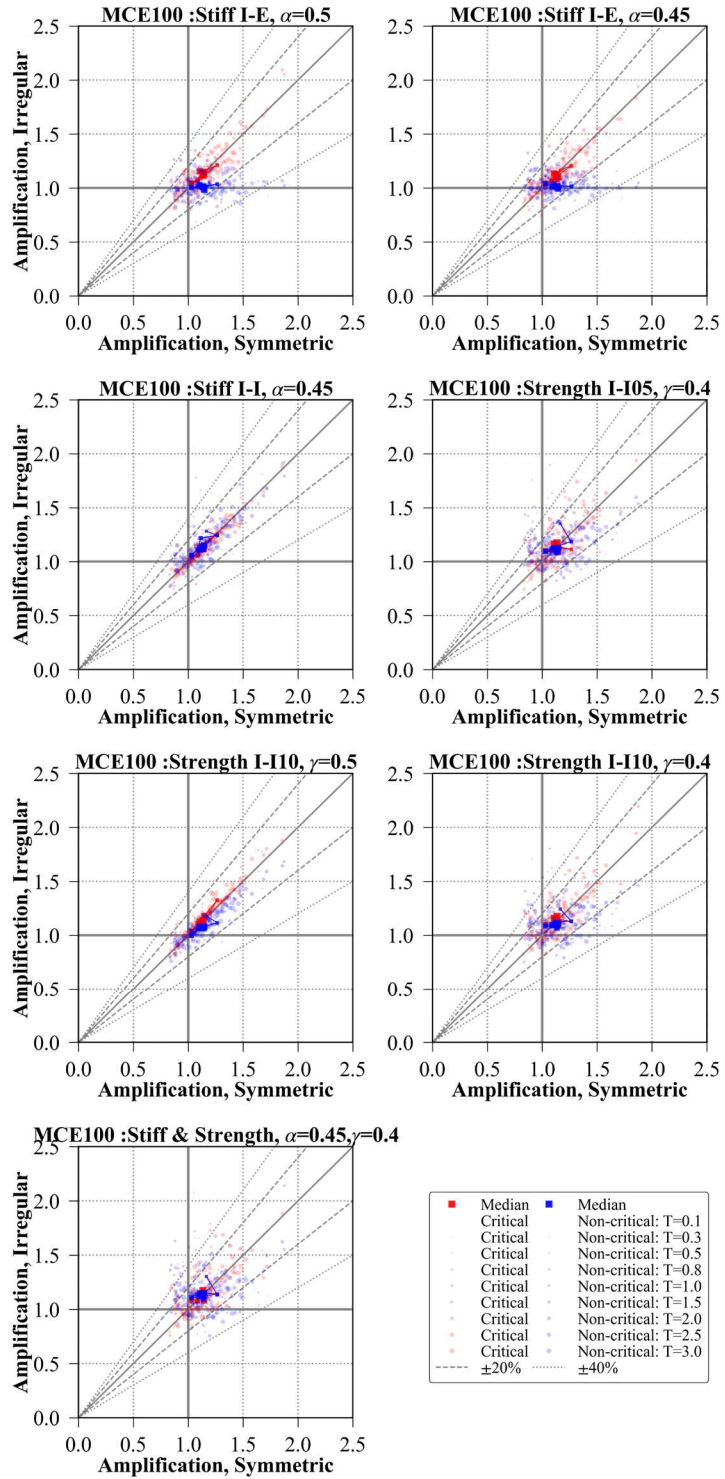


Figure B-67 Comparison of displacement demand amplification in MCE100 between symmetric and irregular systems.

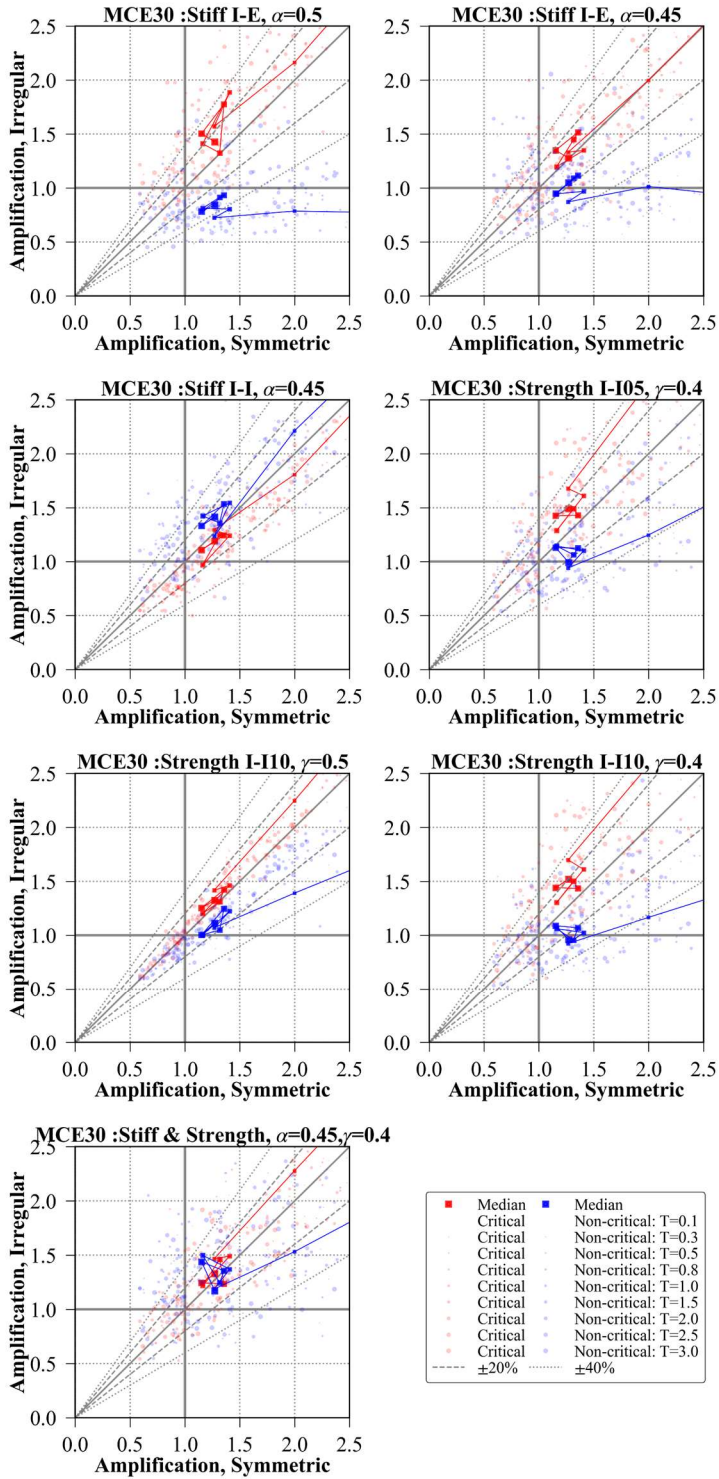


Figure B-68 Comparison of displacement demand amplification in MCE30 between symmetric and irregular systems.

B.4.4 Summary and Conclusions

This section presented the results of analyses for 2DOF oscillators to investigate the effect of prior earthquake events on displacement demand. The 2DOF oscillators represented symmetric systems and several stiffness/strength irregular systems. The oscillators were subjected to single or sequential earthquake inputs. Amplification in displacement demand due to the prior earthquake loading was investigated, where “amplification” is defined as the ratio of displacement demand in a damaged oscillator to the displacement demand in same earthquake in an undamaged oscillator. While this study analyzed a limited number of irregular systems and ground motion inputs, the results are useful to support the outcomes in the other studies in Appendix-B.

Key Outcomes

1. Torsional response did not significantly affect the amplification in displacement demand for the irregular systems considered in this study.
2. The median amplification for critical/noncritical sides and at CM stays within +/- 20% of the results for a symmetric system when both sides have similar yield strength and within +/-40% when there is irregularity in yield strength.
3. Significant amplification can occur in cases with a big earthquake input followed by a smaller earthquake input relative to the amplification in a big earthquake input followed by a big earthquake input. This is the same outcome from SDOF studies in Appendix B.3, but it is noted that this is largely due to the displacement demand of the undamaged oscillator to the small earthquake being very small.

Other findings or notes.

1. The amplification in smaller earthquake events was higher in short period range (i.e., < 0.5 sec) because of the issue with dividing by small numbers. Displacement demand in short period systems was small in both symmetric and irregular systems, and also observed in SDOF study.
2. Prior MCE earthquake inputs have more impact in cases where elastic response is expected for undamaged oscillators.
3. Ductility demand in damaging MCE input was around 3-4 at CM in both symmetric and yielding irregular systems.

More dispersion in amplification of irregular system against symmetric systems is observed when yield-strength irregularity exists in the system

References

- ASCE, 2016, *Minimum Design Loads and Associated Criteria for Buildings and Other Structures*, ASCE/SEI 7-16, American Society of Civil Engineers, Structural Engineering Institute, Reston, Virginia.
- ASCE, 2017, *Seismic Evaluation and Retrofit of Existing Buildings*, ASCE/SEI 41-17, American Society of Civil Engineers, Structural Engineering Institute, Reston, Virginia.
- De la Llera, J.C. and Chopra, A.K., 1995, "Estimation of accidental torsion effects for seismic design of buildings," *Journal of Structural Engineering*, Vol. 127, No. 5, pp. 475-481.
- FEMA, 1999, *Repair of Earthquake Damaged Concrete and Masonry Wall Buildings*, FEMA 307, prepared by the Applied Technology Council for the Federal Emergency Management Agency, Washington D.C.
- Kam, Y. W., Pampanin S., Elwood, J. K., 2011, "Seismic Performance of Reinforced Concrete Buildings in the 22 February Christchurch (Lyttelton) Earthquake," *Bulletin of the New Zealand Society for Earthquake Engineering*, Vol. 44, No. 4, pp. 239-178.
- PEER, 2014, *PEER Ground Motion Database, NGA-West2*, Pacific Earthquake Engineering Research Center, Berkeley, California.
- Shahi, S.K. and Baker, J.W., 2014, "An Efficient Algorithm to Identify Strong Velocity Pulses in Multi-component Ground Motions," *Bulletin of the Seismological Society of America*, Vol. 104, No. 5, pp. 2456-2466.
- Takeda, T., Sozen, M.A., and Nielsen, N.N., 1970, "Reinforced Concrete Response to Simulated Earthquakes," *Journal of the Structural Division*, Vol. 96, No. 12, pp. 2557-2573.
- Zhu, M., McKenna, F., and Scott, H.M., 2018, "OpenSeesPy: Python Library for the OpenSees Finite Element Framework," *SoftwareX*, No. 7, pp. 6-11.

B.5 System Assessment for Repair Triggers

B.5.1 Introduction

This section describes the methods proposed to determine the repair triggers, and their application to quantify the repair triggers for code-conforming RC frame structures. It also examines what characteristics of these structures and ground motions influence the selected drift limits.

B.5.2 Methods

As summarized in Figure B-69, the framework for quantifying reparability involves, first, assessing the performance, in terms of drift demands, of an *undamaged* building in a set of maximum considered earthquake (MCE_R)-level ground motions. This intensity level is the basis for U.S. seismic design, and was chosen to quantify drift demands under rare ground motions as a proxy for life safety performance. Drift demands have been shown to be a reliable indicator of future performance (Raghunandan et al., 2015). We then assess the performance of the *damaged* building in the same MCE_R -level motions and quantify the change in drift demands of the damaged building relative to the undamaged building. We relate this change to the level of damage, quantified by the peak story drift in the damaging motion, to identify the effect of prior damage on future performance. These assessments require the development of a nonlinear simulation model for the buildings of interest that is capable of capturing seismic performance of the system well into the nonlinear range, as described subsequently.

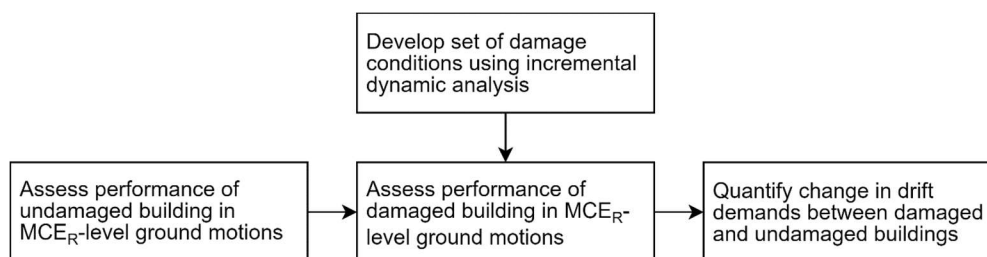


Figure B-69 Framework for assessing the level of damage at which a building's seismic performance is impaired

B.5.2.1 Assess Performance of Undamaged Building

The performance of the undamaged structure is first assessed under MCE_R -level ground motions. Here, 15 of these so-called "performance assessment" motions, or 15 orthogonal motion pairs for 3D analysis, are selected from the PEER NGA-West2 database (PEER, 2020) to represent the MCE_R -level at a site of interest. These motions were selected based on the conditional mean spectrum considering the building of interest's first-mode period, using the

tool developed by Baker (2011), to capture expected spectral shape (and variability therein). For the example building described later, it is assumed that they are located at a high seismic site with $S_{M1} = 0.91$ g in Oakland, California (site class C) (ATC, 2020). The hazard deaggregation needed to do the conditional mean spectrum calculations was obtained from the USGS Unified Hazard Tool (USGS, 2020), consistent with ASCE/SEI 7-16 (ASCE, 2017b). If story drifts in the undamaged building exceed 10% in any story during the MCE_R -level motion, the record is not considered in the determination of drift amplifications, but is considered in determining median peak story drifts for the undamaged building. In non-conforming buildings, if any records caused story drifts to exceed 10% in the undamaged building, we selected additional MCE_R -level motions so 15 drift amplifications could be considered.

B.5.2.2 Develop Set of Damage Conditions

The next step is to develop a varied set of potential damage conditions for each building. This is accomplished by subjecting the structure to incremental dynamic analysis (IDA) (Vamvatsikos and Cornell, 2002). In IDA, a suite of ground motion records are scaled to a range of ground motion intensities to capture the effects of intensity and record to record variability on response (Vamvatsikos and Cornell, 2002). The IDA employed here uses 22 (pairs of) motions in the FEMA P-695 (FEMA, 2009) Far-Field set and (for some buildings) 22 long-duration motions selected by Chandramohan et al. (2016). The long-duration motions are spectrally matched to the FEMA P-695 set. The Far-Field set are intended to be representative of ground motion records for significant events recorded farther than 10 km from the fault rupture (FEMA, 2009). Each input motion is scaled at increasing intensities, quantified as the *geomean* $Sa(T_i)$ for each building, until 10% story drift limit is reached. For 2D analysis, we applied one component from each record pair; for 3D analysis, the record pair was applied simultaneously in each orthogonal building direction.

Each analysis in the IDA (i.e., ground motion record and intensity) creates a damage condition in the building. This damage condition is defined in terms of peak story drift, residual drift, and damaged period. The set of damage conditions produced by this set of ground motions is intended to represent the range of possible damage outcomes for a building. Figure B-70 shows the set of damage conditions generated through IDA for one building.

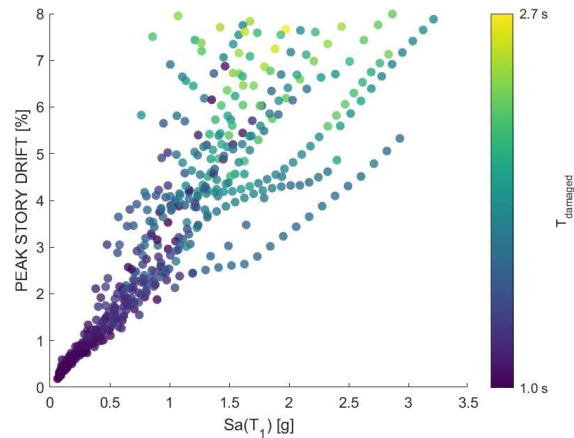


Figure B-70 Set of damage conditions for a code-conforming RC frame, showing how peak story drift and the period of the damaged structure vary with ground motion intensity. The damaged period is calculated using eigenvalue analysis at the end of the analysis; T_1 for this undamaged building is 1.0 sec.

B.5.2.2.1 Selection of damaging ground motions for use in subsequent analysis

From all generated damage conditions, a selection algorithm is used to select a subset of cases for further analysis. With this selection, we aim to represent the entire set of damage conditions, while minimizing the number of analyses conducted subsequently in the framework, thereby greatly reducing computational time from back-to-back nonlinear analyses. To that end, we use stratified random sampling (Parsons, 2014) to select points. Stratified random sampling is appropriate when a proportional, representative sample of a data set is sought. We stratify here based on peak story drift. We primarily quantify damage in terms of the peak story drift, which is strongly correlated with seismic performance metrics, including economic losses (e.g., Ramirez et al. (2012)) and aftershock performance (e.g., Raghunandan et al. (2015)). Figure B-71 illustrates the result of this selection process for one of the buildings. While we selected motions based on peak story drifts only, the distribution of ground motion intensities is also well represented by the selected set. We start with 15 damage conditions for each structure, adding conditions as needed to capture trends in performance.

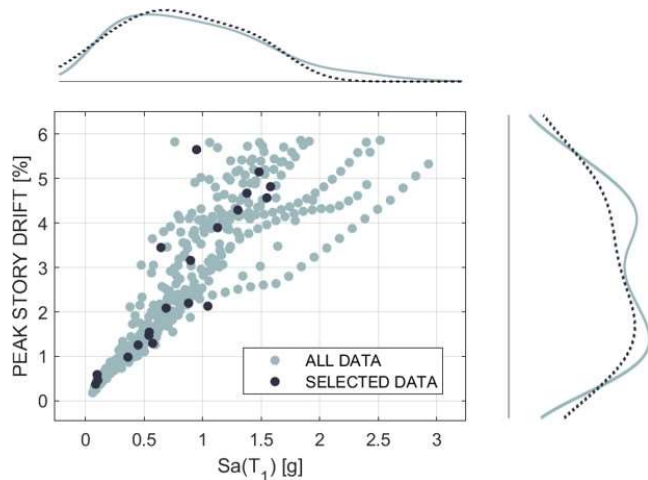


Figure B-71 Set of damage conditions, and the selected conditions, for a code-conforming structure. The distribution of damage conditions along each axis are also shown.

B.5.2.3 Assess Performance of Damaged Building

Next, the change in drift demands on a building when it has been damaged is quantified. We compare the response of the building to each of the performance assessment motions defined in Section B.5.2.1 when the building has and has not experienced prior damage. The prior damage is represented by the selected damage conditions (defined in Section B.5.2.2.1).

To quantify drift demands in the damaged building, analyses for each of the performance assessment motions are run for each selected damage condition. In each analysis, the building model is subjected to two ground motions: the damaging motion, which replicates the damage condition, and one of the performance assessment (MCE_R -level) motions. Figure B-72 shows the set drift histories from the analyses for one damage condition and one MCE_R -level motion.

B.5.2.4 Quantify Change in Drift Demands Between Damaged and Undamaged Buildings

The response of the undamaged structure in each of the performance assessment motions is compared to the damaged structure in Equation 1, as a ratio of peak story drift, Δ_{peak} , in the damaged structure to the peak story drift in the undamaged structure in the same MCE_R -level performance assessment motion. For each damage condition, there are therefore 15 such drift amplification ratios. The peak drift may occur in any story, and in either orthogonal direction. If the building collapsed during the second motion, we assumed a damaged peak story drift value of 10% in determining the drift amplification ratio.

$$\text{Drift amplification ratio} = \frac{\Delta_{\text{peak,damaged}}}{\Delta_{\text{peak,undamaged}}} \quad (\text{B-1})$$

We plotted the drift amplification ratio against the peak story drift in the damaging motion. The results for one case are shown in Figure B-73. We also calculated the moving median value to capture the trend in drift amplifications as damage (quantified as peak story drift) increases. We took the median value for all drift amplifications within each 1% drift bin at increments of 0.25% drift (i.e., 0 - 1% drift, 0.25 - 1.25% drift, etc.). In each bin, we computed the 10th and 90th percentile to quantify the dispersion of drift amplifications.

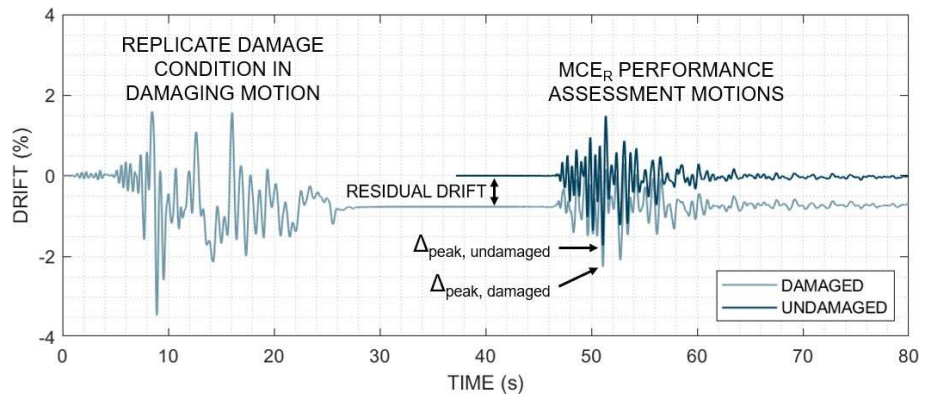


Figure B-72 Story drift time history of analyses for one damage condition and one MCER-level performance assessment motion.

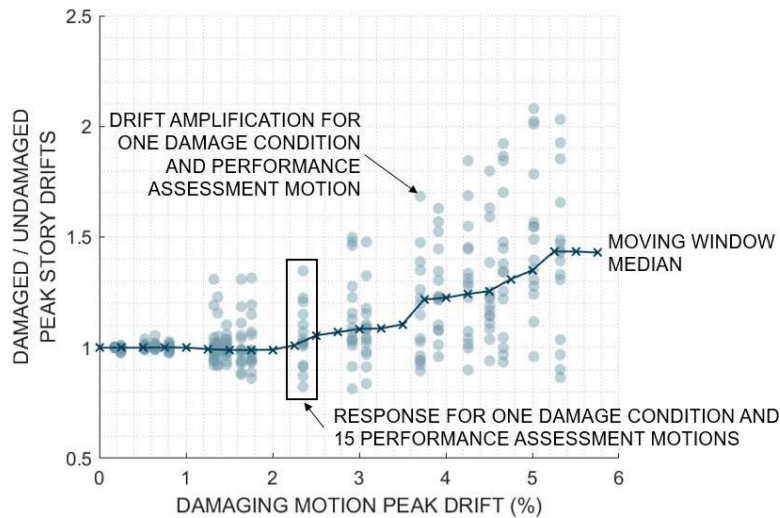


Figure B-73 Median drift amplification ratios over a moving window for one building model subjected to 50 damage conditions and 15 MCER-level motions.

This moving median illustrates the increase in demands associated with damage, and can be used to assess building reparability. This assessment reveals damage (drift) levels below which performance is largely not

impaired, when compared to the same building in an undamaged state. However, we note that the denominator of the drift amplification ratio is based on the existing undamaged building, and may differ greatly from building to building, with implications discussed in the results.

In this Appendix, we preliminarily identify a repair trigger as the level of damage at which the moving 90th percentile curve indicates a 15% increase in drifts has occurred relative to the undamaged building. This range and threshold are somewhat arbitrary, but used here to illustrate the selection of a repair trigger. Further study into appropriate limits should be selected by the judgment of the committee.

B.5.3 Single Degree of Freedom Study to Isolate Building Characteristics

In this section, we employ nonlinear SDOF models of buildings to explore how building characteristics such as deformation capacity, strength, stiffness, period, deterioration, post-yield slope and sensitivity to $P - \Delta$ effects affect the reparability assessment. In the subsequent section, we apply the framework to assess reparability of more realistic multi-DOF building models for RC frames.

B.5.3.1 SDOF Building Models

We modeled the SDOF structures using open source structural analysis software OpenSees (McKenna et al., 2009) with a fixed base, a zero-length tri-linear Ibarra-Medina-Krawinkler IMK hinge (Ibarra et al., 2005), and an elastic element. The IMK hinge captures the nonlinear behavior and stiffness and strength degradation as the model undergoes shaking. The models have a lumped mass and axial load applied at the top of the SDOF model.

Table B-13 lists the range of values used for each structure parameter considered in this study. The median drifts during 15 MCE_R -level motions ranged from 0.9 % to 3.24 % for the SDOF structures. These values were selected to develop SDOF models that capture the range of characteristics of real buildings, and isolate the effects of these characteristics with 50 different models. The baseline SDOF model is representative of a 4-story, code-conforming perimeter moment frame building, with a first mode period, $T = 1.0s$, strength, $V_{max}/W = 0.35$, deformation capacity, $(\theta_p) = 0.06$ rad, and total gravity load equivalent to the seismic weight of the 4-story building, P . Figure B-74 shows the static pushover (backbone) response for models with variation in deformation capacity, strength, and $P - \Delta$ effects. The median drifts during 15 MCE_R -level motions ranged from 0.9 to 3.2% for the undamaged SDOF building models.

Table B-13 Range of values for each SDOF model parameter.

Parameter	Values considered
Strength, V_{max}/W	0.2 - 0.7
Stiffness, T (s)	0.5 - 1.5
$P - \Delta$ effects	$0.25P - 4.0P$
Post-yield slope, M_c/M_y ¹	1.0 - 1.5
Yield drift ² (%)	0.1 - 2.8
Deformation capacity (θ_p) ³	0.0001 - 0.08
Cyclic deterioration	Low - high

¹ Typical value is $M_c = 1.13M_y$ (Haselton et al., 2016)

² Drift is calculated assuming an effective height, $h = 0.7L$

³ Defined as rotation capacity between yield and capping drifts

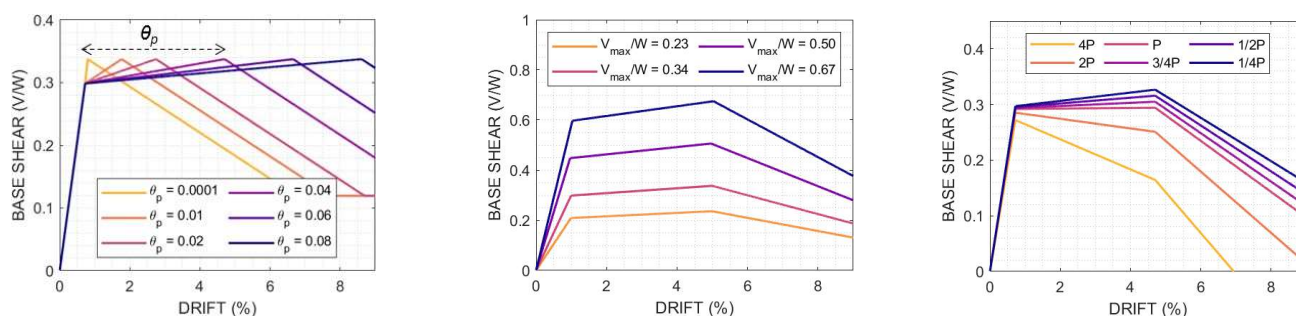


Figure B-74 Static pushover response of SDOF models with (a) varied deformation capacity (θ_p) and constant strength and stiffness, and (b) varied strength and stiffness with constant yield and capping drifts, and (c) $P - \Delta$ effects.

B.5.3.2 Reparability Assessment Results

We applied the framework for assessing reparability to all 50 SDOF models. We considered 50 damage conditions, with 15 performance assessment (MCE_R -level) motions. Figure B-75 shows the response of five models with variation in deformation capacity (Figure B-74a) in a selected damaging motion, and subsequent performance assessment motion.

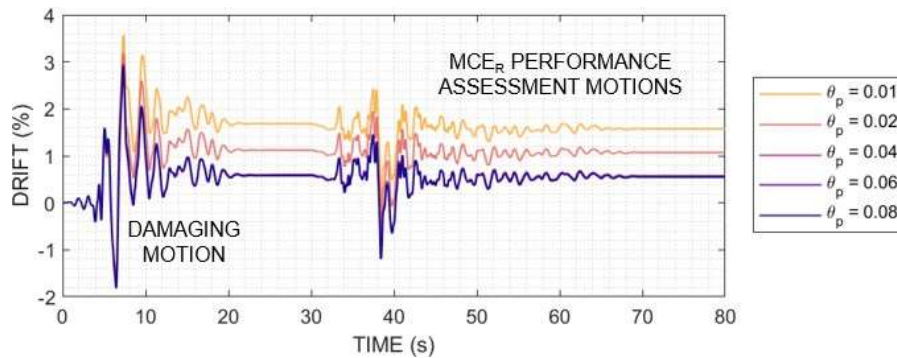


Figure B-75 Drift histories of SDOF models with varied deformation capacities (θ_p) subjected to a back-to-back ground motion.

First, we analyzed how deformation capacity affects future seismic performance and reparability in Figure B-76a. For relatively small damaging motion drifts, i.e. relatively less damage, the ratio of drifts in the damaged and undamaged SDOF models is 1, indicating performance has not been impaired. Figure B-76a shows, however, the steeper increase in drift amplifications in structures with less deformation capacity. Those structures with less deformation capacity have more deteriorated strength and stiffness, largely due to in-cycle deterioration, such that they tend to see larger drifts (relatively to the same undamaged oscillator) in the performance assessment motion. The less ductile structures also have larger residual drifts after the damaging motions, as illustrated by the hysteretic response of each of these models in the same set of damaging and performance assessment motions shown in Figure B-76b, which contribute to the drift amplifications. The jaggedness in the curves in Figure B-76a also reflects the complexity of the structural responses; with larger drifts in the damaging motion, the period of the building tends to elongate and increase effective damping, and decreasing spectral demand. Results of analyses not shown indicated that cyclic deterioration in the hysteresis model did not have a large effect on reparability outcomes.

We also isolated the effect of increased $P - \Delta$ effects, with results shown in Figure B-77. These results show that models with higher $P - \Delta$, and lower effective deformation capacity, see bigger amplifications at lower damage. However, even structures with the most extreme $P - \Delta$, the drift amplifications do not become significant until there is significant residual drift.

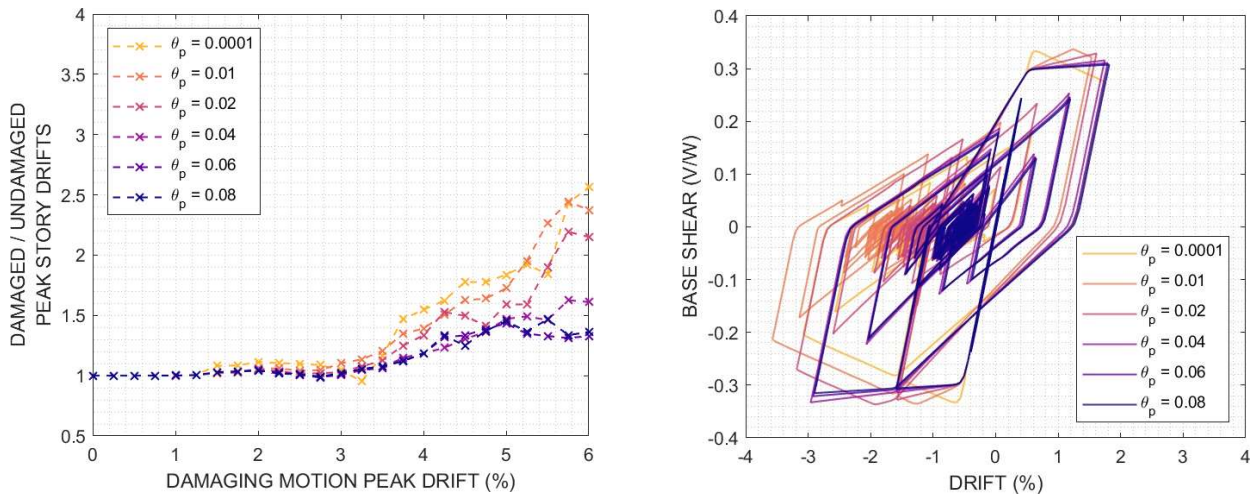


Figure B-76 SDOF models with variation in deformation capacity (defined as θ_p) showing (a) medians, and (b) hysteretic response during one damage condition and performance assessment.

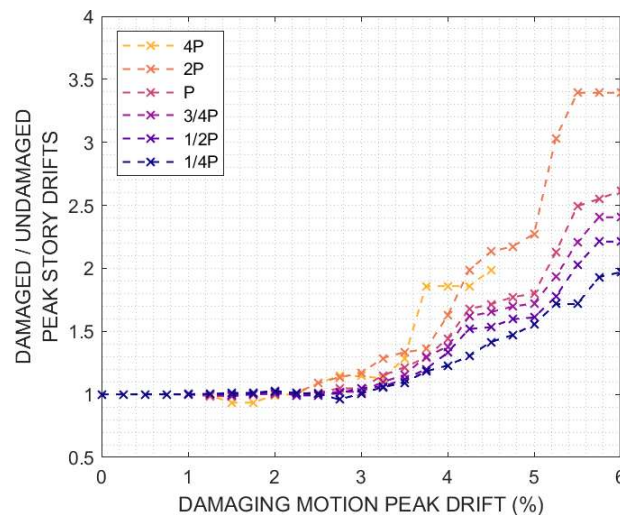


Figure B-77 SDOF models with variation in $P - \Delta$ showing (a) moving window medians, and (b) hysteretic response during one damage condition and performance assessment.

Figure B-78 shows the effect of stiffness, k , and first mode period, T , on drift amplifications. Stiffness alone (Figure B-78b) does not strongly influence response, in terms of when damage impairs performance. However, period matters (Figure 78a) with shorter period structures seeing higher drift amplifications at lower levels of damage (drift). This trend is pronounced for $T < 1.0s$, where the equal displacement "rule" is known to break down (Sozen, 2003). Structure strength does not significantly affect a building's capacity to withstand damage, particularly in longer period structures ($T > 1.0s$), as illustrated by Figure B-79. In the short period case, drifts in the undamaged oscillators were strongly inversely correlated with strength and the drift amplification ratios were controlled by the small denominator in

Equation 1. stronger buildings had smaller drifts in the undamaged case, which is consistent with the equal displacement "rule" (Sozen, 2003).

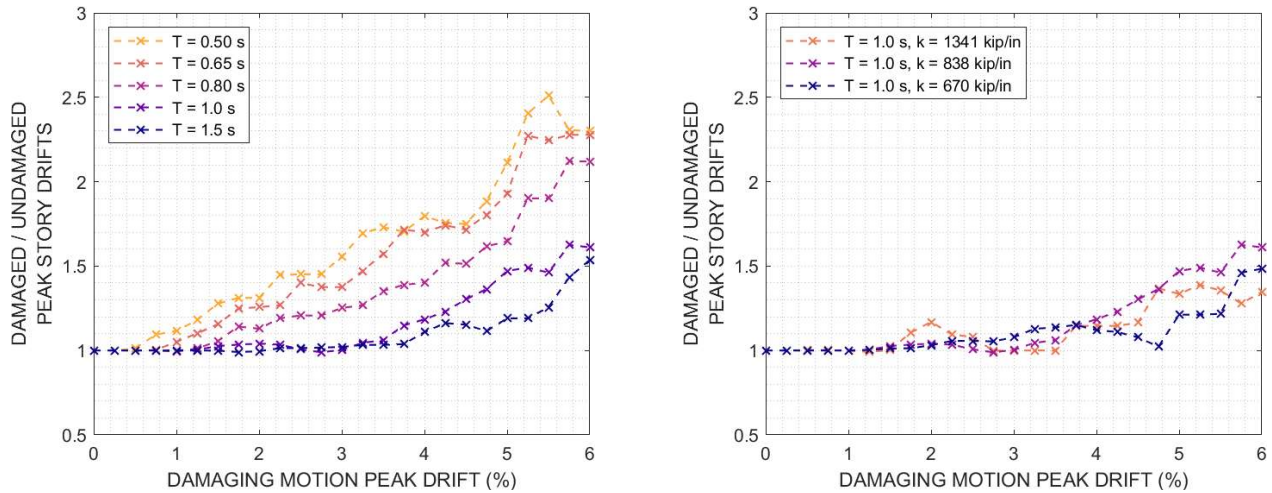


Figure B-78 Median drift amplifications for SDOF models with variation in (a) stiffness and period, and (b) stiffness only.

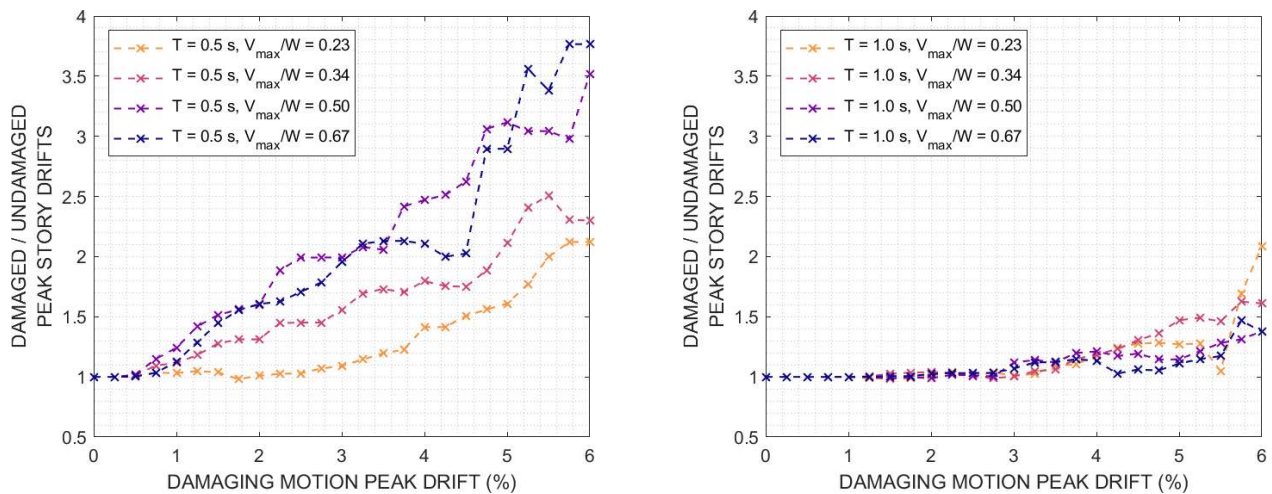


Figure B-79 Median drift amplifications for SDOF models with variation strength and a first mode period (a) $T = 0.5$ s, and (b) $T = 1.0$ s.

B.5.4 RC Frame Buildings of Interest

B.5.4.1 Building Selection and Design

The framework was applied to five RC frame buildings that are based on Haselton et al. (2011), and were updated in FEMA P-2012 (FEMA, 2018). The code-conforming buildings follow ASCE/SEI 7-16 (ASCE, 2017b) standards, and were designed for seismic design category (SDC) D with design and detailing provisions for special moment frames (SMF). The non-conforming, less ductile, buildings are based on the ordinary moment frames (OMF) described in FEMA P-2012 (FEMA, 2018) (see also FEMA P-695 (FEMA, 2009)) and originally designed for SDC B; these designs were also

assessed in SDC D as examples of non-conforming buildings. Based on the building characteristics identified as potentially significant through the SDOF study, we selected buildings for this study that represented a variation in height, building period, sensitivity to $P - \Delta$ effects, detailing and deformation capacity to quantify the difference in reparability associated with these characteristics. Table B-14 lists these buildings and key design parameters: Building C4 is a 4-story code-conforming RC frame building. Building N4 is the same height, but non-conforming, and is weaker and less ductile. Building C1 is a single-story, code-conforming structure. Buildings C12 and N12 are 12-story buildings where C12 is code-conforming, and N12 is non-conforming.

Table B-14 RC frame buildings assessed for reparability in this study

ID	Stories	Design	T(s) ¹	V_{max}/W^2	Ultimate story drift (%) ³	MCER story drifts (%) ⁴	Repair trigger (% drift) ⁵
C4	4	Code-conforming	1.0	0.33	4.9	2.7	2.2
N4	4	Non-conforming	1.4	0.24	3.0	3.6	1.8
C12	12	Code-conforming	2.4	0.16	5.8	2.4	2.0
N12	12	Non-conforming	3.5	0.12	3.9	2.8	2.8
C1	1	Code-conforming	0.4	0.68	5.0	1.5	1.5

¹ Measured using eigenvalue analysis, with elements modeled with cracked sections

² Peak strength from static pushover analysis, normalized by building weight

³ Drift at capping (onset of negative slope) in controlling story during pushover

⁴ Median peak drifts of undamaged building in performance assessment motions

⁵ Level of drift at which the 90th percentile of drift amplifications exceeds 1.15, representing a 15% increase relative to the undamaged building

Figure B-80 shows one exterior frame of the 4-story RC frame building, indicating typical building geometry. In all of the buildings, seismic loads are resisted by three-bay perimeter moment frames. Interior beams and columns are designed only for gravity loading. Column spacing is 20 ft in both (orthogonal plan) directions. The first story height is 15 ft; upper story heights are 13 ft. All buildings have a floor system consisting of a 6 in RC floor slab. Each of the buildings was designed for this geometry and dead, live, and seismic loads (FEMA, 2018) and other requirements from ASCE/SEI 7-16 (ASCE, 2017b). For the 4-story code-conforming building (Bldg C4), for example, in the perimeter frame, beam sizes range from 20 x 34 in to 18 x 24 in, and column sizes range from 22 x 30 in to 22 x 26 in. In columns, reinforcement ratios (ρ) are typically around 1.7% and ties spaced at 2.5 - 3.5 in in the hinge regions ($\rho_s = 0.011$). The perimeter frames were designed by the FEMA P-2012 and FEMA P-695 project teams (FEMA, 2018; FEMA, 2009), and reviewed by practicing engineers. We also designed a beam-column gravity frame system following ASCE/SEI 7-16 (ASCE, 2017b)

requirements. Typical gravity-system beams are 12 x 18 in and columns are 14 x 14 in.

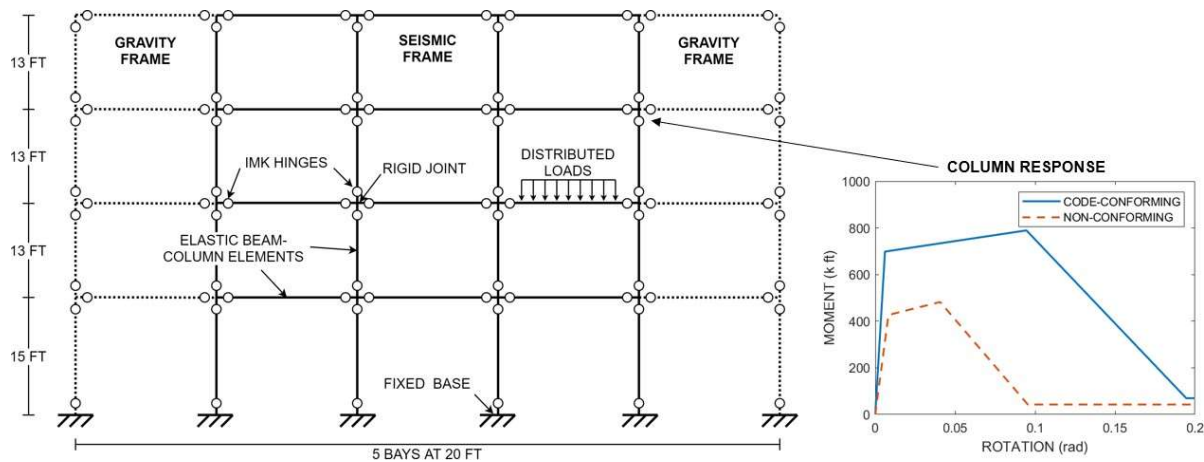


Figure B-80 Diagram of geometry and modeling of exterior frames, with three-bay seismic-resisting bays perimeter frame and two gravity frame bays. Typical column backbones for perimeter frame in 4-story buildings definition are shown.

B.5.4.2 Nonlinear Modeling of RC Frame Buildings

We developed a three-dimensional (3D) nonlinear model of each building in the open source structural analysis software OpenSees (McKenna et al., 2009). This model employs lumped plasticity for beam and column elements, with zero-length hinges at both ends of each element, as shown in Figure B-80. We chose this approach for computational efficiency and for its advantages in capturing, phenomenologically, softening behavior of flexurally-controlled elements in the severely nonlinear range due to spalling and rebar buckling (Haselton et al., 2009). All beams and columns are flexure or flexure-shear critical, such that the response can be captured with a rotational spring. Here, the zero-length moment-rotation hinges were modeled using the IMK peak-oriented hysteretic model (Ibarra et al., 2005) to represent beam and column flexural behavior. Figure B-80 shows backbone curves for perimeter frame first-story columns in two buildings; backbone and cyclic deterioration parameters were determined using the empirical calibration equations developed by Haselton et al. (2016), based on each building's design details. According to these equations, even the non-conforming buildings in this study have significant plastic rotation capacity due to their design detailing.

The model assumes cracked stiffness properties for beams and columns based on Haselton et al. (2016). Columns are assumed to be fixed at the base. At the beam-column joint, the finite size panel zone was modeled with nearly rigid, elastic elements. The floor slab is not explicitly modeled; rather a rigid diaphragm condition and corresponding loads and mass are incorporated into

the model. $P - \Delta$ effects are considered with the PDelta geometric transformation (McKenna et al., 2009). Distributed loads representative of an office building (FEMA, 2018) are applied to beams before dynamic analysis, considering unfactored dead load and the expected (small) fraction of live load (Ellingwood, 1980). Masses are based on these distributed loads and are applied at all model nodes. Three-percent Rayleigh damping (ASCE, 2017a) is applied at the first and third lateral modes (because the building is symmetric, the modes are the same in both orthogonal directions). Damping is based on current stiffness, and is updated throughout the analysis.

We used eigenvalue analysis to determine the building periods, and static pushover analysis to quantify building strength and deformation capacity to summarize building characteristics in Table B-14. The static pushover responses of the buildings under inverted triangular loading used in this study are shown in Figure B-81. These results indicate that the strength of the buildings and range of periods are typical of RC frame structures, and shows variation among the buildings.

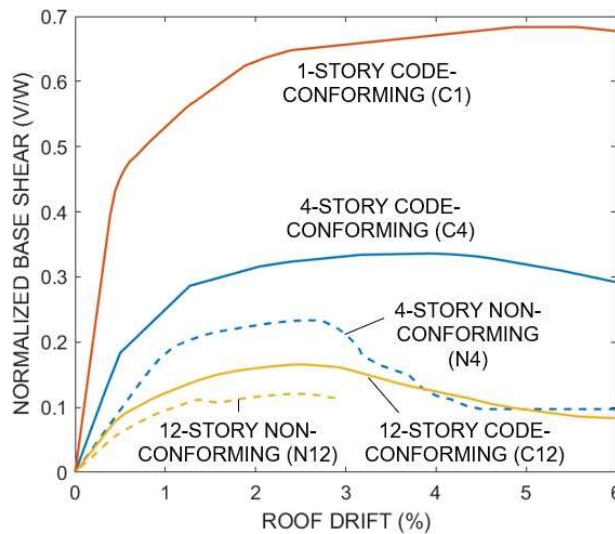


Figure B-81 Response of RC frame buildings under static pushover loading. Base shear is normalized by building weight.

B.5.5 Repair Trigger for RC Frames

Through this framework, we assess reparability, quantifying the relationship between damage and impaired performance in a MCE_R -level event for the RC frame buildings of interest. These results are summarized in Figures B-82, B-83, and B-84. These figures illustrate the range of drift amplifications, as well as the level of damage at which the range of amplifications increase drift demands by 15%.

B.5.5.1 Effect of Building Deformation Capacity

We studied the two 4-story RC moment frame structures, Buildings C4 and N4, with variation in strength and deformation capacity (see Table B-14). These differences in deformation capacity are partially due to component detailing differences (typical column tie spacing, s/d , is of 0.1 vs. 0.4 in in C4 and N4, respectively), and partially due to system effects (stronger columns relative to beams in Bldg C4: typical beam-column strength ratios, $\frac{\Sigma M_C}{\Sigma M_B}$, are 1.4 and 1.1 in Bldg C4 and Bldg N4, respectively).

Figure B-82 shows the median drift amplification ratio over a moving window in these two buildings, along with the 10th to 90th percentiles of each window. In this Appendix, the upper end of this range is compared to a 15% increase in drift demands to identify a building-specific repair trigger. The repair triggers for these buildings are 2.0% and 1.7% for Bldgs C4 and N4, respectively. We see larger drift amplifications in the non-conforming structure (Bldg N4), though in both structures, damage does not significantly impair performance until the building experiences story drifts in excess of 1.5% in a damaging motion. We attribute the worse performance of Bldg N4 primarily to its smaller deformation capacity because the SDOF study found that strength and stiffness are not critical for $T > 1.0$ s. Further, drift demands in Bldg N4 are larger in both the undamaged and damaged cases, as reported in Table B-14. In Bldg N4, higher damage is associated with larger drift amplifications and increased scatter.

In some analyses, the drift amplification is less than one, indicating that peak drifts were smaller in the damaged building. Buildings often experience period elongation as a result of shaking, which can lead to changes in the intensity of shaking felt by the damaged building. We scaled ground motions to the period of the undamaged building, considering a cracked initial stiffness assumption, such that damaged and undamaged cases are subjected to the same motions. If a building is then oscillating at a longer period, it may not be as affected by a motion scaled for a shorter period. In addition, the motions selected according to the conditional mean spectrum slightly underestimated the demand at the elongated period.

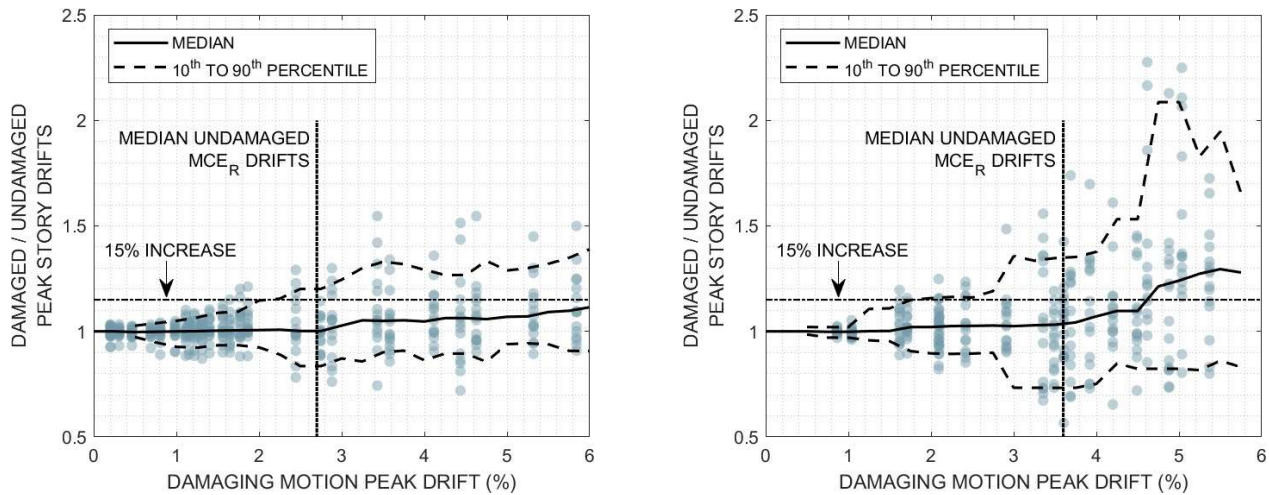


Figure B-82 Reparability of 4-story RC frame buildings, showing the change in response of (a) code-conforming (Bldg C4) and (b) non-conforming (Bldg N4) frames in MCE_R -level motions, as a function of peak story drift in a damaging motion.

B.5.5.2 Effect of Building Period and $P - \Delta$ Sensitivity

We also compared the performance of three code-conforming buildings with different heights and as a result, periods. These buildings include a 1-story structure (Bldg C1) with an initial period of 0.4 s, a 4-story structure (Bldg C4) with an initial period of 1.0 s, and a 12-story structure (Bldg C12) with an initial period of 2.4 s. Figure B-83 shows the responses of the 1-story building, Figure B-84a shows the 4-story response, and Figure B-84 shows the 12-story response. The 1-story structure sees drift amplifications earlier than the 4- and 12-story counterparts, consistent with results of short-period SDOF structures. The repair trigger (i.e., level of damaging motion drift at which the 90th percentile exceeds a 15% increase in demands) is 1.5% in the one-story building, and 2% in the 12-story building. Bldg C12 is more susceptible to $P - \Delta$ effects than Bldgs C1 or C4 because of its longer period and additional stories. While this likely contributed to the higher drift demands experienced by Bldg C12 when it was undamaged (when compared to the other code-conforming structures, as reported in Table B-14), $P - \Delta$ has not amplified the effect of damage on drift demands. Although we find significant effects of $P - \Delta$ in the SDOF study, modern seismic design procedures mitigate these effects through drift limits and $P - \Delta$ design; the presence of gravity system also reduces the effect.

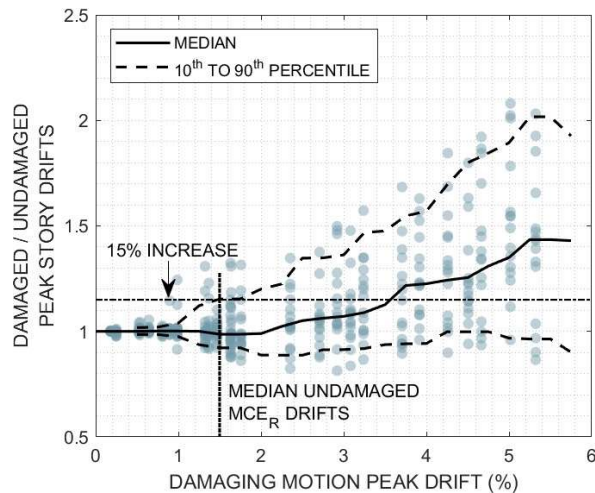


Figure B-83 Reparability of 1-story code-conforming RC frame (Bldg C1) building, showing the change in response of in MCE_R -level motions, as a function of peak story drift in a damaging motion.

We analyzed two 12-story buildings in this study: Bldg C12 is code-conforming, Bldg N12 is non-conforming. The reparability results for these buildings are compared in Figure B-84. Bldg N12 is weaker and saw larger drifts in the MCE_R -level motions in its undamaged state than the stronger Bldg C12. However, both 12-story buildings have relatively similar deformation capacities (see Figure B-81, and thus similar repair triggers. The presence of a gravity system also dilutes the effects of the differences in design between C12 and N12.

B.5.5.3 Other Measures of Damage

We considered other damage measures as predictors of drift amplification, namely period elongation and residual drift. Figure B-85 shows the relationship between drift amplifications and these damage measures for the 1-story, code-conforming building (Bldg C1). Period elongation, which indicates lost stiffness, is strongly correlated with drift amplification, as shown in Figure B-85a, especially once period elongates by a factor of approximately 2. The damaged building period is determined using eigenvalue analysis of the numerical model following the damaging ground motion, but is difficult to determine in a real building without instrumentation. Figure B-85b illustrates the relationship between residual drift and drift amplifications, showing significant amplifications where residual drifts exceed about 0.5% drift.

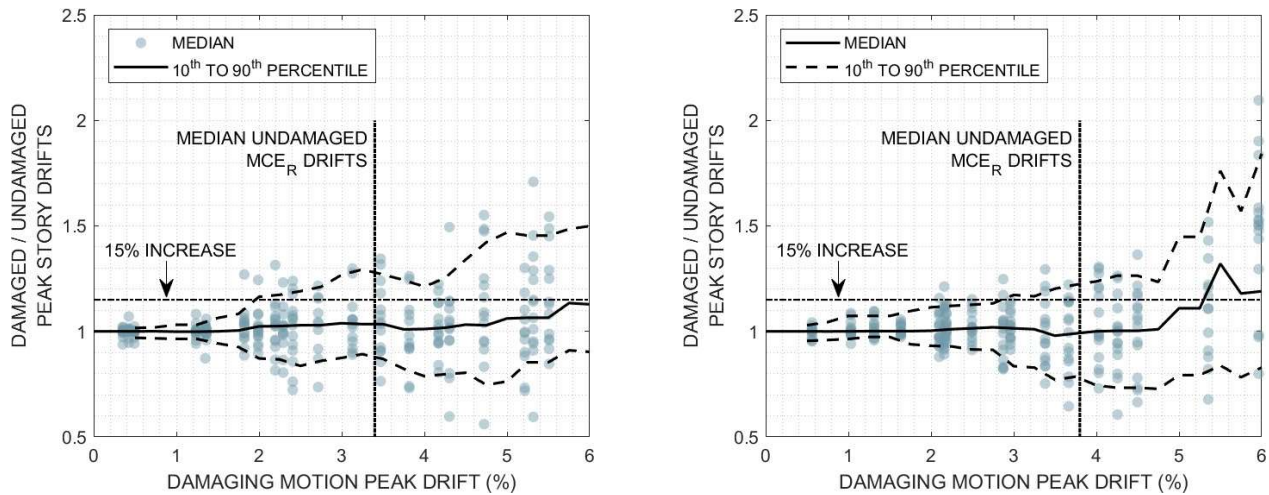


Figure B-84 Reparability of 12-story RC frame buildings, showing the change in response of (a) code-conforming (Bldg C12) (b) non-conforming (Bldg N12) buildings in MCE_R -level motions, as a function of peak story drift in a damaging motion.

For these reasons, and because peak story drifts have been shown to capture damage well (e.g., Elwood and Moehle (2004); Ruiz-García and Aguilar (2015); Jeon et al. (2013); Paal et al. (2015)), we primarily quantify damage in terms of peak story drifts in this study. However, we do consider the effects of residual drift in our quantifying of peak drifts. We considered both "total" drifts (i.e., peak drift relative to the initial, undamaged state), and "in-run" (i.e., peak drift in the second motion, relative to the building state at the end of the damaging motion). In some cases, the second motion counteracted the residual drift, and peak drifts appeared to be smaller as a result, but in others, the residual drift amplified the displacement in the second motion. Overall, we found that trends in drift amplification were largely the same when calculated as total and in-run drifts, though there was variation within individual drift amplification ratios.

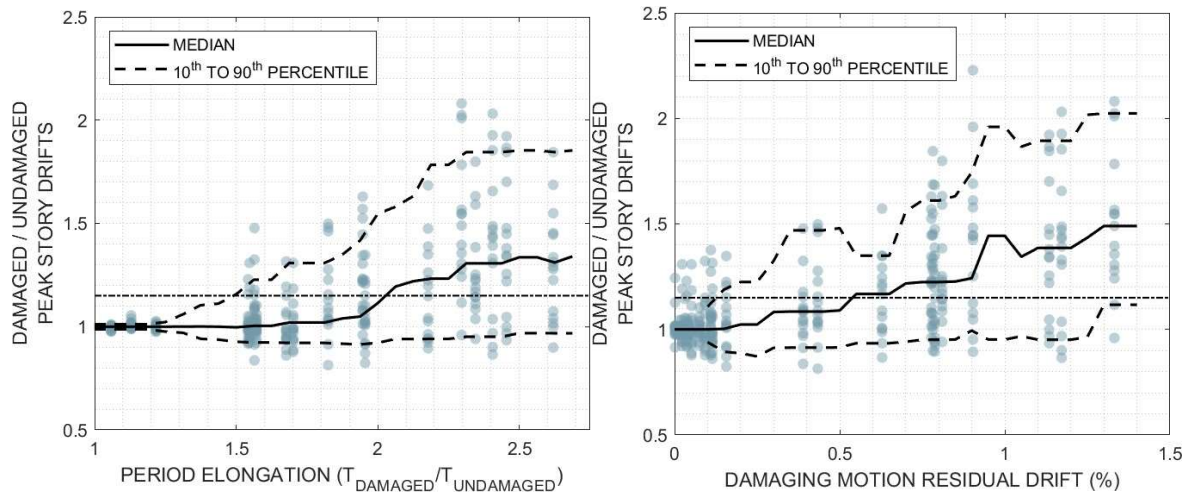


Figure B-85 Relationship between drift amplifications and (a) period elongation and (b) residual drift in a 1-story, code-conforming building.

B.5.5.4 Effect of Damaging Ground Motion Duration

Several studies have shown that collapse performance of buildings is worsened if they are subjected to longer duration shaking by increasing the number of cycles and cyclic energy dissipation demands. In this section, we explore whether the ground motion duration affects reparability. If so, the repair trigger may be sensitive to the seismic environment, and, specifically, the contribution of subduction motions to the hazard (Chandramohan et al., 2016). Recall that for some of the buildings (specifically, Bldgs C1 and C4), we considered some subduction longer duration motions in the development of set of damage conditions. Long duration motions are those for which the 5-75% significant duration (Bommer and Martinez-Pereira, 1999), $D5-75$, is greater than 20 seconds.

To interrogate the effect of the duration of the damaging ground motion, we considered the effect of duration on peak story drift and on reparability. Figure B-86a shows the relationship between duration and peak story drift in the damaging motion; the two are not correlated (R^2 is 0.02). We also considered separately median drift amplifications for the long and short duration motion damage conditions. Figure B-86 illustrates a nearly-identical trend in reparability between damage conditions that result from long and short duration motions. These results indicate that duration is not a significant ground motion for reparability.

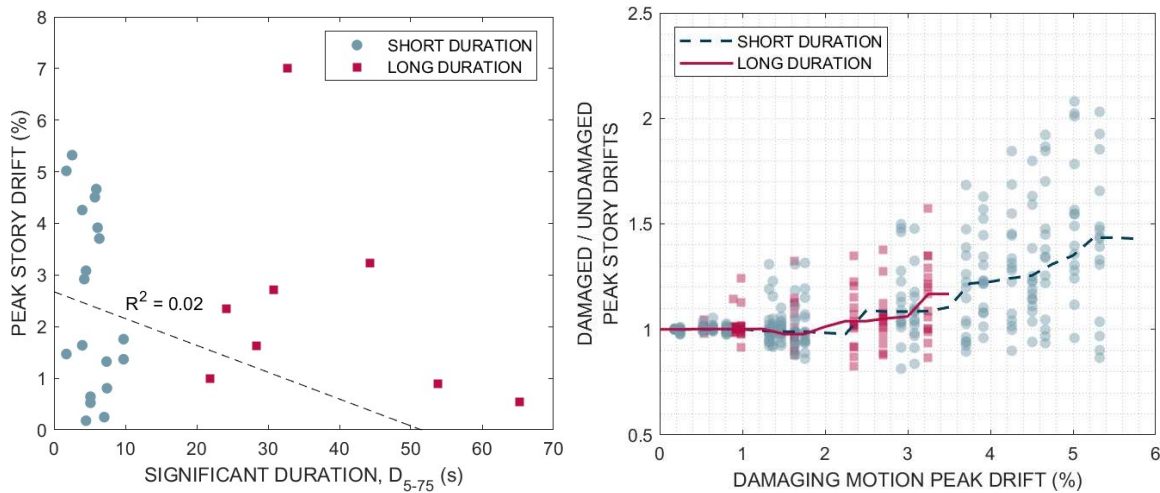


Figure B-86 (a) Relationship between the duration of the damaging motion and associated peak drift for selected damage conditions in a 1-story, code-conforming structure (Bldg C1). (b) Reparability of Bldg C1 for long and short duration ground motions.

References

- ASCE, 2016, Minimum Design Loads and Associated Criteria for Buildings and Other Structures, ASCE/SEI 7-16, American Society of Civil Engineers, Structural Engineering Institute, Reston, Virginia.
- Baker, J. W, 2011, "Conditional mean spectrum: Tool for ground motion selection," *Journal of Structural Engineering*, Vol. 137, No. 3, pp. 322-331.
- Chandramohan, R., Baker, J.W., and Deierlein, G.G., 2016, "Quantifying the influence of ground motion duration on structural collapse capacity using spectrally equivalent records," *Earthquake Spectra*, Vol. 32, No. 2, pp. 927-950.
- Eads, L., Eduardo M., and Lignos, D., 2016, "Spectral shape metrics nad structural collapse potential," *Earthquake Engineering & Structural Dynamics*, Vol. 45, No. 10, pp. 1643-1659.
- FEMA, 2018a, Assessing Seismic Performance of Buildings with Configuration Irregularities, FEMA P-2012, prepared by the Applied Technology Council for the Federal Emergency Management Agency, Washington, D.C.
- FEMA, 2018b, *Seismic Performance Assessment of Buildings*, FEMA P-58, prepared by the Applied Technology Council for the Federal Emergency Management Agency, Washington, D.C.
- FEMA, 2009, *Quantification of Building Seismic*

- Performance Factors*, FEMA P-695, prepared by the Applied Technology Council for the Federal Emergency Management Agency, Washington, D.C.
- Haselton, C.B, Liel, A.B., Taylor-Lange, S.C., and Deierlein, G.G., 2016, "Calibration of Model to Simulate Response of Reinforced Concrete Beam-Columns to Collapse," *ACI Structural Journal*, Vol. 113, No. 6.
- Ibarra, L.F., Ricardo, A. M., and Krawinkler, H., 2005, "Hysteretic models that incorporate strength and stiffness deterioration," *Earthquake Engineering & Structural Dynamics*, Vol. 34, No. 12, pp. 1489-1511.
- Malhotra, P.K., 2002, "Cyclic-demand spectrum." *Earthquake Engineering & Structural Dynamics*, Vol. 31, No. 7, pp. 1441-1457.
- Parsons, V.L., 2014, "Stratified sampling." *Wiley StatsRef: Statistics Reference Online*.
- Raghunandan, M., Liel, A.B., and Luco, N., 2015, "Aftershock collapse vulnerability assessment of reinforced concrete frame structures," *Earthquake Engineering & Structural Dynamics*, Vol. 44, No. 3, pp. 419-439.
- Uang, C.M., and Bertero, V.V., 1991. "UBC seismic serviceability regulations: Critical review," *Journal of Structural Engineering*, Vol. 117, No. 7, pp. 2055-2068.
- Vamvatsikos, D., and Cornell, A.C., 2002, "Incremental dynamic analysis," *Earthquake Engineering & Structural Dynamic*, Vol. 31, No. 3, pp. 491-514.

Appendix C

Fatigue Capacity Models and Background

C.1 Overview

This appendix provides details of the analysis undertaken as the basis for the recommendations made in section 3.3.3.2 of the report regarding assessment of the impact of low cycle fatigue (LCF) on the future performance of earthquake damaged reinforced concrete frame structures.

C.2 Fatigue Capacity Models for Reinforcing Bars

Starting with work undertaken by Mander et al. (1994), numerous researchers have conducted experimental investigations of the LCF capacity of steel reinforcing bars (e.g., Brown and Kunnath, 2000, 2004; Hawileh, Abdalla, et al. 2010; Hawileh, Rahman, et al. 2010; Kunnath et al. 2009; Marder 2018; Slavin and Ghannoum 2016). The results of these experiments have generally been used to calibrate fatigue life relationships in the form of

- the Coffin-Manson equation (Coffin, 1953; Manson, 1953) that relates plastic strain amplitude (ϵ_{ap}) to the number of half cycles required to cause fracture ($2N_f$) or
- Koh and Stephens (1991) equation that relates total strain amplitude (ϵ_a) to the number of half cycles required to cause fracture.

The Coffin-Manson equation is typically presented as:

$$\epsilon_{ap} = \epsilon'_f (2N_f)^c \quad (C-1)$$

where:

ϵ_{ap} = plastic strain amplitude

ϵ'_f = an empirical coefficient

$2N_f$ = number of half-cycles to failure, and

c = an empirical coefficient

The Koh and Stephens equation has a similar form, being:

$$\epsilon_a = M(2N_f)^m \quad (C-2)$$

where:

ε_a = total strain amplitude

M = an empirical coefficient, and

m = an empirical coefficient

Coefficients derived by different researchers for the Coffin-Manson and Koh and Stephens equations are summarized in Table C-1. Where coefficients are given for only one or other of the equations this reflects the data presented by the researcher.

Table C-1 Fatigue Coefficients Derived by Different Researchers

Researcher – reinforcement type	ε'_f	c	M	m
Mander et al. - G40	0.08	-0.49	0.08	-0.45
Brown & Kunnath - No 6a			0.12	-0.47
Brown & Kunnath - No 6b			0.09	-0.45
Brown & Kunnath - No 7	0.13	-0.51	0.11	-0.44
Brown & Kunnath - No 8	0.09	-0.42	0.08	-0.36
Brown & Kunnath - No 9	0.07	-0.37	0.07	-0.31
Kunnath et al. – No. 14			0.10	-0.49
Hawileh et al. - A615	0.13	-0.57	0.10	-0.43
Hawileh et al. - A706	0.10	-0.54	0.09	-0.41
Hawileh et al. - BS 460B	0.36	-0.63	0.25	-0.42
Hawileh et al. - BS B500B	0.22	-0.54	0.15	-0.27
Marder - $s/d_b \leq 4$			0.09	-0.41
Slavin & Ghannoum - M1 G60 4db			0.08	-0.35
Slavin & Ghannoum - M1 G60 5db			0.08	-0.36
Slavin & Ghannoum - M1 G60 6db			0.08	-0.39
Slavin & Ghannoum - M1 G80 4db			0.07	-0.34
Slavin & Ghannoum - M1 G80 6db			0.06	-0.41
Slavin & Ghannoum - M1 G100 4db			0.05	-0.22
Slavin & Ghannoum - M1 G100 5db			0.05	-0.25
Slavin & Ghannoum - M1 G100 6db			0.05	-0.27
Slavin & Ghannoum - M2 G60 4db			0.06	-0.27
Slavin & Ghannoum - M2 G60 5db			0.06	-0.30
Slavin & Ghannoum - M2 G60 6db			0.06	-0.33
Slavin & Ghannoum - M2 G100 4db			0.04	-0.18
Slavin & Ghannoum - M2 G100 5db			0.04	-0.19
Slavin & Ghannoum - M2 G100 6db			0.04	-0.22

Figures C-1 and C-2 show the Koh and Stephens fatigue life relationships summarized in Table C-1, plotted respectively on natural and logarithmic axes.

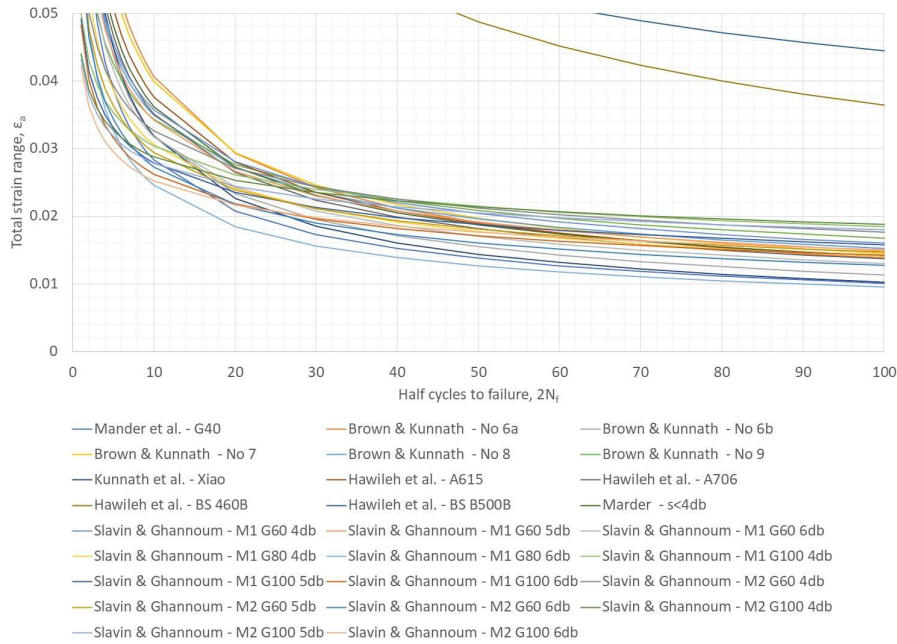


Figure C-1 Koh and Stephens fatigue life relationships for reinforcing steel – natural axes.

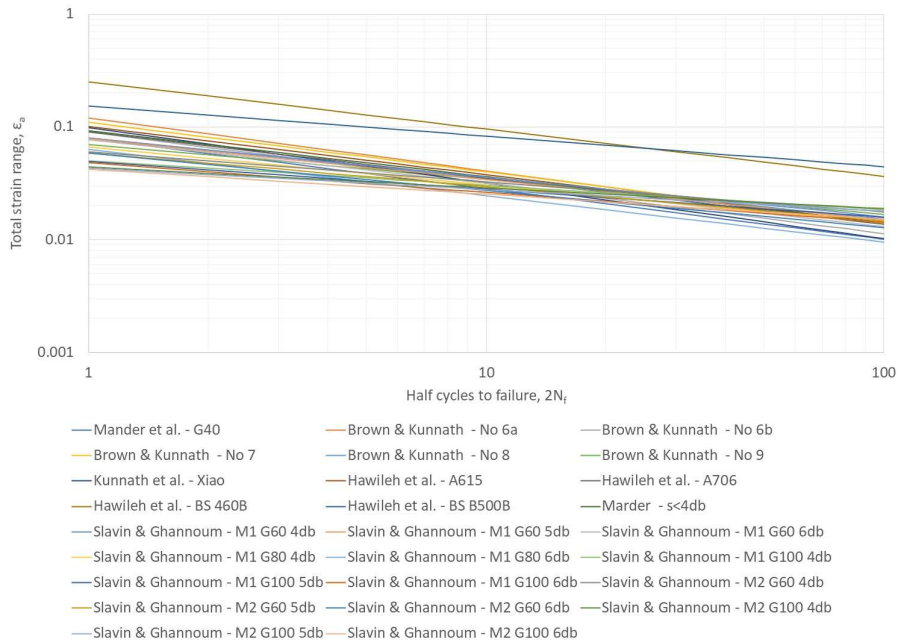


Figure C-2 Koh and Stephens fatigue life relationships for reinforcing steel – logarithmic axes.

It is evident from Figures C-1 and C-2 that there is a significant degree of variation between the fatigue life relationships determined by different researchers and for different types of reinforcing steel.

Recent work by Zhong and Deierlein (2019) has led to development of a parametric approach to defining the coefficients required for the Coffin-Manson equation. This approach accounts for major variables understood to impact the fatigue life of reinforcing bars, being:

- Yield strength (f_y)
- Ratio of ultimate strength to yield strength (T/Y)
- Bar diameter (d_b), and
- Spacing of transverse reinforcement relative to bar diameter (s/d_b)

Table C-2 shows example Coffin-Manson coefficients calculated using Zhong and Deierlein’s method. Fatigue life relationships based on these coefficients and others summarized in Table C-1 are plotted in Figure C-3.

Table C-2 Fatigue Coefficients Calculated Using Zhong & Deierlein’s Relationships

Researcher – reinforcement type	ϵ'_f	c	M	m
Zhong and Deierlein with $s/d_b = 4^{(1)}$	0.12	-0.31		
Zhong and Deierlein with $s/d_b = 6^{(1)}$	0.11	-0.37		
Zhong and Deierlein with $s/d_b = 8^{(1)}$	0.11	-0.42		

⁽¹⁾ Calculated assuming $d_b = 25$ mm, $f_y = 500$ MPa, T/Y = 1.4, $E_s = 200,000$ MPa.

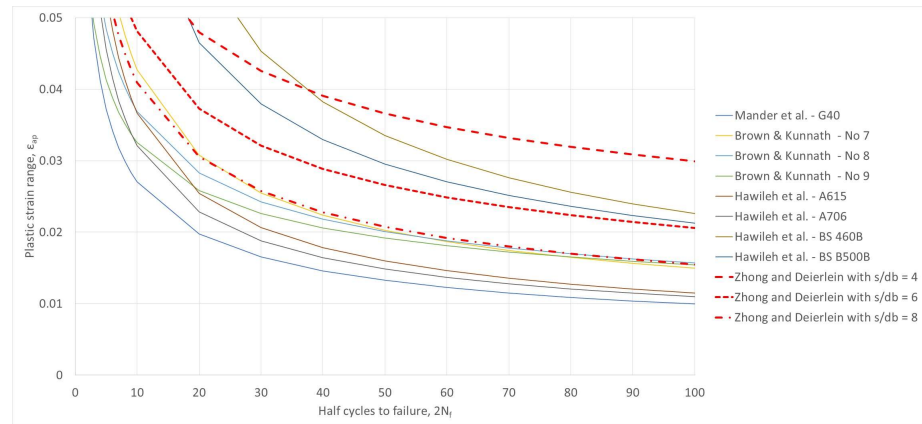


Figure C-3 Coffin-Manson fatigue life relationships for reinforcing steel – natural axes.

Zhong and Deierlein’s work confirms the finding of Marder (2018) and others that materially less fatigue damage occurs when reinforcement is supported by closely spaced transverse reinforcement that reduces the

occurrence of reinforcement buckling. Reinforcement buckling significantly reduces fatigue life because it induces large local plastic strains and can lead to cracking at deformations (Restrepo-Posada, 1993) that in turn leads to failure of the bar. Consideration of the likelihood of buckling also explains the two relationships shown in Figures C-1 and C-2, those determined by Hawileh et al. (Hawileh, Abdalla, et al. 2010) for BS 460B and BS B500B reinforcement, that predict notably greater fatigue life than the majority of the relationships. These were developed based on tests where the bars were supported at a spacing of only twice the bar diameter.

Consequently, different fatigue life relationships have been considered here depending on whether or not buckling of reinforcement may have occurred during the damaging earthquake. Specifically:

- Hawileh’s parameters for BS460B steel have been considered where buckling cannot have occurred, and
- Marder’s parameters, along with those of Kunnath et al. for No 7 and No 8 bars have been considered where buckling may have occurred.

C.3 Definition of Acceptable Levels of Fatigue Damage

Fatigue damage is commonly quantified using ‘Miner’s rule’ (Miner 1945), which can be formulated as:

$$D = \sum 1/2N_{f(i)} \quad (C-3)$$

where:

D = a damage index where a value of 1.0 is generally linked to incipient fracture, and

$2N_{f(i)}$ = number of half-cycles to failure that can be sustained for the strain imposed during cycle i .

Miner’s damage summations have been considered in this work, though it is recognized that other, more sophisticated, methods of quantifying damage are available (e.g., Zhong and Deierlein, 2019).

Two performance measures are considered to represent reasonable alternatives for determining whether the residual fatigue life of reinforcement in an earthquake damaged structure is sufficient. These are:

1. The fatigue life of the reinforcement not having been reduced by more than 10% by the imposed earthquake demands, or
2. The residual fatigue life being sufficient to withstand the impacts of a future ‘maximum considered’ earthquake (MCE).

Fulfillment of either of these criteria is considered sufficient to demonstrate that the reinforcement has not been compromised by fatigue damage significantly enough to impact the building safety. It is not necessary for a structure to fulfill both.

The first criterion is considered to represent a level of fatigue degradation that has no more than a minor impact on the risk of fatigue failure during a future earthquake. Such a threshold is obviously subjective, and there is no specific science that justifies the value of 10%. However, a similar threshold has been proposed on occasions as ‘de minimis’ by building owner’s engineers during discussions of earthquake damage insurance claims in New Zealand where the required standard of repair is generally more onerous than the assurance of future safety of a building that is the focus here. Moreover, the premise of not impacting the building’s future performance is similar to the rationale behind the limiting drift demands, considered in the safety assessment described in Section 3.3 of this report.

The second criterion is considered to show that a structure has sufficient residual fatigue life to resist future demands irrespective of any fatigue degradation that has occurred in the past damaging earthquake. The MCE is not defined here as it is anticipated it may vary between jurisdictions but should be consistent with the definition that would apply to design of a similar building intended for the same use and located on the same site.

Out of necessity, the analyses described in the remainder of this appendix and that form the basis of the recommendations made in section 3.3.3.2 of the report have been based on application of the first criteria. This was necessary because application of the second criteria requires knowledge of the specific characteristics of a building and the hazards it is exposed to that cannot practically be applied in a generic study. The first criterion is also more consistent with criteria applied to the drift demand and other criteria for the post-earthquake assessment.

C.4 Assessment of Fatigue Degradation

Calculation of fatigue damage requires not only an estimate of the peak deformation imposed on a structural element, but also an estimate of the complete deformation history (i.e., cyclic response) imposed during a damaging earthquake. As elaborated on in section C4.2, detailed analysis to determine this deformation history is complex and influenced by the specific characteristics of the structure and the damaging earthquake.

The aim of this study has been to identify thresholds delineating scenarios where fatigue damage can conservatively be considered unimportant from

scenarios where more detailed consideration of fatigue damage is warranted. To achieve this aim based on application of (scaled) earthquake records to different structural configurations would be computationally demanding and require stochastic interpretation of the results.

In lieu of such an approach, a simplified method of estimating fatigue damage has been developed for this study as described in section C4.1. This simplified approach has been used to identify the thresholds demarcating the scenarios where fatigue damage may be a concern.

The simplified approach may also be applied to determine whether fatigue damage is problematic for cases that exceed the thresholds established in this report, for example where the estimated peak drift is greater than 2.0%. The simplified method is expected to be conservative in assessing such cases. More realistic assessment of fatigue damage may instead be achieved based on the type of detailed assessment outlined in section C4.2, albeit at the expense of considerably greater engineering effort.

C.4.1 Simplified Fatigue Life Assessment

The premise of the simplified fatigue life assessment is that the cyclic deformation imposed by an earthquake may be satisfactorily approximated by consideration of an artificial displacement history of the type described in FEMA 461, *Interim Testing Protocols for Determining the Seismic Performance Characteristics of Structural and Non-Structural Components*, (FEMA, 2007) for quasi-static cyclic testing. The reinforcement strains arising in a cantilever beam-column element are then calculated for each displacement increment, followed by the fatigue damage resulting from the strain at each displacement increment. The summation of fatigue damage is then compared to the fatigue damage limits described in section C.3 to determine whether remediation of the reinforcement is required.

C.4.1.1 Displacement History

The FEMA 461 displacement history for quasi-static cyclic testing specifies that increasing increments of displacement be applied to a component, with:

- two reversed cycles applied at each drift increment,
- each drift increment being 1.4 times larger than the preceding increment, and
- the first increment being at an amplitude that is not expected to cause damage to the component.

For the purposes of the simplified fatigue assessment described here, the basis of the displacement history can be defined by setting the drift anticipated to have occurred during the damaging earthquake as the maximum drift in the displacement history, and then defining prior displacement increments by dividing by 1.4. An example of this approach is shown in Figure C-4 where the drift during the damaging earthquake is estimated as 2.0%. While generally inconsequential for estimation of fatigue damage, it is recommended that the number of displacement increments (9 in Figure C-4) is such that the first increment is approximately 0.15% drift as suggested in FEMA 461.

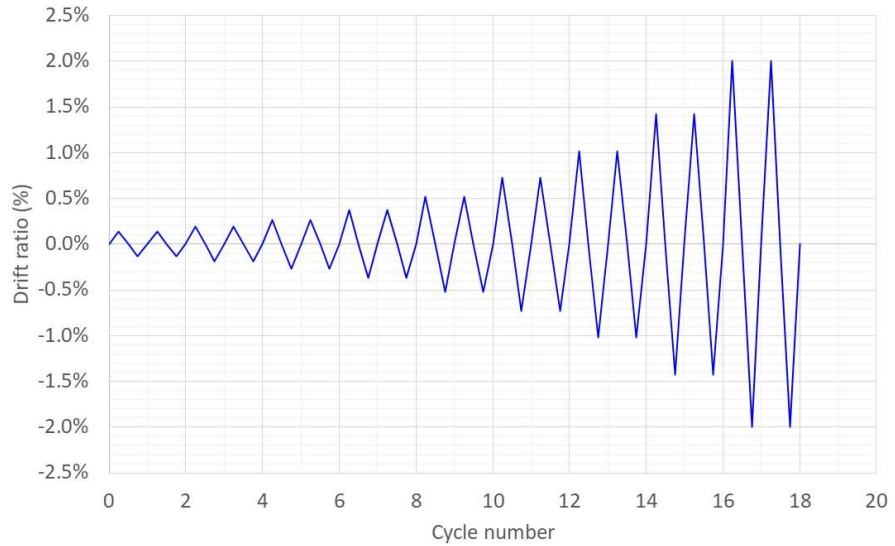


Figure C-4 Example FEMA 461 displacement history with maximum drift of 2.0%

While deemed appropriate for testing of structural components, application of two reversed cycles per drift increment as suggested in FEMA 461 and shown in Figure C-4 is not necessarily representative of the fatigue demands imposed by a particular earthquake.

Various methods are available for calculating the number of effective demand cycles imposed by an earthquake (e.g., Hancock and Bommer 2005). Here the simple definition of Malhotra (2002) has been used to compare the effective number of cycles (i.e., the equivalent number of cycles to the maximum displacement) imposed by the FEMA 461 displacement history to the effective number of cycles that might be expected during an earthquake.

Malhotra states that the effective number of cycles :

$$N_{cy} = \frac{1}{2} \sum_{i=1}^{2n} \left(\frac{u_i}{u_{max}} \right)^c \quad (C-4)$$

where:

- u_i = the displacement during cycle i
- u_{max} = the maximum displacement,
- n = the number of half cycles of displacement imposed, and
- c = an empirical coefficient as used in the Coffin-Manson equation, and taken by Malhotra as 2.

Malhotra published cyclic demand spectra for 71 earthquakes, recorded on both rock and soil sites, which show the number of effective cycles imposed on structures with different periods relative to the period of the site.

Malhotra's plot is reproduced here as Figure C-5.

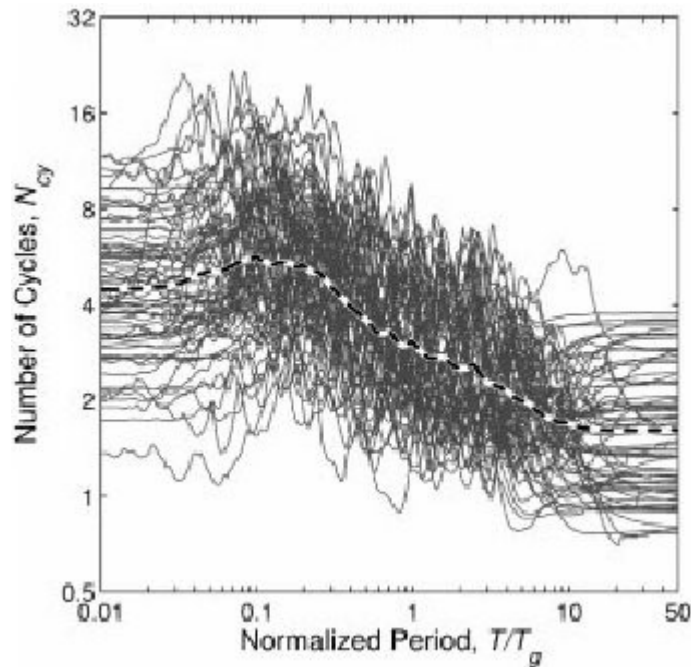


Figure C-5 Cyclic-demand spectra for 71 ground motions for 10% of critical damping and exponent of $c = 2$ (Malhotra 2002)

Malhotra's research indicates that for structures with periods in excess of 0.3 seconds, the number of effective cycles would typically be expected to be 4 or less.

Calculation using equation C-4 shows that the number of effective cycles for a FEMA 461 type displacement history is 2.03 times the number of cycles to each displacement increment. Thus, for the 2 cycles per increment specified by FEMA 461 the number of effective cycles is 4.06. To provide a degree of conservatism in the simplified fatigue assessment described here, the number of cycles per displacement increment is instead taken as 3, corresponding to 6.1 effective cycles at the maximum displacement.

If the simplified approach is being applied to determine whether fatigue damage is problematic for cases that exceed the thresholds established in this report, it is recommended that 3 cycles per displacement increment are considered unless the duration of the damaging earthquake is unusually long in which more cycles per displacement increment may be appropriate. Further work is required to refine recommendations pertaining to longer duration earthquakes.

C.4.1.2 Discussion of Strain Calculation

The strain imposed on reinforcement is the critical factor in estimating fatigue damage. Noting that the strain quantum of interest is either the plastic or total strain amplitude depending on whether fatigue damage is calculated using the Coffin-Manson or Koh and Stephens equations, consideration must be given to the magnitudes of both the tensile and compressive strains imposed.

If the simplified method described here is being applied by a practitioner to estimate the fatigue damage to a structure caused by a particular earthquake, any reasonable method may be used to estimate the strains imposed on the longitudinal reinforcement.

For the purpose of deriving thresholds demarcating the potential onset of excessive fatigue damage, this study has considered the reinforcement strains in simple cantilever elements subjected to an imposed drift. For elements that form part of a frame structure this approach is equivalent to determining a chord rotation rather than a drift. Treating this value as a drift imposed on a frame would be conservative, because it ignores the potentially significant elastic deformation that occurs in other parts of the structure. For example, if the cantilever element considered here is taken to represent a beam, Priestley (1998) suggests that column and joint deformation would increase the effective yield drift by 60% compared to the beam alone.

The calculations undertaken for this study assume a triangular distribution of curvature along the element until yield. The effective yield curvature has been calculated with account made for non-flexural sources of deformation such as shear and slip using the method published by Opabola et al. (2020).

Following yield, plastic deformation has been assumed to occur within an effective plastic hinge length centered on the base of the cantilever, i.e., extending into the support. Assumed plastic hinge lengths have been used in this study as outlined in section C.5.

The fatigue damage calculation is sensitive to the reinforcement compression strain. This is not readily calculable due to its dependence on the tensile strain arising from previous displacement in the reverse direction. For this study it has been assumed that the compression strain is equal to -0.5 times the tensile strain, but not more than -0.01. Further refinement of this aspect is required.

C.4.2 Recommendations for Detailed Fatigue Damage Assessments

Detailed assessment of fatigue damage is a complex process. Only limited comments on the recommended approach are given here.

The aim of detailed assessment of fatigue damage should be to obtain the best possible estimate of the strain history for the reinforcing bars considered. This necessitates use of non-linear response history analysis, with the input ground motion used for the analysis being the best available estimate of shaking at the site of the damaged building. If multiple, similarly representative, records of nearby ground shaking are available it is recommended that multiple analyses should be undertaken, and the results averaged unless comparison to other observable damage suggests that particular shaking records are more appropriate.

Where response history analysis is used to verify that the residual fatigue capacity of reinforcement is sufficient to withstand the MCE for the site (performance measure 2 as defined in section C.3), ground motions representative of the MCE should be chosen in accordance with appropriate guidance for new building design in the same jurisdiction.

Following completion of the response history analyses, fatigue damage should be determined based on either the Coffin-Manson or Koh and Stephens equations as specified in section C.2. Damage summation should be completed using Miner's sum or other appropriate summation method, with effective cycle strain magnitudes calculated following a 'rainflow' counting approach.

C.5 Parametric Analysis to Determine Thresholds Below Which Fatigue Damage is Not Consequential

Based on the approaches outlined in this Appendix, individual and parametric simplified fatigue analyses have been undertaken to identify thresholds below which fatigue damage is expected to be less than 10% of the reinforcement fatigue life (i.e., a Miner's sum not exceeding 0.1).

Output from an example analysis is shown in Figure C-6. This shows:

- the typical displacement history used, comprising 3 cycles per displacement increment with a maximum displacement of 2.0%, and
- the Miner’s fatigue damage sum, in this case determined using Brown & Kunnath’s parameters for No. 8 bars.

The results of parametric analyses undertaken using three different sets of fatigue life parameters are shown in Figures C-7, C-8, and C-9. In each case the variation of fatigue sum is plotted against cantilever aspect ratio (a/h) for different effective plastic hinge lengths. Solid lines show the damage sums calculated including account of non-flexural deformation characteristics, while dashed lines show how the fatigue damage increases with reducing aspect ratio if these sources of deformation are ignored. The results plotted are based on an assumption that the member effective depth is 90% of the total depth, i.e., $d = 0.9h$. Reduced damage sums are estimated if the effective member depth is reduced, e.g., so that $d = 0.8h$.

Considering the solid lines, it can be identified that the fatigue damage sum does not exceed approximately 10% provided the effective plastic hinge length is 0.4h (40% of the member depth) or greater.

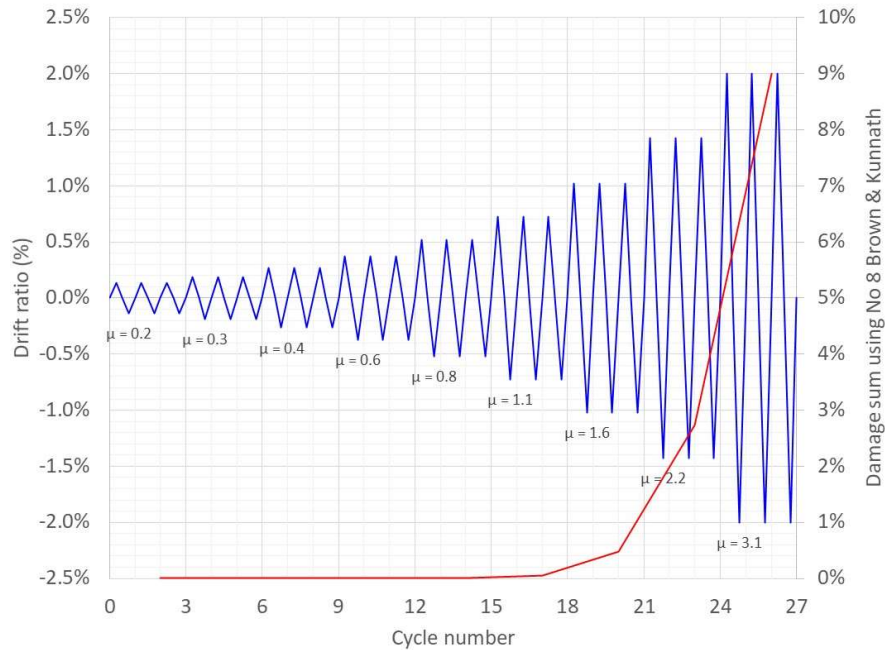


Figure C-6 Fatigue damage progression for cantilever element with aspect ratio of $a/d = 4$, $d/h = 0.9$, and $l_p/h = 0.4$ subjected to maximum drift of 2.0%

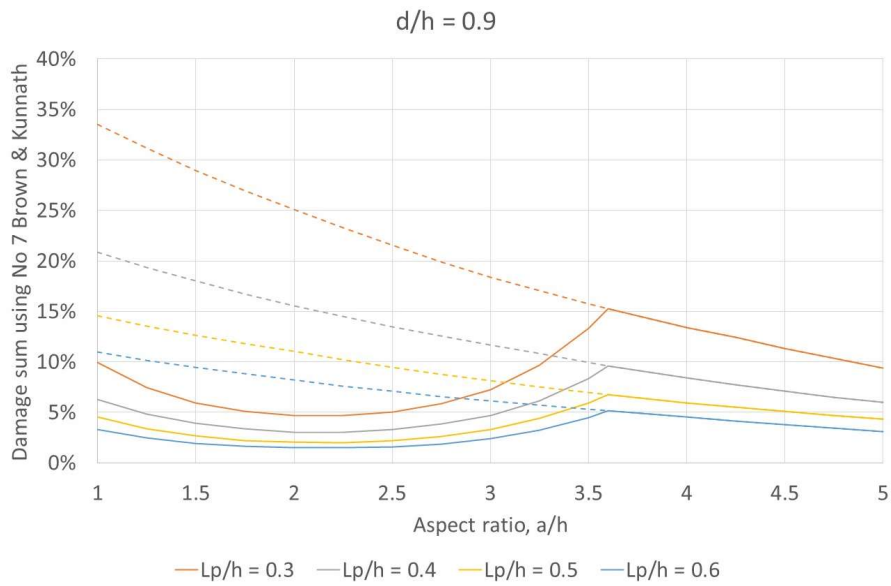


Figure C-7 Impact of aspect ratio and plastic hinge length on fatigue damage sum calculated using Brown and Kunnath parameters for No 7 bars

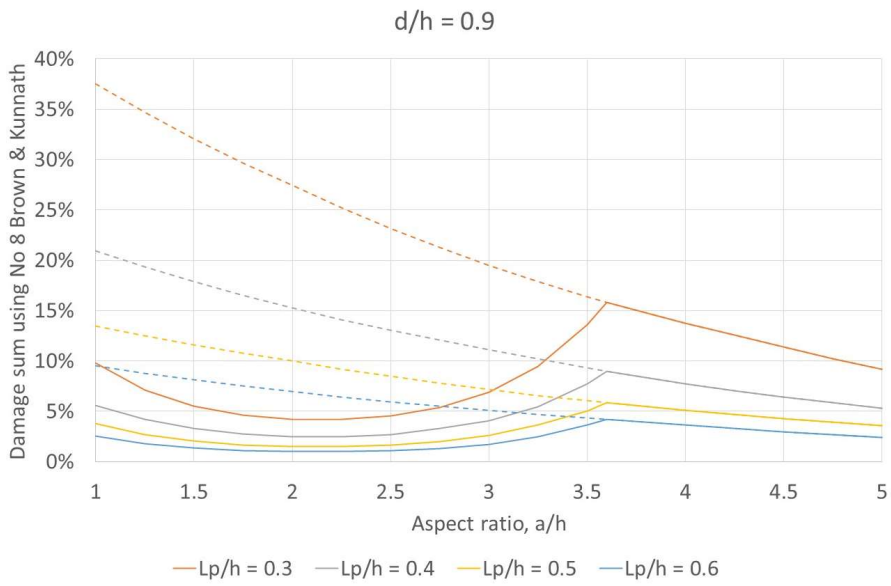


Figure C-8 Impact of aspect ratio and plastic hinge length on fatigue damage sum calculated using Brown and Kunnath parameters for No 8 bars

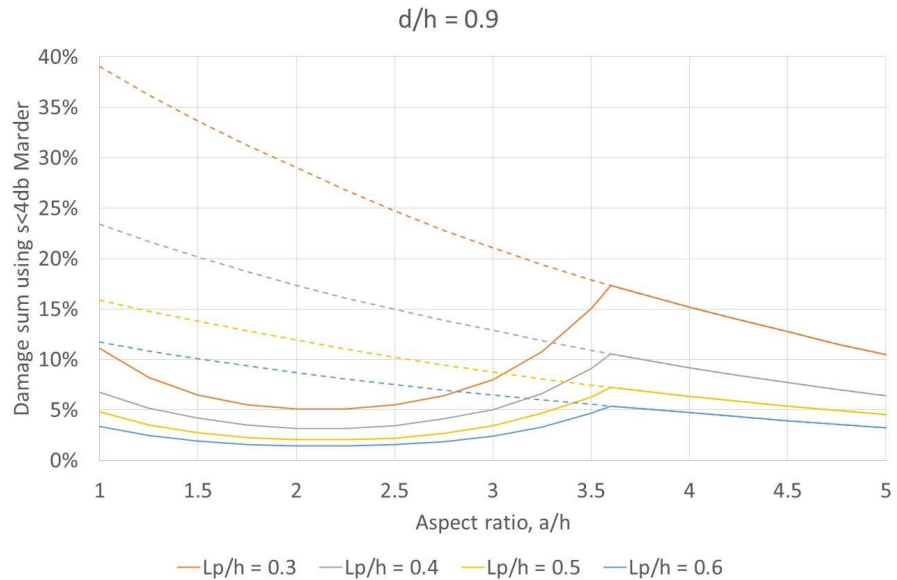


Figure C-9 Impact of aspect ratio and plastic hinge length on fatigue damage sum calculated using Marder fatigue parameters

If non-flexural sources of deformation are ignored or assumed not to occur, the fatigue damage sum increases markedly for aspect ratios where $a/d < 4$ (i.e., in Figures C-7 to C-9 where $a/h < 3.6$). Consideration of these scenarios suggests that in this situation, a fatigue damage sum of approximately 10% or less is predicted provided that:

$$a/d \geq 10 - 15 L_p/h \quad (C-5)$$

where:

a = shear span

d = member effective depth

L_p = effective plastic hinge length

h = member depth

In contrast to the figures above, Figure C-10 shows the outcome of a similar parametric analysis based on Hawileh's parameters for BS460B reinforcing steel. As noted previously these tests were undertaken over a gauge length of only twice the bar diameter, and consequently may be assumed to be unaffected by buckling. It is evident that for this scenario no combination of parameters results in unacceptable levels of fatigue damage. On this basis it is concluded in this study that fatigue damage can be assumed to be inconsequential to future performance if bar buckling has not occurred, and by extension in locations where spalling has not occurred.

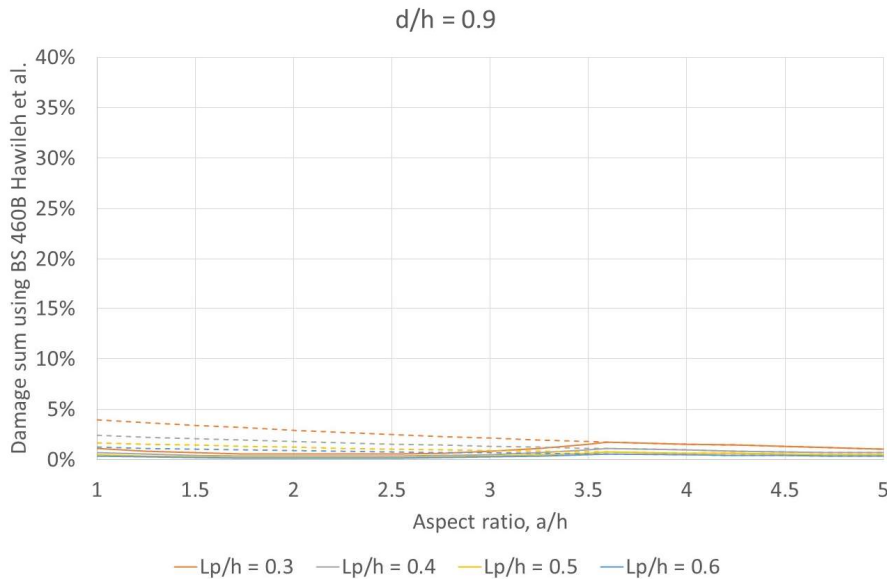


Figure C-10 Impact of aspect ratio and plastic hinge length on fatigue damage sum calculated using Hawileh BS460B fatigue parameters.

C.6 Future Work: Incorporation of Reinforced Concrete Walls

This section outlines the future work needed to address fatigue issues in reinforced concrete structural walls. The goal is not to develop an entirely new appendix for fatigue capacity of walls but to update and expand the approaches in this appendix such that they cover fatigue issues of structural walls and frame members (similar to Appendix H). A significant portion of the material presented in this appendix is generic and can be applied to reinforced concrete walls, with little to no changes. Literature review and parametric studies will be conducted to develop recommendations for plastic hinge length of walls and strain calculations, along with a “deemed-to-comply” approach for various types of walls. The outcome will be used to update the approach outlined in this Appendix.

In the following, the various sections and subsections of this Appendix are briefly described, along with the potential work, if any, needed to address fatigue issues specific to walls.

- C6.1 Overview:** This section indicates the scope of the appendix, which includes recommendations for fatigue capacity of reinforced concrete frame members subjected to earthquakes. A one or two sentences are needed to indicate that the content of the Appendix is also applicable to reinforced concrete walls. If the approach is applied to a specific class of walls, it should be noted here.

- **C.6.2 Fatigue Capacity Models for Reinforcing Bars:** This section focuses solely on fatigue capacity of reinforcing bars, regardless of the element type; therefore, it is applied to reinforcing bars in reinforced concrete walls, and no changes are needed.
- **C.6.3 Definition of Acceptable Levels of Fatigue Damage:** In this section, two performance measures are considered to represent reasonable alternatives for determining whether the residual fatigue life of reinforcement in an earthquake damaged structure is sufficient. This section is also generic (rebar-level) and can likely be applied to reinforcing bars in reinforced concrete walls. In this section or subsequent sections, it should be noted whether the threshold of acceptable fatigue damage (i.e., 10%) is applied to the extreme layer of longitudinal bars or multiple extreme layers (i.e., how many layers of bars need repair?). Wall test results have shown that fracture of the extreme layer of longitudinal bars causes a roughly 20% lateral strength loss from peak strength (i.e., lateral failure), while fracture of the extreme layer of longitudinal bars in a frame member could result in total or significant loss of the lateral strength, depending on how many layers of bars are used. Therefore, it is worthwhile to look into whether the 10% failure damage is appropriate or too conservative for walls.
- **C.6.4 Assessment of Fatigue Degradation**
 - **C.6.4.1 Simplified Fatigue Life Assessment:** This subsection describes a simplified fatigue life assessment approach to determine whether remediation of the reinforcement is required based on an artificial displacement history of the type described in FEMA 461 (FEMA, 2007) for quasi-static cyclic testing. This section might only need minor editorial changes.
 - **C.6.4.1.1 Displacement History:** This subsection describes the displacement history used in the simplified fatigue assessment, which is basically the displacement history described in FEMA 461 (FEMA, 2007), with setting the drift anticipated to have occurred during the damaging earthquake as the maximum drift in the displacement history. To provide a degree of conservatism, the number of cycles per displacement increment is increased from two to three. Since wall buildings generally have shorter periods than frame buildings, it might be worthwhile to investigate whether the 3-cycle per displacement increment is also

appropriate for walls. Other than that, this section is generic, and no changes are likely needed.

- **C.6.4.1.2 Discussion of Strain Calculation:** This subsection provides recommendations for calculation of tensile and compressive strains in frame members. It is largely applicable to walls; however, the issue of using an appropriate plastic hinge length for walls and how to address non-rectangular sections needs to be addressed here. A comprehensive literature of models for wall plastic hinge length is likely needed. Of particular interest is the issue of whether distributed cracking is expected or not. Walls with low longitudinal reinforcement ratios and low axial demands can be particularly susceptible to fatigue failure due to concentration of strain demands at one or two primary cracks. Sensitivity studies are likely needed to address this issue. Additionally, recommendation on simplified approaches to calculate tensile and compressive strains might be needed if a detailed sectional analysis is not performed.
- **C.6.4.2 Recommendations for Detailed Fatigue Damage Assessments:** This subsection is generic and will likely not need any changes.
- **C.6.5 Parametric Analysis to Determine Thresholds Below Which Fatigue Damage is Not Consequential:** In this section, individual and parametric simplified fatigue analyses are undertaken to identify thresholds below which fatigue damage is expected to be less than 10% of the reinforcement fatigue life. The material presented is only applicable to frame members. To develop similar information for walls - i.e., “a deemed-to-comply type approach” given in section 3.3.3.2 of the source report, a ground-up development and parametric studies are needed. For walls, it is expected that there might be more parameters for requiring consideration than for frames.
- **Source Report Chapter 3, Simplified LCF Assessment Procedure:** The simplified assessment procedure of Source Report Chapter 3 and Guidelines Chapter 6 will also need to be reviewed in terms of applicability to walls. In particular, this simplified procedure relies on being able to say that if there is no significant spalling then there is no bar buckling and hence no LCF concerns. This may be valid for typical

walls with sufficient longitudinal reinforcement to develop distributed cracking but may not work for walls with light longitudinal steel where high strains may be concentrated at limited number of cracks. An alternative simplified process will need to be developed for such walls. It is not practical to expect most components to be assessed using the details of Appendix C.

References

- Brown, J., and Kunnath, S. K., 2000, *Low Cycle Fatigue Behaviour of Longitudinal Reinforcement in Reinforced Concrete Bridge Columns*, MCEER-00-0007, Department of Civil and Environmental Engineering, University of Central Florida, Orlando, Florida, pp. 87.
- Brown, J., and Kunnath, S. K., 2004, “Low-Cycle Fatigue Failure of Reinforcing Steel Bars,” *ACI Materials Journal*, Vol. 101, No. 6, pp. 457–466.
- Coffin, L.F., 1953, *A Study of the Effects of Cyclic Thermal Stresses on a Ductile Material*, Knolls Atomic Power Laboratory, Schenectady, New York, pp. 129.
- FEMA, 2007, *Interim Testing Protocols for Determining the Seismic Performance Characteristics of Structural and Non-Structural Components*, FEMA 461, prepared by the Applied Technology Council for the Federal Emergency Management Agency, Washington, D.C.
- Hancock, J., and Bommer, J.J., 2005, “The Effective Number of Cycles of Earthquake Ground Motion,” *Earthquake Engineering & Structural Dynamics*, Vol. 34, No. 6, pp. 637–664.
- Hawileh, R. A., Abdalla, J. A., Oudah, F., and Abdelrahman, K., 2010, “Low-Cycle Fatigue Life Behaviour of BS 460B and BS B500B Steel Reinforcing Bars,” *Fatigue & Fracture of Engineering Materials & Structures*, Vol. 33, No. 7, pp. 397–407.
- Hawileh, R. A., Rahman, A., and Tabatabai, H., 2010, “Evaluation of the Low-Cycle Fatigue Life in ASTM A706 and A615 Grade 60 Steel Reinforcing Bars,” *Journal of Materials in Civil Engineering*, Vol. 22, No. 1, pp.65–76.
- Koh, S. K., and Stephens, R.I., 1991, “Mean Stress Effects on Low Cycle Fatigue for a High Strength Steel,” *Fatigue & Fracture of Engineering Materials and Structures*, Vol. 14, No. 4, pp.413–428.

- Kunnath, S. K., Kanvinde, A., Xiao, Y., and Zhang, G., 2009, *Effects of Buckling and Low Cycle Fatigue on Seismic Performance of Reinforcing Bars and Mechanical Couplers for Critical Structural Members* (CA/UCD-SESM-08-01), University of California, Davis, California.
- Malhotra, P.K., 2002, “Cyclic-Demand Spectrum,” *Earthquake Engineering & Structural Dynamics*, Vol. 31, No. 7, pp. 1441–1457.
- Mander, J. B., Panthaki, F. D., and Kasalanati, A., 1994, “Low-Cycle Fatigue Behaviour of Reinforcing Steel,” *Journal of Materials in Civil Engineering*, Vol. 6, No. 4, pp. 453–468.
- Manson, S.S., 1953, *Behaviour of Materials Under Conditions of Thermal Stress*, Technical Note 2933, Lewis Flight Propulsion Laboratory, Cleveland, Ohio.
- Marder, K., 2018, *Post-Earthquake Residual Capacity of Reinforced Concrete Plastic Hinges (PhD Thesis)*, University of Auckland, Auckland, New Zealand.
- Miner, M. A., 1945, “Cumulative Damage in Fatigue,” *Journal of Applied Mechanics*, Vol. 12, No. 3, pp. 159–164.
- NZSEE, MBIE, EQC, NZGS, and SESOC, 2018, *Technical Proposal to Revise the Engineering Assessment Guidelines - Part C5 Concrete Buildings*, Ministry of Business, Innovation, and Employment, Wellington, New Zealand, pp. 252.
- Opabola, E., and Elwood, K. J., 2020, “Simplified Approaches for Estimating Yield Rotation of Reinforced Concrete Beam-Column Components.” *ACI Structural Journal*, Vol. 117, No. 4, pp. 279–291.
- Opabola, E., Best, T., Elwood, K. J., Hogan, L., and Synge, A. J., 2018, “Deformation Capacity of Reinforced Concrete Beams with a Single Crack,” *Proceedings of the NZSEE Conference*, New Zealand Society for Earthquake Engineering, Auckland, New Zealand, pp. 11.
- Priestley, M.J.N., 1998, “Brief Comments on Elastic Flexibility of Reinforced Concrete Frames and Significance to Seismic Design.” *Bulletin of the New Zealand National Society for Earthquake Engineering*, Vol. 31, No. 4, pp. 246–259.

Priestley, M. J. N., Calvi, G. M., and Kowalsky, M. J., 2007, Displacement-Based Seismic Design of Structures, IUSS Press, Pavia, Italy, pp. 721.

Restrepo-Posada, J. I., 1993, Seismic Behaviour of Connections between Precast Concrete Elements, Department of Civil Engineering, University of Canterbury, Christchurch, New Zealand, pp. 385.

Slavin, C. M., and Ghannoum, W. M., 2016, “Low-Cycle Fatigue Performance of High-Strength Steel Reinforcing Bars.” *ACI Materials Journal*, Vol. 113, No. 6, pp. 803–814.

Zhong, K., and Deierlein, G.G., 2019, *Low-Cycle Fatigue Effects on the Seismic Performance of Concrete Frame and Wall Systems with High Strength Reinforcing Steel* (Final Report CPF Research Project RGA #02-16), Stanford University, Stanford, California, pp. 175.

Appendix D

Stiffness of Damaged and Epoxy-repaired RC Components

D.1 Introduction

Prior earthquake loading is known to reduce the stiffness of RC components. For components not sustaining chord rotations exceeding the safety limit recommended in Appendix A, a portion of this stiffness can be recovered through epoxy injection of cracks. This Appendix provides data to assess the likely reduction in stiffness for damaged or repaired components, thus enabling the serviceability assessment of the performance of a damaged or epoxy-repaired RC frame, as described in Section 3.4.

D.2 Stiffness of Damaged Beam-column Elements

A number of factors contribute to the degradation of stiffness that occurs in moderately damaged reinforced concrete plastic hinges, including cracks and crack closure, bond degradation, concrete degradation, inelastic shear deformations, and the Bauschinger effect. Quantifying the effects of each of these factors on the residual stiffness is not feasible for the purposes of a post-earthquake assessment. Distinction between unloading and reloading stiffness is also impractical. Instead, a single degraded stiffness parameter that is presented as a fraction of the initial secant stiffness to yield, such as the stiffness reduction factors used in FEMA 306, is desirable. This section investigates simple methods for approximating the residual stiffness of moderately damaged plastic hinges.

The definition of secant stiffness used in this study is illustrated in Figure D-1. The stiffness is taken as the secant line between the point at which the loading commences and the first point at which a force threshold (shown as M_n in Figure D-1) is reached in either the positive or negative loading direction. Cycles that occur below the force threshold are not considered in the secant stiffness definition. This definition applies for both the initial and reloading secant stiffness, with the difference being whether the point at which the loading commences is the origin (in the case of initial secant stiffness) or the residual deformation (in the case of reloading stiffness).

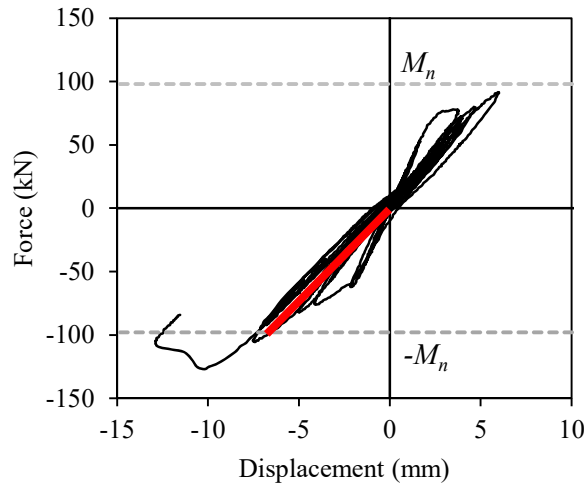


Figure D-1 Definition of secant stiffness (red line) used in this study (Marder et al 2020)

One method of assessing residual stiffness is as a function of the observable damage. Figure D-2 compares total and maximum residual crack width data against reloading stiffness data for the beam specimens by Marder et al (2020). The reloading stiffness is taken as the secant line between the residual deformation (the deformation at which the crack widths were measured) and the first instance of reaching the nominal moment strength M_n . The reloading stiffness is expressed in terms of both kN/mm and using the appropriate ratio of $E_c I_g$ with the theoretical flexural stiffness $3EI/L^3$, where E_c was calculated as $4700\sqrt{f'_c}$ (MPa units). Data corresponding to the stiffness immediately after earthquake loadings are shown in red and data corresponding to cyclic loading are shown in black.

The residual crack width metrics, and particularly the total crack width [Figure D-2(a)], are inversely correlated with the reloading stiffness during cyclic loading, regardless of the prior loading protocol or the level of axial restraint. However, the inverse relationship does not hold for the reloading stiffness immediately after initial earthquake loadings, where higher stiffness values for a given crack width were observed. This implies that a model calibrated on total residual crack width data from cyclic tests may be able to provide a lower-bound residual stiffness following arbitrary earthquake-type loadings.

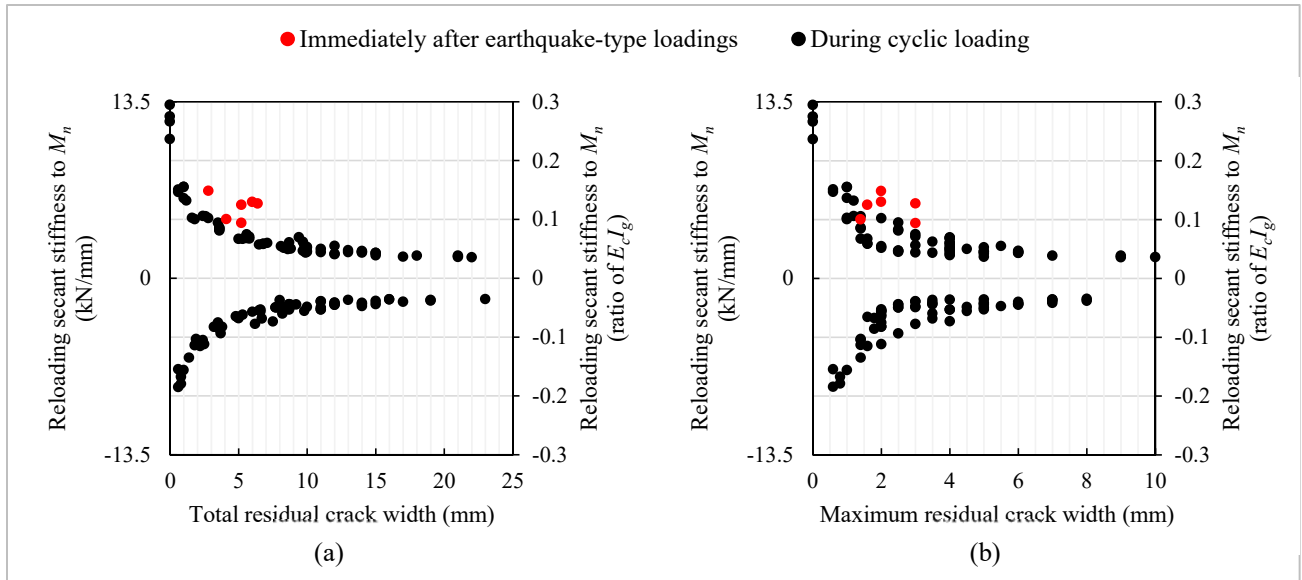


Figure D-2 Reloading stiffness versus (a) total residual crack width and (b) maximum residual crack width

Figure D-3 presents a least-squares power regression model relating total residual crack width to the reloading stiffness of the beam specimens. The model was derived using all total residual crack width data from Marder et al (2020) collected during cyclic loading [i.e., all black data points from Figure D-2(a)]. The total residual crack width is presented as a fraction of the beam depth and the reloading stiffness is presented using the appropriate fraction of $E_c J_g$ in order to give a non-dimensional relationship. The model has a coefficient of determination of 0.93. A simplified version of the model, with less implied precision, is also overlaid on the data.

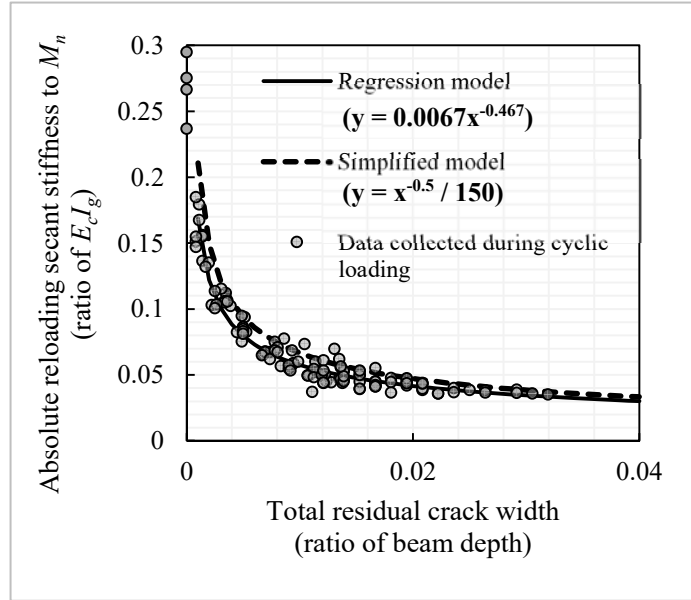


Figure D-3 Least-squares regression power model for total residual crack width versus reloading stiffness

Despite the strong correlation between total residual crack width and stiffness degradation, residual crack width metrics have limitations for informing post-earthquake assessments of residual stiffness. A lack of non-hairline residual cracks does not necessarily indicate that a component was not pushed into the inelastic range. Cracks may close in components subjected to axial compression. In these situations, using the residual crack widths alone as a metric for predicting the residual stiffness would be inappropriate, as zero residual crack width would imply no reduction in the secant stiffness to yield. Such an assessment would be clearly inaccurate, as factors such as bond degradation, concrete degradation, and the Bauschinger effect can affect the residual stiffness regardless of the residual crack width. Furthermore, spalling of cover concrete can preclude the measurement of cracks, making residual crack widths an unusable metric in certain situations. Finally, Figure D-3 shows that a large proportion of the stiffness degradation occurred due to relatively small total residual crack widths, on the order of 0.5% of the beam depth. Identification of such minor cracking in all plastic hinges of a moment frame building may be impractical in post-earthquake situations. Distinguishing earthquake-induced cracking from cracks due to other causes (e.g., shrinkage) may also present problems.

An alternate method of assessing residual stiffness is to use a function of the estimated deformation demands during the damaging earthquake. Use of deformation demand parameters to define the residual stiffness is a commonly employed method in non-linear hysteretic models. Figure D-4

illustrates the peak-oriented reloading stiffness model, which has found widespread use in modelling of reinforced concrete plastic hinges (e.g., Clough and Johnston, 1966; Takeda et al., 1970).

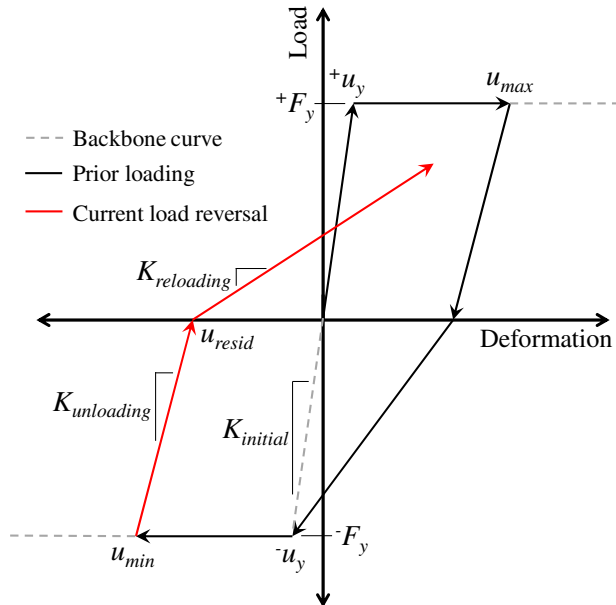


Figure D-4 Peak-oriented reloading stiffness model for an elastic-perfectly plastic element

Figure D-5(a) shows that the reloading stiffness response of the Marder et al (2020) beam specimens was strongly correlated with the difference between the residual drift and the prior peak drift in the reloading direction (i.e., the deformation parameters that define a peak-oriented reloading stiffness model). These results support the use of peak-oriented stiffness models; however, obtaining sufficient knowledge of the deformation history in order to calculate a peak-oriented stiffness is not feasible in post-earthquake situations. Figure D-5(b) shows that, when the maximum prior drift demand is used as a deformation metric, the reloading stiffness degradation of the beam specimens during cyclic loading followed a consistent pattern, but this pattern did not hold for the first half-cycle immediately following the initial earthquake loadings (similar to the finding for the residual crack width metrics). Data points corresponding to the reloading stiffness measured immediately after earthquake-type loadings have notably higher stiffness values for a given peak drift demand. Again, this implies that while cyclic stiffness data may not be representative of residual stiffness following arbitrary earthquake loadings, development of a lower-bound stiffness model by calibrating to cyclic test data may be appropriate.

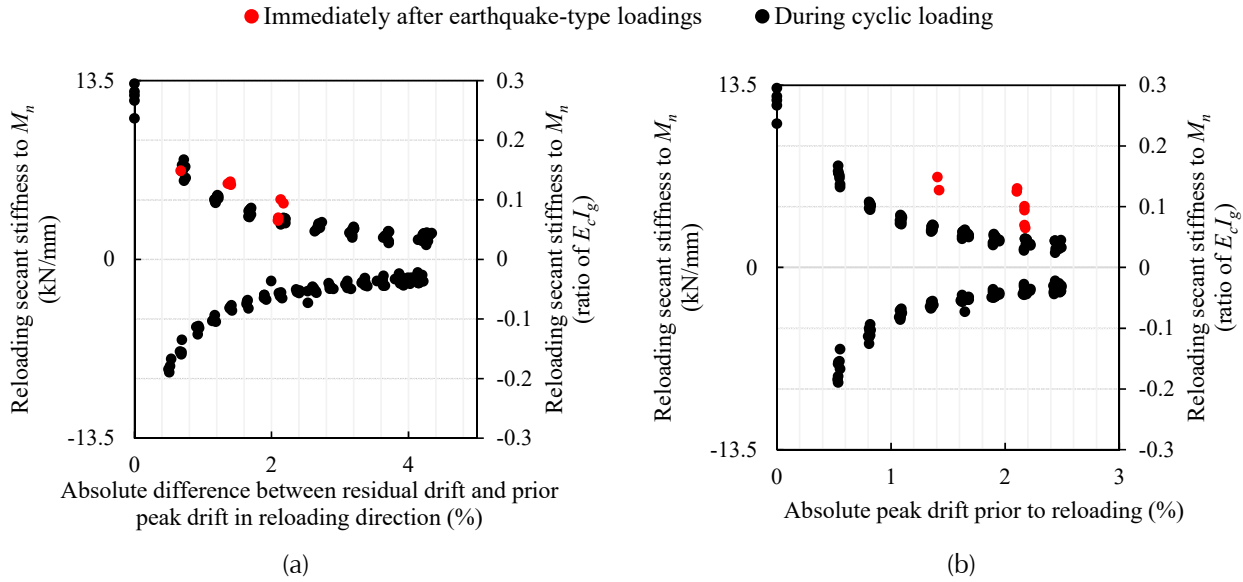


Figure D-5 Reloading stiffness versus (a) the deformation demand metrics used to define a peak-oriented model, and (b) peak drift demand

The data presented in Figure D-5(b) came from nominally identical beam specimens, and therefore similar results would be obtained using any lateral deformation metric. Marder (2018) identified that for components with varying yield rotations, displacement ductility provided a better correlation with reloading secant stiffness than did peak drift demand. Di Ludovico et al. (2013) previously used a database of 23 reversed-cyclic column tests to derive the expression $K_r/K_y = 1 - (1.07 - 1.15\mu^{-0.92})$, where K_r is the peak-to-peak residual stiffness, K_y is the initial secant stiffness to yield, and μ is the displacement ductility. The empirical model proposed by Di Ludovico et al. (2013) is very similar to the expression $K_r/K_y = 1/\mu$, which can be derived from the peak-to-peak stiffness of an elastic-perfectly plastic system subjected to symmetric reversed-cyclic loading, as demonstrated in Figure D-6. Furthermore, $K_r/K_y = 1/\mu$ was previously proposed by Gulkan and Sozen (1974) for estimating secant stiffness of a substitute structure and expected to be a conservative estimate of residual stiffness for an earthquake-damaged plastic hinge.

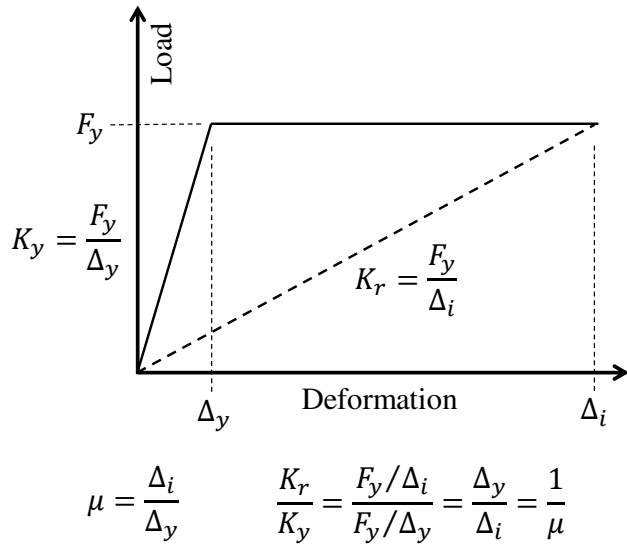


Figure D-6 Relationship between origin-to-peak stiffness degradation and ductility demand

In order to investigate the applicability of the $K_r/K_y = 1/\mu$ model as a lower-bound stiffness following arbitrary earthquake loadings, additional relevant experimental data were required for validation. The following information was deemed necessary in each experiment: (i) an initial arbitrary earthquake-type loading, (ii) a subsequent loading to allow assessment of residual stiffness, and (iii) a limited residual drift (<1.0%) after the initial loading. The limit on residual drift is to prevent the direction of reloading from unduly affecting the measured residual stiffness. As shown in Figure D-4, increased residual drifts can result in increased differences between ‘unloading’ and ‘reloading’ stiffness values in plastic hinges exhibiting a peak-oriented reloading stiffness. Reloading due to earthquake shaking can occur in either direction (i.e., either the ‘unloading’ or ‘reloading’ stiffness could occur), and the measured residual stiffness is therefore sensitive to the residual drift. The intent of the $K_r/K_y = 1/\mu$ model is to give an approximate value of residual stiffness that neglects the distinction between unloading and reloading behaviour. Data used for validation of this model therefore require low residual drifts prior to measurement of residual stiffness.

Shake table tests that involve the application of multiple earthquake ‘runs’ to a test specimen satisfy each of these three criteria. A dataset of relevant shake table tests on ductile reinforced concrete columns was compiled, consisting of four test programs (Arias Acosta, 2011; Hachem et al., 2003; Laplace et al., 1999; Schoettler et al., 2015), eight specimens, and 34 runs. If any specimen exhibited more than moderate damage (e.g., crushing of core concrete or buckling of longitudinal reinforcement) all future runs on that specimen were omitted from the analysis. All specimens were cantilever

columns with a circular or oval cross-section and spiral transverse reinforcement, typical of bridge column construction in seismically active areas of the United States.

Figure D-7 shows the normalized stiffness versus the absolute maximum ductility demand reached in any preceding run for all columns in the dataset. (Estimation of the normalized stiffness based on plotted data was required in cases where numerical data was not available.) The stiffness data immediately following earthquake loadings for the Marder et al. beam specimens (previously shown as the red data points in Figure D-5) are also included in Figure D-7. The stiffness was defined as the secant line between the residual drift and the first instance of reaching 80% of the maximum base moment. In Figure D-7(a), the residual stiffness values were normalized against the initial secant stiffness to 80% of the maximum base moment, which is used here as the measured secant stiffness to yield (similar to the approach used by Paulay and Priestley, 1992, and Elwood and Eberhard, 2009). The displacement ductility of the columns was calculated using a yield rotation that was approximated as the rotation corresponding to the first instance of reaching 80% of the maximum base moment. (The yield rotation of the beam specimens was visually estimated, as sharp changes in the load-deformation response occurred at the first yield of extreme tension steel.)

In practice, a measured initial secant stiffness to yield is not available to normalize against. In Figure D-7(b), the residual stiffness values are normalized against an initial secant stiffness calculated as a ratio of the gross flexural stiffness, as per the provisions of ASCE 41-17 (note that $0.3E_cI_g$ was used in all cases, as all the test specimens had initial axial load ratios of approximately 0.1 or below). A measured yield rotation is also not available for calculating the displacement ductility in practical situations; a theoretical formulation must instead be used. The displacement ductility shown in Figure D-7(b) was determined using a yield rotation calculated from Equation D-1. (It is noted that this formulation significantly under-predicted the yield rotation of the beam specimens.)

$$\theta_y = \frac{M_y L}{3E_c I_{eff}} \quad (\text{Equation D-1})$$

where θ_y is the yield rotation, M_y is the yield moment (taken as the nominal moment M_n using lower characteristic strengths), L is the shear span length, E_c is the Young's Modulus of the concrete (taken as $4700\sqrt{f'_c}$), and I_{eff} is the effective moment of inertia, taken as a fraction of the gross section moment of inertia based on the recommendations of ASCE 41-17.

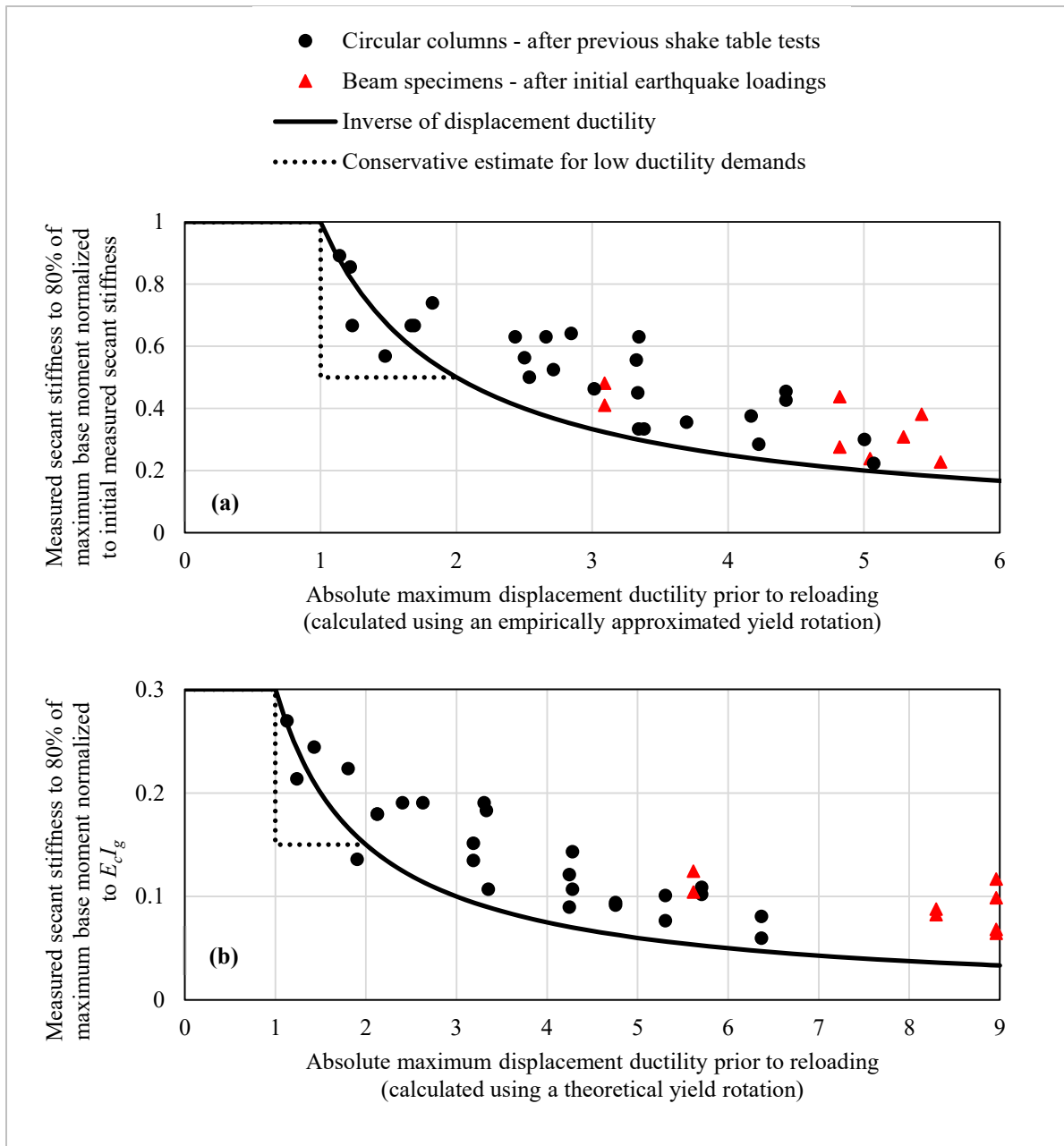


Figure D-7 Proposed stiffness degradation relationship versus experimental stiffness values normalized against (a) an empirical initial secant stiffness and yield rotation, and (b) an initial secant stiffness as a function of $E_c I_g$ and a theoretical yield rotation.

Figure D-7 shows that the proposed $K_r/K_y = 1/\mu$ equation gives a lower-bound prediction of the residual stiffness of the test specimens following arbitrary earthquake-type loadings. The exception to this is at low displacement ductility demands (less than 2.0), likely due to the variability involved in quantifying the yield deformation of reinforced concrete columns. Furthermore, the model is sensitive to estimated ductility demand at low values of ductility (i.e., stiffness reduction varies by a factor of 2

between ductility of 1 and 2). Given the uncertainty involved in estimating the displacement ductility in post-earthquake situations, the stepwise function shown in Figure D-7 may be considered a more appropriate option for estimating a lower-bound residual stiffness in this low ductility region. This approach suggests that any component which is estimated to have been subjected to a displacement ductility greater than 1.0 should be considered to have a residual stiffness that does not exceed 50% of its initial secant stiffness to yield. Thus, a lower-bound estimate of residual stiffness as a function of displacement ductility is given by Equation D-2.

$$\frac{K_r}{K_y} = \begin{cases} 1.0, & \mu < 1.0 \\ 0.5, & 1.0 \leq \mu \leq 2.0 \\ 1/\mu, & \mu \geq 2.0 \end{cases} \quad (\text{Equation D-2})$$

It is important to note that the data in Figure D-7 do not account for the full variability that exists in post-earthquake situations. While variations in the prior loading history and the theoretical versus empirical initial stiffness and yield rotation are accounted for, the variation in the estimated versus actual peak drift demand are not. Estimation of the ductility demand involves considerable uncertainty as it relies on the judgement of the assessor or a numerical model of the building (see Section 3.2). The use of a displacement ductility of 1.0 as the onset of the stepwise function is useful, as non-hairline residual crack widths can be used as indicators that yielding of the longitudinal reinforcement has occurred. However, a lack of non-hairline residual crack widths does not necessarily indicate a lack of yielding in columns, or other members subjected to axial compression.

D.3 Stiffness of Epoxy-repaired Frame Components

The database on the reparability of moderately damaged frame elements in Appendix E outlines the effectiveness of epoxy repairs on initial stiffness recovery. A series of beams, columns, and joints were assessed, and appropriate stiffness recovery factors were recommended in Section E.6.1 of Appendix E.

D.4 Cyclic Stiffness Degradation in Ductile Beam Elements

Data from two of the beam tests in the repair database of Appendix E were used to investigate the rate of degradation in stiffness during repeated inelastic loading. Data was obtained from studies by Marder et al. (2020) and Sarrafzadeh (2021) which performed epoxy repairs on moderately damaged ductile beams. Results and discussions for each study is provided below.

D.4.1 Methodology for Cyclic Stiffness Degradation Calculation

Assessments of post-repair stiffness in Appendix E was based on backbone specimen behavior, used to quantify the extent to which epoxy injection recovered specimen initial stiffness to yield, with respect to undamaged conditions. Further understanding of the performance of repaired structures under varying levels of earthquake shaking can be achieved through analyzing the cycle-to-cycle stiffness degradation of repaired and unrepaired components. In this section a secant stiffness value will be determined for each loading step applied to specimens. This will allow for the step-by-step variations in stiffness to be assessed, allowing differentiation between the variations in stiffness under small and large amplitude displacement demands. This is particularly important when attempting to differentiate between stiffness of components under serviceability or design level shaking following repair.

The results presented in this chapter are based on the calculation of stiffness throughout the application of cyclic loading protocols. Secant stiffness to 70% of peak specimen strength is calculated at each displacement cycle in line with the methodology used in Appendix E and component databases such as the ACI 369 Rectangular Column Database (Ghannoum et al. (2015)). Where smaller amplitude cycles did not reach or exceed the 70% peak strength threshold for each specimen, the secant stiffness to peak was calculated for those individual cycles. This is shown below in Figure D-8 where the determination of stiffness for the first four positive loading cycles of specimen LS-CYC from Sarrafzadeh (2021) is shown. This figure demonstrated the use of the 70% of peak force point for cycle 4 (Figure D-8d) while the previous cycles were determined based on the peak force achieved in the individual cycle, which were all below the 70% threshold. In addition, this figure demonstrates that secant stiffness values were determined based on the residual deformation at zero force at the start of each cycle.

Results in this chapter are presented for cyclic loading in the positive loading direction only. As cyclic loading protocols were always initiated with loading in the positive direction, this limited the impact of loading and residual deformations following negative displacement cycles on stiffness results, particularly during the initial half cycle at each new peak displacement cycle. Despite this, the trends and results outlined in this section are expected to hold and apply regardless of the direction of loading based on data presented by Marder (2018).

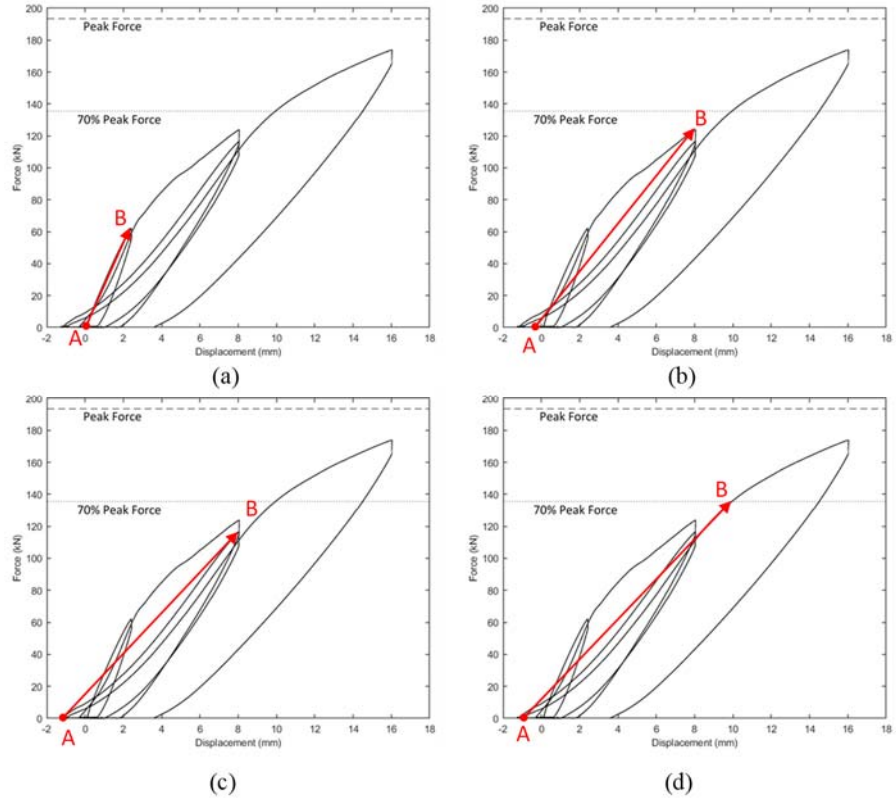


Figure D-8 Determination of cycle-to-cycle stiffness values based on the first four cycles in the positive loading direction for specimen LS-CYC from Sarrafzadeh (2021). (a) Cycle 1 (b) Cycle 2 (c) Cycle 3 (d) Cycle 4.

D.4.2 Component Stiffness Degradation

Throughout this section the calculated stiffness values will be presented as a flexural rigidity, in line with recommendations of ASCE-41 and Equation D-1 and Equation D-2.

$$\text{Flexural Rigidity} = \alpha \cdot K \quad (\text{D-1})$$

$$\alpha = \frac{a^3}{3E_c I_g} \quad (\text{D-2})$$

Where K is the calculated stiffness value in kN/mm based on the methodology outlined in Section D.4.1, a is the shear span of the specimen, E_c is the concrete modulus of elasticity calculated in accordance with NZS 3101:2006 (design code for the tested specimens) and I_g is the second moment of area of the specimen's cross section.

D.4.3 Marder et al. (2020)

Marder et al. (2020) conducted epoxy-injection repairs on moderately-damaged RC ductile beam specimens. The repaired beams were part of a set

of 17 beam specimens tested by Marder et al., under a variety of initial conditions and loading protocol. This included the testing of beams under axial elongation restraint, using spring loaded systems which mimicked the restrained elongation of internal frame beams. Further details of this restraint system can be found in Marder (2018). Specimens were tested under single curvature using variations of loading protocols as presented in Figure D-9. The force-displacement data for 10 of these beams is utilized here to assess their stiffness degradation, as listed in Table D-1. While the focus of this section is on epoxy repaired beams, comparisons are made with differing sets of specimens to investigate the impact of variations in loading rate, restraint condition, loading protocol, and initial conditions on the stiffness degradation of ductile RC beams as well.

Figure D-10 presents results for specimens which were tested under loading categories A and B (Table D-1), where cyclic loading protocols were applied to failure from an undamaged state. Figure D-10a compares results for specimens with varying loading rates and restraint conditions. Dynamic loading rate and axial restraint appear to cause a slight increase in cyclic stiffness up to 1% drift, however the variations are not significant with a peak increase of 4% in comparison to the static unrestrained specimen.

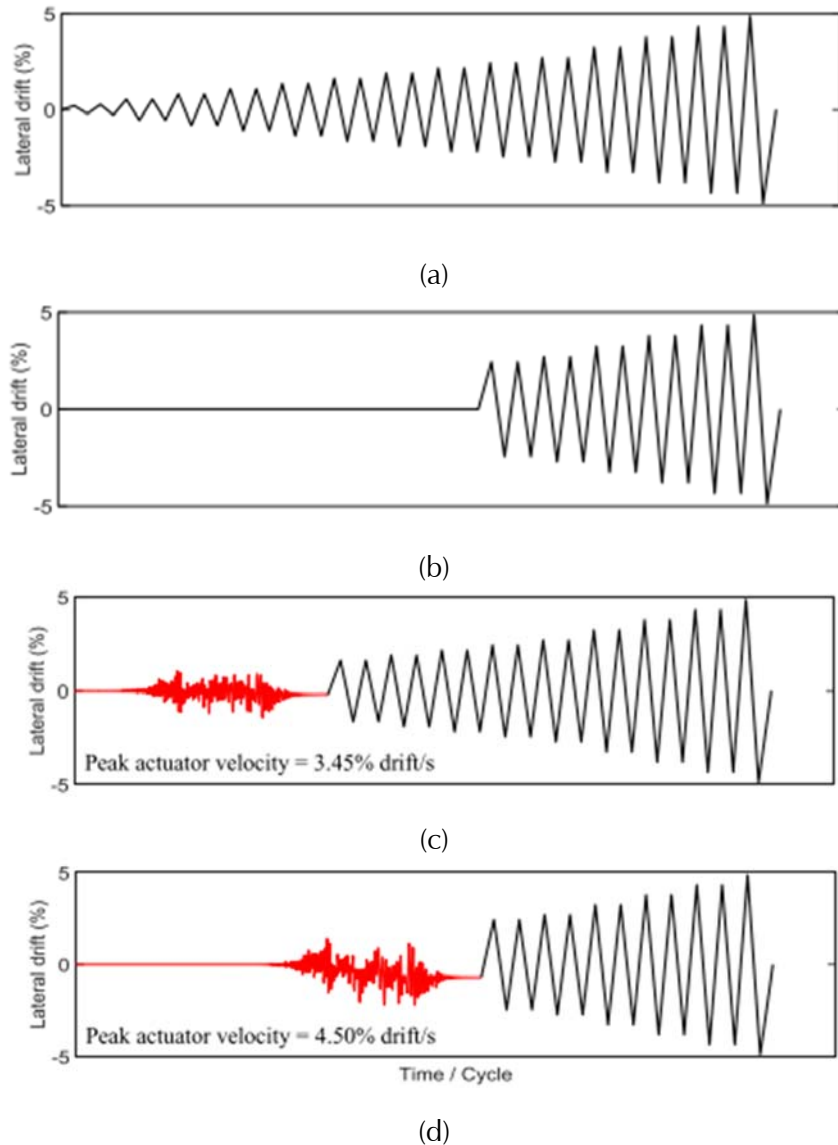


Figure D-9 Loading Protocols of analyzed specimens from Marder et al. (2020) corresponding to loading categories in Table D-1 for specimens (a) CYC, CYC-DYN, and CYC-LER (b) CYC-NOEQ (c) LD-1 and LD-1-R (d) LD-2, LD-2-R, LD-2-LER, and LD-2-LER-R.

Figure D-10b compares the results for variation in loading protocol. Stiffness degradation is shown for a standard cyclic loading protocol (specimen CYC) and the same loading protocol omitting all cycles at or below 2.2% drift (specimen CYC-NOEQ). Following the first cycle at 2.4% drift for specimen CYC-NOEQ, both the stiffness and the rate of cyclic stiffness degradation for the two specimens is very similar, indicating that the cyclic stiffness of the specimens is primarily dependent on the peak demands applied to the component and variations in cycles below the peak did not appear to have an impact. In Figure D-10b, the initial cycle of specimen CYC-NOEQ is similar

in stiffness with the second cycle of specimen CYC. These stiffness values were determined at a drift demand of 0.2% for the CYC specimen and 2.4% for the CYC-NOEQ specimen. These results indicate that it may be more appropriate to use the same effective stiffness in analysis regardless of the considered loading case or level of shaking i.e., serviceability or ultimate limit state loading scenarios.

Table D-1 Testing parameters for beams included from Marder et al. (2020)

Specimen ID	Loading Rate	Loading Category*	Axial Elongation Restraint (Y/N)	Epoxy Repair (Y/N)	a/D
CYC	Static	A	N	N	3.58
CYC-NOEQ	Static	B	N	N	
CYC-LER	Static	A	Y	N	
CYC-DYN	Dynamic	A	N	N	
LD-1		C	N	N	
LD-1-R			N	Y	
LD-2	Dynamic	D	N	N	
LD-2-R	+		N	Y	
LD-2-LER	Static		Y	N	
LD-2-LER-R			Y	Y	

*A Standard cyclic loading to failure.

B Standard cyclic loading to failure, excluding all cycles at or below 2.2% drift.

C Dynamic loading with a peak demand of 1.4% drift, followed by cyclic loading to failure with cycles above 1.4% drift. Repairs applied following dynamic loading where applicable.

D Dynamic loading with a peak demand of 2.2% drift followed by cyclic loading to failure with cycles above 2.2% drift. Repairs applied following dynamic loading where applicable.

Figure D-11 compares results for specimens which had simulated earthquake damage or repair (LD-1, LD-2, LD-2-LER). The results for each set of damaged and repaired beams are compared against an equivalent undamaged cyclic specimen. This corresponded to specimen CYC where unrestrained beams were tested, and specimen CYC-LER where specimens were tested with axial restraint.

Plots showing the results for the LD-1, LD-2 and LD-2-LER specimen sets are shown in Figure D-11a to c, respectively. The results for the post-repair backbone stiffness of these specimens were previously included in Appendix E, demonstrating that epoxy injection was able to recover ~90% of their undamaged backbone stiffness. Here the cyclic degradation behaviour of these specimens is outlined. The same trend was observed in all three sets of specimens. Once again, a clear benefit from the epoxy injection is shown during the first cycle following repair. This initial cycle is the first cycle above the prior peak demands applied during the earthquake loading.

Following this initial loading cycle, the behaviour of the repaired specimen converges with that of the undamaged specimen with little deviations observed from this point onwards.

The same loading protocol was applied to the damaged specimens. While the stiffness of the first half cycle of the damaged specimens following the earthquake-loading was 40-60% of the repaired specimen, it exceeds the undamaged cyclic specimen at the same deformation demand by 40-50%. Di Ludovico et al. (2013) and Marder (2018) noted this observation where the initial stiffness following an arbitrary loading sequence was slightly higher than a cyclic loading protocol with the same peak deformation demand. While Figure D-10b indicated that the peak demands were directly responsible for the cyclic stiffness, the results here point to a contribution from the cumulative impact of consecutively larger loading cycles resulting in a lower stiffness than an arbitrary earthquake type loading. This was reflected in the results presented in Section D.2 and Figure D-7 where a conservative estimate of post-earthquake secant stiffness was presented using data generated from backbone analysis. It should also be noted that the cyclic stiffness following the first half cycle of loading was the same for all specimens once the prior peak was exceeded and the continuation of the same cyclic loading protocol was applied.

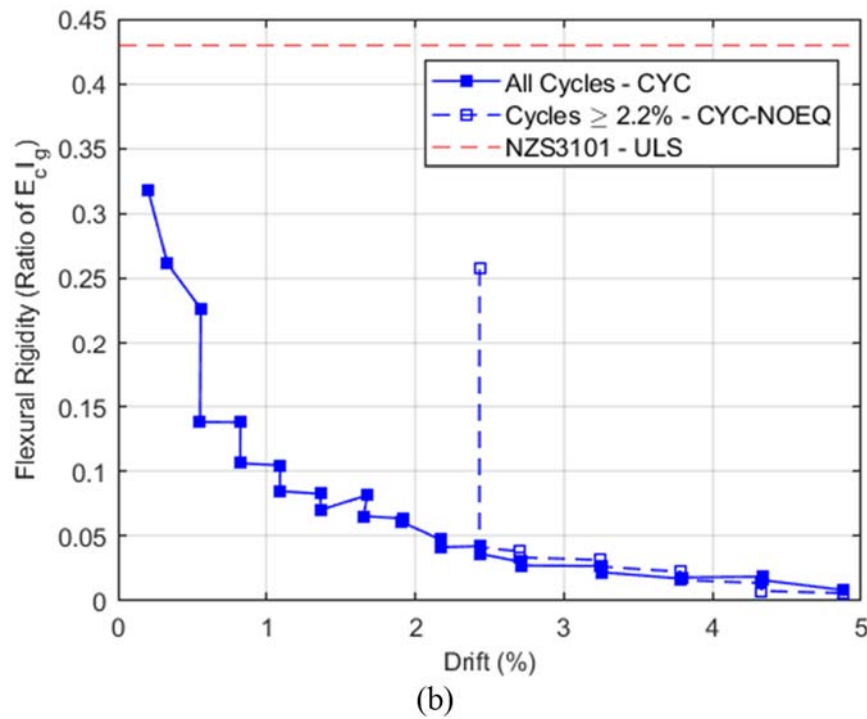
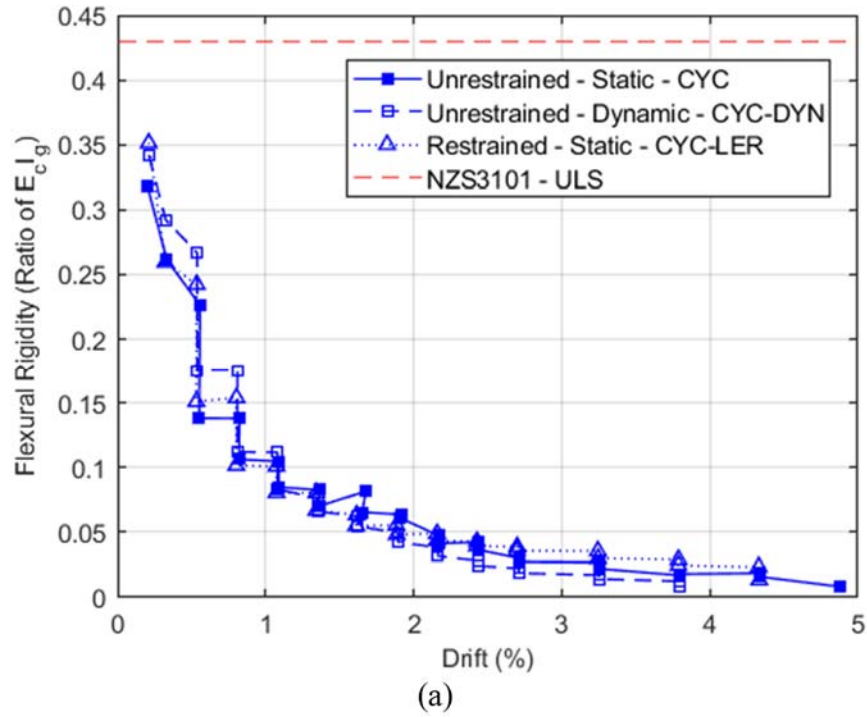


Figure D-10 Stiffness degradation for specimens tested with cyclic loading protocols by Marder (2018). (a) Comparison of static unrestrained, dynamic unrestrained and static restrained conditions (b) Comparison of variations in initial cycle displacement amplitude.

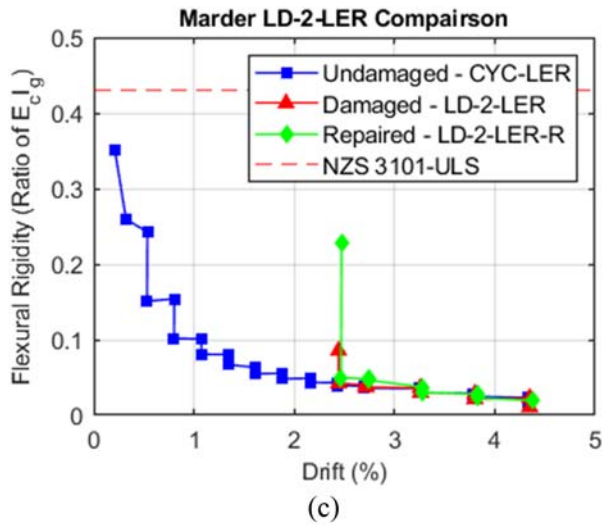
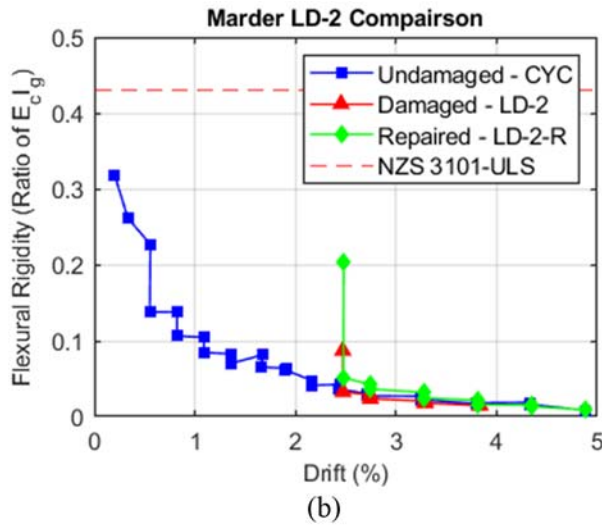
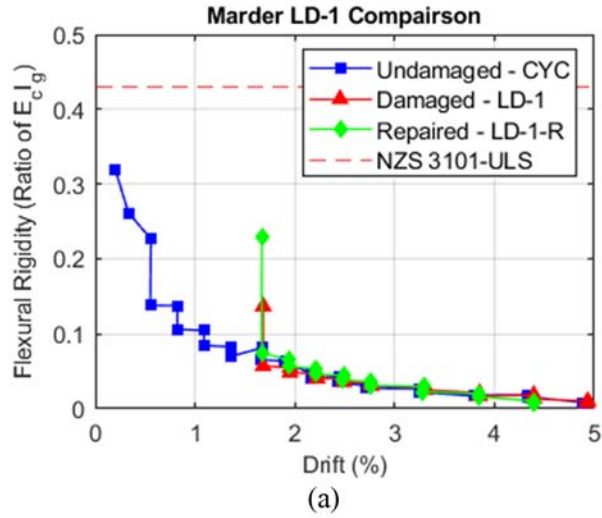


Figure D-11 Cyclic stiffness degradation under undamaged, damaged, and repaired conditions from Marder (2018) for (a) LD-1 (b) LD-2 (c) LD-2-LER specimen sets.

D.4.4 Sarrafzadeh (2021)

In this section, cyclic stiffness degradation for ductile RC beams tested by Sarrafzadeh (2021) is outlined. These tests also assessed the impact of earthquake damage and epoxy injection on ductile RC beam specimens, with lower aspect ratios than those tested by Marder (2018). Two sets of beams, LS (long span) and SS (short span) were tested under single curvature with shear span to depth (a/D) ratios of 2.94 and 2.48, respectively as outlined in Table D-2. In both sets of specimens, standard cyclic loading was used to tests undamaged specimens. In the remainder of specimens, a dynamic earthquake history was used to simulate damage, followed by a cyclic loading protocol to failure. Repaired specimens were treated with epoxy crack injection between the dynamic and cyclic loading protocols. Both applied loading protocols are shown in Figure D-12. The beams were constructed with a cold joint between the specimen and foundation blocks, representing the typical construction procedure of pre-cast beams and cast in-situ joints and columns. The beams were observed to be governed by bond-slip deformation, with the primary crack at the beam-foundation interface being along the cold-joint, while distributed shear-flexure cracking was also observed in the plastic hinge region.

Table D-2 Testing parameters for beams from Chapter 3.

Specimen ID	Loading Rate	Loading Category*	Epoxy Repair (Y/N)	a/D
LS-CYC	Static	A	N	2.94
LS-EQ	Dynamic + Static	B	N	
LS-R			Y	
SS-CYC	Static	A	N	2.48
SS-EQ	Dynamic + Static	B	N	
SS-R			Y	

*A Standard cyclic loading to failure.

B Dynamic loading with a peak demand of 2.5% drift, followed by cyclic loading to failure. Repairs applied following dynamic loading where applicable.

A primary point of difference in the loading protocol in comparison to the Marder et al. (2020) beams is the application of all cycles in the cyclic loading protocol, following the simulated earthquake damage. This allows for observations of specimen behaviour at lower amplitude cycles following repair or earthquake damage. The peak demands during the dynamic earthquake loading for both sets of specimens was 2.5% drift. The results for the LS and SS specimens are shown in Figure D-13a and b respectively.

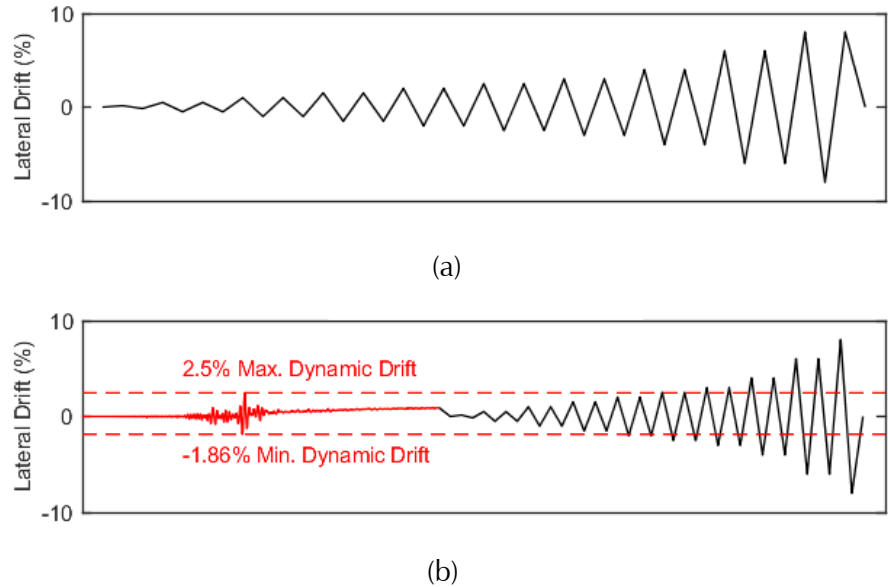


Figure D-12 Loading Protocols of analyzed specimens from Sarrafzadeh (2021) corresponding to loading categories in Table D-2 for specimens (a) LS-CYC and SS-CYC (b) LS-EQ, LS-R, SS-EQ, and SS-R.

Like the results from the previous section, the cyclic stiffness of the specimens, regardless of initial conditions converged, once the prior peak displacement demands of the earthquake loading (2.5%) was exceeded. This also applies to the rate of stiffness degradation. The primary differences are observed in the loading cycles below the prior peak demands. Damaged specimens LS-EQ and SS-EQ were consistently lower in stiffness and showed fluctuations in stiffness up to 1.5% drift. This can be attributed to the significantly pinched hysteretic behaviour observed in these specimens up to 1.5% drift and is demonstrated below in Figure D-14, where above 1.5% the pinching is less pronounced. These specimens were loaded around the original point of zero displacement, despite having a residual deformation of approximately +0.5% drift. As such, a softening effect is observed, particularly during positive cycles below 1% drift which contributed to the unusual cyclic stiffness results at lower displacements. Above 1.5%, a gradual stiffness degradation is observed, converging with the undamaged and repaired specimens at 2.5% drift.

The impact of the epoxy injection during cycles below prior peak earthquake demands is also evident in Figure D-13. While undamaged specimens observed a significant drop off following initial loading due to cracking, a lower rate of degradation is observed in repaired specimens. Repaired specimens saw a 39% reduction in stiffness up to drift of 1.5% while equivalent undamaged specimens saw a 70-75% reduction in stiffness over

the same deformation range. The cumulative reduction in initial stiffness for all undamaged and epoxy-repaired specimens is presented below in Figure D-15. From this plot it is evident that up to 1%, the epoxy-repaired specimens had a significantly lower rate of stiffness reduction in comparison to the undamaged specimens. The rate of stiffness reduction is visibly increased above 1% drift in the epoxy repaired specimens, resembling a more similar rate of stiffness reduction to the undamaged specimens.

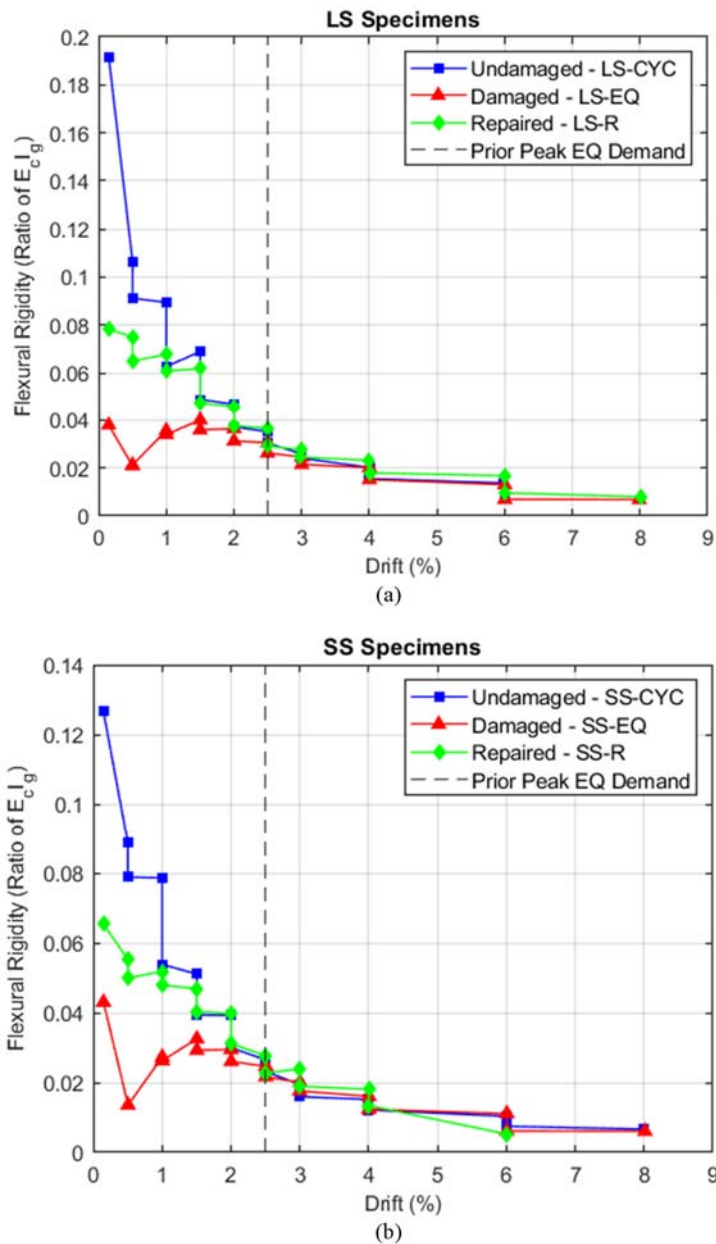


Figure D-13 Cyclic stiffness degradation plots from Chapter 3 test results for (a) LS and (b) SS specimen sets based on initial undamaged, damaged, and repaired specimen conditions.

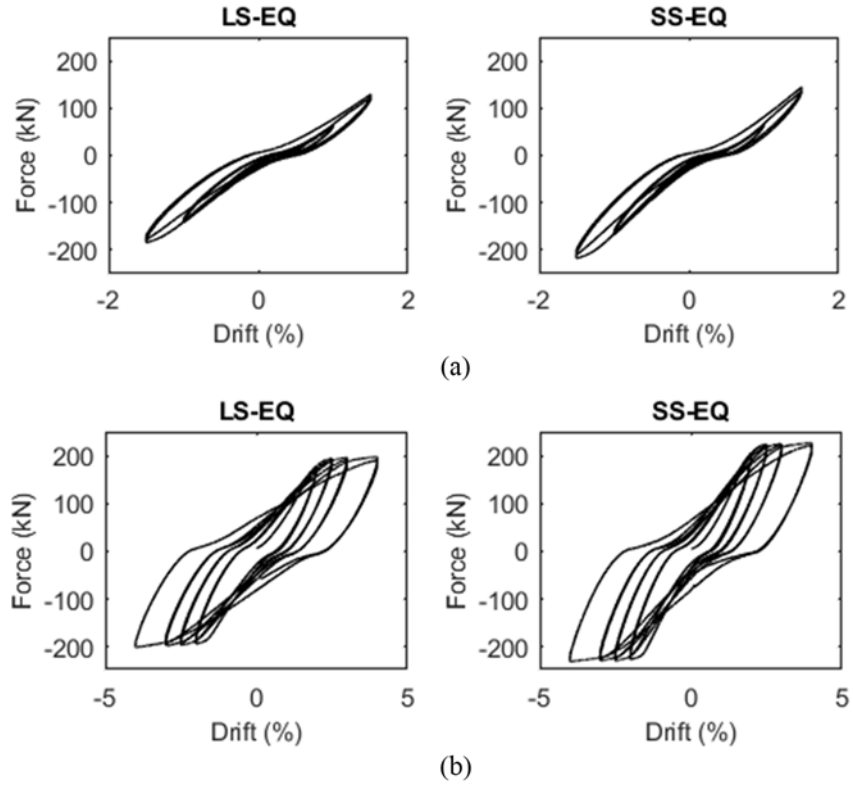


Figure D-14 Hysteresis plots for damaged LS and SS specimens showing cycles at (a) 0-1.5% and (b) 2% and above.

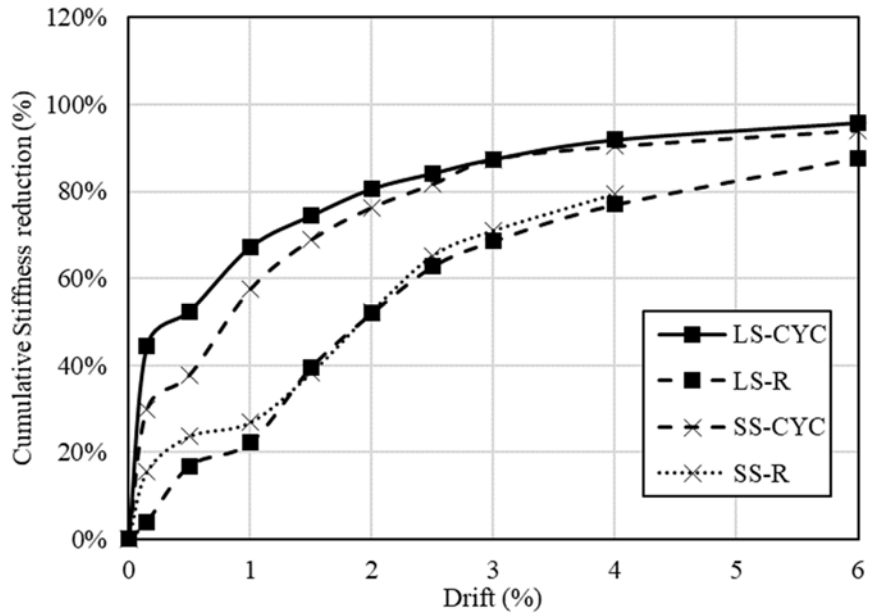


Figure D-15 Cumulative reduction in cycle-cycle stiffness for undamaged and epoxy-repaired beams.

D.5 Discussion and Recommendations

Cycle-to-cycle stiffness degradation data from ductile RC beam specimens was utilized in this chapter to better understand the impact of epoxy-repairs on the performance of frame elements under varying amplitudes of seismic loading. The results from the study by Marder et al. (2020) showed that while epoxy-repairs increased the initial stiffness of moderately-damaged ductile beams, once the prior peak demands from the damaging earthquake were exceeded, the stiffness and the rate of degradation for repaired and undamaged specimens converged. The same was observed with damaged specimens which had the same stiffness and rate of degradation as the undamaged specimens, once the prior peak demands were exceeded. Analyzing the specimens from Sarrafzadeh (2021) which included the application of a full cyclic loading protocol following damage and repair, the same general conclusions were observed, regardless of specimen aspect ratio. The application of smaller amplitude cycles showed that epoxy-repaired specimens had a lower rate of stiffness degradation during small amplitude loading cycles below 1% drift. The stiffness and rate of stiffness degradation of undamaged and epoxy-repaired specimens was seen to converge following cycles at 1% drift, while the peak earthquake demands from the damaging earthquake loading was 2.5% drift. The same observation was not made with damaged specimens which had consistently lower stiffness until the prior peak earthquake demands of 2.5% drift were exceeded. Variations in loading rate, level of axial elongation restraint and loading protocols did not have an impact on the stiffness degradation behaviour of specimens subjected to cyclic loading protocols. Based on these results, and as summarized in Table D-3, the following recommendations are made, for the consideration of component level stiffness changes on global analysis of ductile frame structures:

D.5.1 Analysis of Moderately-damaged RC Ductile Frames

- Under design level earthquake loading - No change in component effective stiffness required.
- Under serviceability level earthquake loading - The reduction in stiffness of damaged components is dependent on the prior deformation demands. Based on comparison with shake table test data, and considerations of challenges of estimating the prior ductility demand, the following model is recommended for estimating a lower-bound reduced stiffness of damaged beam and column components:

$$\frac{K_r}{K_y} = \begin{cases} 1.0, & \mu < 1.0 \\ 0.5, & 1.0 \leq \mu \leq 2.0 \\ 1/\mu, & \mu \geq 2.0 \end{cases}$$

Where K_y is the stiffness of the original component based on standard procedures such as those given in ASCE 41. It should be noted that this model has been compared with column specimens with relatively low axial loads. Further study is required to assess the validity of the model for columns with moderate and high axial loads.

D.5.2 Analysis of Epoxy-repaired Ductile RC Frames Following Moderate Earthquake Damage

- Under design level earthquake loading – No reduction factors should be applied when considering ULS loading cases.
- Under serviceability level earthquake loading – The following reduction factors should be applied to component effective stiffness values for epoxy-repaired beams and columns (as proposed in Appendix E Section E.6.1):

Beams: $\lambda_K = 0.11 (a/D) + 0.42 \leq 1.0$ where $a/D \geq 2$

Columns: $\lambda_K = 0.5$

References

- Arias Acosta, J., 2011, *Seismic performance of circular and interlocking spirals R/C bridge columns under bi-directional shake table loading (PhD thesis)*, University of Nevada, Reno, Nevada.
- ASCE, 2017, *Seismic Evaluation and Retrofit of Existing Buildings*, ASCE/SEI 41-17, American Society of Civil Engineers, Structural Engineering Institute, Reston, Virginia.
- Clough, R.W. and Johnston, S.B., 1966, “Effect of Stiffness Degradation on Earthquake Ductility Requirements,” *Proceedings of Japan Earthquake Engineering Symposium*, Tokyo, Japan.
- Di Ludovico, M., Polese, M., Gaetani d’Aragona, M., Prota, A. and Manfredi, G., 2013, “A proposal for plastic hinges modification factors for damaged RC columns” *Engineering Structures*, Vol. 51 pp. 99–112.
- Elwood, K.J. and Eberhard, M., 2009, “Effective stiffness of reinforced concrete columns,” *ACI Structural Journal*, Vol. 106, pp. 476–484.
- FEMA, 1998, *Evaluation of Earthquake Damaged Concrete and Masonry Wall Buildings*, FEMA 306, prepared by the Applied Technology

Council for the Federal Emergency Management Agency,
Washington, D.C.

- Ghannoum, W., Sivaramakrishnan, B., Pujol, S., Catlin, A.C., Fernando, S., Yoosuf, N. and Wang, Y., 2015, *NEES: ACI 369 Rectangular Column Database*, <https://datacenterhub.org/resources/255>.
- Gulkan, P. and Sozen, M. A., 1974, “Inelastic responses of reinforced concrete structure to earthquake motions,” *Journal Proceedings*, Vol. 71, No. 12, pp. 604-610.
- Hachem, M.M., Moehle, J.P. and Mahin, S.A., 2003, *Performance of circular reinforced concrete bridge columns under bidirectional earthquake loading*, Pacific Earthquake Engineering Research Center, Berkeley, California.
- Laplace, P.N., Sanders, D., Saiidi, M.S. and Douglas, B., 1999, *Shake table testing of flexure dominated reinforced concrete bridge columns*, Center for Earthquake Engineering Research, University of Nevada, Reno, Nevada.
- Marder, K.J., 2018, *Post-Earthquake Residual Capacity of Reinforced Concrete Plastic Hinges*, University of Auckland, Auckland, New Zealand.
- Marder, K.J., Elwood, K.J., Motter, C.J. and Clifton, G.C., 2020, “Quantifying the Effects of Epoxy Repair of Reinforced Concrete Plastic Hinges”, *Bulletin of the New Zealand Society for Earthquake Engineering*, Vol. 53, pp. 37–51.
- Paulay, T. and Priestley, M.J., 1992, *Seismic design of reinforced concrete and masonry buildings*, John Wiley and Sons, New York, New York.
- Sarrafzadeh, M.M., 2021, *Residual Capacity and Reparability of Moderately-Damaged Reinforced Concrete Ductile Frame Structures*, *PhD Thesis (under review)*, University of Auckland, Auckland, New Zealand.
- Schoettler, M, Restrepo, J., Guerrini, G., Duck, D. and Carrea, F., 2015, *A full-scale, single-column bridge bent tested by shake-table excitation*, Pacific Earthquake Engineering Research Center, Berkeley, California.
- Takeda, T., Sozen, M.A. and Nielsen, N.N., 1970, “Reinforced concrete response to simulated earthquakes,” *Journal of the Structural Division*, 1970, Vol. 96, No. 12, pp. 2557-2573.

Appendix E-1

Repair Database: Reinforced Concrete Walls

The lack of robust reparability guidelines for reinforced concrete (RC) structures hinders recovery in earthquake-impacted communities worldwide. Although the reparability of earthquake-damaged structures is a multi-faceted issue involving many stakeholders and variables, the lack of engineering technical guidance must be addressed in-order to allow better informed decisions to be made on the repair of earthquake-damaged RC structures.

As an initial step in the development of such guidelines, a database of existing research on the repair of RC walls was created. To assess the depth of available knowledge, a broad approach was taken in collecting the studies included in this database. A wide range of damage levels and complexity of repair were considered, to capture the full extent of post-earthquake repair options and their effectiveness on seismic performance. The data considered in this study includes 70 wall specimens.

The observed damage states of specimens prior to repair in the database are summarized in Table E1-1. These damage states are an overview of the primary observed damage in tested specimens, which in most cases existed alongside 1 or 2 other observed damage states. These were classified into slight, moderate and heavy damage states which in general represent an increasing complexity of repair necessary to address the damage. Light damage was limited to very minor cracking while moderate damage ranged from cracking to crushing of boundary elements in wall components. Heavy damage was defined as damage requiring more extensive repair such as core crushing to fracture and buckling of reinforcement, necessitating complete replacement.

The repair techniques considered vary from simple methods such as epoxy injection, to complex procedures such as a full replacement of concrete and reinforcing steel. In recent years, the use of different fiber reinforcement polymer (FRP) sheets as a repair technique have also been investigated. A general overview of the repair techniques included in the database can be seen in Table E1-2, categorizing repairs by increasing complexity.

Table E1-1 Categorization of Observed Damage States

Light Damage	Moderate Damage	Heavy Damage
Minor Cracking (indicative of reaching first yield of reinforcement)	Cracking	Core Crushing
	Bond Splitting	Bar Buckling
	Spalling	Opening/Fracture of Stirrups
	Bar Pull-out	Shear Failure
		Bar Fracture
		FRP Fracture
		Boundary Crushing
		Boundary Buckling
		Web Crushing

Table E1-2 Repair Techniques Included in Database

Category 1 Simple Repair	Category 2 Complex Repairs (targeting similar capacity)	Category 3 Complex Repairs + Strengthening (targeting higher capacity)
Epoxy injection	Concrete Replacement (Repl. C)	FRP/CFRP/GFRP ⁽¹⁾
Epoxy Injection + Epoxy Mortar	Repl. C + Epoxy Injection	FRP + Epoxy Injection + Epoxy Mortar
	Repl. C + Steel (Repl. C + S)	FRP + Epoxy Injection + Epoxy Mortar + Str.
	Repl. C + S + Epoxy Injection	Repl. C + FRP
		Repl. C + FRP + Epoxy Injection
		Repl. C + Strengthening (Repl. C + Str.)
		Repl. C + S + Str.
		Repl. C + S + FRP
		Steel Jacketing
		Steel Jacketing + External Prestressing
		SMA spiral ⁽²⁾ + Repl. S + Epoxy Injection + Epoxy Mortar

⁽¹⁾ FRP – Fiber Reinforced Polymers, CFRP – Carbon Fiber Reinforced Polymers, GFRP – Glass Fiber Reinforced Polymers.

⁽²⁾ SMA Spiral – Smart Metallic Alloy transverse spiral reinforcement jacketing original section.

E1.1 Database Format and Specifications

The parameters of the studies, as well as specimen specifications, were captured through population of 31 pre-defined data points which included the following general parameters:

- Year of Publication
- Design Code
- Author
- Element Type
- Specimen IDs
- Applied drifts & Loading Protocols
- Damage level classification
- Observed damage states
- Repair techniques
- Specimen cross section and dimensions
- Shear span ratios
- S/d_b , Reinforcement ratio, Scale and material properties
- Axial load
- Applied Shear Stress
- Aspect Ratio

In addition to the information available in the publications of the considered studies, data was generated by the authors of the database to assess the performance of the tested specimens. This was carried out through the digitization of backbone curves generated from the published hysteresis plots. This was done in a consistent manner as discussed further below. The parameters deemed most critical for assessing the effectiveness of repairs were the stiffness, strength and deformation capacity of these specimens, both prior and following repairs. These parameters are defined below and in Figure E1-1:

Stiffness, K. Defined as the secant stiffness to 80% of peak strength, determined from the positive loading backbone of each component test.

Deformation Capacity, D. Defined as the displacement at which the specimen drops to 80% of its peak strength, a definition often used as an arbitrary indication of failure in experimental testing.

Strength, Q. The peak strength of the specimen, determined as the largest of the positive or negative peak strength. Comparisons of pre and post repair strengths were kept consistent for each specimen.

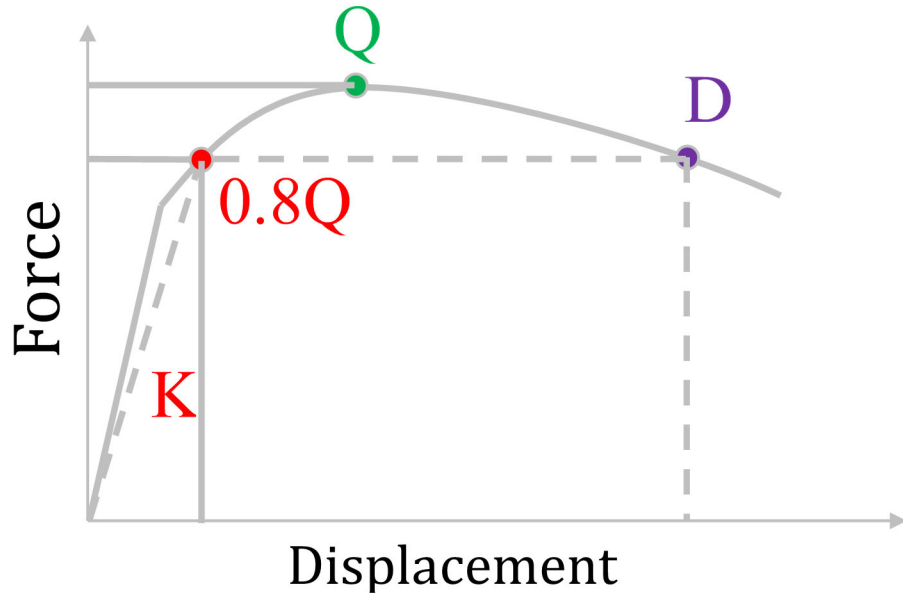


Figure E1-1 Stiffness, strength and deformation capacity determined from backbone data.

To assess the effectiveness of the repairs on the performance of each component, modification factors were determined for the change in stiffness, strength, and deformation capacity through comparison of the pre and post-repair backbones generated from the published hysteresis plots. These modification factors are defined below in addition to in Figure E1-2.

Stiffness Modification Factor, λ_K . The proportional change in secant stiffness to 80% of peak strength following repairs of damaged components.

Deformation Capacity Modification factor, λ_D . The proportional change following repair, in the displacement at the point of 20% reduction in strength. In determining the deformation capacity factor, λ_D , a variety of scenarios were encountered where this definition did not produce a logical result. Comparison of hysteresis plots, where either the pre or post repair hysteresis curves do not see a 20% degradation in strength or no degradation at all, does not produce a useful observation of the change in deformation capacity. In cases where the deformation capacity of the specimen could not

be reasonably assessed, and no signs of a reduction in deformation capacity were present, a value of 1 was assigned.

Strength Modification Factor, λ_Q . The proportional change in peak strength following the repair of the damaged component.

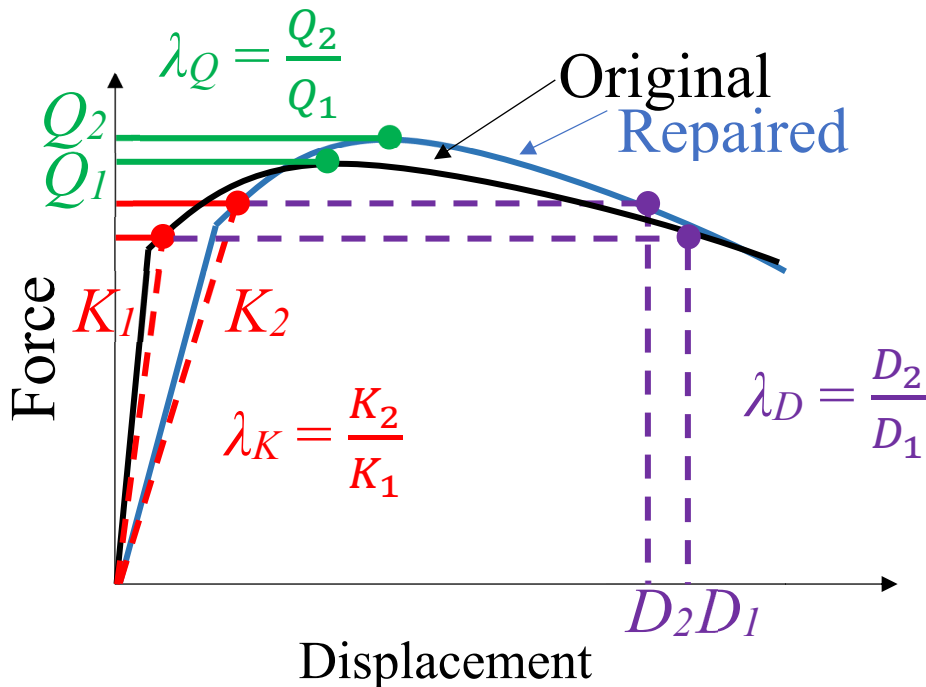


Figure E1-2 Determination of Post Repair Performance Modification Factors.

E1.2 Digitization of Published Hysteresis Plots

To extract the information described in the previous section, the plots of the hysteretic behavior of each specimen were manually digitized into backbone curves. This was done for positive and negative loading cycles both pre and post-repair. The plots were converted into data points using conventional digitization software which allows manual tracing of hysteresis plots into raw data. Figure E1-3a) is an example of the digitization software used to trace the hysteresis plot published in the study by Celebi and Penzien (1973). Figure E1-3 b) then shows a plot of the raw data extracted from the digitization software, depicting the backbone curve for the positive loading cycles of the specimen shown in the previous figure.

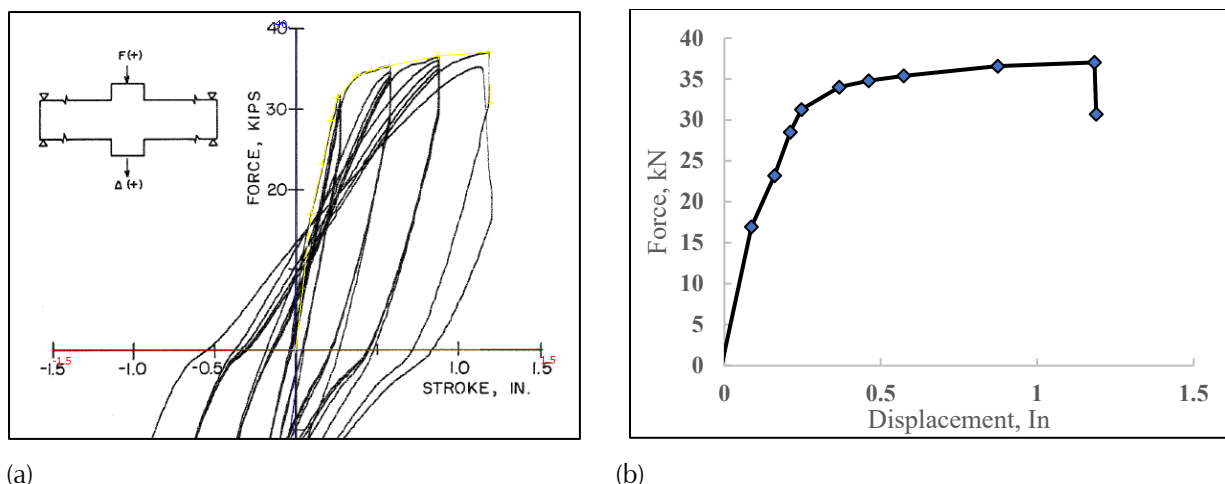


Figure E1-3 Manual digitization of published hysteresis plots b) Plotting of raw data obtained from digitization software. Hysteresis plot in Figure E-a) obtained from Celebi and Penzien, 1973.

Following the extraction of the study parameters the procedure outlined above was carried out for each study, generating the stiffness, deformation capacity and strength for the pre and post-repair backbones, as well as the corresponding modification factors. The full results of these values are discussed in the following section. A condensed summary of the collected data and results for each study individual study included in the database are also included in the appendices of this report.

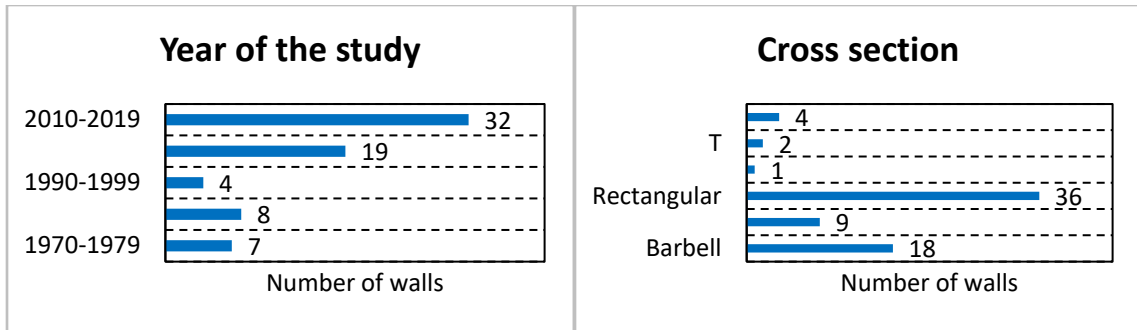
E1.3 Summary of Database Findings

A total of 70 previously tested repaired RC walls were found in the literature, dating back to 1975. The main characteristics of the walls, as Year of the study, Cross section, Aspect ratio, Shear depth to span ratio, Wall thickness, Axial force ratio (defined as the ratio of the vertical axial load over the compressive strength of the section) and Scale factor are categorized in Figure E1-4. The increasing amount of studies over the decades shows that repair of RC walls is not fully understood, and it is a global topic that must be addressed. The most common cross section is the rectangular, but just represents a 51% of the total. Cross section which induces higher shear stresses like Barbell and “H” shape represent the 39% of the total. The 4% of the database studied asymmetrical walls, which generally triggers failure in the boundary zone without the flange. According to the aspect ratio and the shear depth to span ratio there is slight tendency for studying flexural walls (generally defined with a shear depth to span ratio closer or bigger to two), but even tough 40% of the total can be defined as walls with a high influence of shear in their behavior. Thickness equal or bigger than 150 [mm] just represents a 22% of the total, which aligns with the scale factors lesser than 50% in most of the cases. 34% of the walls did not define a specific scale

factor but considering the wall thickness it can be assumed scale factors lesser than 50%. In addition, the scale factors show the inability of smaller values because the difficulty on finding proper reinforcement and aggregates for the concrete.

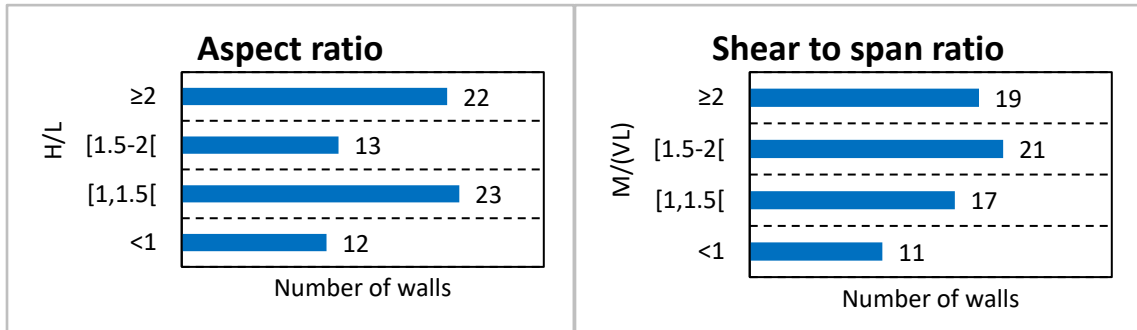
In terms of reparability, two extra variables of interest are the damage state prior to repair and the repair technique used. The maximum damage applied to the walls prior to repair reported by the authors is categorized in Figure E1-5. Boundary buckling and boundary crushing refer to damage in the end zone of the wall (to distinguish between concrete crushing at the boundaries and concrete crushing at the web). Crushing category was defined for the wall with openings where the boundary and the middle zone is hard to define. As can be seen in the figure, for most test walls the maximum damage present in the wall can be categorized as Heavy (bar buckling, bar fracture, boundary buckling, boundary crushing, concrete crushing, web crushing, sliding and lap splice slip), representing a 93% of the total. Generally, this damage state can be associated with the failure of the element, triggered by a lateral strength drop close to 20%. Most of the failure modes of RC walls, as flexural, boundary compression, shear tension, shear compression, sliding and lap splice slip are captured by the damage state defined in the figure.

The different repair techniques used are summarized in Figure E1-6. The main categories are replacement of material of the cross section, Fiber Reinforcement Polymer or FRP (any type of FRP, made of carbon or glass, and installed at any position), and epoxy (which includes resin, grout and similar). The replacement can cover concrete (C), steel (S) and both (C+S). The FRP sheets can affect strength, stiffness and displacement capacity. The strengthening of the section adding more steel, increasing the cross section of the wall, or doing one of the above added to FRP (but no as the main component in the procedure) is cover by “Stre.”.



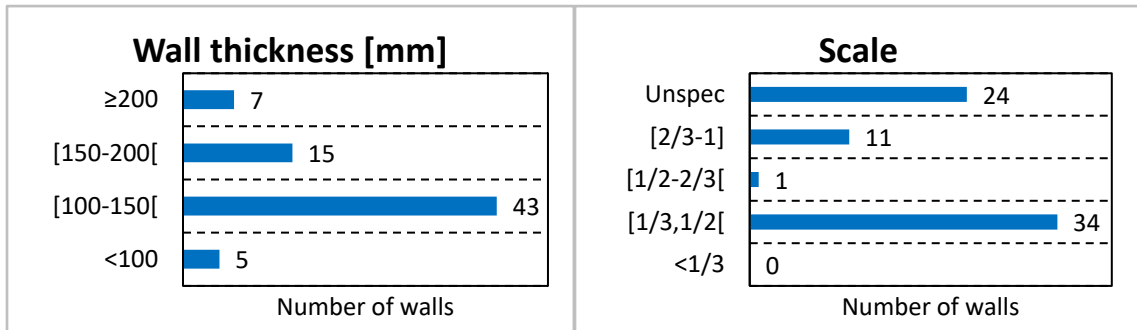
(a)

(b)



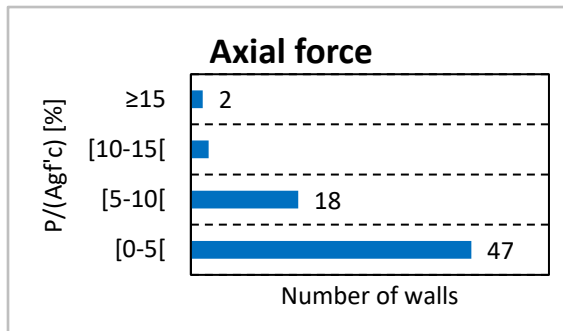
(c)

(d)



(e)

(f)



(g)

Figure E1-4 Data categorized according to: (a) year of the study, (b) cross section, (c) aspect ratio, (d) shear to span ratio, (e) wall thickness, (f) axial force, and (g) shear stress.

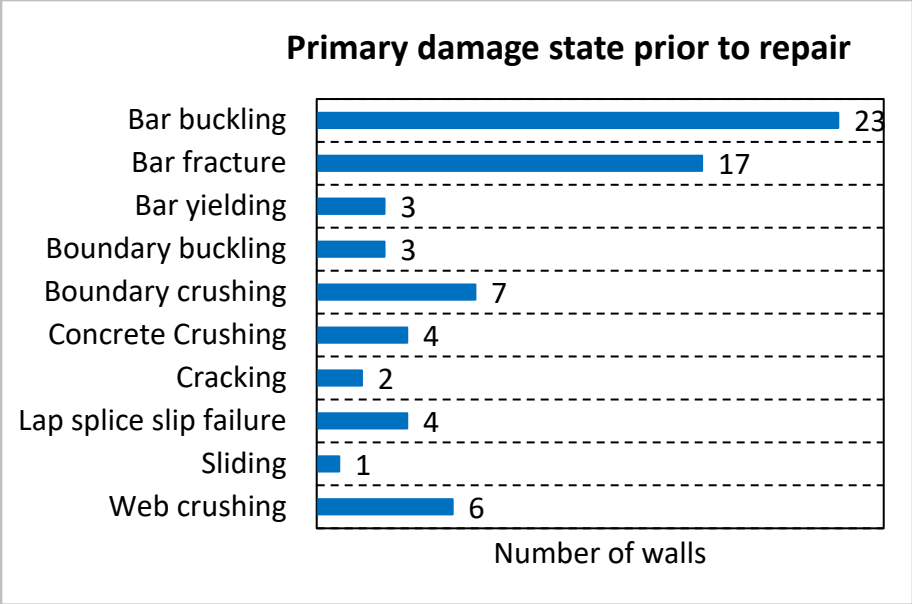


Figure E1-5 Data categorized according to primary damage state prior to repair.

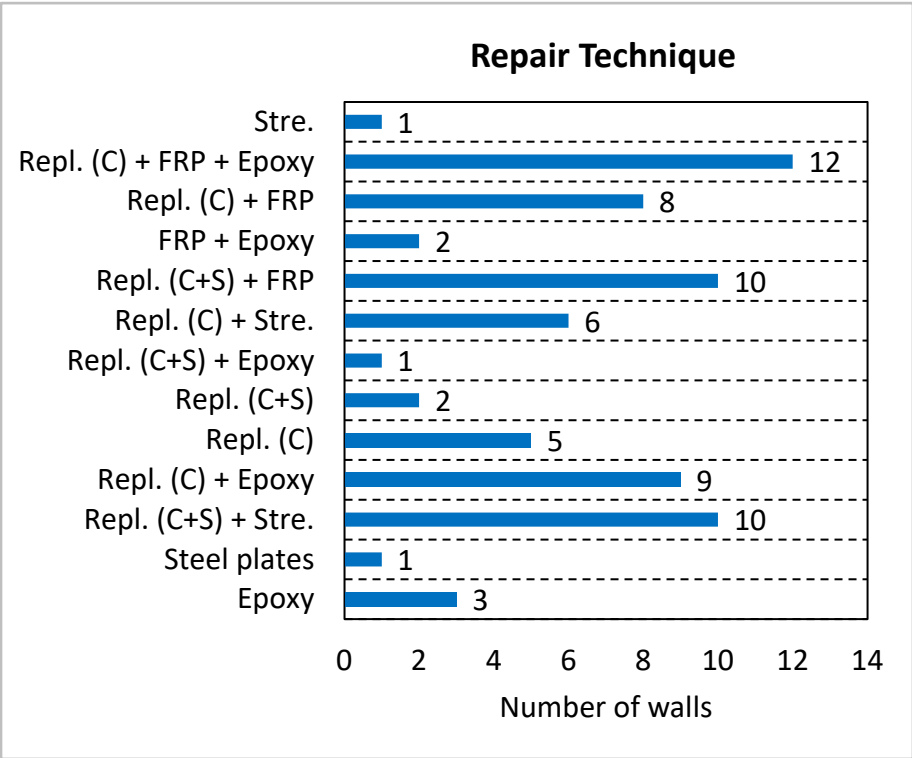


Figure E1-6 Walls categorized by the repair technique.

The four main repair techniques aforementioned are combined with other less popular alternatives to create all the categories of the Figure E1-6. One of the techniques that became popular in the last decades is the FRP sheets, as can be seen in Figure E1-7. This method has been frequently used because their simplicity in the installation compared to other strengthening techniques

such as jacketing or increasing the wall section. However, removing this alternative from the total of the studies, it can be seen a lesser evident tendency in the repair of RC walls.

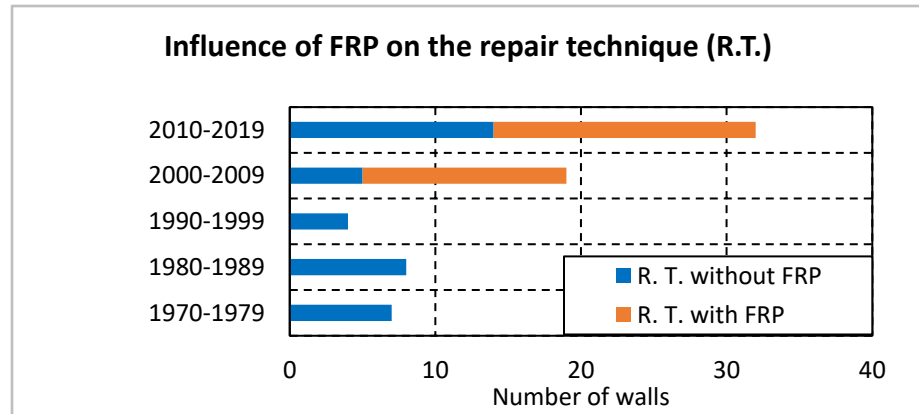


Figure E1-7 Use of FRP sheets over time.

In terms of the type of repair, 50 of the 70 RC repaired walls are classified as “strengthening” in the last column of Table E1-2. Wang, Vallenias and Iliya tested flexural RC walls extracted from an archetype building with complex loading protocols, which makes difficult the comparison of the results. The walls were tested under monotonic, cyclic and mixed loading protocols and the repair techniques under this category generally was concrete and steel replacement and strengthening of the section. Fiorato presents three repaired walls as part of the research made by the Portland Cement Association. Two of them were repaired and strengthened, and the third one only repaired replacing the concrete in the web of the barbell cross-section. Pinho studied different repair and retrofit techniques, but unfortunately, the main work was not found. Just one wall repaired and strengthened was found, but slight on details. Dan, Todut , Li, Zhou, Zhang, Li, Woods, and Cruz-Noguez used different arrangements of FRP, sometimes added to steel and concrete replacement. The failure of the repaired specimens was always triggered by the FRP sheets. Antoniades used FRP as well in walls with low to medium shear to span ratio, but also have a benchmark-repaired wall (repaired using concrete and steel replacement). Riva tested a full scale 4 story RC wall repairing it concrete and steel replacement and strengthening of the critical section to increase sliding strength. Layssi used steel and concrete jacketing for the repair of single reinforced slender RC walls. Yüksel studied walls reinforced with welded wire mesh fabric and the effectiveness of increasing the section with longitudinal and transversal reinforcement. Li proposed a novel web reinforcement to increase the performance of a repaired wall using concentric circular reinforcement. Cortés-Puentes repaired two slender RC wall using Shape Memory Alloys bars as boundary reinforcement to

minimize the inelastic deformation on the steel. The use of steel plates anchored to the foundation without any repair in the wall was used by Taghdi. This technique can be associated to a fast and temporary repair, but hard to think about it as a definitive alternative.

Eighteen repaired RC walls with a repair technique that tries to achieve a similar capacity were found. Wang previously mentioned had a wall with epoxy injection and concrete replacement, without steel replacement. However, unrepaired buckled steel reinforcement accelerates the strength degradation in the repaired wall. Lefas tested three slender repaired walls monotonically replacing the concrete in the boundary region. Barda, Bucci and Haro de la Peña focused on walls with low shear to span ratio and high shear stress because the “H” cross-section used. Because of this the steel reinforcement was not heavily damaged and just the concrete was replaced. Motter tested two repaired wall replacing concrete and steel, and using epoxy resin to fill the cracks. Durga repaired squat walls with high shear stresses tested monotonic and cyclically replacing concrete and using epoxy to fill the cracks.

Finally, simple repair techniques were used just on three walls. Iliya tested two repaired walls but only with slight damage. The walls were tested initially just up to the first yielding, then minor cracking was the main damage observed. Okamoto was part of a study where a full-scale seven-story RC building was tested, but after the repair, non-structural elements were added then a direct comparison is not allowed.

As can be seen, most of the previous tests are focused on heavy damage prior to repair and complex repair techniques. However, the residual capacity and the improvements of simple repair technique on flexural dominant rectangular reinforced concrete walls are not adequately addressed up to the present work. Besides, as any of the previous tests do not have a benchmark wall, the displacement capacity of walls damaged prior to failure have never been studied directly.

E1.3.1 Summary of Performance Modification Factors for Wall Specimens

As previously defined, the behavior of both the original (or undamaged) and the repaired RC elements will be defined through the three main components in a backbone curve: secant stiffness, strength, and displacement capacity. The ratio of the parameter in the repaired wall over the same parameter in the original wall is defined as the Performance Modification Factors (PMF). Thus, λ_K is the PMF for stiffness, λ_Q for strength, and λ_D for deformation capacity. The average of the PMF of all walls per each damage state prior to

repair found in the literature is presented in Table E1-6. Considering all damage states and repair techniques, more than 80% of the initial stiffness can be recovered, and both the strength and the displacement capacity achieve values higher than the originals. However, many of the repair techniques involves complex methodologies which aims to increase all or some of the main variables in the overall behavior of the wall.

Table E1-6 Performance Modification Factors of the Wall Database

Performance Modification Factors	λ_K	λ_Q	λ_D
Average	0.83	1.08	1.19

Categorizing the damage state prior to repair and the repair technique used, the stiffness PMF, the strength PMF, and the displacement capacity PMF are presented in Table E1-7, Table E1-8, and Table E1-9, respectively. Unfortunately, the database does not cover all the combinations to fill the tables, since the heavy damage state and the complex repair techniques (category 3) accumulates most of the walls. Just for slight damage state under repair category 1 achieve a repaired stiffness bigger than 100%, but the walls under this category (Iliya) had different loading protocols pre and post repair which may influence in the secant stiffness derivation. Without considering this study, the repaired stiffness of both categories 1 and 2 are close to 50%, and even using complex techniques in category 3, the repaired stiffness achieves 93%. The strength PMF values presented in Table E1-4 for slight damage state and simple repair shows a similar trend, but again the different loading protocols of the study may influence in this abnormal increase. Considering the repair category 2 and heavy damage state, it can be seen almost a total strength recovery, which is barely affected when moving to complex repair techniques (from 96% to 108%). If the damage state is moderate and complex repair techniques are used, the repaired increase up to 159%. This could indicate that the state of the element before repair can be more influencing in repaired strength rather than the repair technique used. Unfortunately, there is no walls with moderate damage state repaired using some of the techniques of the category 2 to complete this analysis. The optimistic values for displacement capacity in Table E1-9 are because generally the walls with lower shear span to depth ratio and barbell or “H” cross-section failed under shear compression and the repaired specimen had a lower stiffness and higher displacement capacity, as can be seen in example shown in Figure E1-8. The combination of a low recovered stiffness and a high recovered displacement capacity can generate a λ_D value of 411%. Then, even with this categorization, it is important to use similar walls (cross-section, shear depth to span ratio, damage state prior to repair and repair technique) to obtain reliable data.

Table E1-7 λ_K Categorized by Damage State and Repair Technique Category

Damage state	Repair category 1	Repair category 2	Repair category 3	Total
Heavy	-	51%	93%	82%
Moderate	49%	-	93%	82%
Slight	120%	-	-	120%
Total	96%	51%	93%	83%

Table E1-8 λ_Q Categorized by Damage State and Repair Technique Category

Damage state	Repair category 1	Repair category 2	Repair category 3	Total
Heavy	-	96%	108%	105%
Moderate	-	-	159%	159%
Slight	117%	-	-	117%
Total	117%	96%	111%	108%

Table E1-9 λ_D Categorized by Damage State and Repair Technique Category

Damage state	Repair category 1	Repair category 2	Repair category 3	Total
Heavy	-	145%	107%	117%
Moderate	-	-	176%	176%
Slight	-	-	-	-
Total	-	145%	110%	119%

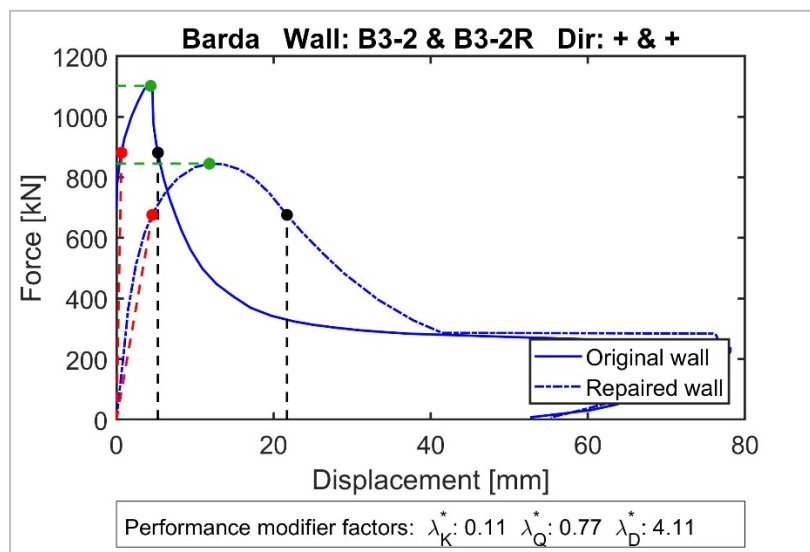


Figure E1-8 Backbones curves of Barda [24] with high repaired displacement capacity and low stiffness.

The stiffness, strength and displacement capacity modification factor versus the repaired technique used are presented in Figure E1-9, Figure E1-10, and Figure E1-11, respectively. The number at the base of each column represents the number of walls used, and the error bars shows one standard deviation. The repair technique with the highest stiffness modification factor is concrete and steel replacement plus FRP, and the repair technique with the lowest stiffness modification factor is the use of steel plates at the base. Discarding Epoxy and except for concrete replacement plus FRP, a band between 75% and 50% separates the repair category 2 and 3. Finally, the high variability in the studies generates high standard deviation which may force a detail analysis when looking for information for assessment of a damaged and repaired RC wall. The strength modification factor of Figure E1-12 shows that no matter the repair technique used, an average value over 90% is achievable. The differences between all the repair techniques, and the variability inside each repair technique, are lower respect to the changes in stiffness. The highest average repaired strength is achieved using steel plates at the base, but also achieved the lowest stiffness as previously discussed. The lowest average repaired strength is achieved by concrete replacement plus FRP, but even though this value is 90% of the original value. The displacement capacity modification factor shows the biggest variability and differences between the repair techniques, from 63% for concrete and steel replacement plus FRP to 225% for concrete replacement plus strengthening. However, this value is highly influenced by the study of Layssi [17] who used concrete and steel jacketing in non-ductile singly reinforced concrete walls, achieving λD values bigger than 400%. Similar results are obtained for concrete replacement as previously discussed, where a low repaired stiffness and a high repaired displacement capacity can induce high displacement capacity modification factors.

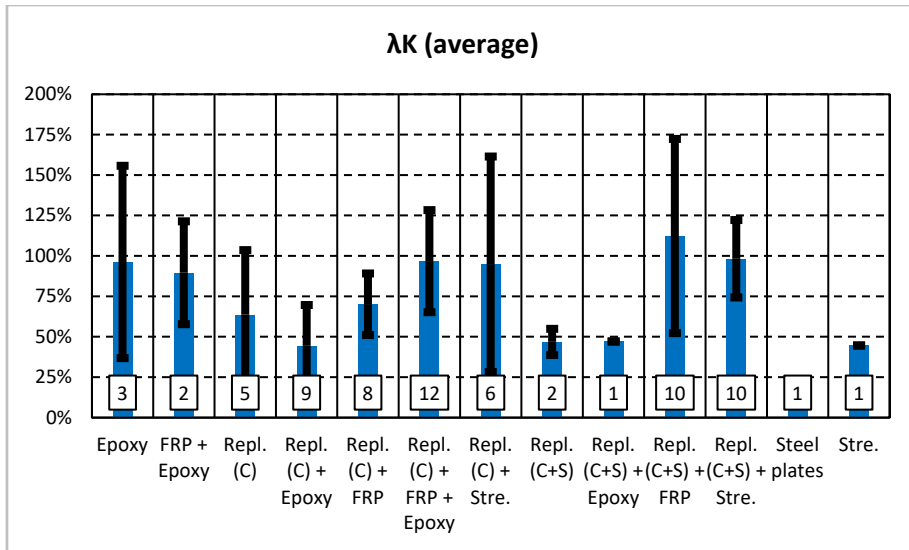


Figure E1-9 Average stiffness modification factor, λ_K , for each repair technique.

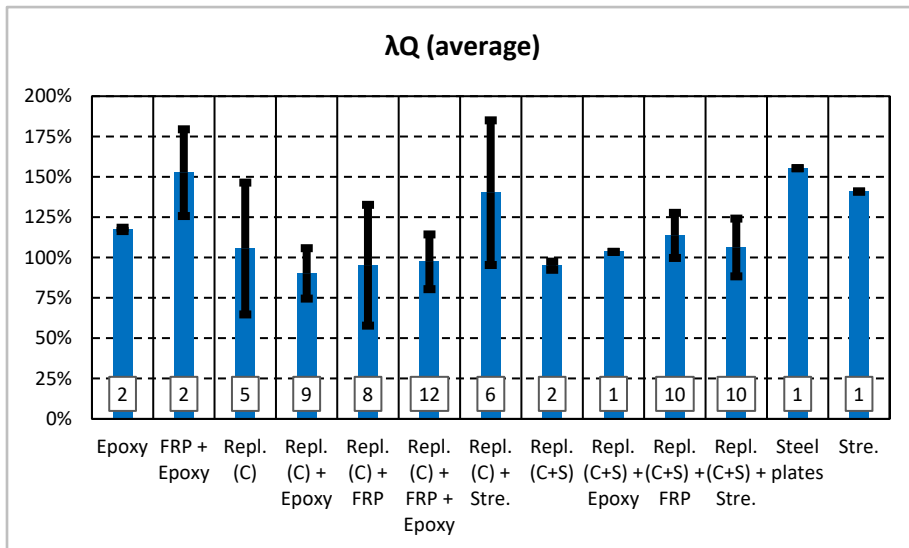


Figure E1-10 Average strength modification factor, λ_Q , for each repair technique.

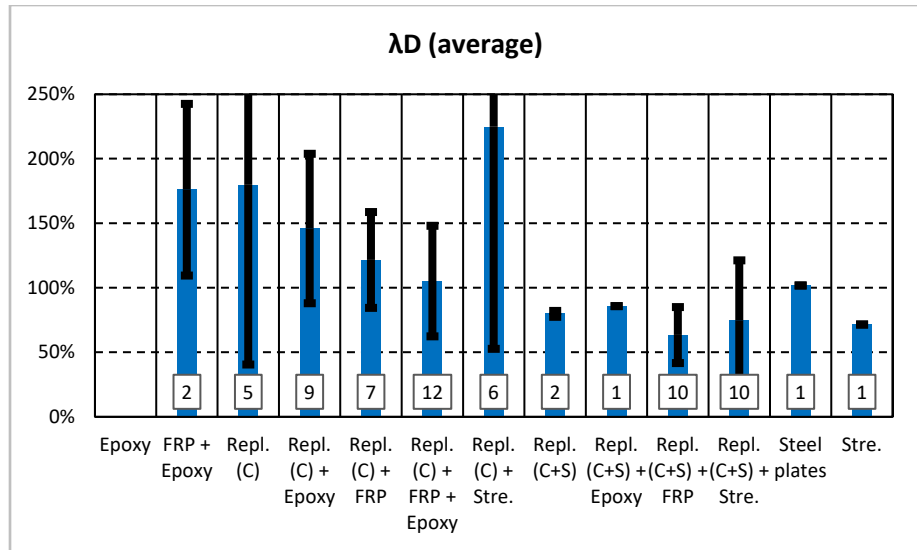


Figure E1-11 Average displacement capacity modification factor, λ_D , for each repair technique.

The stiffness, strength and displacement capacity modification factor versus the primary damage observed are presented in Figure E1-12, Figure E1-13, and Figure E1-14, respectively. In this case, no matter the primary damage observed, the average stiffness modification factor is bigger than 50%. The two walls with cracking as primary damage used complex repair techniques and one of them was tested under different loading protocols pre and post repair. The strength modification factors presented in Figure E1-13 show a minimum average value of 73%, and most of the categories with values bigger than 100%. The category concrete crushing was defined to be used in the walls tested by Todut because the walls had big openings which makes difficult to distinguish between boundary concrete crushing and web concrete crushing. The walls with cracking as the primary damage show high values again, but this is because the complex repair technique used to increase the overall performance of the walls. Finally, the displacement capacity modification factors show the biggest differences between the damage states and inside of each category. The cracking category which shows good results for stiffness and strength here have a poorest performance compared to the other categories. The good performance of the walls with lap splice failure (Layssi) was discussed previously.

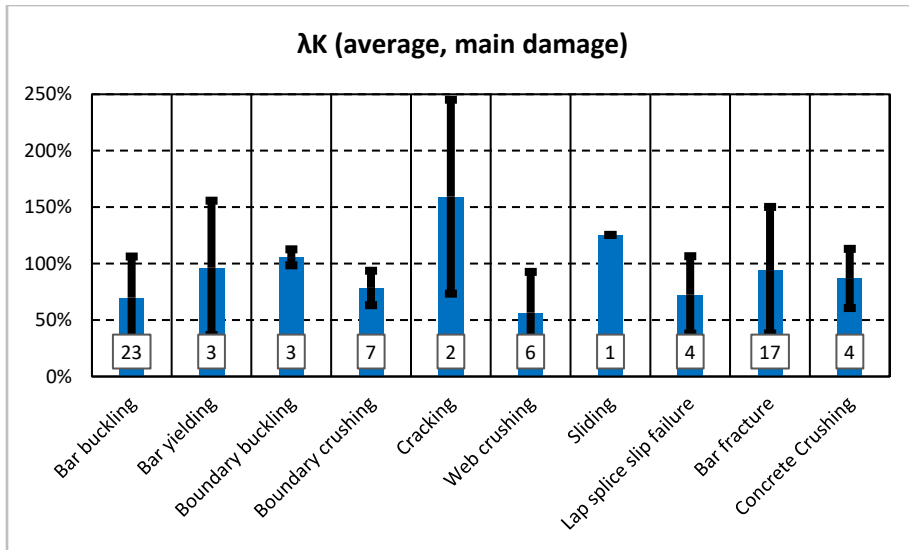


Figure E1-12 Average stiffness modification factor, λ_K , for each repair technique.

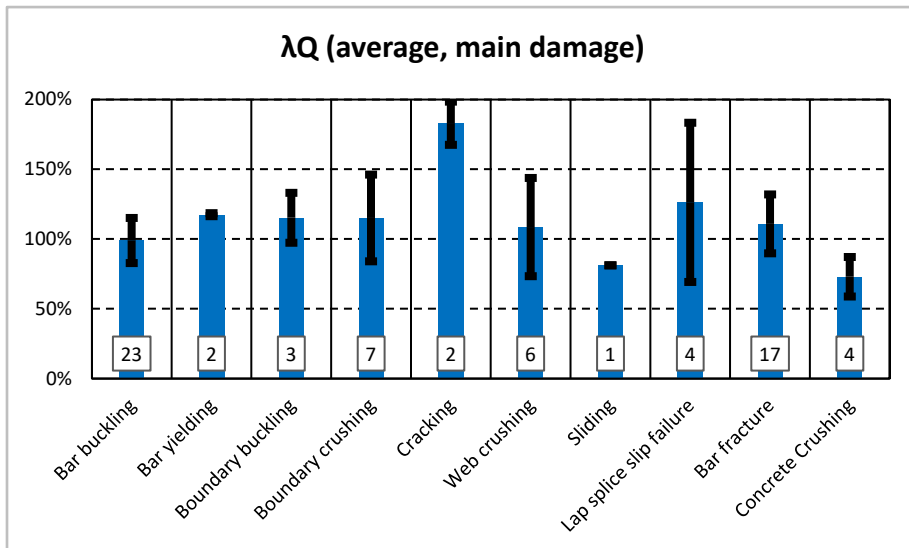


Figure E1-13 Average strength modification factor, λ_Q , for each repair technique.

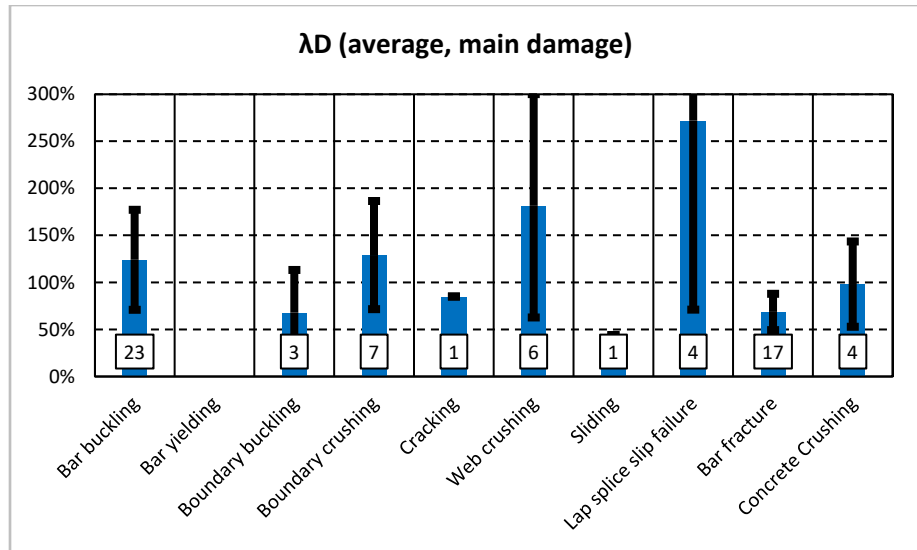


Figure E1-14 Average displacement capacity modification factor, λ_D , for each repair technique.

As can be seen in the last three figures, 40 of the walls presented bar buckling and bar fracture as the primary observed damage, which represent more than 57% of the total. The strength modification factor for these damage states categorized by the repair technique is shown in Figure E1-15. An increment in the average values is observed when the repair techniques is getting more complex. The differences between the maximum and the minimum values is 26% only when bar buckling occurred and 87% when bar fracture occurred. This could indicate that when the damage in the wall induces only bar buckling the repair technique becomes less relevant than when the damage generates bar fracture. The same information is presented for the displacement capacity modification factor in Figure E1-16. When bar fracture happens, the trend is similar to the strength performance. This could be explained considering when the reinforcement bar fractured the repaired performance is more dependent of the new elements. When bar buckling happens, depending on the repair technique some of the original elements still contributes to the wall overall response.

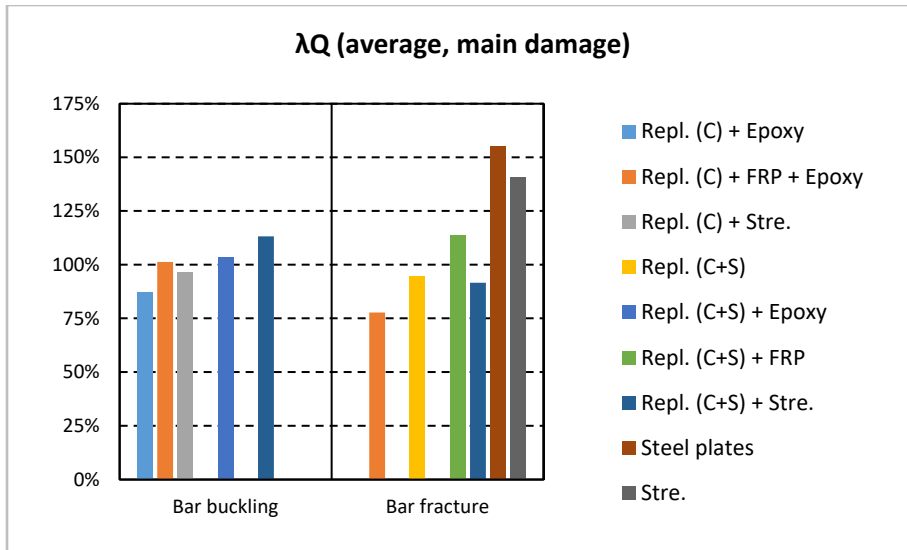


Figure E1-15 Strength modification factor for bar buckling and bar fracture.

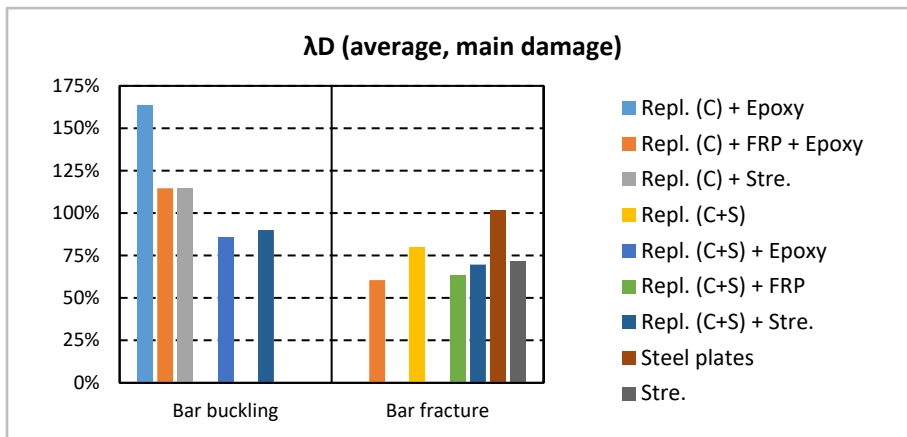


Figure E1-16 Displacement capacity modification factor for bar buckling and bar fracture.

E1.4 Future Work

This appendix was developed in Year 1 of the ATC-145 project. The following future work is planned to make it consistent with Appendix E-2 for frame components.

- Update of introduction to make it specific to walls.
- Explore the results for lambda values based on:
 - Damage in the reinforcement steel before repair,
 - Replacement of the steel reinforcement,
 - Change of the critical section, and

- Variability in the performance of FRP repaired walls. Deeper analysis to distinguish between confinement, flexural or shear strengthening, and checking of the requirements of ACI 440.
- Comparison with values proposed by FEMA 306.
- Identification of characteristics of repair techniques with λ_D and λ_D less than unity.

References

- Antoniades, K.K., Salonikios, T.N., and Kappos, A.J., 2005, “Tests on Seismically Damaged Reinforced Concrete Walls Repaired and Strengthened Using Fiber-Reinforced Polymers,” *Journal of Composites for Construction*, Vol. 9, No. 3, pp. 236–246.
- Antoniades, K.K., Salonikios, T.N., and Kappos, A.J., 2007, “Evaluation of hysteretic response and strength of repaired R/C walls strengthened with FRPs,” *Engineering Structures*, Vol. 29, No. 9, pp. 2158–2171.
- Barda, F., Hanson, J., and Gene, C.W., 1976, “Shear strength of low-rise walls with boundary elements,” *Reinf. Concr. Struct. Seism. Zo.*, Vol. SP-53, pp. 149–202.
- Bucci, F., 1998, *Finite element analysis of repaired concrete structures*, National Library of Canada.
- Cortés-Puentes, L., Zaidi, M., Palermo, D. and E. Dragomirescu, 2017, “Cyclic loading testing of repaired SMA and steel reinforced concrete shear walls,” *Engineering Structures*, Vol. 168, pp. 128–141.
- Cruz-Noguez, C.A. et al., 2014, “Seismic Behavior of RC Shear Walls Strengthened for In-Plane Bending Using Externally Bonded FRP Sheets,” *Journal of Composites for Construction*, Vol. 19, No. 1.
- Dan, D., 2012, “Experimental tests on seismically damaged composite steel concrete walls retrofitted with CFRP composites,” *Engineering Structures*, Vol. 45, pp. 338–348.
- Fiorato, A.E., Oesterle, R.G., and Corley, W.G., 1983, “Behavior of Earthquake Resistant Structural Walls Before and After Repair,” *ACI Journal Proceedings*, Vol. 80, No. 5, pp. 403–413.
- Iliya, R. and Bertero, V., 1980, *Effects of amount and arrangement of wall-panel reinforcement on hysteretic behavior of reinforced concrete walls*, University of California, Berkeley, California.

- Haro de la Peña, O. A., 2001, *Modelling and Analysis of Retrofitted Reinforced Concrete Structures*, University of Toronto, Toronto, Canada.
- Kanaka Durga, S. and Appa Rao, G., 2016, “Performance of Partially Damaged Squat Shear Walls under Reversed Cyclic Loading,” *9th International Conference on Fracture Mechanics of Concrete and Concrete Structures*.
- Layssi, H. and Mitchell, D., 2012, “Experiments on seismic retrofit and repair of reinforced concrete shear walls,” pp. 1–8.
- Lefas, I.D. and Kotsovos, M.D., 1990, "Strength and deformation characteristics of reinforced concrete walls under load reversals," *ACI Structural Journal*., Vol. 87, No. 6, pp. 716–726.
- Li, B. and Lim, C.L., 2010 “Tests on Seismically Damaged Reinforced Concrete Structural Walls Repaired Using Fiber-Reinforced Polymers,” *Journal of Composite Construction*, Vol. 14, No. 5, pp. 597–608.
- Li, Y.F., Huang, C. L., Lin, C. and Hsu, T.H., 2012, “A study on the high seismic performance of RC structural walls under reversed cyclic loading,” *Advances in Structural Engineering*, Vol. 15, No. 7, pp. 1239–1252.
- Li, B., Qian, K. and Ngoc Tran, C.T., 2014, “Retrofitting Earthquake-Damaged RC Structural Walls with Openings by Externally Bonded FRP Strips and Sheets,” *Journal of Composites for Construction*, Vol. 16, No. 1, pp. 10–20.
- Motter, C.J., Clauson, A.B., Petch, J.C., Hube, M.A., Henry, R.S., and Elwood, K. J., 2017, “Seismic performance of repaired lightly reinforced concrete walls,” *Bulletin of the New Zealand Society for Earthquake Engineering*, Vol. 50, No. 4, pp. 574–585.
- Okamoto, S., Wight, J. K., Nakata, S., Yoshimura, M. and Kaminosono, T. 1985, “Testing, Repair and Strengthening, and Retesting of Full-Scale Seven Story Reinforced Concrete Building,” *ACI Special Publication No. 84*.
- Pinho, R., 2000, *Selective retrofitting of RC structures in seismic areas*, University of London, London, United Kingdom.
- Riva, P., Meda, A., and Giuriani, E., 2004, “Experimental test on a full scale repaired RC structural wall,” *13th World Conference on Earthquake Engineering*.

- Taghdi Mustafa, S. M., and Bruneau, M., 2000, “Seismic retrofitting of low-rise masonry and concrete walls using steel strips,” *Journal of Structural Engineering*, Vol. 126, pp. 1017–1026.
- Todut, C., Dan, D., and Stoian, V., 2015, “Numerical and experimental investigation on seismically damaged reinforced concrete wall panels retrofitted with FRP composites,” *Composite Structures*, Vol. 119, pp. 648–665.
- Vallenas, J., Bertero, V. and Popov, E., 1979, *Hysteretic behavior of reinforced concrete structural walls*, University of California, Berkeley, California.
- Wang, T., Bertero, V. and Popov, E., 1975, *Hysteretic behavior of reinforced concrete framed walls*, University of California, Berkeley, California.
- Woods, J.E., Lau, D.T., and Shaheen, I.K., 2017, “Repair of Earthquake Damaged Squat Reinforced Concrete,” *16th World Conference on Earthquake Engineering*.
- Yüksel, S.B., 2019, “Experimental investigation of retrofitted shear walls reinforced with welded wire mesh fabric,” *Structural Engineering and Mechanics*, Vol. 70, No. 2, pp. 133–141.
- Zhang, Z., Li, B. and Qian, K., 2016, “Experimental investigations on seismically damaged nonrectangular reinforced-concrete structural walls repaired by FRPs,” *Journal of Composite Construction*, Vol. 20, No. 1, pp. 1–14.
- Zhou, H., Attard, T. L., Zhao, B., Yu, J., Lu, W., and Tong, L., 2013, “Experimental study of retrofitted reinforced concrete shear wall and concrete-encased steel girders using a new CarbonFlex composite for damage stabilization,” *Engineering Failure Analysis*, Vol. 35, pp. 219–233.

Repair Database: Ductile Reinforced Concrete Frames

E2.1 Introduction and Objectives

This appendix leverages experimental work from existing literature, to assess the reparability of earthquake damaged reinforced concrete (RC) frame elements. Existing guidance on the reparability and residual capacity of earthquake damaged RC components is limited, particularly for frame structures. While repair guidance is provided in documents such as FEMA 306/308, this is confined to RC walls and is based on very limited experimental data. When considering frame elements such as beams and columns, little is available beyond the Japanese Damage Evaluation Guidelines (JDEG), which primarily focus on residual capacity. In addition, the JDEG guide is based heavily on observations of field and experimental damage in Japan. Given the unique design philosophy of Japanese RC structures which generally result in much stronger and stiffer structures (Sarrafzadeh et al., 2016), there is limited transferability of JDEG guidelines outside of Japan. As such this appendix focuses on addressing this gap in guidance by focusing on the reparability of ductile RC frame elements. The findings of this appendix can be used for the recommendations of required repairs based on the results of the safety assessment phase of Chapter 3.

E2.2 Database of Component Repair Tests

A database of experimental programs on the repair of RC components was created. To assess the depth of available knowledge, a broad approach was taken in collecting the studies included in this database. A wide range of damage levels and repair methods were considered, to capture the full extent of post-earthquake repair options and their effectiveness for seismic performance. With a focus on RC frame structures, data for columns, beams and joint specimens of varying detailing and failure mechanisms was collected to provide a holistic view of post-earthquake reparability for these structures. A total of 89 specimens were identified in existing literature, comprising of 39 columns, 36 joints and 14 beams.

The observed damage states of specimens prior to repair in the database are summarized in Table E2-1. These were classified into low, moderate, and

heavy damage, which in general represent an increasing complexity of required repair. A guide for defining each damage state is presented below. It should be noted that these damage states are generally based on RC frame elements with detailing for ductility, which is the primary focus of this appendix, while some non-ductile elements are also included in the database.

Low Damage – Minor cracking of concrete in potential plastic hinge or joint regions. Cracks should be hairline (< 0.2mm).

Moderate Damage – Limited to concrete damage in the plastic hinge region **without** damage to steel reinforcement. This includes distributed cracking with multiple non-hairline cracks and spalling of cover concrete. Significant damage beyond cracking to the core concrete is **NOT** included as moderate damage, which would require more complex repairs.

Heavy Damage – This includes any damage where steel reinforcement is damaged – buckled, fractured, or opened (transverse bars) and bar pull-out where significant yielding and strain penetration of reinforcement is unrepairable. Heavy damage also includes concrete core crushing in addition to other undesirable (non-ductile) failure mechanisms such as shear, axial or bond failure.

Table E2-1 Categorization of Observed Damage States Prior to Repair.

Low Damage	Moderate Damage	Heavy Damage
Hairline Residual Cracking (< 0.2mm)	Non-Hairline Residual Cracking	Core Crushing
	Spalling	Bar Buckling
		Opening/Fracture of Stirrups
		Wide Inclined Cracking
		Bar Fracture
		FRP Fracture
		Bar Pull-out
		Bond Failure ⁽¹⁾

⁽¹⁾ Bond failure is in reference to a failure mechanism which was observed in columns with longitudinal bar lap splices in the potential plastic hinge region. Spalling of cover concrete in the plastic hinge region resulted in a loss of bond to the reinforcement in these specimens and required a retrofit.

A summary of the repair techniques which have been applied to the specimens included in the database can be found in Table E2-2. Repairs addressing low and moderate damage states were relatively simple repair techniques such as epoxy injection and mortar. Heavy damage was typically

addressed via more complex repairs, often combining multiple repair methods, attempting to reinstate initial specimen conditions, or retrofit components to increase their strength, deformation capacity, or both. The repair categories presented in Table E2-2 are intended to reflect the level of complexity and intended outcome of the repairs outlined above. Category 0 represents relatively simple repairs intended to reinstate the initial condition of components which have typically undergone low to moderate damage. Category 1 repairs represent more complex repairs intended to reinstate specimen initial conditions which have typically undergone heavy damage. Category 2 repairs are similar in complexity to Category 1 repairs, however, represent retrofit type repairs where the specimen initial conditions such as strength and deformation capacity are increased.

Table E2-2 Repair Techniques Included in Database

Category 0	Category 1	Category 2
E.I	Repl. C ⁽⁶⁾	FRP-L ⁽⁴⁾
E.M + E.I	Repl. C + E.I	E.I + FRP (C+L)
E.M + FRP-C ⁽³⁾	Repl. (C + S)	Repl. C + E.I. Str.
E.M + E.I + FRP-C ⁽³⁾	Repl. (C + S) + E.I	Repl. C + FRP (C+L) + E.I
	Repl. (C + S) + FRP-C	Repl. C + Str.
		Repl. (C + S) + Str.
		Steel Jacketing
		SMA ⁽⁵⁾ + Repl. (C+S) + E.I + E.M
		E.M + E.I + FRP-C ⁽³⁾ + Str.
		E.M + FRP (C+L)

⁽¹⁾ Notations used in the table are defined as follows: E.I. = Epoxy Injection, E.M = Epoxy Mortar, FRP = Fiber Reinforced Polymer, FRP-C = FRP Confinement, Repl. C = Concrete Replacement, Repl. S = Steel Replacement, FRP-L = Longitudinal FRP, Str. = Strengthening, SMA = Shape Memory Alloy.

⁽²⁾ FRP includes both glass and carbon-based fiber repairs.

⁽³⁾ Where FRP is only used as additional confinement (FRP-C) in specimens with ductile detailing, it is still considered a Category 0 repair. Where FRP-C is used in specimens with deficient detailing it is considered a Category 2 repair intended to improve the original specimen characteristics as a retrofit.

⁽⁴⁾ Where FRP is used longitudinally (FRP-L), it is seen as a complex repair included in Category 1, often requiring invasive concrete drilling, and anchoring in addition to being used for strengthening of specimens.

⁽⁵⁾ SMA – Shape Memory Alloy transverse spiral reinforcement applied in a jacketing method to the original section.

⁽⁶⁾ Concrete replacement refers to repairs where significant portions of damaged concrete are re-cast up to and including the full replacement of core concrete.

For each study included in the database, general study parameters as well as the metadata outlined below were collected based on available published information.

- Year of Publication
- Design Code
- Author
- Element Type
- Specimen IDs
- Applied drifts & Loading Protocols
- Damage level classification
- Observed damage states
- Repair techniques
- Specimen cross section and dimensions
- Shear span
- Reinforcement details (s/d_b , reinforcement ratio)
- Scale
- material properties
- Axial load
- Shear stress

In addition to the information available in the publications of the considered studies, data was generated to assess the performance of the tested specimens, in line with the objectives of this study. This was carried out through the digitization of backbone curves generated from the published hysteresis plots in both the positive and negative loading directions. A consistent methodology was used to generate backbone data, as discussed further below. The parameters deemed most critical for assessing the effectiveness of repairs were the stiffness, strength, and deformation capacity of these specimens, both prior and following repairs. These parameters are defined below and in Figure E2-1a.

Stiffness, K – Defined as the secant stiffness to 70% of peak strength, determined from the positive loading backbone of each component test. This definition is comparable to that of other databases such as the ACI 369 Rectangular Column Database (Ghannoum et al., 2012). Data from the positive backbone is used, as due to residual deformations following positive loading, the initial stiffness of the negative loading direction is not accurately represented in a backbone curve derived from published hysteresis plots.

Deformation Capacity, D – Defined as the displacement at which the specimen drops to 80% of its peak strength, a definition often used as an arbitrary indication of failure in experimental testing. Lower of the positive or negative loading direction deformation capacity is taken.

Strength, Q – The peak strength of the specimen, determined as the largest of the positive or negative peak strength. Comparisons of pre- and post-repair strengths were kept consistent for each specimen (i.e., if peak strength was in the positive direction pre-repair, the comparison was made to the same loading direction following repair).

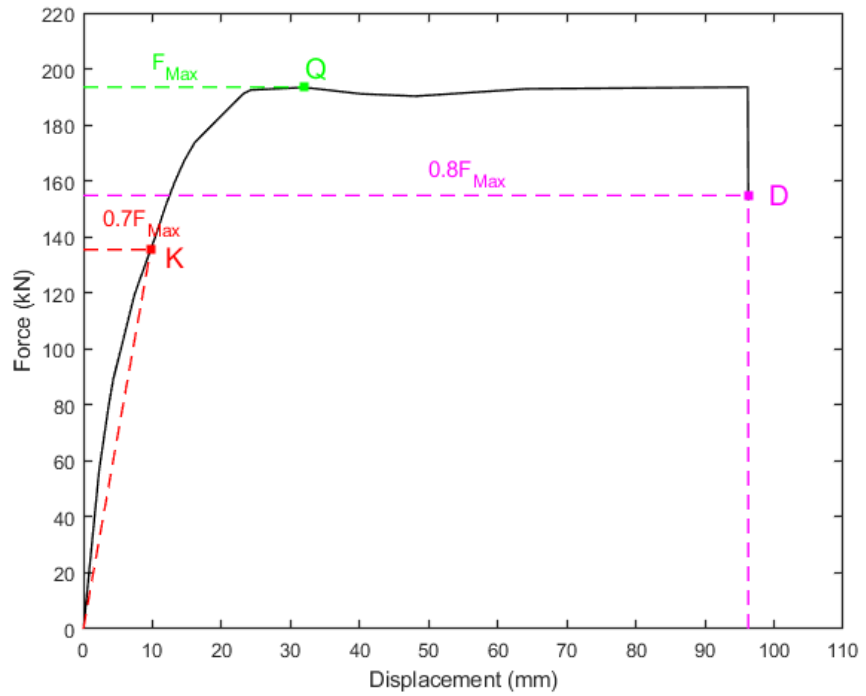
Based on the parameters outlined above, modification factors were determined for the change in stiffness, strength, and deformation capacity to quantify the effectiveness of repairs for each specimen in the database. These modification factors are defined below, in addition to in Figure E2-1b.

Stiffness Modification Factor, λ_K – The proportional change in secant stiffness to 70% of peak strength following repairs of damaged components.

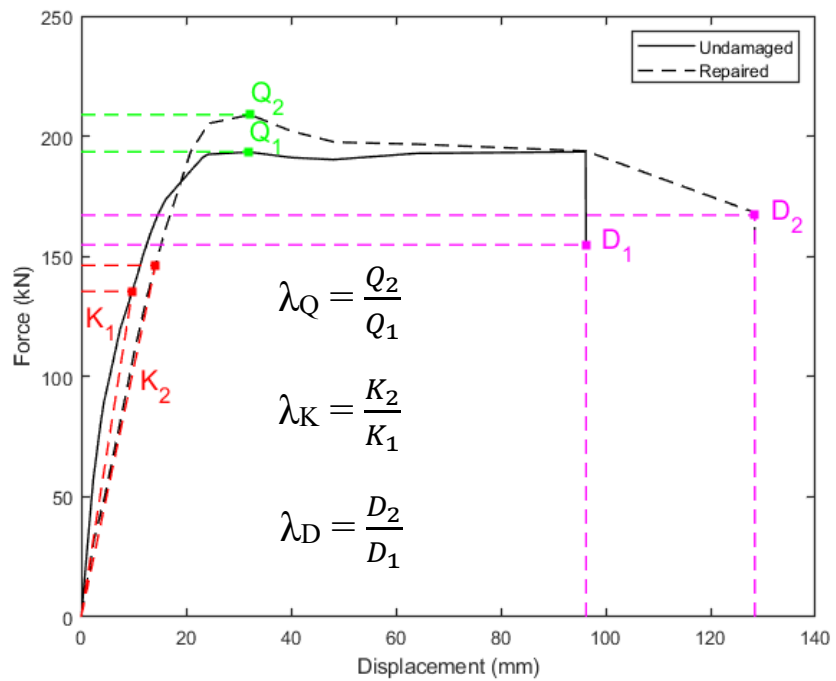
Deformation Capacity Modification factor, λ_D – The proportional change following repair, in the displacement at the point of 20% reduction in strength. In determining the deformation capacity factor, λ_D , a variety of scenarios were encountered where this definition did not produce a logical result. Comparison of hysteresis plots, where either the pre- or post-repair hysteresis curves do not see a 20% degradation in strength or no degradation at all, does not produce a useful observation of the change in deformation capacity. In cases where the deformation capacity of the specimen could not be reasonably assessed, and no signs of a reduction in deformation capacity were present, a value of 1 was assigned.

Strength Modification Factor, λ_Q – The proportional change in peak strength following the repair of the damaged component.

To allow for further analysis of the data collected from the included studies, the observable damage indicators (e.g., spalling, bar buckling etc.) were further categorized into primary, secondary, and tertiary damage indicators. The designation *primary* was assigned to the most severe of the observable damage indicators, with damage to steel reinforcement often outranking concrete damage and more severe damage indicators outranking lower levels of damage (i.e., heavy > moderate > light).



(a)



(b)

Figure E2-1 (a) Determination of strength (Q), stiffness (K) and deformation capacity (D) based on specimen backbone data. (b) Determination of repair modification factors for strength (λ_Q), stiffness (λ_K) and deformation capacity (λ_D) based on the comparison of undamaged and repaired specimen backbone data.

The database can be found in M. Sarrafzadeh’s PhD Thesis (under review) entitled “Residual Capacity and Reparability of Moderately-Damaged Reinforced Concrete Ductile Frame Structures” (Sarrafzadeh, 2021).

E2.2.1 Digitization of Published Hysteresis Plots

To extract the information described in the previous section, the plots of the hysteretic behavior of each specimen were manually digitized into backbone curves, based on available published materials. This was done for positive and negative loading directions for each specimen in both pre- and post-repair tests. The plots were converted into data points using conventional digitization software which allows manual tracing of hysteresis plots into raw data. Figure E2-2a is an example of the digitization software used to trace the hysteresis plot published in Celebi and Penzien (1973). Figure E2-2b then shows a plot of the extracted data, depicting the backbone curve for the positive loading cycles of the specimen shown in Figure E2-2a.

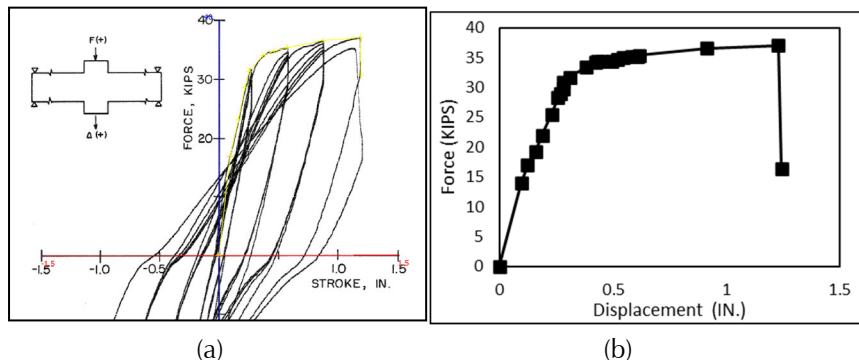


Figure E2-2 (a) Digitisation process of published hysteresis plots – hysteresis plot shown for specimen 7R from [90] (b) Plot of backbone data extracted through digitization process shown in plot (a).

Following the extraction of the backbones, the procedure outlined above was carried out for each study, generating the stiffness, strength, and deformation capacity for the pre- and post-repair backbones, as well as the corresponding modification factors. The full results of these values are discussed in the following sections, with attention given to each component type, level of damage, and repair methods.

E2.3 Database Summary for Columns

The repair database contains 39 column specimens from experimental programs listed in Tables E2-15 to E2-22 of Section E.8. An overview of some general column specimen parameters is presented in Figure E2-3. Most of the column specimens were designed to the Caltrans Highway Design Guide, with a circular cross section also being the most common,

representative of the large number of bridge type columns in the database. Axial load up to a maximum of 17.7% ($P/A_g f'_c$) was applied to the columns, with 68% of the specimens tested with an axial load ratio between 5-10% and 21% between 10-20%. It is worth noting that no columns in the database were tested at higher axial loads, near to or above balance point. Higher axial loads may impact the effectiveness of repairs, particularly where cracks may close and become visually not observable.

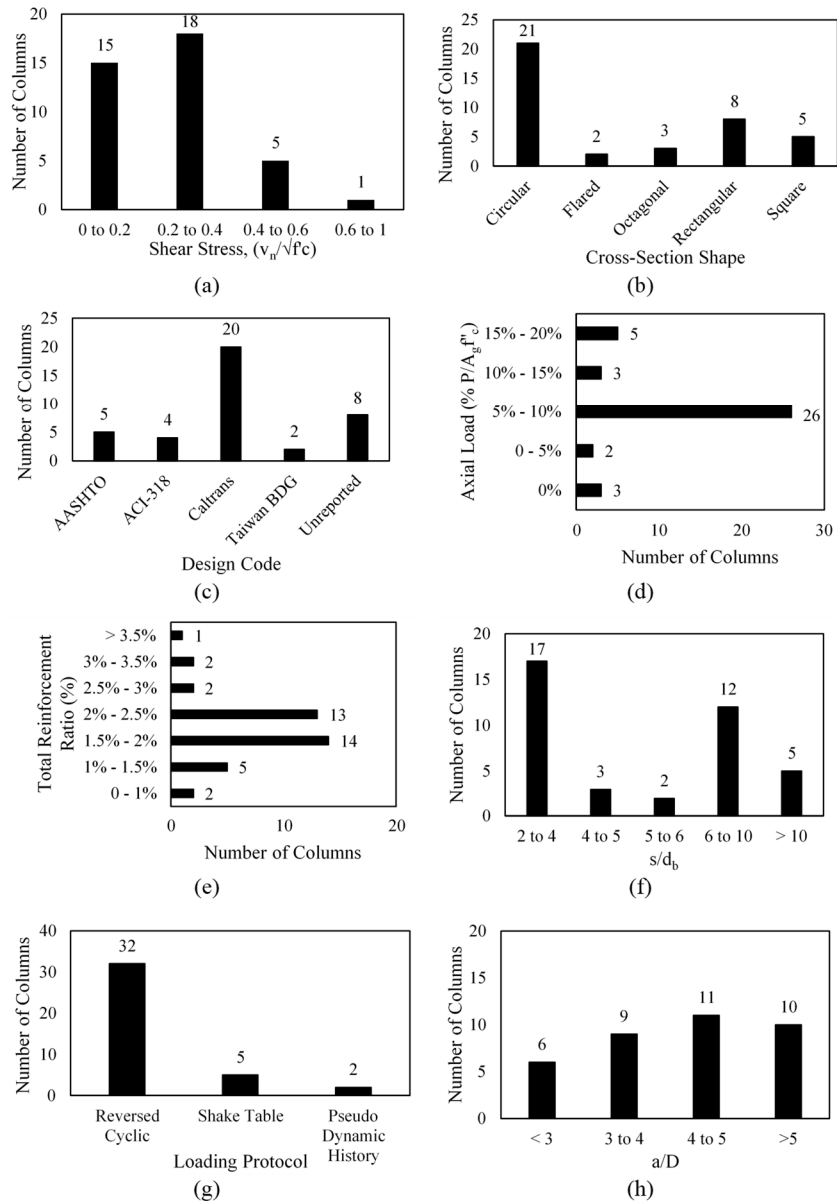


Figure E2-3 Distribution of column specimen (a) Shear stress normalised by $\sqrt{f'_c}$ (b) Specimen cross sections (c) Design code (d) Axial load ratio (e) Total reinforcement ratio (f) transverse reinforcement spacing ratio (g) loading protocol and (h) Shear span to depth ratio.

Approximately 70% of the specimens had a total reinforcement ratio (A_s/A_g) between 1.5 – 2.5% with an overall maximum of 5.5% and a minimum of 0.75%. Transverse reinforcement spacing ratio, s/d_b ranged between 2-15.8, with ~60% of the specimens having an $s/d_b \leq 6$ in line with current ductile detailing requirements of current ACI 318-19.

Static cyclic or reversed cyclic loading, typical of laboratory components tests, were the most common loading type, with a minority (18%) of the specimens being tested under dynamic earthquake histories or via shaketable testing. All specimens which made use of a shake table as part of their loading protocol were from studies by Vosooghi et al. (2008) and Vosooghi and Saiidi (2013).

The shear span to depth ratio (a/D) for the columns ranged between 2.3-8.6, with 85% being >3 , representing a minimal number of squat or shear dominated specimens.

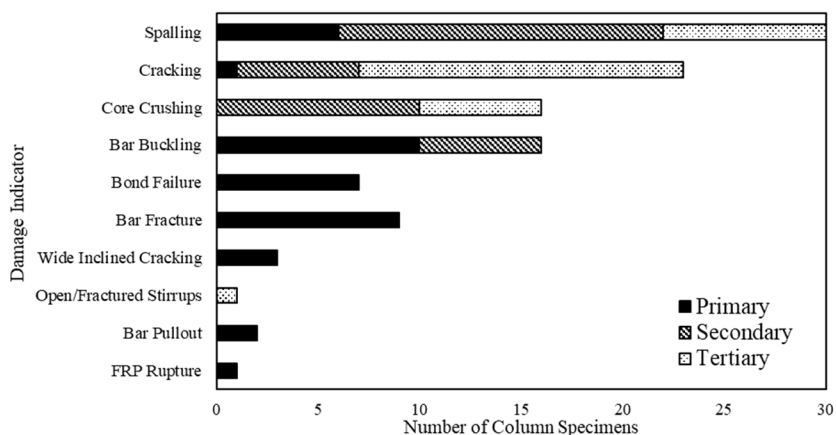


Figure E2-4 Distribution of primary, secondary and tertiary damage indicators observed in column specimens prior to repair. A dashed line is used to separate light/moderate and heavy primary observed damage indicators.

Figure E2-4 provides a summary of the observed damage indicators for columns in the database. These are separated into primary, secondary, and tertiary damage indicators prior to repair, where the primary damage represents the most significant observed damage, often existing along one or more other damage indicators. In total, 82% were classified to have a heavy damage state with the remaining 18% classified as moderately damaged. For heavy damage, bar buckling was the most common primary indicator, occurring in 31% of heavily damaged columns, followed by bar fracture at 28%. Almost all cases of longitudinal bar fracture were preceded by bar buckling, apart from the retrofitted columns in Saiidi and Cheng (2004),

which did not see buckling as a result of additional confinement provided by a large steel jacket prior to damage. Bond Failure was observed in 21% of the heavily damaged columns, and in all cases was due to the termination of longitudinal lap splices in the potential plastic hinge region. As outlined in Table E2-1 this damage was classified as heavy, as it represents a deficient detail, requiring a retrofit type repair and a change in failure mechanism. For moderately-damaged columns, the observable damage can be separated into cracking and spalling. As would be expected, all moderately-damaged columns exhibited cracking, and six experienced spalling as a primary indicator, with one experiencing a primary damage of only cracking. A summary of the combinations of repairs used for the columns in the database are presented in Figure E2-5a with an additional breakdown of the category of repairs for both moderate and heavily damaged columns in Figure E2-5b. Moderately-damaged columns were repaired largely by category 0 repairs, while heavily damaged columns were dominated by category 2 repairs, where specimens were often strengthened or retrofitted to address deficient detailing.

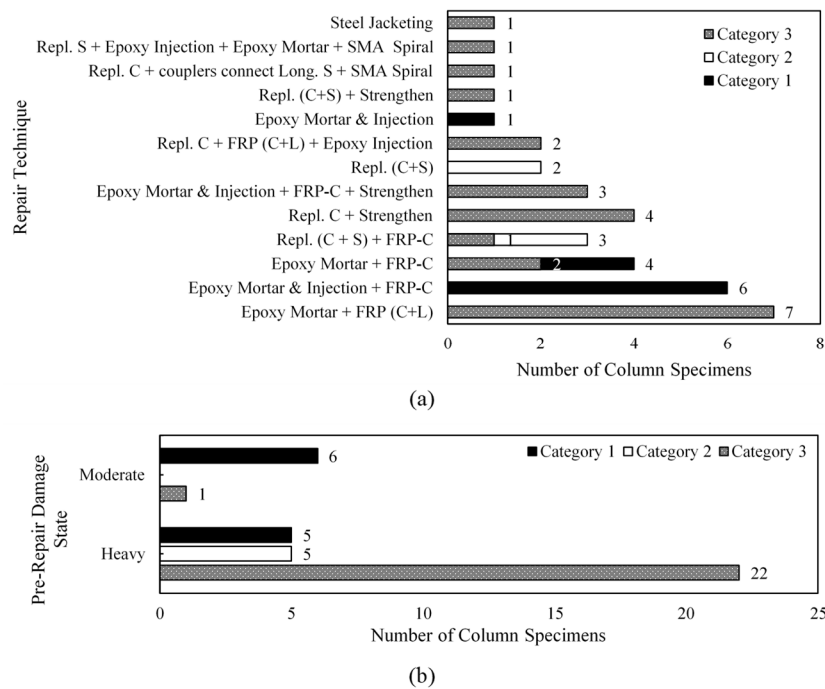


Figure E2-5 (a) Distribution of repair techniques applied to column specimens in the database. Blue bars represent simple repair techniques (category 0) and yellow hatched bars represent complex repair techniques (category 1 or 2). (b) Distribution of complex and simple repair methods utilized in rehabilitation of moderate and heavily damaged column specimens.

E2.3.1 Overall Effectiveness of Column Repairs

In this section, an overview of the backbone analysis is provided based on specific repair techniques. The average recovery in stiffness, strength, and deformation capacity for each repair technique is presented below in Figure E2-6 and Figure E2-7 for moderate and heavily damaged columns respectively. These results do not account for the category of the repairs and simply focus on the effectiveness of the various repair methods, based on the pre-repair damage state. In these figures, bars represent the average modification factor for each respective repair technique, while error bars represent +/- 1 standard deviation from the presented average. The number of specimens repaired by the respective repair technique are shown at the base of each bar.

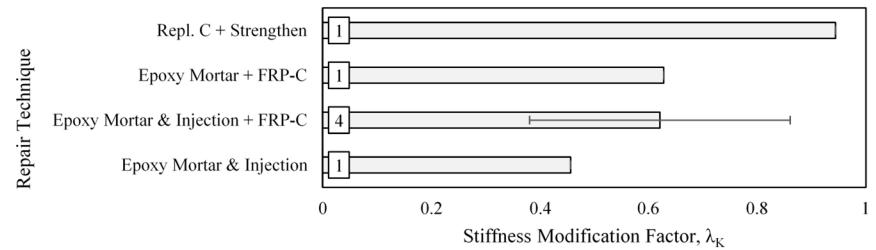
The data encompass a wide range of specimen specifications, damage indicators, and combinations of repair techniques. As such, overall database averages encompass large variations, which do not convey meaningful information on the overall effectiveness of specific repair techniques. Outliers were omitted from the overall averages presented in Table E2-3. The omission of results is also indicated in Figure E2-6 and Figure E2-7 with hatched bars for the corresponding repair technique where specimens were omitted.

Based on the averages in Table E2-3 we can conclude that in general, stiffness of damaged specimens is not fully recoverable, with averages for both moderate and heavily damaged specimens being between 60-80% of the original specimen stiffness. Original column strength however is fully recovered in all columns and exceeded in most cases, regardless of pre-repair damage state. Strength increases can be due to changes in material properties, such as the strain hardening and aging of reinforcement following prior loading, in addition to the impact of specific repairs. The results for deformation capacity also reflect successful recovery for both moderate and heavy damage states with averages above 1. A larger spread in the data in heavily damaged columns is observed with a standard deviation of +/- 1.34. This is reflective of both the large increases observed following retrofit type repairs (category 2), in addition to signaling the greater difficulty in recovering deformation capacity following heavy damage, as indicated by the minimum λ_D of 0.58.

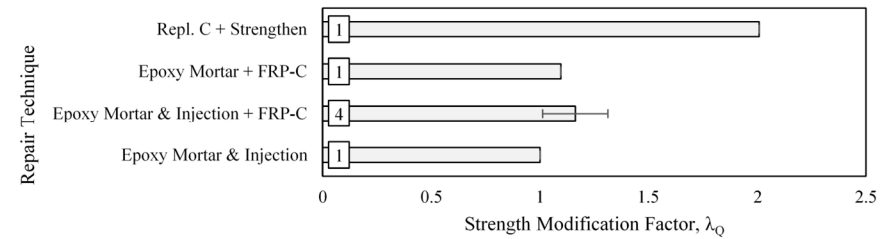
The variability in the test results shows that a more refined analysis beyond just moderate or heavy damage states could be of value, as addressed in the following section.

Table E2-3 Average Stiffness, Strength, and Deformation Capacity Modification Factors for Column Specimens

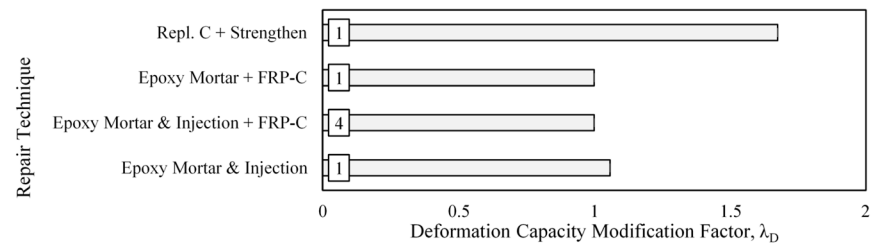
Damage State Mod. Factors	Moderate				Heavy			
	Min	Max	Avg.	Std. Dev.	Min	Max	Avg.	Std. Dev.
Stiffness, λ_K	0.34	0.94	0.64	0.22	0.32	1.37	0.83	0.24
Strength, λ_Q	1.00	2.01	1.25	0.36	0.68	1.59	1.14	0.22
Deformation Capacity, λ_D	1.00	1.67	1.10	0.25	0.58	6.00	1.73	1.34



(a)



(b)



(c)

Figure E2-6 Summary of (a) Stiffness, λ_K (b) Strength, λ_Q and (c) Deformation Capacity, λ_D modification factors for all repair techniques applied to moderately-damaged column specimens. Bars represent average value for the considered repair technique. Error bars represent +/- 1 standard deviation from the average. The number of specimens repaired via each technique is presented at the base of each bar. Hatched bars represent results which are omitted from the final averages presented in.

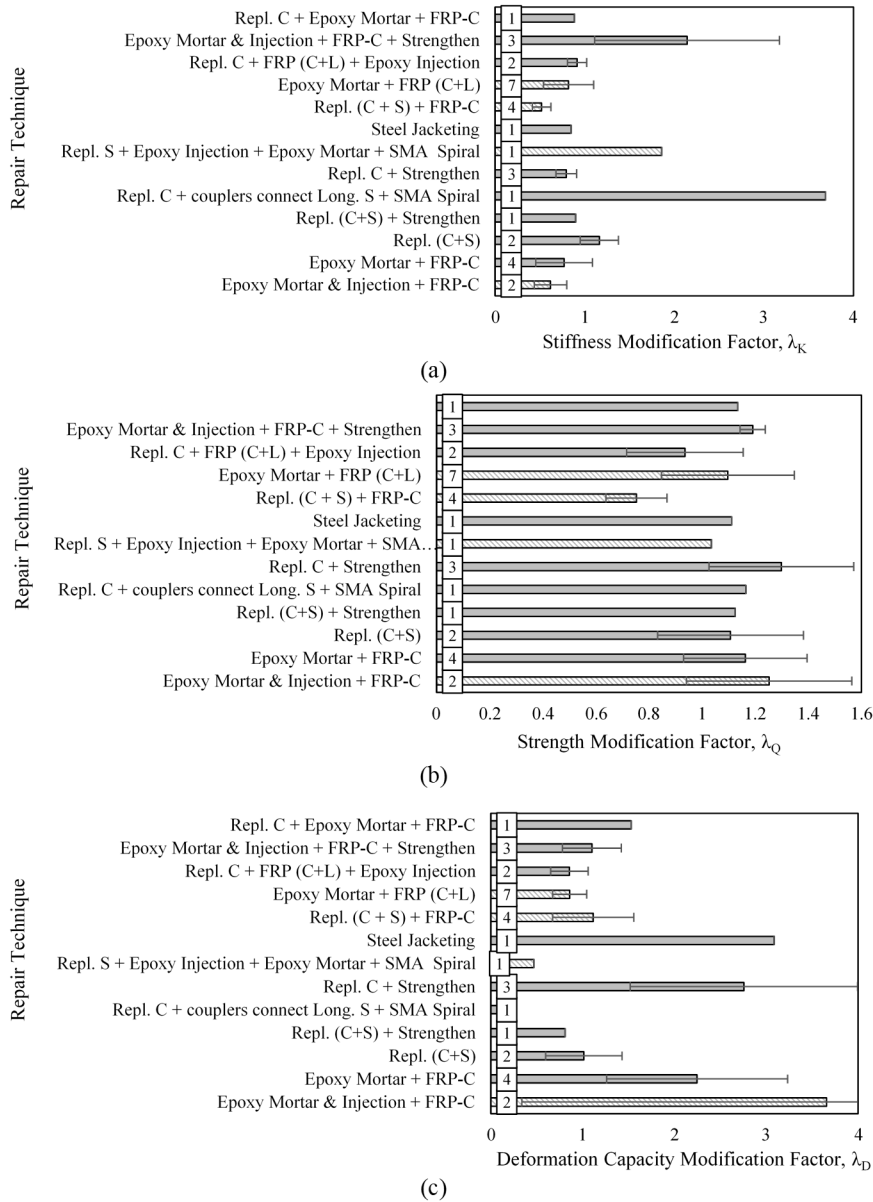


Figure E2-7 Summary of (a) Stiffness, λ_K (b) Strength, λ_Q and (c) Deformation Capacity, λ_D modification factors for all repair techniques applied to heavily damaged column specimens. Bars represent average value for the considered repair technique. Error bars represent +/- 1 standard deviation from the average. The number of specimens repaired via each technique is presented at the base of each bar. Hatched bars represent results which are omitted from the final averages.

E2.3.2 Effectiveness of Column Repair Based on Specific Damage

In this section, further analysis of the data is used to provide context with respect to specific primary damage states. The results are separated based on

repair Categories 0, 1, and 2, with the accompanying discussions used to provide recommendations on the effectiveness of column repairs.

E2.3.2.1 Category 0 Repairs

As previously outlined in Section E.2, Category 0 repairs aim to reinstate the initial specimen characteristics, without significant changes to behavior or failure mechanism. Such repairs are generally applied to specimen with lower levels of damaged and seismic detailing conforming to modern design codes such as the $s/d_b \leq 6$ and continuous reinforcement through the plastic hinge zone. Eight specimens fell into this category, with primary damage indicators of spalling or bar buckling. Table E2-4 outlines the average modification factors for each primary damaged indicator, with discussions presented below.

Table E2-4 Effectiveness of Category 0 Repairs on RC Columns based on Primary Damage Indicators

Primary Damage	Spalling			Bar Buckling		
Damage State	Moderate			Heavy		
Modifier	λ_K^*	λ_Q	λ_D	λ_K	λ_Q	λ_D
Average	0.53	1.06	1.01	0.40	0.92	1.15
Standard Deviation	0.09	0.08	0.03	0.12	0.15	0.22
Maximum	0.63	1.16	1.06	0.49	1.03	1.31
Minimum	0.46	1.00	1.00	0.32	0.82	1.00
Column Database IDs	C4, C12, C18, C19 (*C18 omitted as outlier)			C13, C14		

Spalling

Spalling as a primary damaged indicator is considered a moderate damage state. All four columns with this primary damage state (C4, C12, C18 and C19) also experienced some level of cracking as secondary damage, and were repaired via the repair techniques Epoxy Mortar + Injection, Epoxy Mortar + FRP-C or Epoxy Mortar and Injection + FRP-C. An example of a column with this primary damage indicator is presented in Figure E2-8, showing specimen NHS1 from Vosooghi and Saiidi (2013) prior to repair. Overall, the results for strength and deformation capacity show full recovery, reflecting the same result as that discussed for the overall database in Section E.3.1. Stiffness recovery however appears relatively low, with an average λ_K of 0.53 and a range of 0.46 – 0.63. It should be noted that the stiffness recovery of specimen NHS1 was omitted from the overall average ($\lambda_K = 0.34$), citing the use of low-quality repair mortar by the authors as a contributing factor to the poor performance. All specimens were tested at

axial load ratios between 6.6 – 10%. Of the four columns in this category, only one did not use FRP-C in its repair (C4), achieving the lowest in-group λ_K of 0.46. The remaining columns were repaired via combinations of epoxy and FRP-C. Comparison of the results for specimens tested through dynamic shaketable excitation (C18 and C19) vs. those tested under static loading (C4 and C12) show no significant variation in post-repair performance, with averages tightly in line with those presented in Table E2-4.

It was not made clear in the analyzed studies if axial load was removed prior to repair or not, however the assumption was made that axial load was removed based on typical laboratory testing procedures and safety considerations. This may point to a lower level of stiffness recovery when conducting such repairs in the field, as the presence of axial load during repairs may make cracks less visible and more difficult to inject with epoxy resin. This is observed within this database, with methods involving epoxy injection and mortar, resulting in more modest recovery in stiffness in columns damaged under axial load, in comparison to elements tested without axial load, such as beams, based on results outlined in Section E.4.

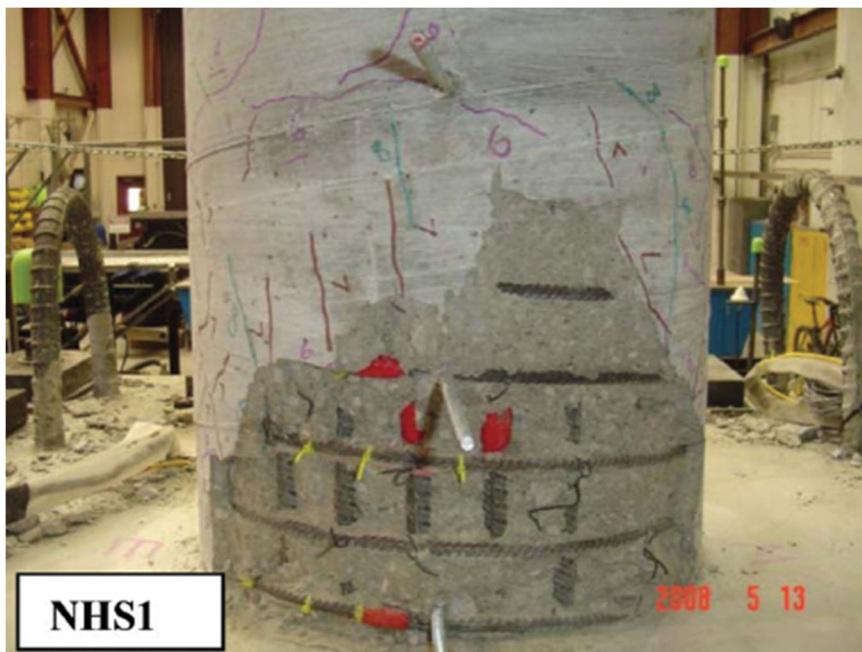


Figure E2-8 Specimen NHS1 (C18) from Vosooghi and Saiidi (2013) following failure, shown as an example of a column with spalling as its primary damage state.

Bar Buckling

Columns C13 and C14 reported bar buckling as their primary damage indicator and were repaired via Category 0 repair methods of Epoxy Mortar

+ FRP-C and Epoxy Mortar and Injection + FRP-C respectively. Deformation capacity was fully recovered in both specimens; however, strength was only recovered in column C14. Column C13 was only able to recover 82% of its original peak strength. The recovery of stiffness was between 32% and 49% of specimen initial stiffness. Specimen C-R from Chang and Loh (2004) was responsible for the λ_K of 0.32 and assessment of the repair methodology identifies that the lack of crack injection, particularly at the column-foundation interface where a crack was noted following initial damage. Yield penetration at interface cracks can significantly contribute to the loss of stiffness in RC components Opabola and Elwood (2020) and as such not addressing cracks in this area and the loss of bond at the interface will result in minimal recovery of stiffness. This specimen was also the one column with bar buckling, repaired via simple methods which did not recover its strength and as such, the repairs in this test appeared to be ineffective in rehabilitating the specimen.

Buckled reinforcement was left as is during repairs in both tests, and despite this, no fracture of reinforcement occurred during the re-testing of either specimen to failure. It should be noted that buckling in specimen C14 was very minor and resembled the early onset of bar buckling.

Although a limited number of tests are presented here for the category, it is clear the recovery of deformation capacity using epoxy mortar and FRP-C is possible, even with the presence of some reinforcement buckling. Comparison of the two specimens shows that the absence of epoxy injection and the lack of treatment for significantly buckled reinforcement resulted in poor post-repair strength and stiffness recovery. As such, the application of Category 0 repairs when significant buckling has occurred is not a suitable repair technique, and an even modest stiffness recovery cannot be relied on if epoxy injection is not applied during Category 0 repairs.

E2.3.2.2 Category 1 Repairs

Only two specimens, columns C1 and C3 were classified as having a Category 1 repair, where a relatively complex repair method, involving the complete replacement of materials was used, without the aim to enhance the specimen characteristics beyond original capacity. Both specimens underwent the full replacement of steel and concrete in the damaged plastic hinge region, with primary damage indicators of bar fracture and bar buckling. The results for the post-repair recovery of stiffness, strength and deformation capacity are presented in Table E2-5.

The data presented here is of interest considering both columns were from the same study (Lehman et al., (2001)), nominally identical and were

subjected to the same peak displacement demand of 7.3% component drift. Where the tests differ is in the application of the Repl. C + S repair method.

Columns 430SR (C3) which suffered bar buckling was repaired using a RC jacket. The aim of the repair was to contain yielding at the base of the column. This was achieved by severing all existing reinforcement and relying on the new jacket reinforcement to maintain the specimen original strength. Meanwhile, column 407SR (C1) approached the repair by carrying out concrete and steel replacement over a length equal to 1.8D from the base of the column. This was carried out to ensure the replacement of any steel which may have yielded. Mechanical couplers were used at the top of the replacement region and below a strain penetration depth in the foundation to replace longitudinal bars, in addition to new transverse reinforcement. Concrete was also fully recast along the full 1.8D + strain penetration depth. The new longitudinal bars were also of a higher grade than the initial reinforcement, although it is unclear if this was an intentional detail during the design of the repairs.

Table E2-5 Effectiveness of Category 1 Repair Techniques on Heavily Damaged RC Columns Based on Primary Damaged Indicators.

Primary Damage	Bar Buckling			Bar Fracture		
Damage State	Heavy			Heavy		
Modifier	λ_K	λ_Q	λ_D	λ_K	λ_Q	λ_D
Average	1.31	0.91	0.72	1.01	1.30	1.31
Standard Deviation	-	-	-	-	-	-
Column Database IDs	C3			C1		

Both methods were successful in stiffness recovery, with specimen 430SR (C3) increasing the initial stiffness as a result of the change in specimen cross section. The change in strength was largely as intended based on the design of the repairs, with geometric construction constraints resulting in the slight reduction observed in specimen 430SR. The recovery in deformation capacity is however where a difference in the effectiveness of the repairs is observed. The use of mechanical couplers in this instance was very successful, with an increase in deformation capacity observed, without a change in failure mechanism. While no change in failure mechanism was observed for specimen 430SR, the concrete jacket still saw a substantial reduction in deformation capacity with a λ_D of 0.72. Comments by the authors seem to indicate that a model of the repaired column had predicted such a reduction.

It is noted that the repairs using mechanical couplers can be logistically difficult, especially if a column is heavily reinforced. However, the results in this case indicate a very successful repair and a viable method where practical. Despite the shortcomings of the concrete jacketing method, the method is considered here to also be a viable option for this level of damage, considering the reductions in capacity were in line with pre-repair calculations. This suggests that the method may be appropriate in scenarios where the geometry of the column section allows for a full recovery in all three performance categories.

E2.3.2.3 Category 2 – Strengthening and Retrofit Type Repairs

A total of 22 columns were repaired via methods which were classified as Category 2. These repairs were considered a type of retrofit, aimed at changing the mechanism of the columns or intended to enhance the original specimen characteristics. As such, columns which had deficient seismic detailing (e.g., presence of lap splices in the potential plastic hinge region, or wide transverse reinforcement) or those with brittle failure mechanism such as shear failure, were classified in this category, in addition to specimens which were strengthened or enhanced following heavy damage. In total, three moderately-damaged and 19 heavily damaged columns were classified in this category.

Moderate Damage Indicators

The moderately-damaged columns included one column which suffered cracking and two which suffered spalling as their primary damage indicator, the results for which are outlined in Table E2-6.

Table E2-6 Effectiveness of Category 2 Repair Techniques on Moderately-Damaged RC Columns Based on Primary Damaged Indicators

Primary Damage	Cracking			Spalling		
	λ_K	λ_Q	λ_D	λ_K	λ_Q	λ_D
Average	0.94	2.01	1.67	0.82	1.24	1.00
Standard Deviation	-	-	-	0.05	0.17	-
Maximum	-	-	-	0.85	1.37	1.00
Minimum	-	-	-	0.78	1.12	1.00
Column Database IDs	C5			C20, C21		

Cracking

Column C5 exhibiting the primary damage indicator of cracking and was repaired via the method of Repl. C + Strengthen. This column had an s/d_b

ratio of 10.67 and an axial load ratio of 10%. The strengthening portion of the repair involved the addition of transverse reinforcement to reduce the s/d_b ratio to 3.33, increase of the section depth and width by 23% and the addition of a new reinforcement cage, jacketing the original section. This resulted in the strength of the section to double ($\lambda_Q = 2.01$) and a 67% increase in deformation capacity. The stiffness of the section was recovered to 94% of the original undamaged section. This repair was conducted following earthquake damaged, to simulate strengthening of an element with inadequate detailing, which would typically be carried out during a retrofit. The peak displacement demand prior to repairs was 2% component drift. Strength degradation had initiated, given the deficient seismic detailing of the specimen, however, the observable damage was still moderate when the test was stopped. An equivalent column strengthened prior to any damage performed similarly to column C5, suggesting the repairs were successful in enhancing the seismic performance of the column, and the application of prior loading did not compromise the retrofit.

Spalling

The two Category 2 specimens which suffered spalling as their primary damage were columns C20 and C21. Both specimens were tested using dynamic shaketable loading and were loaded under a constant axial load of 7.5%. Both columns were designed to represent older construction and included longitudinal lap splices in the potential plastic hinge region. The s/d_b for columns C20 and C21 was 10 and 8 respectively, with both being larger than the maximum of 6 currently permitted by seismic code provisions. Both columns were repaired via the Epoxy Mortar & Injection + FRP-C method. Due to the presence of a lap splice and large transverse reinforcement spacing in the potential plastic hinge region, this repair addresses the deficient detailing, particularly with the added confinement from the FRP-C. The results indicate that the recovery of strength and deformation capacity were successful and resulted in a full recovery of both parameters. Stiffness recovery was also substantial in with an average λ_K of 0.82. Despite the authors citing no indication of bar slip or bond failure during initial damage, it is likely that some level of bond loss has occurred in these specimens given the presence of lap splices terminating in the plastic hinge region. The results for stiffness recovery of specimens with bond failure, outlined later in this section, support this theory which also achieved an average λ_K of 0.82 using similar repair methods. In addition, the presence of vertical cracking (bond splitting cracks) following damaging excitation, as shown below in Figure E2-9 points to the presence of bond degradation.

Overall, the results for the columns outlined here are more indicative of the post-repair recovery of specimens with bond failure, however the repairs were still considered to be successful in rehabilitating the performance of the columns close to a pre-damage condition. Changes in deformation capacity were not directly assessed as the specimens did not see failure during initial loading. Deformation demands following repairs were significantly larger however and as such both columns were assessed to have λ_D values of 1.00, given no evidence of a reduction was observed.

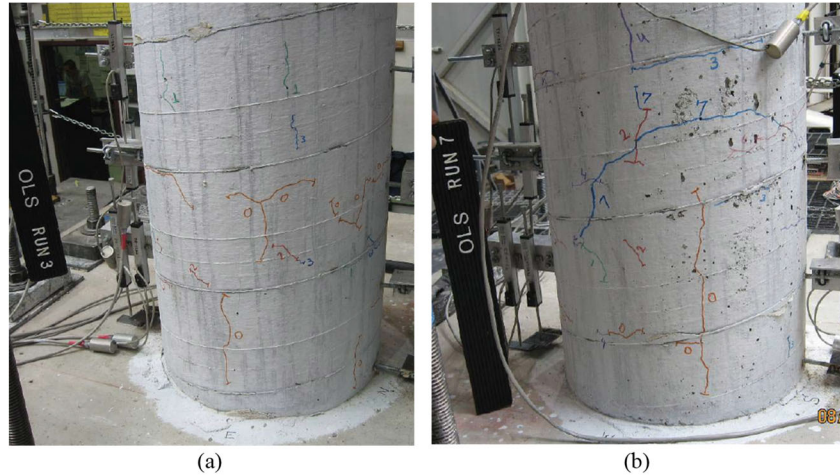


Figure E2-9 Post-excitation damage of specimen OLS from Vosooghi and Saiidi (2013), showcasing the vertical cracking likely indicative of bond degradation. Damage photos obtained from Vossoghi and Saiidi (2013) following (a) excitation run 3 and (b) excitation run 7.

Four main primary damage indicators were identified for the 19 heavily damaged columns, including bar buckling, bar fracture, bond failure, and wide inclined cracking. The results for these damage indicators are outlined in the following two sections, separated into steel related primary damage and non-conforming or brittle columns.

Heavy Damage Indicators – Steel Damage

The results for bar buckling and fracture are presented below in Table E2-7. In total, six columns suffered bar buckling and five suffered bar fracture prior to repairs.

Table E2-7 Effectiveness of Category 2 Repair Techniques on Heavily Damaged RC Columns Based on Primary Damaged Indicators with Steel Damage

Primary Damage	Bar Buckling			Bar Fracture		
Modifier	λ_K	λ_Q	λ_D	λ_K	λ_Q	λ_D

Average	0.90	1.15	1.02	0.78	0.99	0.79
Standard Deviation	0.24	0.18	0.30	0.21	0.25	0.13
Maximum	1.37	1.32	1.53	0.99	1.26	1.00
Minimum	0.72	0.84	0.58	0.44	0.68	0.64
Column Database IDs	C8, C22-24, C26, C27			C2, C25, C28-30		

Bar Buckling

Columns C8, C22-24, C26 and C27 were repaired following bar buckling, using either the Repl. C + Epoxy Mortar + FRP-C or the Epoxy Mortar + FRP (C+L) methods. All specimens, except column C8, had seismic detailing in line with modern code provisions ($s/d_b \leq 6$ and no lap splice termination in potential plastic hinge region), while column C8 had an s/d_b ratio of 7, which is not significantly higher than the permitted spacing and in the range of construction tolerances. On average, the specimens were able to fully recover their strength and deformation capacity, while reinstating 90% of their initial stiffness, indicating successful repairs from a safety-level consideration. However, instances where strength or deformation capacity were not recovered can be observed based on the minimum values presented in Table E2-7 and are further discussed below. A note of interest here is that none of the tests treated the buckled reinforcement as part of their repairs, and despite this were able to in most instances increase or maintain their deformation capacity. Although the results are favorable here, leaving buckled reinforcement untreated is not recommended in non-emergency repairs such as the repair of frames in buildings, which are intended for long term and permanent recovery. A short description is provided below for specimens which did not satisfactorily recover their strength or deformation capacity outlining areas of concern for such repairs.

Specimen 2-R – He et al. (2013):

Specimen 2-R (column C22) failed to recover its deformation capacity and achieved a λ_D of 0.58, a substantial reduction from original capacity. Failure in this column occurred due to concrete crushing in the plastic hinge region, as well as rupture of the FRP-L. Pull-out of the mechanical anchorage system applied for the FRP-L was also reported. It should be noted that a torsional load was applied to this column simultaneously to the lateral loading, with a torque to moment ratio, T/M of 0.2, however the failure was still flexural dominated. Despite the successful recovery in strength, the shortcomings of deformation capacity recovery can be attributed to lack of guidance and consistency in the design and anchorage of FRP strengthening repairs, which are further highlighted in the bar fracture section.

Specimen 4-R – He et al. (2013):

In the case of column 4-R (column C24), an almost full height FRP (C+L) repair was applied due to a large height of damage from torsional loading ($T/M = 0.6$). The failure was judged to be torsional dominated and occurred when a concrete crushing initiated in a small unrepaired region of the column at the top of the specimen. This was followed by rupture of the FRP near the crushing region, resulting in a reduction in strength and a $\lambda_Q = 0.84$. Previous specimens from the same study with lower T/M ratios and lower FRP height did not suffer a reduction in strength and as this is a torsion dominated failure, it does not address the overall reparability of heavily damaged Category 2 columns following bar buckling.

Bar Fracture

Columns C2, C25 and C28-30 suffered bar fracture as their primary damage indicator and were repaired using one of the following three methods:

- Epoxy Mortar + FRP (C+L).
- Repl. (C+S) + Strengthen
- Repl. C + FRP (C+L) + Epoxy Injection

The columns were constructed with s/d_b ratios ranging between 2 – 4.1 and continuous longitudinal reinforcement. Specimens were tested under axial load ratios between 5.5 to 16% and shear span to depth ratios, a/D between 2.5 and 6, representing a wide range of squat to slender columns with low to moderate levels of axial load.

In general, the results for post-repair performance of these columns were too inconsistent to be deemed successful, with four of the five columns seeing either a reduction in strength, deformation capacity, or both. Despite this, stiffness was relatively successful in being recovered, with an average λ_K of 0.78 or 0.86 if column 25, which left cracks up the height of the specimen un-injected is discounted.

Brief summaries are presented in Section E.7.1.3 for the columns which were not able to recover their strength and/or deformation capacity. The results indicate that the performance of FRP-L is of concern in these cases, as was alluded to with specimen 2-R in the buckling section. Shortcomings of this repair method stem from a lack of widely accepted and robust guidance on the design of such repairs, particularly in the applied anchorage solutions. Various methods of anchorage have been captured in this study with little consistency in performance. Both mechanical (He et al., (2013)) and substrate based (Rutledge and Kowalsky (2014), Saiidi and Cheng (2004))

anchorage systems failed when relied on to replace fractured reinforcement. In all cases, fractured reinforcement was left untreated, resulting in demands which the FRP-L anchorage systems could not reliably handle. Once again, repairs which do not address the steel damage and rely on external FRP-L strengthening to recover strength are not consistent enough to be recommended in a frame structure reparability scenario. Such repairs are more suitable for emergency and short-term situations, more in line with addressing issues such as emergency bridge repairs addressing transportation network issues.

Based on the tests outlined for repairs involving FRP-L following buckling or fracture of reinforcement, 56% of specimens failed to recover their strength or deformation capacity, highlighting the inconsistency in the use of such repairs, with the current state of widely implemented knowledge or guidance.

Heavy Damage Indicators – Non-Conforming and Brittle Columns

This section outlines the results for columns which were considered to be non-conforming to modern seismic codes, with brittle failure mechanisms or deficient seismic detailing such as large transverse reinforcement spacing ($s/d_b > 6$) or termination of reinforcement in the potential plastic hinge region. The primary damage indicators which were captured in this section were bond failure and wide inclined cracking. Cases of bond failure were identified as a significant spalling, exposing lap spliced reinforcement terminating in the plastic hinge region, which occurred in six columns. Wide inclined cracking was observed in two specimens, which was indicative of a clear shear dominated, brittle failure mechanism. The results for the post-repair recovery of both damage indicators are presented in Table E2-8.

Table E2-8 Effectiveness of Category 2 Repair Techniques on Heavily Damaged RC Columns Based on Primary Damaged Indicators for Non-ductile Behavior

Primary Damage	Bond Failure			Wide Inclined Cracking		
	λ_K	λ_Q	λ_D	λ_K	λ_Q	λ_D
Average	0.82	1.26	2.83	0.90	1.39	4.17
Standard Deviation	0.08	0.19	0.88	0.22	0.12	2.58
Maximum	0.93	1.59	3.68	1.05	1.47	6.00
Minimum	0.73	1.05	1.35	0.74	1.31	2.35
Column Database IDs	C6, C7, C9, C15-17			C10, C11		

Bond Failure

Database columns C6, C7, C9, C15-17 experienced the primary damage indicator of bond failure following initial damage. The specimens all consisted of lap splice termination in the plastic hinge region and had s/d_b ratios ranging between 6.7 – 14. All six had spalling and cracking as their secondary and tertiary damage indicators, with an example shown in Figure E2-10 from the study by Saadatmanesh et al. (1997). The applied repair techniques consisted of:

- Repl. C + Strengthen
- Epoxy Mortar + FRP-C
- Steel Jacketing

The columns which were repaired via the Repl. C + Strengthen method included complete replacement of concrete in the splice zone and the addition of transverse bars to reduce the s/d_b ratio to between 2.5-3.6 from 10-14.3. Columns C15-17 were tested without axial load. Following repairs, the columns were able to recover and increase their initial strength and increase their deformation capacity. A recovery in stiffness between 73-93% was observed, given reinforcement was able to maintain bond strength, and yield following repairs. Cracking and spalling of cover concrete were again observed following repair, however the onset of this damage was delayed due to the additional confinement and concrete repair.

Column C6 was repaired via Steel Jacketing and was tested under an axial load ratio of 17.7% and an s/d_b ratio of 6.67. The steel jacket was placed over the splice zone and filled with epoxy grout. The objective of the repair was once again to increase the level of confinement and delay the onset of spalling and loss of bond in the spliced region. A similar result was obtained with a significant increase in deformation capacity ($\lambda_D = 3.09$) and an increase in strength. Stiffness was recovered to 85% of its pre-damage condition. This repair resulted in a more ductile behavior of the specimen, with failure occurring much later due to bond loss and yielding of the steel jacket.



Figure E2-10 Specimen C-1 from Saadatmanesh et al. (1997) following failure, shown as an example of a column with bond failure as its primary damage state.

Columns C7 and C9 from Saadatmanesh et al. (1997) were repaired via Epoxy Mortar + FRP-C method. Both columns saw an increase in strength and deformation capacity as a result of the repair, primarily due to the additional confinement of the FRP-C. Hysteresis plots, pre- and post-repair for both columns show a clear change in mechanism with a more prolonged peak and significantly larger hysteresis loops following repairs. The recovery in stiffness was relatively high, up to 90%, likely due to increased bond stability between the reinforcement and the repair mortar, in conjunction to the confining pressures and delay in concrete cover degradation due to the FRP-C. In addition, the rate of stiffness degradation was reported to be significantly reduced in the repaired columns in comparison to the original columns. These results are of value when considering the repair of columns with deficient seismic detailing.

In all six columns, the additional confinement and bond stability provided by FRP-C, steel jacketing or additional transverse reinforcement significantly improved the performance of the columns. In every case, a drastic change in the hysteretic behavior of the specimens was observed with a shift from non-ductile behavior where steel was not allowed to yield and dissipate energy, to large hysteresis loops and sustained peak strength. An example of this shift in mechanism is shown below in Figure E2-11 which is representative of what was observed for all six specimens.

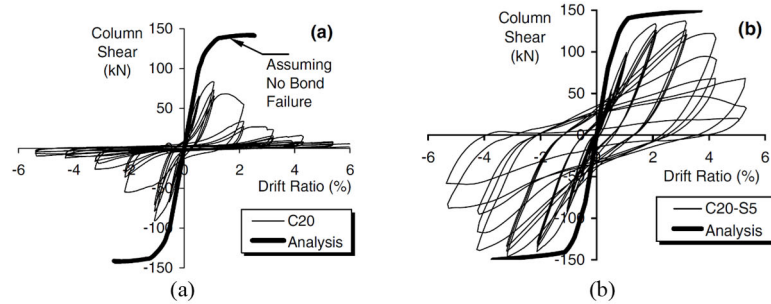


Figure E2-11 Example of shift from brittle to ductile mechanism in columns with lap splice termination in the potential plastic hinge region following retrofit type repairs. Figures adapted from El-Souri and Harajli (2011) for column C17.

Wide Inclined Cracking

Columns C10 and C11 suffered shear failure characterized by significant inclined cracking within the body of the specimen as shown in Figure E2-12.

A summary of the performance of each specimen can be found in Section E.7.1.4. The repair of both specimens involved reinstating the column section through epoxy mortar and injection, while providing additional confinement through externally bonded FRP-C. As indicated by the results in Table E2-8, the repairs were able to enhance the strength and significantly increase the deformation capacity of both columns. Stiffness was full restored in column C10 while column C11 was able to only recover 74% of its original stiffness. In both cases a complete shift in failure mechanism was observed, moving away from a shear failure to a more ductile, flexural controlled failure mechanism, largely as a result of the additional confinement from the FRP-C. The repair of shear critical columns with this repair technique can overall be considered successful, despite the inconsistent recovery in stiffness.

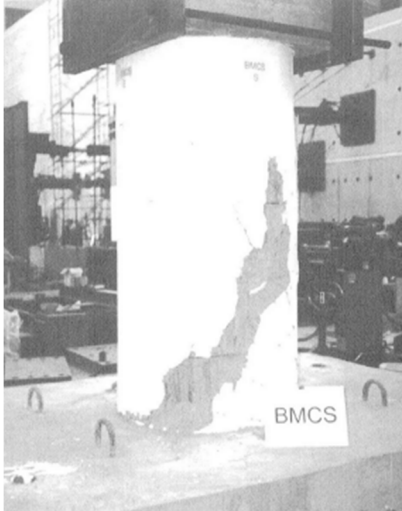


Figure E2-12 Specimen BMCS from Li and Sung (2003) following failure, shown as an example of a column with shear failure as its primary damage state.

E2.4 Database Summary for Beams

A total of seventeen beam specimens were included in the database from with full specimen characteristics and database results provided in Section E.8 Table E2-22 to E2-27. Specimens are identified with ID numbers B1 to B17 as indicated in Section E.8. A general summary of the beams database is provided in Figure E2-13.

A wide range of beam repair studies were captured here with publications ranging from the early 1970s to present day, in addition to representing components designed in accordance with seismic guidelines in New Zealand, Japan, and the United States.

All beam specimens are designed and detailed for ductile performance, while satisfying the transverse reinforcement spacing ratios, $s/d_b \leq 6$, in line with modern seismic detailing requirements. Three specimens with s/d_b ratios of 6.25 were deemed to be compliant, given construction tolerances will result in such variations.

While almost all specimens were tested without the presence of any axial loading or restraint, one specimen included the use of a passive restraint system, applying up to a maximum of 2.5% axial load ($P/A_g f'_c$) during loading, as a result of the specimen's axial elongation.

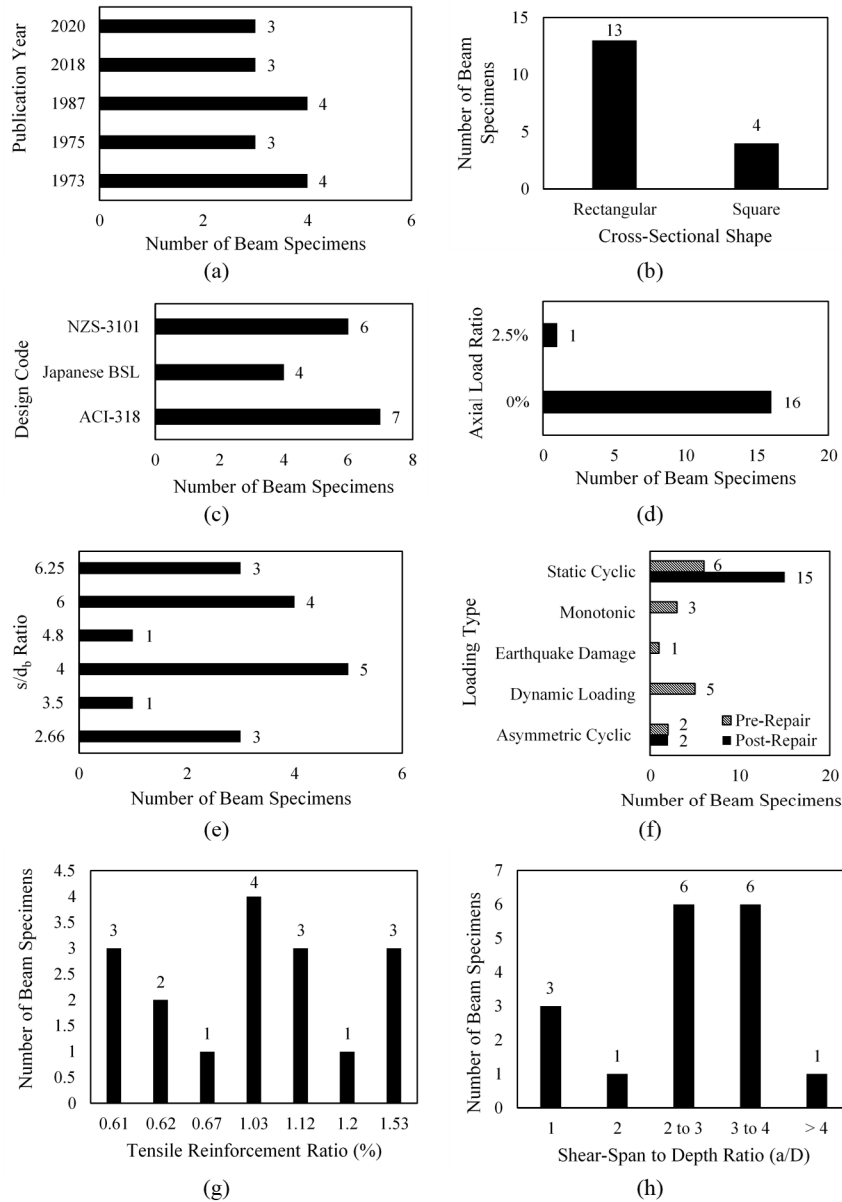


Figure E2-13 Distribution of beam specimens in accordance with (a) Publication year (b) Cross-sectional shape (c) Design code (d) Axial load (e) s/d_b ratio (f) Pre- and post-repair loading protocol (g) Beam tensile reinforcement ratio and (h) Shear-span to depth ratio.

A variety of loading types were used to simulate seismic damage prior to the repairs, ranging from in-situ earthquake damage from a real building, to typical laboratory type static cyclic or monotonic loading. Post-repair performance however was almost always assessed through static cyclic loading.

A wide range of component behavior was also captured in the database, with specimens ranging from squat coupling beam type specimens ($a/D = 1$) to flexural dominated, slender beams ($a/D > 4$). In addition, specimens ranging in tensile reinforcement ratios close to minimum requirements ($\rho_{\text{tens}} = 0.61\%$) up to more heavily reinforced beams with $\sim 1.5\%$ are captured.

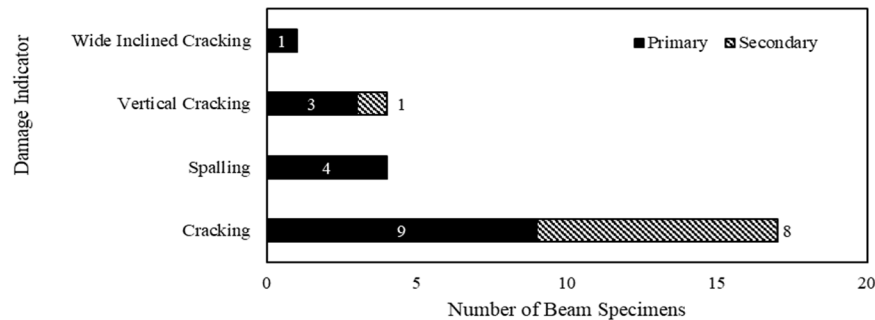


Figure E2-14 Observed damage state for beam specimens.

All of the beams in the database were assessed to have suffered a moderate damage state prior to repairs, as defined in Table E2-1. A breakdown of the damage indicators observed in the beams has been presented in Figure E2-14. Cracking was the most commonly observed damage, noted as the primary damage in 53% of specimens and the secondary damage in the remaining 47%. Spalling, vertical cracking, and wide inclined cracking were observed as the other primary damage indicators. Vertical cracking was noted where cracks along longitudinal bars were observed, indicating a degradation or loss of bond between concrete and reinforcement.

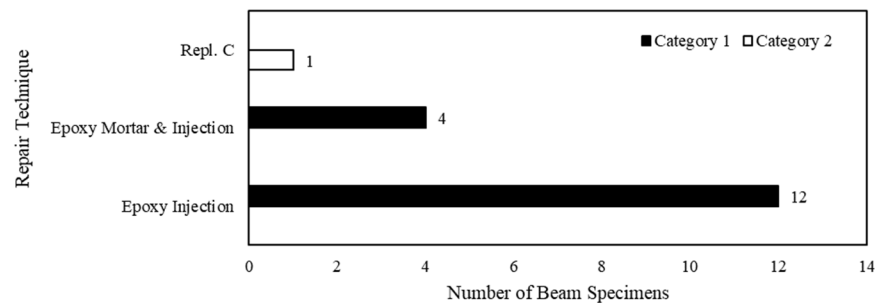


Figure E2-15 Distribution of repair techniques and repair categories applied to beam specimens in the database.

Beam repairs were conducted via the methods outlined in Figure E2-15. Three different repair techniques were identified, with only 1 specimen being repaired using a Category 1 repair (Repl. C), while all other specimens used Category 0 repairs involving epoxy injection and/or mortar.

E2.4.1 Overall Effectiveness of Beam Repairs

Based on the analysis of the pre- and post-repair backbone curves, a discussion is presented in this section to assess the overall effectiveness of the applied repairs. The results here only reflect the post-repair performance of moderately-damaged beams, as data beyond this is not presented in the database. As presented in Table E2-9, the repairs were largely successful in the rehabilitation of these moderately damage beams. On average an ~10% increase in strength was observed, likely due to the pre-repair inelastic strain demands resulting in changes in material properties. Deformation capacity was also largely recovered, with only one specimen failing to achieve a λ_D of 1.00 due to reinforcement rupture following repair. This specimen is not considered to be emblematic of a deficiency in the post-repair performance of these specimens and rather is likely an outlier. Stiffness recovery was once again less effective, with an average λ_K of 0.83 and a range of 0.59-1.12. The results presented in Table E2-9 were based on a subset of 12 specimens from the database. Data from beams B5-8 and B15 were omitted from these overall averages. Beams B5-7 were deemed to be more representative of coupling beams than seismic frame elements, while beam B8 was deemed to be an outlier with a recovery in stiffness much higher than the remainder of the results in the database ($\lambda_K = 1.55$).

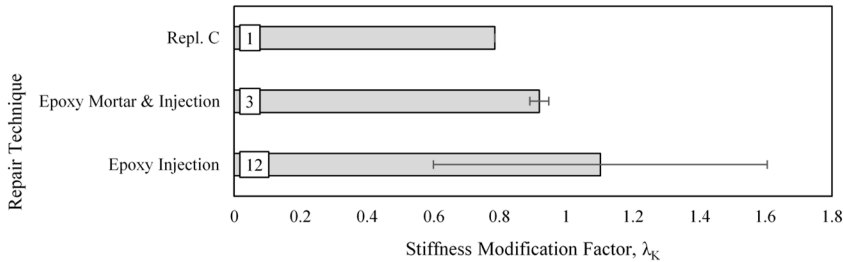
Table E2-9 Average Stiffness, Strength and Deformation Capacity Modification Factors for Beam Specimens

Mod. Factors Results	Stiffness, λ_K	Strength, λ_Q	Deformation Capacity, λ_D
Average	0.83	1.09	0.98*
Standard Deviation	0.18	0.07	0.05
Maximum	1.12	1.26	1.00
Minimum	0.59	1.04	0.83

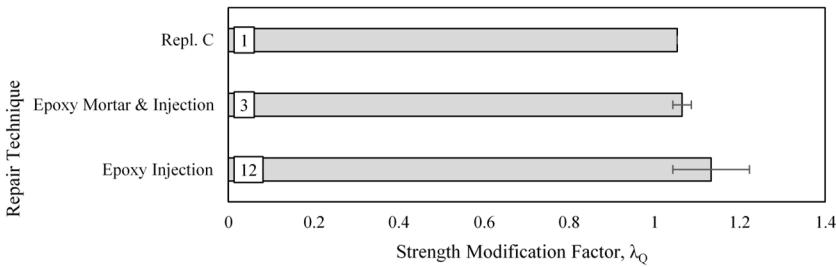
* λ_D for beam B17, which represents specimen SS-R from Sarrafzadeh (2021) which was omitted here as a reduction in deformation capacity was observed due to the specimen's foundation failure which is not representative of the beam performance.

A breakdown for the recovery in stiffness, strength and deformation capacity for each repair technique is provided in Figure E2-16a to c. The results show consistent recovery in strength and deformation capacity regardless of the repair technique. Some variation is observed in the recovery of stiffness amongst the three repair methods, however this level of variation is due to the inclusion of specimens B5-8 in the epoxy injection category, which represented coupling beams and were not similar in performance to the

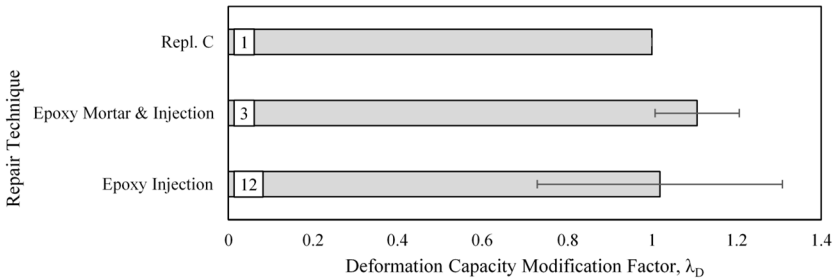
remainder of the database, as such a large standard deviation is also observed in Figure E2-16a for epoxy injection. Discounting this, the results for stiffness are more consistent amongst the various repair methods, including the Category 1, *Repl. C* method.



(a)



(b)



(c)

Figure E2-16 Summary of (a) Stiffness, λ_K (b) Strength, λ_Q and (c) Deformation Capacity, λ_D modification factors for all repair techniques applied to heavily moderately-damaged beam specimens. Bars represent average value for the considered repair technique. Error bars represent ± 1 standard deviation from the average. The number of specimens repaired via each technique is presented at the base of each bar.

E2.4.2 Effectiveness of Beam Repair Based on Specific Damage

This section assesses the effectiveness of repairs on beam specimens in accordance with the specific damage state and repair category

Category 0 Repairs

As all beams in the database were classified with only moderate damage and were detailed for ductile behavior, Category 0 repairs were adequate in the repair of the observed damage. As such, these repairs account for all but one of the beam specimens in the database. The two repairs which are accounted for in this section were Epoxy Mortar & Injection and Epoxy Injection, both aimed at repairing cracks and reinstating specimen original conditions and form.

The results for the backbone analysis of each primary damaged indicator are presented below in Table E2-10. As little variation was observed between the results for cracking and spalling and the applied repairs were similar, these results were combined to encompass a larger sample size.

Table E2-10 Effectiveness of Category 0 Repairs on Moderately-Damaged RC Beams Based on Primary Damage Indicators

Primary Damage	Cracking and Spalling			Wide Inclined and Vertical Cracking		
	λ_K^*	λ_Q	λ_D^{**}	λ_K	λ_Q	λ_D
Average	0.77	1.09	0.98	1.70	1.20	1.00
Standard Deviation	0.13	0.07	0.06	0.31	0.06	-
Maximum	1.12	1.26	1.00	2.17	1.26	1.00
Minimum	0.59	1.04	0.83	1.54	1.13	1.00
Beam Database IDs	B1-4, B9, B11-14, B16, B17			B5-8		

* λ_K for beams B1 and B4 were deemed to be outlier in relation to the remainder of the specimens with both being above 1. As such they are omitted from the averages.

** λ_D for beam B17, was omitted here as a reduction in deformation capacity was observed due to the specimen's foundation failure which is not representative of the beam performance.

Cracking and Spalling

Specimens which were repaired via a combination of epoxy mortar and injection following cracking and/or spalling were on average able to fully recover their strength and deformation capacity. Database beam B3 was not able to fully recover its deformation capacity after suffering bar rupture within its central loading stub. A similar failure was observed in beam B17, where a premature foundation failure resulted in the lowering of deformation capacity. As the underlying reason for this failure was able to be identified, this result was omitted from the overall averages. The failure in beam B3 was not able to be clearly attributed to external factors such as construction quality but is considered to be an outlier in this study and the full recovery of

deformation capacity is expected for moderately-damaged ductile beam elements. Inelastic strains during initial loading cause the strain hardening and aging of longitudinal reinforcement and ultimately result in an increase in strength following repairs. As such, on average, an approximately 10% increase in strength was observed among specimens with cracking and spalling. Epoxy injection was utilized in all cases, and the results are largely in line with the studies by Marder (2018) and Sarrafzadeh (2021), with a complete stiffness recovery not possible in most cases. While beams B1 and B4 were able to fully recover their stiffness, most specimens ranged between 0.59-0.95. Considering beams B1 and B4 as outliers, an overall average of 0.77 is achieved. Comparison of stiffness recovery vs. shear span to depth ratio did find a correlation between the two which is further discussed in conjunction with the results for joint specimens in Section E.6.

Wide Inclined and Vertical Cracking

Vertical cracking in conjunction with distributed shear-flexure cracking was observed in beams B5-8 from the study by Tasai et al (1987). As previously stated, these specimens were representative of coupling beams with beams B5-7 having an a/D of 1 and beam B8 having an a/D of 2. The vertical cracks were indicative of the loss in bond between concrete and the longitudinal reinforcement resulting in failure. Beam B5 experienced failure due to the combination of bond splitting and wide inclined cracking, following a monotonic push. This specimen did not experience a sudden failure, however failed in the negative loading direction following initial damage, due to significant degradation in bond and subsequently strength and stiffness.

Following repairs, a significant increase in stiffness and strength was observed in all specimens, as shown in Table E2-10. The applied epoxy repairs resulted in a change in failure mechanism for specimens B6-8, where a significant improvement in bond occurred, and vertical bond splitting cracks were not observed. Beam B5 saw no change in performance and failed once again during loading in the negative direction following a large monotonic positive push. Overall, the restoration of bond strength and the change in failure mechanism resulted in an average λ_K of 1.70, with a range of 1.54-2.17. Deformation capacity was fully restored and a 20% increase in strength was also observed. The increase in strength was due to a combination of strain hardening in the steel and increased bond strength following epoxy repairs.

Category 1 Repairs

As outlined in the previous sections, only one specimen was repaired via a Category 1 repair method. This was database beam B10 from the study by

Popov and Bertero (1975), which used the concrete replacement method (Repl. C) following the primary damage indicator of cracking. In this study, the complex repair was more successful than the epoxy injection method based on a greater level of stiffness recovery. The beam repaired via concrete replacement had a λ_K of 0.78 compared to a λ_K of 0.59 and 0.62 for the other specimens repaired via epoxy injection in the same study. The specimen also observed a 5% increase in strength and a full recovery in deformation capacity.

The result should be taken into context in the absence of epoxy injection. While epoxy injection can effectively reinstate lost reinforcement bonding, particularly at critical regions, it is clear that the complete replacement of concrete has been more effective in this study, as would be expected. However, the lack of full stiffness recovery is also of note. Epoxy injection may have addressed any loss of stiffness due to bond slip deformation at the beam-column interface or cracking outside of the plastic hinge region. As such, a combination of the two repairs would have likely increased the effectiveness of stiffness recovery in beam B10. Alternatively, a more comprehensive replacement of concrete extending beyond the plastic hinge zone and considering a yield penetration depth into the column may have resulted in a higher stiffness recovery, such as the method used by Lehman et al. (2001) on column C1.

E2.4.3 Stiffness Recovery and Shear Span to Depth Ratio

Stiffness recovery for moderately-damaged beam specimens ranged between 0.59 – 0.95. Sarrafzadeh (2021) highlighted a relationship between λ_K and shear span to depth ratio, (a/D). As a/D increases, trending towards more flexural dominated deformations, the recovery in stiffness using epoxy repairs becomes more effective. This is also observed in the beams in this database. This data is highlighted when presenting the recommendations for the stiffness recovery of moderately damaged beams in Section E.6.1.

E2.5 Database Summary for Joints

A total of 36 beam-column subassemblies were included in the database with full specimen characteristics and database results provided in Section E2.8 Table E2-28 to E2-34.

A variety of specimen characteristics were captured in the database, as indicated by the general overview presented in Figure E2-17. The majority of specimens were tested without axial restraint in the beam specimens, with only specimens from the study by Adin et al. (1993) providing this through post-tensioning and as such, the results largely reflect un-restrained beam

conditions. As seen with both beam and column specimens, a range of specimen geometries and reinforcement detailing was also captured. The distributions in Figure E2-17 place a focus on beam reinforcement and aspect ratio, as the primary focus of this study is on the behavior of ductile frames, which typically rely on a weak beam-strong column failure mechanism. A range of flexure to shear dominated beams are captured in the database with a/D ratios between 1.2 to 5.2. In addition, the specimens represent lightly reinforcement beams ($<0.5\%$) up to a tensile reinforcement ratio of 1.3%. A wide range of transverse reinforcement spacing is also captured with s/d_b ratios seen between 3.2-30.

As highlighted above and in Figure E2-17, the studies in the database captured a variety of subassembly types, both with and without seismic detailing. This ranged from the complete absence of reinforcement in the joint region to specimens which had brittle beam or column detailing and even those with undesirable column to beam moment capacity ratios. These joints were tested to reflect existing structures without adequate seismic detailing in the respective country of each study. During discussions of the overall results, deficient joints will be separated from those with adequate seismic detailing. Joints with seismic detailing and ductile behavior were classified as Type-1 while non-seismic or deficient joints were categorized as Type-2. This is indicated in the full database results in Section E2.8, with Type-2 joints highlighted in red in all tables. In total, 22 Type-2 and 14 Type-1 joints are represented in the database.

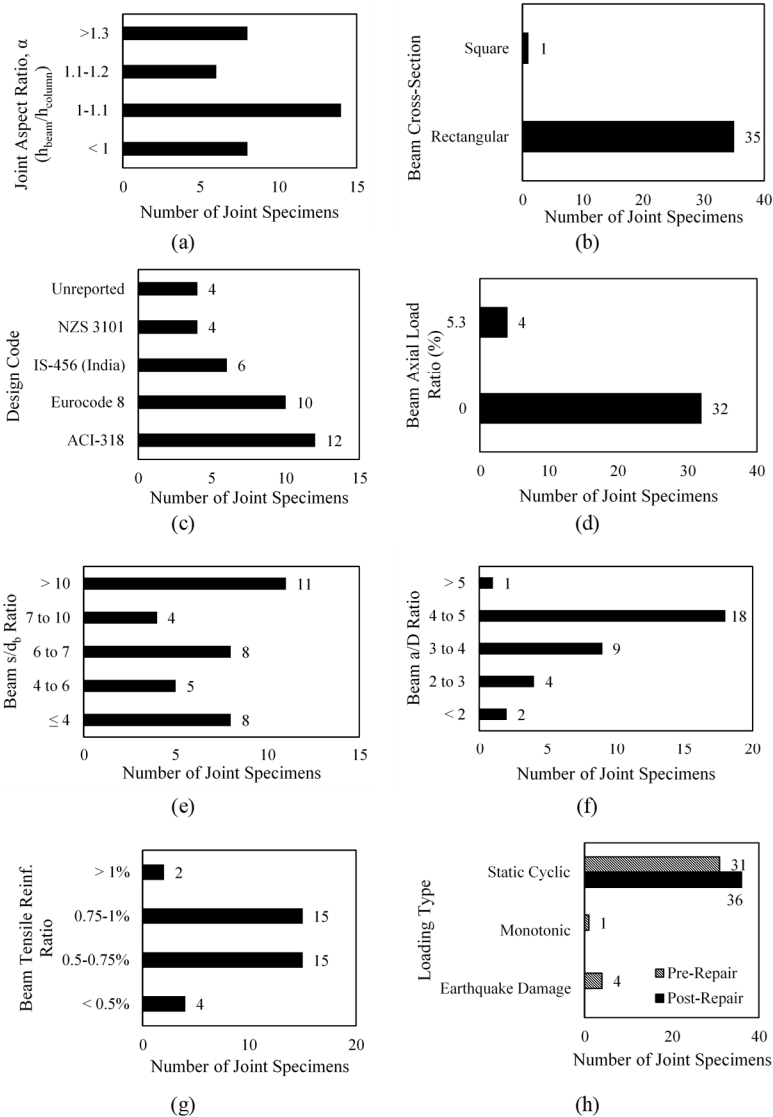


Figure E2-17 Distribution of joint specimens in accordance with (a) Joint aspect ratio (b) Cross-sectional shape (c) Design code (d) Axial load (e) beam s/d_b ratio (f) Shear-span to depth ratio (g) Beam tensile reinforcement ratio and (h) Pre- and post-repair loading protocol.

Figure E2-18 outlines the various damage indicators observed in the joint specimens prior to repairs. The figure also provides a breakdown for each damage indicator of when they are identified as primary, secondary, or tertiary damage. Cracking was overall the most common damage indicator, followed by spalling. As primary damage, cracking and spalling were both observed in 25 specimens, 15 being cracking and 10 spalling. Bar buckling as the primary damage was also observed in nine instances. In total, 25 joints suffered moderate damage with 11 being Type-1 joints, while a total of 11 suffered heavy damage with only three being Type-1 joints. A summary of

the repair techniques used in accordance with repair category and damage state are also presented in Figure E2-19a and b.

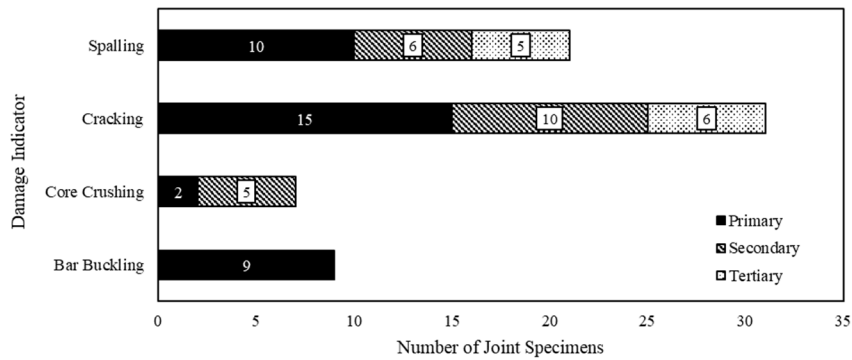
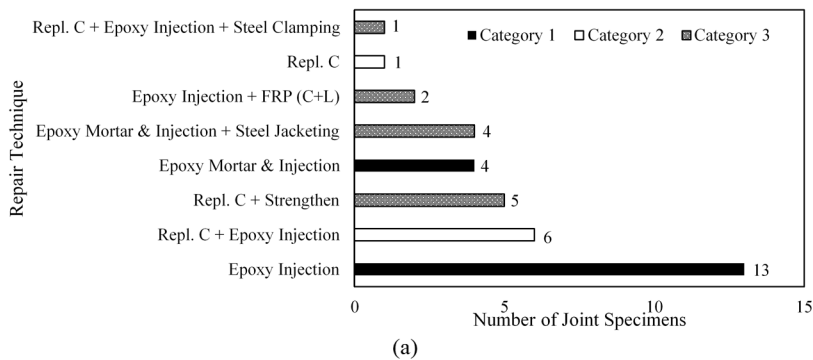
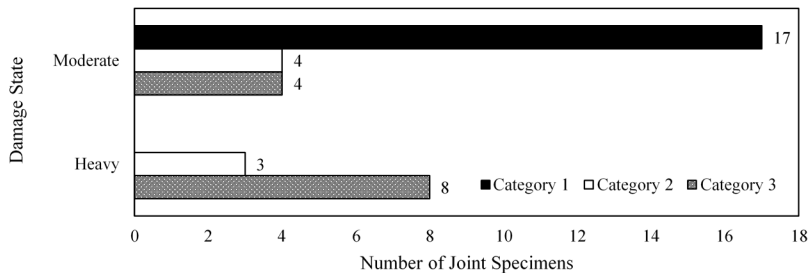


Figure E2-18 Observed damage states for joint specimens.



(a)



(b)

Figure E2-19 (a) Distribution of repair techniques and repair categories applied to joint specimens (b) Distribution of joint specimen damage state and repair category.

E2.5.1 Overall Effectiveness of Joint Repairs

In this section, a summary of the backbone analysis is provided in addition to results of individual repair techniques. As with the previous sections on column and beam specimens, the overall effectiveness of the applied repairs is presented below for moderate and heavily damaged joint specimens in Table E2-11. The results presented in this section are only representative of

Type-1 joints, with a summary of Type-2 joints presented later in Section E.5.4. The results from Table E2-11 indicate that moderately damage joint specimens performed similarly to moderately-damaged beams, with a full recovery of deformation capacity, a 10% increase in strength and an average stiffness recovery of ~80%.

Table E2-11 Average Stiffness, Strength and Deformation Capacity Modification Factors for Joint Specimens with Seismic Detailing (Type-1)

Damage State Mod. Factor	Moderate				Heavy				All	
	Min.	Max.	Avg.	Std. Dev.	Min.	Max.	Avg.	Std. Dev.	Avg.	Std. Dev.
Stiffness, λ_K	0.64	0.89	0.79 ⁽¹⁾	0.09	0.56	1.14	0.76	0.33	0.78	0.16
Strength, λ_Q	0.99	1.29	1.11 ⁽²⁾	0.10	1.04	1.32	1.15	0.15	1.10	0.12
Deformation Capacity, λ_D	0.84	1.25	1.01	0.10	0.96	1.05	1.00	0.04	1.01	0.09

1 Stiffness recovery for database joint J10 and J11 from Walsh (2015) were omitted due to the lack of a completely undamaged equivalent.

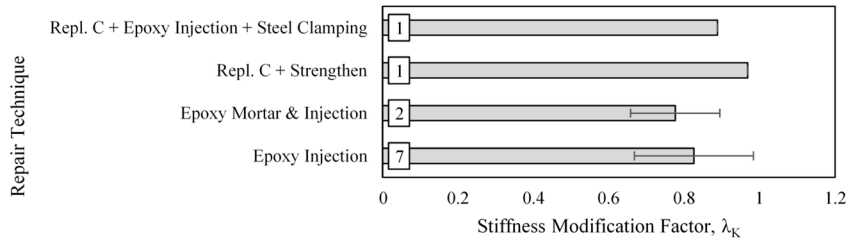
2 Strength recovery for database joint J1 from Popov and Bertero (1975) was omitted as it was the only case where a reduction in strength (- 9%) was observed for a moderately-damaged specimen deemed to be an outlier.

Heavily damaged joints in this database fared similarly on average, with a slight reduction in stiffness recovery at 76%. However, this result is based on only three specimens from two studies, which achieved significantly different results. As such, while it is indicative of the average, a consistent recovery in stiffness was not observed for heavily damaged specimens in the database. Figure E2-20 and Figure E2-21 separate the stiffness, strength and deformation capacity modification factors for each repair technique applied to moderate and heavily damaged Type-1 joints respectively. Based on these results, no particularly unsuccessful repair methods were identified for moderately-damaged joints with the results being largely in line with the averages presented for the overall database.

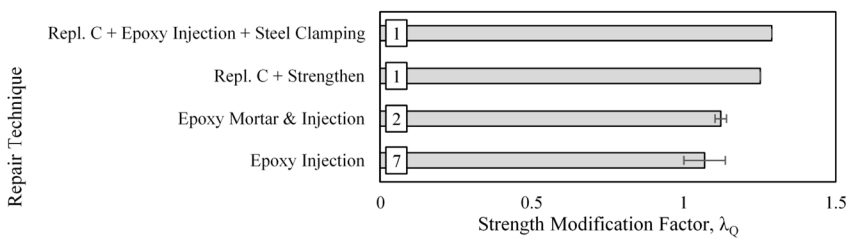
While a limited number of heavily damaged specimens are represented in Figure E2-21, a clear distinction in the stiffness recovery can be seen between the two repair methods.

Database joints J4 and J5 from Tsonos and Papanikolaou (2003) were noted to not be successful in their stiffness recovery, due to unsuccessful recovery in reduced anchorage, following epoxy injection. Meanwhile, database joint J3 from Lee et al. (1976), which suffered a similar failure mechanism was able to fully recover its stiffness without the use of epoxy injection. It should be noted that both studies indicated no yielding of transverse reinforcement and hence limited damaged in the joint region. While the results for joints J4

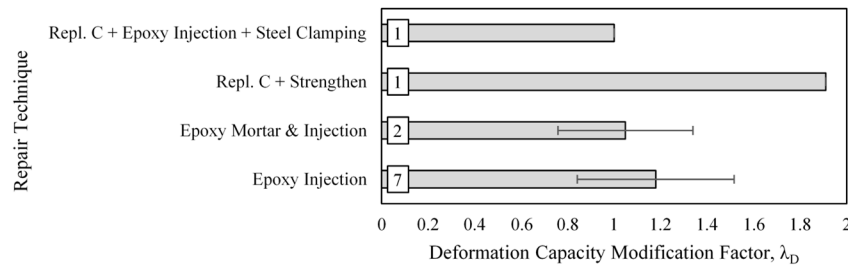
and J5 are not considered invalid here, the quality of the repair is brought under question and the effectiveness of stiffness recovery not representative of the repair technique.



(a)



(b)



(c)

Figure E2-20 Summary of (a) Stiffness, λ_{κ} (b) Strength, λ_Q and (c) Deformation Capacity, λ_D modification factors for all repair techniques applied to moderately-damaged type-1 joints specimens. Bars represent average value for the considered repair technique. Error bars represent +/- 1 standard deviation from the average. The number of specimens repaired via each technique is presented at the base of each bar.

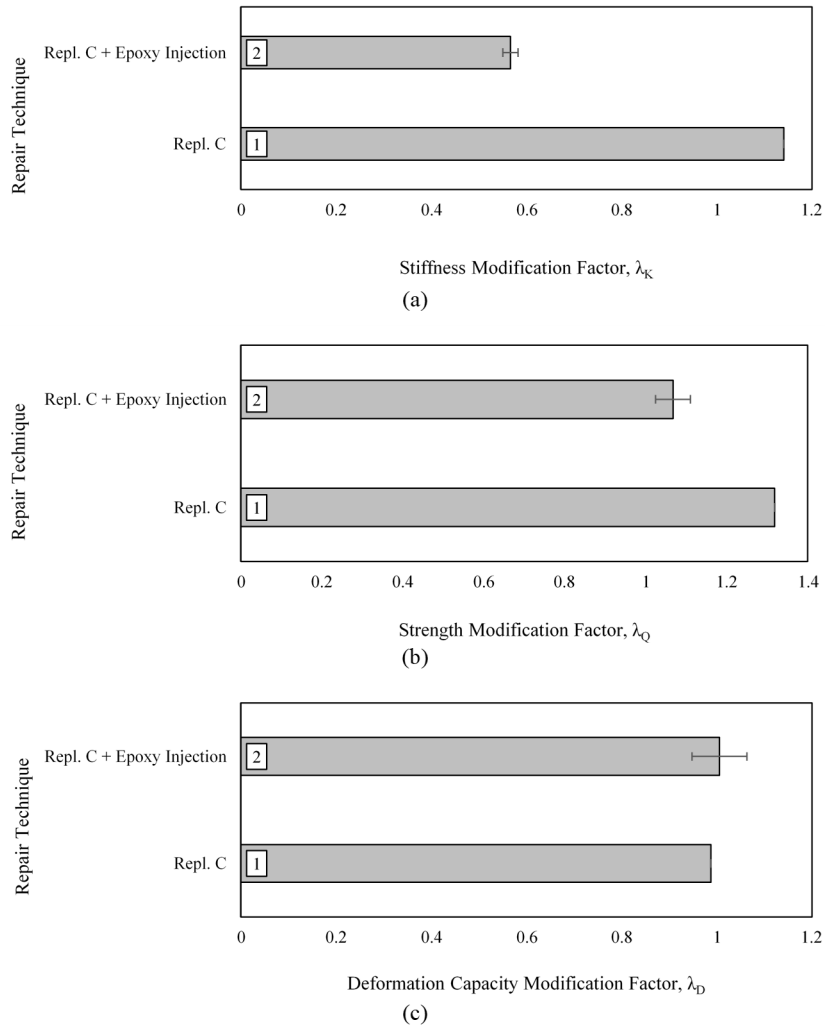


Figure E2-21 Summary of (a) Stiffness, λ_K (b) Strength, λ_Q and (c) Deformation Capacity, λ_D modification factors for all repair techniques applied to heavily damaged type-1 joints specimens. Bars represent average value for the considered repair technique. Error bars represent +/- 1 standard deviation from the average. The number of specimens repaired via each technique is presented at the base of each bar.

E2.5.2 Effectiveness of Joint Repair Based on Specific Damage

In line with the discussions provided in the previous sections on column and beam specimens, a breakdown of the joint repairs in accordance with primary damage states is provided in this section. The overall effectiveness of repairs is presented for joints in accordance with the complexity of the repair and the primary damage indicator. Only the repair of type-1 joints is discussed in this section and the results pertaining to type-2 specimens joints J15-J36 are not included here as discussed in the previous section.

E2.5.2.1 Category 0 Repairs

A total of nine specimens had category 0 repairs using either the Epoxy Injection or Epoxy Mortar & Injection methods following either cracking or spalling as the primary damage indicator.

Table E2-12 Effectiveness of Category 0 Repair Techniques for Moderately-Damaged Type-1 Joints Based on Primary Damage Indicator

Primary Damage	Cracking			Spalling		
	λ_K^*	λ_Q^*	λ_D	λ_K	λ_Q	λ_D
Average	0.78	1.06	1.00	0.78	1.12	1.05
Standard Deviation	0.09	0.09	-	0.12	0.02	0.29
Maximum	0.88	1.19	-	0.86	1.13	1.25
Minimum	0.64	0.91	-	0.69	1.11	0.84
Joint Database IDs	J1, J2, J8, J9, J11-13			J6, J7		

* Result for database joint J11, representing specimen H2 from Walsh (2015) not included in average stiffness and the result for database joint J1, representing specimen BC4 from Popov and Bertero (1975) was not included in the average for strength, with both being deemed outliers.

Cracking

The seven joints indicated in Table E2-12 suffered cracking in the beam and joint regions prior to all being repaired via the Epoxy Injection method. The results present similar overall effectiveness as for moderately-damaged joints in Table E2-11. On average a 7% increase in strength was observed, likely due to the strain hardening of reinforcement prior to the repairs. Average stiffness recovery was at 78%, with a range of 64-88%. In all cases, deformation capacity was recovered or presented no signs of a reduction. Visual observations following repairs also indicated that epoxied cracked remained closed and new cracks formed adjacent to them. Where cracking was left unrepaired in the joint region, new cracks were not observed following re-loading.

Closer observation of individual results for stiffness recovery showed that only two of the specimens applied the epoxy injection method both in the beam and joint region. These were database joints J8 and J9 from French et al. (1990) which achieved 86% and 88% recovery in initial stiffness respectively. In addition, this study made use of slip wire transducers to measure the recovery in bond strength inside the joint area. The results indicated that bond strength was fully recovered and only degraded ½ loading cycle earlier than in the undamaged specimens, despite peak story

drifts of 4.6% being applied prior to repairs. These results indicate that as expected, the effectiveness of stiffness recovery is improved when joint cracks are also treated.

Another observation with respect to the performance of joints following cracking was based on strain gauge data from Lee et al. (1976) and Tsonos and Papanikolaou (2003) which indicated that transverse reinforcement did not yield during initial loading with cracks of up to 0.25mm. In addition, no damaged was noted in the columns of any of the specimens discussed here. The results indicated that when applied correctly, epoxy injection can successfully reinstate bond between reinforcement and concrete in the joint and result in substantial recovery in stiffness.

Spalling

Database joints J6 and J7 from Marthong et al. (2013) suffered spalling as a primary damaged indicator and were repaired with Epoxy Mortar & Injection. While both specimens were designed to behave in a ductile manner with a strong column-weak beam mechanism, the damage pattern, as shown in Figure E2-22 suggests this was not successful. In both cases damage in the beam was concentrated at a single significant crack with some spalling at the beam-column interface in addition to significant joint cracking. Joint cracks also extended well into the column region and were more significant following repairs.

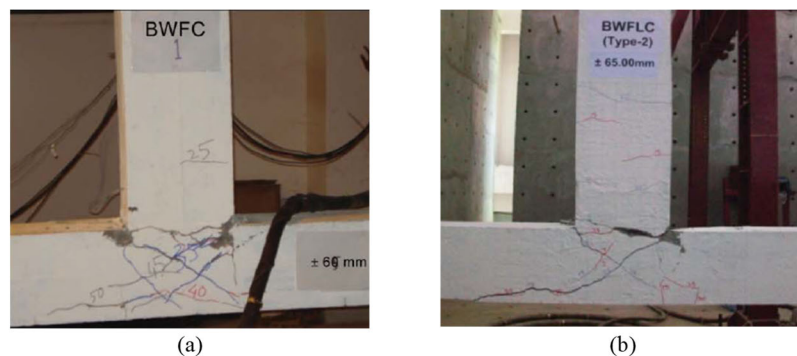


Figure E2-22 Pre-repair damage state for (a) Specimen BWFC-1 (database joint J6) and (b) BWFC-2 (database joint J7). Photographs obtained from Marthong et al. (2013).

These specimens are not considered to be accurate examples of spalling damage which would be expected in a ductile moment frame found in regions of high seismicity due to the unfavorable damage pattern. Despite this, the average post-repair performance was similar to the specimens with cracking for strength and stiffness recovery. Deformation capacity was reduced in joint J6 with a λ_D of 0.84 while a 25% increase was seen in joint

J7. No clear indication of the reason for a reduced deformation capacity was provided in the study, however due to the inconsistencies the repairs cannot be thought of as completely successful.

E2.5.2.2 Category 1 Repairs

The various complex repairs applied to the damaged joint specimens were previously outlined in Sections E.6. The results of these repairs are categorized based on moderate and heavy primary damage indicators prior to repairs in Table E2-13. A discussion for the results of each primary damage indicator is also provided following each corresponding table.

Table E2-13 Effectiveness of Category 1 Repairs on Heavily Damaged Type-1 Joints Based on Damage Indicators.

Primary Damage	Core Crushing			Buckling		
	λ_K	λ_Q	λ_D	λ_K	λ_Q	λ_D
Average	0.57	1.07	1.01	1.14	1.32	0.99
Standard Deviation	0.02	0.04	0.06	-	-	-
Maximum	0.58	1.10	1.05	-	-	-
Minimum	0.56	1.04	0.96	-	-	-
Joint Database IDs	J4, J5			J3		

Core Crushing

Database joints J4 and J5 from Tsonos and Papanikolaou (2003) suffered concrete core crushing prior to repairs via the Repl. C + Epoxy Injection method. The joints were representative of buildings adhering to the design codes at the time of study (2002). Joint J4 was designed in accordance with ACI318-95 and ACI-ASCE Committee 352 guidelines (1985) while joint J5 was designed in accordance with Eurocode 3 & 8. Both specimens suffered cracking, significant spalling and degradation of the concrete core in the beam while joint J5 also suffered some spalling at the back of the joint region due to anchorage failure of the longitudinal reinforcement. The primary detailing difference between the two specimens was the use of three smaller bars (joint J4) vs. two large bars (joint J5) for longitudinal beam reinforcement, while maintaining the same reinforcement ratio. The loss of anchorage in joint J5 also resulted in hairline joint cracking, which was not observed in joint J4, while transverse joint reinforcement remained elastic in both specimens. While no buckling was reported, the study states that some level of buckling may have been present prior to repair, resulting in bar rupture during final loading. While concrete replacement was used for repairs, the entire core was not replaced, despite crushing of the concrete not being limited to the cover, as shown in Figure E2-23.



Figure E2-23 Database joint J5 (Specimen RE1) during repairs, following removal of loose concrete. Photograph obtained from Tsonos and Papanikolaou (2003).

The repairs were successful in recovering the strength and deformation capacity of the specimen and allowing them to maintain a ductile response with no relocation of the plastic hinge region. Joint J5 also saw a shift in failure mechanism where anchorage failure was not observed, likely due to the increased bond strength of the beam reinforcement in the joint, following epoxy injection. However, the recovery of initial stiffness was not favorable, with λ_K values of 0.56 and 0.58. One potential explanation for this is the partial recasting of crushed beam concrete, despite significant deterioration as shown in Figure E2-23. As discussed for the specimen for bar buckling below, a complete replacement of damaged beam concrete may have significantly improved this result.

Bar Buckling

Database joint J3 suffered bar buckling as its primary damage indicator, prior to being repaired via the Repl. C method. Damaged following initial loading was primarily observed in the beam region with only hairline cracking in the joint and no damage observed in the columns. All loose concrete was removed including the core in the damaged beam region and recast with fresh concrete. Buckled reinforcement was also manually straightened as far as possible using hammer blows. This is not a recommended method of straightening with more appropriate methods now available using heat treatment or replacement of damaged steel.

Following repairs, deformation capacity was fully recovered, and a strength increase of 32% was recorded, with this being attributed to significant inelastic strains pushing the steel well into the strain hardening phase. Initial stiffness recovery saw a 14% increase in comparison to the undamaged specimen, significantly more successful than the comparable database joints

J4 and J5. In addition, while joint cracking was not treated, no new cracks were found in the joint during re-testing.

E2.5.2.3 Category 2 – Strengthening and Retrofit Type Repairs

Table E2-14 Effectiveness of Category 2 Repair Techniques on Moderately-Damaged Type-1 Joints based on Primary Damage Indicators

Primary Damage	Cracking			Spalling		
	λ_K	λ_Q	λ_D	λ_K	λ_Q	λ_D
Modifiers	0.97	1.25	1.82	0.89	1.29	1.00
Standard Deviation	-	-	-	-	-	-
Database Joint IDs	J10			J14		

Cracking

Database joint J10 was an H-frames extracted from a damaged structure following the 2011 Canterbury earthquakes to assess post-earthquake capacity and reparability. The specimen was very similar to a laboratory-built unit (Unit 4) tested by Restrepo et al. (1995) which was used as the equivalent undamaged specimen for assessment of repair effectiveness. This specimen suffered distributed cracking in the beam and joint region and was repaired using a repair and retrofit strategy which included addition of transverse reinforcement in the beams and replacement of concrete. This methodology was expected to increase the ductility of the unit, as was observed in the results with an 82% increase in deformation capacity in comparison to the unit from Restrepo et al. (1995). Overall, the results can be considered to be successful, with almost a full recovery in stiffness and a 25% increase in strength following the retrofit. The experiments are a valuable case study, however, are somewhat specific to specimens tested in the study and are of limited value for general repair recommendations.

Spalling

Database joint J14 suffered cover spalling as the primary damage prior to being repaired via the Repl. C + Epoxy Injection + Steel Clamping method. The repairs included full replacement of cover concrete, epoxy injection of beam core cracks and joint cracks, in addition to steel stiffening clamps used to shift the plastic hinge away from the column face. The specimen resembled an ordinary moment frame designed in accordance with ACI 318. Overall, the specimen saw a full recovery of deformation capacity and an approximately 30% increase in strength, owing to the relocation of its plastic hinge region as shown in Figure E2-24. The initial stiffness of the specimen was also recovered to 89% of its undamaged state. Overall, the repair

technique was seen to be effective in rehabilitating the specimen, however given the relocation of the plastic hinge, accompanied by a 30% increase in strength it can be argued that the simple repair techniques discussed in the previous section may have been more appropriate if a shift in plastic hinge or a retrofit of the specimen is not required.

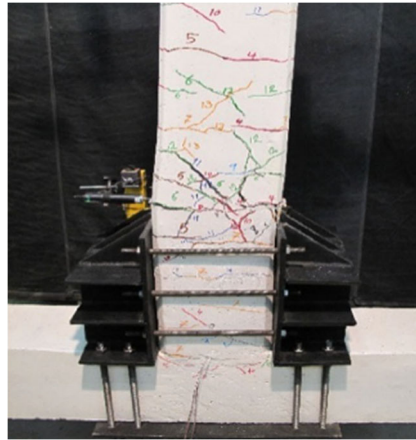


Figure E2-24 Post-failure damage state of specimen PO from Torabi and Maheri (2017) showing the relocation of the plastic hinge away from the beam-column interface. The steel clamping system used in the repairs are also visible in this image.

E2.5.3 Beam-Joint Stiffness Contributions

To account for joint distortion in RC frames, ASCE-41 Section 10.4.2.2 (2017) provides a simple modelling method which adjusts for the over-estimation of RC frame stiffness using purely rigid joint elements (Figure E2-25). The recommended models extend the beam section partially, or fully (depending on beam to column capacity ratio) to the centerline of the joint region. This method provides a practical and simple method to account for joint shear distortion and bar slip in frames, resulting in a more realistic frame stiffness in comparison to typical rigid joint elements.

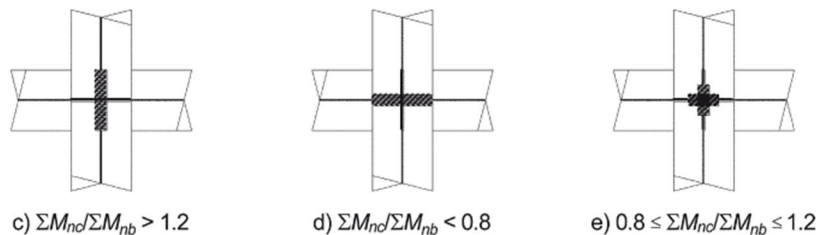


Figure E2-25 Part of Figure 10-2 from ASCE-41 Section 10.4.2.2, demonstrating the simplified joint region models for beam-column joints. The various recommendations based on column to beam moment capacity ratios are shown in the three joint

regions above. Hatched regions represent rigid element lengths while lines represent the continuation of frame elements.

Based on the database results for individual beams and beam-column subassemblies, it is recommended here that the modification factors recommended for stiffness recovery need only be applied to beam elements during post-repair analysis. This recommendation can then be used in conjunction with the modelling recommendations of ASCE-41 for joint regions.

Database averages indicate that post-repair stiffness of both beams and subassemblies following Category 0 repairs were similar (average λ_K beams = 0.77 +/- 0.13, λ_K subassembly = 0.78 +/- 0.10), noting that all Category 0 joints had $M_{nc}/M_{bc} \geq 1.8$. While detailed data is not available in this database to breakdown the contributions of these stiffness changes, these results point to stiffness changes likely being concentrated in the beam region. While detailed joint models are not often used in global frame analysis, they are appropriate in other circumstances or in academically focuses numerical analysis. There is room here for more experimental and numerical studies to be conducted, to further understand the contributions of beam-joint stiffness changes following Category 0 repairs such as epoxy injection. The rationale listed below from studies in the database, add support to the recommendations in this section.

- Many tests (database joints J1- 4) reported limited to no new damage beyond hairline cracking in the joint following reloading after repair. This was reported in conjunction with no damage observed in the columns.
- Strain gauge data from database joints J2-5 showed that all reinforcement in the joint remained in the elastic region even during reloading to failure following repairs. Significant inelastic strains in beam reinforcement were observed simultaneously, highlighting the “protection” of the joint region by the repaired plastic hinges, in line with limited joint damage progression outlined above.
- While studies such as database joints J3 from Lee et al. (1976) indicate a moderate increase in shear distortion when joint cracks are left unrepaired (~33%), this was deemed to be a result of an increase in shear stresses, due to beam strength increases.

E2.5.4 Repair of Joints with Inadequate Seismic Design (Type-2)

Joints which were designed with inadequate seismic detailing, often resembling older structures in regions of low seismicity, were categorized as

type-2 joints. A total of 22 joints were placed in this category with database joint IDs J15-36 as presented in Section E.8. Summaries for the performance and repair of these specimens are provided in Section E.7.4.

Based on the brief overviews provided for each study, by in larger the repairs applied to the type-2 specimens were successful in recovering the pre-damage capacity of the joints. However, in most cases, the repairs did not address the inadequate seismic detailing or design of the specimens. Consistent recovery in strength was observed across all specimens but the recovery in stiffness and deformation capacity proved to be inconsistent for similar specimens and damage states. When considering the reparability of RC frame structures, it is difficult to make generalized recommendations with regards to the repair of joints with inadequate seismic design and detailing from these results. The large variation in the behavior of the type-2 specimens, make the results more meaningful as individual studies where specific details and scenarios can be considered, as outlined in Section E.7.4.

E2.6 Implications for Reparability of Seismic Frames

Based on the analysis of the database results, this section provides conclusions and recommendations for the reparability of RC frames, for post-earthquake repair and retrofit. The recommendations presented here are based on the repair of components alone and do not consider external factors such as global residual deformations and damage to non-frame components such as flooring systems and diaphragms.

E2.6.1 Low to Moderately-damaged Ductile Frames

This section provides recommendations for the repair of low to moderately-damaged frame components. In line with the definitions presented in Table E2-1, the damage considered here is limited to cracking and spalling of cover concrete and does not include any significant damage to the concrete core or reinforcement buckling or fracture. The focus is also on ductile frames, while components with non-ductile detailing such as splice termination in potential plastic hinge region or large transverse reinforcement spacing ($s/d_b > 6$) are not considered here. Recommendations, summarized in Table E2-15, are based on moderately-damaged specimens in the database, however, based on the discussions of this chapter, equally apply to components with low damage.

Table E2-15 Recommendations for Stiffness, Strength, and Deformation Capacity Modification Factors for Epoxy-repaired Ductile RC frame Components

Mod. Factors \ Component	Component	
	Columns*	Beams
Stiffness, λ_k	0.5	$0.11(a/D) + 0.42 \leq 1.0$ where $a/D \geq 2$
Strength, λ_Q	1.05	1.1
Deformation Capacity, λ_D	1.0	1.0

*Note: data only available for columns with axial load ratio < 10%

Columns

The recommendations presented here are limited to ductile columns with axial load ratios ($P/A_g f'_c$) of $\leq 10\%$. A subset of columns was presented in this study with axial load ratios $> 10\%$, however these columns were all repaired via retrofit type solutions following non-ductile damage states (Columns C6-C11). It is recommended that future experimental programs investigate effective repair methods for the repair of moderately-damaged ductile columns with higher levels of axial load. Columns which are primarily designed for gravity systems with large axial loads closer to balance (30-40%) are of particular interest.

Based on the results presented in Section E.3 for database columns C4, C12, C18 and C19, it is evident that combinations of epoxy mortar and injection and FRP-C repairs are adequate to fully reinstate the strength and deformation capacity of moderately-damaged ductile RC columns. This is a key point as both parameters are critical for life-safety and collapse prevention performance objectives. As indicated in the stiffness data presented in Figure E2-26, the results also show that FRP-C slightly improved the recovery of stiffness in moderately-damaged ductile columns compared to cases where only epoxy injection and mortar were used. It should be noted that this is based on a limited dataset and warrants further testing, particularly for specimens with only epoxy injection and mortar repair.

Under moderate damage, no shifting of the plastic hinge zone was observed, in line with the limited increase in strength and no reduction in deformation capacity as shown in Figure E2-26. The data is presented in relation to the displacement ductility prior to repair, which shows no observable correlation to the discussed modification factors. Other parameters such as shear stress, axial load, reinforcement ratio, a/D and s/d_b were also explored with no correlations identified.

Based on the Category 0 repair methods applied to the specimens outlined in Section E.3.2.1, and the key points outlined above, the repair method Epoxy Mortar & Injection + FRP-C is recommended for the repair of moderately-damaged RC ductile columns with axial load ratios $\leq 10\%$. Post-repair modification factors of $\lambda_K = 0.5$, $\lambda_Q = 1.05$ and $\lambda_D = 1$ are proposed based on the available data presented in Figure E2-26.

Sensitivity analysis should be conducted for strength with a range of 1 - 1.15 based on the spread of the considered data to ensure that undesirable mechanisms do not develop based on these changes in column peak strength. Sensitivity analysis for stiffness can be conducted by considering a λ_K range of 0.4-0.6 based on the spread of the stiffness data considered. In cases where stiffness recovery is identified to be a critical parameter, higher category repairs should be considered. Additional datapoints based on future research should be used to refine the stiffness modification factor.

A concern for the repair of these columns in the field is the difficulty in identifying and injecting of cracks which are repaired without the removal of axial load. Further investigations into the application of epoxy injection under real-world conditions, particularly with respect to the injection of small cracks under axial load is recommended.

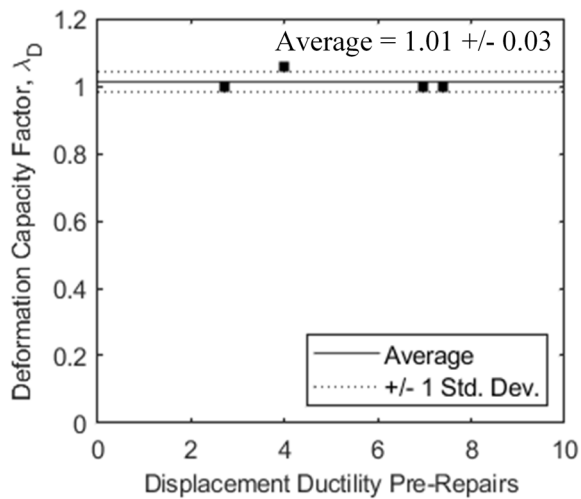
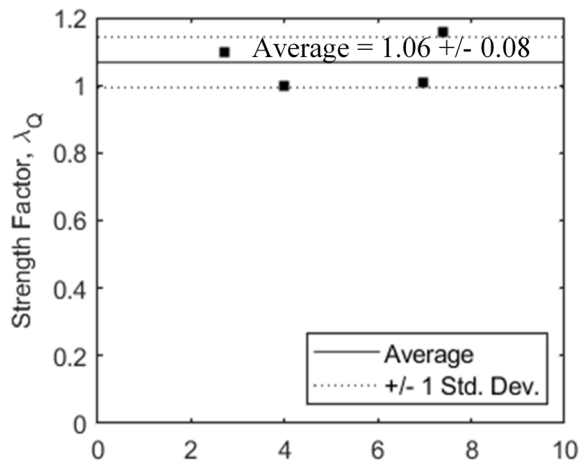
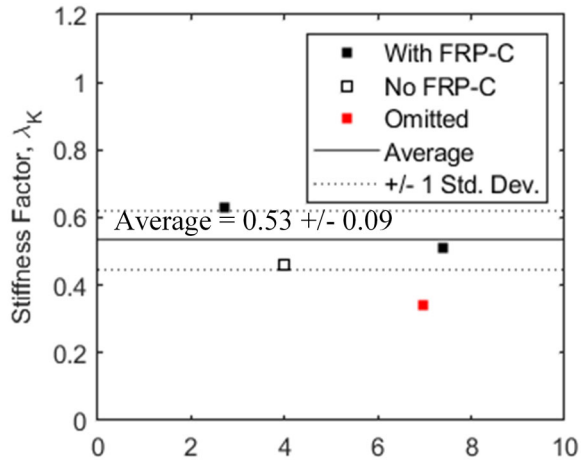


Figure E2-26 Data from database columns C4, C12, C18 and C19 presenting stiffness, strength and deformation capacity recovery for moderately-damaged ductile columns with category 0 repairs.

Beams and Joint Regions

The recommendations presented here are based on the beam specimens and joint specimens outlined in Section E.4 and E.5. As discussed in Section E.5.3 based on observed experimental results and recommendations for the modelling of joint regions based on ASCE-41 Section 10.4.2.2, all proposed modification factors should be applied to beam elements in beam-column subassemblies. The assumption is also made here that damage in the beam-column joints is limited to the beam and joint area and columns remain undamaged, in line with a strong-column-weak-beam failure mechanism.

Based on the data presented in this chapter for RC ductile beams and joints, the recommendations in this chapter will be based on the Category 0 repairs method of Epoxy Injection and Epoxy Mortar. While limited data is available for the Concrete Replacement method following low to moderate damage (only database beam B10), the results of this repair were very much in line with the epoxy injection and mortar method. The modification factors presented in this section for epoxy injection and mortar can also be applied for concrete replacement following low to moderate damage. Future experimental programs should consider the concrete replacement to expand available data on the effectiveness of this repair method. As discussed in Section E.4.2, there is potential for greater effectiveness of stiffness recovery where the concrete replacement and epoxy injection methods are combined, or where concrete replacement is applied in a more comprehensive manner, addressing any regions of potential bar yielding and hairline cracking and catering for yield penetration into joint regions.

The recommended repair methods are in general able to fully recover the deformation capacity of the components, and result in an ~10% increase in strength. Repaired component stiffness was on average 77% of the initial undamaged specimen stiffness. As outlined in Section E.2.4.1, the collected data also suggests a positive relationship between shear span to depth ratio (a/D) and the effectiveness of epoxy injection on stiffness recovery. This is evident in Figure E2-27 based on the data from moderately-damaged beam and joints specimens in the database. Rather than a singular stiffness modification factor for initial stiffness, a relationship based on a linear regression is shown in Figure E2-27 and proposed in Equation E2-1. The relationship only applies to beams with $a/D > 2$, consistent with the specimens in the database. An upper λ_K limit of 1.00 is also recommended, acknowledging that particularly in field repairs, it is difficult to reinstate the undamaged component stiffness following even moderate damage. The residual sum of squares (RSS) is used as a measure of error for the proposed

relationship and is represented in Figure E2-27 as a +/- 0.1 range for the regression line.

$$\lambda_K = 0.11(a/D) + 0.42 \leq 1.0 \quad (E2-1)$$

where, $a/D > 2$.

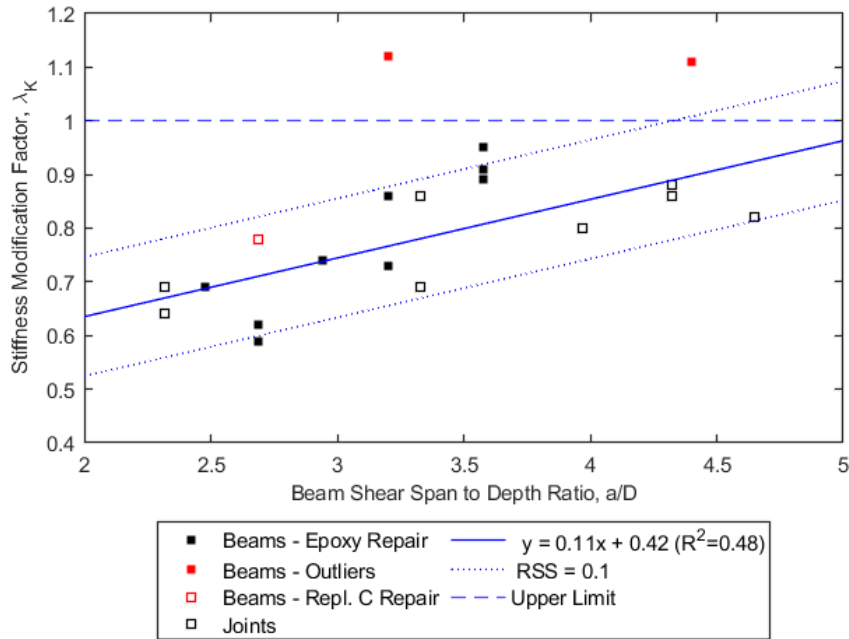
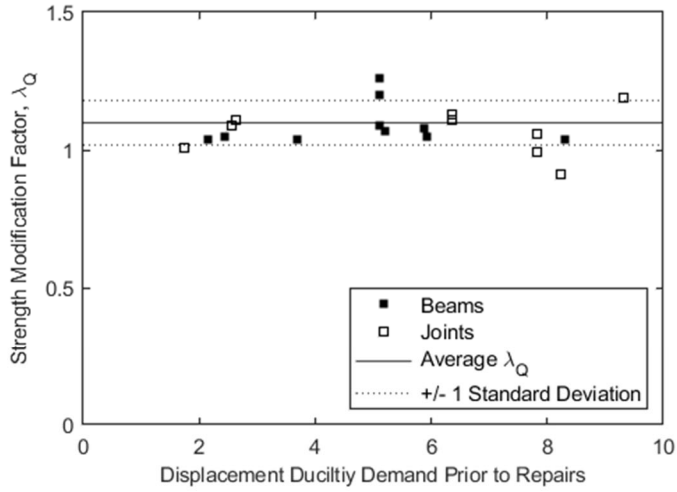


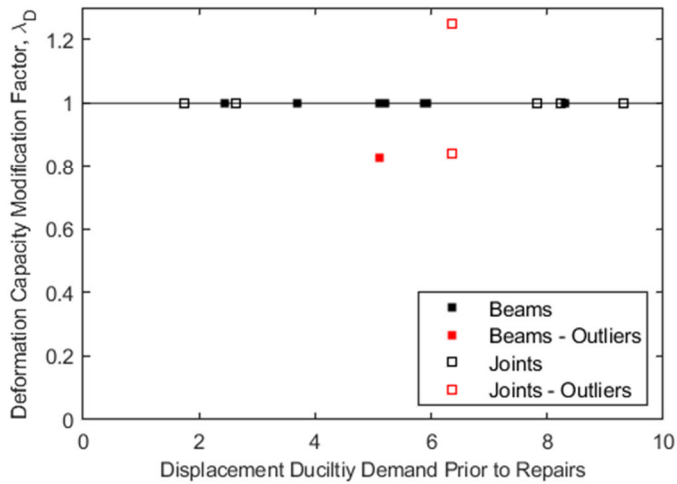
Figure E2-27 Stiffness recovery factor, λ_K plotted against beam shear span to depth ratio (a/D) for all beam and joint specimens repaired with Category 0 repairs, following moderate damage.

Based on the data for both beams and joints presented in Figure E2-28a, an average strength increase of 10% is observed, in line with the individual results outlined in Sections E.4.2 and E.5.2. As such, the strength modification factor for low to moderate damage following the recommended repair techniques, to be applied at beam plastic hinge locations for strength is $\lambda_Q = 1.10 \pm 0.1$. It is recommended that a sensitivity analysis also be conducted, using the standard deviation of the data presented above, to ensure that unfavorable failure mechanisms would not arise following the specified strength changes. No trend with changes in strength in relation to various specimen parameters was observed, as such the data in Figure E2-28a is simply plotted against prior ductility demand with no trend.

The data for deformation capacity was much more uniform as presented in Figure E2-28b. Apart from some outliers which were highlighted in the appropriate sections for beam and joint specimens, deformation capacity was recovered in all cases. As such a λ_D of 1.00 is recommended.



(a)



(b)

Figure E2-28 (a) Strength modification factors, λ_Q and (b) Deformation capacity modification factors for all beam and joint specimens repaired using Category 0 repairs following moderate damaged.

E2.6.2 Heavily Damaged Ductile Frames

This section provides recommendations for the repair of heavily damaged ductile frame components. In line with the definitions presented in Table E2-1, the damage considered here is anything beyond what has been defined as moderate. This typically includes crushing of the concrete core and/or damage to the reinforcement such as buckling or fracture. Once again, a focus is also placed on ductile frames and non-ductile detailing such as splice termination in potential plastic hinge region or large transverse reinforcement spacing ($s/d_b > 6$) is not considered here.

Columns

The results for heavily damaged ductile RC columns encompassed many repair techniques which varied greatly in complexity. These included Category 0 repairs utilising epoxy in conjunction with FRP-C, to Category 1 and 2 repairs which included the complete replacement of damaged materials and the strengthening beyond original column capacity.

Based on the discussions outlined in Section E.3.2.1 the use of Category 0 repairs is not recommended where reinforcement has been damaged, including noticeable buckling or rupture of longitudinal reinforcement.

The results in Section E.3.2.3 indicate that FRP-C and FRP-L were able to recover specimen strength and deformation capacity in 63% of cases which suffered bar buckling (database columns C8, C14, C23, C26, C27), without replacement of the reinforcement. This was not observed following bar fracture where only one of four columns with FRP-L was able to recover its strength and deformation capacity (database column C30) while not replacing damaged reinforcement. Failures in FRP-L performance was attributed to unreliable FRP anchorage systems and increased demands on FRP-L for strength recovery without addressing reinforcement damage. Complete replacement of steel and concrete in the damaged region (database column C1), with consideration of yield penetration lengths and the use of mechanical couplers was found to reliably reinstate specimen stiffness, strength and deformation capacity (i.e. λ_K , λ_Q , and $\lambda_D \geq 1.00$).

Based on the points outlined above the following recommendations are provided for the repair of heavily damaged ductile RC columns:

- Where heavy damage is observed such as core crushing and reinforcement damage, category 0 repairs are not an appropriate solution.
- FRP-L is not recommended as a long-term solution for strength and deformation capacity recovery, where damaged longitudinal reinforcement is not replaced.
- The complete replacement of steel and concrete, in line with the methodology for database column C1 from Lehman et al. (2001) was observed to be the most effective solution for heavily damaged ductile RC columns.

Beams and Joint Regions

No data on heavily damaged ductile beams and limited data on heavily damaged ductile joints (three specimens – J3-5) are presented in the

database, and as such no recommendations of modification factors are presented here. However, the following conclusions are made based on available tests and data:

- While no damage beyond bar buckling was observed in this database, complete concrete replacement of beams (database beam B10 and database joint J3) were very successful in rehabilitating specimens, particularly in complete strength and deformation capacity recovery.
- Based on database joints J4 and J5, it is recommended that even if only partial crushing of the concrete core has occurred, complete replacement of concrete in the plastic hinge region is recommended, to avoid significant reductions in post-repair initial stiffness.
- Due to the lack of data, the result outlined for heavily damaged columns are extended to apply to beams. It is recommended that damaged steel reinforcement be replaced and a reliance on FRP-L without addressing reinforcement damage be avoided.
- Future research is required on the replacement of reinforcement in beams following heavy damage, such as the use of mechanical couplers or welding. Further work is also required on the straightening of buckled reinforcing bars using heat treatment, this is while some work has been done demonstrating favorable results for structural steel member buckling (Aydin and Aktas (2015), Kim et al. (2004), Hirohata and Kim (2007), (2008a, 2008b), Bachman (2004)).

E2.6.3 Frames with Non-conforming or Brittle Elements

The reparability of non-conforming frames is outside the scope and focus of this study, however the repair of non-ductile frame elements was covered in this database and as such the following conclusions can be presented.

Columns Susceptible to Bond Failure

The results for six database columns (C6, C7, C9, C15-17) indicate that multiple forms of additional confinement, namely FRP-C, steel jacketing and additional transverse reinforcement were all effective in rehabilitating columns which were susceptible to bond failure. These included columns with lap-splice termination in the potential plastic hinge region and transverse reinforcement with $s/d_b > 6$. These specimens successfully transitioned from brittle to ductile failure mechanisms following the Category 2 repairs outlined in this chapter. As such, no specific repair

technique is recommended here, rather the repair philosophy of concrete repair (through mortar or replacement) in conjunction with additional confinement is recommended. Where clearly visible cracking is present outside of the failure zone, epoxy injection is also recommended. Using the data for the aforementioned columns, the following post-repair modification factors are recommended for columns susceptible to bond failure. Values are based on average post-repair recovery figures in the database. Standard deviations are also provided in the recommendations, with the aim that a sensitivity analysis would be conducted with any calculations which make use of these factors. It should be noted that specimens which did not see full bond failure (C20 and C21 from Section E.3.2.3) due to small displacement demands but were detailed to be susceptible to bond failure exhibited very similar post-repair performance to the six columns outlined in this section which were repaired following significant spalling and full exposure of the lap-spliced region such as in Figure E2-10.

Stiffness, $\lambda_K = 0.80 \pm 0.1$

Strength, $\lambda_Q = 1.25 \pm 0.2$

Deformation Capacity = No modification factor is recommended due to large variability in results. In all cases a significant increase in deformation capacity was observed. With an average λ_D of 2.8 ± 0.9 .

Columns Susceptible to Brittle Shear Failure

Epoxy mortar, injection and FRP-C proved to be very effective in the repair and retrofit of columns which had suffered brittle shear failure, indicated by the presence of large, inclined cracks. It should be noted that no reports of significant damage to longitudinal steel reinforcement was noted in these repairs. Due to limited data and the greater level of uncertainty in specimens susceptible to brittle failure mechanisms, no recommendations of modification factors for such repairs are suggested. These repairs were able to successfully transition the columns from a brittle to ductile failure mechanism, accompanied by significant increases in strength and deformation capacity. On average 90% of the initial specimen stiffness was also recovered, however due to the limited dataset, this cannot be recommended as a modification factor.

Beams and Joint Regions

While no beams in the database could be classified with non-ductile behavior, a subset of 22 joint specimens (database joints J15-36) were classified as non-ductile with deficient seismic detailing. While most of the

repair and retrofit schemes were considered to successfully reinstate the specimen's initial conditions, in most instances inadequate detailing was not addressed, and a reliable ductile failure mechanism was not achieved. As such no recommendations are made here for the rehabilitation of non-ductile beams and joints.

References

- Adin, M., D. Yankelevsky, D. Farhey, 1993, Cyclic Behavior of Epoxy-Repaired Reinforced Concrete Beam-Column Joints, *ACI Structural Journal*, Vol. 90.
- Aydin, E., M. Aktas, 2015, “Obtaining a permanent repair by using GFRP in steel plates reformed by heat-treatment,” *Thin-Walled Structures*, Vol. 94, pp. 13–22.
- Bachman, R.E., 2004, “The ATC-58 Project Plan for Nonstructural Components,” *Performance-Based Seismic Design Concepts and Implementation: Proceedings of an International Workshop, Bled, Slovenia*, pp. 125–136.
- Bett, B., R. Klingner, J.O. Jirsa, 1989, “Lateral Load Response of Strengthened and Repaired Reinforced Concrete Columns,” *ACI Structural Journal*, Vol. 85, pp 499–508.
- Celebi, M., J. Penzien, 1973, *Hysteretic behaviour of epoxy repaired RC beams*, Berkeley, California.
- Chai, H., M.J.N. Priestley, F. Seible, 1992, “Seismic Retrofit of Circular Bridge Columns for Enhanced Flexural Performance,” *ACI Structural Journal*, Vol. 88, pp. 572–584.
- Chang, S., Y. Li, C. Loh, 2004, “Experimental Study of Seismic Behaviors of As-Built and Carbon Fiber Reinforced Plastics Repaired Reinforced Concrete Bridge Columns,” *Journal of Bridge Engineering*, Vol. 9, pp. 391–402.
- Cuevas, A., S. Pampanin, 2017, *Post-Seismic Capacity of Damaged and Repaired Reinforced Concrete Plastic Hinges Extracted from a Real Building*, pp. 1–13.
- Elsouri, A.M., M.H. Harajli, 2011, “Seismic Repair and Strengthening of Lap Splices in RC Columns: Carbon Fiber – Reinforced Polymer versus Steel Confinement,” *Journal of Composite Construction*, Vol 15, pp. 721–731.
- French, C.W., G.A. Thorp, W.J. Tsai, 1990, Epoxy repair techniques for moderate earthquake damage, *ACI Structural Journal*, Vol. 87, pp. 416–424.
- He, R., S. Grelle, L.H. Sneed, A. Belarbi, 2013, “Rapid repair of a severely damaged RC column having fractured bars using externally bonded CFRP”, *Composite Structures*, Vol. 101, pp. 225–242.

- He, R., L.H. Sneed, A. Belarbi, 2013, “Rapid Repair of Severely Damaged RC Columns with Different Damage Conditions: An Experimental Study”, *International Journal of Concrete Structures and Materials*, Vol. 7, pp. 35–50.
- Hirohata, M., Y.-C. Kim, 2007, “Dominant Factors Deciding Compressive Behavior of Cruciform Column Projection Panel Corrected by Heating”, *Steel Structures*, Vol. 7, pp. 193–199.
- Hirohata, M., Y.C. Kim, 2008, “Effect of correction by heating/pressing on mechanical behaviour of steel structural members”, *Welding in the World*, Vol. 52, pp. 63–70.
- Hirohata, M., Y.-C. Kim, 2008, “Generality Verification for Factors Dominating Mechanical Behavior under Compressive Loads of Steel Structural Members Corrected by Heating/Pressing”, *Steel Structures*, Vol. 8, pp. 83–90.
- Karayannis, C.G., C.E. Chalioris, K.K. Sideris, 1998, “Effectiveness of RC beam-column connection repair using epoxy resin injections,” *Journal of Earthquake Engineering*, Vol. 2, pp. 217–240.
- Karayannis, C.G., G.M. Sirkelis, 2008, “Assessment of the lognormality assumption of seismic fragility curves using non-parametric representations”, *Earthquake Engineering and Structural Dynamics*.
- Kim, Y.-C., H. Mikihiro, H. Kawazu, 2004, “Safety Evaluation of Cruciform Columns Corrected by Heating (Mechanics, Strength & Structural Design)”, *Transactions JWRI*, Vol 33.
- Lee, D.L.N., J.K. Wight, R.D. Hanson, 1976, *Original and Repaired Reinforced Concrete Beam-Column Subassemblages Subjected to Earthquake Type Loading*, Ann Arbor, Michigan.
- Lehman, D.E., J.P. Moehle, 2000, *Seismic performance of well-confined concrete bridge columns*, Pacific Earthq. Eng. Res. Cent.
- Lehman, D.E., S.E. Gookin, A.M. Nacamull, J.P. Moehle, 2001, “Repair of earthquake-damaged bridge columns,” *ACI Structural Journal*, Vol. 98, pp. 233–242.
- Li, Y., Y.-Y. Sung, 2003, “Seismic repair and rehabilitation of a shear-failure damaged circular...”, *Canadian Journal of Civil Engineering*, Vol 30, pp. 819–829.
- Marthong, C., A. Dutta, S.K. Deb, 2013, “Seismic rehabilitation of RC exterior beam-column connections using epoxy resin injection, *Journal of Earthquake Engineering*, Vol. 17, pp. 378–398.

- Opabola, E.A., K.J. Elwood, 2020, “Simplified approaches for estimating yield rotation of reinforced concrete beam-column components,” *ACI Structural Journal*, Vol. 117, pp. 279–291.
- Popov, E.E., V. V Bertero, 1975, “Repaired R/C Members Under Cyclic Loading”, *Earthquake Engineering and Structural Dynamics*, Vol. 4, pp. 129–144.
- Restrepo, J.I., R. Park, A.H. Buchanan, 1995, “Tests on Connections of Earthquake Resisting Precast Reinforced Concrete Perimeter Frames”, *PCI Journal*, Vol. 40, pp. 44–61.
- Rutledge, S.T., M.J. Kowalsky, D. Ph, R. Seracino, D. Ph, J.M. Nau, D. Ph, 2014, “Repair of Reinforced Concrete Bridge Columns Containing Buckled and Fractured Reinforcement by Plastic Hinge Relocation”, *Journal of Bridge Engineering*, Vol. 19, pp. 1–10.
- Saadatmanesh, H., M.R. Ehsani, L. Jin, 1997, “Repair of Earthquake-Damaged RC Columns with FRP Wraps” *ACI Structural Journal*, Vol. 94, pp. 206–214.
- Saadatmanesh, H., M.R. Ehsani, L. Jin, 1997, “Seismic Strengthening of Circular Bridge Pier Models with Fiber Composites,” *ACI Structural Journal*, Vol. 93.
- Saiidi, M.S., Z. Cheng, 2004, “Effectiveness of Composites in Earthquake Damage Repair of Reinforced Concrete Flared Columns,” *Journal of Composite Construction*, Vol. 8, pp. 306–314.
- Sarrafzadeh, M.M., 2021, *Residual Capacity and Reparability of Moderately-Damaged Reinforced Concrete Ductile Frame Structures, PhD Thesis (under review)*, University of Auckland, Auckland, New Zealand.
- Shin, M., B. Andrawes, 2011, “Emergency repair of severely damaged reinforced concrete columns using active confinement with shape memory alloys,” *Smart Materials and Structures*, Vol. 20.
- Tasai, A., Y. Sakai, S. Otani, H. Aoyama, 1987, *Experimental Study on Repair with Epoxy Resin for Damaged Reinforced Concrete Members*, Tokyo, Japan,.
- Tasai, A., 1988, “Resistance of flexural reinforced concrete members after repair with epoxy resin,” *Ninth World Conf. Earthquake Engineering*, Tokyo, Japan.
- Torabi, A., M.R. Maheri, 2017, “Seismic Repair and Retrofit of RC Beam – Column Joints Using Stiffened Steel Plates”, *Iranian Journal of*

Science and Technology, Transactions of Civil Engineering, Vol. 41, pp. 13–26.

Tsonos, A.G., K. V. Papanikolaou, 2003, “Post-earthquake repair and strengthening of reinforced concrete beam-column connections (theoretical & experimental investigation),” *Bulletin of the New Zealand Society for Earthquake Engineering*, Vol. 36, pp. 73–93.

Vosooghi, A., M.S. Saiidi, J. Gutierrez, 2009, “Rapid repair of RC bridge columns subjected to earthquakes,” *Concrete Repair, Rehabilitation and Retrofitting II*, pp. 397–398.

Vosooghi, A., M.S. Saiidi, 2013, “Shake-Table Studies of Repaired Reinforced Concrete Bridge Columns Using Carbon Fiber-Reinforced Polymer Fabrics,” *ACI Structural Journal*, Vol. 110, pp. 105–114.

Walsh, K., 2015, *Inventory and seismic assessment of earthquake-vulnerable masonry and concrete buildings*, The University of Auckland, Auckland, New Zealand.

Walsh, K., R. Henry, G. Simkin, N. Brooke, B. Davidson, J. Ingham, 2016, “Testing of reinforced concrete frames extracted from a building damaged during the Canterbury earthquakes,” *ACI Structural Journal*, Vol. 113, pp. 349–362.

Wu, R., C.P. Pantelides, 2017, “Rapid repair and replacement of earthquake-damaged concrete columns using plastic hinge relocation,” *Composite Structures*, Vol. 180, pp. 467–483.

Influence of Deformation Capacity on the Repair Assessment of RC Frame Buildings

F.1 Overview

This study investigates how the system-level repair trigger varies with building characteristics, comparing RC frame buildings designed according to ASCE 7-16 for special, intermediate, and ordinary reinforced concrete moment frames (ASCE, 2016) and a building designed according to the 1963 version of ACI 318 (ACI, 1963). The study matrix consists of five 4-story reinforced concrete moment frames with different levels of system and component deformation capacity owing to their different design and detailing. Of the modern designs, the ordinary moment frame (OMF) is the least well controlled by system and component design and detailing requirements. The results indicate the drift thresholds which, if reached, indicate that the future life safety performance of the structure is impaired and are also used to compare system and component limits.

F.2 Design of Frames with Different Deformation Capacities

Four 4-story RC frame buildings are designed to meet ASCE 7-16 and ACI 318-14 requirements (ASCE, 2016; ACI, 2014), as listed in Table F-1. The building details, in terms of the layout of the building, story height, and span of each bay are adopted from FEMA P-2012 (FEMA, 2018). Each building is assumed to have two perimeter frames and five gravity frame lines resisting seismic loads in each direction. The intermediate moment frame (IMF) is designed for Las Vegas, NV ($S_{DS} = 0.51g$; $S_{DI} = 0.20g$). Three variations of OMFs are designed for Boston, MA ($S_{DS} = 0.23g$; $S_{DI} = 0.09g$). The baseline OMF design has flexure-critical columns. The two other OMF exhibit potentially brittle deficiencies related to weak joints and shear-critical columns, respectively. In addition, there is a 4-story RC moment frame designed according to the 1963 version of ACI 318 for California (ACI, 1963). The RC special moment frame described in Appendix B also provides

an additional point of comparison ($S_{DS} = 1.5$; $S_{DI} = 0.6$). The 1963 era building is designed according to ACI 318-63 requirements to represent older less ductile high seismic construction.

Figure F-1 provides the design spectrum and base shear for each building. The gravity system is a beam column system designed to withstand the dead and live loads. The IMF and OMF buildings have the same gravity system; the 1963 era building which has slightly different detailing for these members based on the older code requirements. The gravity system for the SMF is described in Appendix B.

For the OMF, three different versions are considered. The first (baseline) OMF has flexure-critical columns and is not expected to have joint failure. Although columns are not always flexure critical in OMFs, the perimeter framing and bay spacing, story heights, and other dimensions for the baseline building means that this outcome is not a surprising feature of the design. As the OMF design guidelines can produce building designs with various failure modes, the other two ordinary moment frames are designed to fail through shear critical column (OMF-SC) and brittle joint deficiencies (OMF-JC), respectively. In all three cases, load reversal in OMF beam hinges is expected.

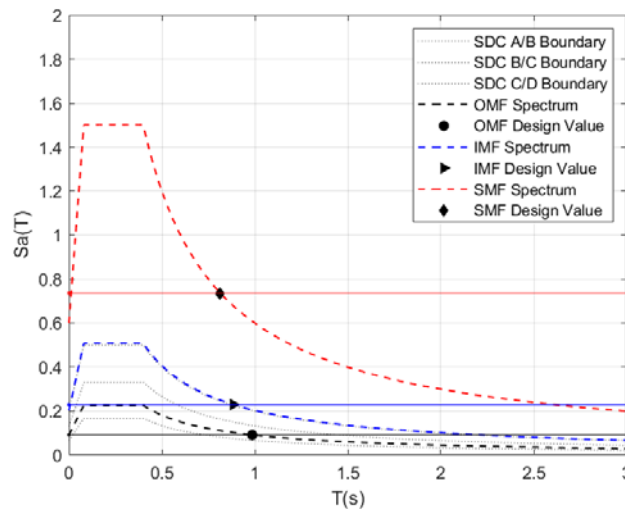


Figure F-1 Design spectrum of studied buildings, with boundaries between Seismic Design Category (SDC) also shown for reference.

Tables F-2 to F-6 provide the design details including member sizes and reinforcement sizing. The designs are governed by strength for the OMFs and drift limits for the IMF. The ACI-63 building design is controlled by strength. In these tables, the size of each member is reported as $h \times b$ [s], where h is the height of the member cross-section, b is the width of the member cross-section, and s is the spacing of the transverse reinforcement.

For the columns, the reinforcing is shown in this format: $[\rho_{total}, \rho_{sh}]$ where ρ_{total} is the longitudinal reinforcement ratio and ρ_{sh} is the shear reinforcement ratio. For beams, the reinforcing is provided in the following format: $[\rho_{top}, \rho_{bot}, \rho_{sh}]$, where ρ_{top} and ρ_{bot} represents the top and bottom reinforcement ratios, respectively. The drift ratios reported in these tables are the amplified linear elastic drifts calculated in accordance with the ASCE 7-16 design requirements.

Figure F-2 presents the outcome of the design process for all the buildings in terms of the columns' ratios of flexural to shear strength, and the column to beam strength ratios. While the OMF and IMF have weaker columns than the SMF, they tend to not have weak columns (relative to beams), due to the geometry of the loading conditions assumed in the design. Similarly, because of the story heights and span lengths, the only case with shear-critical columns is OMF-SC.

Table F-1 RC Frame Systems Studied.

Title	System	Base Shear	T (s)	Mc/Mb	Cu.Ta (s)	Design	Characteristics
SMF	SMF	0.092	1.0	1.7	0.81	Drift	Baseline
IMF	IMF	0.046	1.4	1.1	0.88	Drift	Baseline
OMF	OMF	0.031	1.6	1.1	0.99	Strength	Baseline
OMF-SC	OMF	0.031	1.7	1.0	0.99	Strength	Shear critical columns
OMF-JC	OMF	0.031	1.7	1.0	0.99	Strength	Joint critical
ACI - 63	-	0.092	1.1	1.5	-	-	Baseline

Note: System: the seismic force resisting system of the building. Base shear: the ratio of the base shear to the weight of the building used in the design of the building. T: analytical period obtained from OpenSEES model, considering cracked section. Mc/Mb: the maximum column beam strength ratio of interior joints of the seismic frame. Cu.Ta: the upper limit for the analytical period calculated using ASCE 7-16 requirements used for the base shear calculations. Design: the requirement of the code which primarily controlled the final design.

Table F-2 Summary of Design Properties of IMF

Level	Columns		Beams		Drift(%)
	Exterior	Interior	Exterior	Interior	
4	18 x18 [8.0]	18 x18 [8.0]	24x18 [5.0]	24x18 [5.0]	1.1
	(0.0244,0.0028)	(0.0244,0.0028)	(0.0082,0.0061,0.0024)	(0.0082,0.0061,0.0024)	
3	18 x18 [8.0]	18 x18 [8.0]	24x18 [5.0]	24x18 [5.0]	1.7
	(0.0244,0.0028)	(0.0244,0.0028)	(0.0082,0.0061,0.0024)	(0.0082,0.0061,0.0024)	
2	22x18 [8.0]	22x18 [8.0]	28x18 [6.0]	28x18 [6.0]	1.6
	(0.0239, 0.0028)	(0.0239, 0.0028)	(0.0086,0.0069,0.0020)	(0.0086,0.0069,0.0020)	
1	22x18 [8.0]	22x18 [8.0]	28x18 [6.0]	28x18 [6.0]	1.3
	(0.0239, 0.0028)	(0.0239, 0.0028)	(0.0086,0.0069,0.0020)	(0.0086,0.0069,0.0020)	

Note: The concrete strength of columns is 7.0 ksi. The concrete strength of beams is 5.0 ksi.

Table F-3 Summary of Design Properties of OMF

Level	Columns		Beams		Drift (%)
	Exterior	Interior	Exterior	Interior	
4	18 x18 [7.5]	18 x18 [7.5]	22x18 [9.0]	22x18 [9.0]	0.5
	(0.0244,0.0016)	(0.0244,0.0016)	(0.0113,0.0068,0.0014)	(0.01125,0.00675,0.0014)	
3	18 x18 [7.5]	18 x18 [7.5]	22x18 [9.0]	22x18 [9.0]	1.0
	(0.0244,0.0016)	(0.0244,0.0016)	(0.0113,0.0068,0.0014)	(0.01125,0.00675,0.0014)	
2	18 x18 [7.5]	18 x18 [7.5]	22x18 [9.0]	22x18 [9.0]	1.3
	(0.0244,0.0016)	(0.0244,0.0016)	(0.0113,0.0068,0.0014)	(0.01125,0.00675,0.0014)	
1	18 x18 [7.5]	18 x18 [7.5]	22x18 [9.0]	22x18 [9.0]	1.0
	(0.0244,0.0016)	(0.0244,0.0016)	(0.0113,0.0068,0.0014)	(0.01125,0.00675,0.0014)	

Note: The concrete strength of columns is 7.0 ksi. The concrete strength of beams is 5.0 ksi.

Table F-4 Summary of design properties of OMF-SC

Level	Columns		Beams		Drift(%)
	Exterior	Interior	Exterior	Interior	
4	16x16 [6.5]	16x16 [6.5]	24x16 [10.0]	24x16 [10.0]	0.7
	(0.0494,0.0021)	(0.0494,0.0021)	(0.0115,0.0069,0.0014)	(0.0115,0.0069,0.0014)	
3	16x16 [6.5]	16x16 [6.5]	24x16 [10.0]	24x16 [10.0]	1.3
	(0.0494,0.0021)	(0.0494,0.0021)	(0.0115,0.0069,0.0014)	(0.0115,0.0069,0.0014)	
2	16x16 [6.5]	16x16 [6.5]	24x16 [10.0]	24x16 [10.0]	1.8
	(0.0494,0.0021)	(0.0494,0.0021)	(0.0115,0.0069,0.0014)	(0.0115,0.0069,0.0014)	
1	16x16 [6.5]	16x16 [6.5]	24x16 [10.0]	24x16 [10.0]	1.8
	(0.0494,0.0021)	(0.0494,0.0021)	(0.0115,0.0069,0.0014)	(0.0115,0.0069,0.0014)	

Note: The concrete strength of columns is 4.0 ksi. The concrete strength of beams is 4.0 ksi.

Table F-5 Summary of design properties of OMF-JC

Level	Columns		Beams		Drift (%)
	Exterior	Interior	Exterior	Interior	
4	18x18 [7.5]	18x18 [7.5]	22x18 [9.0]	22x18 [9.0]	0.6
	(0.0244,0.0016)	(0.0244,0.0016)	(0.0113,0.0068,0.0014)	(0.0113,0.0068,0.0014)	
3	18x18 [7.5]	18x18 [7.5]	22x18 [9.0]	22x18 [9.0]	1.1
	(0.0244,0.0016)	(0.0244,0.0016)	(0.0113,0.0068,0.0014)	(0.0113,0.0068,0.0014)	
2	18x18 [7.5]	18x18 [7.5]	22x18 [9.0]	22x18 [9.0]	1.5
	(0.0244,0.0016)	(0.0244,0.0016)	(0.0113,0.0068,0.0014)	(0.0113,0.0068,0.0014)	
1	18x18 [7.5]	18x18 [7.5]	22x18 [9.0]	22x18 [9.0]	1.3
	(0.0244,0.0016)	(0.0244,0.0016)	(0.0113,0.0068,0.0014)	(0.0113,0.0068,0.0014)	

Note: The concrete strength of columns is 4.0 ksi. The concrete strength of beams is 4.0 ksi.

Table F-6 Summary of Design Properties of ACI-63

Level	Columns		Beams		Drifts (%)
	Exterior	Interior	Exterior	Interior	
4	22x18 [10.0]	22x18 [10.0]	24x12 [12.0]	24x12 [12.0]	N/A
	(0.0152,0.0013)	(0.0152,0.0013)	(0.0067,0.0033,0.0015)	(0.0067,0.0033,0.0015)	
3	26x20 [10.0]	26x20 [10.0]	28x16 [9.0]	28x16 [9.0]	N/A
	(0.0154,0.0016)	(0.0154,0.0016)	(0.0087,0.0053,0.0013)	(0.0087,0.0053,0.0013)	
2	30x20 [9.0]	30x20 [9.0]	34x20 [8.0]	34x20 [8.0]	N/A
	(0.0169,0.0015)	(0.0169,0.0015)	(0.0062,0.0047,0.0009)	(0.0062,0.0047,0.0009)	
1	30x24 [9.0]	30x24 [9.0]	34x20 [8.0]	34x20 [8.0]	N/A
	(0.0176,0.0012)	(0.0176,0.0012)	(0.0066,0.0056,0.0009)	(0.0066,0.0056,0.0009)	

Note: The concrete strength of columns is 5.0 ksi. The concrete strength of beams is 5.0 ksi.

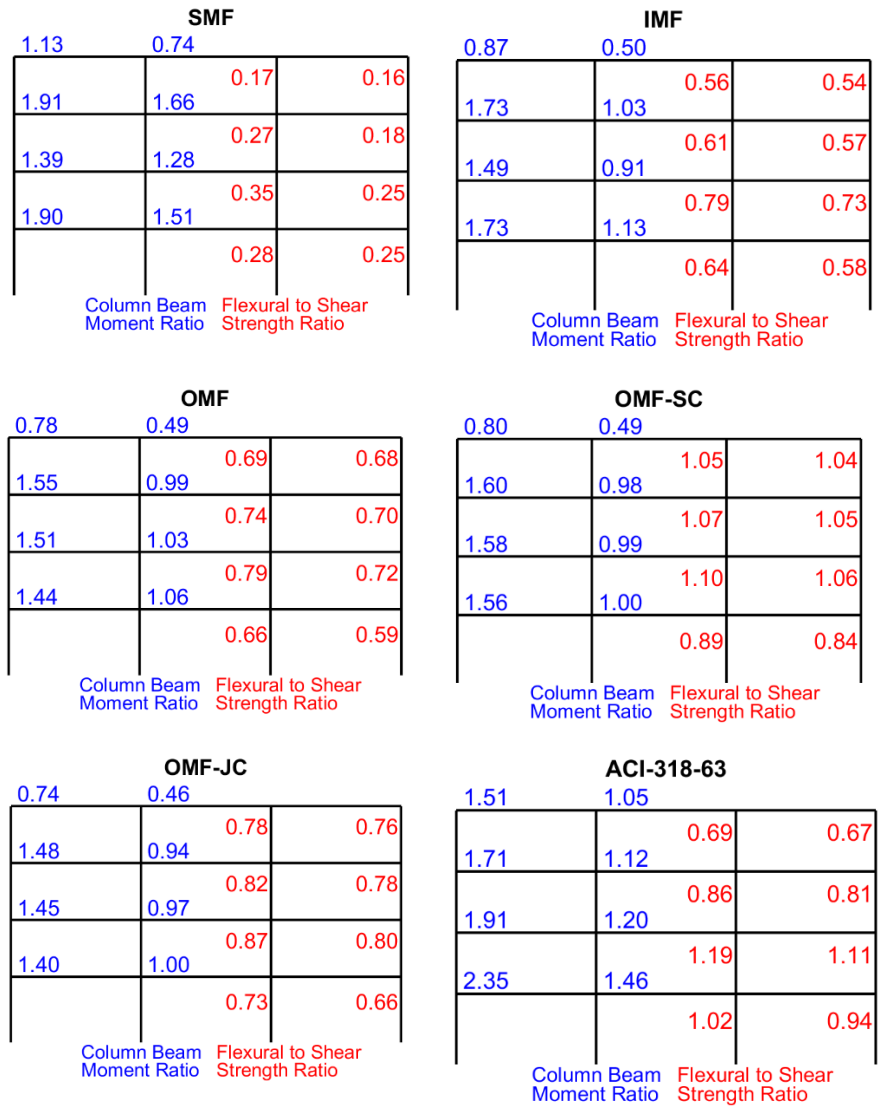


Figure F-2 Summary of column beam moment ratios, calculated as $\frac{\sum M_c}{\sum M_b}$ considering slab effects, and the ratio of column flexural to shear strength, $\frac{V_p}{V_n}$.

F.3 Nonlinear Modeling of Studied Frames

Each building is modeled nonlinearly in two dimensions in the OpenSEES software platform, as shown in Figure F-3. The gravity frames of the building are modeled alongside seismic frames connected via rigid links. Foundations for all buildings assumed to be fully fixed, representing, for example, a basement wall condition. The models also consider P-Delta effects. Rayleigh damping of 3.0% is assumed for all buildings applied to the first and third modes of the vibration using initial stiffness.

To capture nonlinear component response, column and beam response are represented phenomenologically with concentrated plastic hinges. These hinges are modeled with the Ibarra et al. (2015) model, with parameters determined by the equations from Haselton et al. (2016) that relate component properties to model parameters. To represent shear critical columns, the post-“yield” section of the backbone curve of columns is shortened such that the deformation capacity of the column matches the Elwood and Moehle (2005) estimates for shear critical columns. To represent the joint critical case, the strength of beam plastic hinges adjacent to the joints are modified to represent moment demand that causes the adjacent joint reaches to its capacity.

Table F-1 provides a summary of properties of the studied frames. Figure F-4 provides the pushover curves for each studied frame. The SMF is stronger and stiffer than the other buildings. The IMF also exhibits higher strength compared to the OMFs. However, the difference between IMF and OMF is not as great as the difference in design values, which can be attributed to the high contribution of gravity frames and of gravity load design of even perimeter framing elements of the structures designed for lower seismicity. The shear critical and joint critical OMFs are the least ductile buildings, with the baseline OMF, IMF, ACI-318 63, and SMF designed buildings exhibiting greater deformation capacity (in that order). Although the 1963 version of ACI-318 did not have stringent detailing requirements, that building is designed for California (high seismicity), which led to stronger columns than beams in most cases.

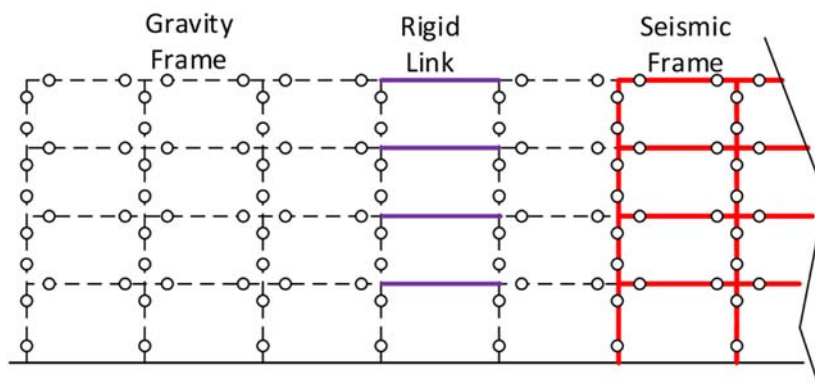


Figure F-3 Idealization of moment frames for nonlinear simulations. In the full model, two gravity frames are connected to the seismic frame via rigid links.

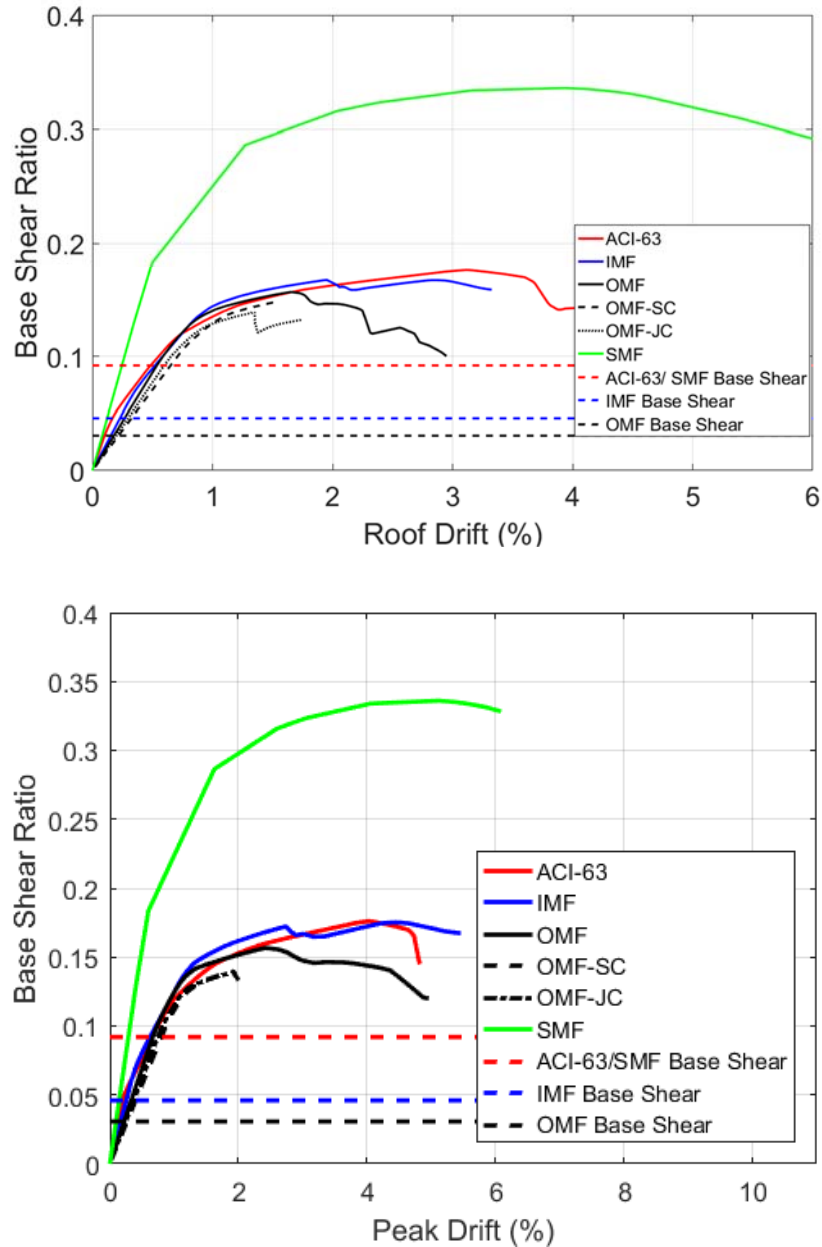


Figure F-4 Pushover curves of the studied RC frames, showing (a) Roof Drift on the x-axis and (b) Peak Drift on the x-axis.

F.4 Summary of Framework for System-Level Repair Assessment

The framework described in Appendix B is adopted for assessment of when system performance is impaired in terms of a drift threshold.

The framework consists of four main steps shown in Figure F-5. The first step evaluates the performance of each undamaged frame building under a set of performance assessment ground motions selected for the site of the

building, scaled to DE level of shaking. For each site, records are selected to represent the design intensity using the conditional mean spectrum approach. The second step involves incremental dynamic analysis to quantify each frame building’s response to a range of ground shaking intensities, producing a range of responses; these results are referred to collectively as “damage conditions”. In the third step, back-to-back analysis is conducted to evaluate the performance of the damaged building by choosing some damaging motions (or conditions) to precede the performance assessment motion; the damaging ground motions are selected based on the statistical approach described in Appendix B that maintains the distribution for peak story drifts from the full IDA. Appendix B shows that 20-30 damaging conditions are sufficient. This step examines how damage in the building affects the drift demands at the DE level shaking. Damage is quantified by the peak story drift incurred in the damaging motion. The fourth step quantifies the amplifications of drift in the performance assessment motions associated with damage, indicating when safety repairs are needed based on the system analyses.

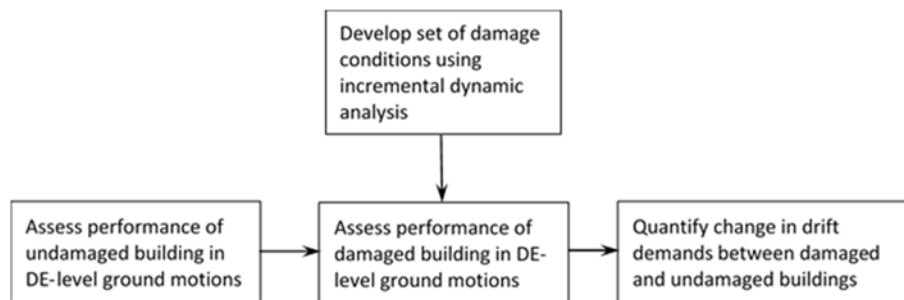


Figure F-5 Framework for assessing the level of damage at which building seismic performance is impaired.

F.5 Repair Assessment Results

F.5.1 System-level drift amplification results

The framework described in the previous section is used to prepare a repair assessment plot for each of the studied frames. The repair assessment plot presents the maximum drift in the damaging motion on the x-axis, and the amplification of the drifts in DE-level performance assessment motions on the y-axis. A value of 1 on the y-axis indicates that the damage does not affect the drift response. Figure F-6 to F-10 presents these plots for each building, including the median and ninetieth percentile curves. In all cases, for small drifts in the damaging motion, there is initially not a significant change in the drifts in the DE performance assessment motions (the median curve is flat). However, as damage, measured by the damaging motion peak drift is increased, both the drifts in the DE motions and the scatter increases.

These plots show also how the initiation of drift amplification can vary from one building to another based on the deformation capacity. Figure F-11 shows a comparison between the median values for all studied building in one plot. Figure F-11 reveals that the OMFs are most prone to drift amplification. In other words, the buildings with the most significant drift amplifications and amplifications at the lowest levels of damage are those with the smallest deformation capacity (see Figure F-4a). The drift amplifications seem to become significant after damaging motion drifts near the story drift associated with the peak pushover response. Figure F-12 shows a comparison between the ninetieth percentile values for all studied building in one plot, showing the same trend.

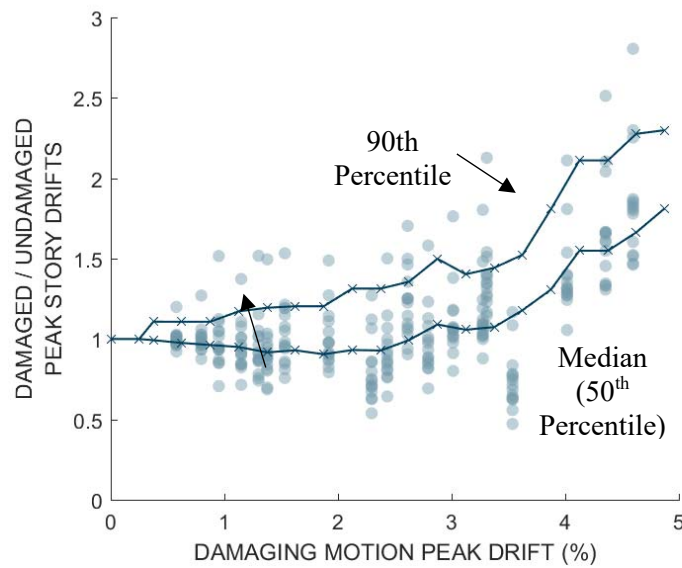


Figure F-6 IMF drift amplifications in DE motions as a function of damaging motion peak drift.

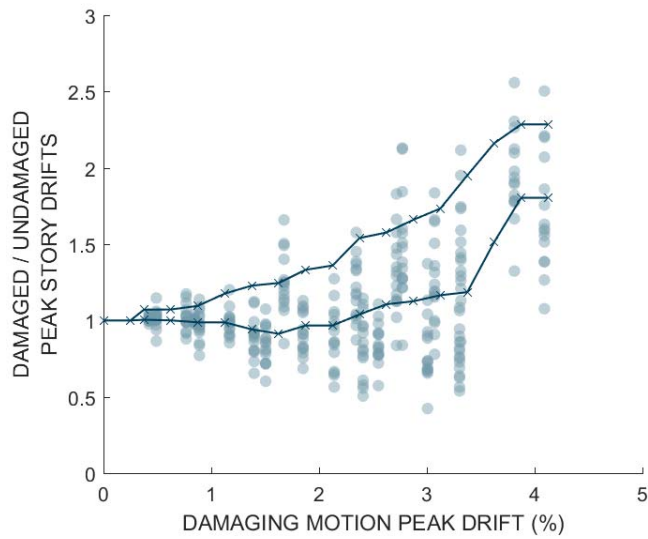


Figure F-7 OMF drift amplifications in DE motions as a function of damaging motion peak drift.

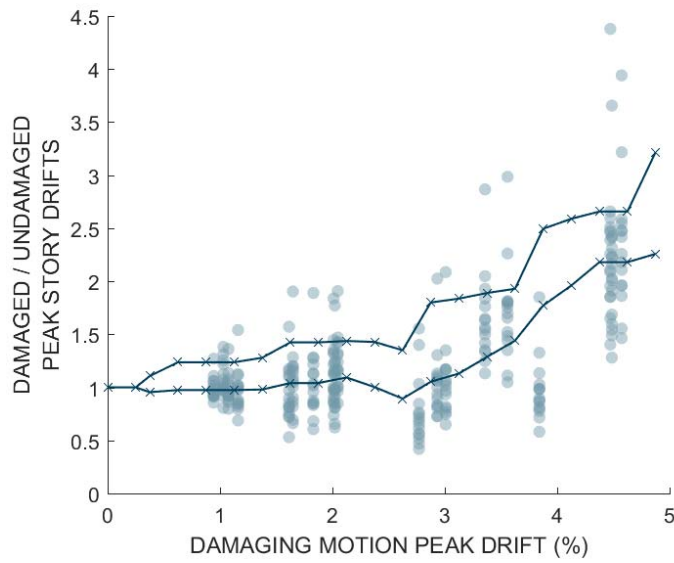


Figure F-8 OMF-SC (shear critical) drift amplifications in DE motions as a function of damaging motion peak drift.

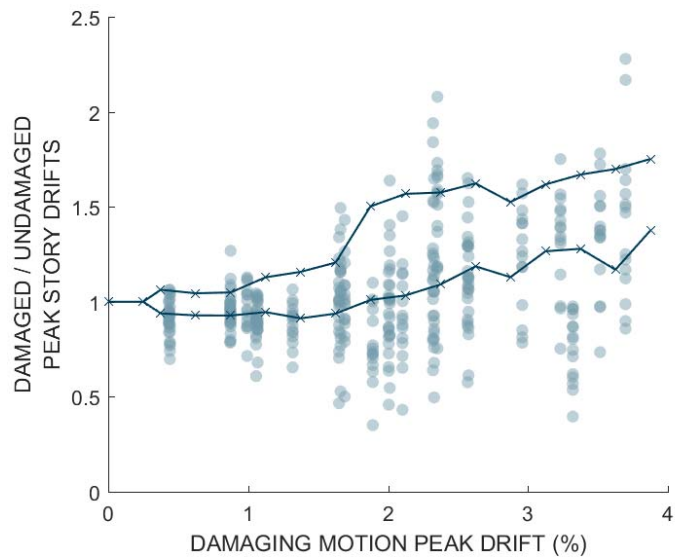


Figure F-9 OMF-JC (joint critical) drift amplifications in DE motions as a function of damaging motion peak drift.

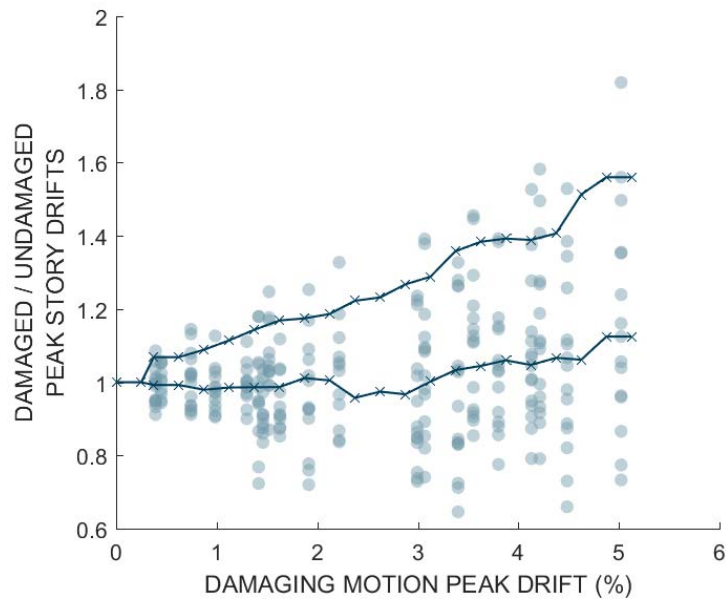


Figure F-10 ACI-318 1963 era building drift amplifications in DE motions as a function of damaging motion peak drift.

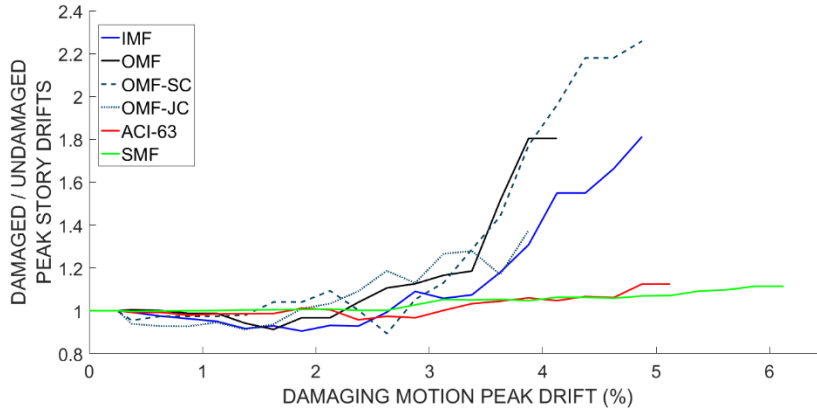


Figure F-11 Comparison of median (50th percentile) drift amplifications in DE motions in the studied frames, showing effect of building deformation capacity.

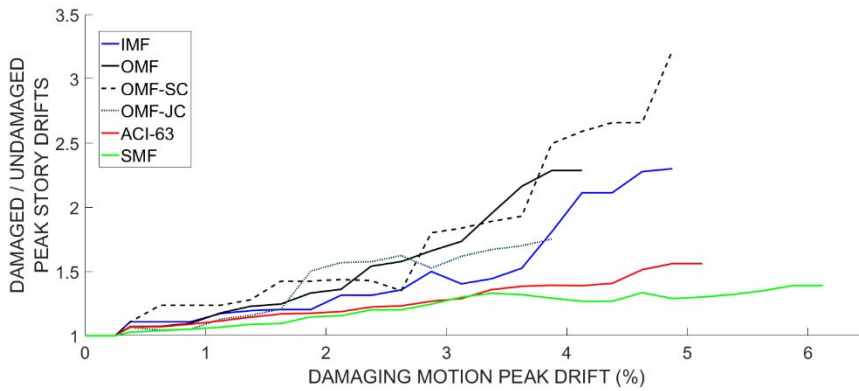


Figure F-12 Comparison of 90th percentile of drift amplifications in DE motions in the studied frames, showing effect of building deformation capacity.

F.5.2 Comparison of System and Component Limits in Repair Guidelines

To compare system and component limits developed in these guidelines, and explore the implications on drift amplifications and repair, we make use of the plastic rotation a values from ASCE 41 (ASCE 41-17), as presented in Figure F-13. These a values define component deformation capacity in terms of the point of lateral strength loss.

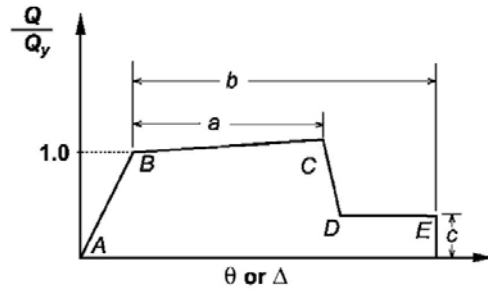


Figure F-13 Definition of plastic rotation a values from ASCE 41 (ASCE 41-17).

Drift amplification results for all the studied frames are replotted in Figure F-14 to Figure F-18, quantifying damage on the x-axis as a ratio of the plastic rotation demand from the damaging motion to a . The value plotted is the maximum over all columns of the ratio of the plastic rotation demand in the columns in the damaging motion to the a value. Results for all the building studied are combined in Figure F-19. Note that these results are more jagged than those provided with damaging motion drift on the x-axis because the damage conditions were selected based on drift from IDA.

Figures F-14 through Figure F-19 show that, in general, for plastic rotation demands less than the a value, median drift amplifications are not significant. Drift amplifications become significant as the plastic rotation demand in the critical elements approaches 1; at this point, the subsequent motion is likely to push the response into a strength degrading negative slope response. In the OMF (Figure F-15), the ratio of plastic rotation demands to a is generally greatest at the first story, and drifts are generally highest in the first or second stories, though this depends on the ground motion characteristics. There is a strong correlation between peak story drift and the ratio of maximum column hinge rotation normalized to the a value.

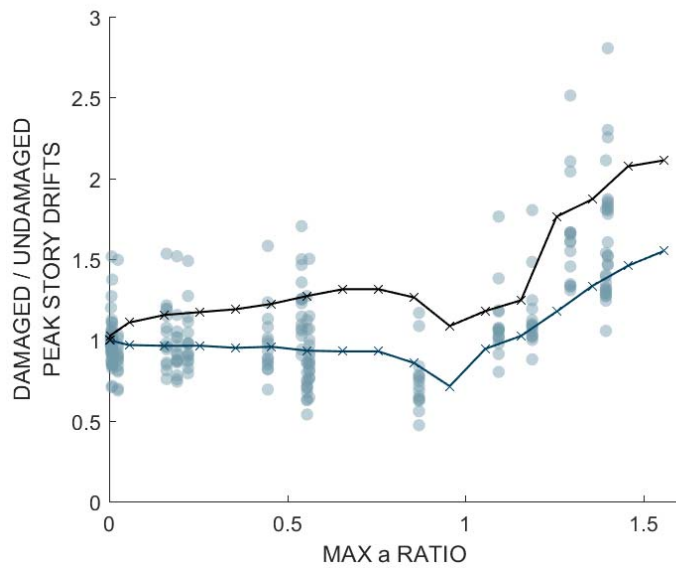


Figure F-14 IMF drift amplifications in DE motions as a function of damage, quantified by the plastic rotation demand to capacity ratio, termed “Max A ratio”.

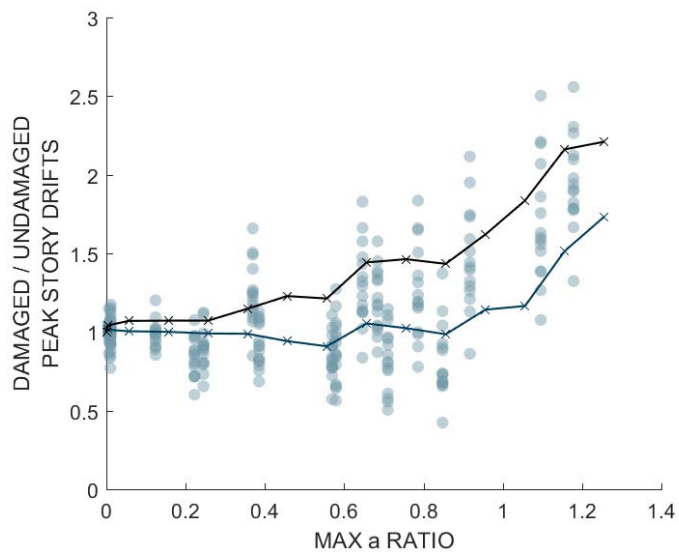


Figure F-15 OMF drift amplifications in DE motions as a function of damage, quantified by the plastic rotation demand to capacity ratio, termed “Max A ratio”.

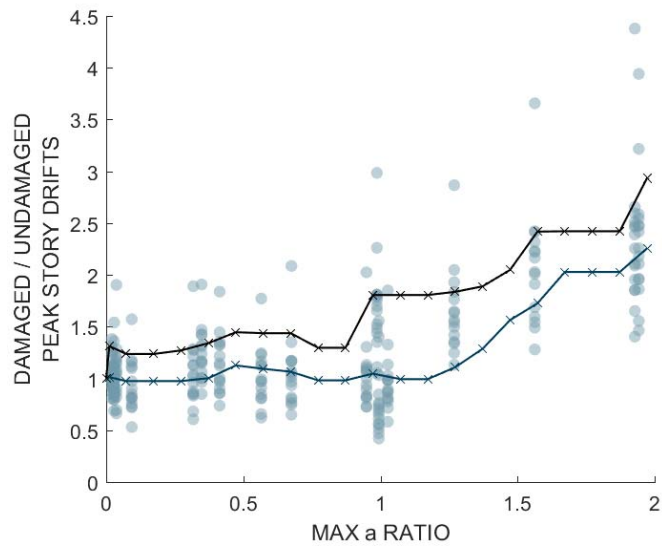


Figure F-16 OMF-SC (Shear critical) drift amplifications in DE motions as a function of damage, quantified by the plastic rotation demand to capacity ratio, termed “Max A ratio”.

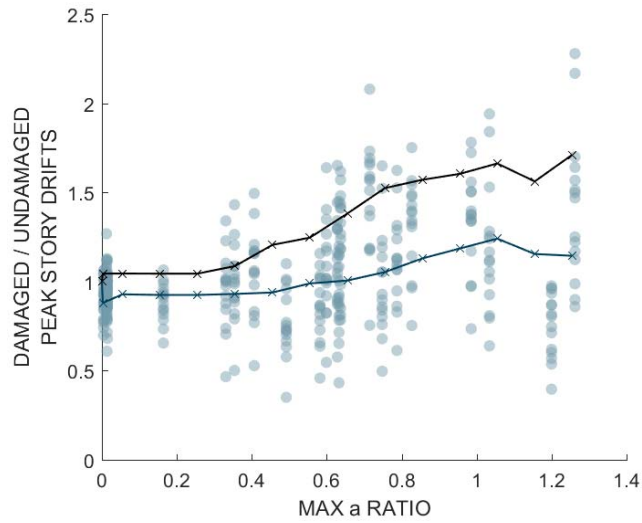


Figure F-17 OMF-JC (joint -critical) IMF drift amplifications in DE motions as a function of damage, quantified by the plastic rotation demand to capacity ratio, termed “Max A ratio”.

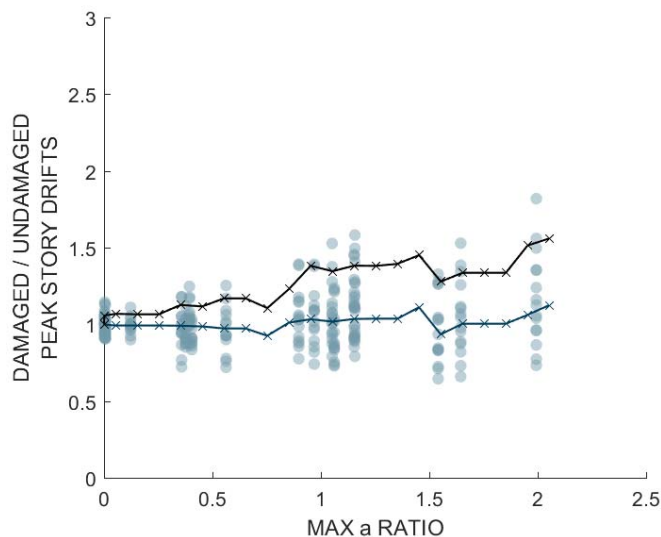


Figure F-18 ACI 1963-era building drift amplifications in DE motions as a function of damage, quantified by the plastic rotation demand to capacity ratio, termed “Max A ratio”.

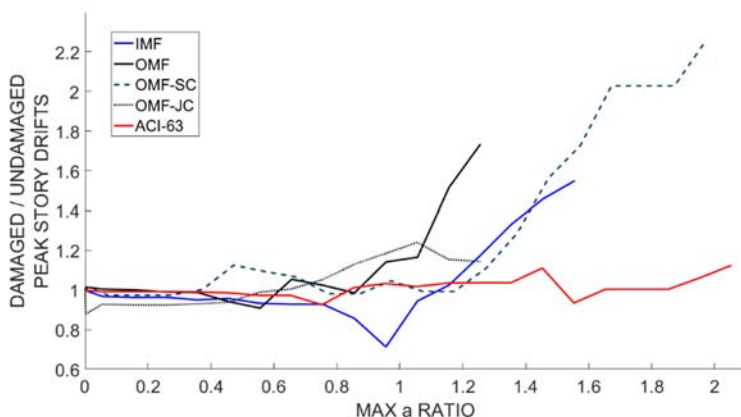


Figure F-19 Comparison of median (50th percentile) of drift amplifications in DE motions in the studied frames, as a function of the column plastic rotation demand to capacity ratio.

In the current version of the repair guidelines, component inspection trigger can be defined in the form of $x \cdot a$, where x may be on the order of 0.15 (See Appendix H). Results in Figure F-19 confirm no impaired performance at this level of deformation demand, which is desirable for an inspection trigger.

Figure F-20 provides a comparison between the visual damage limits (Appendix I) that are being proposed as indicating safety repairs and the system response for the OMF building. To develop this figure, the column component database being developed this project was reviewed to identify experimental specimens with similar aspect ratio, stirrup spacing to effective

depth, transverse reinforcement ratio, axial load ratio and shear capacity ratio to the columns in the first story of the perimeter frame. The selected column is the FSF-15S-0.1 column from Chiu et al. (2019). These results show that DS2 (flexural yielding) is before the onset of significant drift amplification (at least in a median sense). The drift at the onset of lateral strength degradation is near the beginning of the degradation of system response.

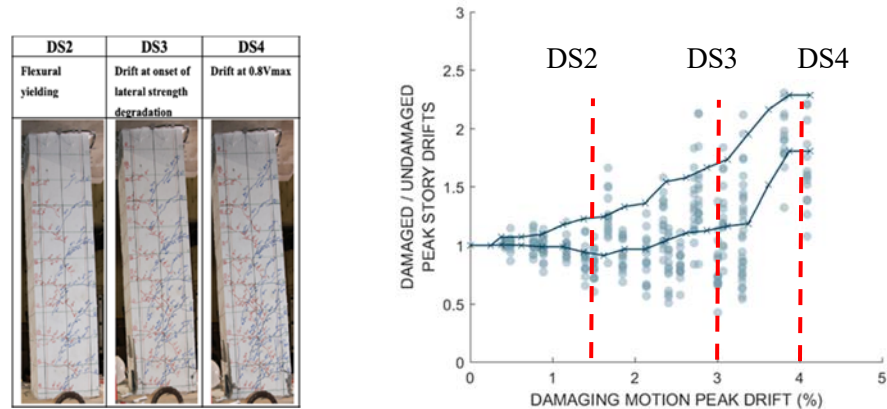


Figure F-20 Comparison of visual damage limit and the system limit for the OMF, considering an experimental specimen with column characteristics similar the studied OMF.

F.5.3 Implications for Substantial Structural Damage

The Repair Guidelines will likely use the concept of Substantial Structural Damage (defined in IEBC, 2018). This concept is currently defined by a loss of 33% of lateral strength (IEBC, 2018).

To relate the damage in the analyses described above to the loss of strength for the OMF, a pushover analysis was conducted at the end of each damaging ground motion. This pushover therefore provides a measure of the strength remaining in the structure after the damaging motion. These pushover plots are presented in Figure F-21, showing a significant change in stiffness after the damaging motion, but not a very significant change in strength. Strength loss after the damaging motion is quantified as the ratio of the pushover strength of the undamaged building to the damaged building, i.e., remaining building strength.

This measure of strength loss is compared with the drift amplifications in Figure F-22. The plot shows that strength loss may not be a good indicator of the impairment of the future seismic performance, because there is not a very strong trend between the strength and the drift amplification. In other words, significant drift amplifications are observed, when the remaining strength is calculated to be high. Likewise, for this building, which is a frame structure

with many components contributing to the mechanism, 33% strength loss was never observed, despite significant degradation in drift performance. This suggests that the current limit may be highly non-conservative.

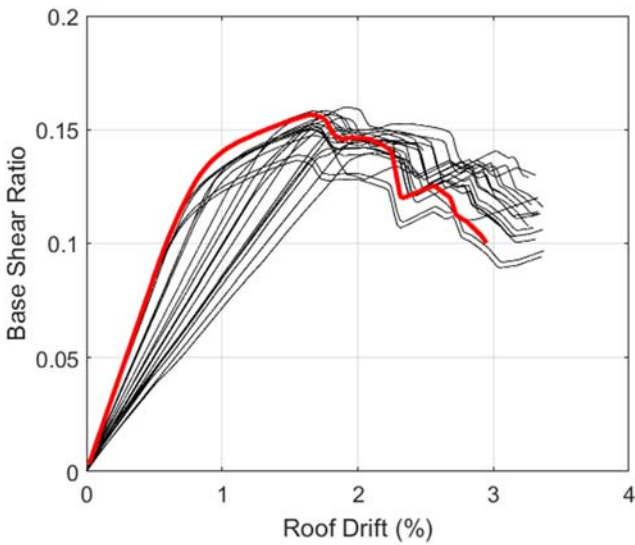


Figure F-21 Comparison of pushover curves of the OMF after different damaging motions; the undamaged pushover curve is presented in red. (the damaging motions had peak drifts between 0.5 and 4% drift).

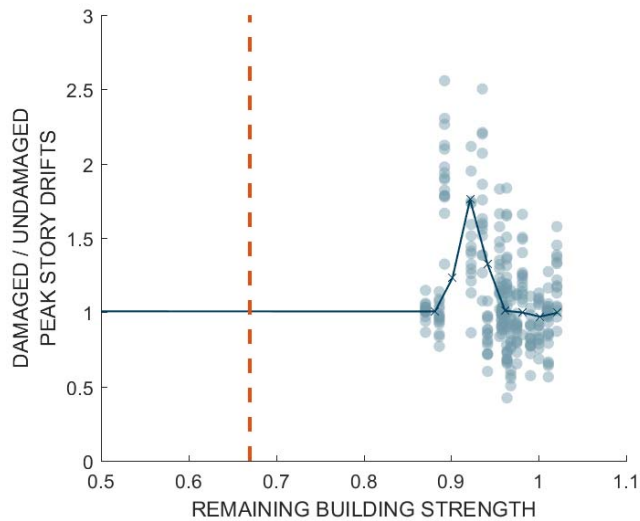


Figure F-22 Repair assessment plot of OMF using strength loss as the measure of the damage. The Remaining Strength is the ratio of damaged to undamaged maximum base shear from pushover analysis (so strength loss is 1 minus this value).

F.6 Conclusions and Summary

This Appendix describes the results of a study of the influence of deformation capacity and detailing on system response and the need for safety repairs. Five 4-story moment frames are designed to represent different characteristics which could impact their deformation capacity. The results show that impairment of system level performance is associated with demands exceeding component and building deformation capacities, and significant amplification of drifts in subsequent motions is not observed until these deformation capacities are reached.

This Appendix also relates system behavior to the component limits for these frame structures. A component-based plastic rotation demand to capacity ratio represents the component limits, showing that the inspection limits are conservative relative to these system responses and that the draft visual damage limits for repair trigger correspond with the observed drift amplifications.

For one of the buildings, pushover analyses are conducted after the damaging motion to assess strength loss. These results suggest that strength loss is not a good predictor of drift amplification, and that for buildings with many components contributing to the mechanism 33% strength loss – as currently used in the IEBC – may be highly non-conservative.

References

- ACI, 2014, *Building Code Requirements for Structural Concrete*, ACI 318-14, and *Commentary*, ACI 318R-14, ACI Committee 318, American Concrete Institute, Farmington Hills, Michigan.
- ACI, 1963, *Building code requirements for reinforced concrete*, ACI Committee 318, American Concrete Institute, Farmington Hills, Michigan.
- ASCE, 2016, *Minimum Design Loads and Associated Criteria for Buildings and Other Structures*, ASCE/SEI 7-16, American Society of Civil Engineers, Structural Engineering Institute, Reston, Virginia.
- ASCE, 2017, *Seismic Evaluation and Retrofit of Existing Buildings*, ASCE/SEI 41-17, American Society of Civil Engineers, Structural Engineering Institute, Reston, Virginia.
- Chiu C., Sung H., Chi K., and Hsiao F., 2019, “Experimental quantification on the residual seismic capacity of damaged RC column members,” *International Journal of Concrete Structures and Materials*, Vol. 13, No. 17.

- Elwood, K., and Moehle, J., 2005, "Drift capacity of reinforced concrete columns with light transverse reinforcement," *Earthquake Spectra*, Vol. 21, No. 1, pp. 71-89.
- FEMA, 2018, *Assessing seismic performance of buildings with configuration irregularities, FEMA P-2012*, prepared by the Applied Technology Council for the Federal Emergency Management Agency, Washington D.C.
- ICC, 2018, *International Existing Building Code, IEBC*, International Code Council, Country Club Hills, Illinois.

G.1 Introduction

This Appendix summarizes the Wall System Studies conducted to assess repair triggers. The studies included the assessment of responses for three building archetypes using two-dimensional (2D) models that included only a single wall to compute responses. Archetypes with more than a single wall were not considered because the design space was too large and the goal was to assess trends. For this study, walls were assumed to be flexure-controlled (no shear failures) and well-detailed, i.e., ACI 318-14 “Special Walls”. Damage trends were evaluated by using ratios of various responses (e.g., drift, hinge rotation) for the damaged structure to the undamaged structure. An assessment of these trends generally indicates that the system studies do not provide valuable information that cannot already be gleaned from inspection and repair triggers developed in Appendix H for components and visible damage summaries being developed in Appendix I. This finding is consistent with the approach used for the system studies, since the study is based on a model of a single wall, where redistribution is not possible. For the models with single wall, the one response parameter that did show a positive correlation for the damaged-to-undamaged ratio trends was the residual response (e.g., residual roof drift) at the end of the damaging ground motion. However, due to concerns related to the ability to reliably predict (compute) residual responses using current modeling approaches and the ability to validate these results, residual responses were not deemed sufficiently reliable at this time to use as a repair trigger.

G.2 Description

Figure G-1 outlines the methods used to assess the influence of damaging ground motions on the subsequent response of a building for code level demands. The goal is to see if trends can be observed using these analyses to help identify a repair trigger. The approach involve conducting a performance assessment of an undamaged building, conducting a performance assessment of a damaged building (considering various levels of damage) and comparing the two. The performance assessment is done at two hazard levels Design Earthquake (DE) and Maximum Considered Earthquake (MCE_R) as defined in ASCE 7-16, and trends are evaluated using the following four parameters: (i)

roof drift; (ii) curvature at the base; (iii) 1st story drift; (iv) plastic hinge total rotation; as well as the residual values of these four parameters. Changes in these parameters of the damaged building relative to the undamaged building are investigated as potential indicators that future performance is impaired, and repairs are needed.

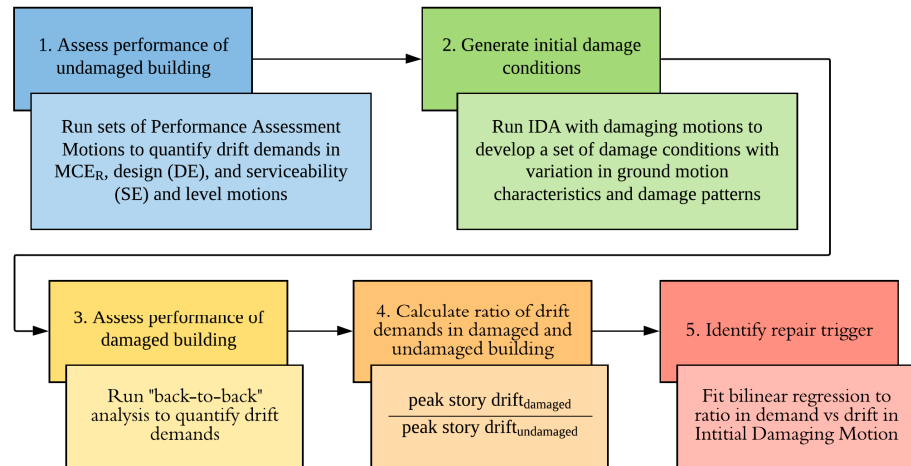


Figure G-1 Flowchart of methods used to assess the effect of pre-damaging ground motions.

Step 1. Assess performance of undamaged building. The performance of the undamaged building is assessed at performance levels associated with safety assessment and involve motions scaled to design earthquake (DE) and risk-targeted maximum considered earthquake (MCE_R) intensities. Two suites of 20 ground motions (GMs) are selected to appropriately represent the spectral shape at the two performance levels considered (DE and MCE_R) at a site located in Westchester, Los Angeles, California (latitude 33.970, longitude -118.38). This location has site-modified spectral acceleration values of $S_{MS} = 2g$ and $S_{MI} = 0.92g$. Each suite of GMs is scaled to a Conditional Mean Spectrum (CMS) for each building fundamental period (Baker, 2011). The selection procedure does not directly consider ground motion duration of the Performance Assessment Motions. Figure G-2 illustrates how the spectra for each set of performance GM datasets matches the same S_a value at T_l .

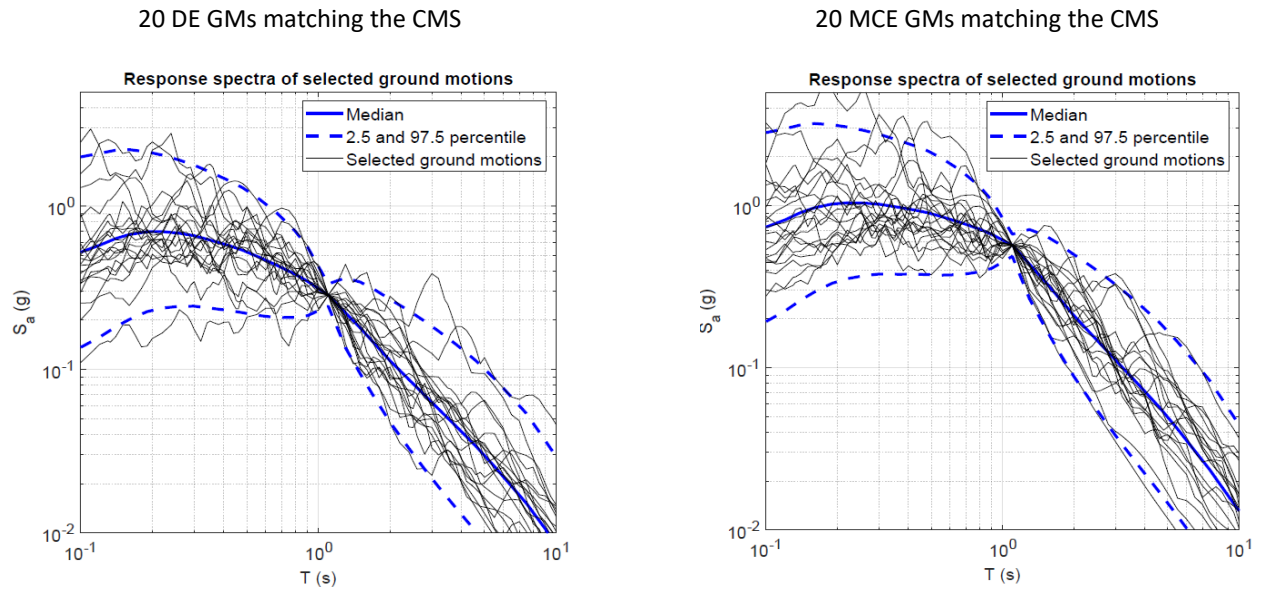


Figure G-2 Suite of DE and MCE GMs matching their respective Conditional Mean Spectrum (CMS).

The period used to match the spectrum is the fundamental period obtained from the Eigen analysis of the structure using seismic weight (mass) defined according to ASCE 7-16 and using nominal material properties to determine flexural stiffness ($0.5E_cI_g$) and shear stiffness ($0.4E_cA_g$).

Step 2. Generate Initial Damage Conditions. The performance of the undamaged building is assessed using Incremental Dynamic Analysis (IDA) to produce roof drift demands varying from almost zero to around 3 times the predicted roof drift capacity of each building.

The FEMA P-695 far field GMs are used as the set of Damaging Motions for the IDA (FEMA, 2009). This set represents motions suitable for assessment of buildings located at sites where strong ground shaking is expected. Figure G-3 provides example results for one of the structures.

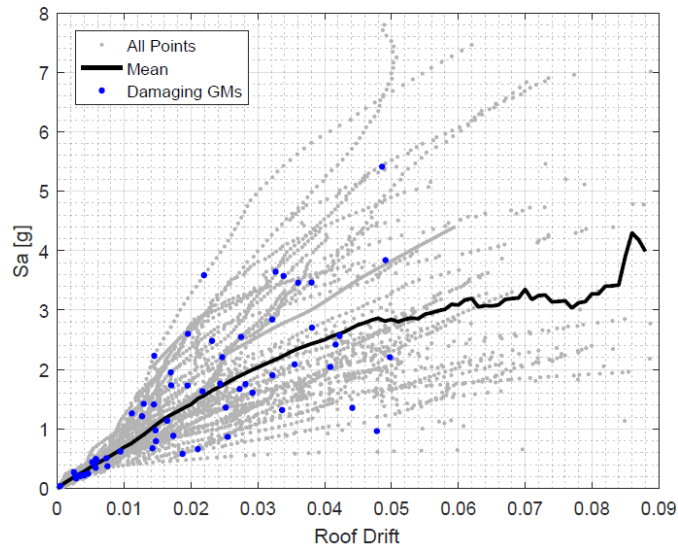


Figure G-3 Illustration of Incremental Dynamic Analysis results for one of the buildings (8-story building). Each dot represents the maximum roof drift demand response in function of the spectral acceleration at the fundamental period of the structure.

These analyses are used to create a set of “Initial Damage Conditions” that represent a wide range of responses and damage for the building for the range of ground motion intensities and characteristics considered.

A subset of 60 of these Initial Damage Conditions is selected for subsequent analysis. A subset of the IDA is used because the analysis is computationally intensive, as will be described below. The subset is identified using stratified random sampling (Parsons, 2014) based on peak roof drift. The stratified random sampling ensures that the distribution of peak roof drifts in the selected Initial Damage Conditions is the same as the entire set. No more than two Initial Damage Conditions were selected from the same ground motion record regardless of scale factor. The selected subset of Initial Damage Conditions covers a sufficient range of demand responses in a way that further analyses do not alter the conclusions of this study (indicated as blue dots in Figure G-3).

Step 3. Assess performance of damaged building. This process uses the same Performance Assessment Motions and performance levels described in Step 1. The difference is that the structure is already damaged when applying the Performance Assessment Motions. The level of pre-damage is determined by the Initial Damage Conditions (Step 2).

The assessment of the damaged building is illustrated in Figure G-4. First, the simulation recreates the Initial Damage Condition using the same Damaging Motion and intensity level. Then, after the simulation has been

allowed to come to rest, one of the Performance Assessment Motions is applied. This process is repeated for that same Initial Damage Condition for all of the Performance Assessment Motions for a given performance level and, subsequently, for the rest of the Initial Damage Conditions and that same performance level.

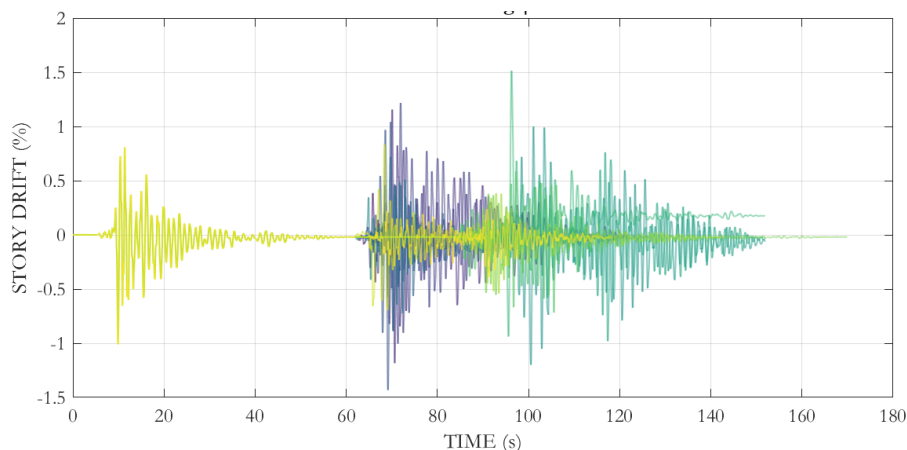


Figure G-4 Illustration of back-to-back analysis used in performance assessment of the damaged building.

Step 4. Compare drift demands in undamaged and damaged building.

The outcome of Steps 1-3 are five sets of peak demands (roof drift, curvature at the base, first story drift, plastic hinge total rotation, and the residuals of these parameters) in the undamaged building that can be compared to the corresponding set of the same demands obtained for the damaged building. These five parameters are expressed as a damaged-to-undamaged ratio, as expressed in Eq. G-1, where y represents the peak demand of any of the five parameters mentioned before, i is the Performance Assessment Motion (DE or MCE_R), and j is the Damaging GM to which the DE or MCE_R GM is concatenated with.

$$\left(Ratio_y \right)_{i,j} = \left(\frac{y_{i,j}^{(damaged)}}{y_i^{(undamaged)}} \right) \quad (G-1)$$

If the ratio in Eq. G-1 is close to 1.0, the demand in the undamaged and damaged building are essentially the same for that motion. If it is greater than 1, the damaged building has amplified the demand, and if it is less than 1.0, there is actually deamplification of the demand in the damaged structure. The ratios of each parameter are plotted and the trends are analyzed to assess the role of preexisting damage on subsequent building responses in safety level events (DE or MCE_R).

Step 5. Analyzing the trends. If the intensity of the Damaging GM that produces the pre-damaged condition before the DE or MCE_R motions are

applied alters the future performance of the building, a trend should be apparent in the plots of $(Ratio_y)_{i,j}$ vs Damaging GM intensity level. However, as it will be shown, no significant trends are observed prior to the Damaging GM producing demands that exceed the deformation capacity (expressed as roof drift or total plastic hinge rotation, and shown with a dashed vertical green line in the corresponding plots in Figure G-5) of the primary lateral force resisting element (in this case, a single wall). After analyzing the results, it is found that a lognormal distribution can be fitted to the ratio data obtained for every Damaging GM intensity level. The trend can be defined by connecting the mean value of each fitted lognormal distribution as schematically shown in Figure G-5. Also, if any point is found beyond $\mu^* \cdot \sigma^{*3}$ after fitting the lognormal distribution, it is considered a residual. The residuals are removed, and a new lognormal distribution is fitted to the remaining data. This process is repeated as many times as needed. This is done because there are a few cases where the damaged-to-undamaged ratio is very high, suggesting that the building model has reached the collapse state, in which case there is no need to consider the ratio because it would introduce bias to the data because the probability of collapse of a building designed accordingly with the codes is very low (<10%) and a repair trigger is not needed for a collapsed building. Figure G-6 shows that only 0.1% of the data (damaged-to-undamaged ratios in this case) are in the $(\mu^* \cdot \sigma^{*3}, +\infty)$ interval.

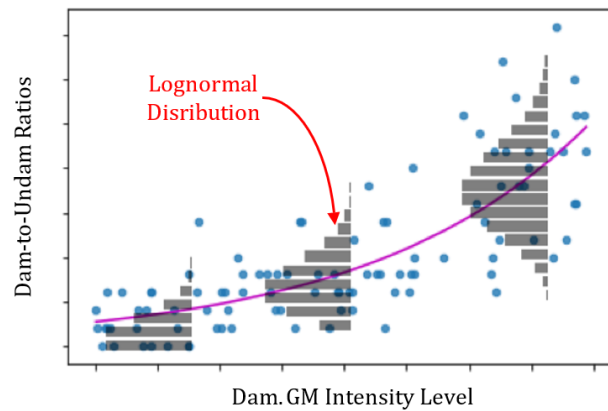


Figure G-5 Conceptual representation of how the trends is defined for analyzing the damaged-to-undamaged ratios.

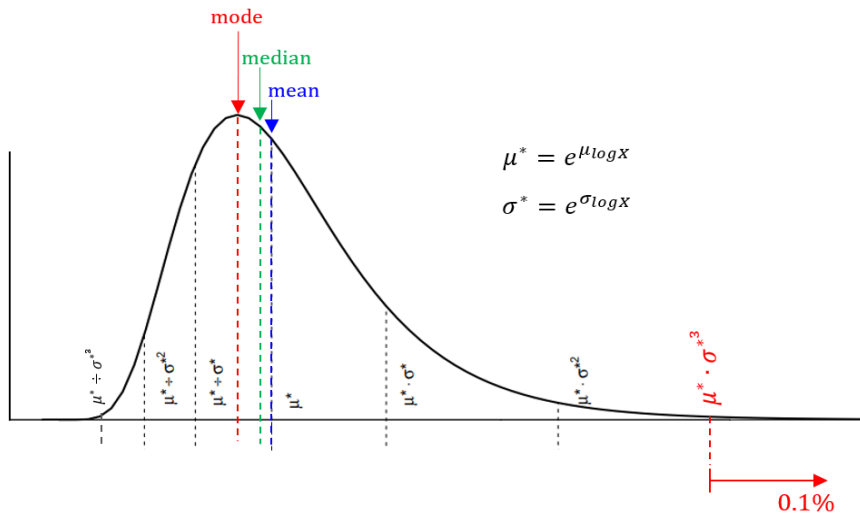


Figure G-6 Criteria to exclude residuals.

G.3 Design of Archetype Buildings

Three archetype buildings are studied as part of this study. Table G-1 presents the main characteristics of the archetypes. All archetypes are Reinforced Concrete (RC) Wall Buildings designed in accordance with the Modal Response Spectrum Analysis (MRSA) of ASCE 7-16 (including accidental torsion). To determine wall design actions, a two-dimensional model of a single wall was created. Effective wall flexural stiffness was set at $0.5E_cI_g$ and shear stiffness at $0.4E_cA_g$ over the entire wall height for the code level analysis.

All walls are designed to be special structural walls with wall aspect ratios $h_w/l_w > 2.0$; therefore, the walls are expected to be controlled by flexural responses. The design and detailing of the walls follows the provisions of ACI 318-19; however, wall shear amplification, which was added to Section 18.10.3 of ACI 318-19, was not considered because this study is focused on the behavior of existing buildings. Therefore, the subsequent assessment using the IDA in some cases produced wall shear responses that exceeded the wall nominal shear strength, which were ignored in this study (since shear-controlled walls were not part of this study). Studies of shear-controlled walls should be considered in a later study.

Table G-1 Main Characteristics of the RC Wall Building Archetypes

	4-story	8-story	12-story
# of stories	4	8	12
Design	Code-conforming except for shear amplification (Section 18.10.3.1 ACI318-19)		
T_1 (s)	0.4	1.08	1.65
Seismic weight, W (kips)	10,332	21,276	32,220
V/W	0.31	0.14	0.10
# of walls (each direction)	2	2	4
$ALR_{min} - ALR_{max}^{(a)}$	1.5% - 4.0%	2.5% - 7.0%	3.8% - 10.6%
Wall spect ratio (h_w/l_w)	2.25	3.53	5.27
f'_c (ksi) ^(b)	5	5	5
f_y (ksi) ^(b)	60	60	60
Wall type	Flexure-Controlled	Flexure-Controlled	Flexure-Controlled
Roof Drift ^(c)	0.72%	0.98%	0.94%
Predicted Roof Drift Capacity ^(d)	2.6%	2.5%	2.7%

Note: Axial load ratio of the wall. The maximum and minimum axial loads come from the LC6 and LC7 of ASCE 7-16, respectively; LC6: $(1.2 + 0.2S_{DS})DL + 0.5LL$; LC7: $(0.9 - 0.2S_{DS})DL$.

Nominal material properties of the wall

From Modal Response Spectrum Analysis (with nominal material properties)

Using equation proposed by Abdullah and Wallace (2019) with expected material properties and expected shear demand and axial load (i.e., considering shear amplification factors of ACI 318-19)

The commentary of ACI 318-19 Section 18.10.6 states that the wall P-M strength over the wall height should be specified so that the critical section (plastic hinge) occurs at the intended location. In this study, this was accomplished by amplifying the ASCE 7-16 moment demand M_u over the wall height by the factor $M_{pr,base}/M_{u,base}$, where $M_{pr,base}$ and $M_{u,base}$ are the maximum probable moment at the base using $f'_s = 1.25f_y = 75$ ksi and the moment demand at the wall base obtained from the MRSA. This process is illustrated in Figure G-7 for the 8-story building archetype. In Figure G-7, the amplified moment demand is less than the moment capacity (ϕM_n), at all locations over the wall height except at the critical section (hinge region).

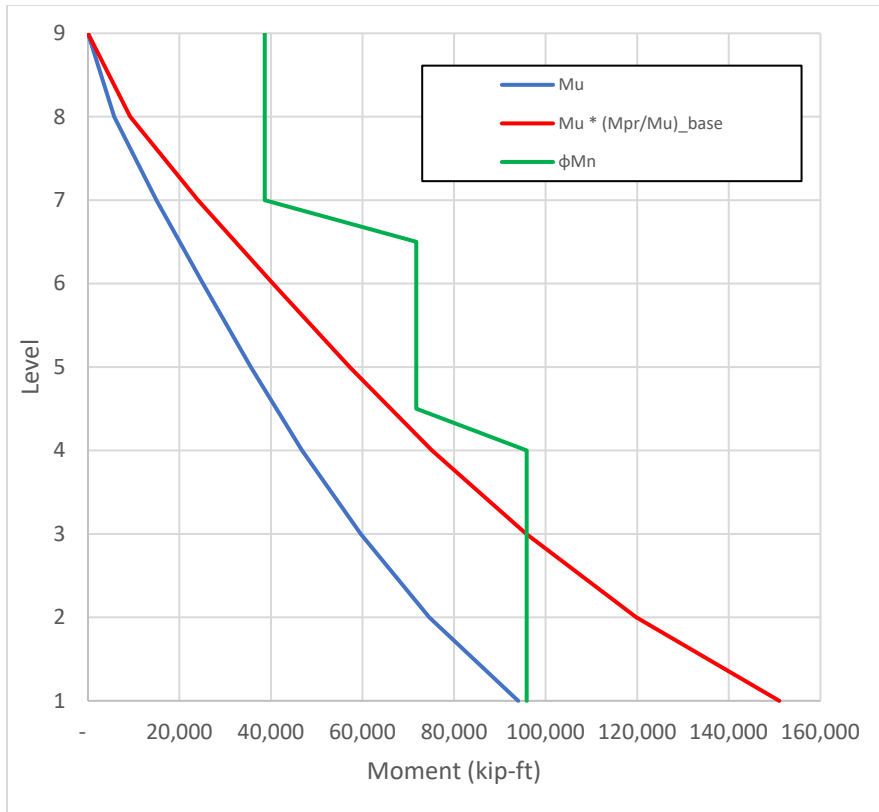


Figure G-7 Moment demand amplified by $(M_{pr}/M_u)_{base}$ – Plot taken from the 8-story.

G.4 OpenSEES Modeling

Due to symmetry of the building layout and the lateral system, and to simplify the modeling process, a 2D model consisting of one wall was used to determine the responses of the building in each direction. The wall was modeled using the Multi-Vertical-Line-Element (MVLE) model in OpenSees (Koložvari et al., 2015). Four elements were used for the first story and subsequent levels were modeled with two elements. The model considers expected material properties ($f_{ye} = 70$ ksi; $f'_{ce} = 1.3 f'_c = 6.5$ ksi) and the unconfined and confined concrete uniaxial stress versus strain relationships were estimated using the Saatcioglu and Razvi (1992) model because this confinement model allowed for consideration of the different levels of confinement for the two principal directions (e.g., x, y) for the boundary elements. Parameters were selected for the Concrete02 model in OpenSEES to fit these stress versus strain relationships. The expected axial load of $P_{u,expected} = 1,959$ kips was calculated with the load combination $DL + 0.25LL$. Reinforcement stress versus strain was modeled using the SteelMPF model in OpenSEES based on the following parameters (list parameters): $f_{ye} = 70$

ksi, $E_s = 29,000$ ksi, and 1% post yielding slope. The process described in this paragraph is the 1st step of the algorithm shown in Figure G-8.

Once the model was created, a monotonic pushover analysis was conducted, e.g., as shown in the 2nd step of Figure G-8, to determine appropriate parameters for modeling strength loss (no strength loss was considered in the initial pushover analysis). The roof drift capacity at significant strength loss ($\geq 20\%$ from peak load) was estimated using the Drift Capacity model proposed by Abdullah and Wallace (2019), which is expected to occur at about 2.5% roof drift for the 8-story building archetype (see Table G-1). To reproduce significant strength loss at the predicted roof drift capacity for each archetype, the neutral axis depth and strain profile at the predicted roof drift capacity are needed (see 3rd step in Figure G-8). The strain at which strength degradation initiates in compression for both confined concrete and longitudinal boundary reinforcement is assumed to be the same (ε_b), i.e., crushing of confined concrete and buckling of longitudinal boundary reinforcement are coupled. If this approach is not adopted, compressive concrete loads are transferred to boundary longitudinal reinforcement, and only moderate strength loss can be achieved. In addition, for this study, the outer steel layer of the boundary element (BE) under tension is assumed to reach its rupture strain when concrete reaches its residual strength in the BE under compression. An upper strain limit, ε_{rupt} , was also set for tension rupture of longitudinal reinforcement (e.g., $\varepsilon_{rupt} = 0.10$ for 8-story building archetype). Step 4 of Figure G-8 details how these values are used to modify the material properties of the BE in the plastic hinge region to achieve strength loss. Step 5 of Figure G-8 demonstrates that the strength loss objectives are achieved for both monotonic and reversed-cyclic pushover analyses (at roof drift capacity of 2.5% for 8-story building archetype). Additional details associated with the modifications to the material stress versus strain relations are described in the following paragraphs and in Figure G-8.

Strain values ε_b and ε_{res}^* , which are associated with strength loss, are selected from the monotonic pushover analysis of the Multi-Vertical-Line-Element-Model (MVLEM) without modified material stress versus strain relations. The strain values are determined from the strain profile at the wall critical section (wall-foundation interface) when the roof drift capacity is reached (see Figure G-9) as noted below:

- ε_b is selected as the strain at half of the neutral axis depth (i.e., half of the strain of the outer compressed fiber). Once this value is reached in the compression BE of the MVLEM, significant strength loss will occur because half of the compressed boundary longitudinal

reinforcement is assumed to buckle and half of the confined concrete in the compressed BE initiates strength loss by starting on the descending branch of the stress-strain relation. The material properties are modified to achieve this objective (of strength loss).

- The modified residual concrete strength is obtained from the following relationship:

$$\varepsilon_{res}^* = \varepsilon_{rupt} \times \left(\frac{c}{l_w - c} \right) \quad \text{G-2}$$

Where ε_{rupt} is the strain at which the bars in tension rupture ($\varepsilon_{rupt} = 0.10$ was used for all archetypes in this study). The above expression produces strength loss because the properties of the boundary longitudinal reinforcement in tension are modified to achieve strength loss exactly when the neutral axis associated to the roof drift capacity is reached (if we were only modifying the material relationships in tension).

It is noted that the material properties also are modified in compression, which also influence wall responses earlier because the strain levels associated for compression are lower than the strain levels associated with strength loss in tension ($\varepsilon_b < \varepsilon_{res}^*$). Once the roof drift capacity is reached, the wall neutral axis depth becomes larger due to degradation in concrete stress capacity, and Eq. G-2 produces rebar rupture in the tension BE when the outer fibers in the compressed BE have failed (reached residual strength) as desired to achieve significant strength loss for both directions of loading.

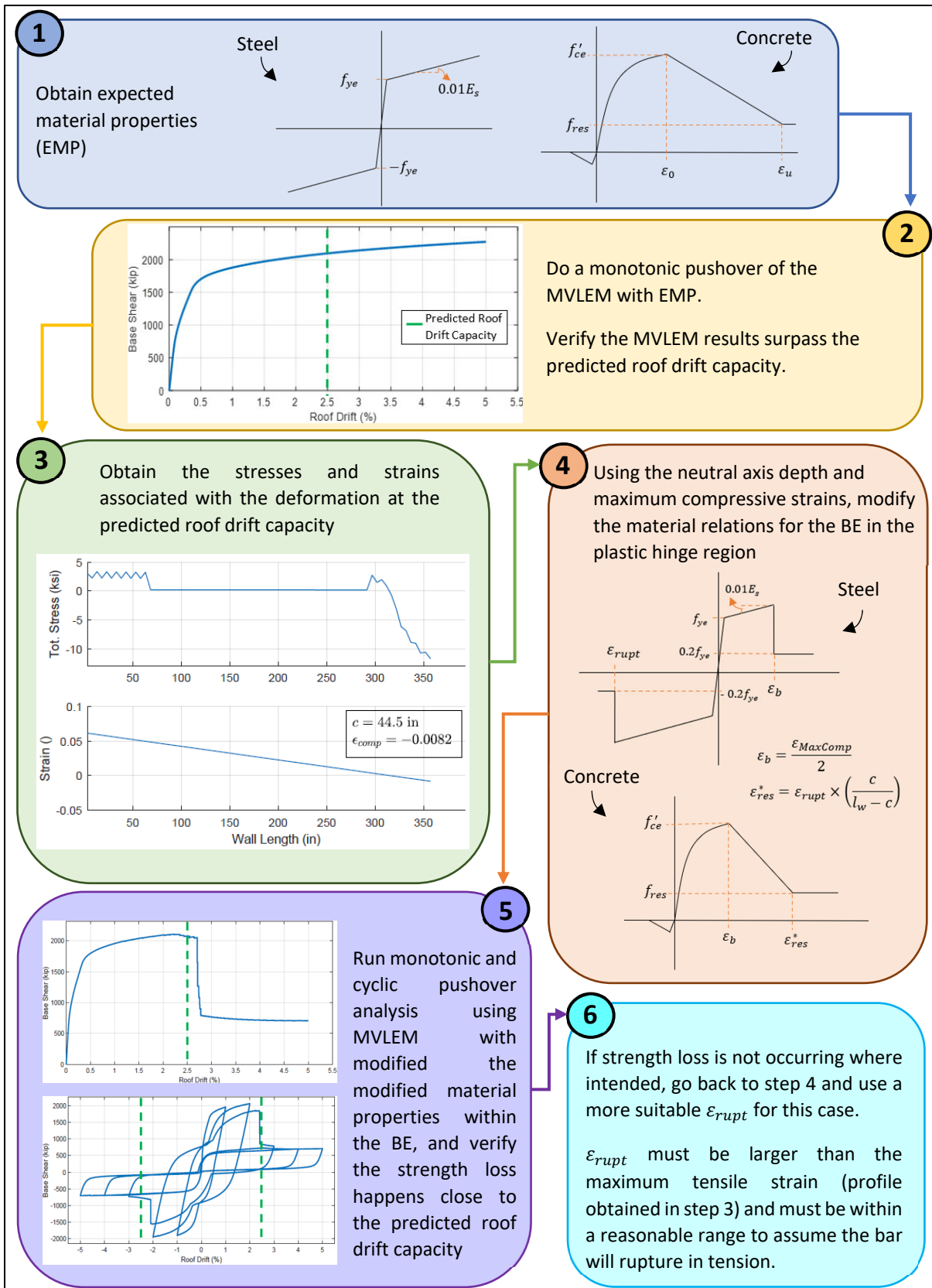


Figure G-8 Algorithm to obtain MVLEM with strength loss at predicted roof drift capacity.

Changing the strains at peak and residual stresses in the Concrete02 material in the OpenSEES model is sufficient to implement the necessary modification to the concrete stress versus strain relations. However, to implement the necessary modifications for the steel behavior it was necessary to define a Parallel material at the BE, one a bilinear SteelMPF material with weight factor of 80% (with a strain hardening ratio equal to 0.0125) to have complete strength loss in tension and compression at the desired strain values (using MinMax option in OpenSees), and another with weight factor of 20% and elastic-perfectly plastic SteelMPF material. This approach was implemented to achieve the desired residual strength.

Although results presented here are for roof level displacement, an alternative approach based on using plastic hinge rotation to define strength loss also was developed. In this case, the plastic hinge rotation at strength loss is determined from the roof drift, e.g., as described by (Abdullah, 2019, PhD Dissertation). Hinge rotation is used in Section 5 since it is commonly used to define component modeling parameters, e.g., in ASCE 41-17.

G.5 Verification of the Dynamic Response of the Model

After modifying the material relationships as explained in the prior section to achieve the desired strength loss at the predicted drift (or hinge rotation) capacity and verifying that the desired result was achieved for monotonic and cyclic pushover analyses, IDA were run to produce the comparisons for the response ratios discussed in Section 2 (Steps 1 through 5).

The IDA was stopped either when the response exceeded 10% of story drift at any level or when the analysis did not converge, which happens when the normalized displacement increment does not meet the tolerance threshold of 10^{-3} . Not meeting the tolerance is most likely to occur when the stiffness is so degraded that the displacement increments obtained in the iterations have too much variance to achieve the tolerance.

As noted above, predicted roof drift capacity was converted into total hinge rotation capacity. The predicted total hinge rotation at strength loss (Figure G-9, red star) was compared with the total hinge rotation at 20% strength loss from the last converged IDA (Figure G-9, blue star) to assess the accuracy of the modeling approach adopted.

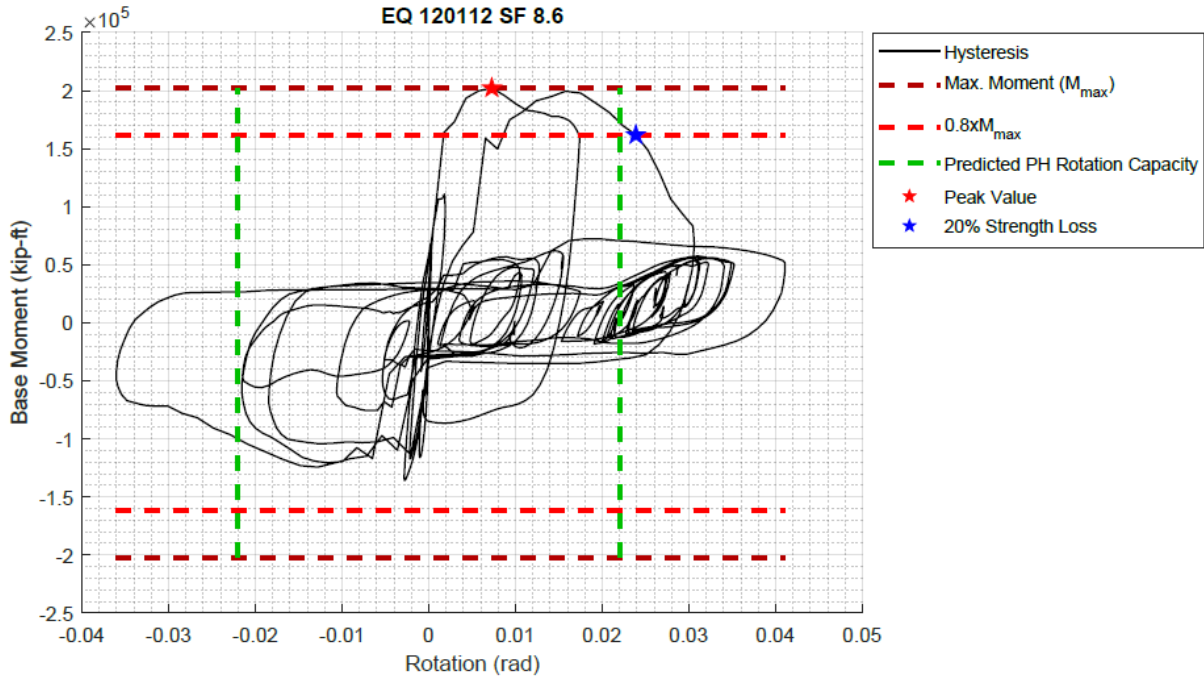


Figure G-9 Example of hysteretic response with strength loss compared against the predicted total hinge rotation capacity (this plot is taken from the 8-story building analysis).

Table G-2 shows the predicted total hinge rotation capacity and the average rotation capacity obtained from the analysis of all three archetypes. The average rotation capacity is obtained using a plastic hinge length $l_{ph} = l_w/2$. The values obtained from the MVLE model are slightly larger than the predicted values; however, this was deemed acceptable because the goal of the study was to assess trends; therefore, it was not necessary to precisely match the predicted value.

Parameter	4-Story	8-Story	12-Story
$l_{ph} = l_w/2$	12'	15'	15'
Average from MVLEM	3.02%	2.71%	2.58%
Predicted	2.36%	2.21%	2.54%

G.6 Results of System Assessment

G.6.1 Results for 4-story Building Archetype

G.6.1.1 Analysis of the Archetype

A Modal Response Spectrum Analysis (MRSA) was done following ASCE 7-16. The details can be found in a separate report. The fundamental period is $T_1 = 0.40s$, the roof drift demand is 0.72%, and the minimum and maximum axial load ratios are 1.5% and 4.0%. shows a summary of the MRSA.

Table G-3 Loads and Displacements of the 4-story Wall

Level	Height (ft)	Axial Load LC6 (kip)	Axial Load LC7 (kip)	Lateral Force (kip)	Story Shear (kip)	Overtuning Moment (kip-ft)	Elastic Deflection (in)	Amplified Deflection (in)	Story Drift (%)
Base	0	1,392	503	0	1,616	65,905	0.00	0.00	0.00
2	15	1,021	370	253	1,479	42,416	0.11	0.53	0.30
3	28	649	238	443	1,176	23,831	0.33	1.64	0.71
4	41	277	106	568	677	8,798	0.62	3.08	0.92
Roof	54	0	0	677	0	0	0.93	4.65	1.01

G.6.1.2 Design of the Archetype

Figure G-10 provides details of the wall design. Additional design details can be found in the Appendix.

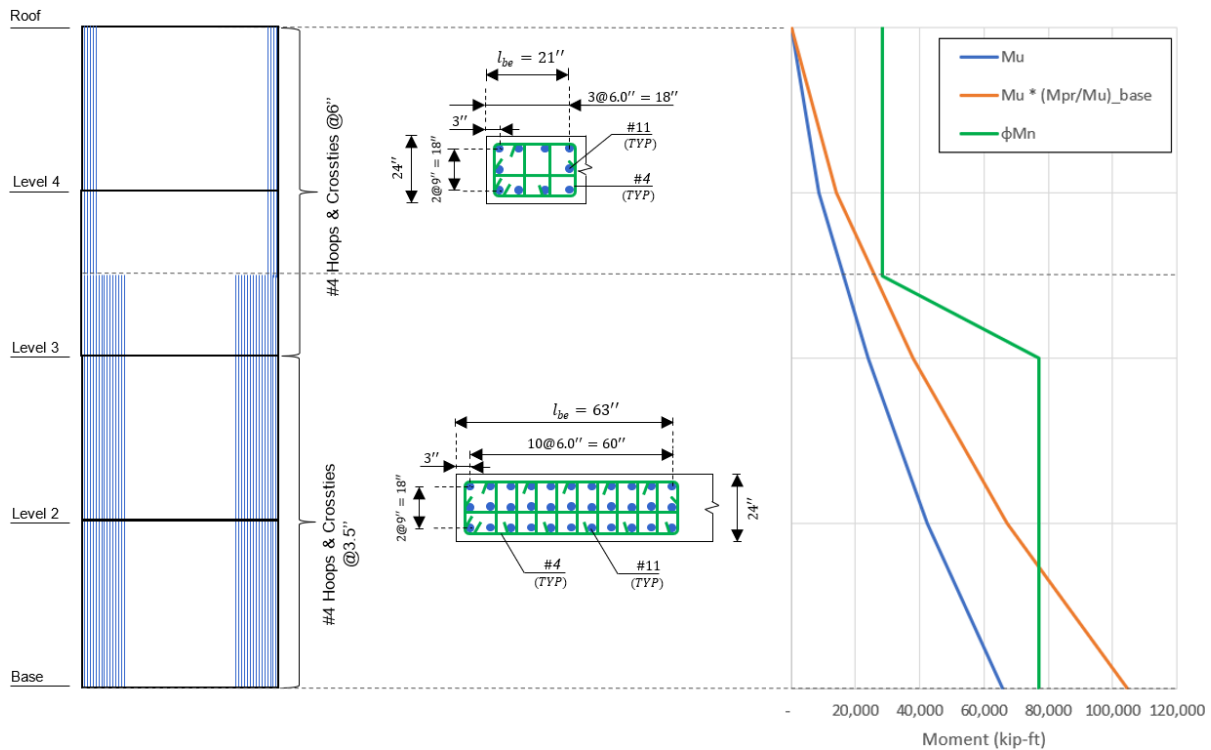


Figure G-10 4-story building design result along with moment demand and capacity profiles.

G.6.1.3 Sectional Analysis with Expected Material Properties

Table G-4 summarizes the expected demands and maximum probable moments and expected moment capacities of each story. The expected shear demands are obtained from the application of the shear amplification parameters of ACI 318-19 and the consideration of expected material properties. The expected axial load (which at the base is $P_{u,expected} = 945$ kips) is obtained with the load combination DL + 0.25LL. The maximum probable

moments and moment capacities are obtained from sectional analysis considering expected material properties. The Saatciouglu and Razvi (1992) models were used to define the unconfined and confined concrete uniaxial stress versus strain relationships.

Table G-4 Expected Demands, Maximum Probable Moment and Expected Capacity Per Story

Level	Height (ft)	Expected Demands		M_{pr} (kip*ft)	M_{ne} (kip*ft)
		V_{ue} (kip) ^(a)	P_{ue} (kip)		
Base	0	3,474	945	104,672	100,454
2	15	3,180	696	101,471	98,404
3	28	2,528	444	96,502	94,582
4	41	1,455	191	42,755	41,855
Roof	54	-	-	-	-

^(a) The shear amplification demands used are $n_s = 4.54$, $\Omega_v = 1.59$ and $\omega_v = 1.35$

G.6.1.4 Monotonic Pushover Results of MVLEM

Figure G-11. Base shear vs roof drift response obtained from monotonic pushover of MLVEM with expected material properties (without modifications) is shown in Figure G-11. More detailed results from this analysis can be found in the Appendix (additional responses, stress and strain profiles associated with the demands at the predicted roof drift capacity, and profiles responses).

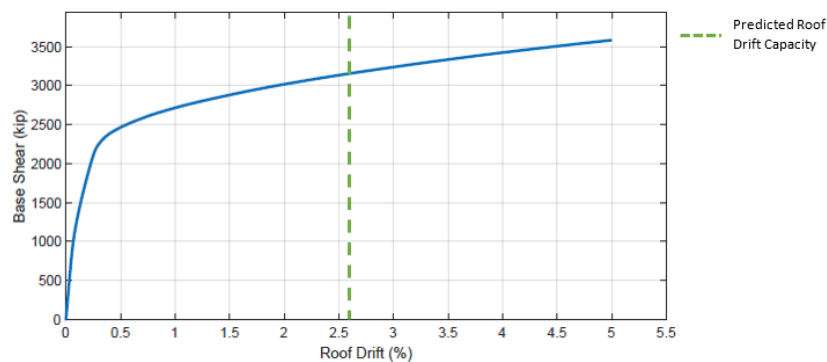


Figure G-11 Base shear vs roof drift response obtained from monotonic pushover of MLVEM with expected material properties (without modifications).

G.6.1.5 Monotonic and Cyclic Pushover Results of MVLEM with Modified Material Relationships

Figure G-12 shows the base shear vs roof drift responses for both monotonic and cyclic pushover analysis of the MVLEM with modified material

relationships (to account for strength loss). More detailed responses from this analysis can be found in the Appendix

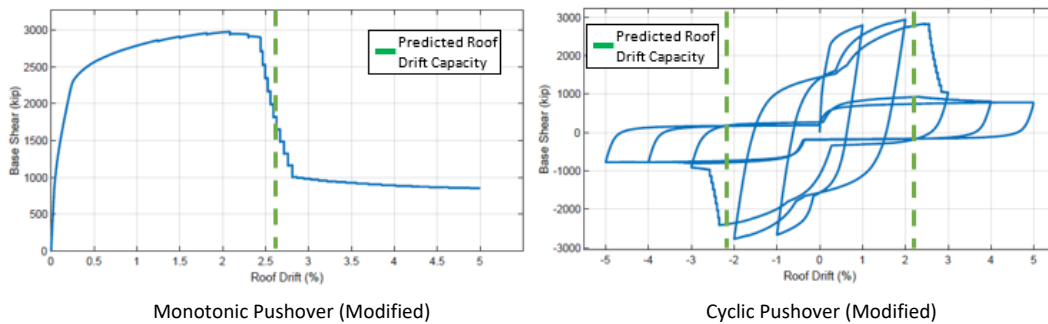


Figure G-12 Base shear vs roof drift response obtained from monotonic and cyclic pushovers of MLVEM with modified material relationship.

G.6.1.6 IDA Results of MVLEM with Modified Material Relationships

Figure G-13 shows a global result of the IDA of the MVLEM with modified material relationships, and the selected records that are used as Damaging GMs. The Appendix presents more detailed results from these analyses; S_a and Roof Drift distributions of all GMs in the IDA and the ones selected as Damaging GMs, the S_a vs Max. Story Drift plot in addition to the one shown in Figure G-21, responses profiles, and identification of total hinge rotation capacity.

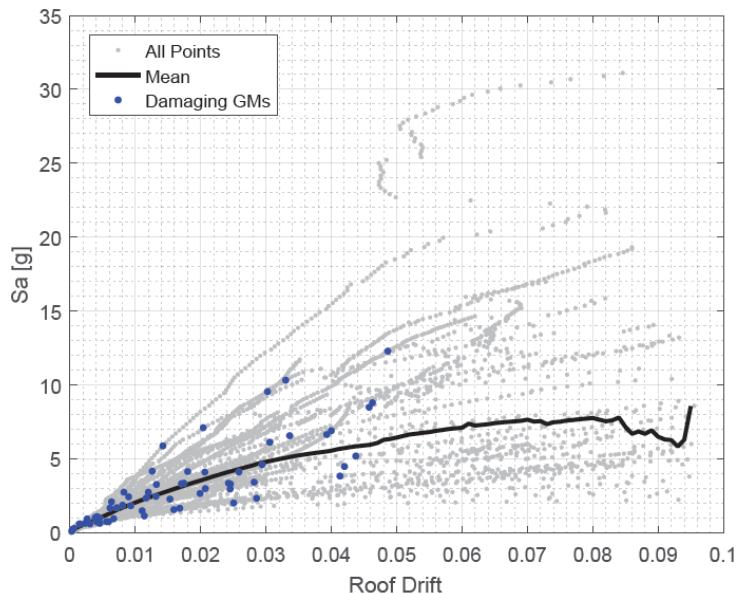


Figure G-13 IDA Global results (MVLEM with modified expected material properties) and selected Damaging GMs.

G.6.1.7 IDA Results of MVLEM with Modified Expected Material Properties

Figure G-14 shows moment profiles over the wall height at different roof drift demand levels. It can be seen the nonlinearity is concentrated within $h = l_w/2$, as expected. In addition to moment profiles, the story drift profiles, curvature profiles, and story shear profiles can be found in the Appendix.

Base moment versus plastic hinge rotation (Figure G-15) is plotted to demonstrate deformation at strength loss for the different GMs and to compare these values with the predicted total hinge rotation capacity indicated with the vertical green line. Additional results are presented in the Appendix.

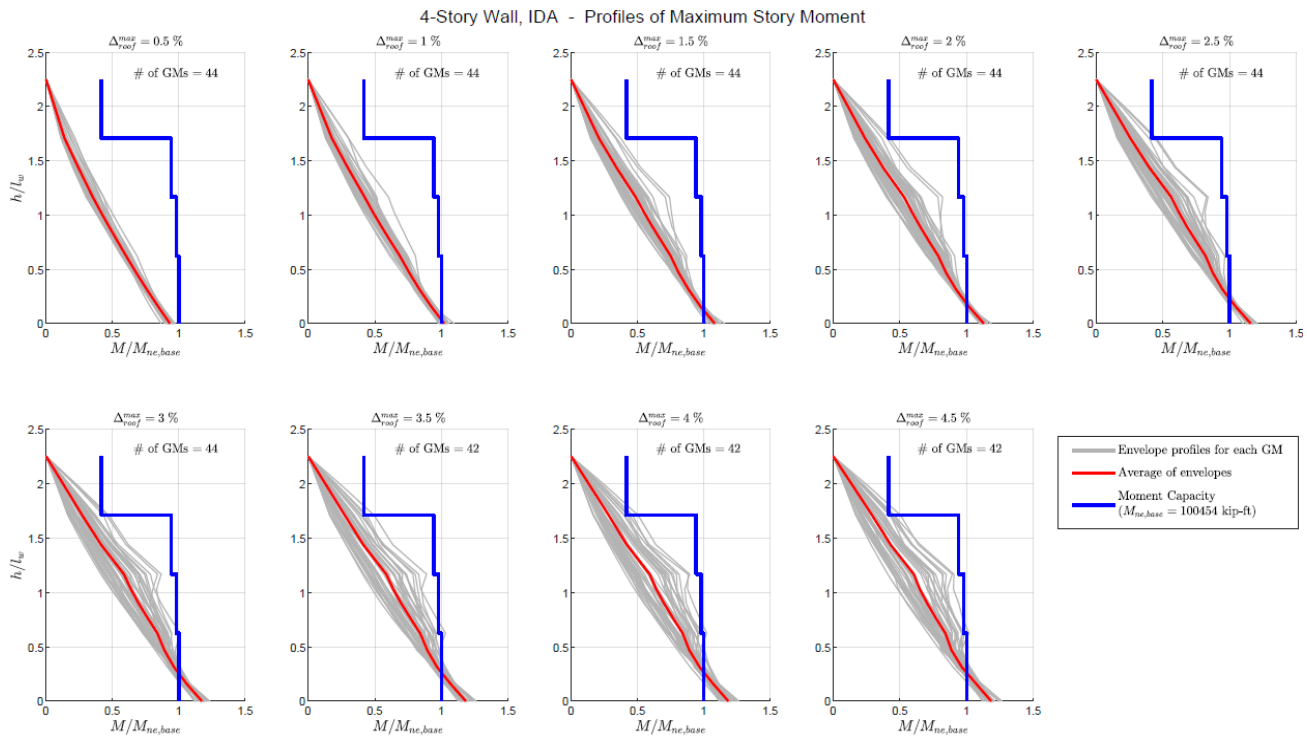


Figure G-14 Moment profile results from the IDA of the MVLEM with modified expected material properties.

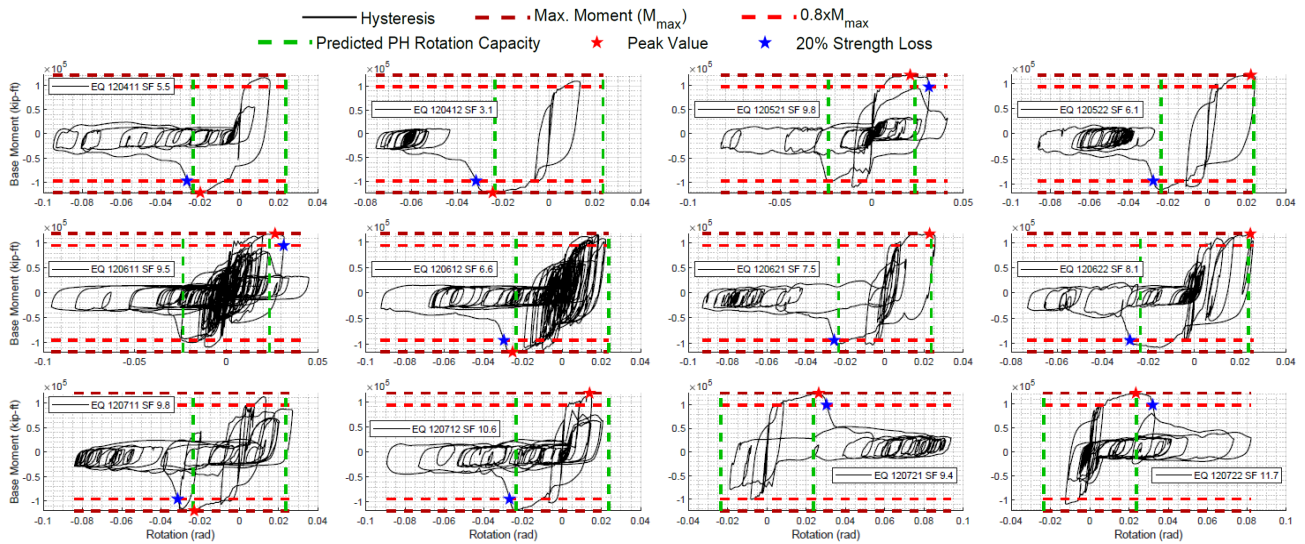


Figure G-15 Extract of plots identifying the total hinge rotation capacity assuming $l_{ph} = l_w/2 = 12'$ (MVLEM with modified expected material properties).

G.6.1.8 Damaged to Undamaged Building Responses Ratios of MVLEM with Modified Expected Material Properties

Figure G-24 shows the damaged-to-undamaged ratios of the “Dam. GMs & DE suite” (the maximum ratios for analysis considering +DE and -DE were selected). Additional results are presented in the Appendix, e.g., damaged-to-undamaged ratios obtained from the “Dam. GMs & +DE suite” and “Dam. Gms & -DE suite” analysis.

The response histories of all four parameters used to calculate the damaged-to-undamaged ratios for the “Dam. GMs & +DE suite” case are presented in the Appendix. Responses ratios associated to the “Dam. GMs & -DE suite” are not presented because the damaged-to-undamaged ratios show the direction in which the second GMs were applied does not affect the trends.

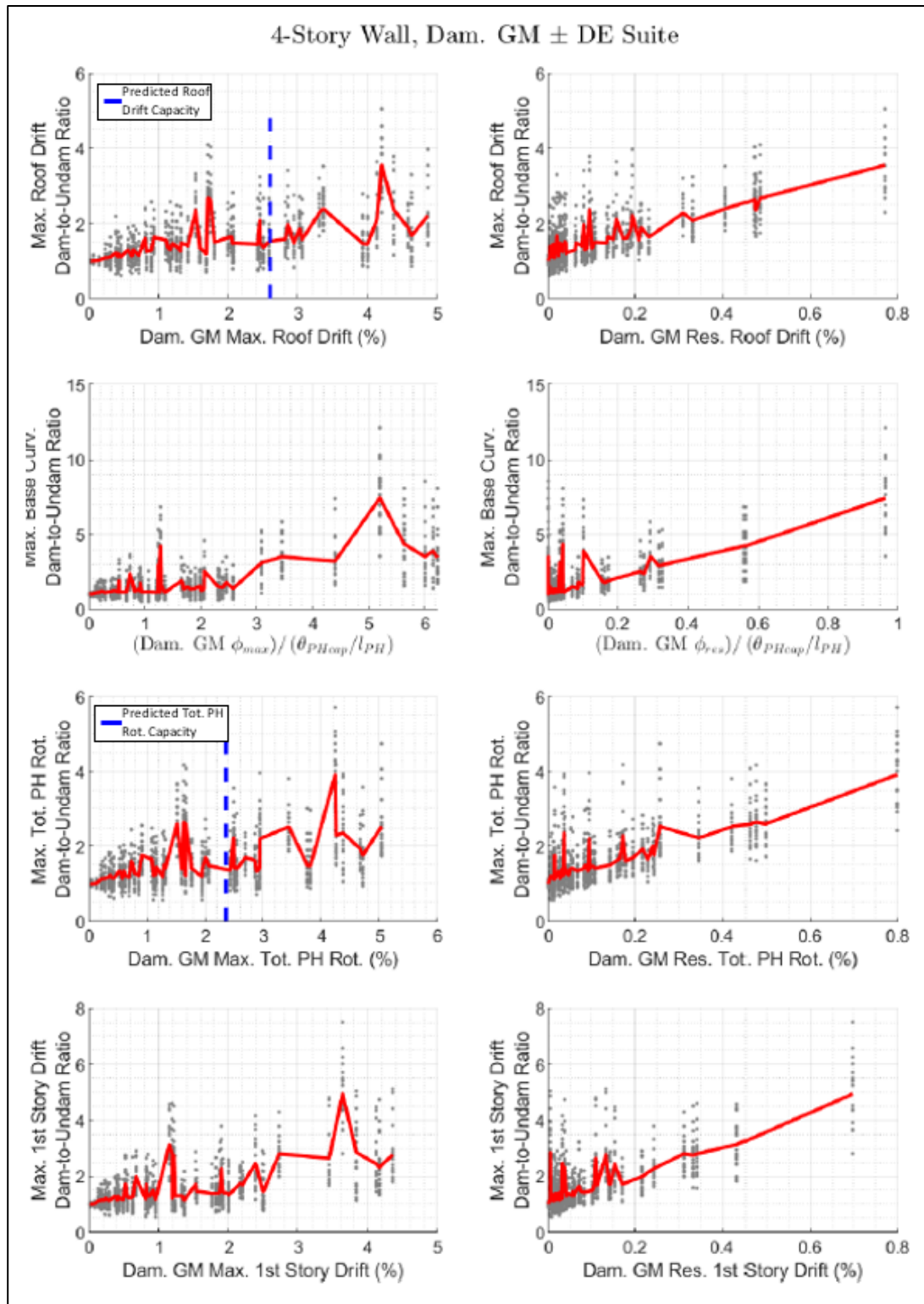


Figure G-16 Maximum damaged-to-undamaged ratios obtained from the "Dam. GMs & \pm DE suite" analyzes.

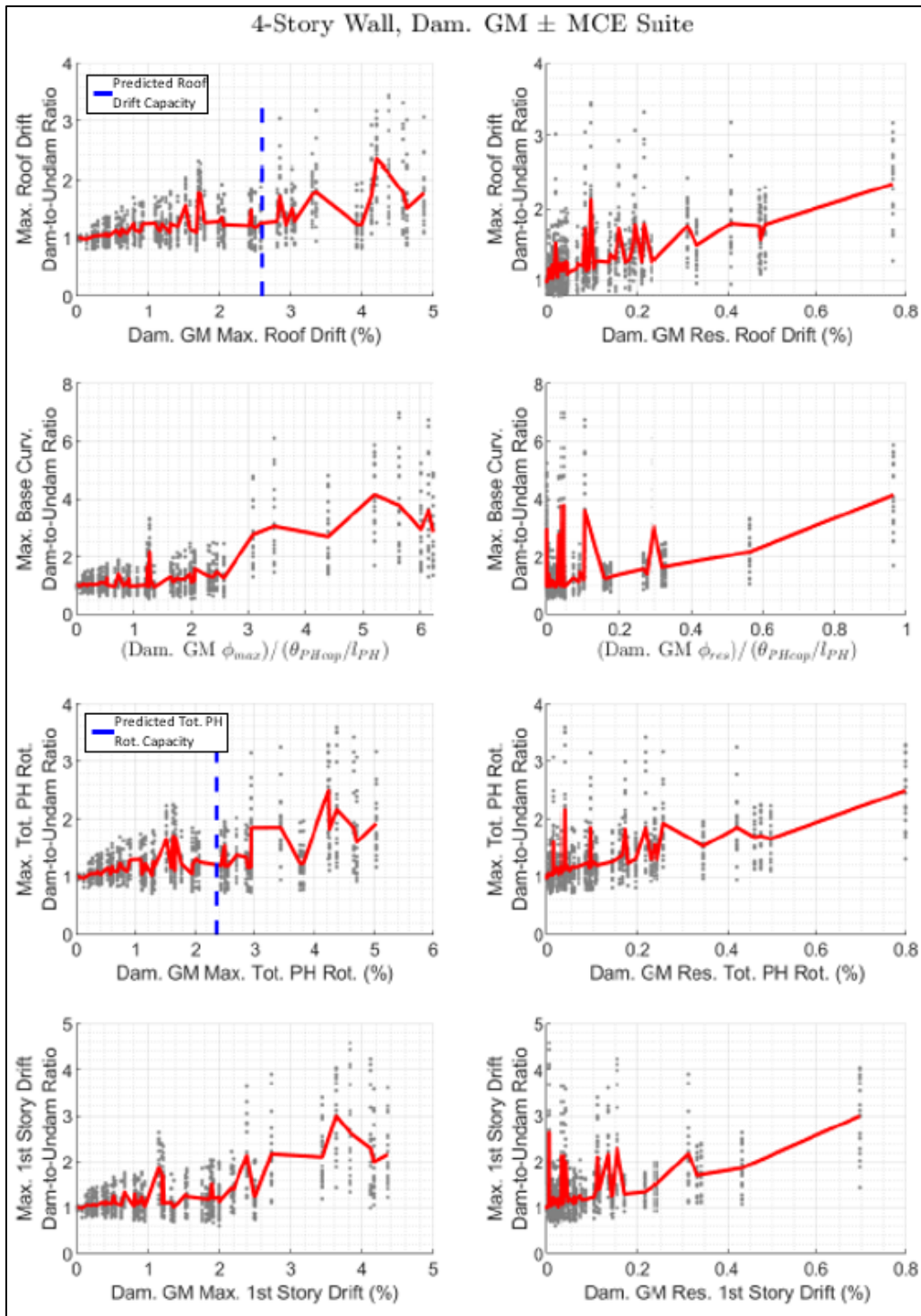


Figure G-17 Maximum damaged-to-undamaged ratios obtained from the “Dam. GMs & \pm MCE suite” analyses.

G.6.2 Results for 8-story Building Archetype

G.6.2.1 Analysis of the Archetype

A Modal Response Spectrum Analysis (MRSA) was done following ASCE 7-16. The details can be found in the Appendix. The fundamental period is $T_1 = 1.08$ s, the roof drift demand is 0.98%, and the minimum and maximum axial load ratios are 2.5% and 7.0%. Table G-5 shows a summary of the MRSA.

Table G-5 Loads and Displacements of the 8-Story Wall

Level	Height (ft)	Axial Load LC6 (kip)	Axial Load LC7 (kip)	Lateral Force (kip)	Story Shear (kip)	Overturning Moment (kip-ft)	Elastic Deflection (in)	Amplified Deflection (in)	Story Drift (%)
Base	0	3,016	1,081	0	1,511	94,004	0.00	0.00	0.00
2	15	2,627	942	127	1,437	74,574	0.08	0.41	0.23
3	28	2,237	804	294	1,273	59,612	0.27	1.34	0.59
4	41	1,848	665	381	1,086	46,798	0.54	2.68	0.86
5	54	1,459	527	389	935	35,604	0.87	4.33	1.06
6	67	1,069	388	362	832	25,161	1.24	6.21	1.20
7	80	680	249	296	718	14,982	1.65	8.23	1.30
8	93	290	111	310	444	5,766	2.07	10.34	1.35
Roof	106	0	0	444	0	0	2.49	12.47	1.37

G.6.2.2 Design of the Archetype

Figure G-18 provides details of the wall design. Additional design details can be found in the Appendix.

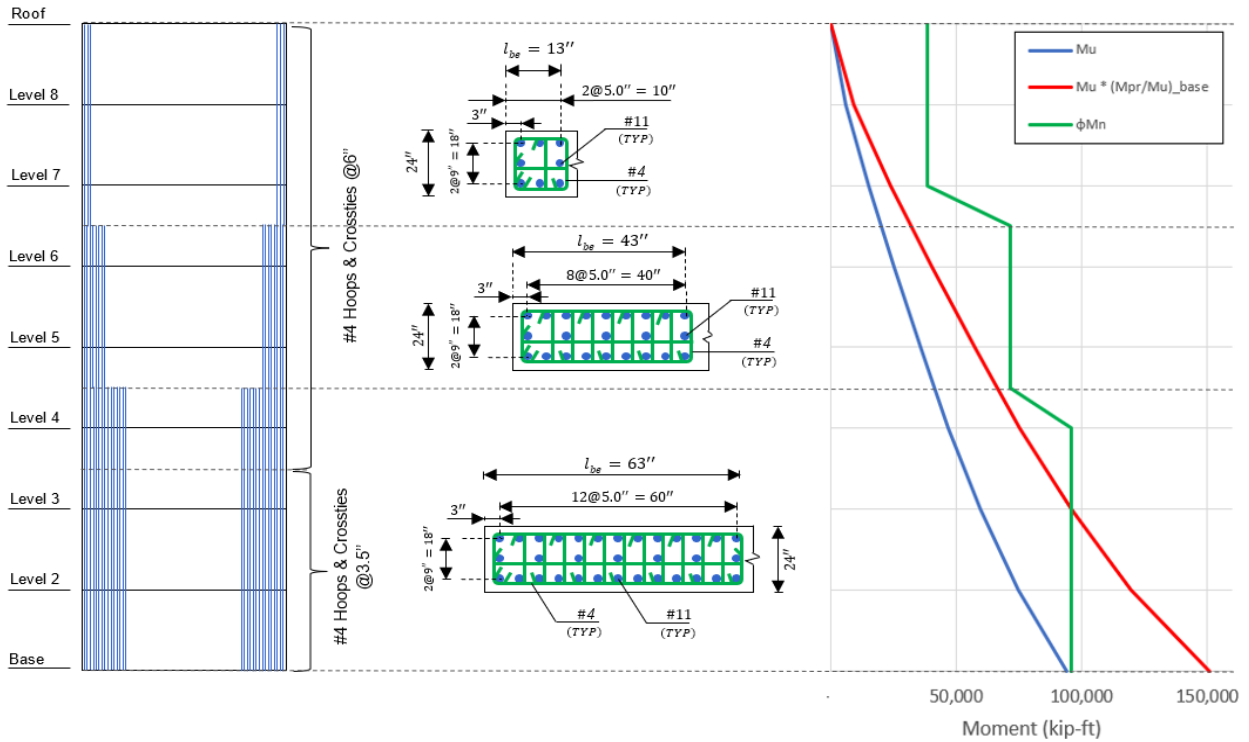


Figure G-18 8-story building design result along with moment demand and capacity profiles.

G.6.2.3 Sectional Analysis with Expected Material Properties

Table G-6 summarizes the expected demands and maximum probable moments and expected moment capacities of each story. The expected shear demands are obtained from the application of the shear amplification parameters of ACI 318-19 and the consideration of expected material properties. The expected axial load (which at the base is $P_{u,expected} = 1,959$ kips) is obtained with the load combination $DL + 0.25LL$. The maximum probable moments and moment capacities are obtained from sectional analysis considering expected material properties using the Saatcioglu and Razvi (1992) models.

Table G-6 Expected Demands, Maximum Probable Moment and Expected Capacity Per Story

Level	Height (ft)	Expected Demands		M_{pr} (kip*ft)	M_{ne} (kip*ft)
		V_{ue} (kip) ^(a)	P_{ue} (kip)		
Base	0	3,876	1,959	151,031	139,806
2	15	3,687	1,706	146,920	137,105
3	28	3,266	1,454	142,772	134,409
4	41	2,786	1,201	137,307	130,417
5	54	2,399	949	97,701	91,980
6	67	2,134	696	93,331	89,143
7	80	1,842	444	61,260	58,580
8	93	1,139	191	56,847	55,749
Roof	106	-	-	-	-

^(a) The shear amplification demands used are $n_s = 8.90$, $\Omega_v = 1.61$ and $\omega_v = 1.60$

G.6.2.4 Monotonic Pushover Results of MVLEM

Figure G-19 shows the base shear vs roof rift response for the monotonic pushover analysis of the MVLEM with expected material properties (without modifications to account for strength loss). More detailed results from this analysis can be found in the Appendix (additional responses, stress and strain profiles associated with the demands at the predicted roof drift capacity, and profiles responses).

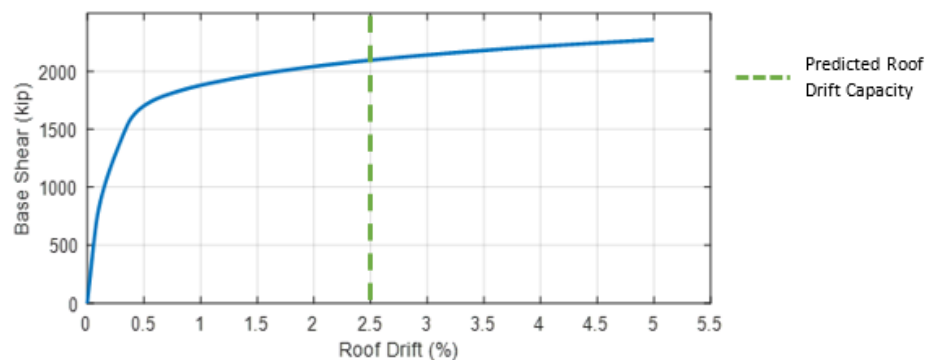


Figure G-19 Base shear vs roof drift response obtained from monotonic pushover of MLVEM with expected material properties (without modifications).

G.6.2.5 Monotonic and Cyclic Pushover Results of MVLEM with Modified Material Relationships

Figure G-20 shows the base shear vs roof drift responses for both monotonic and cyclic pushover analysis of the MVLEM with modified material

relationships (to account for strength loss). More detailed responses from this analysis can be found in the Appendix

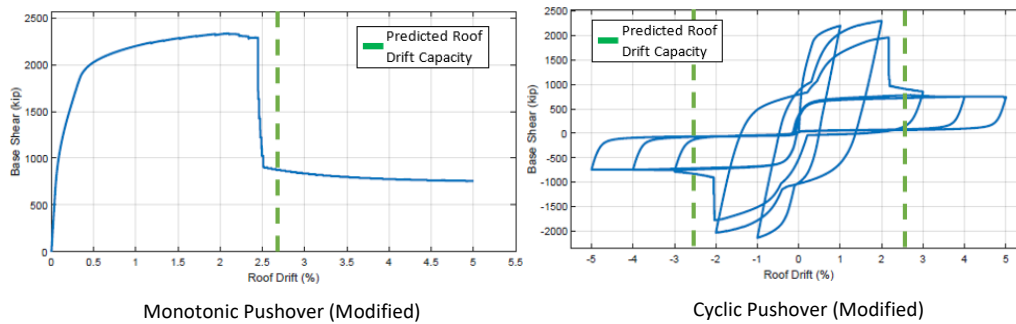


Figure G-20 Base shear vs roof drift response obtained from monotonic and cyclic pushovers of MLVEM with modified material relationship.

G.6.2.6 IDA Results of MVLEM with Modified Material Relationships

Figure G-21 shows a global result of the IDA of the MVLEM with modified material relationships, and the selected records that are used as Damaging GMs. The Appendix presents more detailed results from these analyses; S_a and Roof Drift distributions of all GMs in the IDA and the ones selected as Damaging GMs, the S_a vs Max. Story Drift plot in addition to the one shown in Figure G-21, responses profiles, and identification of total hinge rotation capacity.

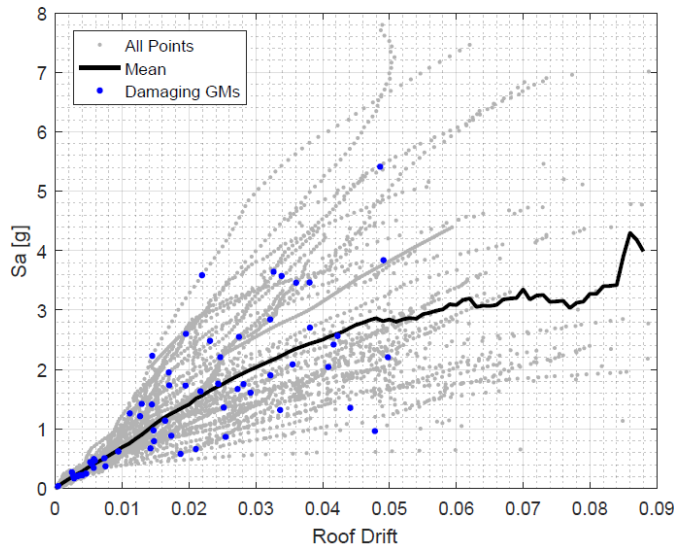


Figure G-21 IDA Global results (MVLEM with modified expected material properties) and selected Damaging GMs.

G.6.2.7 IDA Results of MVLEM with Modified Expected Material Properties

Figure G-22 shows moment profiles over the wall height at different roof drift demand levels. It can be seen the nonlinearity is concentrated within $h = l_w/2$, as expected. In addition to moment profiles, the story drift profiles, curvature profiles, and story shear profiles can be found in the Appendix.

Base moment versus plastic hinge rotation (Figure G-23) is plotted to demonstrate deformation at strength loss for the different GMs and to compare these values with the predicted total hinge rotation capacity indicated with the vertical green line. Additional results are presented in the Appendix.

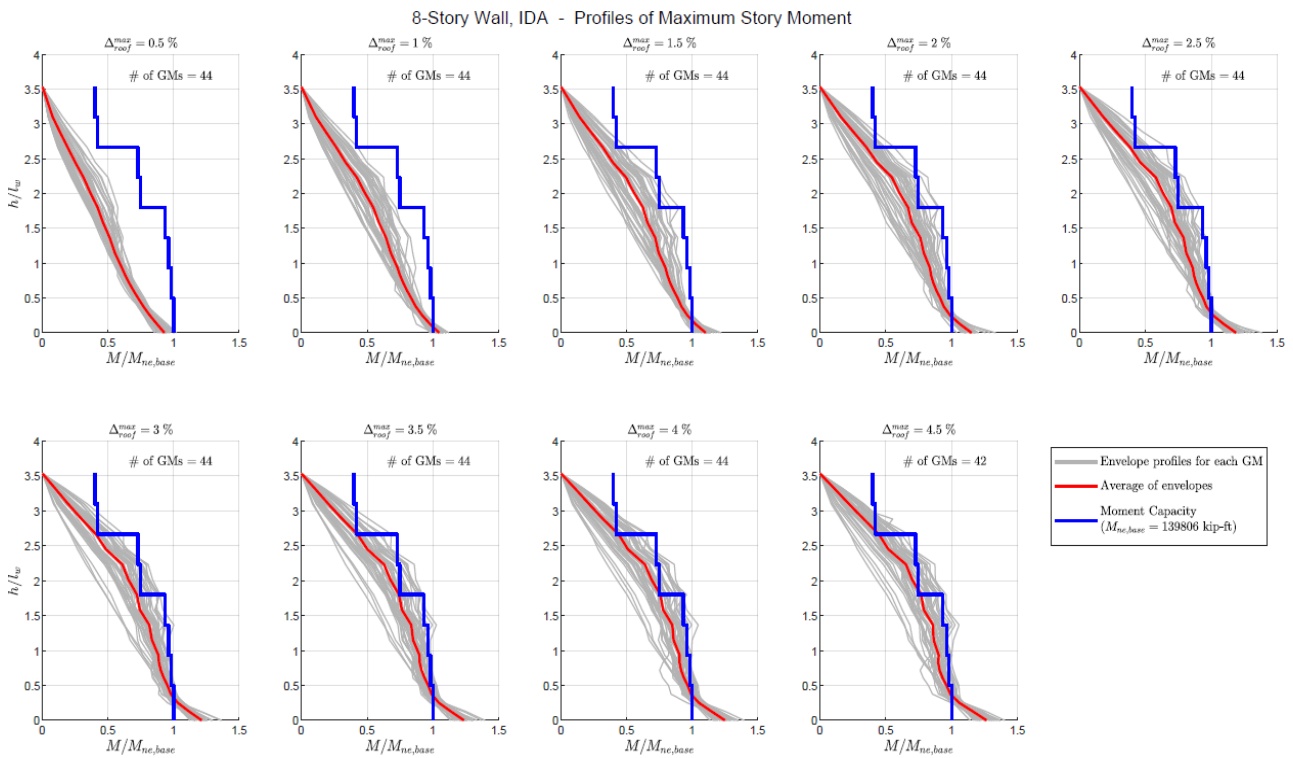


Figure G-22 Moment profile results from the IDA of the MVLEM with modified expected material properties.

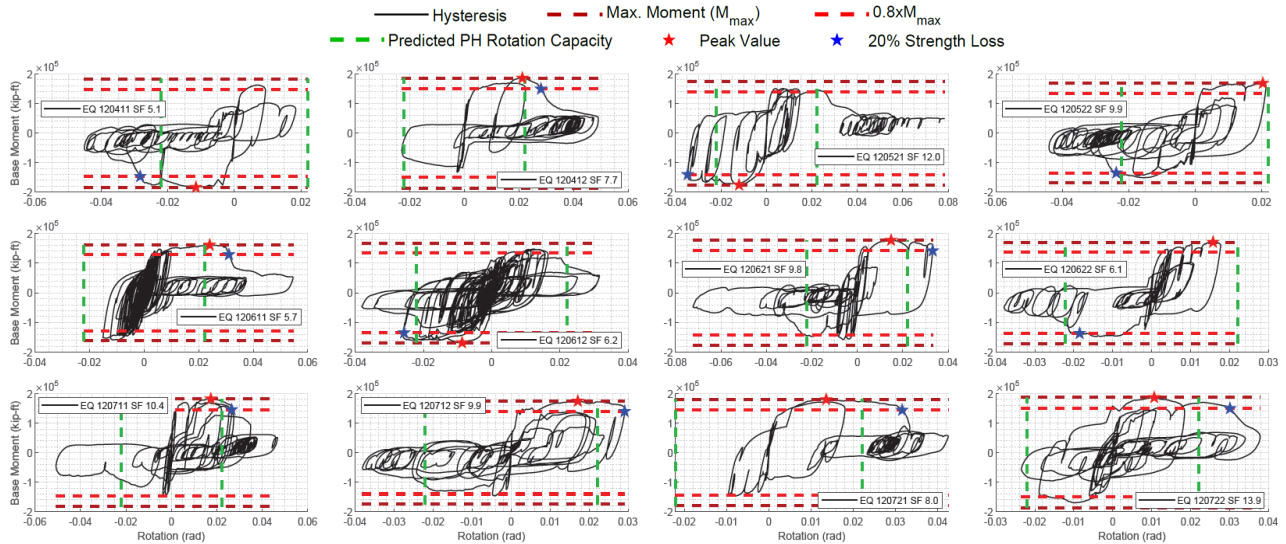


Figure G-23 Extract of plots identifying the total hinge rotation capacity assuming $I_{ph} = I_w/2 = 15'$ (MVLEM with modified expected material properties).

G.6.2.8 Damaged to Undamaged Building Responses Ratios of MVLEM with Modified Expected Material Relationships

Figure G-24 shows the damaged-to-undamaged ratios of the “Dam. GMs & DE suite” (the maximum ratios for analysis considering +DE and -DE were selected). Additional results are presented in the Appendix, e.g., damaged-to-undamaged ratios obtained from the “Dam. GMs & +DE suite” and “Dam. GMs & -DE suite” analysis.

The response histories of all four parameters used to calculate the damaged-to-undamaged ratios for the “Dam. GMs & +DE suite” case are presented in the Appendix. Responses ratios associated to the “Dam. GMs & -DE suite” are not presented because the damaged-to-undamaged ratios show the direction in which the second GMs were applied does not affect the trends.

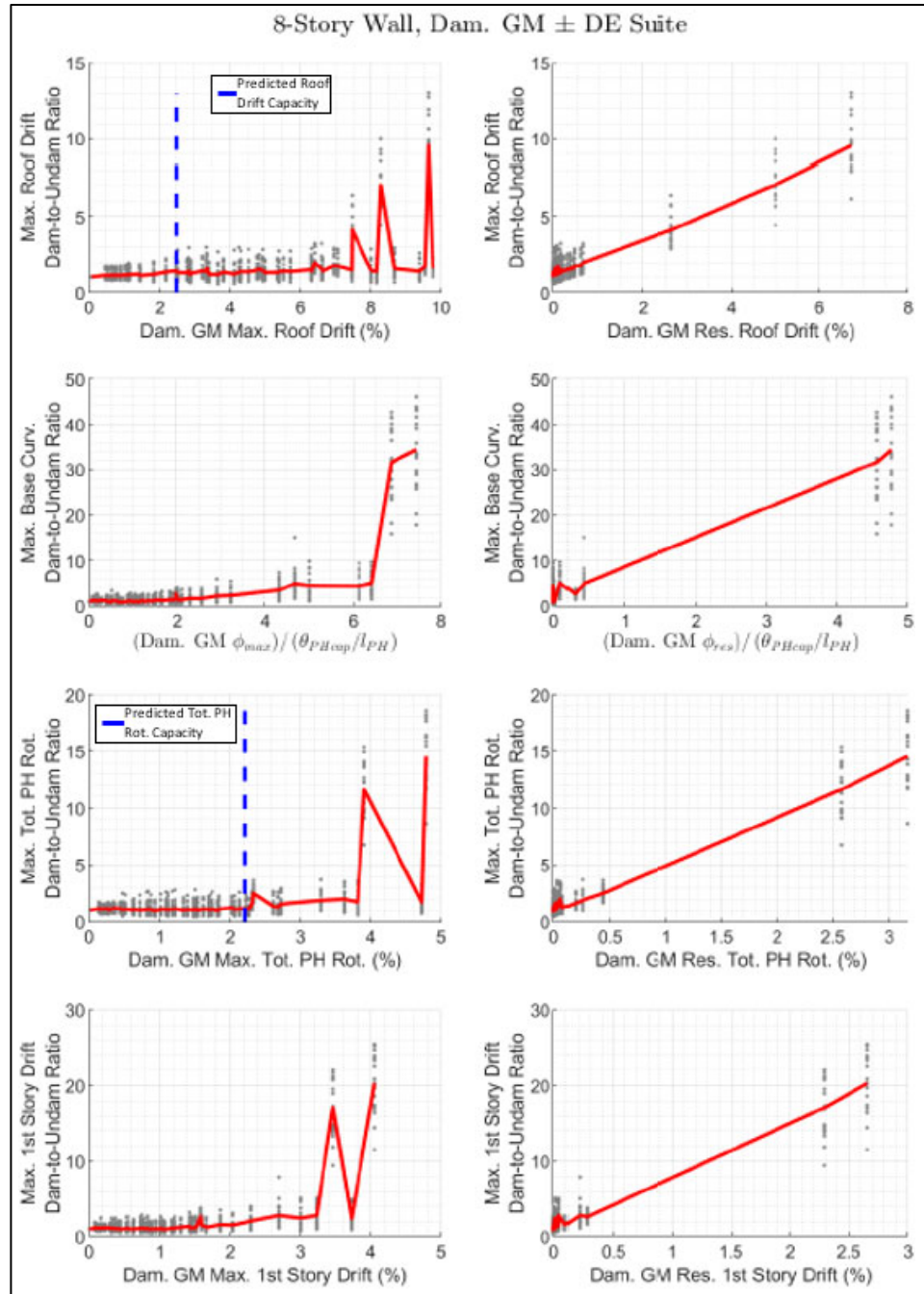


Figure G-24 Maximum damaged-to-undamaged ratios obtained from the “Dam. GMs & ± DE suite” analyzes.

Figure G-25 shows the damaged-to-undamaged ratios of the “Dam. GMs & +MCE suite” (the maximum ratios among the analysis considering +MCE and -MCE were selected). Additional results are presented in the Appendix, e.g., damaged-to-undamaged ratios obtained from the “Dam. GMs & +MCE suite” and “Dam. GMs & -MCE suite”.

The response histories of all four parameters used to calculate the damaged-to-undamaged ratios for the “Dam. GMs & +MCE suite” cases are presented in the Appendix. Response ratios associated to the “Dam. GMs & -MCE suite” are not presented because the damaged-to-undamaged ratios show the direction in which the second GMs were applied does not affect the trends.

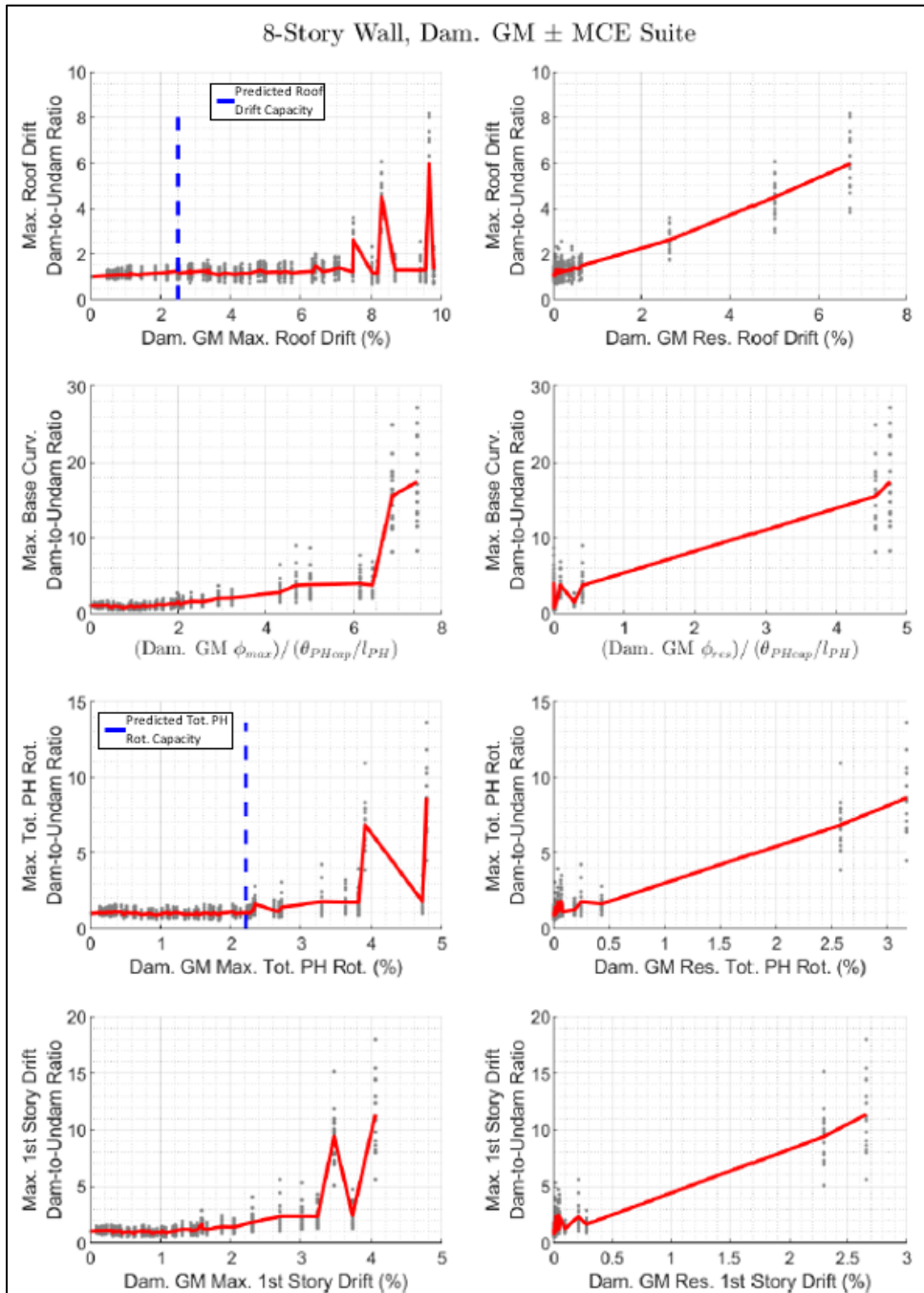


Figure G-25 Maximum damaged-to-undamaged ratios obtained from the “Dam. GMs & ± MCE suite” analyzes.

G.6.3 Results for 12-story Building Archetype

G.6.3.1 Analysis of the Archetype

A Modal Response Spectrum Analysis (MRSa) was done following ASCE 7-16. The details can be found in the Appendix. The fundamental period is $T_1 = 1.65$ s, the roof drift demand is 0.94%, and the minimum and maximum axial load ratios are 3.8% and 10.6%. Table G-7 shows a summary of the MRSa.

Table G-7 Loads and Displacements of the 12-Story Wall

Level	Height (ft)	Axial Load LC6 (kip)	Axial Load LC7 (kip)	Lateral Force (kip)	Story Shear (kip)	Overtopping Moment (kip-ft)	Elastic Deflection (in)	Amplified Deflection (in)	Story Drift (%)
Base	0	4,574	1,635	0	815	61,010	0.00	0.00	0.00
2	15	4,184	1,497	33	794	51,196	0.06	0.28	0.16
3	28	3,795	1,358	88	736	43,717	0.19	0.93	0.42
4	41	3,406	1,220	138	650	37,527	0.38	1.90	0.62
5	54	3,016	1,081	167	557	32,605	0.63	3.13	0.79
6	67	2,627	942	173	477	28,564	0.92	4.58	0.93
7	80	2,237	804	168	422	24,860	1.24	6.20	1.04
8	93	1,848	665	160	398	21,003	1.59	7.97	1.13
9	106	1,459	527	144	397	16,682	1.97	9.84	1.20
10	119	1,069	388	113	391	11,854	2.36	11.80	1.25
11	132	680	249	92	336	6,867	2.76	13.81	1.29
12	145	290	111	146	194	2,521	3.17	15.85	1.31
Roof	158	0	0	194	0	0	3.58	17.91	1.32

G.6.3.2 Design of the Archetype

Figure G-18 provides details of the wall design. Additional design details can be found in the Appendix.

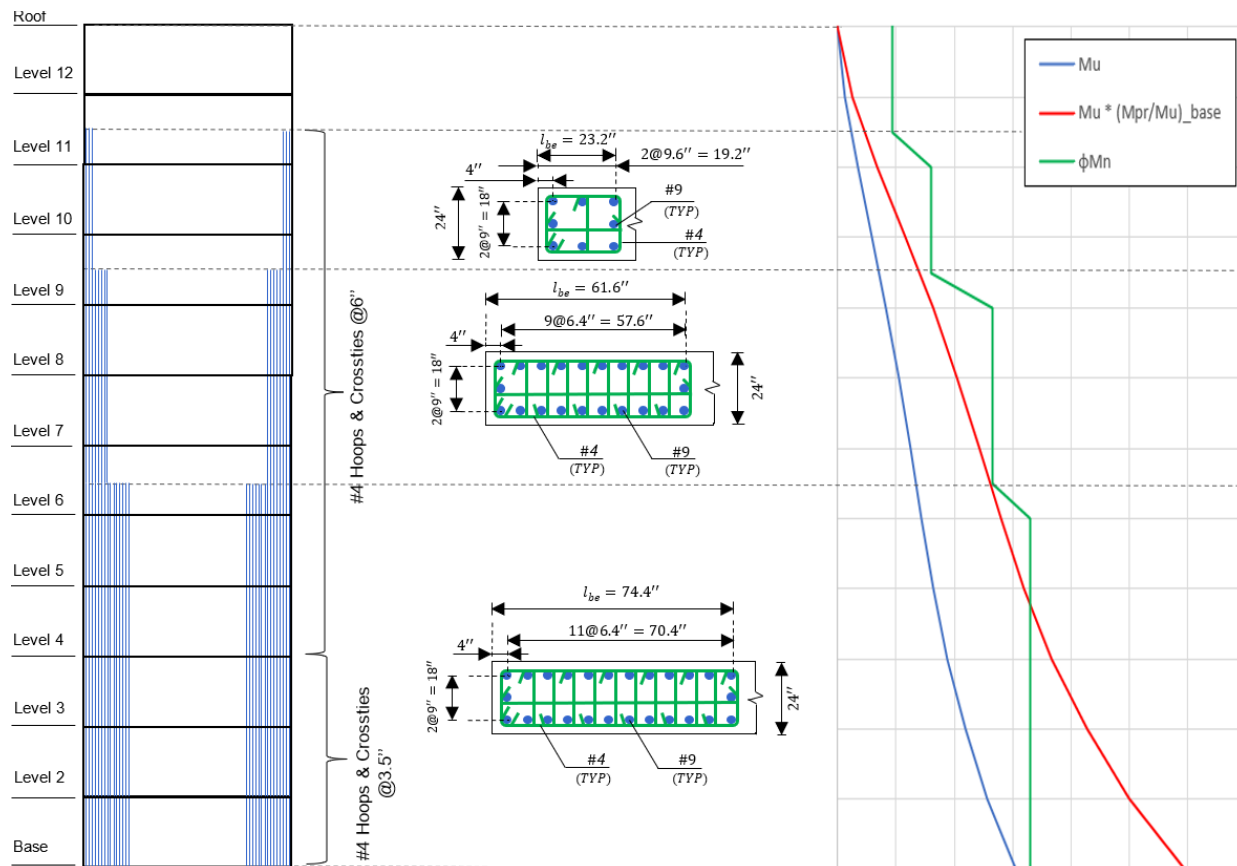


Figure G-26 12-story building design result along with moment demand and capacity profiles.

G.6.3.3 Sectional Analysis with Expected Material Properties

Table G-8 summarizes the expected demands and maximum probable moments and expected moment capacities of each story. The expected shear demands are obtained from the application of the shear amplification parameters of ACI 318-19 and the consideration of expected material properties. The expected axial load (which at the base is $P_{u,expected} = 2,968$ kips) is obtained with the load combination $DL + 0.25LL$. The maximum probable moments and moment capacities are obtained from sectional analysis considering expected material properties. The Saatcioglu and Razvi (1992) models were used to define the unconfined and confined concrete uniaxial stress versus strain relationships

Table G-8 Expected Demands, Maximum Probable Moment and Expected Capacity Per Story

Level	Height (ft)	Expected Demands		M_{pr} (kip*ft)	M_{ne} (kip*ft)
		V_{ue} (kip) ^(a)	P_{ue} (kip)		
Base	0	2,445	2,968	102,065	119,246
2	15	2,382	2,716	99,315	115,138
3	28	2,208	2,464	96,551	111,000
4	41	1,950	2,211	92,805	105,737
5	54	1,671	1,959	90,041	101,547
6	67	1,431	1,706	87,262	97,343
7	80	1,266	1,454	79,135	87,948
8	93	1,194	1,201	76,282	79,199
9	106	1,191	949	73,439	57,986
10	119	1,173	696	48,891	53,312
11	132	1,008	444	45,925	48,701
12	145	582	191	28,843	30,043
Roof	158	-	-	-	-

^(a) The shear amplification demands used are $n_s = 13.27$, $\Omega_v = 1.95$ and $\omega_v = 1.74$

G.6.3.4 Monotonic Pushover Results of MVLEM

Figure G-27 shows the base shear vs roof rift response coming from a monotonic pushover analysis of the MVLEM with expected material properties (without modifications to account for strength loss). More detailed results from this analysis can be found in the Appendix (additional responses, stress and strain profiles associated with the demands at the predicted roof drift capacity, and profiles responses).

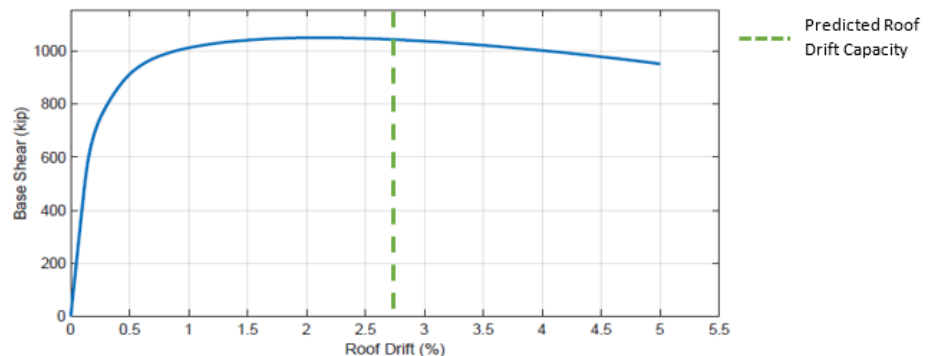


Figure G-27 Base shear vs roof drift response obtained from monotonic pushover of MLVEM with expected material properties (without modifications)

G.6.3.5 Monotonic and Cyclic Pushover Results of MVLEM with Modified Material Relationships

Figure G-28 shows the base shear vs roof drift responses for both monotonic and cyclic pushover analysis of the MVLEM with modified material relationships (to account for strength loss). More detailed responses from this analysis can be found in the Appendix

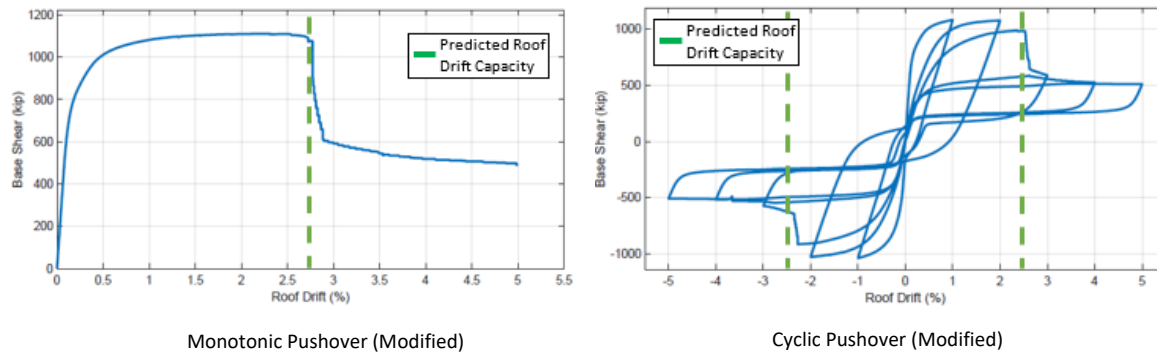


Figure G-28 Base shear vs roof drift response obtained from monotonic and cyclic pushovers of MLVEM with modified material relationship.

G.6.3.6 IDA Results of MVLEM with Modified Material Relationships

Figure G-29 shows a global result of the IDA of the MVLEM with modified material relationships, and the selected records that are used as Damaging GMs. The Appendix presents more detailed results from these analyses; S_a and Roof Drift distributions of all GMs in the IDA and the ones selected as Damaging GMs, the S_a vs Max. Story Drift plot in addition to the one shown in Figure G-21, responses profiles, and identification of total hinge rotation capacity.

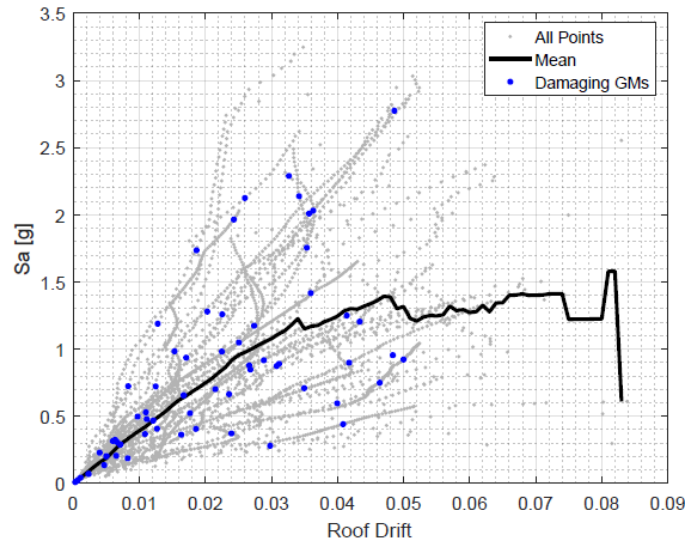


Figure G-29 IDA Global results (MVLEM with modified expected material properties) and selected Damaging GMs.

G.6.3.7 IDA Results of MVLEM with Modified Expected Material Properties

Figure G-30 shows moment profiles over the wall height at different roof drift demand levels. It can be seen the nonlinearity is concentrated within $h = l_w/2$, as expected. In addition to moment profiles, the story drift profiles, curvature profiles, and story shear profiles can be found in the Appendix.

Base moment versus plastic hinge rotation (Figure G-31) is plotted to demonstrate deformation at strength loss for the different GMs and to compare these values with the predicted total hinge rotation capacity indicated with the vertical green line. Additional results are presented in the Appendix.

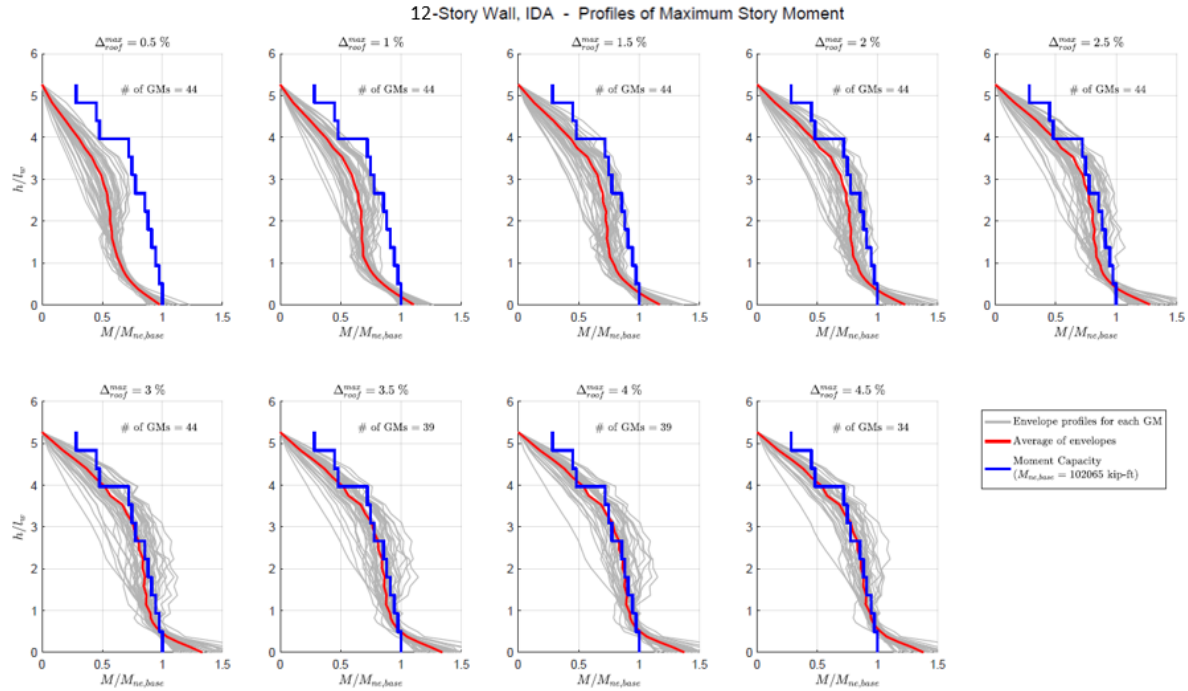


Figure G-30 Moment profile results from the IDA of the MVLEM with modified expected material properties.

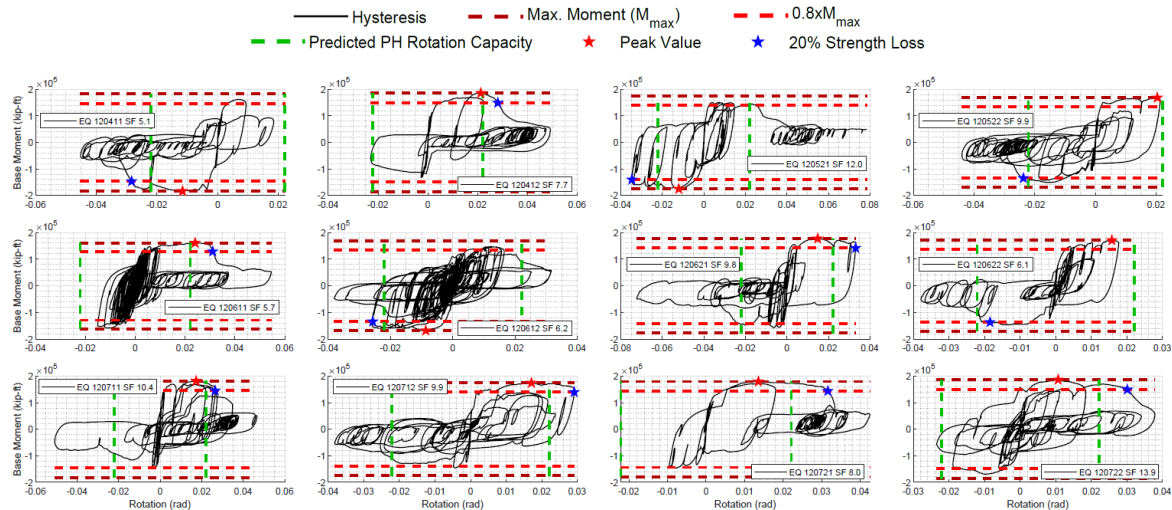


Figure G-31 Extract of plots identifying the total hinge rotation capacity assuming $I_{ph} = I_w/2 = 15'$ (MVLEM with modified expected material properties).

G.6.3.8 Damaged to Undamaged Building Responses Ratios of MVLEM with Modified Expected Material Relationships

Figure G-32 shows the damaged-to-undamaged ratios of the “Dam. GMs & DE suite” (the maximum ratios for analysis considering +DE and -DE were selected). Additional results are presented in the Appendix, e.g., damaged-to-undamaged ratios obtained from the “Dam. GMs & +DE suite” and “Dam. GMs & -DE suite” analysis.

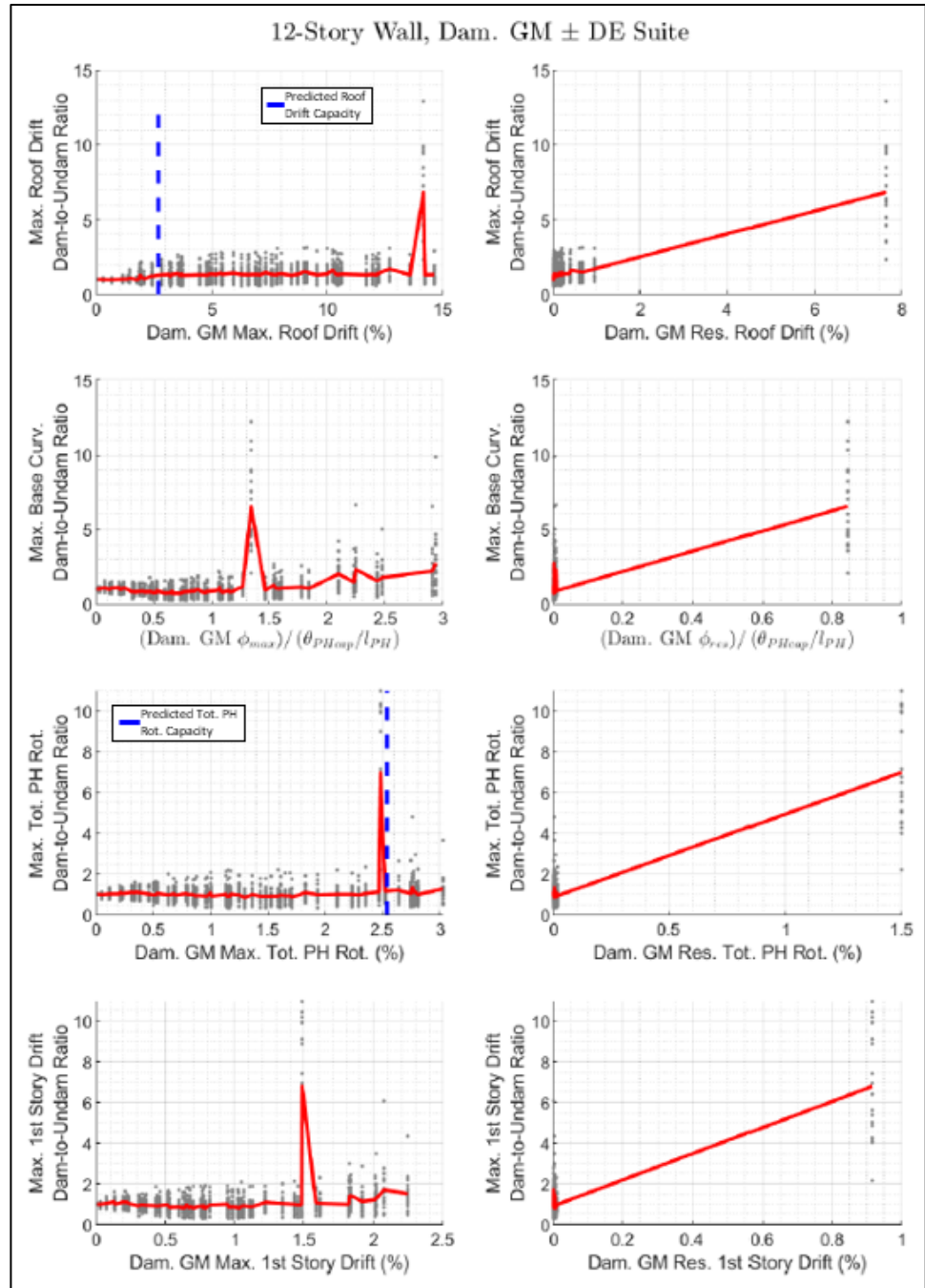


Figure G-32 Maximum damaged-to-undamaged ratios obtained from the “Dam. GMs & ± DE suite” analyzes.

The response histories of all four parameters used to calculate the damaged-to-undamaged ratios for the “Dam. GMs & +DE suite” case are presented in the Appendix. Responses ratios associated to the “Dam. GMs & -DE suite” are not presented because the damaged-to-undamaged ratios show the direction in which the second GMs were applied does not affect the trends.

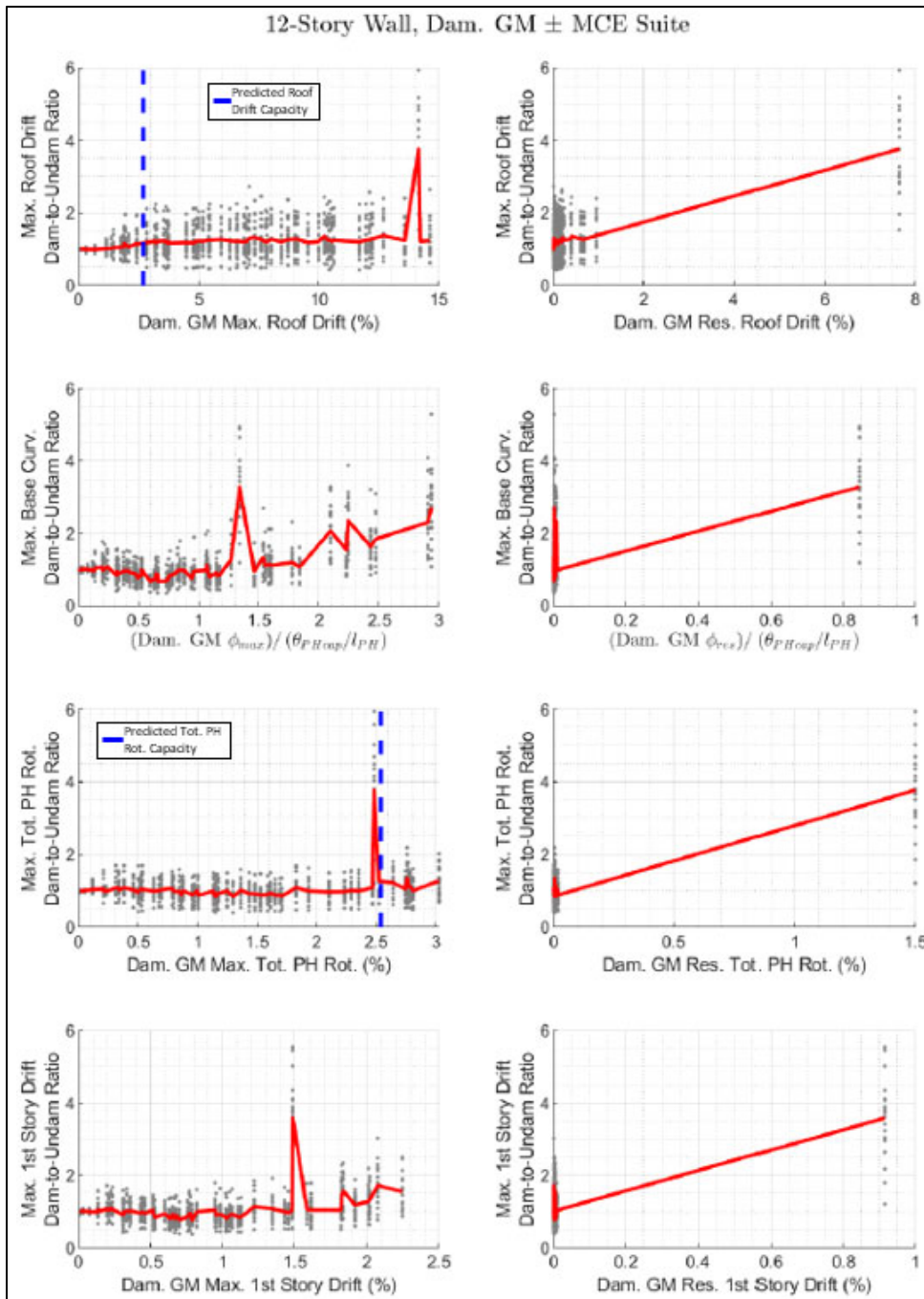


Figure G-33 Maximum damaged-to-undamaged ratios obtained from the “Dam. GMs & ± MCE suite” analyzes.

Figure G-33 shows the damaged-to-undamaged ratios of the “Dam. GMs & +MCE suite” (the maximum ratios among the analysis considering +MCE and -MCE were selected). Additional results are presented in the Appendix, e.g., damaged-to-undamaged ratios obtained from the “Dam. GMs & +MCE suite” and “Dam. GMs & -MCE suite”.

The response histories of all four parameters used to calculate the damaged-to-undamaged ratios for the “Dam. GMs & +MCE suite” cases are presented in the Appendix. Response ratios associated to the “Dam. GMs & -MCE suite” are not presented because the damaged-to-undamaged ratios show the direction in which the second GMs were applied does not affect the trends.

G.7 Analysis of the Damage-to-Undamaged Ratio Trends

Trends for MCE plots are discussed since the conclusions reached for DE and MCE plots are the same. The trends obtained for the 8- and 12-story buildings are very similar (Figure G-25 and Figure G-33, respectively); the ratio of maximum roof drift is relative flat for the entire range of damaging ground motions considered, with maximum ratios generally between 1.0 and 1.1 for the range lower than the predicted roof drift capacity and between 1.0 and 1.4 for the range beyond the roof drift capacity. There is one Damaging GM intensity level that is associated with a damaged-to-undamaged ratio of almost 4.0. This result was examined more closely to determine that this was a result of the relatively large residual deformation that resulted in the Damaging GM. It was also noted that larger ratios sometimes resulted when response values were relatively low (i.e., the denominator of the ratio was small), such that the ratio of the responses appeared large, but the absolute value of the drifts were still relatively small (and no repair would be needed). A possible way to address this issue would be to plot ratios only when the values exceeded a threshold; however, this was not adopted given the overall findings (see conclusions in Section 8). Therefore, even with significant strength loss, which occurs for maximum roof drift ratios beyond about 2.5%, the ratio stays almost flat. By looking at the ratio of maximum base curvature it can be seen that there is some amplification beyond the deformation capacity of the wall; however, that amplification is not observed in the other maximum response ratios because of the linear response (unloading) outside the plastic hinge zone. The ratios between the maximum responses show a clearer trend when plotted against the wall residual responses against the Damaging GM.

A positive correlation can be seen when looking at the trends of the damaged-to-undamaged ratios against residual responses. The trend of the damaged-to-undamaged ratios when plotted against the maximum responses (e.g., max roof drift) stays between 1.0 and 1.2 for the range lower than the predicted deformation capacity, except for a few peaks that are close to ratio values of 1.6 and 1.8. However, as Figure G-34 shows, those cases correspond to analyses that resulted in residual roof drifts of about 0.5%, which are relatively high ratios for this trend. However, due to concerns related to the ability to reliably predict (compute) residual responses using

current modeling approaches and the ability to validate these results, residual responses were not deemed sufficiently reliable at this time to use as a repair trigger (and use of component limits and visual inspection is recommended).

The trends of the 4-story building for all parameters, the maximum roof drift, maximum curvature (within the 1st element at the base of the wall), maximum plastic hinge rotation and maximum 1st story drift, show a distinct trend with an increase after the deformation capacity is surpassed. This increase is associated with strength loss, which occurs when nonlinear curvature concentrates in the element adjacent to the wall-foundation interface (more so than is observed for the taller archetypes). However, the trend is not really helpful for assessing when repair would be needed since the damage associated with strength loss would be better determined by component limits and visual inspection.

In summary, the observed trends of the ratio of maximum responses when plotted against maximum responses from the damaging GM, are not helpful for assessing when repair would be needed since the damage associated with strength loss would be better determined by component limits and visual inspection. In this matter, determining the residual response (e.g., residual roof drift) could be more significant because the trends show a general positive correlation with the damaged-to-undamaged ratios.

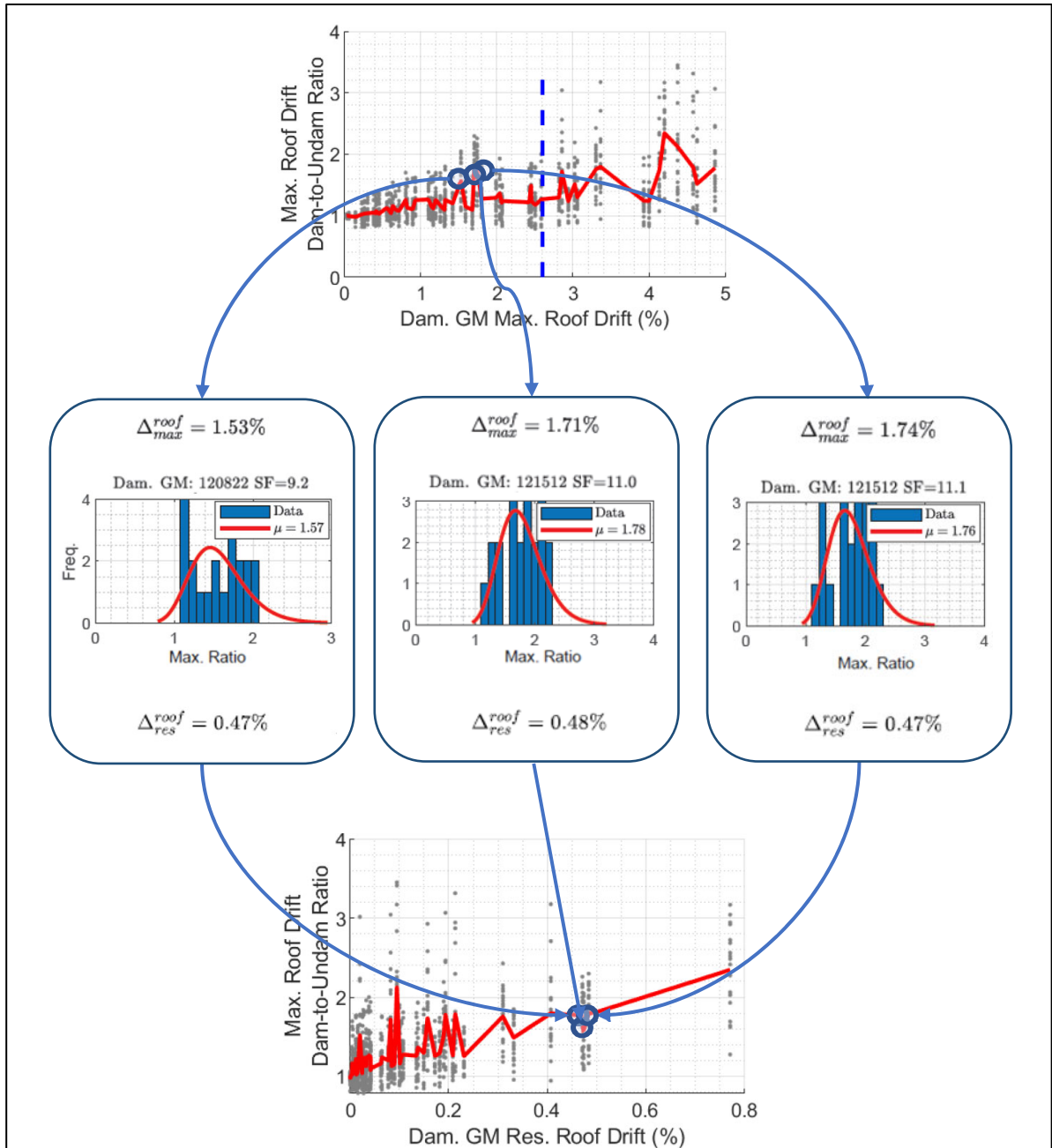


Figure G-34 Relation between peak dam-to-undam ratios and effect of maximum roof drift and residual roof drift.

G.8 Implications for Substantial Structural Damage

The Repair Guidelines will likely use the concept of Substantial Structural Damage (defined in IEBC, 2018), which is defined as a loss of 33% of lateral strength (IEBC, 2018). For the archetype buildings studied, wall strength loss tends to occur rapidly after reaching the roof drift or hinge rotation capacity associated with the initiation of strength loss (e.g., see Figure G-12 and Figure G-15; Figure G-20 and Figure G-23; Figure G-28 and Figure G-31) due to

concrete crushing and reinforcement buckling within the boundary element (for compression-controlled walls) or boundary longitudinal reinforcement fracture (for tension-controlled walls). Damage states for various walls are shown in Appendix I for various levels of drift (or rotation) demand. These plots, along with the damage ratio trends discussed in Section 7, indicate that strength may not be a good indicator of the impairment of the future seismic performance and that 33% strength loss for these wall systems tends to result in substantial visible damage (concrete crushing and reinforcement buckling). In addition, if greater demands are imposed on a wall with 33% strength loss, additional strength loss will occur rapidly to either a residual strength which tends to be low (e.g., 20% of ultimate strength for low values of cl_w/b^2 (e.g., $20 <$), or, in cases with high ratios of cl_w/b^2 (e.g., > 40), near zero residual strength (see Abdullah and Wallace, 2021). An alternative approach, possible one where that indicates that the probability of strength loss is very high could be considered.

G.9 Conclusions

The following observations are derived from a review of the trends observed in the plots of the damaged-to-undamaged response ratios:

- The ratios damaged-to-undamaged responses for all parameters are close to 1.0 (do not show any significant variation from 1.0) until the demand in a Damaging GM exceeds the deformation capacity (e.g., roof drift, 1st story rotation). If the demand in the Damaging GM results in strength loss, then substantial localized damage at the wall boundaries is expected. Therefore, the results of these system level studies indicate that component inspection/repair triggers (App. H) and visual inspection (App. I) should be sufficient to assess the need for repair.
- It is noted that the system studies presented here are based archetypes with a single wall design (cross section, reinforcement). Consideration of other designs, i.e., with different wall geometries and reinforcement is not feasible due to the large design space. Therefore, use of component level inspection and repair triggers should be sufficient to address this larger design space.
- The IDA studies presented included the consideration of applying the performance ground motion (DE or MCE_R suite) with either +/- sign to consider the potential influence of GM direction on the ratios of damaged-to-undamaged responses for all parameters (e.g., to address the potential of ratchetting of the response in one primary direction).

The direction of the applied GM did not significantly influence the response ratios considered.

- Some amplification was observed for the ratios of damaged-to-undamaged responses prior reaching (hinge/roof) deformation capacity for some Damaging GMs. Results for several of these GMs were reviewed to ascertain that this amplification was a result of residual story drift from a limited number of the Damaging GMs (the ratios in these cases tended to be large, which influenced the average value, which is the value plotted). Given the uncertainty associated with prediction of residual story drifts from computer models, use of component level inspection and repair triggers are recommended.

References

- Abdullah, S.A. and Wallace, J.W., 2019, "UCLA-RC walls database for reinforced concrete structural walls," *Proceedings of the 11th National Conference in Earthquake Engineering*.
- Abdullah, S. A., 2019, *Reinforced concrete structural walls: Test database and modeling parameters (Ph.D. dissertation)*, Department of Civil and Environmental Engineering, University of California, Los Angeles, California.
- Abdullah, S.A. and Wallace, J.W., 2021, "Drift capacity at axial failure of RC structural walls and wall piers", *Journal of Structural Engineering*, Vol. 147, No. 6, pp. 04021062.
- ACI, 2019, *Building Code Requirements for Structural Concrete*, ACI 318-19, and *Commentary*, ACI 318R-19, ACI Committee 318, American Concrete Institute, Farmington Hills, Michigan.
- ASCE, 2016, *Minimum Design Loads and Associated Criteria for Buildings and Other Structures*, ASCE/SEI 7-16, American Society of Civil Engineers, Structural Engineering Institute, Reston, Virginia.
- FEMA, 2009, *Quantification of building seismic performance factors*, FEMA P-695, prepared by the Applied Technology Council for the Federal Emergency Management Agency, Washington D.C.
- Kolozvari, K., Orakcal, K., Wallace, J.W., 2015, "Modeling of cyclic shear-flexure interaction in reinforced concrete structural walls. I: theory". *ASCE Journal of Structural Engineering*, Vol. 141, No. 5, pp. 04014135.
- PEER, 2021, *OpenSees—Open System for Earthquake Engineering Simulation*, Pacific Earthquake Engineering Research Center, Berkeley, California, <http://opensees.berkeley.edu/OpenSees/developer.html>.

Parsons, V.L. 2017, "Stratified sampling," *Wiley StatsRef: Statistics Reference Online*, American Cancer Society, pp. 1–11.

Saatcioglu, M., and Razvi, S. R., 1992, "Strength and ductility of confined concrete." *ASCE Journal of Structural Engineering*, Vol. 118, No. 6, pp. 1590-1607.

Component Deformation Limits for RC Components

H.1 Overview

This appendix describes the development of a framework for defining component deformation limits for inspection and repair triggers for reinforced concrete (RC) structural components. These triggers are used in post-earthquake assessment procedures to identify locations for visual inspection and identify locations needing structural repair. As part of this study, experimental test data are initially examined to understand the impact of displacement history on residual capacity of concrete components. The study focuses on defining the deformation limit beyond which: (a) the number of loading cycles starts influencing the cyclic behavior (strength and deformation capacity) of RC components and (b) the prior loading history starts influencing the residual (reserve) capacity (in terms of strength and deformation capacity) of the component for subsequent loading events. This component deformation limit was found to correspond to the deformation at the initiation of lateral strength loss (LSL).

Subsequently, using structural reliability techniques, the component deformation limit for inspection trigger is defined such that there is a low probability (less than about 10%) that deformation at LSL is exceeded. The component deformation limit for repair trigger is defined as the deformation at the initiation of LSL. For ease of implementation, both triggers are expressed as a fraction of deformation at 20% lateral strength loss on ASCE/SEI 41 idealized backbones, i.e., modeling parameter a or d , depending on whether the ASCE/SEI 41 backbone for the component is defined in terms of plastic hinge rotation (Parameter a) or total hinge rotation (Parameter d) (See Figure H-1).

In this appendix, the applicability of the proposed framework is demonstrated for non-ductile frame components and ACI 318 code-conforming flexure-controlled walls. It is, however, believed that the methodology can be applied to other concrete components and components of other materials (e.g., steel components).

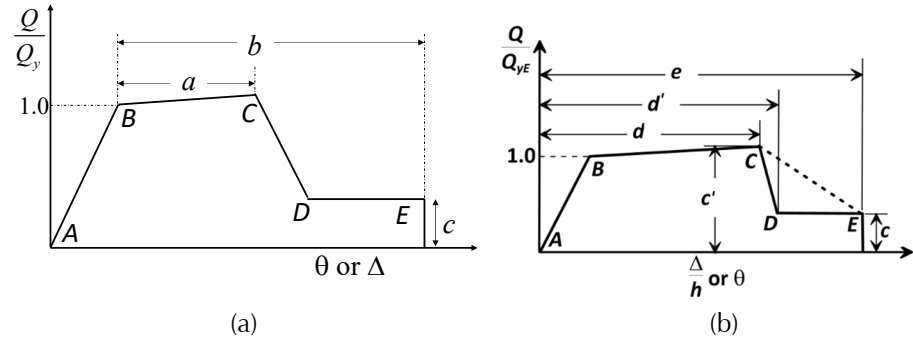


Figure H-1 ASCE/SEI 41 idealized force-deformation (backbone) relation to model hinge region of (a) beam-column components (b) flexure-controlled walls (proposed for adoption in ASCE 41-23).

H.2 Impact of Loading History on Residual Capacity of RC Components

H.2.1 When does the number of cycles starts influencing the cyclic behavior (strength and deformation capacity) of RC components?

Seismic demands on structures impose cyclic deformations on structural and non-structural components. From the perspective of post-earthquake residual capacity assessment, it is important to understand the effect of cyclic displacement history on the seismic performance of concrete components for future earthquake events. To accomplish this, in this section, results from nominally identical components tested under a varying number of cycles at each peak deformation demand are first compared, followed by a discussion on test results from nominally identical components subjected to different loading histories and components subjected to an initial loading protocol followed by a standard loading protocol.

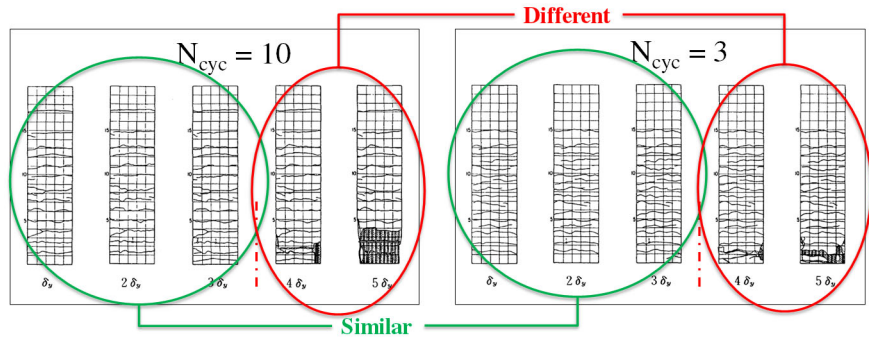
Kawashima and Koyama (1988) studied the cyclic response of three nominally identical, flexure-controlled columns with an aspect ratio of 5.4 to study the damage accumulation and hysteretic response of the columns subjected to cyclic loading protocols containing different numbers of cycles at each drift demand – N_{cyc} = three, five, and ten cycles at each peak drift demand. For the sake of brevity, however, the discussion herein focuses on the columns subjected to three and ten cycles at each peak drift demand (i.e., N_{cyc} equals to three and ten).

As shown in Figure H-2(a), the influence of number of cycles on the component damage level became significant after the drift demand exceeded 2.1% (corresponding to a displacement demand of 52mm and a ductility demand of 4). As can be deduced from Figure H-3(a), this drift demand corresponds to the initiation of lateral strength loss (LSL). Similar

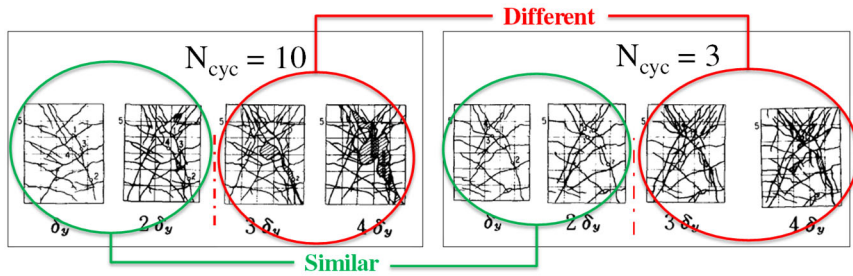
conclusions can be drawn from results of another set of tests on flexure-controlled columns with an aspect ratio of 3.8, reported by the same authors. Kawashima and Koyama (1988) also carried out similar tests on nominally identical shear-controlled columns and observed that the influence of number of cycles on the component damage level became significant once LSL was initiated, as shown in Figure H-2(b) and Figure H-3(b). For shear-controlled columns, given that low-cycle fatigue is not an issue, the assumption that the influence of the number of cycles is not significant until initiation of LSL seems reasonable considering that the shear capacity of the component is attained during the elastic range of response.

Similar results have been observed for RC structural walls. For example, Oesterle et al. (1976) tested two identical flexure-shear-controlled walls with barbell-shaped cross-sections under two different reversed cyclic loading protocols to investigate the significance of loading history on the behavior of the walls, as shown in Table H-1. As can be noted, one reversed cycle at a rotational ductility of five (i.e., roughly drift at the initiation of LSL) resulted in response of Wall B9 being comparable to that of Wall B7 which had sustained three complete reversed cycles at ductility demands of 1, 2, 3, 4, and 5. Thus, they concluded that structural wall behavior under load reversals was not as dependent on the entire previous load history as it was on the previous maximum level of deformations, i.e., whether the wall was previously loaded to initiation of LSL or not.

These experimental results suggest that the number of cycles applied prior to the initiation of LSL does not have a significant influence when comparing components tested under reversed cyclic loading, provided that low-cycle fatigue limit state is not triggered.

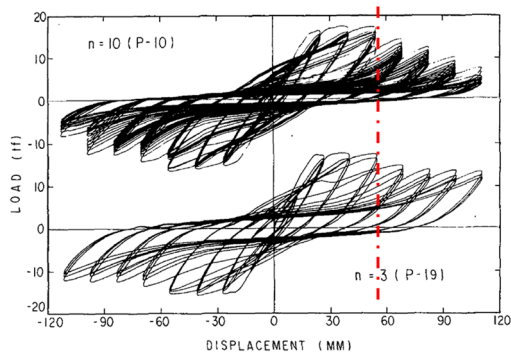


(a) Flexure-controlled columns

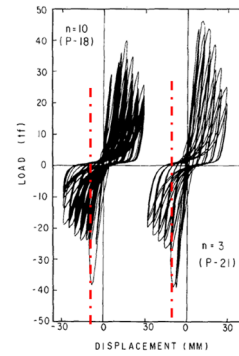


(b) Shear-controlled columns

Figure H-2 Damage accumulation in (a) flexure-controlled (b) shear-controlled columns with number of cycles (N_{cyc}) equal to three and ten (Plots adapted from Kawashima and Koyama 1988).



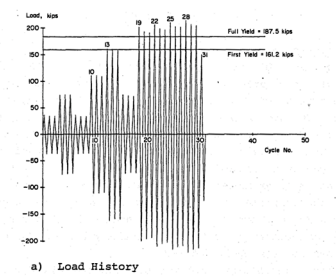
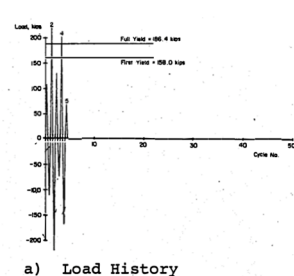
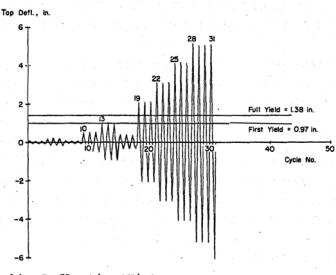
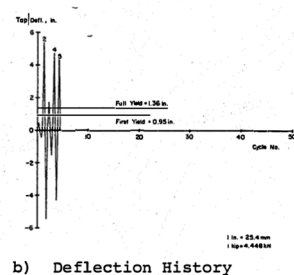
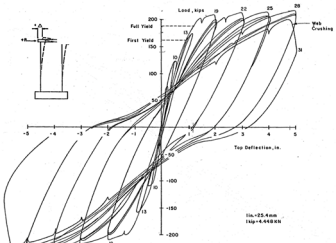
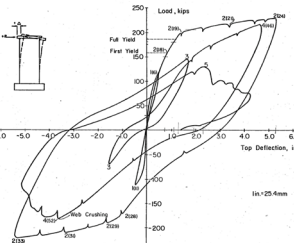
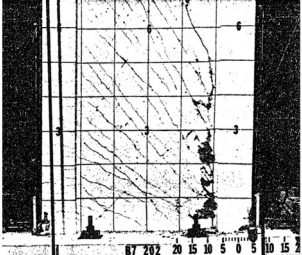
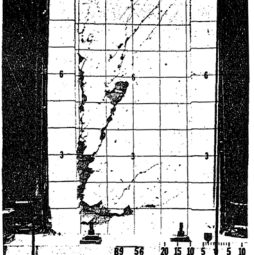
(a) Flexure-controlled columns



(b) Shear-controlled columns

Figure H-3 Measured hysteretic response of the flexure-dominated columns (Plots adapted from Kawashima and Koyama 1988).

Table H-1 Companion Walls Specimens Tested Under Different Load Protocols (Oesterle et al., 1979)

Test ID	Wall B7	Wall B9
Load history	 <p>a) Load History</p> <p>1 in. = 25.4 mm 1 kip = 4.448 kN</p>	 <p>a) Load History</p> <p>1 in. = 25.4 mm 1 kip = 4.448 kN</p>
Displacement history	 <p>b) Deflection History</p> <p>1 in. = 25.4 mm 1 kip = 4.448 kN</p>	 <p>b) Deflection History</p> <p>1 in. = 25.4 mm 1 kip = 4.448 kN</p>
Load-displacement relation	 <p>1 in. = 25.4 mm 1 kip = 4.448 kN</p>	 <p>1 in. = 25.4 mm 1 kip = 4.448 kN</p>
Damage condition	 <p>Flexural yielding following by web crushing</p>	 <p>Flexural yielding following by web crushing</p>

Furthermore, results from shake table tests on three nominally identical shear-controlled columns subjected to different displacement histories (records), from a test program by Nakamura and Yoshimura (2012), were reviewed. As shown in Figure H-4, the three columns were subjected to records producing different numbers of cycles. To make a meaningful comparison, the number of effective cycles (N_{eff}) to drift at the onset of LSL (also the drift at peak strength, V_{max}) was computed for each column using

the Malhotra (2002) formulation (Equation (H-1)). To account for the variation in drift at peak strength between the test specimens, it was decided to compute the N_{eff} corresponding to the smallest drift of the three specimens at LSL, which is 0.66% for specimen C13-J.

$$N_{eff} = \frac{1}{2} \sum_{i=1}^{2n} \left(\frac{u_i}{u_{max}} \right)^c \quad (H-1)$$

where n represents the number of displacement half-cycles experienced by the element, u_i is the peak-to-trough displacement for each half cycle, i , $u_{max} = 2$ times the peak drift considered, and c is the damage parameter, taken equal to 2 as proposed by Malhotra (2002).

Figure H-5 compares the computed number of effective cycles to 0.66% drift and peak strength of the columns. As shown in the figure, increase in N_{eff} did not influence the measured column peak strength. Based on these results, it was concluded that displacement history does not have an influence on the shear capacity of columns – supporting the experimental tests results from the shear-controlled specimens by Kawashima and Koyama (1988).

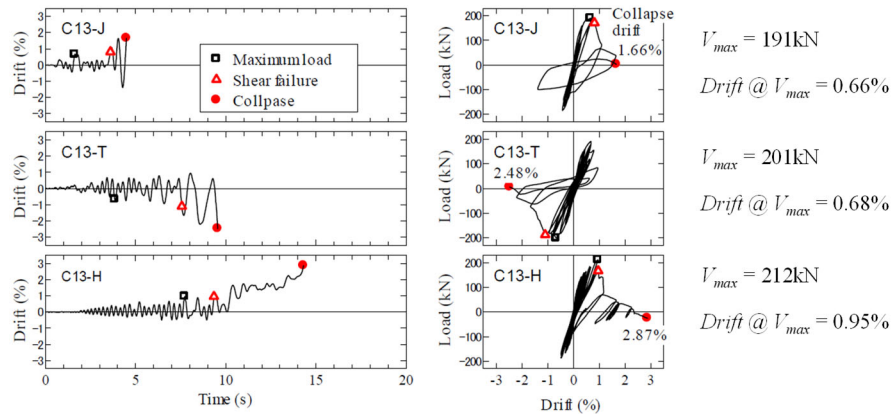


Figure H-4 Response of nominally identical shear-controlled columns subjected to different displacement histories (Nakamura and Yoshimura 2012).

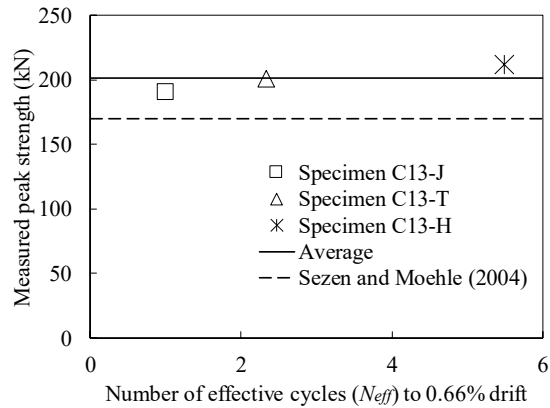


Figure H-5 Influence of number of effective cycles (N_{eff}) on measured peak strength of three nominally identical shear-controlled columns.

Based on the limited test results presented above, it can be concluded that, irrespective of the failure mode (i.e., flexure- or shear-controlled), the force-displacement response (in terms of strength and deformation capacity) and damage progression of RC components subjected to reversed cyclic loading may not be appreciably influenced by the number of cycles applied prior to the onset of LSL, given that low-cycle fatigue is not triggered..

H.2.2 When does prior loading history start influencing residual capacity?

In this subsection, experimental results are reviewed to understand the deformation at which demands from a past seismic event have compromised the probable response of a component in future seismic events. The experimental results are from studies on the residual capacity of concrete components (i.e., Colmenares et al., 2021; Moscoso et al., 2021; Opabola 2021; Chiu et al., 2020; Marder 2018; Maeda et al., 2017). Each considered test program includes two or more tests on nominally identical components – one of which is subjected to a standard cyclic loading protocol (Figure H-6a), while the other tests are subjected to an initial loading protocol (an earthquake or a cyclic loading) prior to applying a standard reversed, cyclic loading protocol (Figure H-6b).

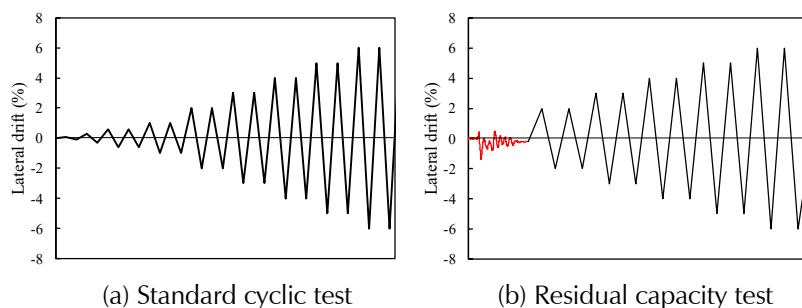


Figure H-6 Typical displacement protocol for considered test sets.

Six nominally-identical ductile beam specimens reported by Marder (2018) were examined. The test specimens included:

1. Specimen CYC subjected to a pseudo-static standard cyclic protocol
2. Specimen CYC-DYN subjected to a pseudo-dynamic standard cyclic protocol
3. Specimen LD-1 subjected to an initial pseudo-dynamic long-duration displacement history (with a peak drift demand of 1.36%) is applied and followed by a pseudo-static standard cyclic protocol
4. Specimen LD-2 subjected to an initial pseudo-dynamic long-duration displacement history (with a peak drift demand of 2.17%) is applied and followed by a pseudo-static standard cyclic protocol
5. Specimen P-1 subjected to an initial pseudo-dynamic pulse-type displacement history (with a peak drift demand of 1.36%) is applied and followed by a pseudo-static standard cyclic protocol
6. Specimen P-2 subjected to an initial pseudo-dynamic pulse-type displacement history (with a peak drift demand of 2.17%) is applied and followed by a pseudo-static standard cyclic protocol

The measured drift at initiation of LSL for specimen CYC-DYN was 1.9%, meaning that specimens LD-1 and P-1 were subjected to an initial pseudo-dynamic loading protocol with a peak drift (1.36%) lesser than the drift at LSL from a nominally identical specimen subjected to a dynamic standard cyclic protocol. On the other hand, specimens LD-2 and P-2 were subjected to an initial dynamic loading protocol with a peak drift (2.17%) larger than the drift at LSL from a nominally identical specimen subjected to a dynamic standard cyclic protocol.

The force-displacement plots of the beam specimens are presented in Figure H-7. In Figure H-7, the force-displacement plots represent the cyclic tests on EQ-damaged specimens LD-1, LD-2, P-1 and P-2. The tests showed that the initial earthquake protocol influenced the initial stiffness of the EQ-damaged specimens (the residual displacements in the EQ-damaged specimens are also noteworthy – see Figure H-7e). Discussions on the influence of initial earthquake protocol on the initial stiffness of the EQ-damaged frame component specimens has been extensively covered in existing literature (De Ludovico et al., 2013; Marder, 2018; and Opabola, 2021). Instead, this appendix focuses on the influence of initial earthquake protocol on residual strength and deformation capacity. As shown in Figure H-7a & b, irrespective of the type of initial earthquake protocol (i.e., long duration or pulse-type), lower initial stiffness and residual displacement in the EQ-

damaged LD-1 and P-1, the force-displacement plots of both specimens were similar to that of specimen CYC once the EQ-damaged LD-1 and P-1 were pushed to drifts larger than 1.36%. On the other hand, the force-displacement plots of EQ-damaged LD-2 and P-2 were significantly different from that of specimen CYC. The similarities in the force-displacement plots of specimens CYC, EQ-damaged LD-1 and P-1 at drift demand $> 1.36\%$ is attributed to the fact that the lateral strength loss was not initiated during the initial EQ-protocol. These experimental observations suggest that the hysteretic behavior of an EQ-damaged component would be similar to that of a pristine nominally identical component in a subsequent event once the EQ-damaged and pristine components are both subjected to a drift demand larger than the initial peak drift demand the EQ-damaged component was subjected to during the initial earthquake. On the other hand, lateral strength loss was initiated by the initial EQ-protocol in specimens LD-2 and P-2, resulting in reduced residual capacity – as observed by lower residual strength and deformation capacity in EQ-damaged LD-2 and lower deformation capacity in EQ-damaged P-2.

It is noteworthy that similar conclusions have been reached in a system-level study on two nominally identical frame structures subjected to different loading histories by Cecen (1979) (Note that this study is also discussed in Appendix B of the 2020 ATC 145 Source report) where Cecen (1979) concluded that two nominally identical EQ-damaged frames, subjected to different displacement histories, will have the similar response under a similar subsequent base motion provided that the intensities of all the preceding displacement histories are not greater than that of the subsequent base motion. Based on the discussions presented in this appendix, the Cecen (1979) conclusion is valid, provided that the drift at LSL of the components is not exceeded.

Ductile beam test specimens from an experimental program by Opabola (2021) were also examined. Conclusions, similar to that of Marder (2018), can be derived from these tests. For the sake of brevity, no detailed information is provided here.

Chiu et al. (2020) carried out residual capacity tests on conforming and non-conforming RC column test specimens. Force-displacement plots from these tests are shown in Table H-2. Similar to Marder (2018), irrespective of the component failure mode (i.e., flexure-controlled or flexure-shear controlled), the EQ-damaged specimens were able to retain their original strength and deformation capacity when the drift demand from the initial EQ protocol was lower than the drift at LSL measured from the standard cyclic test. As shown in Table H-2, in cases where the drift demand from the initial EQ protocol

was larger than the drift at LSL, the residual capacity of the EQ-damaged specimens was affected.

Pseudo-dynamic tests on three nominally identical shear-controlled columns by Nakamura and Yoshimura (2012) were examined – specimens 4J21, 4W21 and 6J21. The three specimens were subjected to different initial and subsequent displacement histories (Figure H-8a). As shown in Figure H-8b, the drift at LSL was not attained in 4J21 and 6J21 during the initial EQ input and the force-displacement response of these components during the subsequent EQ input was uncompromised until the drift at LSL was attained. On the other hand, in specimen 4W21, the drift at LSL was significantly exceeded; hence, the residual capacity of the component was significantly compromised during the subsequent EQ event.

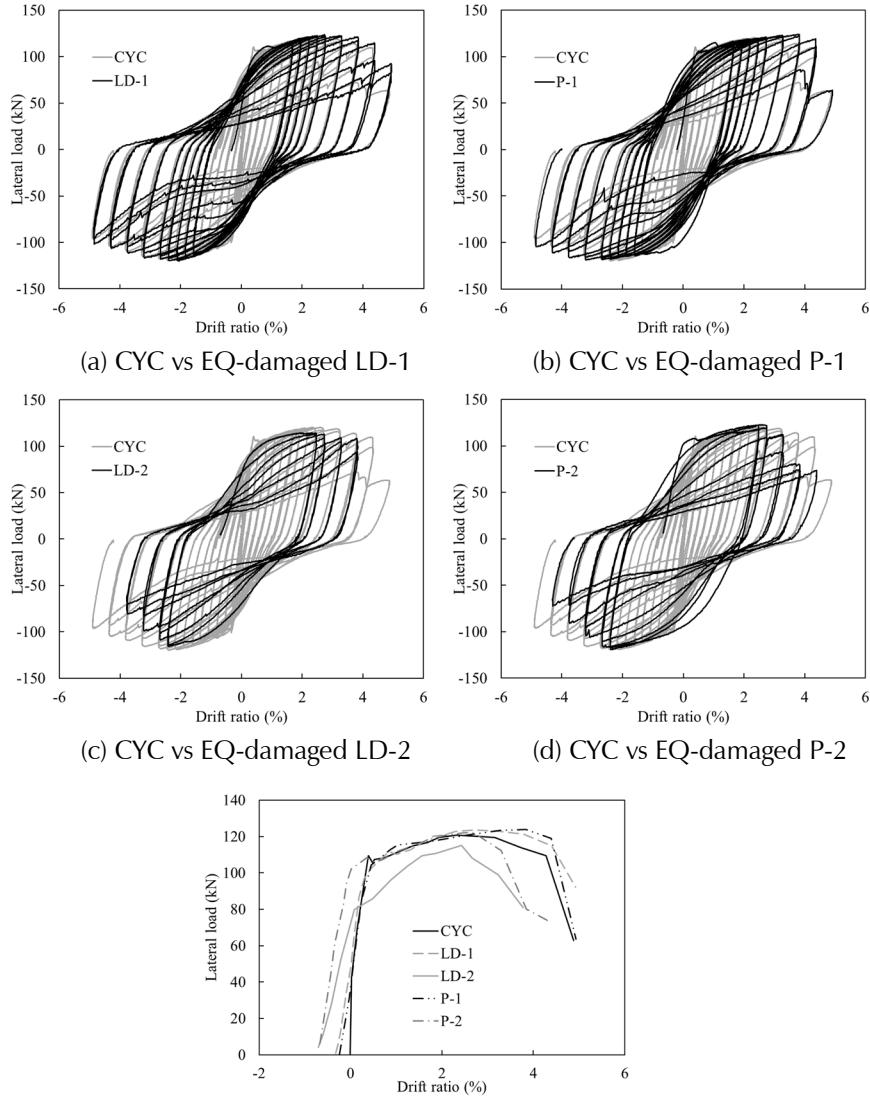


Figure H-7 Force- displacement plots of Marder (2018) beam specimens.

Table H-2 Examples of Force-displacement Plots Showing the Influence of Prior Loading History on Residual Capacity of Columns and Beams (Marder 2018; Chiu et al. 2020)

Failure mode	Hysteresis plot of specimen subjected to standard cyclic protocol	Hysteresis plot of specimen subjected to initial dynamic loading with peak demand less than drift at LSL from standard cyclic protocol	Hysteresis plot of specimen subjected to initial dynamic loading with peak demand equal to or greater than drift at LSL from standard cyclic protocol
Flexure-shear column	<p>Figure 1: Hysteresis plot for specimen SF-30S-0.1. The plot shows lateral force (kN) on the y-axis (ranging from -350 to 350) and displacement (mm) on the x-axis (ranging from -80 to 80). A secondary x-axis at the top shows drift ratio (%) from -4 to 4. The plot includes a strength envelope, experimental data points, and markers for maximum strength point, stirrups yielding, concrete spalling, and concrete crushing. The specimen shows a peak lateral force of approximately 250 kN at a drift ratio of about 4%.</p>	<p>Figure 2: Hysteresis plot for specimen SF-30S-0.1 under initial dynamic loading. The plot shows lateral force (kN) on the y-axis (ranging from -300 to 300) and displacement (mm) on the x-axis (ranging from -150 to 150). A secondary x-axis at the top shows drift ratio (%) from -8 to 8. The plot includes dynamic and static loading curves, a strength envelope, and markers for observed yielding point, maximum strength point, stirrups yielding, concrete spalling, and concrete crushing. The specimen shows a peak lateral force of approximately 200 kN at a drift ratio of about 4%.</p>	<p>Figure 3: Hysteresis plot for specimen SF-30S-0.1 under initial dynamic loading with peak demand equal to or greater than drift at LSL. The plot shows lateral force (kN) on the y-axis (ranging from -300 to 300) and displacement (mm) on the x-axis (ranging from -150 to 150). A secondary x-axis at the top shows drift ratio (%) from -8 to 8. The plot includes dynamic and static loading curves, a strength envelope, and markers for observed yielding point, maximum strength point, stirrups yielding, concrete spalling, and concrete crushing. The specimen shows a peak lateral force of approximately 200 kN at a drift ratio of about 4%.</p>
Flexure-controlled column	<p>Figure 4: Hysteresis plot for specimen FF-15S-0.1. The plot shows lateral force (kN) on the y-axis (ranging from -350 to 350) and displacement (mm) on the x-axis (ranging from -150 to 150). A secondary x-axis at the top shows drift ratio (%) from -8 to 8. The plot includes a strength envelope, experimental data points, and markers for observed cracking point, observed shear point, observed yielding point, maximum strength point, stirrups yielding, concrete spalling, and concrete crushing. The specimen shows a peak lateral force of approximately 250 kN at a drift ratio of about 4%.</p>	<p>Figure 5: Hysteresis plot for specimen FF-15S-0.1 under initial dynamic loading. The plot shows lateral force (kN) on the y-axis (ranging from -300 to 300) and displacement (mm) on the x-axis (ranging from -150 to 150). A secondary x-axis at the top shows drift ratio (%) from -8 to 8. The plot includes dynamic and static loading curves, a strength envelope, and markers for observed yielding point, maximum strength point, stirrups yielding, concrete spalling, and concrete crushing. The specimen shows a peak lateral force of approximately 200 kN at a drift ratio of about 4%.</p>	<p>Figure 6: Hysteresis plot for specimen FF-15S-0.1 under initial dynamic loading with peak demand equal to or greater than drift at LSL. The plot shows lateral force (kN) on the y-axis (ranging from -300 to 300) and displacement (mm) on the x-axis (ranging from -150 to 150). A secondary x-axis at the top shows drift ratio (%) from -8 to 8. The plot includes dynamic and static loading curves, a strength envelope, and markers for observed yielding point, maximum strength point, stirrups yielding, concrete spalling, and concrete crushing. The specimen shows a peak lateral force of approximately 200 kN at a drift ratio of about 4%.</p>
Flexure-controlled beam	<p>Figure 7: Shear force vs lateral drift plot for specimen P-1. The plot shows shear force (kN) on the y-axis (ranging from -150 to 150) and lateral drift (%) on the x-axis (ranging from -5 to 5). The plot shows multiple cycles of loading and unloading, with a peak shear force of approximately 100 kN at a drift ratio of about 5%.</p>	<p>Figure 8: Shear force vs lateral drift plot for specimen P-1 under initial dynamic loading. The plot shows shear force (kN) on the y-axis (ranging from -150 to 150) and lateral drift (%) on the x-axis (ranging from -5 to 5). The plot shows initial dynamic loading followed by static loading, with a peak shear force of approximately 100 kN at a drift ratio of about 5%.</p>	<p>Figure 9: Shear force vs lateral drift plot for specimen P-2. The plot shows shear force (kN) on the y-axis (ranging from -150 to 150) and lateral drift (%) on the x-axis (ranging from -5 to 5). The plot shows initial dynamic loading followed by static loading, with a peak shear force of approximately 100 kN at a drift ratio of about 5%.</p>

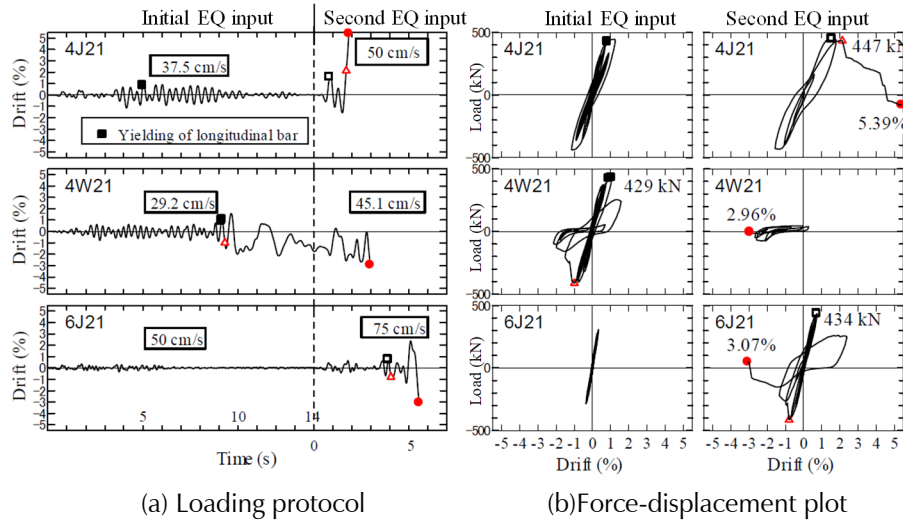


Figure H-8 (a) Loading protocol and (b) force-displacement response of three-nominally identical shear-controlled columns (Nakamura and Yoshimura, 2012).

Similar to frame members, experimental results from studies on residual (reserve) capacity of RC walls are reviewed (i.e., tests involving application of two sequential loading protocols). It is important to note that although the results reviewed herein are from tests on non-conforming (ordinary) flexure-controlled walls and shear-controlled walls, the concepts and conclusions are equally applicable to conforming flexure-controlled walls. As will be discussed later in Section H.5.1, conforming walls are defined as walls that satisfy the requirements of the current or prior versions of ACI 318 since 1983.

Colmenares et al. (2021) conducted an experimental program on four flexure-controlled walls to understand the effect of number of cycles on residual (reserve) capacity of typical Chilean RC structural walls with unconfined boundaries. One specimen, baseline, was tested under a standard cyclic loading protocol, while the other three tests were subjected to a cyclic loading protocol with a constant amplitude at a target drift of about 1.0% prior to applying the standard cyclic loading protocol, as shown in Table H-3. The varied parameter between the three tests was the number of cycles applied during the initial constant-amplitude loading protocol, which ranged from 30 to 120 cycles (Table H-3). Since the target drift of 1.0% is smaller than the drift capacity of the baseline specimen at initiation of LSL (roughly 2.0%), the number of cycles in the first loading protocol did not have a noticeable effect on the strength and deformation capacity of the wall tests. The only observed effect of the initial loading protocol was a reduction in the effective cracked stiffness (secant to general yield) of the walls, as can be seen from the backbones in Table H-3. Further, Moscoso et al. (2021)

conducted an experimental study on flexure-controlled walls with details similar to those used in tests by Colmenares et al. (2021), except that Moscoso et al. (2021) used a standard cyclic loading protocol for the initial loading (versus a constant-amplitude loading protocol), as shown in Table H-4. Specimen RW2-S2.5 was tested initially under a standard cyclic loading protocol with maximum drift demands of +1.76% and -1.57%, which are close to drift capacity at initiation of LSL of a companion specimen (RW1-S2.5) tested to failure only under a standard cyclic loading protocol (Table H-4). As a result, during the subsequent standard cyclic loading protocol, RW2-S2.5 was able to only sustain one additional cycle with a drift demand greater than the maximum drift reached during the initial loading protocol. However, for the other two wall tests (RW4-S2.5 and RW6-S1.75), since the maximum drift reached during the initial loading protocol was only about 50% of drift at initiation of LSL of the companion specimens (RW3-S2.5 and RW5-S1.75), no noticeable effect of the prior cyclic loading protocols was observed on the strength and deformation capacity of RW4-S2.5 and RW6-S1.75 (Table H-4).

Lastly, two series of tests (total of nine wall tests) were performed by Maeda et al. (2017) to investigate the influence of different levels of prior damage on performance of shear-controlled walls during a subsequent loading protocol. All the specimens in each test series were identical. The design parameter varied between the two-test series was the web transverse and longitudinal reinforcement ratios – 1.32% and 0.66% for tests in Series S-13 and Series S-06, respectively. The parameter varied in each test series is the level of damage sustained during the initial loading protocol, as shown in Table H-5. For example, the baseline specimens (S-13-D0 and S-06-D0) were not subjected to any initial loading, whereas specimen S-13-DI was subjected to two cycles at drift demands of 0.025% and 0.05% during the ramp-up and ramp-down of the initial loading protocol and five cycles at drift demand of 0.075%. For Series S-13, since none of the specimens were subjected to a drift demand equal to, or greater than, drift capacity at initiation of LSL of the baseline specimen (~0.8%) during the initial loading protocol, no noticeable effect on the strength, deformation capacity, and damage state of the walls was observed as a result of the damage due to the initial loading protocol, except for a reduction in the initial stiffness of the walls (Figure H-9). Similar results were observed for tests in Series S-06, except for a slight reduction in the lateral strength of specimen S-06-DIV, which, during the initial loading, was subjected to a maximum drift demand that was close to its drift capacity at LSL.

Table H-3 Influence of Prior Loading History on Residual Capacity of Walls—Tests Conducted by Colmenares et al. (2021)

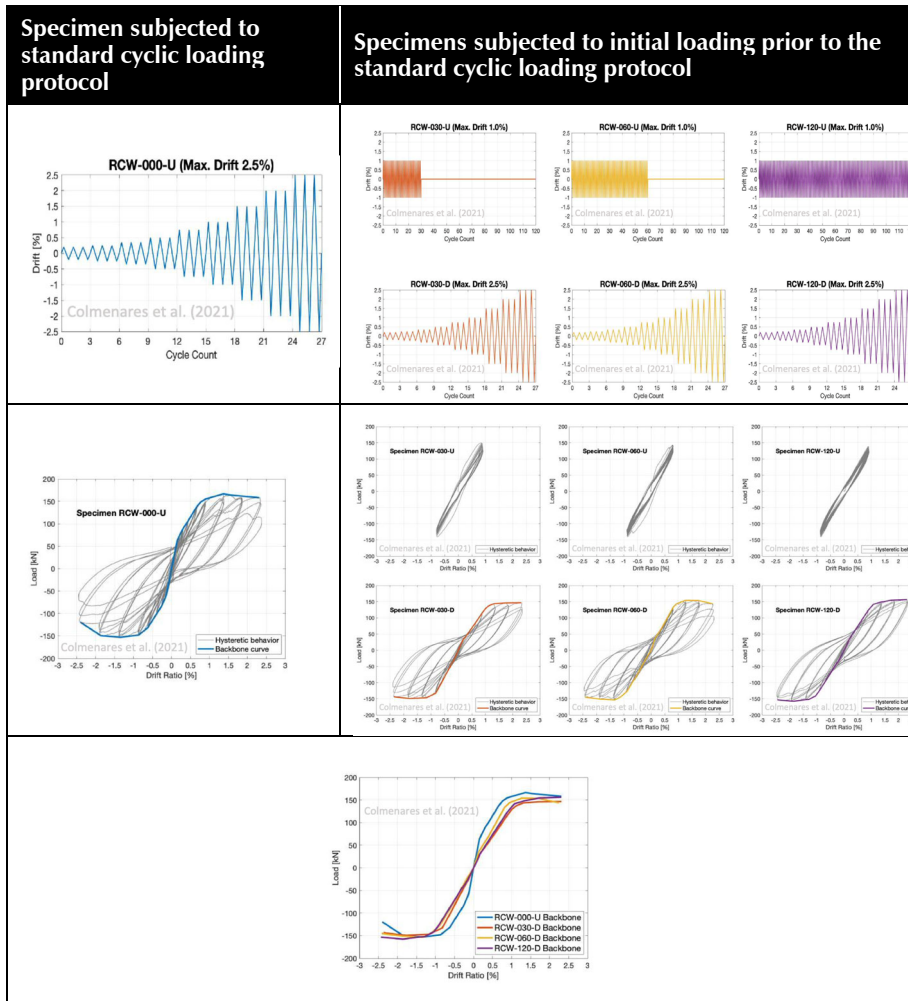


Table H-4 Influence of Prior Loading History on Residual Capacity of Walls—Tests Conducted by Moscoso et al. (2021)

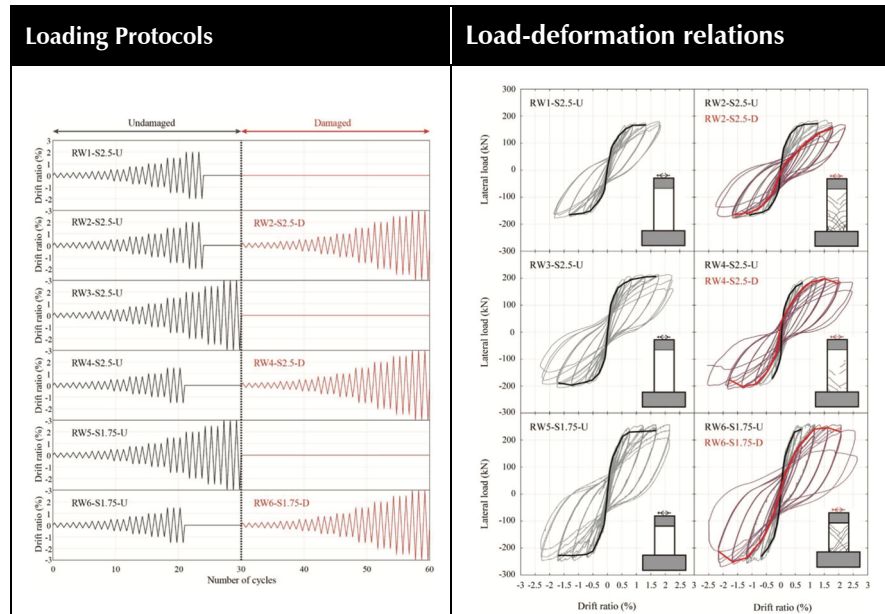
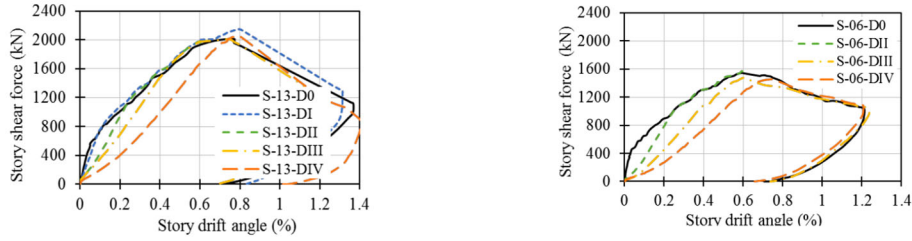
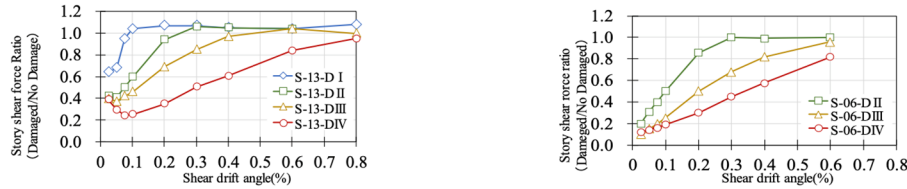


Table H-5 Loading Protocols Used by Maeda et al. (2017) to Conduct Residual Capacity Tests on Shear-controlled Walls

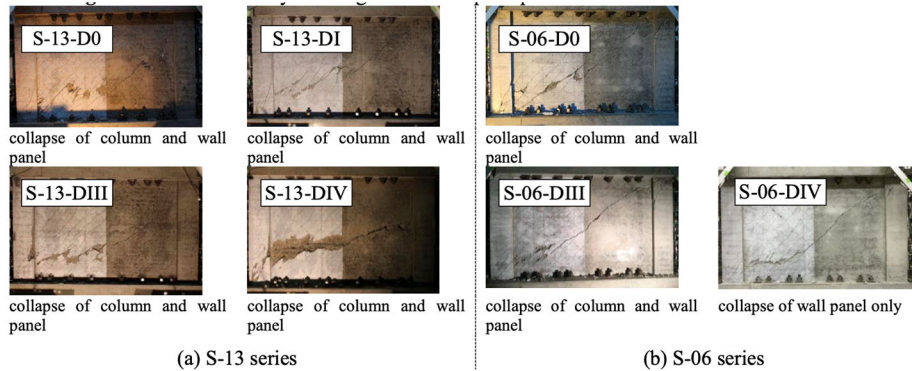
Loading type	Specimens	Story Drift R/(1000rad.) and Number of Each Cycle													
		±0.25	±0.5	±0.75	±1	±2	±3	±4	±6	±4	±3	±2	±1	±0.5	±0.25
Pre	S-13-DI	2	2	5										2	2
	S-13-DII	2	2	2	2	5							2	2	2
	S-13-DIII	2	2	2	2	2	2	5			2	2	2	2	2
	S-13-DIV	2	2	2	2	2	2	2	5		2	2	2	2	2
	S-06-DII	2	2	2	2	5							2	2	2
	S-06-DIV	2	2	2	2	2	2	2	2	5		2	2	2	2
Loading type	Specimens	Story Drift R/(1000rad.) and Number of Each Cycle													
		±0.25	±0.5	±0.75	±1	±1.5	±2	±2.5	±3	±4	±6	±7	8		
Main	All	2	2	2	2	2	2	2	2	2	2	2	2		



(a) Shear force-story drift envelopes with different pre-damage levels



(b) Story shear force ratio at each main drift angle



(c) Damage state at the end of the test

Figure H-9 Results from residual capacity tests of shear-controlled walls conducted by Maeda et al. (2017).

The following conclusions from the examined residual capacity test programs on the frame and wall components are summarized below:

1. Provided that the drift at initiation of LSL is not exceeded in any previous displacement histories (and capacity is not reduced due to low-cycle fatigue), aside from a reduction in initial stiffness, the residual capacity (in terms of strength and deformation capacity) and hysteretic of the earthquake-damaged component is not likely compromised.
2. Damage progression data from experimental tests suggest that the onset of LSL corresponds to the initiation of critical diagonal failure plane in flexure-shear and shear-controlled components, and the onset of bar buckling in flexure-controlled components. Further discussion on this topic is provided subsequently in this appendix.

The conclusions above suggest that the behavior of an earthquake-damaged component follows a ‘peak-oriented’ assumption – i.e., provided the peak

lateral resistance of an earthquake-damaged component was not reached in any preceding displacement histories (and no low-cycle fatigue issues), the residual capacity of the component is uncompromised.

Figure H-10 is a graphical representation of the peak-oriented assumption using an arbitrary force-displacement plot for a component that has been subjected to three events. Figure H-10 shows that a damaged component will only be able to reach its original peak strength if the original component was subjected to initial cyclic demands lower than the drift capacity at initiation of LSL (i.e., point 8). As shown in Figure H-10, ductility demand histories reduce the effective stiffness of a damaged component (from K_1 to K_2 to K_3), irrespective of whether the drift at onset of LSL is reached or not. Further discussions on the influence of prior ductility demands on the stiffness of damaged concrete components are given elsewhere (i.e., De Ludovico et al., 2013; Maeda et al. 2017; Marder 2018; Abdullah et al., 2020; and Opabola, 2021).

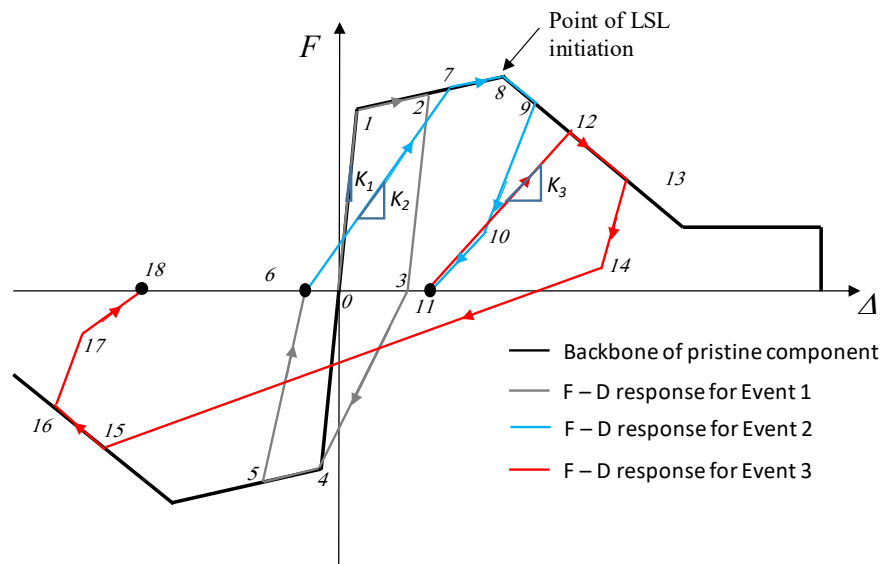


Figure H-10 Peak-oriented reloading assumption.

H.3 Proposed Methodology

H.3.1 Defining the Ultimate Component Deformation Limit

As previously concluded, provided that the low-cycle fatigue limit state is not triggered, the influence of prior loading history on the residual capacity of concrete components becomes significant once the deformation at the initiation of LSL (θ_{LSL}) is reached. Hence, in this section, the ultimate component deformation limit is defined as the deformation beyond which the residual capacity (strength and deformation capacity) of the component is compromised.

State-of-practice documents of seismic evaluation (i.e., ASCE/SEI 41-17) provide formulations or tables for evaluating the component deformation capacities at lateral failure (i.e., 20% lateral strength loss) and axial failure. There are currently no formulations for predicting θ_{LSL} of concrete components. In this study, rather than developing new formulations for predicting θ_{LSL} , it was considered more efficient to adopt a simple methodology of calibrating a multiplier, x , to be applied to the ASCE/SEI 41 deformation capacity at lateral failure (θ_{LF}) to obtain θ_{LSL} (See Figure H-11a and Equation (H-2)).

$$\theta_{LSL} = x \cdot \theta_{LF} \quad (H-2)$$

Using information from collated databases of experimental tests on concrete components (frame elements and walls), the statistical distribution (median and dispersion) of multiplier x is computed (e.g., Figure H-11b).

Sections H.4.3 and H.5.2 provide information on the development of θ_{LSL} for non-ductile columns and code-conforming flexure-controlled walls, respectively.

Future changes to ASCE/SEI 41 modelling parameters may warrant recalibration of the multiplier and statistical distributions for predicting the ultimate component deformation limits presented next.

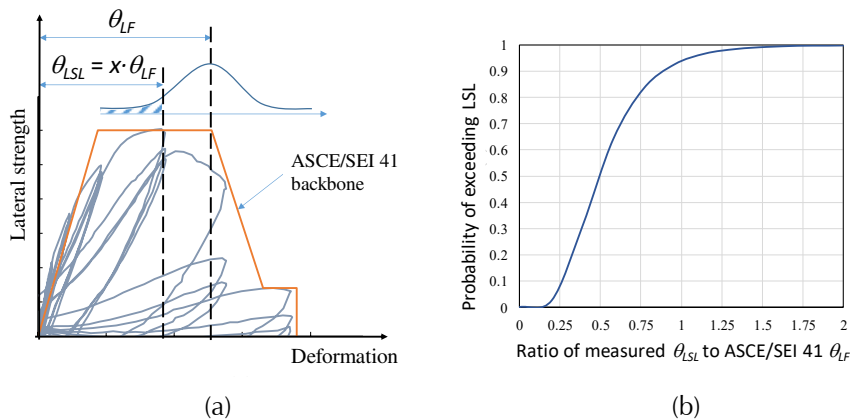


Figure H-11 Definition of the ultimate component deformation limit (a) Definition of LSL (b) Cumulative probability distribution of the ratio of measured deformation at LSL to ASCE/SEI 41 deformation capacity at lateral failure (i.e., 20% lateral strength loss).

The preceding discussion is applicable to deformation-controlled components. For force-controlled components (such as shear-controlled and splice-critical components), the component deformation limit is replaced by a component strength limit. This implies that rather than using deformation,

the inspection triggers are expressed in terms of the computed lateral strength.

H.3.2 Inspection Trigger

A key component of the post-earthquake assessment procedure is identifying locations for visual inspection. In this procedure, the engineer: a) develops an analytical model of the building subjected to ground motions recorded at or near the site, and b) calculates inspection triggers for the various structural components of the building. The demands on these components obtained from the analytical model are compared with the calculated inspection triggers to identify locations that may potentially have sustained damage. It is important that these inspection triggers are developed with the consideration of having a low likelihood of missing damaged components, thereby warranting the need for this trigger to be conservatively defined. In other words, it is better to inspect more locations than required, rather than inspecting fewer locations than necessary. In this section, a general methodology is proposed for defining the deformation limit for inspection triggers (θ_{IT}) of structural components, which is defined such that there is a low likelihood that θ_{LSL} is not exceeded. In other words, the inspection trigger multiplier x_{IT} , where $\theta_{IT} = x_{IT}\theta_{LSL}$, is defined such that there is a $p\%$ probability of exceeding θ_{LSL} . Based on engineering judgment, it is recommended that $p \leq 10\%$. For this reliability analysis, it is necessary to consider all relevant sources of uncertainty in demand and capacity estimates. In addition to considering the uncertainty β_{LSL} in predicting θ_{LSL} (see Figure H-11b), uncertainties in demand estimates by considering ground motion (β_{gm}) and modeling (β_{model}) uncertainties need to be incorporated. The adopted approach in this study accounts for the fact that there could be a significant level of uncertainties in the demand estimates for various reasons, i.e., the proximity of the structure to a recording station, availability and reliability of building instrumentation data, knowledge level of material and structural properties, and complexity of adopted modeling techniques. For example, it is reasonable to assume that β_{gm} and β_{model} would be low for instrumented buildings and high for non-instrumented buildings. β_{gm} would be low for a building situated near a ground motion station. The argument for β_{model} follows the assumption that numerical models of instrumented buildings can be properly calibrated using data from the instrumentation. From a post-earthquake assessment perspective, β_{model} could be further reduced if the engineer is able to make post-event observations on the expected behavior and eventual failure modes of the components.

The authors are unaware of available studies that have recommended values of β_{gm} and β_{model} for adoption in post-earthquake probabilistic modeling and

analysis. Table 5-2 of FEMA P-58 recommends values for β_{model} depending on the quality and completeness of the analytical model, where β_{model} values of 0.10, 0.25, and 0.40 are recommended for superior, average, and limited quality models. In this study, it is assumed that the β_{model} for instrumented and non-instrumented buildings would be in the range of 0.10 to 0.40. On the other hand, the record-to record variability values (β_{RTR}) provided in Table 5-3 of FEMA P-58 are deemed too conservative for adoption as β_{gm} because it is expected that there would be a fair amount of available information on the actual ground motion record from ground motion stations and the post-earthquake assessment would likely not involve analyses using a suite of ground motion records. This appendix assumes that β_{gm} ranges from 0.0 for buildings with ground motion station on site to 0.70 for buildings without any ground motion stations on a similar site class within approximately 50km (Abrahamson, 2021).

The inspection trigger multiplier x_{IT} is defined using structural reliability methods such that there is a $p\%$ probability of exceeding θ_{LSL} under a given component deformation demand. In this appendix, it is assumed that the random variables representing the deformation parameters (demand and capacity) are statistically independent and lognormally distributed (Melcher 1999). In structural reliability terms, the limit state function for triggering the median $\tilde{\theta}_{LSL}$ can be written as Equation (H-3), where $\tilde{\theta}_D$ is the median component deformation demand:

$$G = \ln(\tilde{\theta}_{LSL}) - \ln(\tilde{\theta}_D) \quad (H-3)$$

The reliability index Z , accounting for the uncertainties in capacity and demand, can be computed as:

$$Z = \frac{\ln\left(\frac{\tilde{\theta}_{LSL}}{\tilde{\theta}_D}\right)}{\sqrt{\beta_{gm}^2 + \beta_{model}^2 + \beta_{LSL}^2}} \quad (H-4)$$

The reliability index Z defines probability p of $\tilde{\theta}_D$ exceeding $\tilde{\theta}_{LSL}$. The relationship between Z and p is defined as:

$$p = \Phi(-Z) \quad (H-5)$$

where $\Phi(\cdot)$ is standard normal distribution function.

In this section, the limit state of interest is the inspection trigger, which is activated when $\tilde{\theta}_D \geq \theta_{IT}$. Replacing $\tilde{\theta}_D$ with θ_{IT} in Equation (H-4), θ_{IT} can be expressed as:

$$\theta_{IT} = \frac{\tilde{\theta}_{LSL}}{e^{Z\sqrt{\beta_{gm}^2 + \beta_{model}^2 + \beta_{LSL}^2}}} \quad (H-6)$$

where $1/e^{Z\sqrt{\beta_{gm}^2 + \beta_{model}^2 + \beta_{LSL}^2}}$ is the multiplier with respect to the median value of $\tilde{\theta}_{LSL}$, and it defines the fraction of $\tilde{\theta}_{LSL}$ that θ_{IT} needs to be equal to, or exceed, in order to trigger a limit state of interest. As previously stated, θ_{LSL} is defined as a fraction of the deformation capacity at lateral failure (θ_{LF}), i.e., $\theta_{LSL} = x \cdot \theta_{LF}$.

Hence, θ_{IT} is defined as:

$$\theta_{IT} = \frac{\tilde{\theta}_{LSL}}{e^{Z\sqrt{\beta_{gm}^2 + \beta_{model}^2 + \beta_{LSL}^2}}} = \frac{1}{e^{Z\sqrt{\beta_{gm}^2 + \beta_{model}^2 + \beta_{LSL}^2}}} \cdot \tilde{x} \cdot \tilde{\theta}_{LF} = x_{IT} \tilde{\theta}_{LF} \quad (H-7)$$

As such, the inspection trigger multiplier x_{IT} is defined using the probability p of exceeding θ_{LSL} (defined in terms of a reliability index Z), considering various sources of uncertainty. In Equation (H-7), β_{LSL} and x are the only parameters influencing x_{IT} which are dependent on the component.

Subsequently, parametric studies are carried out in this appendix to provide a range of multipliers, x_{IT} , for various combinations of ground motion uncertainty β_{gm} , modeling uncertainty β_{model} , capacity uncertainty β_{LSL} , and reliability index Z for non-ductile columns and code-conforming flexure-controlled walls.

H.3.3 Repair Trigger

The purpose of the repair trigger is to identify structural damage that needs repair. Repair trigger of a component is defined as a deformation limit beyond which the lateral strength of the component is compromised (i.e., the residual lateral strength of the component is less than the lateral strength of the undamaged component) and that structural repair may be required to restore the structural characteristics of the component. Additionally, the repair trigger is used to finetune the analytical model of the building to accurately predict demands and damage, i.e., to reconcile model results and observed damage. Therefore, the repair trigger should not be conservatively defined, as was the case for the inspection trigger because the need for repair has to be confirmed by visual inspection using the guidance in Appendix I.

The proposed repair trigger is the median estimate of θ_{LSL} . As will be discussed later, this typically corresponds to the deformation at the initiation of the critical diagonal failure plane in flexure-shear-controlled components and the initiation of longitudinal bar buckling in flexure-controlled components.

H.3.4 Components Always Requiring Inspection

This appendix recognizes the fact that there are vertical load-carrying components whose probable residual capacity may not be reliably assessed or their post-LSL behavior is very brittle (i.e., once the lateral strength degradation initiates, the component possess little or no additional deformation capacity before axial failure occurs) and thus failure of such components in a subsequent event may result in catastrophic consequences. It is recommended that such components be inspected regardless of whether the inspection trigger is exceeded or not. Also, careful engineering judgement should be exercised when classifying such components as those not requiring repair. Examples of columns or walls falling in this category include:

- Non-ductile columns with significant axial loads (typically $s/d > 0.5$ and $P/A_g f'_c > 0.3$)
- Shear-controlled walls with axial loads ratios, $P/A_g f'_c$, exceeding 0.15 and shear-flexure strength ratios, $V_{ne}/V_{@Mne}$, lower than 0.5.
- Flexure-controlled walls with values of $l_w c/b^2$ exceeding 70.

H.4 Non-Ductile Frame Elements

H.4.1 Description of Database

As part of this study, a database of cyclic tests on non-ductile columns was collated. In this study, non-ductile columns were defined as columns with reinforcement detailing typical of pre-1970s structures i.e., columns with widely spaced transverse reinforcement ($s/d \geq 0.5$), poorly anchored transverse reinforcement (i.e., 90 degree hooks), and columns with short splices in the region of maximum moment demands (defined as columns with provided splice length $l_{s,provided} \leq 30d_b$). Columns with plain longitudinal reinforcement were not considered in this study.

The collated database consists of 162 non-ductile columns – 68 flexure-shear controlled columns, 70 shear-controlled columns, 24 splice-critical columns. Flexure-shear failure is characterized by flexural yielding of the column followed by failure in shear due to imposed shear demands that catalyze shear capacity degradation. As ductility demand increases, inclined cracks in concrete and degradation of aggregate interlock mechanism leads to reduction of concrete contribution to shear capacity. In shear-controlled columns, the column experiences a brittle shear failure without flexural yielding. This failure occurs when the un-degraded shear strength is less than the shear demand corresponding to expected or probable flexural strength. Brittle shear failure is also characterized by diagonal cracking and is often

associated with columns with low aspect ratios (typically $a/d < 2$). Columns with inadequate lap-splices experience bond-failure without flexural yielding because the maximum developable tensile stress in the lap-spliced longitudinal bars is lower than the yield stress of the longitudinal bars. The column behavior is dominated by vertical bond-splitting cracks along the lap-splice region.

In the collated database, a column specimen is classified as shear-controlled if it fails through a diagonal failure plane, flexural yielding is not reported by the test authors and the measured peak strength is lower than the calculated flexural strength. Otherwise, the column is classified as flexure-shear controlled. Columns with lap-splices of longitudinal bars are classified as splice-critical if the measured peak strength is lower than the calculated flexural strength, and available photos and measured data suggest a bond-dominated mechanism.

The distribution of key parameters of the columns in the database is presented in Table H-6. One and four columns with short splices (e.g., Lynn et al. 1996) are classified as shear-controlled and flexure-shear-controlled, respectively. Additional information on the columns with short splices is available in Opabola and Elwood (2021).

Table H-6 Distribution of Key Parameters of the Non-ductile Columns in the Database

Parameter	Range of parameters		
	Shear-controlled	Flexure-shear	Splice-critical
Aspect ratio (a/d)	1.2 – 3.8	2.2 – 7.3	3.6 – 9.3
Longitudinal reinforcement ratio ρ_l (%)	1.3 – 3.9	1 – 3.8	1 – 3.3
Transverse reinforcement ratio ρ_t (%)	0.07 – 0.3	0.07 – 0.33	0.07 – 0.4
Stirrup spacing to effective depth (s/d)	0.5 – 1.2	0.55 – 1.2	0.5 – 1.2
Concrete compressive strength (MPa)	13.5 – 37	13 – 45	24 – 40
Axial load ratio $N/A_g f'_c$	0 – 0.5	0 – 0.6	0 – 0.33
Provided splice length $l_{s,provided}/d_b$	20	20 – 30	20 – 30

For each column in the database, information of four drift quantities was extracted from the measured force-displacement backbone, namely:

1. Elastic rotation: estimated by drawing a secant line from the origin to pass through the backbone curve at 70% of maximum lateral load (V_{max}) and made to intersect the horizontal line corresponding to V_{max} . The elastic drift would correspond to the yield rotation in a component that experienced flexural yielding.
2. Drift at initiation of LSL: estimated as the drift at which the components start suffering lateral strength loss.
3. Drift at lateral failure: defined as drift corresponding to $0.8V_{max}$.
4. Drift at axial failure: defined as the drift where the author(s) reported loss of initial axial capacity or at which the lateral resistance has degraded to zero.

Apart from force-displacement data, damage progression photos were collated for specimens where such photos are available. For more information, refer to the visual damage database presented in Appendix I.

H.4.2 Failure mode Classification

One of the initial steps in adopting the methodology presented in this Appendix is the identification of the component failure mode. For beam-column components, it is proposed that the strength-based failure mode classification procedure adopted in ASCE/SEI 41-13 (Table H-7) be adopted for beam-column components. The ASCE/SEI 41-13 failure mode classification methodology adopts the shear capacity ratio (defined as the ratio of flexural strength to undegraded shear strength) of the column. The undegraded shear strength of a column can be evaluated using ASCE/SEI 41-17 provisions (see Section 10.4.2.3.1 of ASCE/SEI 41-17). It is noteworthy that studies (e.g., Opabola and Elwood (2018)) have shown that adopting the ASCE/SEI 41-17 undegraded shear capacity equation helps provide a better failure mode prediction than adopting the ASCE/SEI 41-13 undegraded shear capacity equation.

Splice-critical columns are defined as ‘columns controlled by inadequate development or splicing along the clear height’ in ASCE/SEI 41-17. Columns can be classified as splice-critical if the maximum developable tensile stress (computed using Equation 10-1a of ASCE/SEI 41-17) is lesser than the expected yield strength of the longitudinal bars.

Table H-7 Failure mode classification according to ASCE/SEI 41-13

Shear capacity ratio	ACI 318 conforming seismic details with 135-degree hooks	Closed hoops with 90-degree hooks	Other (including lap-spliced transverse reinforcement)
$V_y/V_o \leq 0.6$	Flexure	Flexure-shear	Flexure-shear
$1.0 \geq V_y/V_o \geq 0.6$	Flexure-shear	Flexure-shear	Shear
$V_y/V_o > 1.0$	Shear	Shear	Shear

H.4.3 Defining the Deformation at Initiation of LSL

It was of interest to identify the damage state of flexure-shear- and shear-controlled columns corresponding to the deformation at initiation of LSL. Using the database presented in Appendix I, a study was carried out to identify what damage level corresponds to the deformation at initiation of LSL. From the data presented in Appendix I, a subset of shear-controlled and flexure-shear controlled columns with axial load ratio ($N/A_g f'_c$) ≤ 0.35 was collated. Columns with high axial load were not selected as it was assumed that the axial load level would make the observation of inclined crack widening more difficult, thereby introducing some bias to the study.

Based on the adopted axial load criteria, 10 shear-controlled and 11 flexure-controlled columns were selected. All selected column specimens have damage state photographs to define the onset of the critical inclined crack widening. Figure H-12 presents data on the ratio of measured drift corresponding to onset of widening of critical inclined crack to the measured drift at LSL for shear-controlled and flexure-shear controlled columns. The data presented in Figure H-12 show that the widening of the critical inclined crack starts after the drift at LSL is attained. The average ratios of measured drift corresponding to onset of widening of critical inclined crack to the measured drift at LSL for shear-controlled and flexure-shear controlled columns were 1.03 and 1.05 respectively. Based on the data presented in Figure H-12, it was concluded that the drift at LSL in shear-controlled and flexure-shear controlled columns correspond to the onset of the critical inclined crack widening.

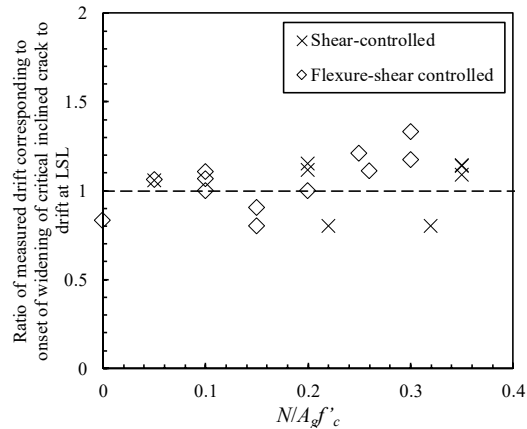


Figure H-12 Ratio of measured drift corresponding to onset of widening of critical inclined crack to the measured drift at LSL for shear-controlled and flexure-shear controlled columns versus axial load ratio.

A plot similar to Figure H-12 could not be generated for splice-critical column as there are currently no sufficient test programs with damage progression photographs.

H.4.3.1 Shear-Controlled and Splice-critical Components

Experimental results show that shear-controlled and splice-critical columns suffer significant strength degradation immediately after the peak lateral resistance is attained. The peak lateral strength corresponds to attainment of shear capacity in shear-controlled columns and lateral strength corresponding to bond strength in splice-critical columns. As earlier mentioned, given that the LSL is attained during the elastic portion of the force-displacement curve, it is reasonable to treat these components as force-controlled.

The post-earthquake assessment of shear-controlled and splice-critical components will entail comparing force demands and lateral strength capacity of the components. In this section, we propose adopting the lateral strength provisions as provided in ASCE/SEI 41-17 – i.e., Section 10.4.2.3.1 for shear-controlled columns and Section 10.3.5 for splice-critical columns.

Figure H-13 presents the adequacy of the ASCE/SEI 41-17 provisions in predicting the lateral strength of 70 shear-controlled columns (Figure H-13a) and 24 splice-critical columns (Figure H-13b). ASCE/SEI 41-17 provides a lateral strength estimate for shear-controlled columns with a median measured-to-predicted ratio of 1.1 and dispersion of 0.3. The cumulative distribution function (CDF) of the adequacy of ASCE/SEI 41-17 provisions in predicting the lateral strength of the shear-controlled columns is presented in Figure H-14a. For splice-critical columns, ASCE/SEI 41-17

recommendation provides an estimate with a median measured-to-predicted ratio of 1.1 and a coefficient of variation of 0.17 (See Figure H-14b for CDF of model error). The relatively higher adequacy of the formulation for splice-critical components may be attributed to data size. Further studies are needed to validate this.

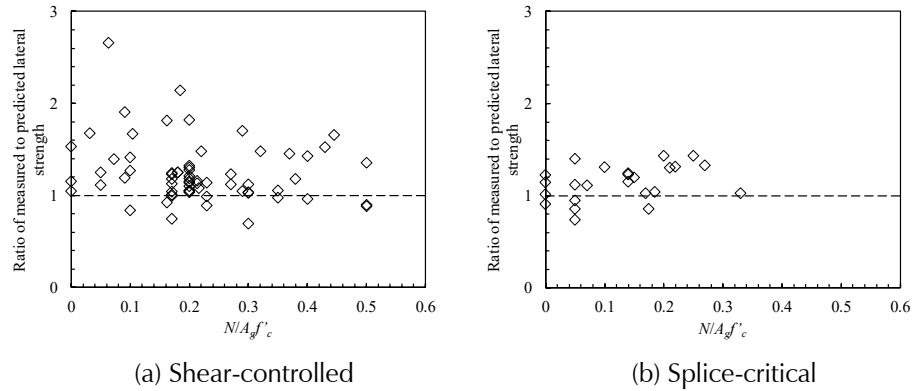


Figure H-13 Adequacy of ASCE/SEI 41-17 in predicting the lateral strength of (a) shear-controlled columns (b) Splice-critical columns in the collated database.

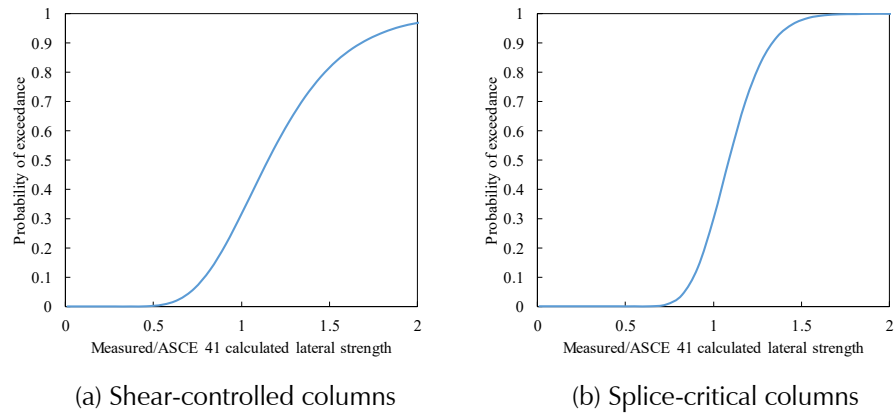


Figure H-14 Model error in predicting the lateral force at LSL for (a) shear-controlled columns (b) Splice-critical columns.

H.4.3.2 Flexure-Shear-Controlled Non-Ductile Columns

The deformation capacity at lateral failure (20% drop in lateral strength) of beam-column components in ASCE/SEI 41-17 is defined in terms of modeling parameter a which represents the plastic rotation capacity at 20% drop in lateral resistance. Following the methodology outlined in section H.3.1, this section seeks to define a multiplier x that needs to be applied to ASCE/SEI 41 modelling parameter a (See Equation (H-8)) for defining the component deformation limit corresponding to LSL (θ_{LSL}).

$$a_{ASCE41-17} = 0.042 - 0.043 \frac{N}{A_g f'_c} + 0.63 \rho_t - 0.023 \frac{V_y}{V_o} \quad (H-8)$$

Where N is the axial load, A_g is the gross cross-sectional area, f'_c is concrete strength, ρ_t is the transverse reinforcement ratio, V_y is the flexural yield strength, and V_o is the undegraded shear strength as provided in section 10.4.2.3.1 of ASCE/SEI 41-17.

For flexure-shear controlled columns, as a first step, column specimens subjected to a loading protocol in which the first cycle results in deformation demands \geq deformation at LSL (e.g., Wight 1973) were filtered out. This was done to ensure all specimens had gone through cyclic deformation demands prior to onset of loss of lateral resistance. Secondly, the dataset was separated into two bins based on axial load level – Bin I contains columns with $N/A_g f'_c < 0.30$ and Bin II contains columns with $N/A_g f'_c \geq 0.30$. This binning process recognizes the influence of axial load on seismic performance.

Also, given that the ASCE/SEI 41 column modeling parameters are provided in terms of plastic rotation, the measured deformation at LSL was also expressed in terms of plastic rotation – defined as the difference between the measured total rotation at LSL and the yield rotation of the column.

Figure H-15 presents the adequacy of the ASCE/SEI 41-17 provisions in predicting the plastic deformation at LSL for the flexure-shear controlled columns in Bins I and II. Figure H-15a compares the measured plastic deformation at LSL and computed modeling parameter a for the column dataset. Figure H-15b shows the distribution of the multiplier x to the ASCE/SEI 41-17 modeling parameter a to predict the plastic rotation at LSL for columns in Bins I and II. For Bin I, the multiplier x has a median value of 0.5 with a dispersion of 0.5. For Bin II, the multiplier x has a median value of 0.7 with a dispersion of 0.45. The difference in multipliers between Bins I and II highlights the fact that the difference between plastic rotation at LSL and plastic rotation at lateral failure is smaller in columns with high axial load – i.e., rapid strength degradation following LSL.

It is important to be conservative in defining the deformation at LSL for non-ductile columns with high axial load; hence, it was decided to adopt the multiplier for columns with low axial load for columns with high axial load – i.e., adopting a median multiplier of 0.5 (as well as the dispersion of 0.5) for flexure-shear controlled columns irrespective of axial load. As earlier discussed, non-ductile columns under high axial load should be classified as requiring inspection and further actions may be warranted before concluding that such columns have sufficient residual capacity.

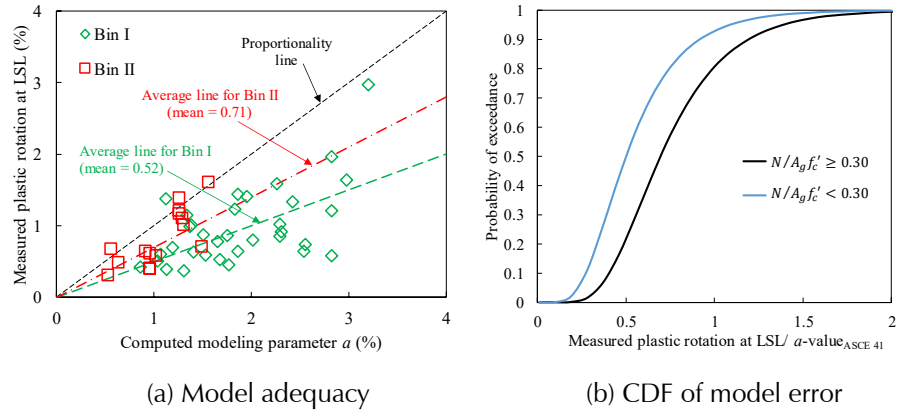


Figure H-15 Predicting the plastic rotation at LSL in flexure-shear controlled columns.

H.4.4 Proposed Inspection Trigger

H.4.4.1 Inspection Trigger for Shear-controlled and Splice-critical Columns

As previously mentioned, to avoid false negatives, the inspection trigger needs to be a lower-bound estimate with a high confidence level that there is a low probability of exceeding component deformation limit at LSL. Recall that shear-controlled and splice-critical columns are considered to be force-controlled. Hence, the inspection trigger is defined such that there is a low probability of exceeding the component peak strength.

Using the adopted methodology presented in Section H.3.2 and the proposed Equation (H-7), Table H-8 and Table H-9 present results of a parametric study, considering ground motion (β_{gm}), modeling (β_{model}) uncertainties and values of safety index Z (a function of p – the probability of exceeding V_{max}), to define a range of multipliers x_{IT} to the computed lateral strength of shear-controlled columns for the inspection trigger. For this parametric study, the computed x value of 1.1 and dispersion β_{LSL} of 0.3 were adopted for the parametric study. The average multiplier is computed as 0.45. Examples of damage state photos at an elastic force demand of $0.5V_{max}$ in shear-controlled columns are presented in Figure H-16.

As mentioned previously, V_{max} is computed using ASCE/SEI 41-17 provisions. For shear-controlled columns, V_{max} is the undegraded shear capacity of the column as defined in Section 10.4.2.3.1 of ASCE/SEI 41-17. For splice-critical columns, V_{max} is the lateral resistance corresponding to the maximum developable tensile stress in the lap splices, as defined in Section 10.3.5 of ASCE/SEI 41-17.

It is also recommended that whether the inspection trigger is exceeded or not, it may be worthwhile to inspect shear-controlled columns with high axial load ($P/A_g f'_c > 0.3$) (See section H.3.4).

Table H-8 Selecting a Multiplier χ_{IT} to Computed Lateral Strength for Assessing the Inspection Trigger of Shear-controlled Columns Based on a 5% Probability of Exceeding the Undegraded Shear Strength (i.e., $Z = 1.645$)

β_{model}	β_{gm}							
	0.0	0.1	0.2	0.3	0.4	0.5	0.6	0.7
0.1	0.65	0.64	0.59	0.54	0.48	0.42	0.36	0.31
0.15	0.63	0.62	0.58	0.52	0.47	0.41	0.36	0.31
0.2	0.61	0.59	0.56	0.51	0.45	0.40	0.35	0.30
0.25	0.58	0.57	0.53	0.49	0.44	0.39	0.34	0.29
0.3	0.55	0.54	0.51	0.47	0.42	0.37	0.33	0.29
0.35	0.52	0.51	0.48	0.45	0.40	0.36	0.32	0.28
0.4	0.48	0.48	0.45	0.42	0.38	0.34	0.30	0.27
Average	0.57	0.56	0.53	0.48	0.43	0.38	0.34	0.29
0.45								

Table H-9 Selecting a Multiplier χ_{IT} to Computed Lateral Strength for Assessing the Inspection Trigger of Shear-controlled Columns Based on a 10% Probability of Exceeding the Undegraded Shear Strength (i.e., $Z = 1.28$)

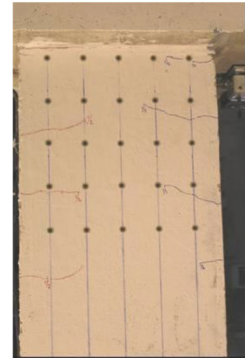
β_{model}	β_{gm}							
	0.0	0.1	0.2	0.3	0.4	0.5	0.6	0.7
0.1	0.73	0.72	0.68	0.63	0.57	0.52	0.46	0.41
0.15	0.72	0.70	0.67	0.62	0.56	0.51	0.46	0.41
0.2	0.69	0.68	0.65	0.60	0.55	0.50	0.45	0.40
0.25	0.67	0.66	0.63	0.59	0.54	0.49	0.44	0.39
0.3	0.64	0.63	0.60	0.57	0.52	0.48	0.43	0.39
0.35	0.61	0.60	0.58	0.54	0.50	0.46	0.42	0.38
0.4	0.58	0.57	0.55	0.52	0.48	0.44	0.40	0.37
Average	0.66	0.65	0.62	0.58	0.53	0.48	0.44	0.39
0.55								



(a) Tran (2010)



(b) Henkhaus et al. (2013)



(c) Wood (2009)

Figure H-16 Examples of damage photos at force demands $\sim 0.5V_{max}$ in the shear-controlled column damage database.

Table H-10 and Table H-11 present a range of multipliers to the lateral strength of splice-critical columns for the inspection trigger. For splice-critical columns, the computed x value of 0.5 and dispersion β_{LSL} of 0.5 were adopted for the parametric study. The average multiplier is computed as 0.53. Splice-critical columns under high axial load ($P/A_g f'_c > 0.3$), inspection processes are recommended, whether the inspection trigger is exceeded or not. It is noteworthy that the dispersion β_{LSL} of 0.17 for splice-critical columns was derived based on a limited dataset. If a higher level of conservatism is desired, a dispersion β_{LSL} of 0.3 (similar to shear-controlled columns) can be adopted. In such a case, the multipliers in Table H-8 and Table H-9 can be adopted for splice-critical columns.

Table H-10 Selecting a Multiplier x_{IT} to Computed Lateral Strength for Assessing the Inspection Trigger of Splice-critical Columns Based on a 5% Probability of Exceeding the Lateral Strength Corresponding to the Maximum Developable Tensile Stress in the Lap Splices (i.e., $Z = 1.645$)

β_{model}	β_{gm}							
	0.0	0.1	0.2	0.3	0.4	0.5	0.6	0.7
0.1	0.80	0.76	0.69	0.61	0.53	0.45	0.39	0.33
0.15	0.76	0.73	0.67	0.59	0.52	0.45	0.38	0.33
0.2	0.71	0.69	0.64	0.57	0.50	0.43	0.37	0.32
0.25	0.67	0.65	0.61	0.55	0.48	0.42	0.36	0.31
0.3	0.62	0.61	0.57	0.52	0.46	0.41	0.35	0.30
0.35	0.58	0.57	0.54	0.49	0.44	0.39	0.34	0.29
0.4	0.54	0.53	0.50	0.46	0.42	0.37	0.33	0.28
Average	0.67	0.65	0.60	0.54	0.48	0.42	0.36	0.31
	0.50							

Table H-11 Selecting a Multiplier x_{IT} to Computed Lateral Strength for Assessing the Inspection Trigger of Splice-critical Columns Based on a 10% Probability of Exceeding the Lateral Strength Corresponding to the Maximum Developable Tensile Stress in the Lap Splices (i.e., $Z = 1.28$)

β_{model}	β_{gm}							
	0.0	0.1	0.2	0.3	0.4	0.5	0.6	0.7
0.1	0.85	0.83	0.77	0.69	0.62	0.55	0.49	0.43
0.15	0.82	0.80	0.75	0.68	0.61	0.54	0.48	0.43
0.2	0.79	0.77	0.72	0.66	0.60	0.53	0.48	0.42
0.25	0.75	0.73	0.69	0.64	0.58	0.52	0.47	0.41
0.3	0.71	0.69	0.66	0.61	0.56	0.51	0.45	0.41
0.35	0.67	0.66	0.63	0.59	0.54	0.49	0.44	0.39
0.4	0.63	0.62	0.60	0.56	0.52	0.47	0.43	0.38
Average	0.75	0.73	0.69	0.63	0.57	0.52	0.46	0.41
	0.60							

H.4.4.2 Inspection Trigger for Flexure-shear Controlled Non-ductile Columns

The parametric study results for flexure-shear controlled columns are presented in Table H-12 and Table H-13. For flexure-shear controlled columns, the computed x value of 0.5 and dispersion β_{LSL} of 0.5 were adopted for the parametric study. As shown in Table H-12, adopting a Z -value of

1.645 (i.e., probability of exceeding $\theta_{LSL} p = 0.05$) results in a multiplier to modeling parameter a with an average value of 0.16. It is noteworthy that the immediate occupancy (IO) limit in ASCE/SEI 41-17 is defined as $0.15a$. There is a 30% increase in the multiplier to 0.21 for a Z-value of 1.28 (i.e., $p = 0.10$).

A multiplier of 0.15 is proposed as an inspection trigger for flexure-shear controlled non-ductile columns. Similar to ASCE/SEI 41 IO provisions for columns, it is recommended that an upper plastic rotation limit of 0.5% be adopted for the inspection trigger (i.e., $0.15a \leq 0.5\%$).

If a higher level of conservatism is required, a Z-value larger than those adopted in Table H-12 and Table H-13 can be applied. As the Z-value increases, the multiplier tends to zero (a case where the repair trigger of flexure-shear controlled columns corresponds to the computed yield rotation).

Table H-12 Selecting a Multiplier x_{IT} to Computed Modelling Parameter a for Assessing the Inspection Trigger of Flexure-shear-controlled Columns Based on a 5% Probability of Exceedance (i.e., $Z = 1.645$)

β_{model}	β_{gm}							
	0.0	0.1	0.2	0.3	0.4	0.5	0.6	0.7
0.1	0.22	0.21	0.20	0.19	0.17	0.15	0.14	0.12
0.15	0.21	0.21	0.20	0.19	0.17	0.15	0.14	0.12
0.2	0.21	0.20	0.19	0.18	0.17	0.15	0.13	0.12
0.25	0.20	0.20	0.19	0.18	0.16	0.15	0.13	0.11
0.3	0.19	0.19	0.18	0.17	0.16	0.14	0.13	0.11
0.35	0.18	0.18	0.17	0.16	0.15	0.14	0.12	0.11
0.4	0.17	0.17	0.17	0.16	0.14	0.13	0.12	0.11
Average	0.20	0.19	0.19	0.17	0.16	0.14	0.13	0.11
	0.16							

Table H-13 Selecting a Multiplier x_{IT} to Computed Modelling Parameter a for Assessing the Inspection Trigger of Flexure-shear-controlled Columns Based on a 10% Probability of Exceedance (i.e., $Z = 1.28$)

β_{model}	β_{gm}							
	0.0	0.1	0.2	0.3	0.4	0.5	0.6	0.7
0.1	0.26	0.26	0.25	0.23	0.22	0.20	0.18	0.17
0.15	0.26	0.25	0.24	0.23	0.22	0.20	0.18	0.16
0.2	0.25	0.25	0.24	0.23	0.21	0.20	0.18	0.16
0.25	0.24	0.24	0.23	0.22	0.21	0.19	0.18	0.16
0.3	0.24	0.23	0.23	0.22	0.20	0.19	0.17	0.16
0.35	0.23	0.23	0.22	0.21	0.20	0.18	0.17	0.15
0.4	0.22	0.22	0.21	0.20	0.19	0.18	0.16	0.15
Average	0.24	0.24	0.23	0.22	0.21	0.19	0.17	0.16
	0.21							

H.4.5 Repair Trigger

The component deformation limits corresponding to the repair trigger are proposed to correspond to the median estimate of the deformation at the initiation of LSL (i.e., initiation of critical diagonal failure plane), which corresponds to a plastic rotation capacity of $0.5a$ for flexure-shear controlled columns. It is noteworthy that $0.5a$ corresponds to approximately 3 times the average component deformation limit for inspection trigger (i.e., $0.16a$).

The damage control (DC) performance level is defined in ASCE/SEI 41-17 to correspond to a post-earthquake damage state defined to be halfway between life safety (LS) and immediate occupancy (where life safety corresponds to the post-earthquake damage state where components are damaged but retain a margin of safety against onset of partial or total collapse). If the definition of the DC limit state is assumed to represent the limit where a repairable level of damage is acceptable, DC may be assumed to be equivalent to the repair trigger. Hence, it was considered interesting to see what deformation limit the DC performance level correspond to.

Given that the ASCE/SEI 41-17 LS acceptance criteria for columns are provided in terms of modeling parameter b while the IO acceptance criteria are provided in terms of a , it is not a straightforward process to derive an expression for the DC acceptance criteria in terms of a . However, Opabola and Elwood (2018) proposed $0.75a$ as an alternative LS acceptance criteria for non-ductile columns. Adopting this value, DC would correspond to

$0.5(0.15a + 0.75a) = 0.45a$ (corresponding to 3 times IO) – which is close to the proposed repair trigger.

Shear-controlled and splice-critical columns should be treated as force-controlled. The component strength limit corresponding to repair trigger for shear-controlled and splice-critical columns is defined as the undegraded shear capacity and the lateral resistance corresponding to the maximum developable tensile stress in the lap splices respectively.

H.5 Conforming Flexure-Controlled Walls

H.5.1 Description of Database

A comprehensive database (Abdullah 2019; Abdullah and Wallace 2019), which stores data on more than 1100 reinforced concrete (RC) wall tests reported in the literature, was utilized to obtain a dataset of conforming flexure-controlled walls. The reported information includes three major clusters of data: (1) information about the test specimen, test setup, and axial and lateral loading protocols; (2) computed data, e.g., moment-curvature relationships (depth of neutral axis, c , nominal moment capacity, M_n , moment corresponding to first yield of longitudinal reinforcement, M_y , curvature at M_n , ϕ_n , curvature at M_y , ϕ_y) and wall shear strength according to ACI 318-19; and (3) test results, e.g., backbone relations and failure modes. A significant portion of the database is dedicated to the reinforcement details in the web and boundary elements. Database information related to the objectives of this study are briefly presented below; however, detailed information about the database can be found elsewhere (Abdullah 2019; Abdullah and Wallace 2019).

For buildings assigned to Seismic Design Category D, E, and F, design of RC structural walls is currently governed by the requirements of ASCE/SEI 7-16 and ACI 318-19, which includes provisions for structural walls with special boundary elements (SBE) that satisfy ACI 318-19 §18.10.6.4. Detailing requirements for walls with SBEs have changed over the years and are likely to keep changing in the future; therefore, the database was filtered using the following criteria to obtain a dataset of ACI 318-19 code- or nearly code-compliant walls, which are the focus of this study. Since the recommendations provided herein are applied for post-earthquake assessment of buildings designed based on prior version of ACI 318, as well as the current version, the selected detailing criteria below are less restrictive than the detailing requirements of ACI 318-19 §18.10.6.4 to cover walls that are compliant to previous version of ACI 318 since 1983:

1. General criteria:

- a. Flexure-controlled walls, i.e., ratio of nominal shear strength to shear associated with nominal moment capacity, $V_n/V_{@Mn} > 1.0$,
 - b. Walls with various cross-sections (planar, T-shaped, H-shaped, Barbell-shaped, half barbell-shaped),
 - c. Walls tested under quasi-static, reversed cyclic loading,
 - d. Walls with measured concrete compressive strength, $f'_c \geq 21$ MPa [3 ksi],
 - e. Walls with ratio of measured tensile-to-yield strength for boundary longitudinal reinforcement, $f_u/f_y \geq 1.2$, and
 - f. Walls with web thickness, $t_w \geq 80$ mm [3.15 in.],
2. Detailing criteria:
- a. A minimum of two curtains of web vertical and horizontal reinforcement,
 - b. Ratio of provided-to-required (per ACI 318-19 Eq 18.10.6.4b) area of boundary transverse reinforcement, $A_{sh,provided}/A_{sh,required} \geq 0.7$,
 - c. Ratio of vertical spacing of boundary transverse reinforcement to minimum diameter of longitudinal boundary reinforcement, $s/d_b < 8.0$, and
 - d. Centerline distance between laterally supported boundary longitudinal bars, h_x , between 25 mm [1.0 in.] and 240 mm [9.4 in.].

Based on the above selected filters, a total of 188 wall tests (hereafter referred to as conforming dataset) were identified. Histograms for various dataset parameters for the 188 tests are shown in Figure H-17, where $P/A_g f'_c$ is the compressive axial load normalized by the measured concrete compressive strength (f'_c) and gross concrete area (A_g), and M/Vl_w is the ratio of base moment-to-base shear normalized by wall length (l_w). Analysis of reported failure modes of about 1000 wall tests by Abdullah (2019) indicated that the flexure- and shear-controlled walls have a nominal shear-to-flexure strength ratio ($V_n/V_{@Mn}$) > 1.0 and < 1.0 , respectively, whereas walls with failure modes reported as flexure-shear are mainly scattered between $0.7 < V_n/V_{@Mn} < 1.3$. A limit of 21 MPa [3 ksi] was specified on f'_c in accordance with requirements of ACI 318-19 §18.2.5 for conforming seismic systems. At least two curtains of web reinforcement were specified to be consistent with ACI 318-19 §18.10.2.2. Walls with t_w less than 88 mm [3.5 in.] were excluded because use of two curtains of web reinforcement along with realistic concrete cover is not practical in such thin walls. The limit on ratio f_u/f_y is slightly less restrictive than the limit of 1.25 specified in ACI 318-19

§20.2.2.5. The specified limits on $s/d_b \leq 8.0$ and $A_{sh,provided}/A_{sh,required}$ (A_{sh} required by ACI 318-19 Eq 18.10.6.4b) ≥ 0.7 are slightly less restrictive than the current limits in ACI 318-19 §18.10.6.4 of 6.0 and 1.0, respectively.

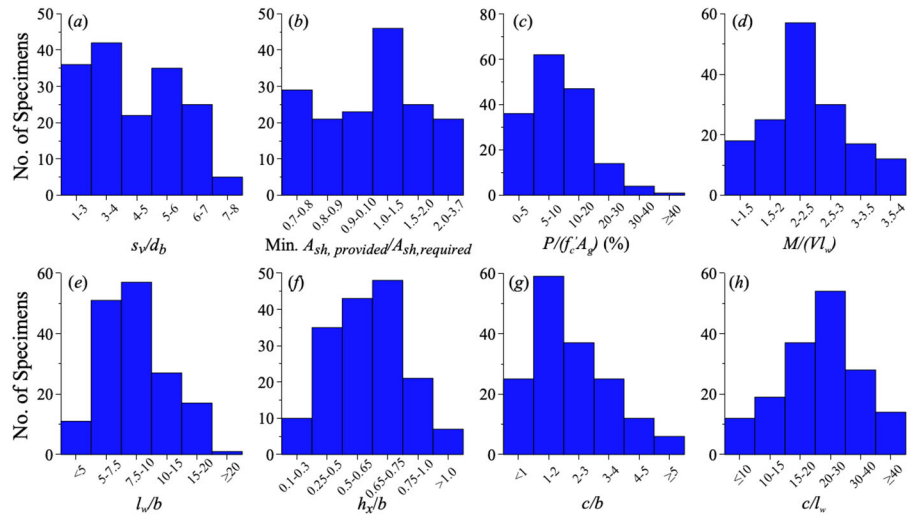


Figure H-17 Histograms of the first dataset (188 tests) for walls with conforming detailing.

The database includes backbone relations (e.g., base shear-total top displacement), consisting of seven points (origin, cracking, general yielding, peak, ultimate, residual, and collapse), as shown in Figure H-18. Abdullah (2019) describes the approach used to define each point on the backbone curve from experimental load-deformation relationships. In addition to backbones and failure mode information, the database includes reported deformation at key damage states such as initiation of concrete cover spalling, initiation longitudinal bar buckling, and longitudinal bar fracture, if such information was reported in the reference document. Out of the 188 wall tests in the conforming dataset, 62 walls had reported deformation on at least cover spalling and bar buckling. This smaller subset (62 walls) was closely studied for the recommendations proposed herein, especially identifying at deformation capacity at initiation of LSL (θ_{LSL}).

Additionally, the walls in the conforming dataset are tested under quasi-static, reversed cyclic loading protocols. Out of the 62 wall tests in the smaller dataset, 38 walls were tested using loading protocols that contained three repeated cycles at each load/deformation demand, 23 walls with two repeated cycles at each load/deformation demand, and only one wall with one cycle at each load/deformation demand.

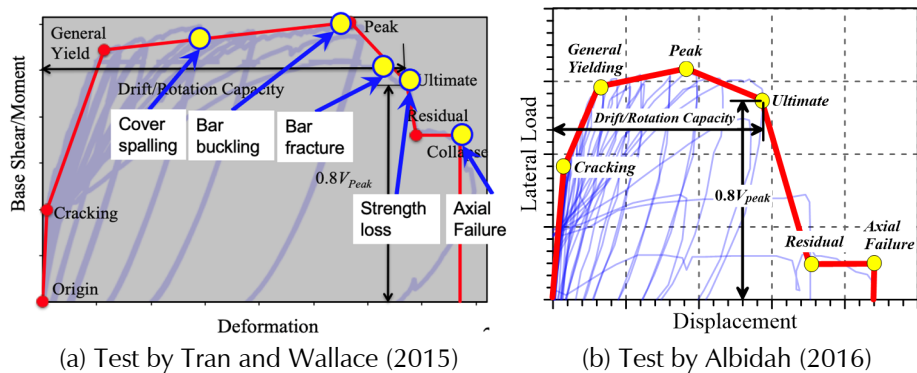


Figure H-18 Example wall backbone curve contained in UCLA-RCWalls database.

As noted previously, ASCE/SEI 41-17 nonlinear deformation-based modeling parameters for structural walls are given as plastic hinge rotations (i.e., Parameters a and b corresponding to plastic rotation at lateral and axial failure, respectively). Recent updates of these provisions (planned to be adopted in ACI 369-23 and ASCE/SEI 41-23), however, use total hinge rotation capacities (hereafter referred to simply as rotation capacity) for the deformation-based modeling parameters of flexure-controlled walls (Figure H-1b), which include both the elastic and plastic deformations contributed by the hinge region (Abdullah, 2019). This is because, by using total hinge rotation, modeling parameters are not sensitive to approaches (or assumptions) used to calculate yield rotation, θ_y , are consistent with the total drift ratio or chord rotation used to define modeling parameters for shear-controlled walls and coupling beams, respectively, and can be converted to strain limits, which is convenient for fiber models that are becoming increasingly popular in engineering practice.

As will be shown in the next section, the proposed inspection and repair triggers are expressed as fractions of ASCE/SEI 41-23 modeling parameter d (Figure H-1b), corresponding to 20% lateral strength loss from peak strength (hereafter called $d_{ASCE\ 41}$). Therefore, the experimental drift capacity values of the dataset are converted to total hinge rotation capacities. The approach used to convert drift ratios (or top displacements) to total hinge rotations is described by Abdullah (2019), which is the same approach used to develop the updated ASCE/SEI 41-23 modeling parameters. Additionally, fragility curves are developed for hinge rotation capacities at each key damage states normalized by $d_{ASCE\ 41}$, as shown in Figure H-19. It is noted that only half of the walls in the reduced dataset had reported bar fracture because this information was either not reported or the wall did not experience longitudinal bar fracture and failed due to out-of-plane instability or, in a rare case, due to crushing of concrete in the web region next to the boundary

elements (common in barbell or flanged walls). The statistics (means and standard deviations, Beta value) for rotations at each key damage state normalized by $d_{ASCE\ 41}$ are presented in Table H-14. Results presented in Figure H-1 and Table H-14 will later in Sections H.5.3 and H.5.4 be used to propose triggers for inspection and repair using the methodology described previously. The ASCE 41-23 models for Parameter d for conforming flexure-controlled walls are compared with experimental data in Figure H-20. Further details can be found elsewhere (Abdullah, 2019).

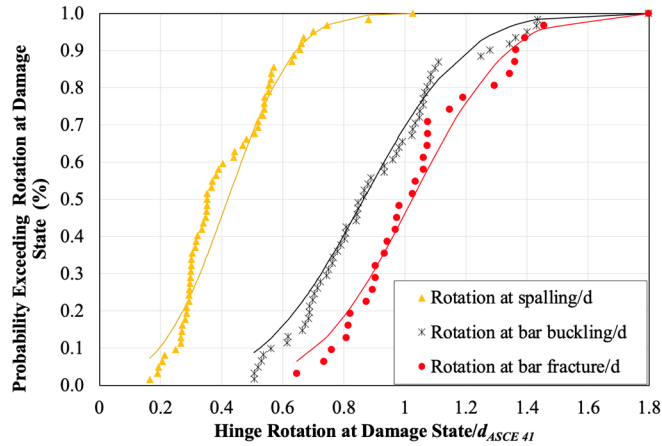


Figure H-19 Fragility curves for key damage states.

Table H-14 Statistics for rotation at key damage states of conforming flexure-controlled walls as fractions of $d_{ASCE\ 41}$

Damage State	Mean	Median	Standard Deviation
Cover Spalling	0.42	0.35	0.18
Bar Buckling	0.91	0.86	0.27
Bar Fracture	1.05	1.02	0.25

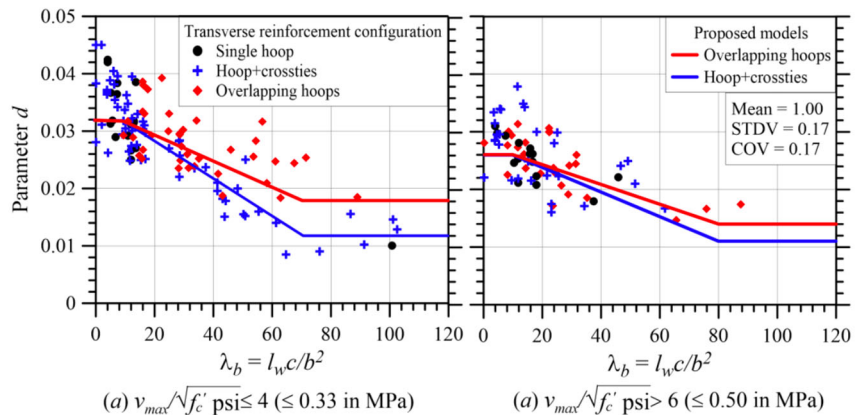


Figure H-20 Comparison of data and Proposed ASCE 41-23 models for Parameter d for conforming flexure-controlled walls (Note: the statistics shown are for the ratios of predicted-to-experimental values for the entire dataset).

H.5.2 Deformation at initiation of LSL for conforming flexure-controlled walls

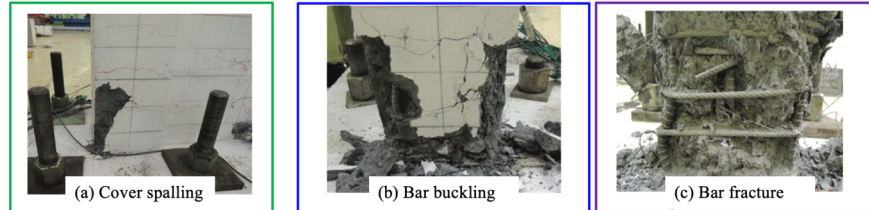
In this subsection, damage states typical of conforming flexure-controlled walls, as well as results from the conforming dataset, are reviewed to identify the rotation capacity at initiation of LSL, which will be used to propose inspection and repair triggers in the subsequent subsections.

For conforming flexure-controlled walls subjected to gradual increase of cyclic demands, the damage sequence typically involves:

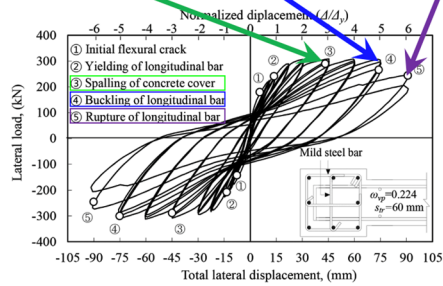
- a. Formation of horizontal cracks initiating from the extreme edges of the wall with or without diagonal (tension) shear cracks in the web,
- b. Sequential yielding of longitudinal bars till the effective yield strength of the wall is reached,
- c. Spalling of concrete cover at the extreme fibers of the wall (boundary elements),
- d. Buckling of extreme longitudinal bars in the boundaries, resulting in initiation of lateral strength loss (LSL),
- e. Fracture of buckled longitudinal bars combined with concrete core crushing, opening or fracture of hoops and crossties, or local instability, leading to significant loss of lateral strength (at least by 20%). In walls with nominal shear stress exceeding $6\sqrt{f'_c}$ (in psi), loss of lateral strength is likely due to crushing of the web region adjacent to the boundary elements,
- f. Gradual loss of lateral strength as a result of sequential fracture of longitudinal bars and concrete crushing for walls with low compression demands (depth of neutral axial/width of flexural compression zone, c/b , < 2) and squat cross-sections ($l_w/b \sim \leq 10$), or crushing of concrete or out-of-plane instability across the entire length of the wall for walls with significant compression demands and slender cross-sections (c/b , > 4 and $l_w/b > 15$), leading to abrupt loss of axial load-carrying capacity.

Examples of some of these damage states are presented in Figure H-21, which includes walls with a wide range of characteristics (low and high compression demands; squat and slender cross-sections). These figures suggest that initiation of LSL in conforming flexure-controlled walls is associated with buckling of longitudinal bars. Once longitudinal bars buckle, the concrete core loses part of the confining pressure and the depth of neutral axis shifts inward, leading to a smaller moment arm and thus reduction in moment capacity. As thus, longitudinal bar buckling can be considered as the damage state beyond which the residual capacity of the wall (in terms of

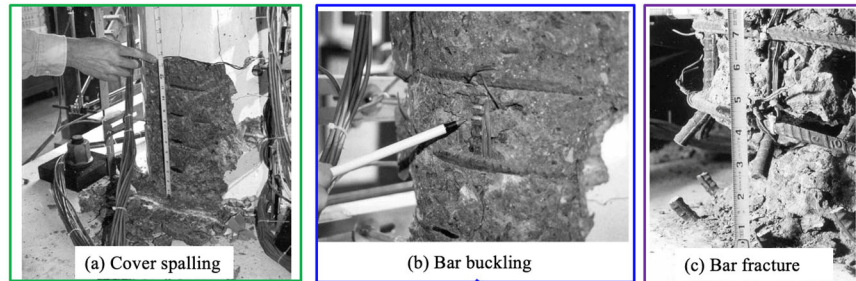
strength and deformation capacity) is compromised, and that structural repair might be needed to restore the structural characteristic of the wall for future events. Further discussion on rotation capacity at initiation of LSL is given below based on review of limited test data; however, a more detailed discussion on the damage states and damage photos of conforming flexure-controlled walls are presented in Appendix I.



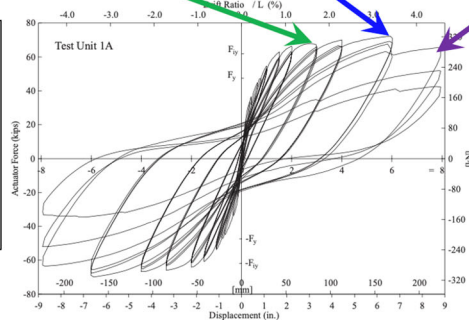
Note: $\frac{l_w c}{b^2} \approx 4$
 → Wall with low compression demands and squat cross-section (barbell-shaped wall)



(a) Mun et al. (2016)



Note: $\frac{l_w c}{b^2} \approx 6$
 → Wall with low compression demands and squat cross-section (barbell-shaped wall)



(b) Hines et al. (2002)

Figure H-21 Examples of damage states of conforming flexure-controlled walls.

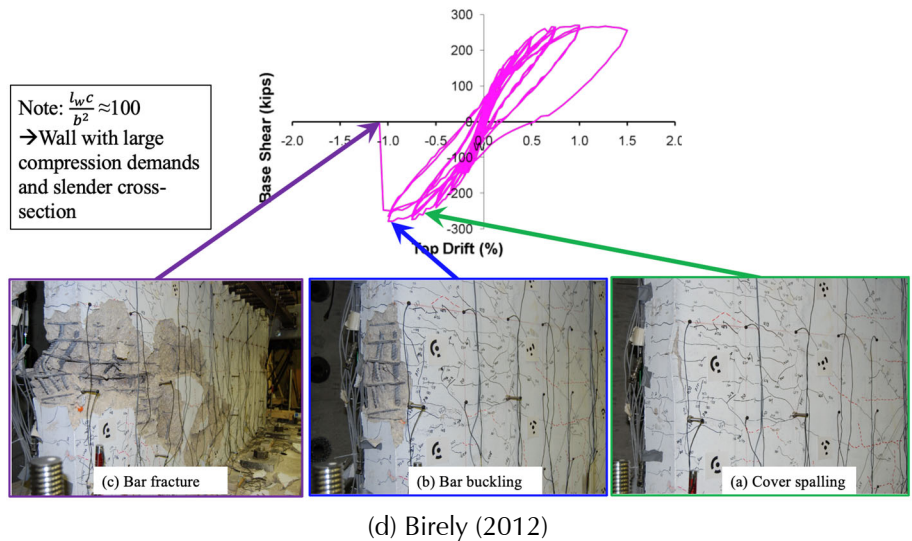
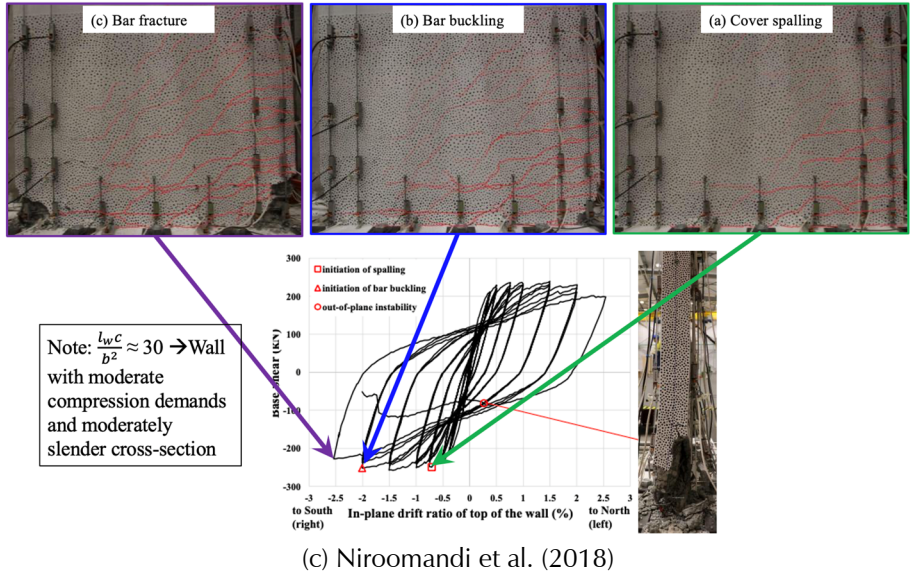


Figure H-21 Examples of damage states of conforming flexure-controlled walls (continued).

Figure H-22 compares the rotation capacities of the reduced dataset of 62 wall tests at three key damage states and indicates that rotation capacities for all three damage states vary significantly (by a factor of 2.0 to 4.0), although all the walls are fully or nearly code-compliant. Additionally, there is significant buffer zone (on average about 1.0% rotation) between occurrence of initiation of cover spalling and initiation of bar buckling, indicating that it is unlikely for cover spalling and bar buckling damage states to happen simultaneously. As was shown in Table H-14, the median values of rotation at cover spalling and bar buckling normalized by $d_{ASCE 41}$ are 0.35 and 0.86, respectively, indicating that on average rotation at bar buckling is more than twice the rotation at cover spalling. This suggests that use of cover spalling

as the component deformation limit is very conservative. Figure H-22 and Table H-14 also indicate that there is only slight reserve rotation capacity (buffer zone) between bar buckling and bar fracture (ratio of median values of rotation at bar buckling to bar fracture ≈ 0.86), and that fracture of extreme layer of longitudinal bars results in roughly 20% lateral strength loss, which is typically defined as lateral failure (ratio of median values of rotation at bar fracture to lateral failure ≈ 1.0). These results support the conclusion of considering the damage state of longitudinal bar buckling as the component deformation limit for conforming flexure-controlled walls, which is used to propose inspection and repair triggers in the following subsections.

Lastly, Figure H-22 indicates that there is a significant correlation between rotation capacity and a slenderness parameter, $(l_w/b)(c/b) = l_w c/b^2$, where l_w is the length of the wall, c is the depth of neutral axial corresponding to a concrete compressive strain of 0.003, and b is the width of the flexural compression zone. This parameter provides an efficient means to account for the slenderness of the cross section (l_w/b) and the slenderness of the flexural compression zone of the cross section (c/b) on the deformation capacity of conforming flexure-controlled walls (Abdullah and Wallace, 2019; 2020). Walls with values of $l_w c/b^2$ lower than 10 tend to be flexure-tension controlled and generally have large deformation capacities (e.g., Figure H-21a,b), whereas walls with values of $l_w c/b^2$ exceeding 70 (slender cross-section and large compression zone) tend to be flexure-compression controlled and generally have low deformation capacities and simultaneous occurrence of lateral and axial failures (e.g., Figure H-21 d) (Abdullah and Wallace, 2021), suggesting that these walls could be considered as components always requiring inspection, as described in Section H.3.4. Additional discussion on the impact of parameter $l_w c/b^2$ is given in Appendix I, where this parameter can be used to select wall tests similar to an actual wall in a building. Further review of the data revealed that rotation at initiation of bar buckling is moderately impacted by the longitudinal bar slenderness ratio, s/d_b , which ranges from 2.5 to 8.0 in the reduced dataset.

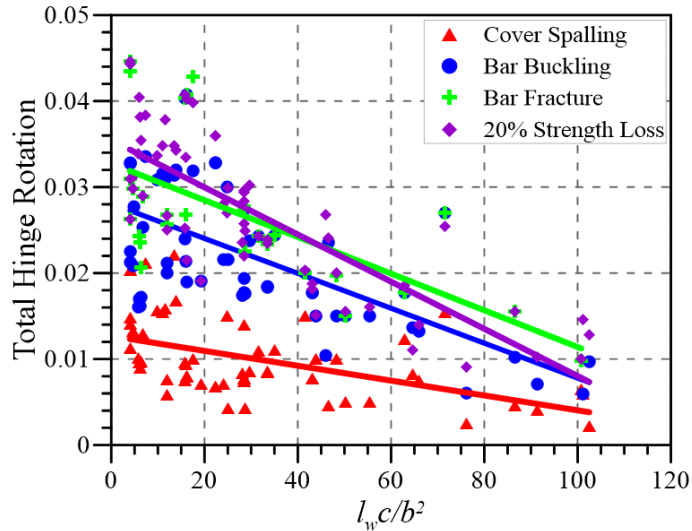


Figure H-22 Comparison of rotation capacity of the dataset at key damage states.

H.5.3 Inspection Trigger

As discussed previously, the purpose of the inspection trigger is to help the engineer identify locations that may have potentially sustained structural damage for visual inspection. Therefore, it is important that this trigger is developed such that there is a very low likelihood of missing damaged components.

In accordance with the proposed methodology in Section H.3.2 and the capacity uncertainty ($\beta_{LSL} = 0.27$) reported in Table H-14, a parametric study was carried out to determine the range of multipliers on $d_{ASCE 41}$ for inspection trigger of code-conforming flexure-controlled walls. Table H-15 and Table H-16 present the results of the parametric study for 5% and 10% probabilities of exceedance, respectively. It can be seen that, depending on the variability in the model and the ground motion, the multipliers between the two tables range from 0.23 to 0.59, with average values of 0.36 and 0.44 for 5% and 10% probabilities of exceedance, respectively. Therefore, an inspection trigger of $0.4d_{ASCE 41}$ is proposed for conforming flexure-controlled walls.

Figure H-23 and Figure H-24 indicate that an inspection trigger of $0.4d_{ASCE 41}$ roughly corresponds to a median value of rotation at cover spalling, which confirms the rationale of the approach used to select the inspection trigger. That is, when there is 50% probability that cover spalling has occurred, visual inspection should be conducted to confirm whether the element has sustained structural damage or not.

In the updated nonlinear acceptance criteria for flexure-controlled walls in ASCE 41-23, Immediate Occupancy (IO) performance objective is defined

as the sum of elastic hinge rotation and 10% of the inelastic hinge rotation (i.e., $IO = \theta_y + 0.1(d - \theta_y)$). For conforming flexure-controlled walls, θ_y typically ranges from 0.3% to 0.4%. Assuming $\theta_y \approx 0.35\%$, $IO \approx 0.4\%$ to 0.64% rotation and ≈ 0.2 to $0.4 d_{ASCE 41}$. Thus, the proposed inspection trigger ($0.4d_{ASCE 41}$) is roughly 1 to 2 times IO, as can be seen in Figure H-24.

Table H-15 Selecting a Multiplier χ_{IT} to Computed Modelling Parameter d for Assessing the Inspection Trigger for Code Conforming Flexure-controlled Walls Based on a 5% Probability of Exceedance (i.e., $Z = 1.645$)

β_{model}	β_{gm}							
	0.0	0.1	0.2	0.3	0.4	0.5	0.6	0.7
0.1	0.54	0.52	0.48	0.43	0.38	0.33	0.29	0.25
0.15	0.52	0.50	0.47	0.42	0.37	0.33	0.28	0.24
0.2	0.49	0.48	0.45	0.41	0.36	0.32	0.28	0.24
0.25	0.47	0.46	0.43	0.39	0.35	0.31	0.27	0.23
0.3	0.44	0.43	0.41	0.38	0.34	0.30	0.26	0.23
0.35	0.42	0.41	0.39	0.36	0.32	0.29	0.25	0.22
0.4	0.39	0.38	0.36	0.34	0.31	0.27	0.24	0.21
Average	0.47	0.46	0.43	0.39	0.35	0.31	0.27	0.23
	0.36							

Table H-16 Selecting a Multiplier x_{IT} to Computed Modelling Parameter d for Assessing the Inspection Trigger for Code Conforming Flexure-controlled Walls Based on a 10% Probability of Exceedance (i.e., $Z = 1.28$)

β_{model}	β_{gm}							
	0.0	0.1	0.2	0.3	0.4	0.5	0.6	0.7
0.1	0.59	0.58	0.55	0.51	0.46	0.41	0.37	0.33
0.15	0.58	0.57	0.54	0.50	0.45	0.41	0.36	0.32
0.2	0.56	0.55	0.52	0.48	0.44	0.40	0.36	0.32
0.25	0.54	0.53	0.50	0.47	0.43	0.39	0.35	0.31
0.3	0.51	0.51	0.48	0.45	0.42	0.38	0.34	0.31
0.35	0.49	0.48	0.46	0.43	0.40	0.37	0.33	0.30
0.4	0.46	0.46	0.44	0.42	0.39	0.35	0.32	0.29
Average	0.53	0.52	0.50	0.46	0.43	0.39	0.35	0.31
	0.44							

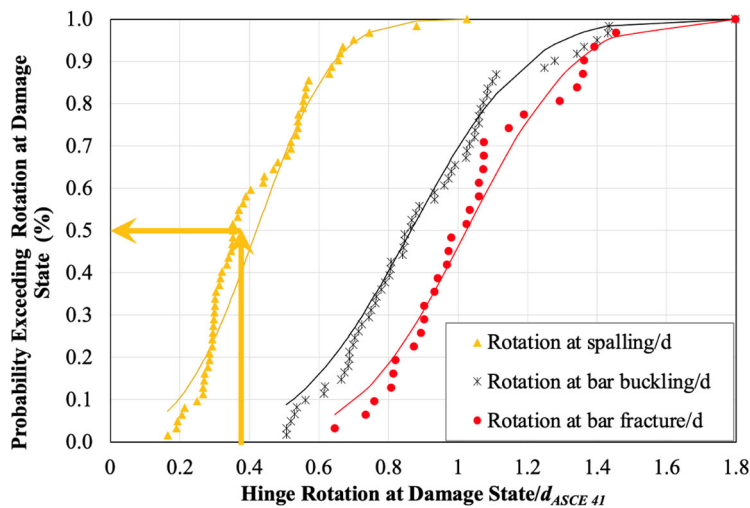


Figure H-23 Fragility curves for key damage states-Inspection trigger roughly corresponds to median value of rotation at cover spalling.

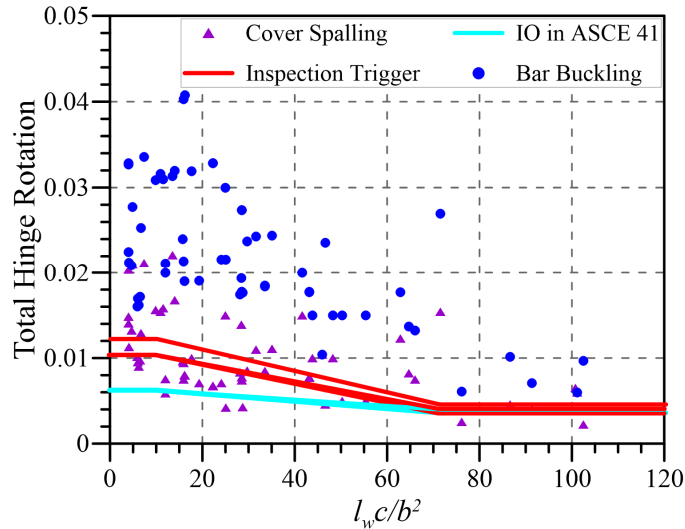


Figure H-24 Comparison of proposed Inspection Trigger with rotation capacity data at cover spalling and bar buckling and with IO performance objective in ASCE 41-23.

H.5.4 Repair Trigger

As discussed previously, the purpose of the repair trigger is to identify damaged components that need structural repair and to finetune the analytical model to reliably predict demands and damage. For conforming flexure-controlled walls, longitudinal bar buckling (initiation of LSL) is the damage state that requires structural repair because, as noted previously, at demands beyond deformation at bar buckling, walls have little residual capacity left before reaching lateral failure. Therefore, this trigger is defined as the median value of hinge rotation at bar buckling, i.e., 50% probability of reaching initiation of LSL. If repair is triggered for a wall critical section, it is confirmed by visual inspection (per Appendix I) before repair is carried out.

Figure H-25 and Table H-14 show that the median value of rotation at bar buckling corresponds to a repair trigger of $0.86 d_{ASCE\ 41}$. To account for the possibility of bar buckling occurring prior to the reported observation (i.e., buckled bars being concealed by split but un-spalled concrete cover), a slightly smaller multiplier for repair trigger, i.e., $0.8 d_{ASCE\ 41}$, is proposed. Figure H-25 also shows that median value of rotation at bar buckling corresponds to roughly 25% probability of bars fracturing and almost 100% probability of cover spalling.

The Life Safety (LS) performance objective in ASCE/SEI 41-23 is defined as $0.75 e_{ASCE\ 41}$, which is roughly equal to $0.9 d_{ASCE\ 41}$, resulting in the repair trigger ($0.8 d_{ASCE\ 41}$) being equal to about 0.9 times LS. Figure H-26

compares the proposed repair trigger with the rotation capacity data of the reduced dataset and LS performance objective.

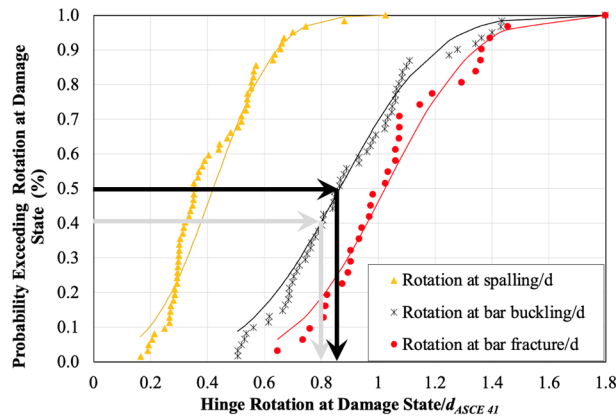


Figure H-25 Fragility curves for key damage states-identifying repair trigger as median value of rotation at bar buckling.

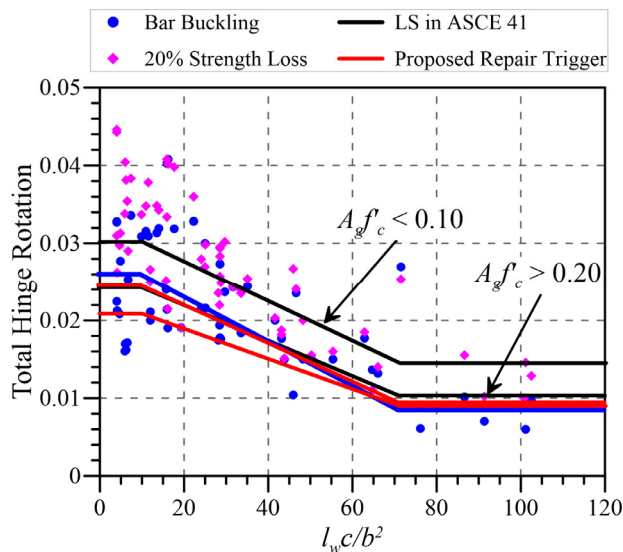


Figure H-26 Comparison of proposed Repair Trigger with rotation capacity data at bar buckling and 20% LSL and with LS performance objective in ASCE 41-23.

H.6 Conclusions and Recommendations

Based on the results presented in this appendix, the following conclusions can be drawn with regards to the impact of loading protocol on the behavior of RC components and proposed triggers for inspection and repair.

H.6.1 Impact of Loading Protocol on Residual Capacity of Concrete Components

1. Provided that the deformation at initiation of lateral strength loss (LSL) of an RC component is not exceeded in any previous loading histories (prior earthquakes) and low-cycle fatigue is not triggered, aside from a

reduction in initial stiffness, the residual (reserve) capacity (in terms of strength and deformation capacity) of the earthquake-damaged component is not likely compromised, irrespective of the expected failure mode (i.e., flexure- or shear-controlled).

2. Damage progression data from experimental tests suggest that the initiation of LSL corresponds to the initiation of critical diagonal failure plane in flexure-shear and shear-controlled components, and the onset of bar buckling in flexure-controlled components.

H.6.2 Triggers

H.6.2.1 Inspection Trigger

1. During post-earthquake assessment of a building, demands on the components obtained from analysis of an analytical model of the building are compared with inspection triggers to identify locations that may potentially have sustained damage. To ensure there is a low likelihood of missing damaged components, inspection triggers are conservatively defined.
2. A general methodology is proposed for defining the deformation limit for inspection triggers (θ_{IT}) of structural components, which is defined such that there is a low probability of exceeding θ_{LSL} . As such, the inspection trigger multiplier x_{IT} is defined such that there is a $p\%$ probability of exceeding θ_{LSL} . Based on engineering judgment, it is recommended that $p \leq 10\%$. For this reliability analysis, all sources of uncertainty in demand and capacity estimates are considered such as uncertainty β_{LSL} in predicting θ_{LSL} and uncertainties in demand estimates by considering ground motion (β_{gm}) and modeling (β_{model}) uncertainties.
3. Brittle components such as shear-controlled and splice-critical columns should be treated as force-controlled. For force-controlled components, the inspection trigger multiplier x_{IT} is defined such that there is a $p\%$ probability of exceeding V_{max} . A $p \leq 10\%$ is also recommended for force-controlled components.
4. The proposed inspection triggers are given in Table H-17

H.6.2.2 Repair Trigger

1. The purpose of the repair trigger is to identify structural damage that needs repair. Repair trigger of a component is defined as a deformation limit beyond which the lateral strength of the component is compromised (i.e., the residual lateral strength of the component is less than the lateral strength of the undamaged component) and that structural repair may be required to restore the structural characteristics of the component.

2. Additionally, the repair trigger is used to finetune the analytical model of the building to accurately predict demands and damage, i.e., to reconcile model results and observed damage. Therefore, the repair trigger should not be conservatively defined, as was the case for the inspection trigger because the need for repair has to be confirmed by visual inspection using the guidance in Appendix I.
3. The proposed repair trigger is the median estimate of θ_{LSL} , which corresponds to the deformation at the initiation of the critical diagonal failure plane in flexure-shear-controlled components and the initiation of longitudinal bar buckling in flexure-controlled components.
4. The proposed repair triggers are given in Table H-17.

Table H-17 Recommended Component Deformation Limits for Inspection and Repair Triggers

Component	Inspection trigger	Repair trigger
Shear-controlled non-ductile columns	$0.5V_{max}$	$1.0V_{max}$
Splice-critical non-ductile columns	$0.5V_{max}$	$1.0V_{max}$
Flexure-shear-controlled non-ductile columns	0.15a	0.5a
Code conforming flexure-controlled walls	$0.4d$	$0.8d$

H.7 References

- Abdullah, S. A., 2019, *Reinforced concrete structural walls: Test database and modeling parameters (Ph.D. dissertation)*, Dept. of Civil and Environmental Engineering, University of California, Los Angeles, California.
- Abdullah S. A., and J. W. Wallace, 2019, “Drift capacity of RC structural walls with special boundary elements.” *ACI Structural Journal*, Vol. 116, No 1, pp. 183–194. <https://doi.org/10.14359/51710864>.
- Abdullah S. A., and J. W. Wallace, 2020, “Reliability-based design methodology for reinforced concrete structural walls with special boundary elements” *ACI Structural Journal*, Vol. 117, No. 3, pp. 17–29.
- Abdullah, S.; Aswegan, K.; Klemencic, R.; and Wallace, J., 2020, “Experimental Study of Concrete Coupling Beams Subjected to Wind and Seismic Loading Protocols,” Report Number UCLA SEERL 2020/01, Submitted to Magnusson Klemencic Associates

Foundation, University of California, Los Angeles, Los Angeles, California, pp. 268.

Abdullah S. A., and J. W. Wallace, 2021, “Drift Capacity at Axial Failure of RC Structural Walls and Wall Piers.” *ASCE Journal of Structural Engineering*, Vol. 147, No. 6, pp. 04021062.

Abrahamson N., 2021. Personal communication, 2 September.

ACI, 2019, *Building Code Requirements for Structural Concrete*, ACI 318-19, ACI Committee 318, American Concrete Institute, Farmington Hills, Michigan.

ACI, 2017, *Standard requirements for seismic evaluation and retrofit of existing concrete buildings*, ACI 369.1-17, ACI Committee 369, American Concrete Institute, Farmington Hills, Michigan.

Albidah, A., 2016, *Vulnerability and risks of collapse of structural concrete walls in regions of low to moderate seismicity (Ph.D. dissertation)*, Dept. of Infrastructure Engineering, University of Melbourne., Melbourne, Australia.

ASCE. 2017. *Seismic evaluation and retrofit of existing buildings*. ASCE/SEI 41-17. Reston, VA: ASCE.

ASCE, 2016, *Minimum Design Loads and Associated Criteria for Buildings and Other Structures*, ASCE/SEI 7-16, American Society of Civil Engineers, Structural Engineering Institute, Reston, Virginia.

Birely, A. C., 2012, *Seismic performance of slender reinforced concrete structural walls (Ph.D. dissertation)*, Dept. of Civil and Environmental Engineering, Univ. of Washington, Seattle, Washington.

Boys, A., 2009, *Assessment of the Seismic Performance of Inadequately Detailed Reinforced Concrete Columns (Master’s thesis)*, Dept. of Civil and Environmental Engineering, Univ. of Canterbury, Christchurch, New Zealand.

Chiu, C.K., Sung, H.F., and Chiou, T.C., 2020, “Quantification of the reduction factors of seismic capacity for damaged RC column members using the experiment database,” *Earthquake Engineering and Structural Dynamics*; 1–21

Colmenares J. and Santa María, H., 2021, “Effect of Number of Cycles on the Residual Capacity of RC Structural Walls with Unconfined Boundaries,” *Presentation at 2nd Workshop on Residual Capacity*.

- Di Ludovico, M., Polese, M., d’Aragona, M.G., Prota, A., and Manfredi, G., 2013, “A proposal for plastic hinges modification factors for damaged RC columns,” *Engineering Structures*, Vol. 51, pp. 99-112.
- Hines, E. M., Seible, F., and Priestley, M. J. N., 2002, “Seismic Performance of Hollow Rectangular Reinforced Concrete Piers with Highly Confined Corner Elements—Phase I: Flexural Tests, and Phase II: Shear Tests,” *Structural Systems Research Project 99/15*, University of California, San Diego, California, 266 pp.
- Kawashima K, Koyama T., 1988, “Effect of number of loading cycles on dynamic characteristics of reinforced concrete bridge pier columns,” *Structural Engineering / Earthquake Engineering*, Vol. 5, No. 1, pp. 205-21
- Lynn, A.C., Moehle, J.P., Mahin, S.A. and Holmes, W.T., 1996, “Seismic evaluation of existing reinforced concrete building columns,” *Earthquake Spectra*, Vol. 12, No. 4, pp. 715-739.
- Maeda, M., Koike, T., Hosoya, N., Suzuki, Y., Tsurugai, K., and Nimura, A., 2017, “Damage and residual seismic performance evaluation of reinforced concrete shear walls,” *Proceedings of 16th World Conference on Earthquake (16WCEE 2017)*, January 9-13, Santiago Chile.
- Malhotra, P.K., 2002, “Cyclic-Demand Spectrum,” *Earthquake Engineering & Structural Dynamics*, Vol. 31, No. 7, pp.1441–1457.
- Marder, K., 2018, *Post-Earthquake Residual Capacity of Reinforced Concrete Plastic Hinges (PhD Thesis)*, University of Auckland, Auckland, New Zealand, 302pp.
- Melchers, R.E., 1999, *Structural Reliability Analysis and Prediction*, Second Edition, John Wiley and Sons Ltd., West Sussex, England.
- Moscoso, J., Hube, M., and Santa María, H., 2021, “Residual Seismic Capacity of Reinforced Concrete Walls with Unconfined Boundaries,” *ACI Structural Journal*, Vol. 118, No. 5.
- Mun, J. H., Yang, K. H., and Lee, Y., 2016, “Seismic tests on heavyweight concrete shear walls with wire ropes as lateral reinforcement,” *ACI Structural Journal*, Vol. 113, No. 4, pp. 665–675.
- Nakamura, T., and Yoshimura, M., 2012 “Simulation of Old Reinforced Concrete Column Collapse by Pseudo-Dynamic Test Method,” *Proceedings of 15th World Conference on Earthquake Engineering*, 24-28 September 2012, Lisbon, Portugal.

- Niroomandi, A., Pampanin, S., Dhakal, R.P., Soleymani Ashtiani, M., and De La Torre, C., 2018, "Rectangular RC Walls Under Bi-Directional Loading: Recent Experimental and Numerical Findings," *Proceedings of New Zealand Concrete Industry Conference*, October 11-13, Hamilton, New Zealand.
- Oesterle, R. G., A. E. Fiorato, L. S. Johal, J. E. Carpenter, H. G. Russell, and W. G. Corley, 1976, *Earthquake resistant structural walls—Tests of isolated walls*, Report to National Science Foundation (GI-43880). Skokie, IL: Construction Technology Laboratories, Portland Cement Association.
- Opabola, E. and Elwood, K.J., 2018, "Comparative study on acceptance criteria for non-ductile reinforced concrete columns," *Bulletin of the New Zealand Society for Earthquake Engineering*, Vol. 51, No. 4, pp.183-196.
- Opabola, E. A., 2021, *Seismic Vulnerability Assessment of Existing Reinforced Concrete Frame Structures: A Failure Mode-Based Approach (PhD Thesis)*, University of Auckland, Auckland, New Zealand, 440pp.
- Opabola, E.A. and Elwood, K.J., 2021, "Seismic assessment of reinforced concrete columns with short lap splices," *Earthquake Spectra*.
- Tran, T. A., and J. W. Wallace, 2015, "Cyclic testing of moderate-aspect-ratio reinforced concrete structural walls." *ACI Structural Journal*. Vol. 112, No. 6, pp. 653–666. <https://doi.org/10.14359/51687907>.
- Wight, J.K., 1973, *Shear strength decay in reinforced concrete columns subjected to large deflection reversals*. University of Illinois at Urbana-Champaign, Urbana-Champaign, Illinois.

Visual Damage Limits

I.1 Introduction and Objectives

Visual inspection of earthquake-damaged components is an important step in the post-earthquake assessment of buildings. Decisions on the structural conditions and the need for structural repair of earthquake-damaged components can be made based on the information collected from the visual inspection process. Certain post-earthquake assessment guidelines (e.g., JBDPA 2014; FEMA 306) adopt residual crack width as a metric to evaluate the residual capacity of concrete structures. At the time this appendix was developed, however, there was no sufficient residual crack width data from experimental tests to develop and validate an approach based on residual crack width for assessment of residual capacity and repairability of earthquake-damaged buildings. Additionally, crack widths in concrete components following an earthquake can be influenced by a number of factors (e.g., displacement history, loading rate, and so on) and might not be a reliable indicator of the demands experienced by the concrete components. Finally, while use of residual crack width might provide some useful information for shear-controlled components, it might not be as useful for flexure-controlled components as soon as the cover spalls. Therefore, in this appendix, a different approach has been explored as a visual inspection technique for concrete structures. The approach involves developing damage progression databases for various concrete components (beam, column, and wall). In addition to visual damage data, the databases include specimen data such as reinforcement detailing, geometry, material properties, and axial and lateral loadings to enable engineers identify test specimens representative of the earthquake-damaged components they are assessing. By comparing the damage pattern/level of the earthquake-damaged component and the damage progression data from the selected representative test specimens, engineers can efficiently identify the damage state of the component and assess the need for structural repair.

I.2 Description of Key Damage States

I.2.1 *Non-ductile Frame Elements*

Typical cyclic tests are based on drift increments of 0.5% to 1.0%, and in certain cases, test photos at peak drifts are the only published photos. Hence,

it may be difficult to use test photos to determine the exact onset of any damage state with a sufficient level of certainty. For example, a column subjected to a standard cyclic loading protocol with a drift increment of 1.0% may experience an onset of bar buckling at 1.2% during a push to 2.0%. Suppose photos are only available at peak drifts (as done by most experiments), a drift of 2.0% may be the ‘observed’ drift at the onset of bar buckling (a deviation of 0.8% from the actual value). To overcome this uncertainty, it was decided to define the damage states in terms of performance for beam-column components.

Majority of collated tests do not discuss if the published photos were taken at peak or residual displacement (i.e. zero force). Future work could look at clarifying this information with the authors of the cyclic test programs. Also, a possible direction to pursue in a future study is the possibility of having two data bins – one for tests with photos at peak displacements and the other with photos at residual displacement.

In this study, four damage states were defined for brittle beam-column components that do not experience flexural yielding (e.g., shear-controlled and splice-critical columns) and five damage states for beam-column components that experience flexural yielding (e.g., flexure-shear and flexure-controlled columns).

For brittle beam-column components, the four damage states are (Figure I-1):

- a) **DS1** – Damage state corresponding to (or close to) the attainment of $0.7V_{max}$ on the force-displacement backbone. DS1 represents a damage state in the elastic phase of the component response.
- b) **DS2** – Damage state corresponding to (or close to) the drift at the initiation of lateral strength loss (LSL). The study presented in Appendix H concluded that the deformation at LSL is significant for assessing the residual capacity of concrete components.
- c) **DS3** – Damage state corresponding to (or close to) the drift at the onset of lateral failure. This damage state is defined at a drift corresponding to 20% drop in peak lateral resistance.
- d) **DS4** – Damage state corresponding to (or close to) a drift at which loss of initial axial capacity is reported or the lateral resistance has degraded to zero.

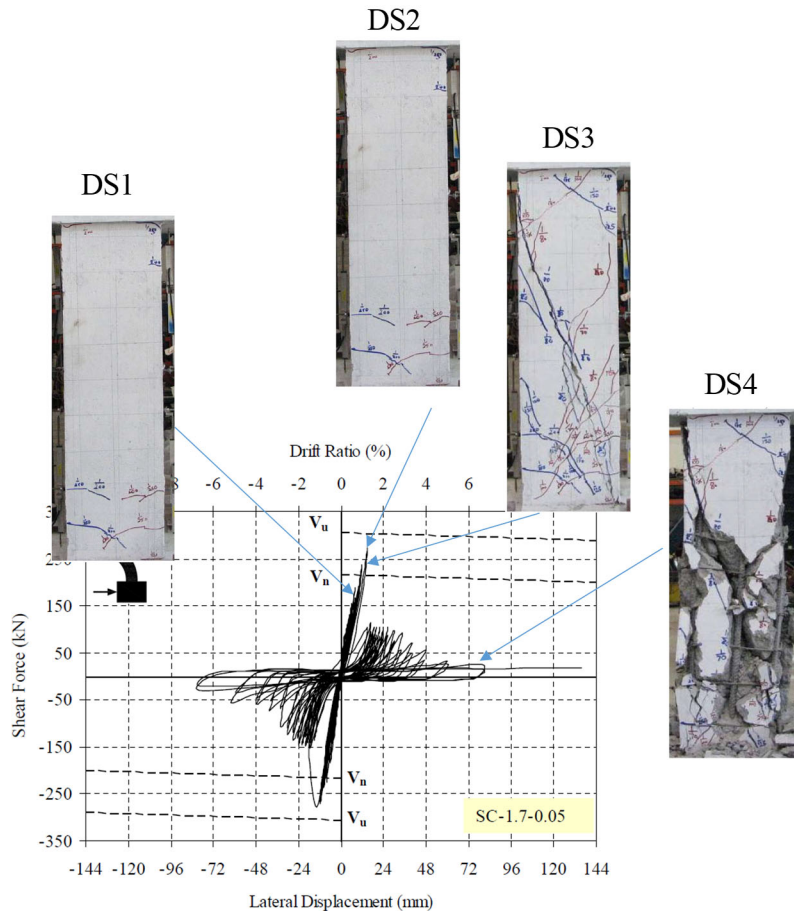


Figure I-1 Definition of the five considered damage states on the force-displacement response of a column (Tran, 2010)

It is noteworthy that the term ‘close to’ (in the damage state definition) recognizes that if the drift corresponding to a defined damage state is not equal to one of the peak drifts, there is a high likelihood that there may not be corresponding photos (because authors report photos at peak drifts); hence, the adopted approach was to use available photos at the peak drift closest to the defined damage state.

Five damage states (DS) were defined as Figure I-2:

- a) **DS1** – Damage state corresponding to (or close to) the first yield of the component. The drift at first yield is defined to correspond to the attainment of $0.7V_{max}$ on the force-displacement backbone. DS1 represents a damage state in the elastic phase of the component response.
- b) **DS2** – Damage state corresponding to (or close to) to the effective yield of the component (i.e., measured yield rotation). The effective yield (or yield rotation) is defined by drawing a secant line from the

origin to pass through the backbone curve at 70% of maximum lateral load (V_{max}) and made to intersect the horizontal line corresponding to V_{max} .

- c) **DS3** – Damage state corresponding to (or close to) the drift at initiation of lateral strength loss (LSL).
- d) **DS4** – Damage state corresponding to (or close to) the drift at onset of lateral failure. This is defined as drift corresponding to 20% drop in peak lateral resistance.
- e) **DS5** – Damage state corresponding to (or close to) drift when the experimental study reported loss of initial axial capacity or at which the lateral resistance has degraded to zero.

The current approach (i.e., defining four and five damage states for brittle- and flexure-shear columns respectively) recognizes that brittle columns do not have the effective yield point. For flexure-shear controlled columns, DS2 coincides with the proposed limit for an undamaged component (See Section I.5). If consistency in the number of DSs for brittle- and flexure-shear columns is desired, future studies can address this.

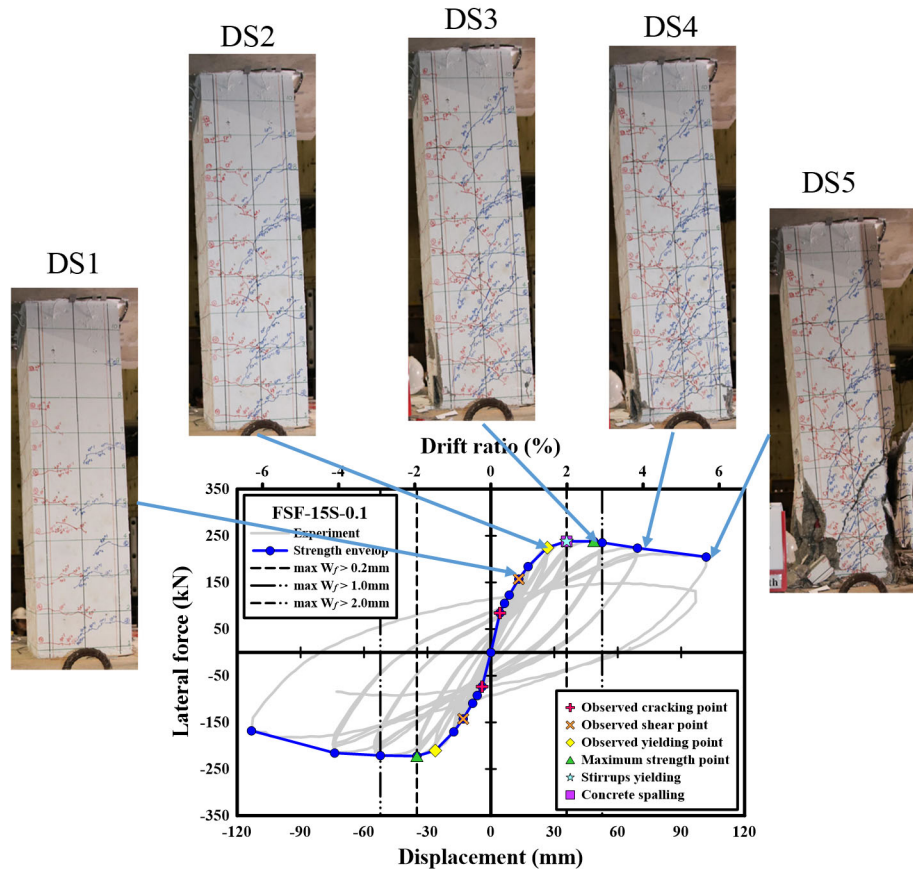


Figure I-2 Definition of the five considered damage states on the force-displacement response of a flexure-shear controlled column (Chiu et al. 2019)

I.2.2 Conforming Flexure-Controlled Walls

For code-conforming flexure-controlled walls subjected to gradual increase of cyclic demands, the damage states (DS) can typically be classified as follows. These DSs, along with the inspection and repair trigger defined in Appendix H, are shown on a typical backbone in Figure I-3. As an example, photos of the damage condition at, or close to, these DSs are shown in Table I- 1.

- a) **DS1** – Formation of horizontal cracks initiating from the extreme edges of the wall with or without diagonal (tension) shear cracks in the web, followed by sequential yielding of longitudinal bars till the effective yield strength of the wall is reached. Walls with rotation/displacement demands not exceeding effective yield strength (i.e., DS1) can be classified as *undamaged components*, where the prior loading does not have any noticeable effect on the cracked behavior of the component.

- b) **DS2** – Spalling of concrete cover at the extreme fibers (boundary elements) of the wall. This damage state coincides with the Inspection Trigger defined in Appendix H.
- c) **DS3** – Initiation of lateral strength loss (LSL) which is typically due to buckling of extreme longitudinal bars in the boundary elements. As discussed in Appendix H, this damage state is used as Repair Trigger.
- d) **DS4** – 20% lateral strength loss from peak strength, which is typically defined as lateral failure, due to fracture of buckled longitudinal bars at the extreme layer combined with concrete core crushing, opening or fracture of hoops and crossties, or local instability. In walls with significant shear stress demands (exceeding $\sim 6\sqrt{f'_c}$ (in psi)), 20% loss of lateral strength is likely due to crushing of the web region adjacent to the boundary elements.
- e) **DS5** – Loss of axial load-carrying capacity or total loss of lateral strength as a result of sequential fracture of longitudinal bars and concrete crushing for walls with low compression demands and squat cross-sections (i.e., $l_w c/b^2 < 20$ or 15), or crushing of concrete or out-of-plane instability across the entire wall length for walls with significant compression demands and slender cross-sections ($l_w c/b^2 < 60$ or 70), leading to abrupt loss of axial load-carrying capacity. Abdullah and Wallace (2021) concluded that conforming flexure-controlled walls with $P/A_g f'_c$ and $l_w c/b^2$ less than about 0.20 and 60, respectively, exhibit moderate-to-significant deformation capacity beyond 20% lateral strength loss prior to the onset of axial failure, whereas walls with $P/A_g f'_c > 0.20$, regardless of the value of $l_w c/b^2$, exhibit lateral strength loss and axial failure essentially simultaneously. In walls with high values of $l_w c/b^2$ (i.e., > 60), brittle compression and/or out-of-plane failure occurs with generally no post lateral-strength-loss deformation capacity.

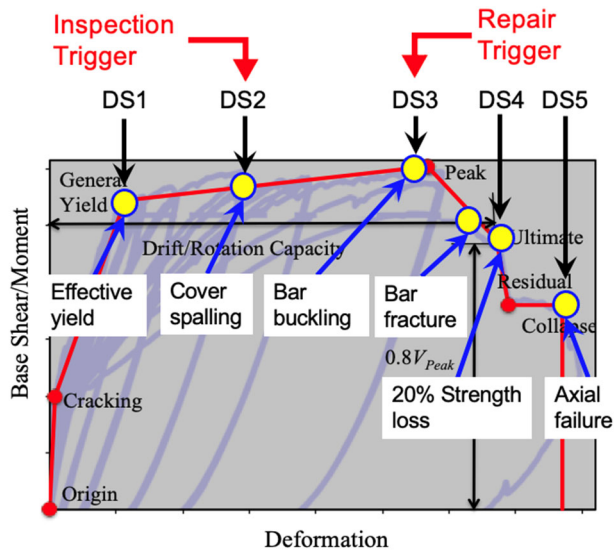
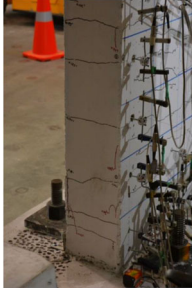
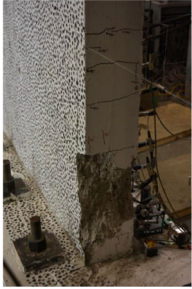


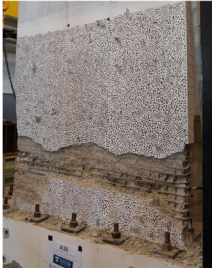


Figure I-3 Backbone relationship showing damages states for a code-conforming wall.

Table I-1 Damage States of Code-conforming Flexure-controlled Walls (Shegay, 2019)

Damage State	Description	Example of Damage Condition
DS1	At general (effective) yielding	
DS2	At concrete cover spalling	
DS3	At longitudinal bar buckling	
DS4	At 20% lateral strength loss (due to bar fracture, or out-of-plane instability, etc.)	
DS5	At axial failure (loss of axial load-carrying capacity)	

I.3 Datasets of Component with Damage Photos

I.3.1 Frame Elements

A database of 16 shear-controlled and 15 flexure-shear controlled columns was collated. The main criteria for selecting these column specimens is the availability of damage progression images. In the collated database, a column specimen is classified as shear-controlled if it fails through a diagonal failure plane, the test authors do not report flexural yielding, and the measured peak strength is lower than the calculated flexural strength. Otherwise, the column is classified as flexure-shear controlled.

The key information reported in the database for each column specimen are the column dimension, axial load ratio ($P/A_g f'_c$), aspect ratio (a/d), stirrup spacing to effective depth ratio (s/d), transverse reinforcement ratio (ρ_t), longitudinal reinforcement ratio (ρ_L), concrete compressive strength (f'_c), expected flexural strength (V_p), expected undegraded shear capacity (V_o) defined according to the ASCE/SEI 41-17, shear capacity ratio (V_p/V_o), damage progression images and hysteresis plot. The database does not provide information on residual crack width. Most test programs do not report residual crack widths; hence, this residual crack width is scarce. The database is provided in an accompanying spreadsheet file.

Key parameters worth considering when identifying representative test specimens from the database include transverse reinforcement ratio (ρ_t), shear capacity ratio (V_p/V_o), axial load ratio ($P/A_g f'_c$) and aspect ratio (a/d).

I.3.2 Conforming Flexure-Controlled Walls

I.3.2.1 Description of Database

A dataset of 62 code-conforming flexure-controlled wall tests was described, in detail, in Appendix H, which is obtained from comprehensive database of RC structural wall tests reported in the literature (Abdullah 2019; Abdullah and Wallace 2019). The database includes three major clusters of data: (1) information about the test specimen, test setup, and axial and lateral loading protocols; (2) computed data, e.g., moment-curvature relationships (depth of neutral axis, c , nominal moment capacity, M_n , moment corresponding to first yield of longitudinal reinforcement, M_y , curvature at M_n , ϕ_n , curvature at M_y , ϕ_y) and wall shear strength according to ACI 318-19; and (3) test results, e.g., backbone relations and failure modes.

Out of the 62 walls in the dataset, photos at the damage states described in Section I.2.2 for 32 wall tests were collected and reported in the dataset (Figure I-4). If available, two photos for each damage state are included,

showing both boundary elements or an overall view of the wall with a close-up view. Under each photo, a brief description is provided to primarily indicate the drift demand at that damage state. In addition to damage photos, the photos of the force-displacement plots are included. It should be noted that the reported deformation in these plots are typically either top total displacement or top total drift ratio, whereas the earthquake demands on a wall estimated from an analytical model are typically in terms of total flexural rotations over an assumed plastic hinge length, similar to the proposed inspection and repair triggers in Appendix H. The wall database is provided in an accompanying spreadsheet file.

Test #	Series		Force-Deformation Response	Damage States				
	Author(s)	Specimen Name		DS1 (Up to yielding)	DS2 (Up to Cover Spalling)	DS3 (Up to Bar Buckling)	DS4 (Up to bar fracture or 20% strength loss)	DS5 (Up to axial failure)
9	Wang et al. 2001	19						
10	Wang et al. 2001	20						
11	Wang et al. 2001	21						

Figure I-4 Partial view of database showing the damage states and photos.

I.3.2.2 Guidance on Identifying Representative Tests

Figure I-5 indicates that there is a significant correlation between rotation capacity and a slenderness parameter, $(l_w/b)(c/b) = l_w c/b^2$, where l_w is the length of the wall, c is the depth of neutral axial corresponding to a concrete compressive strain of 0.003, and b is the width of the flexural compression zone. This parameter provides an efficient means to account for the slenderness of the cross section (l_w/b) and the slenderness of the flexural compression zone of the cross section (c/b) on the deformation capacity of conforming flexure-controlled walls (Abdullah and Wallace, 2019; 2020). Walls with values of $l_w c/b^2$ lower than 10 tend to be flexure-tension controlled and generally have large deformation capacities, whereas walls with values of $l_w c/b^2$ exceeding 70 (slender cross-section and large compression zone) tend to be flexure-compression controlled and generally have low deformation capacities and simultaneous occurrence of lateral and axial failures (Abdullah and Wallace, 2021). Therefore, it is recommended that the engineer estimates the $l_w c/b^2$ of the wall(s) they are evaluating and uses this value or a range close to this value (e.g., calculated $l_w c/b^2 \pm 5$) to identify representative tests from the database. If further refinement is desired, it is recommended that longitudinal bar slenderness ratio, s/d_b , be used. This is because, as was discussed in Appendix H, the initiation of

lateral strength loss typically coincides with initiation of longitudinal bar buckling, which is moderately impacted by s/d_b (Figure I-6).

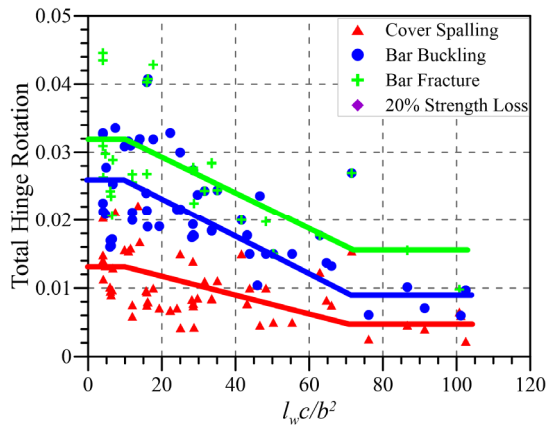


Figure I-5 Comparison of rotation capacity of the dataset at key damage states.

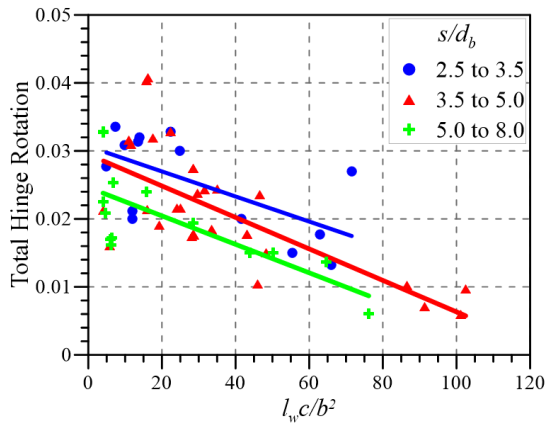


Figure I-6 Influence of s/d_b on total hinge rotation of conforming flexure-controlled walls.

The variables in $l_w c / b^2$ are primarily geometries of the wall (i.e., l_w and b) and are readily available, except for c . For the purpose of preliminary analysis, the empirical equation of Eq. I-1 can be used to compute the approximate depth of neutral axis c :

$$\frac{c}{l_w} = k_1 + k_2 \frac{P}{A_g f'_c} \quad (\text{I-1})$$

where values of k_1 and k_2 are obtained from Table I- 2 based on the cross section shape of the wall.

Eq. I-1 is derived based on data from 696 walls with $P/(A_g f'_c) > 0$ (Abdullah and Wallace, 2020). The first term considers the impact of longitudinal reinforcement (ratio and strength) and concrete strength, whereas the second

term addresses the impact of axial load. Figure I-7 compares the depth of neutral axis computed from Eq. I-1 with that computed from detailed sectional analysis. The statistics of the Eq. I-1 are shown in Table I- 2.

Table I-2 Neutral axis depth parameters in Eq. I-1

Wall cross-section shape	k_1	k_2	Mean	COV
Rectangular	0.10*	1.2	1.04	0.17
Barbell and Flanged	0.03	1.4	1.05	0.27
T-, L-shaped, and half-barbell: flange in compression	0.03	0.7	1.00	0.30
T-, L-shaped, and half-barbell: web in compression	0.20	2.0	1.01	0.24

* This value is for walls with longitudinal reinforcement concentrated in the boundary elements. For wall with uniformly distributed reinforcement, $k_1 = 0.05$ and 0.20 when longitudinal reinforcement ratio < 0.005 and ≥ 0.015 , respectively. For intermediate values, linear interpolation is applied.

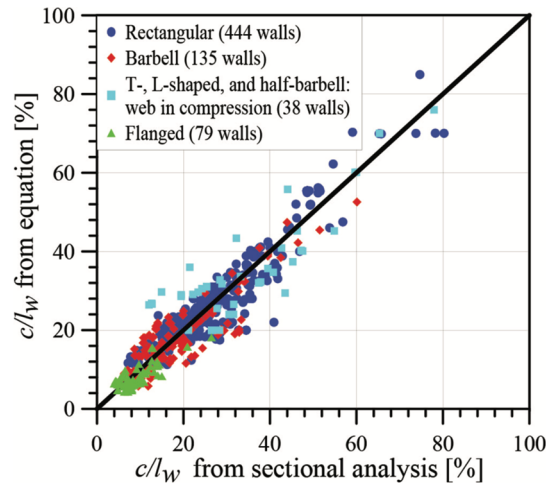


Figure I-7 Comparison of c computed from Eq. I-1 with that from detailed sectional analysis.

I.4 Undamaged Components

An undamaged component can be defined as a component that essentially retains its pre-earthquake structural characteristics (effective stiffness, strength, and deformation capacity). The component effective stiffness is defined as the secant stiffness to yield (i.e. not the uncracked stiffness). Prior research (e.g., De Ludovico et al., 2013; Marder, 2018; Abdullah et al., 2020) have shown that residual stiffness of earthquake-damaged concrete components (walls, beams, and columns) can be assessed based on the maximum ductility demand previously experienced, and that component

effective stiffness degradation is inversely proportional to the maximum ductility demand. In other words, for a component to retain its original effective stiffness, the ductility demand must not be greater than unity (i.e., deformation demand \leq effective yield deformation capacity). A force-controlled component (e.g., shear-controlled or splice-critical column) is classified as undamaged if 70% of the computed component lateral strength (using expected properties) is not exceeded.

I.5 Future Work

The current visual damage databases provide limited data for shear-controlled columns, flexure-shear controlled columns, and code-conforming flexure-controlled walls. Future efforts should focus on:

1. Expanding and updating the databases described here such that they cover element with a broad range of variables and characteristics and provide alternative approaches to present the damage photos and data. For walls, multiple photos might be needed to capture the damage over the full wall length; therefore, adding more than two photos for each damage state should be considered.
2. Developing similar databases for other types of concrete elements such as splice-critical columns, code-conforming beam and columns, non-code-conforming flexure-controlled walls, shear-controlled walls, flexure-shear controlled walls, and shear-friction-controlled walls.
3. Developing a user-friendly platform/tool to publish the databases such that engineers and researchers can easily access and use the data and information, especially following an earthquake.

I.6 Conclusions

This appendix presents an approach to conduct visual damage inspection of earthquake-damaged concrete components to assess the level of damage and the need to perform structural repair. Unlike existing approaches, which depend on residual crack width, the proposed approach depends on comparing the damage pattern and level of earthquake-damaged components with damage states of representative component tests identified from visual damage databases. As a preliminary work, two small databases are developed – one for shear- and flexure-shear-controlled columns (31 tests) and the other for conforming flexure-controlled walls (32 tests). The damage states are classified into five categories: DS1 through DS4 or DS5 representing damage observed at first or effective yield through damage at axial failure, respectively.

An undamaged component is one that essentially retains its pre-earthquake structural characteristics (effective stiffness, strength, and deformation capacity). For a flexural-yielding component to retain its original effective stiffness, the ductility demand must not be greater than unity (i.e., deformation demand \leq effective yield deformation capacity). A force-controlled component (e.g., shear-controlled or splice-critical column) is classified as undamaged if 70% of the computed component lateral strength is not exceeded.

References

- Abdullah, S. A., 2019, *Reinforced concrete structural walls: Test database and modeling parameters.* "Ph.D. dissertation, Dept. of Civil and Environmental Engineering, University of California, Los Angeles, California.
- Abdullah S. A., and J. W. Wallace, 2019, "Drift capacity of RC structural walls with special boundary elements," *ACI Structural Journal*, Vol. 116, No. 1: pp. 183–194. <https://doi.org/10.14359/51710864>.
- Abdullah S. A., and J. W. Wallace, 2020, "Reliability-based design methodology for reinforced concrete structural walls with special boundary elements." *ACI Structural Journal*, Vol. 117, No. 3, pp. 17–29.
- Abdullah S. A., and J. W. Wallace, 2021, "Drift Capacity at Axial Failure of RC Structural Walls and Wall Piers." *ASCE Journal of Structural Engineering*, Vol. 147, No. 6.
- ACI, 2019, Building Code Requirements for Structural Concrete, ACI 318-19, ACI Committee 318, American Concrete Institute, Farmington Hills, Michigan.
- ASCE, 2017, Seismic Evaluation and Retrofit of Existing Buildings, ASCE/SEI 41-17, American Society of Civil Engineers, Structural Engineering Institute, Reston, Virginia.
- Chiu, C.K., Sung, H.F., Chi, K.N., Hsiao, F.P., 2019, "Experimental quantification on the residual seismic capacity of damaged RC column members," *International Journal of Concrete Structures and Materials*, Vol, 13, No. 1, pp. 1-22
- Di Ludovico, M., Polese, M., d'Aragona, M.G., Prota, A., and Manfredi, G., 2013, "A proposal for plastic hinges modification factors for damaged RC columns," *Engineering Structures*, Vol. 51, pp. 99-112.

- FEMA, 1998, Evaluation of Earthquake Damaged Concrete and Masonry Wall Buildings, FEMA 306, prepared by the Applied Technology Council for the Federal Emergency Management Agency, Washington, D.C.
- JBDPA, 2014, *Guideline for post-earthquake damage evaluation and rehabilitation* (in Japanese), Japan Building Disaster Prevention Association.
- Marder, K., 2018, *Post-Earthquake Residual Capacity of Reinforced Concrete Plastic” Hinges (PhD Thesis)*, University of Auckland, Auckland, New Zealand, 302pp.
- Shegay, A., 2019, *Seismic Performance of Reinforced Concrete Walls Designed for Ductility, PhD dissertation*, The University of Auckland, New Zealand.
- Tran, C.T.N., 2010, *Experimental and analytical studies on the seismic behavior of reinforced concrete columns with light transverse reinforcement (PhD dissertation)*, Nanyang Technological University, Singapore.

- ATC-38, Database on the Performance of Structures Near Strong-Motion Recordings: 1994 Northridge, California, Earthquake, 2000
<https://atcouncil.org/pdfs/ATC38toc.pdf> (TOC only)
- ATC-52-4, Here Today—Here Tomorrow: The Road to Earthquake Resilience in San Francisco Post-Earthquake Repair and Retrofit Requirements, 2010
https://sfgov.org/esip/sites/default/files/FileCenter/Documents/9761-atc524_compressed.pdf
- FEMA 306, Evaluation of Earthquake Damaged Concrete and Masonry Wall Buildings: Basic Procedures Manual, 1999
<https://www.fema.gov/media-library-data/20130726-1506-20490-1995/fema-306.pdf>
- FEMA 307, Evaluation of Earthquake Damaged Concrete and Masonry Wall Buildings: Technical Resources, 1999 https://www.fema.gov/media-library-data/20130726-1507-20490-6988/fema_307.pdf
- FEMA 308, Repair of Earthquake Damaged Concrete and Masonry Wall Buildings, 1999 <https://www.fema.gov/media-library-data/20130726-1453-20490-4004/fema-308.pdf>
- FEMA 352, Recommended Postearthquake Evaluation and Repair Criteria for Welded Steel Moment-Frame Buildings, 2000
<https://www.fema.gov/media-library-data/20130726-1444-20490-4440/fema-352.pdf>
- FEMA 461, Interim Testing Protocols for Determining the Seismic Performance Characteristics of Structural and Nonstructural Components, 2007 <https://www.atcouncil.org/pdfs/FEMA461.pdf>
- FEMA P-58, Seismic Performance Assessments of Buildings, 2018
<https://femap58.atcouncil.org/reports>
- FEMA P-154, Rapid Visual Screening of Buildings for Potential Seismic Hazards: A Handbook, 2015
<https://www.fema.gov/sites/default/files/2020->

[07/fema_earthquakes_rapid-visual-screening-of-buildings-for-potential-seismic-hazards-a-handbook-third-edition-fema-p-154.pdf](#)

FEMA P-1024, Performance of Buildings and Nonstructural Components in the 2014 South Napa Earthquake, 2015

<https://www.atcouncil.org/docman/fema/2-fema-p-1024-south-napa-earthquake-mitigation-report/file>

FEMA P-2018, Seismic Evaluation of Older Concrete Buildings for Collapse Potential, 2018 [https://www.fema.gov/media-library-](https://www.fema.gov/media-library-data/1557501511786-)

[data/1557501511786-a329579140a17ed6aa865b6591924f7a/FEMA2018_508.pdf](https://www.fema.gov/media-library-data/1557501511786-a329579140a17ed6aa865b6591924f7a/FEMA2018_508.pdf)

FEMA Hazus Earthquake Model Technical Manual, 2020

https://www.fema.gov/sites/default/files/2020-10/fema_hazus_earthquake_technical_manual_4-2.pdf

PEER Tall Buildings Initiative Guidelines for Performance-Based Seismic Design of Tall Buildings, 2017

https://peer.berkeley.edu/sites/default/files/final_tbi_report_10.9.2017_0.pdf

Appendix K

Inspection Reference Material

This appendix provides reference materials for the inspection part of the Inspection and Analysis phase of the Assessment Framework.

(not applicable to ATC-145 scope)

Candidate for Further Study	FEMA P-58 (PACT): <input type="checkbox"/>	FEMA E-74 (Nonstructural): <input type="checkbox"/>
	FEMA P-154 (RVS): <input type="checkbox"/>	Retrofitted URM: <input type="checkbox"/>

ATC-38 POSTEARTHQUAKE BUILDING PERFORMANCE ASSESSMENT FORM

Incorporating modifications by FEMA P-1024 (ATC 66-5) & ATC-145 Specific Notes (red text)

Note: DO NOT LEAVE ANY BLANK SPACES!

Indicate Unknown (UNK), Not Applicable (NA), or None if necessary.

Building Site Information [1]

Inspector(s):	Date:	Bldg. ID#:	Page <u>1</u> of <u>6</u>
Address:		Building Name:	
Type of Survey: <input type="checkbox"/> Exterior Only <input type="checkbox"/> Exterior and Interior		Recording Station ID:	
Existing Posting Placard: <input type="checkbox"/> Red <input type="checkbox"/> Yellow <input type="checkbox"/> Green <input type="checkbox"/> None		Photo ID#s:	
Building Owner/Manager Contact – Name:		Phone:	
Civil/Structural Engineer for Repair – Name:		Phone:	
General Damage Classification (Structural): <input type="checkbox"/> None (N) <input type="checkbox"/> Insignificant (I) <input type="checkbox"/> Minor (m) <input type="checkbox"/> Moderate (M) <input type="checkbox"/> Heavy (H) <input type="checkbox"/> Collapse (C)			
General Damage Classification (Nonstructural): <input type="checkbox"/> None (N) <input type="checkbox"/> Insignificant (I) <input type="checkbox"/> Minor (m) <input type="checkbox"/> Moderate (M) <input type="checkbox"/> Heavy (H) <input type="checkbox"/> Collapse (C)			

[Note: For “M” or “H” classification, fill out Detailed Damage Description Section on page 5]

Building Construction Data [2]

Construction Date:	Design Date:	Sloped Site: <input type="checkbox"/> Yes <input type="checkbox"/> No
Number of Stories Above Ground:		Number of Basement Levels:
Number of Living Units:	Foundation Type:	Soil Type:
Plan Width (ft):	Plan Length (ft):	Approximate Building Area (sq.ft.):
Occupancy Type (see Glossary):	Occupied Prior to Earthquake: <input type="checkbox"/> Yes <input type="checkbox"/> No <input type="checkbox"/> UNK	
Notes:		

Model Building Type [3]

Predominant Model Building Type (see Glossary):	Seismic Retrofit: <input type="checkbox"/> Yes <input type="checkbox"/> No <input type="checkbox"/> UNK
Describe Building if More Than One Model Building Type Present:	
Describe Retrofit if Present:	
Additions? If yes, describe building type, date of construction:	

Figure A-1 Postearthquake Building Performance Assessment Form (page 1 of 6).

Performance Modifiers [4] (refer to FEMA P-154 for pounding and irregularity criteria)		Bldg. ID#:	Page <u>2</u> of <u>6</u>
Discontinuous Columns: <input type="checkbox"/> Yes <input type="checkbox"/> No <input type="checkbox"/> UNK <input type="checkbox"/> NA		Facade Setbacks: <input type="checkbox"/> Yes <input type="checkbox"/> No <input type="checkbox"/> UNK <input type="checkbox"/> NA	
Pounding Potential: <input type="checkbox"/> Yes <input type="checkbox"/> No <input type="checkbox"/> UNK <input type="checkbox"/> NA		Seismic Expansion Joints: <input type="checkbox"/> Yes <input type="checkbox"/> No <input type="checkbox"/> UNK <input type="checkbox"/> NA	
Open Front Plan: <input type="checkbox"/> Yes <input type="checkbox"/> No <input type="checkbox"/> UNK <input type="checkbox"/> NA		Other Torsional Imbalance: <input type="checkbox"/> Yes <input type="checkbox"/> No <input type="checkbox"/> UNK <input type="checkbox"/> NA	
Plan Irregularities: <input type="checkbox"/> Yes <input type="checkbox"/> No <input type="checkbox"/> UNK <input type="checkbox"/> NA		Deterioration of Structure: <input type="checkbox"/> Yes <input type="checkbox"/> No <input type="checkbox"/> UNK <input type="checkbox"/> NA	
Previous Earthquake Damage: <input type="checkbox"/> Yes <input type="checkbox"/> No <input type="checkbox"/> UNK <input type="checkbox"/> NA			
Describe Other Vertical Irregularities:			
Describe Other Plan Irregularities:			
Describe Other Pre-Earthquake Building Conditions:			

Sketch of Building [5]

Plan sketch provided on separate paper: <input type="checkbox"/> Yes <input type="checkbox"/> No
Elevation sketch provided on separate paper: <input type="checkbox"/> Yes <input type="checkbox"/> No

Nonstructural Elements [6]

Exterior Cladding/Glazing Code (see Glossary):
Partitions Code (see Glossary):
Ceilings Code (see Glossary):
Fire Protection: <input type="checkbox"/> Yes <input type="checkbox"/> No <input type="checkbox"/> UNK <input type="checkbox"/> NA
Elevators: <input type="checkbox"/> Yes <input type="checkbox"/> No <input type="checkbox"/> UNK <input type="checkbox"/> NA
Chimneys: <input type="checkbox"/> Yes <input type="checkbox"/> No <input type="checkbox"/> UNK <input type="checkbox"/> NA
Parapets: <input type="checkbox"/> Yes <input type="checkbox"/> No <input type="checkbox"/> UNK <input type="checkbox"/> NA
Major Appendages: <input type="checkbox"/> Yes <input type="checkbox"/> No <input type="checkbox"/> UNK <input type="checkbox"/> NA
Standard Plumbing, Electrical, Lighting, HVAC: <input type="checkbox"/> Yes <input type="checkbox"/> No <input type="checkbox"/> UNK <input type="checkbox"/> NA
Describe Major Fixed Equipment:
Describe Unusual Contents:

Figure A-1 Postearthquake Building Performance Assessment Form (page 2 of 6).

General Damage [7]

Bldg. ID#:

Page 3 of 6

General Damage Classification (repeated from Section [1] on page 1): <input type="checkbox"/> None (N) <input type="checkbox"/> Insignificant (I) <input type="checkbox"/> Minor (m) <input type="checkbox"/> Moderate (M) <input type="checkbox"/> Heavy (H) <input type="checkbox"/> Collapse (C)	
[Note: See Glossary for ATC-13 Damage State Definitions]	
ATC-13 Damage State, Structural:	ATC-13 Damage State, Nonstructural:
ATC-13 Damage State, Equipment:	ATC-13 Damage State, Contents:
Percent of Floor Area Collapsed: _____% <input type="checkbox"/> UNK <input type="checkbox"/> NA	
Building off Foundation: <input type="checkbox"/> Yes <input type="checkbox"/> No <input type="checkbox"/> UNK <input type="checkbox"/> NA	Story out of Plumb: <input type="checkbox"/> Yes <input type="checkbox"/> No <input type="checkbox"/> UNK <input type="checkbox"/> NA
Damage to Structural Members: <input type="checkbox"/> Yes <input type="checkbox"/> No <input type="checkbox"/> UNK <input type="checkbox"/> NA	Hazmat: <input type="checkbox"/> Yes <input type="checkbox"/> No <input type="checkbox"/> UNK <input type="checkbox"/> NA
Parapet Damage: <input type="checkbox"/> Yes <input type="checkbox"/> No <input type="checkbox"/> UNK <input type="checkbox"/> NA	Chimney Damage: <input type="checkbox"/> Yes <input type="checkbox"/> No <input type="checkbox"/> UNK <input type="checkbox"/> NA
Exterior Non-building Damage: <input type="checkbox"/> Yes <input type="checkbox"/> No <input type="checkbox"/> UNK <input type="checkbox"/> NA	Pounding Damage: <input type="checkbox"/> Yes <input type="checkbox"/> No <input type="checkbox"/> UNK <input type="checkbox"/> NA
Comments about General Damage:	

Nonstructural Damage [8] (only complete to extent that this is useful to estimate peak demands on structure)

Cladding Separation or Damage: _____% of wall area <input type="checkbox"/> UNK <input type="checkbox"/> NA
Partitions Damage: <input type="checkbox"/> None (N) <input type="checkbox"/> Insignificant (I) <input type="checkbox"/> Minor (m) <input type="checkbox"/> Moderate (M) <input type="checkbox"/> Heavy (H) <input type="checkbox"/> UNK <input type="checkbox"/> NA
Windows Damage: _____% of windows <input type="checkbox"/> UNK <input type="checkbox"/> NA
Lights and Ceilings Damage: <input type="checkbox"/> None (N) <input type="checkbox"/> Insignificant (I) <input type="checkbox"/> Minor (m) <input type="checkbox"/> Moderate (M) <input type="checkbox"/> Heavy (H) <input type="checkbox"/> UNK <input type="checkbox"/> NA
Buildings Contents Damage: <input type="checkbox"/> None (N) <input type="checkbox"/> Insignificant (I) <input type="checkbox"/> Minor (m) <input type="checkbox"/> Moderate (M) <input type="checkbox"/> Heavy (H) <input type="checkbox"/> UNK <input type="checkbox"/> NA
Comments about Nonstructural Damage:

(not applicable to ATC-145 scope)

Injuries or Fatalities [9]

No. of Minor Injuries: _____ <input type="checkbox"/> UNK	No. of Major Injuries: _____ <input type="checkbox"/> UNK	No. of Fatalities: _____ <input type="checkbox"/> UNK
Comments about Injuries or Fatalities:		

Figure A-1 Postearthquake Building Performance Assessment Form (page 3 of 6).

(not applicable to ATC-145 scope)

Functionality [10]		Bldg. ID#:	Page <u>4</u> of <u>6</u>
Percent Usable Space Immediately: ___% <input type="checkbox"/> UNK	Percent Usable Space in 1-3 Days: ___% <input type="checkbox"/> UNK		
Percent Usable Space within 1 Week: ___% <input type="checkbox"/> UNK	Percent Usable Space within 1 Mo.: ___% <input type="checkbox"/> UNK		
Percent Usable Space in 1-6 Months: ___% <input type="checkbox"/> UNK	Time Until Full Occupancy: ___ <input type="checkbox"/> UNK <input type="checkbox"/> NA		
Comments about Functionality:			

Geotechnical Failures [11]

Lateral Ground Movement: <input type="checkbox"/> Yes <input type="checkbox"/> No <input type="checkbox"/> UNK <input type="checkbox"/> NA	Buckled Sidewalks: <input type="checkbox"/> Yes <input type="checkbox"/> No <input type="checkbox"/> UNK <input type="checkbox"/> NA
Ground Settlement: <input type="checkbox"/> Yes <input type="checkbox"/> No <input type="checkbox"/> UNK <input type="checkbox"/> NA	Liquefaction Indicators: <input type="checkbox"/> Yes <input type="checkbox"/> No <input type="checkbox"/> UNK <input type="checkbox"/> NA
Separation Between Building and Ground: <input type="checkbox"/> Yes <input type="checkbox"/> No <input type="checkbox"/> UNK <input type="checkbox"/> NA	
Landslide: <input type="checkbox"/> Yes <input type="checkbox"/> No <input type="checkbox"/> UNK <input type="checkbox"/> NA	
Comments about Geotechnical Features:	

Additional Comments

Additional Comments Pertaining to Any Section of Survey Form (use additional pages if necessary):

Figure A-1 Postearthquake Building Performance Assessment Form (page 4 of 6).

DETAILED DAMAGE DESCRIPTION

Bldg. ID#:

Page 5 of 6

Vertical Elements

Racking of Main Walls: <input type="checkbox"/> None (N) <input type="checkbox"/> Insignificant (I) <input type="checkbox"/> Moderate (M) <input type="checkbox"/> Heavy (H) <input type="checkbox"/> UNK <input type="checkbox"/> NA
Racking of Cripple Walls: <input type="checkbox"/> None (N) <input type="checkbox"/> Insignificant (I) <input type="checkbox"/> Moderate (M) <input type="checkbox"/> Heavy (H) <input type="checkbox"/> UNK <input type="checkbox"/> NA
Buckling, Crippling, Tearing of Steel Beams, Columns, or Braces: <input type="checkbox"/> None (N) <input type="checkbox"/> Insignificant (I) <input type="checkbox"/> Moderate (M) <input type="checkbox"/> Heavy (H) <input type="checkbox"/> UNK <input type="checkbox"/> NA
Spalling or Cracking of Concrete Columns or Beams: <input type="checkbox"/> None (N) <input type="checkbox"/> Insignificant (I) <input type="checkbox"/> Moderate (M) <input type="checkbox"/> Heavy (H) <input type="checkbox"/> UNK <input type="checkbox"/> NA
Column Crushing Due to Overturning or Discontinuous Lateral Resisting Elements: <input type="checkbox"/> None (N) <input type="checkbox"/> Insignificant (I) <input type="checkbox"/> Moderate (M) <input type="checkbox"/> Heavy (H) <input type="checkbox"/> UNK <input type="checkbox"/> NA
Shear Cracking in Columns: <input type="checkbox"/> None (N) <input type="checkbox"/> Insignificant (I) <input type="checkbox"/> Moderate (M) <input type="checkbox"/> Heavy (H) <input type="checkbox"/> UNK <input type="checkbox"/> NA
Cracked Shear Walls: <input type="checkbox"/> None (N) <input type="checkbox"/> Insignificant (I) <input type="checkbox"/> Moderate (M) <input type="checkbox"/> Heavy (H) <input type="checkbox"/> UNK <input type="checkbox"/> NA
Percentage of Shear Walls with Cracks: _____% <input type="checkbox"/> UNK <input type="checkbox"/> NA
Rocking of Shear Walls: <input type="checkbox"/> None (N) <input type="checkbox"/> Insignificant (I) <input type="checkbox"/> Moderate (M) <input type="checkbox"/> Heavy (H) <input type="checkbox"/> UNK <input type="checkbox"/> NA
Damage to Shear Wall Boundary Elements: <input type="checkbox"/> None (N) <input type="checkbox"/> Insignificant (I) <input type="checkbox"/> Moderate (M) <input type="checkbox"/> Heavy (H) <input type="checkbox"/> UNK <input type="checkbox"/> NA
Damage to Shear Wall Coupling Beams: <input type="checkbox"/> None (N) <input type="checkbox"/> Insignificant (I) <input type="checkbox"/> Moderate (M) <input type="checkbox"/> Heavy (H) <input type="checkbox"/> UNK <input type="checkbox"/> NA
/ % of Tiltup Wall Panels Leaning or Fallen Out: _____ / _____% <input type="checkbox"/> UNK <input type="checkbox"/> NA
Infill Walls Damaged or Fallen Out: <input type="checkbox"/> None (N) <input type="checkbox"/> Insignificant (I) <input type="checkbox"/> Moderate (M) <input type="checkbox"/> Heavy (H) <input type="checkbox"/> UNK <input type="checkbox"/> NA

Horizontal Elements

Roof Collapse: _____ % of Diaphragm <input type="checkbox"/> UNK <input type="checkbox"/> NA	Floor Collapse: _____ % of Diaphragm <input type="checkbox"/> UNK <input type="checkbox"/> NA
Loss of Vertical Roof Support: _____ % of Roof Area Affected <input type="checkbox"/> UNK <input type="checkbox"/> NA	
Tearing of Diaphragms at Other Points of High Stress: _____ % of Diaphragm <input type="checkbox"/> UNK <input type="checkbox"/> NA	
Damage at Re-entrant Corners: <input type="checkbox"/> None (N) <input type="checkbox"/> Insignificant (I) <input type="checkbox"/> Moderate (M) <input type="checkbox"/> Heavy (H) <input type="checkbox"/> UNK <input type="checkbox"/> NA	
Damage to Collectors at Walls: <input type="checkbox"/> None (N) <input type="checkbox"/> Insignificant (I) <input type="checkbox"/> Moderate (M) <input type="checkbox"/> Heavy (H) <input type="checkbox"/> UNK <input type="checkbox"/> NA	
Cross Grain Bending Damage at Roof-to-Wall Connections: _____ % of Connection Length <input type="checkbox"/> UNK <input type="checkbox"/> NA	

Figure A-1 Postearthquake Building Performance Assessment Form (page 5 of 6).

DETAILED DAMAGE DESCRIPTION (Continued)

Bldg. ID#:	Page <u>6</u> of <u>6</u>
------------	---------------------------

Connections

Girder-Column Connection Damage Including Panel Zones: <input type="checkbox"/> None (N) <input type="checkbox"/> Insignificant (I) <input type="checkbox"/> Moderate (M) <input type="checkbox"/> Heavy (H) <input type="checkbox"/> UNK <input type="checkbox"/> NA
Column Splice Damage: <input type="checkbox"/> None (N) <input type="checkbox"/> Insignificant (I) <input type="checkbox"/> Moderate (M) <input type="checkbox"/> Heavy (H) <input type="checkbox"/> UNK <input type="checkbox"/> NA
Damage to Brace Connections: <input type="checkbox"/> None (N) <input type="checkbox"/> Insignificant (I) <input type="checkbox"/> Moderate (M) <input type="checkbox"/> Heavy (H) <input type="checkbox"/> UNK <input type="checkbox"/> NA
Damage to Column-to-Foundation Connections: <input type="checkbox"/> None (N) <input type="checkbox"/> Insignificant (I) <input type="checkbox"/> Moderate (M) <input type="checkbox"/> Heavy (H) <input type="checkbox"/> UNK <input type="checkbox"/> NA
Damage to Connections of Precast Elements that are Part of the Lateral Force Resisting System: <input type="checkbox"/> None (N) <input type="checkbox"/> Insignificant (I) <input type="checkbox"/> Moderate (M) <input type="checkbox"/> Heavy (H) <input type="checkbox"/> UNK <input type="checkbox"/> NA

Foundations

Foundations Cracked or Otherwise Damaged: <input type="checkbox"/> None (N) <input type="checkbox"/> Insignificant (I) <input type="checkbox"/> Moderate (M) <input type="checkbox"/> Heavy (H) <input type="checkbox"/> UNK <input type="checkbox"/> NA
Slabs-on-Grade Cracked or Otherwise Damaged: <input type="checkbox"/> None (N) <input type="checkbox"/> Insignificant (I) <input type="checkbox"/> Moderate (M) <input type="checkbox"/> Heavy (H) <input type="checkbox"/> UNK <input type="checkbox"/> NA

Equipment and Systems (only complete to extent that this is useful to estimate peak demands on structure)

Electrical Equipment Damage Including Backup Generators: <input type="checkbox"/> None (N) <input type="checkbox"/> Insignificant (I) <input type="checkbox"/> Moderate (M) <input type="checkbox"/> Heavy (H) <input type="checkbox"/> UNK <input type="checkbox"/> NA
Damage to Boilers, Chillers, Tanks, etc.: <input type="checkbox"/> None (N) <input type="checkbox"/> Insignificant (I) <input type="checkbox"/> Moderate (M) <input type="checkbox"/> Heavy (H) <input type="checkbox"/> UNK <input type="checkbox"/> NA
HVAC Damage (Fans, Ducts) : <input type="checkbox"/> None (N) <input type="checkbox"/> Insignificant (I) <input type="checkbox"/> Moderate (M) <input type="checkbox"/> Heavy (H) <input type="checkbox"/> UNK <input type="checkbox"/> NA
Damage to Water and Sprinkler Lines and Fire Pumps: <input type="checkbox"/> None (N) <input type="checkbox"/> Insignificant (I) <input type="checkbox"/> Moderate (M) <input type="checkbox"/> Heavy (H) <input type="checkbox"/> UNK <input type="checkbox"/> NA
Elevator Equipment Damage (Car and Counterweight Rails, Cars, Penthouse Equipment): <input type="checkbox"/> None (N) <input type="checkbox"/> Insignificant (I) <input type="checkbox"/> Moderate (M) <input type="checkbox"/> Heavy (H) <input type="checkbox"/> UNK <input type="checkbox"/> NA

Additional Comments (use additional pages if necessary):
--

Figure A-1 Postearthquake Building Performance Assessment Form (page 6 of 6).

ATC-38 POSTEARTHQUAKE BUILDING PERFORMANCE ASSESSMENT FORM

SURVEYOR INSTRUCTIONS

This form should be filled out as completely as possible by the surveyor(s). Do not leave blank spaces; use "UNK" for "Unknown", "NA" for "Not Applicable", or "None" when appropriate. Talk with the owner to obtain as much information as possible. Assure him/her that detailed name and address information will not be released to the public. Photos should be taken of each exterior building elevation, and of any locations where significant damage is visible. For each strong motion site, obtain or sketch a map of the block or blocks surveyed to identify the locations of each building relative to the strong motion instrument. Distances from the buildings to the instrument should be determined wherever possible.

The ATC-38 Postearthquake Building Assessment Form includes 11 sections as listed below. Refer to the *Glossary of Terms and Codes* for classifications and codes that should be used on the form. The form is intended to be self-explanatory; however, some clarifying comments are included here for each of the 11 sections. In all cases, write down as much information as possible, and state any assumptions you need to make about the building and/or its performance. Too much or repeated information is always better than incomplete information.

1. **Building Site Information.** For Building ID#, use the following notation: station owner, last 3 digits of station number, initials of surveyor, and sequential number. (For example: CDMG386-ER-01.) Be sure to include the Building ID number on each page and indicate the number of pages. For Photo ID#, make sure to note the number(s) on the film roll that were taken of the given building. When the film is developed, write the same numbers on the back of each photo so they will be matched to the proper building.
2. **Building Construction Data.** If possible, indicate design date and construction date by year, not decade.
3. **Model Building Type.** If the building has different model building types in different directions or on different floors, describe in the space provided.
4. **Performance Modifiers.** In this section, describe any other vertical or plan irregularities that are not listed on the form, including unusual pre-earthquake building conditions.
5. **Plan Sketch of Building.** Provide a sketch of the building footprint. Annotate the sketch as appropriate. Note on the sketch the assumed east-west and north-south directions if they are used in other sections of the form, and include a north arrow. Surveyors should carry a compass.
6. **Nonstructural Elements.** Refer to the *Glossary* for codes to be used for cladding and partition types.
7. **General Damage.** This section should be descriptive as well as quantitative. Indicate the General Damage Classification that corresponds to the worst damage to any specific element. (This should be the same General Damage Classification as that checked in Section 1.) Estimate the ATC-13 damage state as defined in the *Glossary* for each building area as shown (for residences, consider chimneys and veneer to be nonstructural and water heaters to be equipment). In the space provided for comments, include possible reasons for damage if appropriate. For buildings with General Damage Classification of "M" or "H", fill out the 2-page *Detailed Damage Description* as described below.

Figure A-2 Surveyor instructions (page 1 of 4).

8. **Nonstructural Damage.** Indicate damage to partitions, lights, ceilings, and contents in terms of General Damage Classification as defined in the *Glossary*.
9. **Injuries or Fatalities.** Include comments where appropriate, such as unusual reasons for casualties.
10. **Functionality.** Indicate percentage of space that can be used for the building's original pre-earthquake function for the various time periods listed, as well as the amount of time needed to restore the building to its full pre-earthquake functionality. In the comments section, include any reasons for closure and note if the building can only be accessed for clean-up.
11. **Geotechnical Failures.** In this section, describe any other geotechnical failures or unusual features that are not listed on the form.

After the 11 main sections of the form, space is provided for additional comments pertaining to any section of the form. Attach additional sheets if necessary, making sure to label each sheet with the Building ID number. For buildings with General Damage Classification of "M" or "H", fill out the 2-page *Detailed Damage Description* as briefly described below.

Detailed Damage Description. This part of the form should be filled out as completely as possible for any buildings with General Damage Classification of "M" or "H". It includes sections for Vertical Elements, Horizontal Elements, Connections, Foundations, and Equipment and Systems. In each case the damage should be described in terms of the General Damage Classification defined in the *Glossary*. Make sure to use "NA" or "UNK" as appropriate. Use the notes section to include additional information about the building and the damage, such as differences by direction or floor level in damage or model building type. The notes section may also be used to indicate the location (i.e., ground floor or top story) of extensive damage to equipment and systems. Add extra pages if necessary, making sure to label each one with the Building ID number.

Figure A-2 Surveyor instructions (page 2 of 4).

ATC-38 GLOSSARY OF TERMS AND CODES

General Damage Classification:

Code	Description
N	No damage is visible, either structural or nonstructural.
I	Damage requires no more than cosmetic repair. No structural repairs are necessary. For nonstructural elements this would include spackling partition cracks, picking up spilled contents, putting back fallen ceiling tiles, and repositioning equipment and furnishings.
m	Minor repairable structural or nonstructural damage has occurred. Repairs can be made without significant disruption to occupants. This damage state includes cracked or dislodged masonry requiring repair.
M	Repairable structural damage has occurred. The existing elements can be repaired in place, without substantial demolition or replacement of elements. For nonstructural elements this would include minor replacement of damaged partitions, ceilings, contents, or equipment.
H	Damage is so extensive that repair of elements is either not feasible or requires major demolition or replacement. Includes URM buildings that require partial or complete reconstruction of damaged masonry walls. For nonstructural elements this would include major or complete replacement of damaged partitions, ceilings, contents, or equipment.
C	Partial or complete loss of gravity support with collapse.

Occupancy Type:

Occupancy Type	Code
Apartment	A
Auto Repair	AR
Church	C
Dwelling	D
Data Center	DC
Garage	G

Gas Station	GS
Government	GV
Hospital	H
Hotel	HL
Manufacturing	M
Office	O
Restaurant	R

Retail	RS
School	S
Theater	T
Utility	U
Warehouse	W
Other	OTH
Unknown	UNK

Model Building Type:

Framing System	Reference Codes and Diaphragm Types
Steel Moment Frame	S1 - Stiff Diaphragms; S1A - Flexible Diaphragms
Steel Braced Frame	S2 - Stiff Diaphragms ; S2A - Flexible Diaphragms
Steel Light Frame	S3
Steel Frame w/ Concrete Shear Walls	S4 - Stiff Diaphragms; S4A - Flexible Diaphragms
Steel Frame w/ Infill Masonry Shear Walls	S5 - Stiff Diaphragms; S5A - Flexible Diaphragms
Concrete Moment Frame	C1 - Stiff Diaphragms; C1A - Flexible Diaphragms
Concrete Shear Wall Building	C2 - Stiff Diaphragms; C2A - Flexible Diaphragms
Concrete Frame w/ Infill Masonry Shear Walls	C3 - Stiff Diaphragms ; C3A - Flexible Diaphragms
Reinforced Masonry Bearing Wall	RM1 - Flexible Diaphragms; RM2 - Stiff Diaphragms
Unreinforced Masonry Bearing Wall	URM - Flexible Diaphragm; URMA - Stiff Diaphragm
Precast/Tiltup Concrete Shear Walls	PC1 - Flexible Diaphragms; PC1A - Stiff Diaphragms
Precast Concrete Frame w/ Conc. Shear Walls	PC2
Wood Light Frame	W1
Commercial or Long-Span Wood Frame	W2
Mobile Home/School Portable	MH
Multi-unit, multi-story residential	W1A

Figure A-2 Surveyor instructions (page 3 of 4).

ATC-38 GLOSSARY OF TERMS AND CODES (continued)

Exterior Cladding/Glazing Codes:

Cladding/Glazing Type	Code
Stucco	S
Wood Product	W
Curtain Wall	C
Brick	B
Glass	G
Concrete	O
Metal	M
Exposed Structure	E
Window Wall	I
Pre-cast Panels	P
PC Fascia	F
Stone	N
Marble	R
URM	U
Masonry	Y
Ceramic Tiles	T

Partitions Codes:

Partition Type	Code
Gypsum Board	G
Plaster	P
Wood Lath	W
URM	U
Metal	M
Concrete	C
Brick	B
Marble	R
Masonry	Y

Ceilings Codes:

Ceiling Type	Code
Gypsum Board – nailed directly to framing	G
Gypsum Board - suspended	H
Suspended Tile	S
Lath and plaster – attached directly to framing	L
Lath and plaster - suspended	P
Exposed Slab	E
Metal	M
Wood	W
Glued Tiles	T
Suspended acoustic T-Bar	A

ATC-13 Damage State Definitions:

Damage State	Percent Damage (damaged value ÷ replacement value)
0 Unknown	Unknown
1 None	0%
2 Slight	0% - 1%
3 Light	1% - 10%
4 Moderate	10% - 30%
5 Heavy	30% - 60%
6 Major	60% - 100%
7 Destroyed	100%

Figure A-2 Surveyor instructions (page 4 of 4).